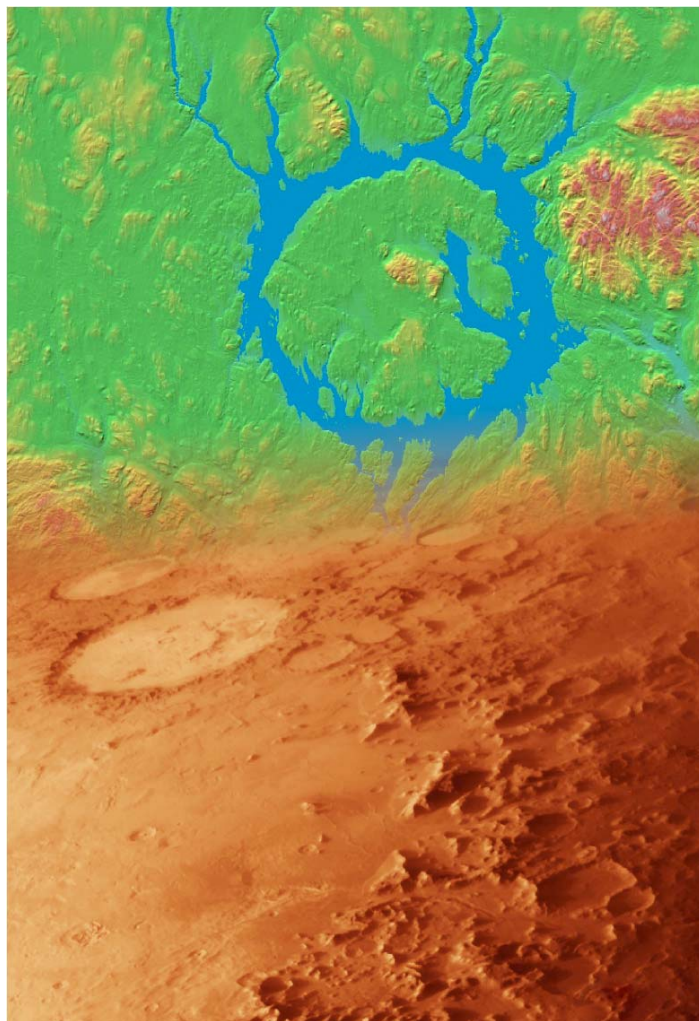


40th ESLAB

First International Conference
on Impact Cratering in the Solar System

08-12 May 2006

Proceedings



European Space Agency
European Space and Technology Centre
ESTEC



Contents

Oral Sessions

S.01 - Asteroids, comets and impact flux	1
Chair: B. Cohen	
Estimates of impact flux from terrestrial crater counts: the role of gravity and target properties	3
M. Dence	
S.02 - Planetary chronology and the Late Heavy Bombardment	9
Chair: N. Barlow	
Progress in Martian Chronological Studies from Crater Counts	11
W.K. Hartmann	
S.04 - Cratering on Mars and Venus	15
Chair: S. Werner	
Martian impact craters and their implications for target characteristics	17
N. Barlow	
Martian alluvial fans: understanding the crater connection	27
E. Kraal	
Venusian impact craters	31
J. Raitala	
S.05 - Terrestrial impact craters and impact petrology	41
Chair: C. Koeberl	
Non-impact origin of the crater field in the Gilf Kebir region (SW Egypt)	43
M. Di Martino	
The Meteor crater, Arizona: A century of exploration and debates	49
V.L. Masaitis	
The geological record of meteorite impacts	55
G. Osinski	
Characterisation of a small crater-like structure in SE Bavaria, Germany	67
W. Rösler	
Geologic setting, properties, and classification of terrestrial impact formations	73
D. Stöffler	

S.07 - Chicxulub: new geophysical studies	79
Chair: G. Osinski	
Chicxulub, anatomy of a large impact structure: From impactite to ejecta distribution P. Claeys	81
S.08 - Physics and chemistry of impact cratering	93
Chair: N. Artemieva	
Shatter cones of the Haughton impact structure, Canada G. Osinski	95
Direct observation of transient crater growth S. Yamamoto	101
S.09 - Computer simulations	107
Chair: M. Gerasimov	
Evaluation of planetary impacts using numerical and experimental techniques E. Baldwin	109
Numerical modeling of impact cratering E. Pierazzo	115
Geological aspects of terrestrial impact cratering rates; simulating the processes and effect of crater removal S. Thackrey	123
S.10 - Laboratory Experiments	129
Chair: E. Pierazzo	
Impact experiments on dry and wet sandstone F. Schaefer	131
S.12 - Catastrophes and extinctions	137
Chair: A. Rossi	
Large bolide impacts - Is it only size that counts? G. Walkden	139
S.14 - Impacts and habitability of Terrestrial Planets	145
Chair: C. Cockell	
The processing of organic matter in impact craters: Implications for the exploration for life J. Parnell	147

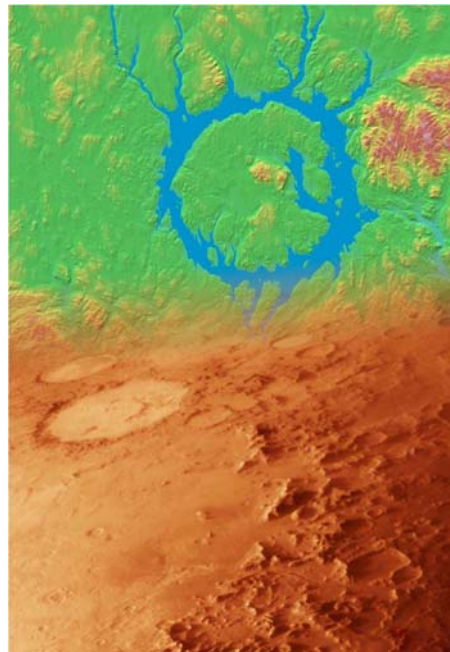
Poster Sessions

Poster Session 1 - Tuesday, 9 May 2006	153
Collisions history in the main-belt by spectroscopic methods M. Birlan	155
21 Lutetia as a possible binary system after photometric, frequency and spectral investigations V. Busarev	161
Preparation Development and preliminary application of novel equations of state for geological materials and ice P. Church	167
Investigation of impact cratering processes into porous targets through hypervelocity experiment and simulations C. Giacomuzzo	175
Laboratory impact cratering on ice-silicate mixture targets K. Hiraoka	181
Shock effects and petrological features of the Ohaba chondrite G.O. Iancu	185
Impact simulation with fracture and porosity M. Jutzi	189
Floor-fractured craters on the terrestrial planets - The Martian perspective J. Korteniemi	193
A time estimate for consolidation and disintegration of an asteroid-rubble pile. The simplest model. A preliminary analysis. G.A. Leikin	199
Modelling crater shapes with Gaussian random spheres T. Tchumatchenko	203
High accuracy matching of planetary images G. Vacanti	209
Sedimentary and Paleoclimatic research on the Promethei Basin in the south polar cap of Mars E. Velasco Dominguez	215
 Poster Session 2 - Thursday, 11 May 2006	 219
The telluric conductivity anomaly at Magyarmecske: Is it a buried impact crater? T. Bodoky	221
Excavation efficiencies in three-dimensional simulations of the Chicxulub meteor impact G. Gisler	225
Glass spherules in upper Eocene Flysch of Croatian Adriatic - Evidence of an impact into carbonate target? T. Marjanac	231
The crater "Yama Korchazhikha" on the website "Catalogue of the Earth's impact structures" A. Mikhееva	237

Session S.01

Asteroids, Comets and Impact Flux

Chair: B. Cohen



ESTIMATES OF IMPACT FLUX FROM TERRESTRIAL CRATER COUNTS: THE ROLE OF GRAVITY AND TARGET PROPERTIES

Michael R. Dence

824 Nesbitt Place, Ottawa ON K2C 0K1 Canada E-mail: mrdenca@rsc.ca

ABSTRACT

Data from terrestrial craters is used to derive estimates of the rate of impact crater formation on Earth and illustrate how gravity and target properties influence crater size. The number of craters with diameter >20 km on the North American and northwest European stable cratons is taken as the flux over the last 500 Ma. This is an average rate of $0.15 \pm 0.1 \times 10^{-14} \text{ km}^{-2} \text{ year}^{-1}$ or one 20km crater per 1.1Ma for the whole Earth. For a given crater formed in crystalline rocks energy released is calculated from the rate of attenuation of shock waves below the impact point and the dynamic tensile fracture strength of the target materials as confined by overburden pressure at the base of the transient cavity. These results support diameter-energy relationships of the form $D = aE^b$ where b is approximately 1/3.5, between energy and gravity scaling.

1. INTRODUCTION

In 1998 French[1] listed three questions that need to be resolved to determine impact flux on Earth: (1) How often is there an impact of a given size? (2) How much energy is released in a given impact? (3) How large a crater is formed? He also pointed out that "individual estimates of the frequency of impact on Earth for objects of the same size vary by factors of 5-10x, especially for larger objects". The recent detailed study by Bland and Artemieva [2] gives a similar five-fold range for craters with diameter >20 km quoting the estimates of Grieve & Shoemaker [3] and of Hughes [4]. While some statistical uncertainty is inevitable, a more precise estimate should be possible by further consideration of Earth's impact crater record in the light of the set of questions raised by French.

Frequency of crater formation depends upon using geological criteria to assess the size and exposure age of the area selected for counting. This gives one measure of crater frequency but questions of energy release and impactor size for a given range of crater diameters must also be addressed. Melosh and Ivanov [5] note that "50 years of study ... have not resulted in a predictive, quantitative model of crater formation". To determine energy released and resulting crater size requires an improved understanding of crater mechanics, the effects

of target material properties and the role of gravity. This paper addresses cases where there is sufficient information from field and laboratory observations and recent experiments on the dynamic tensile strength of rocks to make such calculations.

2. RATE OF CRATER FORMATION

The Earth has a highly variable surface with a sparse population of impact craters concentrated in a few geologically stable regions. Among them, the exposed Canadian Shield, about 1% of the Earth's total area, is the largest with relatively homogeneous properties. C.S.Beals and colleagues first recognized its potential as a collecting surface after the New Quebec and Brent craters were brought to scientific attention in 1950-51. They realized that these craters are of similar size (3-4km) and form, but differ in age by ~ 450 Ma or more, suggesting that other impact scars should be preserved. Inspired by the views of Baldwin [6], they initiated the first systematic search over a large area for terrestrial craters that resembled those on the Moon [7].

By 1972 criteria for recognizing impact craters had advanced to the stage where an estimate of the rate of crater formation on the Canadian Shield was possible [8]. The scope of the estimate was enlarged by Grieve and Dence in 1979 to encompass the stable cratonic areas of North America and northwestern Europe [9], a combined area of $17 \times 10^6 \text{ km}^2$, or about 10% of the land surface of the Earth. By that date all large (>20 km) craters recognized today in those regions had been identified. Their determination of crater production rate showed similar independent rates for the North American and European cratonic regions and a combined rate of $0.35 \pm 0.13 \times 10^{-14} \text{ km}^{-2} \text{ year}^{-1}$ for craters with $D > 20$ km. This estimate was based on an accumulation period of 450 Ma. They note that for craters >22.6 km the distribution slope approximates $N \propto D^{-2}$ with some variation for craters >45 km where the sample size is small. For craters < 22.6 km the distribution slope is much lower, an effect initially attributed to shorter preservation times and difficulty of recognizing small craters. It is now apparent [2] that breakup in the atmosphere of bodies < 1 km in diameter prevents many small craters from being formed.

Three decades of growth in the terrestrial impact database has provided an increase in the number of craters recognized in the North American and Europe but few are within the area originally considered. Those that have been added are too small to affect flux calculations based on the number of craters with $D > 20$ km. Grieve and Dence [9] adopted a -2 size distribution slope and derived an estimate of an average of one impact capable of forming a 20km crater on Earth every 560,000 years. Likewise, for an impact that would be capable of creating a 100km crater on Earth, they project one occurrence on

average every 14 Ma. Bland and Artemieva [2] give very similar estimates for this size range in their Table 2 but adopt different distribution slopes of ~ -1.8 for craters <70 km and ~ -2.6 for larger craters. Their curve lies close to that of Hughes [4] and converges at D near 125km. On the other hand, French [1], in his Table 2.1, based on estimates from Grieve and Shoemaker [3] and Neukum and Ivanov [10], calculates one 20km crater per 350,000 years but only one 100km crater per 26 Ma. His figures imply a mean distribution slope of $N \propto D^{-2.4}$.

However, the most robust portion of the distribution curve for all terrestrial craters is in the interval $D > 20 < 90$ km where the slope approximates -2 [9]. The rate for craters with $D > 20$ km proposed in [9] gives a projection of 28 craters in the combined North American and NW European cratons, for an accumulation period of 450 Ma. On the other hand only 15 craters with diameter >16 km were recognized at the time of the study with the deficiency mainly for $D < 32$ km. With no significant change in the numbers taking place since then a more accurate estimate for the rate for crater formation is obtained if the actual number of known craters with $D > 20$ km is used. Furthermore, as some craters in Scandinavia and possibly Canada are >450 Ma old [11], the accumulation period for these areas may approximate 500Ma. The rate of accumulation then becomes $0.15 \pm 0.1 \times 10^{-14} \text{ km}^{-2} \text{ year}^{-1}$ or one 20km crater per 1.1Ma for the whole Earth. Using a distribution slope of -2 , an impact capable of forming a 100km crater would occur on Earth once per 28 Ma. This is in harmony with current knowledge of three craters with $D > 80$ km formed on land since the end of the Palaeozoic 250 Ma ago.

3. DERIVING ESTIMATES OF ENERGY RELEASE FROM IMPACT CRATER SIZE

To convert from crater size to impactor size requires an estimate of kinetic energy released on impact. Various approaches have been made in the last half-century with differing results. In the case of Barringer Meteor Crater early estimates of energy released by the iron meteorite range over three orders of magnitude, from 3×10^{14} to 5×10^{17} J [12] and in recent papers still vary by a factor of 5-10x [1,2]. Estimates have been derived by scaling from craters formed by nuclear explosion [13], from observations of the volume of fractured [14] or shock-melted rock [15] or by extrapolation from experiments under controlled conditions. More recently calculations have taken into account a number of parameters. Thus Bland and Artemieva [2] convert from crater size to impactor mass by using the scaling relationships of Schmidt and Housen [16] and selecting for impact at 45° , velocity of 18 km.s^{-1} and densities of 3000 kg.m^{-3} for the target, 3400 kg.m^{-3} for stones and 7800 kg.m^{-3} for irons.

3.1 Stages of crater formation

It is now well recognized that crater formation can be discussed as a three-stage process involving initial contact, excavation of a transient cavity and collapse of the cavity to form the final structure [17]. The size of the fully developed transient cavity provides the most accurate expression of the energy released on impact so a prime aim of the observer in analyzing terrestrial craters is to recover the form and size of the transient cavity. This requires deciphering complications that arise from the processes that produce the final crater. In using an array of observations from selected terrestrial craters it is useful to take each parameter into account according to the stage of crater development that it represents. The present discussion specifically relates to targets comprising strong crystalline rocks of low porosity.

In the earliest stage the target is compressed by shock waves generated on contact and the resulting imprint of shock metamorphism is a direct measure of the reaction of the target materials to the energy deposited [18]. Gravity is not an important factor at this stage but becomes so in two ways as shock waves are reflected from the trailing edge of the impactor and from the free surface to unload and modify the elastic and plastic effects of dynamic compression. Gravity is a control on the volume of melted and fragmented material retained within the crater. In addition, where the target retains strength below the zone of total melting the resulting dynamic tensional regime leads to fracturing and fragmentation, allowing the shocked material to flow freely as the cavity is excavated. At this point, as outlined below, gravity acts through the weight of overburden to regulate the limit of fracturing and fragmentation and hence the depth of the cavity.

In the third stage, the rocks of the uplifted crater rim collapse under gravity, enlarging the rim diameter and either partly filling the cavity with breccia to form a simple crater or by enhancing the upwards motion of the center assists in complex crater formation. Craters occurring in crystalline rocks show a morphological and structural progression with size from simple through flat-floored and complex with central peak to peak ring forms, as are recognized in other planets.

3.2 Information needed for the calculation of energy released on impact

The method employed here for calculating released energy uses the dimensions of the imprint of shock metamorphism as a direct expression of the initial shock compression and its subsequent attenuation. It then considers the extent of fragmentation resulting from the reflected shock waves, particularly as seen directly under the point of impact. Most important is the shock level at the limit of down axis fragmentation at the base of the breccia lens. In simple craters where breccias are

preserved this information is obtained by drilling at the center; in complex craters the equivalent fragmentation limit is taken as the maximum shock level at the top of the central peak. Comparative information is needed from laboratory or nuclear explosion experiments along with calculations to derive estimates of the rate of shock pressure decay and expressions of how confining pressure modifies dynamic tensile strength.

In subsequent sections observations from selected impact craters on the Canadian Shield are used as examples of craters formed in crystalline rocks. As discussed in previous papers [19, 20] craters formed in crystalline rocks have the advantage of being formed in relatively homogeneous target materials in which the development and preservation of shock metamorphism in quartz and feldspars is generally well preserved and can be calibrated against laboratory experiments using similar materials. By contrast, data for sedimentary rocks are sparse, more diverse and subject to considerable uncertainty in terms of the effects of variable porosity and contrasts in physical properties across bedding planes.

4. SOURCES OF OBSERVATIONS

4.1 Observations from natural terrestrial craters

An examination of craters formed in the crystalline rocks of the Canadian Shield indicates that the most complete and direct reconstruction of the transient cavity can be made in the case of the Brent crater, the largest known simple crater [19]. Its diameter prior to erosion is estimated as 3.8km. Extensive drilling has provided a detailed cross-section from which the depth to the base of the breccia lens from the original surface is estimated at 1,150m. The Charlevoix crater is taken as the representative complex crater with diameter before erosion estimated at 54km. From the analysis given in [20] the rocks forming its central uplift have risen from below the level of the down axis fragmentation limit. They conform to the general model by moving as large blocks along discrete shear zones rather than as dispersed fragments. At the present level of exposure shock metamorphism at Charlevoix indicates the fragmentation limit in the center was at a shock level of about 25GPa at an original depth of about 11km.

Additional data on shock levels at the limit of fragmentation comes from the craters listed in [20]. They form the basis for the relationship first noted in [19] that the level of shock metamorphism, P (GPa) increases with increasing final crater diameter, D (km) according to the relationship:

$$P = 3.5 D^{0.5} \quad (1)$$

By comparing reconstructions of the transient cavity stage at Brent and Charlevoix the striking difference in the size of the excavation relative to the imprint of shock metamorphism is apparent (Fig.1). In large craters substantially more elastic energy is stored below the fragmentation limit and expands during uplift.

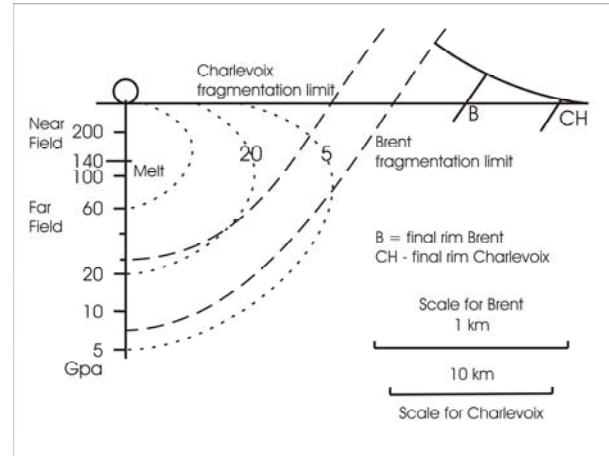


Fig.1 - Comparison of the transient cavities at Brent and Charlevoix normalized to the imprint of shock metamorphism. Note scale difference and that the final rim at Brent (B) is much closer to the transient cavity rim than that of Charlevoix (CH).

In Table 1 the estimated final diameter, transient cavity (TC) diameter and depth from the original surface and shock pressure at the fragmentation limit (FL) is given for the Brent simple crater, Nicholson Lake central peak crater and three peak ring craters.

Table 1 - Craters providing data for energy calculations

Crater	Final diameter (km)	TC diameter (km)	TC depth (km)	Shock pressure at FL (GPa)
Brent	3.8	3.0	1.15	7
Nicholson Lake	14	10	3.5- 4	12.5
Clearwater Lake W	32	18	6.5- 7	20
Charlevoix	54	32	11-13	25
Manicouagan	80	48	17-19	30

The complex craters share the presence of early Paleozoic sedimentary rocks, mainly limestone that formed a relatively thin (<200m) cover over the crystalline rock basement at the time of the respective impacts. These pre-impact sedimentary rocks form the upper part of the transient cavity rim and have first been lifted away from the center and then brought downwards and inwards during late stage collapse. They are thereby preserved in

a structural trough around the center. Their inner limit provides a measure of the radius of the transient cavity after correction for movement towards the center. Knowing the radius allows calculation of a range of values for the depth of the transient cavity according to whether the depth/diameter ratio is about 1/2.5 as at Brent or 1/3 as suggested by the Charlevoix restoration (Fig.1).

Some estimates of the final rim diameter used here differ from those of other authors. Rather than the outermost visible circumferential fracture the rim preferred here is the dominant shear zone activated during late stage collapse. It is generally based on structural, gravity anomaly and other geophysical evidence.

4.2 Experimental data bearing on energy release calculations

Two sets of data are of direct relevance to energy calculations. Hugoniot data and shock experiments that produce distinctive shock effects are required for calibration of shock metamorphism. The data used here are based on the measurements summarized in [1,19] and reinterpreted in [20]. In addition Hugoniot data form the basis for the calculations of Ahrens and O'Keefe [21] to determine shock pressure attenuation in crystalline rocks under various conditions of hypervelocity impact. Their results are used in the next section

In addition, Ai and Ahrens [22] have determined shock pressures the onset of fracturing and at the limit where fracturing results in complete fragmentation in two strong crystalline rocks and in Coconino sandstone. Their results place important constraints on the dimensions of transient cavities in similar materials and provide an explanation for the difference in shock levels at the fragmentation limit noted in fig. 1 and Table 1. However, the shock pressures measured experimentally for the onset of dynamic fracturing and complete fragmentation at room temperature and pressure are 100-500 MPa. These are much lower than the shock pressures of 7-30 GPa inferred from shock metamorphism at the limit of brecciation in terrestrial craters.

Ai and Ahrens note that the fracture and fragmentation limits will be affected by confining pressure. It follows that in natural impact events the confining pressure imposed by gravity and the density of the enclosing rocks governs the extent of dynamic fragmentation and hence the depth of the transient cavity. In Fig.2 the results from experiment are compared apparent dynamic tensile strength from observed shock pressures at selected craters. Confining pressures are calculated as the pressure at the base of transient cavities reconstructed as illustrated in Fig.1 with average basement rock density of 2700 kg.m⁻³.

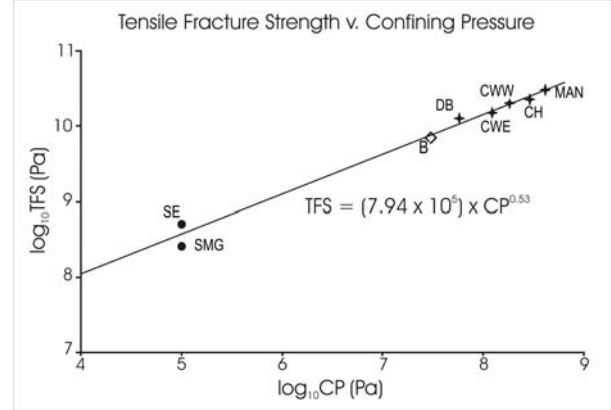


Fig.2 - Dynamic tensile fracture strength v. calculated confining pressure at the fragmentation limit from laboratory data (dots) after [18] and representative Canadian craters: B= Brent, DB = Deep Bay, CWE & CWW = Clearwater East & West, CH = Charlevoix, MAN = Manicouagan

The resulting relationship between confining pressure (CP) and dynamic tensile fragmentation strength (TFS) is remarkably consistent and is given (in Pa) by

$$TFS = 7.94 \times 10^5 CP^{0.53} \quad (2)$$

4.3 Energy calculations from shock metamorphism in simple impact craters

The calculation of energy release on impact can be made from Ahrens and O'Keefe's [21] calculations of shock-wave attenuation from equations of state. They investigate attenuation in low porosity crystalline rocks for impact by spheroidal iron and stony meteorites striking vertically over a range of velocities. In the calculation that most closely simulates a typical asteroidal impact on Earth, a spheroidal stony body of density about 3900 kg.m⁻³ impacting at 15 km.s⁻¹ generates a shock wave with pressure on contact near 300 GPa. Initial decay in the near field is slow as the projectile is embedded but then the calculated rate of attenuation down axis in the far field becomes approximately -2. This result is in good agreement with attenuation rates of shock waves generated in similar rocks by nuclear explosions [19,20]. Since the calculations normalize the centerline distance from the point of impact to the radius of the impactor, R₀(m) the size of the impactor can be calculated from the formula

$$P = 2512 (R/R_0)^{-2} \quad (3)$$

P is the shock pressure in GPa at depth R (m) down axis. Application thus depends on being able to determine the shock pressure at a given depth below an impact point.

This can be most readily done in simple craters if the shock level can be determined at the base of the transient cavity. At Brent the central drill hole penetrates the limit of fragmentation that marks the base of the breccia lens at $R = 1,150\text{m}$ where shock metamorphism indicates a mean shock pressure of 7GPa, with an uncertainty of about 3GPa. Then, from Eq.1 $R_0 = 60.7\text{ m}$, and for the given conditions [21] the mass of the impactor is $3.65 \times 10^9\text{ kg}$ and the energy released on impact is calculated to be $4.1 \times 10^{17}\text{ J}$.

4.4 Energy calculations for complex craters

Reconstructing the transient cavity in complex craters with central peak or peak ring is more difficult as the axial region is strongly distorted by the late stage central uplift process. However, in the cases noted in Table 1 the diameter of the transient cavity can be estimated from the preserved remnants of the thin layer of pre-impact sedimentary rocks that covered the Precambrian basement at the time of impact. In the case of Charlevoix the distribution of shock zones at the present level of erosion gives a basis for reconstructing the transient cavity [20] and demonstrates that as at Brent it has a depth to diameter ratio of about 1:2.5 to 1:2.8. If this ratio is accepted for the other craters that are listed in Table 1 a depth can be calculated in each case. As the shock pressure at the respective fragmentation limit (FL) is also known from the level of shock metamorphism at the center, Eq. 3 can be applied with results given in Table 2.

Table 2 - Impact energy calculations for complex craters

Crater	Final Diameter (km)	Impactor diameter (km)	Energy released (J)
Nicholson L.	14	0.57	4.13×10^{19}
Clearwater Lake West	32	1.28	4.87×10^{20}
Charlevoix	54	2.55	3.83×10^{21}
Manicouagan	80	4.2	1.7×10^{22}

5. GENERALIZATION OF IMPACT ENERGY CALCULATIONS FROM CRATER SIZE

For comparative purposes the diameter to energy relationship is commonly cast in the form $D = a E^b$. Here D is the final diameter, a is a function of target properties, E is the energy released on impact and b varies from 1/3 for energy scaling to 1/4 where gravity dominates. Cooper [23] and others have found that nuclear explosion craters conform to $b = 1/3.4$. Examples of this relationship include that of Shoemaker [24] whose formulation is based on nuclear explosion data and can be expressed as $D = 1.435 \times 10^{-5} E^{1/3.4}$, when D is in km and E in joules. Another example for large craters in crystalline rock also based on nuclear explosion results is

$D = 1.96 \times 10^{-5} E^{1/3.4}$ [12], while French [1] employs simple energy scaling with results that can be expressed as $D = 2.79 \times 10^{-6} E^{1/3}$.

The results in Table 2 along with the result for Brent can be compared to give values for a and b . Taking each pair in turn values for b range from 1/3 to 1/3.9 with an average of 1/3.5; the mean value of a is about 3×10^{-5} . Exponent b is in good agreement with 1/3.4 as obtained from nuclear explosion craters [23] and reinforces indications the importance of gravity in determining the size of the transient cavity and the final diameter of impact craters on Earth. As shown in Table 3, where calculations for $D=20\text{km}$ are compared with those in the papers quoted, the method employed here gives energy estimates close to those of other approaches.

Table 3 - Representative energy calculations for craters with final diameter $D = 20\text{km}$

Author	Ref.	Formula	Calculated Energy (J)
Shoemaker	[24]	$D = 1.435 \times 10^{-5} E^{1/3.4}$	7.8×10^{20}
Dence et al.	[12]	$D = 2.75 \times 10^{-5} E^{1/3.4}$	2.7×10^{20}
French	[1]	$D = 2.79 \times 10^{-6} E^{1/3}$	3.7×10^{20}
This paper		$D = 2.87 \times 10^{-5} E^{1/3.44}$	1.3×10^{20}
Bland & Artemieva	[2]	$D = 2.16 \times 10^{-4} E^{1/3.85}$	1.33×10^{21}

Note that Bland and Artemieva calculate for 45° impacts while all other calculations take the vertical impact case.

6. CONCLUSION

The rate of crater formation adopted here implies that, in the thoroughly explored terrestrial cratons, the terrestrial crater record is essentially complete for craters $>20\text{ km}$ over the last 500Ma. This is similar to the position of Hughes [4] and Bland and Artemieva [2] though they extend the record to craters $>2\text{-}3\text{ km}$ but restrict it to the last 120Ma. A further implication is that the North American and NW European cratons may be slightly over endowed with large ($>32\text{km}$) craters for the area they encompass. Certainly the eastern Canadian Shield is relatively rich in large impacts [8].

It must also be recalled that the database in the two cratons consists largely of craters formed in crystalline rocks. This allows close comparisons with craters on other stony bodies in the Solar system. However, such comparisons must allow for differences in gravity not only in its effect on impact velocity and ejecta

distribution but also on the role of confining pressure in determining the depth of transient cavities. In addition, as approximately half the craters on Earth are formed in sequences of sedimentary rocks >1km thick, other complications must be considered in making interplanetary comparisons. The strength of sedimentary materials is generally lower than that of crystalline rock [22] so tensile fracturing and fragmentation will extend to lower shock levels for a given size of impactor. In addition, stratification and porosity of sedimentary materials may have substantial effects. Attenuation of the initial shock wave is greater in porous media [23] and a larger proportion of the energy is partitioned as heat. Likewise the role of water and may be a significant factor, particularly at the late stage of collapse and central uplift. Although a detailed comparison is beyond the scope of this paper, a general statement can be made to the effect that craters formed in sediments are commonly substantially shallower than craters formed in crystalline rock. Crater by crater evaluation is needed for detailed comparisons between the terrestrial crater database and those for other members of the Solar System.

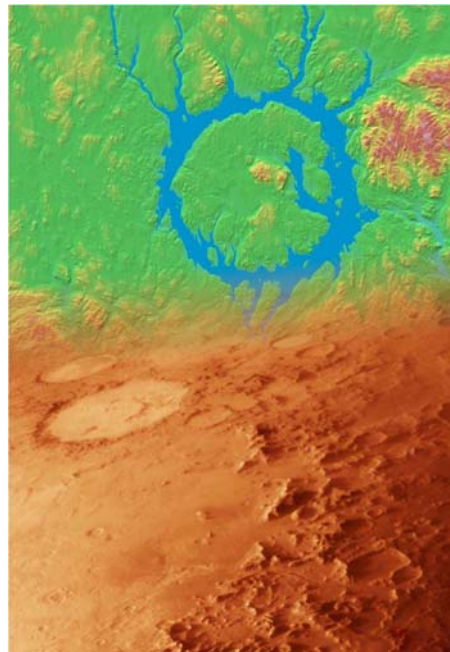
7. REFERENCES

1. French, B.M. 1998. *Traces of catastrophe*. Vol. LPI contribution no. 954. Houston: Lunar and Planetary Institute. 120.
2. Bland, P.A., Artemieva, N.A. 2006. *Meteoritics and Planetary Science*. 41: 607-631.
3. Grieve, R.A.F., Shoemaker, E.M. 1994. In *Hazards Due to Comets and Asteroids*. University of Arizona Press: Tucson.. 417-462.
4. Hughes, D.W. 2000. *Monthly Notices of the Royal Astronomical Society*. 137: 429-437.
5. Melosh, H.J., Ivanov, B.A. 1999. *Annual Review of Earth and Planetary Sciences*. 27: 385-415.
6. Baldwin, R.B. 1949. *The face of the moon*. Chicago: University of Chicago Press. 239.
7. Beals, C.S., Ferguson, G.M., Landau, A. 1956. *Journal of the Royal Astronomical Society of Canada*. 50: 203-211; 250-261.
8. Dence, M.R. 1972. *The nature and significance of terrestrial impact structures*. in *Proceedings, 24th International Geological Congress*. 1972. Montreal.
9. Grieve, R.A.F. and Dence, M.R. 1979. *Icarus*. 38: 230-242.
10. Neukum, G., Ivanov, B.A. 1994. In *Hazards due to comets and asteroids*, T. Gehrels, Editor. University of Arizona: Tucson.. 359-416.
11. Abels, A., et al. 2002. In *Impacts in Precambrian shields*, J. Plado and L.J. Pesonen, Editors. Springer: Berlin.. 1-58.
12. Dence, M.R., Grieve, R.A.F., and Robertson, P.B. 1977. In *Impact and explosion cratering*, D.J. Roddy, R.O. Pepin, R.B. Merrill, Editors. Pergamon Press: New York. 247-275.
13. Shoemaker, E.M. 1960. In *Report of the XX1st International Geological Congress, Norden*: Copenhagen. 418-434.
14. Innes, M.J.S. 1961. *Journal of Geophysical Research*. 66: 2225-2239.
15. Grieve, R.A.F., Dence, M.R., Robertson, P.B. 1977. In *Impact and explosion cratering*, D.J. Roddy, R.O. Pepin, R.B. Merrill, Editors. Pergamon Press: New York.. 791-814.
16. Schmidt, R.M. and Housen, K.R. 1987. *International Journal of Impact Engineering*. 5: 543-560.
17. Melosh, H.J. 1989, *Impact Cratering: A Geological Process*. Oxford University Press: Oxford. 245.
18. Collins, G.S., Melosh, H.J., Ivanov, B.A. 2004. *Meteoritics & Planetary Science*. 39: 217-231.
19. Dence, M.R. 2002. In *Impacts in Precambrian Shields*. J. Plado, L.J. Pesonen, Editors. Springer. Berlin 59-79.
20. Dence, M.R. 2004. *Meteoritics and Planetary Science*. 39: 267-286.
21. Ahrens, T. and O'Keefe, J. 1977. In *Impact and Explosion Cratering*, D.J. Roddy, R.O. Pepin, R.B. Merrill, Editors. Pergamon Press: New York. 639-656.
22. Ai, H.A. and Ahrens, T.J. 2004. *Meteoritics and Planetary Science*. 39: 233-246.
23. Cooper, H.F.J. 1977. In *Impact and Explosion Cratering*, D.J. Roddy, R.O. Pepin, R.B. Merrill, Editors. Pergamon: New York. 11-44.
24. Shoemaker, E.M. 1977. In *Impact and Explosion Cratering*: D.J. Roddy, R.O. Pepin, R.B. Merrill, Editors. Pergamon Press: New York. 617-628.

Session S.02

Planetary Chronology and the Late Heavy Bombardment

Chair: N. Barlow



PROGRESS IN MARTIAN CHRONOLOGICAL STUDIES FROM CRATER COUNTS: ACCUMULATION OF THE SMALLEST CRATERS

William K. Hartmann

1700 E. Fort Lowell Road, Suite 106, Tucson, Arizona 85719-2395 USA

hartmann@psi.edu

ABSTRACT

Nature's process of cratering the worlds of the solar system offers many opportunities for understanding geologic characteristics of planetary surfaces far beyond the cratering process itself. These include assessment of ages, geological processes of modification, and rates of such processes. Recent critiques of this method, and concerns about secondary craters, are overwrought. Remaining issues revolve around use of small craters (diameter $D \lesssim 200$ m). I propose that under any of the suggested models, km-scale surfaces lacking craters of $D \lesssim 50$ m are unlikely to have ages $>$ few 10s My.

1. BACKGROUND: THE CRATERING OPPORTUNITY

On various worlds, nature creates symmetric circular craters with fairly well-known size frequency distributions (SFDs) and crudely known formation rates. Each primary impact (by an interplanetary body) scatters numbers of secondary impactors, which produce "distant secondary craters" (secondaries outside obvious clusters and rays, far removed from their parent primary crater). The total SFD of such craters, prior to any erosional or depositional losses, is called the "production function." An example is shown in Fig. 1, based on counts on the relatively young lava-covered surface of the volcano, Arsia Mons. Studies of the SFDs on different stratigraphic units, and measurements of losses of the smaller craters relative to the "production function" SFD, provide a wealth of information about surface ages and erosional/depositional processes [1]. The total accumulated densities of well-preserved craters – i.e., the total number/km² of primaries plus distant secondaries – give a datum for measuring the crater retention age of the surface. This may give the formation age of the underlying rock unit under ideal conditions, but there is an analogy to radiometric gas retention ages. In ideal conditions, the gas retention age of a rock gives its formation age, but in the presence of disturbances, such as an impact or heating event, the gas retention age may give the date of the disturbance. In the same way, in an erosive or

depositional environment, the crater retention age may measure the retention time, i.e., survival time, of craters and other topographic features of the characteristic scale being considered. In areas of complex history, the combination of the shape of the SFD and morphologies of craters in different diameter ranges gives a valuable tool for estimating the nature and rate of geological processes of obliteration.

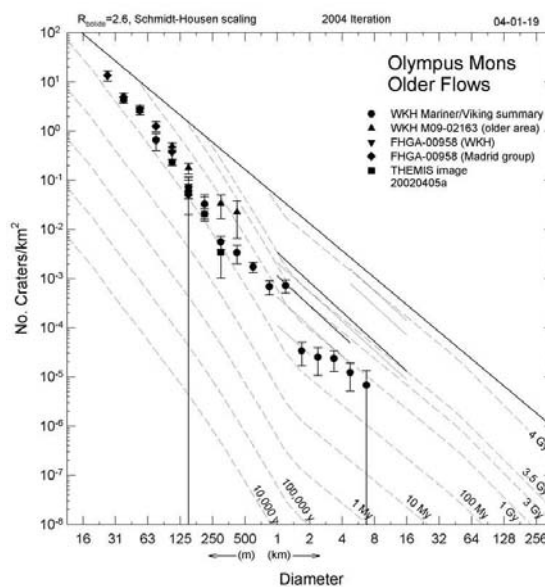


Fig. 1. Data points show size-frequency distribution of total size-frequency distribution (primaries + secondaries) derived from Mars Global Surveyor and other imagery of Olympus Mons. Lava flow surfaces were divided into an older group and a younger group, based on superposition criteria; this plot shows data from the older flows. Images used are listed. Curved lines are isochrons for various ages, and upper solid line is empirically measured saturation equilibrium curve. The counts suggest a good fit to the shape of the isochrons, i.e., "production function" curves, and suggest a characteristic age of a few hundred My for the older surface lavas.

2. BRIEF REVIEW OF RECENT CRITIQUES

Such techniques have recently come under fire, but some of the criticisms are seeing the glass as half empty, instead of recognizing the "glass-half-full" value

of the information supplied by craters. I address some of these issues here.

Malin and Edgett stated that “...it is impossible to date Martian surfaces from impact craters...given the problems of burial and exhumation,” and that a Mars with young volcanism “is not the planet we think we see....” [2] This ignores that the present techniques made a correct pre-Apollo 1965 prediction of “about 3.6” Gy for typical lunar mare ages [3], and also correctly predicted from Mariner 9 data in the 1970s that widespread areas of Martian lavas are only a few hundred My old [4], as evidently confirmed a decade later by basaltic and other igneous meteorites from all but one of 5 to 9 Martian launch sites. The technique can even characterize the date of the exhumation episodes, because typical exhumed surfaces (documented by Malin and Edgett [2]) have a low density of sharp, small craters, and the numbers of those craters give a measurement of the exposure time since exhumation. Furthermore, the SFD contains information on the rate of the exhumation process. If the small sharp craters fit the proposed production function or isochron shape, it means that the exhumation event was short-lived relative to the time since exhumation, because the production function SFD as been preserved ever since. On the other hand, if the SFD is flattened, indicating continuing losses of small craters, it means that the exhumation process has continued over an extended period, such that the surface is still being eroded even as new craters are forming. Moreover, Malin and Edgett proposed no new, revised chronology for Mars. Order-of-magnitude revisions of proposed crater count chronologies would bring them into conflict with the Martian meteorite evidence.

Most other recent critiques have focused on small craters (typically $10\text{m} < D < 250\text{m}$), suggesting that they do not convey useful information on ages or geologic processes [5]. These critiques raise interesting and useful issues, but they all erroneously state that crater chronology systems depend fundamentally on an assumption that all the counted craters are primaries. This is incorrect in my case, since I count not just primaries, but the total mix of primaries plus distant secondaries. It is true that my isochron derivation (converting to Mars from the “calibration SFD” found in lunar maria) involves a velocity ratio more appropriate to primaries than secondaries, but this is a 2nd order correction compared to the errors proposed by the critical authors. An example of the problem is found in the McEwen et al. (2005) paper on Zunil (cf. [5]), which reads numbers off my isochrons and represents them as primary crater numbers, then

concludes that they are off by a factor 2000 – the error being that my isochrons don’t give primary crater numbers, but rather primary + secondary totals. The internal inconsistency in the McEwen et al. (2005) work is shown by the fact that they apply their new understanding to derive a new age for the Athabasca Vallis channel system, but their result (1.5 My to 200 My) is virtually identical to a result for Athabasca Vallis based on my isochron system (few My to <200 My), published three years earlier by Berman and Hartmann [6].

Do my current isochrons really represent the production rate of small craters? Malin et al. have observed a new 25 m crater on Mars, with dramatic ray system of ejecta, which faded in a few years, presumably due to winds and sand mobility. They used their observations of several rapidly-fading ray systems to estimate a production rate for craters of 25m-100m (www.msss.com). As shown in Fig. 1, their rate is within about a factor 3 of my isochrons at that size. Issues may be raised about whether the Malin et al. estimate is correct, but if it is, then the isochrons appear likely to be within an order of magnitude of the correct production rate for small craters of $25\text{m} \leq D \leq 100\text{m}$.

Another critique, by Bierhaus [5], based on his good work on Europa cratering, argues that secondaries are so hopelessly dominated by non-random clustering that age information would be wiped out among small craters. This ignores that crater counters generally avoid obvious clusters and rays, in an attempt to count the relatively randomly distributed craters. Empirical evidence also obviates this criticism. For example, in recent work on some 45 Martian landslides, Quantin et al. [7] showed that in every case the stratigraphically younger landslides have the same or (usually) measurably lower crater density than the older ones or background, which counters the assertion that statistical clustering of secondaries wipes out chronometric information among small craters. It seems clear that crater SFD’s, even at small sizes in small areas, generally do preserve chronographic information.

3. A SIMPLE MODEL OF SMALL CRATER PRODUCTION

In my system, I have made no judgement whether small craters ($D \leq 200\text{m}$) are dominated by primaries or secondaries. The literature is divided on this. However, it is valuable to think through the consequences of either end-member model. If most small craters are primaries, they accumulate randomly but relatively uniformly with time, so that my existing “2004 iteration” isochrons [1] would be correct.

If most such craters are completely dominated by secondaries, they would accumulate not gradually but in showers, each shower caused by an “offstage” primary impact crater some distance away. Head et al. [8] concluded that craters at least 3 km across are needed to eject Martian meteorites from Mars, which means that craters of $D > 3$ km are needed to throw decameter-scale secondary craters over much of Mars. Thus, as a thought experiment, we may consider Zunil-sized (10 km) craters as a test case for understanding the accumulation of secondaries. (Note that larger craters produce more secondaries, but 20 km craters would be $\sim 1/4$ as frequent as “Zunils.”) McEwen et al. (2005, Table 3; cf. [5]), give model results on secondary crater SFDs at different distances from a Zunil-sized crater. McEwen et al. and my isochrons agree that the timescale between formation of Zunil-sized craters is of order 1 My. Therefore, if 20m-scale craters are virtually all secondaries, we would have to wait an average of 1 My for “a Zunil” to cast a sizeable population of 20m secondaries onto randomly chosen fresh surfaces, such as new lava flows. This model can be made more specific. For example, the models of McEwen et al. indicate that Zunil covers only 1/6 of Mars with secondary crater densities comparable to my 1 My isochrons. Thus, as shown in Fig. 1, we would actually have to wait for some 6-10 Zunils (allowing for overlap of secondary fields), or ~ 6 -10 My for secondaries to begin to appear on a newly-formed geologic formation. McEwen et al., invoking a model by co-author Artemieva, use a size distribution for secondaries that appears steeper than I would expect, but after 10 My, a few larger primaries would begin to fill in secondaries at larger sizes. The point is that the McEwen et al. model predicts that on surfaces older than about 10 My years, the accumulated number of craters begins to straddle my isochron for 10 My – indicating a gross consistency between McEwen et al. [5] and my isochrons.

In the same way, the model of McEwen et al. also predicts that after 100 My, the SFD would straddle my isochron for 100 My, and implies that after 100 My, some 100 different primaries would contribute to the population of secondaries at any given spot. This counters concerns about statistics-of-one effects of statistical clustering among spatial distributions of secondaries from single primaries. The same model shows that the small craters begin to reach saturation equilibrium densities (upper solid line on Fig. 2) in about 100 My, so that they become much less useful in dating surfaces.

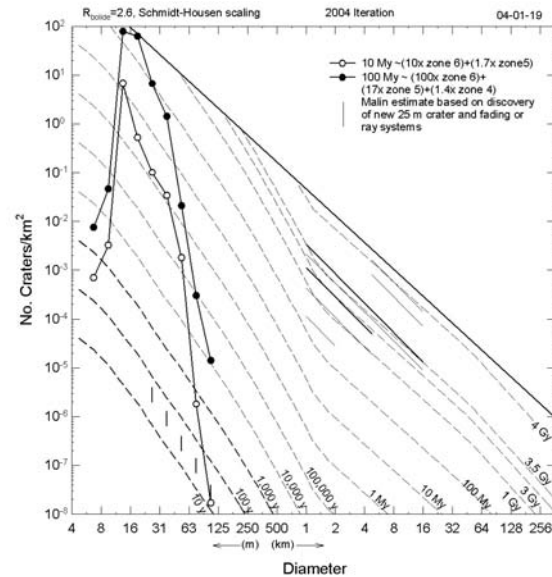


Fig. 2. McEwen predicted SFD's from Zunil secondaries after 10 and 100 My (see text). Tick marks (lower left) show Malin's proposed observed production of 25m-100m craters in 100 years (see text).

To put it another way, for surfaces formed over some 99.8% to 98% of Martian time (all but the last 10 to 100 My), the crater densities should roughly agree with the isochron system, even if the small craters are completely dominated by secondaries. In other words, a Martian lava flow, debris apron, glacier, or similar feature with virtually no 20m-scale craters must be $<$ few My old, while such a surface with saturation density is $>$ few hundred My old, contradicting the frequent assertion [5] that such craters give no chronologic information.

4. CONCLUSION

Existing crater chronology systems using craters of $D \geq 1$ km have a track record of successful prediction of ages on the moon and Mars. Combination of crater density measurements with observations of crater morphologies gives valuable information about not only ages, but also geological processes affecting obliteration. Recent criticisms based on new observations of small crater populations, have been overwrought in their suggestions that impact crater chronology studies, and/or counts of small impact craters, are worthless. Impact crater counts, combined with crater morphology studies, are a valuable addition to the analytic toolkit of planetary geologists.

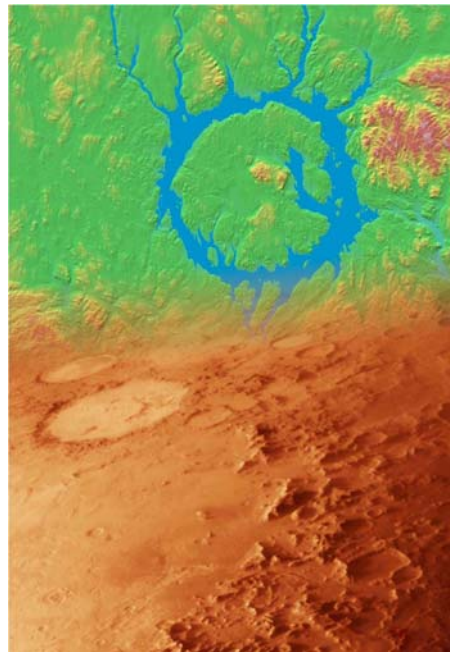
REFERENCES

1. Hartmann W.K., Martian cratering 8: Isochron refinement and the chronology of Mars, *ICARUS*, Vol. 174, 294-320, 2005.
2. Malin M.C. and Edgett K.S., Evidence for Persistent Flow and Aqueous Sedimentation on Early Mars, *SCIENCE*, Vol. 302, 1931-1934, 2003; Malin M.C. and Edgett K.S., *J. GEOPHYS. RES.*, Vol. 106, 23429-23570.
3. Hartmann W.K., Terrestrial and Lunar Flux of Large Meteorites in the Last Two Billion Years, *ICARUS*, Vol. 4, 157-165.
4. Hartmann W.K., Martian Cratering, IV: Mariner 9 Initial Analysis of Cratering Chronology, *J. GEOPHYS. RES.*, Vol. 78, 4096-4116, 1973. Hartmann W.K., Martian Cratering V: Toward an Empirical Martian Chronology, and Its Implications, *GEOPHYS. RES. LETT.* Vol. 5, 450-452, 1978.
5. McEwen A.S. et al., Discovery of a Large Rayed Crater on Mars: Implications for Recent Volcanic and Fluvial Activity and the Origin of Martian Meteorites, LPSC XXXIV, abstract #2040. McEwen A.S. et al., the Rayed Crater Zunil and Interpretations of Small Impact Craters on Mars, *ICARUS*, Vol. 176, 351-381, 2005. Bierhaus E.B. et al., Secondary Craters on Europa and Implications for Cratered Surfaces, *NATURE*, Vol. 437, 1125-1127, 2005. Chapman C.R., Mars Cratering Issues: Secondary Cratering and End-Noachian Degradation, Second Conf. on Early Mars, Abstract #8028, 2004.
6. Berman D.C. and Hartmann W.K., Recent Fluvial, Volcanic, and Tectonic Activity on the Cerberus Plains of Mars, *ICARUS*, Vol. 159, 1-17, 2002.
7. Quantin C. et al., Ages of Valles Marineris (Mars) Landslides and Implications for Canyon History, *ICARUS*, Vol. 172, 555-572, 2004.
8. Head J.N., Melosh H.J., and Ivanov, B.A., Martian Meteorite Launch: High-Speed Ejecta from Small Craters. *SCIENCE*, 298, 1752-1756, 2002.

Session S.04

Cratering on Mars and Venus

Chair: S. Werner



MARTIAN IMPACT CRATERS AND THEIR IMPLICATIONS FOR TARGET CHARACTERISTICS

Nadine G. Barlow

*Northern Arizona University, Department of Physics and Astronomy, Flagstaff, AZ 86011-6010 USA
Nadine.Barlow@nau.edu*

ABSTRACT

Martian impact craters display a number of characteristics which differ from those associated with impact craters on volatile-poor bodies such as the Moon or Mercury. These characteristics include the morphometric properties of the crater, ejecta and interior morphologies, and the range of preservational states due to modification from the Martian environment. Both the thin Martian atmosphere and the presence of volatiles within the target material can contribute to these unusual characteristics, but the role of target volatiles appears to dominate.

1. INTRODUCTION

Lunar impact craters have become the “standard” to which impact craters on other bodies have been compared. However, the Moon is a volatile-poor body, with no substantial atmosphere or presence of volatiles within the target material. The presence of volatiles substantially affects impact craters, both during crater formation and through subsequent modification. Examples of these effects are clearly evident in Martian impact craters, which serve as better analogs to terrestrial craters than do lunar craters.

Martian impact craters were identified in the early imagery from Mariners 4, 6, 7, and 9, but it was not until the Viking missions in the late 1970’s that the full range of morphologic features could be appreciated. The latest armada of orbiting spacecraft (Mars Global Surveyor (MGS), Mars Odyssey, and Mars Express (MEx)) has dramatically enhanced the amount of information about Martian impact craters by providing multispectral, stereo, topographic, and mineralogic data. The recent addition of the Mars Reconnaissance Orbiter (MRO) together with in situ analysis of impact crater materials by the Mars Exploration Rovers (MER) are adding additional layers of information to help us better understand how the Martian environment, and particularly the presence of atmospheric and subsurface volatiles, has influenced the formation and subsequent modification of impact craters on our neighboring world. Peering below the surface with MEx’s MARSIS and MRO’s SHARAD ground penetrating radars will provide direct

constraints on the role of subsurface volatiles in producing the observed morphologies and morphometries of Martian impact craters.

2. CRATER MORPHOMETRY

Viking-based analysis of Martian impact craters using shadow measurements and photoclinometry suggested that many of the morphometric parameters were quite different from those of lunar craters [1, 2]. The detailed topographic information produced by MGS’s Mars Orbiter Laser Altimeter (MOLA) instrument has confirmed that crater morphometric properties are quite different between Mars and volatile-poor bodies such as the Moon and Mercury [3, 4].

The gravity-dependence of the transition between simple and complex crater forms is well-established, predicting that the simple-to-complex transition diameter (D_{sc}) should be smaller on larger and/or more massive bodies [5]. Gravity scaling predicts that D_{sc} on Mars should be about 10 km, similar to D_{sc} on smaller but more massive Mercury. The actual value for Mars is closer to 7 km, although D_{sc} is observed to be smaller at higher latitudes [3]. These observations suggest that the crust is weakened by the presence of ice within the near-surface materials.

Other morphometric properties also show variations with latitude. For example, the relationship between the depth (d) and the diameter (D) of fresh complex craters [3, 6] at near-polar latitudes is

$$d = 0.03 D^{1.04} \quad (1)$$

while the relationship in near-equatorial regions is

$$d = 0.19 D^{0.55} \quad (2)$$

Similar latitudinal dependencies are observed for other morphometric parameters (see [3] for more details). These latitudinal variations in crater morphometries are consistent with the proposed latitudinal distribution of near-surface ice, based on geothermal models [7-9].

3. EJECTA MORPHOLOGIES

Fresh lunar impact craters are surrounded by a radially-oriented ejecta blanket, emplaced by dry material ejected along ballistic trajectories. Such ejecta blankets, referred to here as “lunar radial ejecta”, are comprised of an inner thick, hummocky deposit called the continuous ejecta blanket surrounded by the more dispersed, secondary crater-dominated discontinuous ejecta blanket [5]. Fresh Martian impact craters, however, are typically surrounded by ejecta blankets displaying a more lobate or fluidized appearance. Such ejecta morphologies are called “layered ejecta”, and are subdivided into several classes based on the appearance of the ejecta [10]. Craters displaying one complete layer of ejecta are called single layer ejecta (SLE) craters, while those displaying two complete ejecta layers are double layer ejecta (DLE) craters. Multiple layer ejecta (MLE) craters are surrounded by three or more partial or complete ejecta layers. Two models have been proposed for the formation of the layered ejecta morphologies: (1) vaporization of volatile-rich target material during impact [11, 12], and (2) interaction of the ejecta plume with the thin Martian atmosphere [13, 14].

3.1. Single Layer Ejecta

SLE craters display a single ejecta blanket surrounding the crater (Fig. 1). They are the most common type of ejecta morphology surrounding fresh craters on Mars [15]. The smallest craters which show a SLE morphology (the “onset diameter”) range from about 3 to 5 km in the equatorial region to less than 1 km near the poles, although regional variations are seen in the equatorial region [16-18]. The SLE morphology is associated with craters up to about 25 km in diameter in the equatorial region and up to >70-km-diameter near the poles. The ejecta blanket is characterized by two quantitative measurements, the ejecta mobility (EM) ratio and lobateness (Γ), which are believed to provide information about the fluidity of the ejecta during emplacement. The EM ratio describes how far the ejecta extends from the crater and is defined as [19, 20]

$$EM = \frac{(\text{maximum extent of ejecta from crater rim})}{(\text{crater radius})} \quad (3)$$

Lobateness is a measure of the sinuosity of the ejecta deposit. It is defined in terms of the area covered by the ejecta (A) and the perimeter (linear distance along outer edge) of the ejecta deposit (P) [21]:

$$\Gamma = P/(4\pi A)^{1/2} \quad (4)$$

A circular ejecta blanket will have $\Gamma = 1$ while more sinuous ejecta have higher values. Martian SLE craters have EM ratios between 0.20 and 6.60, with a median of 1.53. Their lobateness values vary from 1.00 to 3.57, with an average of 1.10. Hence, most SLE craters have ejecta deposits which extend ~1.5 crater radii from the rim and which are generally close to circular. EM and Γ values typically indicate more fluid ejecta as one approaches the poles, consistent with the proposed higher concentrations of subsurface volatiles in these regions from geothermal and hydrologic models [8, 9] as well as the observed high hydrogen concentrations from the Gamma Ray Spectrometer/Neutron Spectrometer on Mars Odyssey [22-24].

Both the subsurface volatile [11, 12] and atmospheric [13, 14] models can replicate the general features of the SLE morphology. However, the observed latitudinal variations in onset diameter, EM, and Γ strongly suggest that subsurface volatiles dominate the formation process.

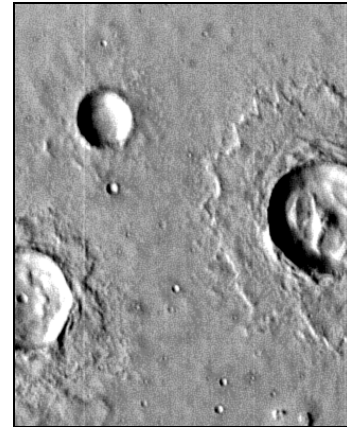


Figure 1. Examples of single layer ejecta (SLE) craters on Mars. Crater on right is 11.6 km in diameter and located at 23.63°N 101.71°E. (THEMIS image I02493005)

3.2 Double Layer Ejecta

DLE craters display two complete ejecta layers (Fig. 2) and are commonly found around craters in the mid-latitude (~40°-65°) zone in both hemispheres. This ejecta morphology is seen around craters up to ~25-km-diameter. Detailed analysis of the DLE ejecta blankets using MGS’s Mars Orbiter Camera (MOC) and Odyssey’s Thermal Emission Imaging System (THEMIS) visible (VIS) camera suggest that the inner ejecta layer is emplaced before the outer layer [25]. Contrary to earlier reports, DLE craters are seen at a range of elevations and in materials with varying

thermal inertia values [15, 26], but they are most strongly concentrated in low-lying regions of the northern hemisphere between 40°N and 65°N.

EM ratios vary from 0.40 to 3.30 for the inner ejecta layer, with an average value of 1.49. The outer ejecta layer has an EM range of 1.20 to 10.60 with an average of 3.24 [27]. Thus the outer ejecta layer displays much greater fluidity than the inner layer, which is similar in its EM values to those of SLE craters. The outer layer also displays high lobateness values, ranging from 1.01 to 2.27 with an average of 1.14. Inner layer Γ ranges between 1.00 and 1.38, with an average of 1.04.

The high EM and Γ values, as well as onset diameters of <1 km and concentrations within latitude zones expected to be ice-rich, all suggest that target volatiles are responsible for the DLE morphology. The inner layer displays many characteristics which are similar to those of SLE craters in these same regions and likely form by a similar mechanism. The very high EM ratios for the outer layers may indicate interaction of the ejecta plume with the Martian atmosphere, such as through a base surge process [25].

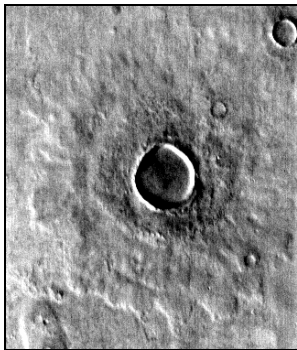


Figure 2: This double layer ejecta (DLE) crater is 6.8 km in diameter and located at 46.7°N 325.7°E. (THEMIS image I03484002)

3.3. Multiple Layer Ejecta Craters

The MLE morphology is most commonly associated with craters in the 25-50-km-diameter range, although craters as small as 8-km-diameter can show this ejecta pattern. Multiple layer craters display three or more ejecta layers which can extend completely around the crater or only as partial segments (Fig. 3). Most MLE craters are concentrated along the highlands/lowlands dichotomy boundary [15].

Analogous to the outer layer of DLE craters, the outermost complete ejecta deposit of the MLE craters has very high EM and Γ values, indicating that the

ejected material was very fluid at the time of emplacement. EM ratios range from 0.30 to 4.70, with an average value of 2.17; lobateness has an average value of 1.18 with a range of 1.02 to 1.74 [27].

The generally large size of MLE craters suggests that they are excavating to depths of around 1 km or more, within the regions where groundwater reservoirs could exist based on geothermal models [8, 9]. Both incorporation of liquid water within the ejected material [28] and interaction of the vapor plume with the Martian atmosphere [27] have been proposed to explain the extreme fluidity of the MLE ejecta deposits.

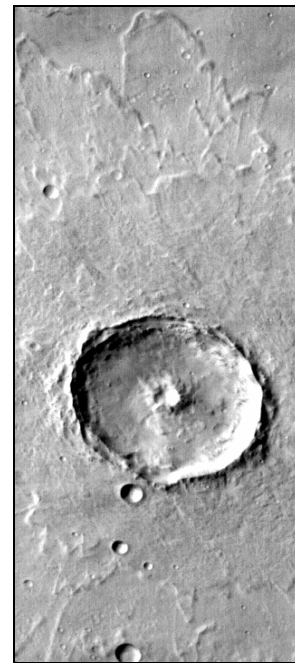


Figure 3: Multiple layer ejecta (MLE) craters display 3 or more partial or complete ejecta layers. This 25 km MLE crater at 6°N 304°E also displays a summit pit. (THEMIS image I03218002)

3.4. Other Ejecta Morphologies

The SLE, DLE, and MLE morphologies constitute 89% of all the ejecta morphologies associated with Martian impact craters ≥ 5 -km-diameter [27]. Although the other ejecta morphologies are numerically minor, the size and regional distributions of these features provide additional insights into the properties of the target materials.

Very small (typically <3-km-diameter in the equatorial region) and very large (typically >50-km-diameter) craters often display a radial (Rd) ejecta pattern, which

is qualitatively similar to the lunar radial ejecta patterns (Figure 4). Secondary crater chains are common in this ejecta pattern and can extend for 100's of crater radii from the crater rim [29]. This has led some researchers to conclude that the small crater population (<1-km-diameter) is dominated by secondary craters, which has important implications for terrain ages derived from small crater statistics.

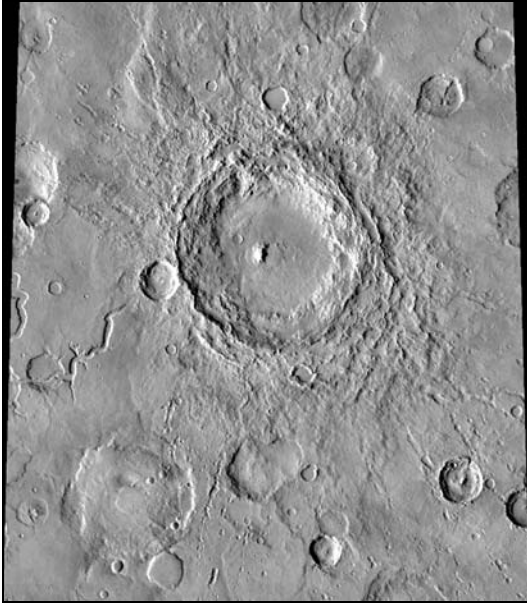


Figure 4: Radial (Rd) ejecta craters, like this 114-km-diameter example, show little or no evidence of ejecta fluidization, but chains of secondary craters are obvious. Crater is located at 32.14°N 21.99°E. (Viking mosaic image)

Diverse (Di) ejecta display components of both layered and radial ejecta patterns. Typically, chains of secondary craters extend from beneath the outer edge of the layered ejecta deposit (Fig. 5), indicating that the secondary craters are emplaced before the layered deposit. This suggests that volatile-poor but coherent target material is excavated before the volatile-rich region is encountered. The onset diameter for Di ejecta craters varies with age of the surface: Craters on young, Amazonian-aged volcanic lava flows show the Di pattern for craters as small as 10-km-diameter. Intermediate-aged Hesperian surfaces require craters to be at least 19 km in diameter before the Di pattern is seen, and craters on the old Noachian-aged surface are at least 45 km in diameter before showing this ejecta morphology [30]. This diameter-terrain age relationship likely reflects the varying thickness of a weak, fragmented regolith, which would be thicker on older units. Excavation through this thicker regolith to an underlying coherent bedrock layer, necessary for

production of the blocks responsible for secondary crater formation, requires a larger crater.

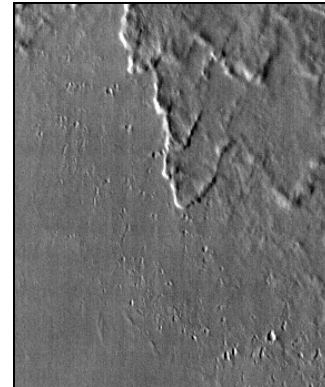


Figure 5: Example of a diverse (Di) ejecta morphology, with small secondary craters extending beyond the outer edge of the multiple layer ejecta blanket. This crater is located at 23.19°N 207.76°E (THEMIS image V01990003)

Pancake (Pn) ejecta craters are associated with ejecta deposits where the outer edge drops off in a convex shape rather than terminating in a distal rampart (Fig. 6). This morphology is primarily seen around craters <20-km-diameter at the higher latitudes, usually in the same 40-65° latitude zone where DLE craters dominate. Costard [20] suggested that Pn craters were simply the inner layer of a double layer crater where the thin outer ejecta layer had been either destroyed or was below detection limits. A more recent analysis of these craters using MOC and THEMIS data supports this idea [26]. Not only are many craters classified as Pn craters using Viking imagery found to actually be DLE craters using higher resolution data, but the EM and Γ values for Pn craters are statistically identical to the inner layer of DLE craters.

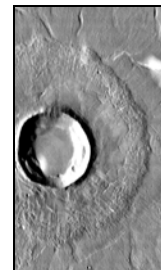


Figure 6: Pancake (Pn) craters do not display a terminal ridge (rampart) to their ejecta deposits. Crater is 14.1 km in diameter and located at 34.90°N 102.58°E. Higher resolution suggests this is actually a degraded DLE crater (THEMIS image I04378002)

Pedestal (Pd) craters are an unusual landform where both the crater and ejecta blanket are elevated above the surrounding terrain (Fig. 7). Pd craters are very small (typically <5-km-diameter) and are concentrated in the 45-60° latitude zone in both hemispheres. The original explanation for these features was that eolian deflation of surrounding fine-grained materials left the crater and ejecta blanket perched above the surroundings. However, Pd craters tend to be found within the ice-rich fine-grained mantles proposed to be deposited during high obliquity periods. A new model has been proposed by which sublimation of the ice within this mantling material causes the lowering of the surrounding terrain and the perched characteristics of the Pd craters [26].

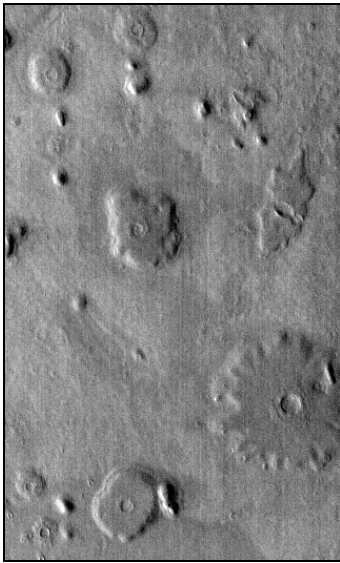


Figure 7: Pedestal (Pd) craters often occur in clusters, as seen in this image from the Arcadia Planitia region of Mars. The largest crater (lower right) is 1.8 km in diameter and located near 42.4°N 154.6°E. (THEMIS image I11416010)

4. INTERIOR MORPHOLOGIES

Martian impact craters display a variety of interior morphologies, including central peaks, peak rings, flat floors, and wall terraces. Collapse pits are seen on the floors of some craters while others have their floors covered with sedimentary deposits of eolian or possibly lacustrine origin. One class of interior features which is common on Mars but absent on volatile-poor bodies like the Moon are central pits.

4.1. Central Pits

Central pits are depressions found in the center of crater floors. There are two types of central pits: floor pits, where the pit lies directly on the floor of the crater, and summit pits, where the pit is found on a central rise or on top of a central peak. Fig. 8 shows an example of a floor pit while a summit pit is seen in Fig. 3. Over 1500 central pit craters have been identified on Mars, with floor pits approximately twice as common as summit pits [31]. Both floor pits and summit pits are found in craters with a similar range in sizes (5 to 57 km in diameter) and over a similar latitude zone (50°N to 70°S). The ratio of the pit diameter to the crater diameter (D_p/D_c) is strongly peaked for floor pits near 0.15 (range: 0.07 to 0.29). Summit pits tend to be smaller relative to their parent crater than floor pits (median = 0.11), but are not as strongly peaked over the range of 0.05 to 0.19 (Fig. 9). Pit craters are found in craters with a wide range in preservational state, from very degraded to pristine. Among fresh craters with preserved ejecta morphologies, most display a multiple layer ejecta morphology.

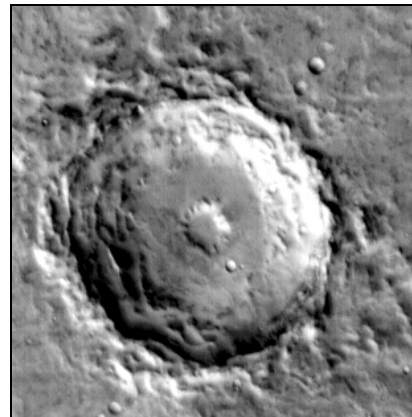


Figure 8: This 20.7-km-diameter crater displays a central floor pit. Crater is located at 22.46°N 340.41°E. (THEMIS image I01199005)

Central pits are believed to result from the release of volatiles from the center of the crater during crater formation. Croft [32] suggested that this resulted from cometary impacts, but the lack of central pit craters on volatile-poor bodies such as the Moon and Mars argues against central pits being solely a result of impactor composition. Because central pit craters are also common on icy moons such as Ganymede [33, 34] and Europa [35], the most widely accepted model of central pit formation involves impact into volatile-rich target materials [36]. Recent numerical modeling of both asteroid and comet impacts into ice-soil mixed targets shows that temperatures within the central region of the

transient cavity can reach temperatures well above the vaporization point of water ice [37]. A sudden release of this vapor could be responsible for the formation of central pits. The fact that craters in a wide range of preservational states (and thus a range of ages) display central pits suggests that the target volatiles responsible for central pit formation have been present on Mars for most if not all of its history.

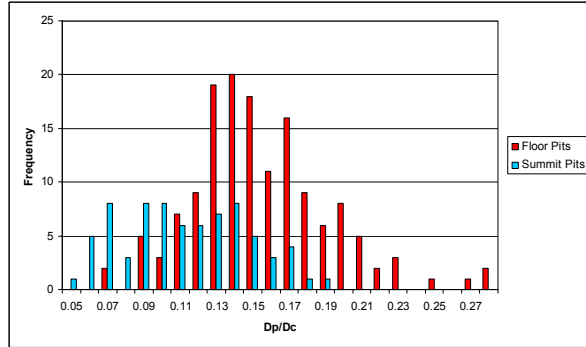


Figure 9: Comparison of D_p/D_c values for floor and summit pits. Floor pits show a stronger peak and tend to be larger relative to their parent crater than summit pits.

Major questions which still remain for central pits are: (1) why are some pits found on crater floors while others occur on top of central rises, and (2) why do some craters display central pits when adjacent craters of similar size and age do not? An on-going study to compare central pit craters on Ganymede with their Martian analogs may help to resolve these questions [38].

5. DEGRADATION OF MARTIAN CRATERS

While the layered ejecta morphologies and central pits strongly suggest the presence of volatiles in the target material at the time of crater formation, a number of processes related to volatiles operate to modify Martian impact craters after their formation. Mars today is cold and dry, with no liquid water remaining stable for extended periods of time on the surface or in the atmosphere. However, many impact craters on the ancient Noachian surface units are highly degraded, suggesting that degradation rates were much higher early in Martian history [39] (Fig. 10). While a variety of geologic processes (including eolian deposition, volcanic lava flows, and impact cratering and ejecta deposition) were operating at higher rates during this early time period, analysis of how the topographic profile of these impact craters has been altered also suggests that rainfall and surface water flow were

responsible for much of the degradation during this time [40].

The presence of liquid water on the Martian surface during the planet's early history is problematic because temperatures on Mars, even with a thicker carbon dioxide-rich atmosphere, are expected to have been too low to support liquid water because the Sun is expected to have been fainter when the solar system first formed. However, numerical modeling of atmospheric effects from impacts into volatile-rich materials during this early period suggests that regional microclimates can be produced where excess greenhouse warming can allow conditions favorable for liquid water [41]. Valley network channels and alluvial fans within impact craters may have formed from such microclimate conditions.

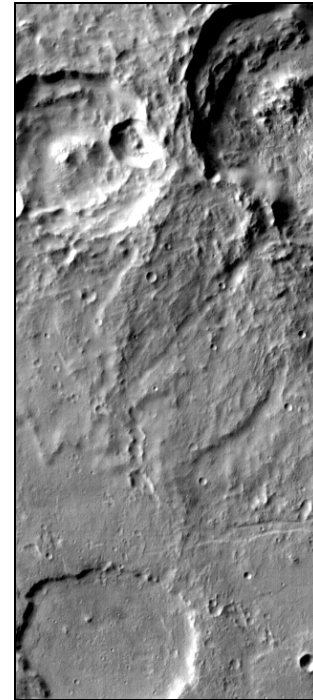


Figure 10: Example of the range of crater degradation seen in the ancient regions of Mars. Fresher craters, like that in the upper right, display prominent interior and ejecta features, while highly degraded craters, such as the one at the bottom, have had most of their features removed. Image is 32 km across and centered near 27°S 198°E. (THEMIS image I10579004)

The volatile-rich target affects impact craters in the mid-latitude regions of Mars through relaxation of crater topography, a process called “terrain softening” [42-44] (Fig. 11). The presence of ice in the target material weakens the crust, allowing relaxation of

topographic features over geologically short time periods. Sharp features such as crater rims and ejecta ramparts become rounded and material on steep slopes display features indicative of subsurface creep. Terrain softening is most common in the mid-latitude regions (~30°-60° latitude zone) because of the large presence of ice and the warmer temperatures which can be achieved in these regions due to seasonal and long-term obliquity cycles.



Figure 11: This 17-km-diameter crater shows features characteristic of terrain softening, caused by creep in target materials with high ice content. The rounded crater rim and ejecta features along with flow-type features on the crater floor are typical features seen in terrain softened craters on Mars. Crater is centered near 32°N 44°E (THEMIS image I11582007)

6. CONCLUSIONS

Martian impact craters display a variety of features which suggest that volatiles, both in the target material and the atmosphere, play a major role in crater formation and modification. Characteristics and distributions of the layered ejecta morphologies suggest that impact into volatile-rich surface materials is the dominant cause of these unusual features, although atmospheric interactions cannot be ignored as a contributor to the outermost ejecta deposit of double layer and multiple layer morphologies. Central pits are another strong indicator that the Martian near-surface region contains large concentrations of volatiles. Studies of onset diameters for single layer ejecta craters as a function of crater age suggest that the depth to the ice-rich layer has increased over time [45], but the deep reservoir seems to have maintained approximately the same volatile concentration for much of Mars' history [46].

Volatiles influence not only the initial morphologies and morphometries of Martian impact craters but also

their subsequent evolution. Ancient craters have undergone a substantial amount of degradation due to eolian, volcanic, tectonic, impact, and fluvial processes. Large impact events, particularly during the first 10⁹ years of Mars' history, may have produced regional microclimates with enhanced fluvial and/or glacial activity. Present-day near-surface ice affects crater morphology through creep processes and sublimation of surface ice deposits emplaced at mid-latitudes during periods of high obliquity may be responsible for the unusual pedestal crater morphology.

Impact craters on Mars display numerous characteristics which differentiate them from craters on volatile-poor bodies like the Moon. Differences in impact velocities and surface gravity between Mars and the Moon can explain some of these observed differences, but many others must be the result of the volatile-rich Martian environment. The presence of both an atmosphere and surface/subsurface volatiles on the Earth makes Mars a better analog for understanding the original morphologies expected with terrestrial impact craters.

REFERENCES

1. Pike R. J., Control of crater morphology by gravity and target type: Mars, Earth, Moon, *PROCEEDINGS OF THE 11TH LUNAR AND PLANETARY SCIENCE CONFERENCE*, 2159-2189, 1980.
2. Davis P. A. and Soderblom L. A. Modeling crater topography and albedo from monoscopic Viking Orbiter imagers, 1, Methodology, *J. GEOPHYSICAL RESEARCH*, Vol. 89, 9449-9457, 1984.
3. Garvin J. B. et al. North polar region craterforms on Mars: Geometric characteristics from the Mars Orbiter Laser Altimeter, *ICARUS*, Vol. 144, 329-352, 2000.
4. Smith, D. E. et al. Mars Orbiter Laser Altimeter: Experiment summary after the first year of global mapping of Mars, *J. GEOPHYSICAL RESEARCH*, Vol. 106, 23,689-23,722, 2001.
5. Melosh, H. J., *Impact Cratering: A Geologic Process*, Oxford University Press, New York, 1989.
6. Garvin J. B. et al. Craters on Mars: Global geometric properties from gridded MOLA topography, *6th INTERNATIONAL CONFERENCE ON MARS*, Lunar and Planetary Institute Abstract #3277, Houston, TX, 2003
7. Rossbacher L. A. and Judson S. Ground ice on Mars: Inventory, distribution and resulting landforms, *ICARUS*, Vo. 45, 39-59, 1981.
8. Fanale F. P. Martian volatiles: Their degassing history and geochemical fate, *ICARUS*, Vol. 28, 179-202, 1976.

9. Clifford S. M. A model for the hydrologic and climatic behavior of water on Mars, *J. GEOPHYSICAL RESEARCH*, Vol. 98, 10973-11016, 1993.
10. Barlow N. G. et al. Standardizing the nomenclature of Martian impact crater ejecta morphologies, *J. GEOPHYSICAL RESEARCH*, Vol. 105, 26733-26738, 2000.
11. Carr M. H. et al. Martian impact craters and emplacement of ejecta by surface flow, *J. GEOPHYSICAL RESEARCH*, Vol. 82, 4055-4065, 1977.
12. Stewart S. T. et al. The relationship between rampart crater morphologies and the amount of subsurface ice, *LUNAR AND PLANETARY SCIENCE XXXII*, Abstract #2092, Lunar and Planetary Institute, Houston, TX, 2001.
13. Schultz P. H. Atmospheric effects on ejecta emplacement, *J. GEOPHYSICAL RESEARCH*, Vol. 97, 11623-11662, 1992.
14. Barnouin-Jha O. S. et al. Investigating the interactions between an atmosphere and an ejecta curtain. 2. Numerical experiments, *J. GEOPHYSICAL RESEARCH*, Vol. 104, 27117-27131, 1999.
15. Barlow N. B. and Perez C. B. Martian impact crater ejecta morphologies as indicators of the distribution of subsurface volatiles, *J. GEOPHYSICAL RESEARCH*, Vol. 108, #E08, 5085, doi: 10.1029/2002JE002036, 2003.
16. Kuzmin R. O. et al. Structural inhomogeneities of the Martian cryosphere, *SOLAR SYSTEM RESEARCH*, Vol. 22, 121-133, 1988.
17. Barlow N. G. et al. Variations in the onset diameter for Martian layered ejecta morphologies and their implications for subsurface volatile reservoirs, *GEOPHYSICAL RESEARCH LETTERS*, Vol. 28, 3095-3098, 2001.
18. Boyce J. M. et al. Distribution of onset diameters of rampart ejecta craters on Mars, *LUNAR AND PLANETARY SCIENCE XXVIII*, Abstract #1404, Lunar and Planetary Institute, Houston, TX, 1998.
19. Mouginis-Mark P. Martian fluidized ejecta morphology: Variations with crater size, latitude, altitude, and target material, *J. GEOPHYSICAL RESEARCH*, Vol. 84, 8011-8022, 1979.
20. Costard F. M. The spatial distribution of volatiles in the Martian hydrolithosphere, *EARTH, MOON, AND PLANETS*, Vol. 45, 265-290, 1989.
21. Barlow N. G. Sinuosity of Martian rampart ejecta deposits, *J. GEOPHYSICAL RESEARCH*, Vol. 99, 10927-10935, 1994.
22. Boynton W. V. et al. Distribution of hydrogen in the near-surface of Mars: Evidence for subsurface ice deposits, *SCIENCE*, Vol. 297, 81-85, 2002.
23. Feldmann W. C. et al. Global distribution of near-surface hydrogen on Mars, *J. GEOPHYSICAL RESEARCH*, Vol. 109, E09006, doi: 10.1029/2003JE002160, 2004.
24. Mitrofanov I. G. et al. Soil water content on Mars as estimated from neutron measurements by the HEND instrument onboard the 2001 Mars Odyssey spacecraft, *SOLAR SYSTEM RESEARCH*, Vol. 38, 253-257, 2004.
25. Boyce J. M. and Mouginis-Mark P. J. Martian craters viewed by the THEMIS instrument: Double-layered ejecta craters, *J. GEOPHYSICAL RESEARCH*, in press, 2006.
26. Barlow N. G. Impact craters in the northern hemisphere of Mars: Layered ejecta and central pit characteristics, *METEORITICS AND PLANETARY SCIENCE*, in press, 2006.
27. Barlow N. G. A review of Martian impact crater ejecta structures and their implications for target properties, in *Large Meteorite Impacts III* (T. Kenkmann, F. Hörz, and A. Deutsch, eds.), Geological Society of America Special Paper 384, 433-442, 2005.
28. Barlow N. G. and Bradley T. L. Martian impact craters: Correlations of ejecta and interior morphologies with diameter, latitude, and terrain, *ICARUS*, Vol. 87, 156-179, 1990.
29. McEwen A. S. et al. The rayed crater Zunil and interpretations of small impact craters on Mars, *ICARUS*, Vol. 176, 351-381, 2005.
30. Hartmann W. K. and Barlow N. G. Nature of the Martian uplands: Effect on Martian meteorite age distribution and secondary cratering, *METEORITICS AND PLANETARY SCIENCE*, in press, 2006.
31. Barlow N. G. and Hillman E. Distributions and characteristics of Martian central pit craters, *LUNAR AND PLANETARY SCIENCE XXXVII*, Abstract #1253, Lunar and Planetary Institute, Houston, TX, 2006.
32. Croft S. K. A proposed origin for palimpsests and anomalous pit craters on Ganymede and Callisto, *PROCEEDINGS OF THE 14TH LUNAR AND PLANETARY SCIENCE CONFERENCE, JOURNAL OF GEOPHYSICAL RESEARCH*, Vol. 88, B71-B89, 1983.
33. Horner V. M. and Greeley R. Pedestal craters on Ganymede, *ICARUS*, Vol. 51, 549-562, 1982.
34. Schenk P. H. Central pit and dome craters: Exposing the interiors of Ganymede and Callisto, *J. GEOPHYSICAL RESEARCH*, Vol. 98, 7475-7498, 1993.
35. Moore J. M. et al. Impact features on Europa: Results of the Galileo Europa Mission (GEM), *ICARUS*, Vol. 151, 93-111, 2001.
36. Wood C. A. et al. Interior morphology of fresh Martian craters: The effects of target characteristics, *PROCEEDINGS OF THE 9TH LUNAR AND PLANETARY SCIENCE CONFERENCE*, 3691-3709, 1978.
37. Pierazzo E. et al. Starting conditions for hydrothermal systems underneath Martian craters: Hydrocode modeling, in *Large Meteorite Impacts III* (T. Kenkmann, F. Hörz, and A. Deutsch, eds.),

Geological Society of America Special Paper 384, 443-457, 2005.

38. Klaybor K. M. and Barlow N. G. Interior morphologies of impact craters on Ganymede, *LUNAR AND PLANETARY SCIENCE XXXVII*, Abstract #1360, Lunar and Planetary Institute, Houston, TX, 2006.

39. Chapman C. R. and Jones K. L. Cratering and obliteration history of Mars, *ANNUAL REVIEWS OF EARTH AND PLANETARY SCIENCE*, Vol. 5, 515-540, 1977.

40. Craddock R. A. and Howard A. D. The case for rainfall on warm, wet early Mars, *J. GEOPHYSICAL RESEARCH*, Vol. 107, No. E11, 5111, doi: 10.1029/2001JE001505, 2002.

41. Colaprete A. et al. The effect of impacts on the Martian climate, *WORKSHOP ON THE ROLE OF VOLATILES AND ATMOSPHERES ON MARTIAN IMPACT CRATERS*, LPI Contribution No. 1273, Lunar and Planetary Institute, Houston, TX, 32-33, 2005.

42. Squyres S. W. and Carr M. H. Geomorphic evidence for the distribution of ground ice on Mars, *SCIENCE*, Vol. 231, 249-252, 1986.

43. Jankowski D. G. and Squyres S. W. The topography of impact craters in “softened” terrain on Mars, *ICARUS*, Vol. 100, 26-39, 1992.

44. Turtle E. P. and Pathare A. V. “Softening” of Martian impact craters by creep of ice-rich permafrost, *WORKSHOP ON THE ROLE OF VOLATILES AND ATMOSPHERES ON MARTIAN IMPACT CRATERS*, LPI Contribution No. 1273, Lunar and Planetary Institute, Houston, TX, 110-111, 2005.

45. Reiss D. et al. Ages of rampart craters in equatorial regions on Mars: Implications for the past and present distribution of ground ice, *METEORITICS AND PLANETARY SCIENCE*, in press, 2006.

46. Barlow N. G. Martian subsurface volatile concentrations as a function of time: Clues from layered ejecta craters, *GEOPHYSICAL RESEARCH LETTERS*, Vol. 31, L05703, doi: 10.1029/2003GL019075, 2004

MARTIAN ALLUVIAL FANS: UNDERSTANDING THE CRATER CONNECTION

Erin R. Kraal^(1, 2) and Erik Asphaug⁽¹⁾

⁽¹⁾UC Santa Cruz, Department of Earth Science, 1156 High Street, Santa Cruz, CA, USA 95064,
Email:ekraal@pmc.ucsc.edu, asphaug@pmc.ucsc.edu

⁽²⁾Now at Utrecht University, Faculty of Geosciences, Department of Sedimentology, Postbus 80021, 3508 TA Utrecht,
The Netherlands, Email:kraal@geo.uu.nl

ABSTRACT

Our global survey of alluvial fans has found 28 locations that contain more than 50 large alluvial fans. Twenty-seven of these locations are impact craters. All alluvial fans originate from the rim of the crater and deposit their apron into the basin. The locations of alluvial fans are regionally groups and focused in three main locations, all in the southern hemisphere. The correlation between alluvial fans and impact craters on Mars indicates that some part of the impact process may help set conditions favourable to fan formation.

1. INTRODUCTION

The results of a global survey (Figure 1a) for Martian alluvial fans shows an important relationship, that alluvial fans on Mars are found almost exclusively to originate from the inside rims of impact craters.

Our survey has found ~50 fans on the Martian surface, primarily through a global search of THEMIS data. While our survey is global, and not limited to impact craters, only one fan has been discovered so far that does not originate on an interior crater wall. This single fan is located in Capris Chasm (Figure 1c).

Here we report on work devoted to understanding why impact craters are the preferred site locales for alluvial fans on Mars. Crater walls are steep and they are heavily faulted, but the same is true for other Mars locales, so that explanation requires a very careful evaluation. Nor is it obvious why craters should be favorable, topographically, for the tapping of groundwater near their rims, given that rims are raised above the mean ground surface. The source of groundwater associated with these fans is not readily evident; if it is water originating from precipitation then one is challenged by the fact that fans are strictly localized, as discussed below.

And so, one is compelled to search for genetic links with cratering. Plausible explanations we are exploring include radial and subsurface faulting [1] that may lead to effective mobilization of groundwater, or impact-induced hydrologic cycles proximal to a recently

formed crater, or impact-triggered mobilization of ground ice towards a freshly formed crater (see abstract by Plesko *et al.* in this volume), or the possibility that isostatic rebound after crater formation provides the uplift associated with the formation of many terrestrial alluvial fans.

2. GLOBAL SURVEY RESULTS

We conducted our global survey using THEMIS IR images at ~100 m/pixel resolution. 27 craters have been found that contain fans, and to date we have identified ~50 alluvial fans in these craters, with some craters contain multiple fans originating from different directions (Figure 1b, 1d). Thus, 98% of the alluvial fans detected in this survey are located within impact craters. While we have searched globally, all fans identified are located in the southern hemisphere.

One interesting finding of our survey is the confirmation, after a global survey down to 20 km diameter crater sizes, of the initial finding [2] that a majority of fans are located in three distinct regions, with the two exceptions shown in Figure 1b and 1d.

The craters that contain alluvial fans range in diameter from 27 km to 157 km; the craters that contain the most fans are between 80 km and 90 km in diameter. The search for fans in smaller sized craters may be limited by our ability to resolve thin depositional layers at small scale, so a lower crater limit has not been established. For example, Williams *et. al* have reported on fan-like structures in Mojave Crater, a 60 km diameter crater where the structures are too small to be resolved in THEMIS 100m/pixel imagery [3].

Fan orientation (location on the rim where the fan originates) has a broad spread, as shown in Figure 2, and does not show a preferential orientation overall. We are studying the statistics of fan distribution within craters that contain multiple fans, to understand whether there is a preferential alcove spacing.

3. CRATER CONNECTION

The striking connection between alluvial fans and impact craters indicates that some aspect of the cratering process is responsible for helping set initial conditions that can be exploited to form alluvial fans on Mars.

The simplest hypothesis to be tested is that craters of a certain dimension simply define the most advantageous topographic profile for fan formation, and thus are the most common site. This effort involves a first-order comparison of topographic profiles wherever fans are located on Mars, both inside of craters and elsewhere, e.g. on valley walls. We are in the process of examining topographic profiles as a function of crater diameter, for any indication of whether alluvial fan preference for craters of a given diameter may simply be correlated with the typical profiles inside of craters of that diameter.

This explanation is already challenged by observations, in THEMIS images, of multiple apparently similar craters that have formed in very similar geologic units, in close proximity. Only one will have a fan or fans, while the proximal nearly identical craters have none. So topography alone may not be able to offer an explanation.

Another aspect being examined is sediment production. In order to form alluvial fans, there must be a source of clastic sediments in the alcove. The bedrock geology of the crater rim is an integral aspect of this sediment production function. While many aspects of cratering are scale similar, the differential scaling of melt production is well known to lead to large craters being more melt rich, owing to the greater energy required per unit volume for excavation. The same is likely to be true regarding clast size production, with larger craters resulting in the production of finer clasts.

Another aspect of the cratering process involves the formation of large-scale radial faults that may be advantageous for alluvial fan production, given that in terrestrial settings, alluvial fan alcoves tend to initiate along pre-existing faults or joints. Separate from issues of hydrology, we are examining alcove distribution within the craters that contain multiple fans (FIGURE) to see whether this correlates with the expected distribution of radial structures resulting from impact fracture.

4. CONCLUSION

We report on our global survey of alluvial fans on Mars, which extends the initial fan survey [2] globally to craters of much smaller diameter. In related work, the curious distribution of fan-containing craters seen in Figure 1a is being explored for its possible climate significance (e.g. Santiago et al., LPSC 2006). Here we are challenged to understand why craters are the preferred setting for fan formation, especially given that fans can exist inside of one crater and be absent from almost identical craters in the same THEMIS image. Examining the setting for fan formation may reveal not only evidence of past Martian hydrological activity, but may reveal how impact cratering events interacted with Martian subsurface geology in the Hesperian to produce appropriate conditions for fan formation.

5. REFERENCES

- [1] Xia, K. and T.J. Ahrens, Impact induced damage beneath craters, GRL 28, 3525-3527, (2001)
- [2] Moore, J. M. and Howard, A. H. (2005) JGR, V 110, DOI: 10.1029/2004JE002352.
- [3] Williams, R. M. E., Edgett, M. C., and Malin, M. C., LPSC XXXV, abstract #1415.

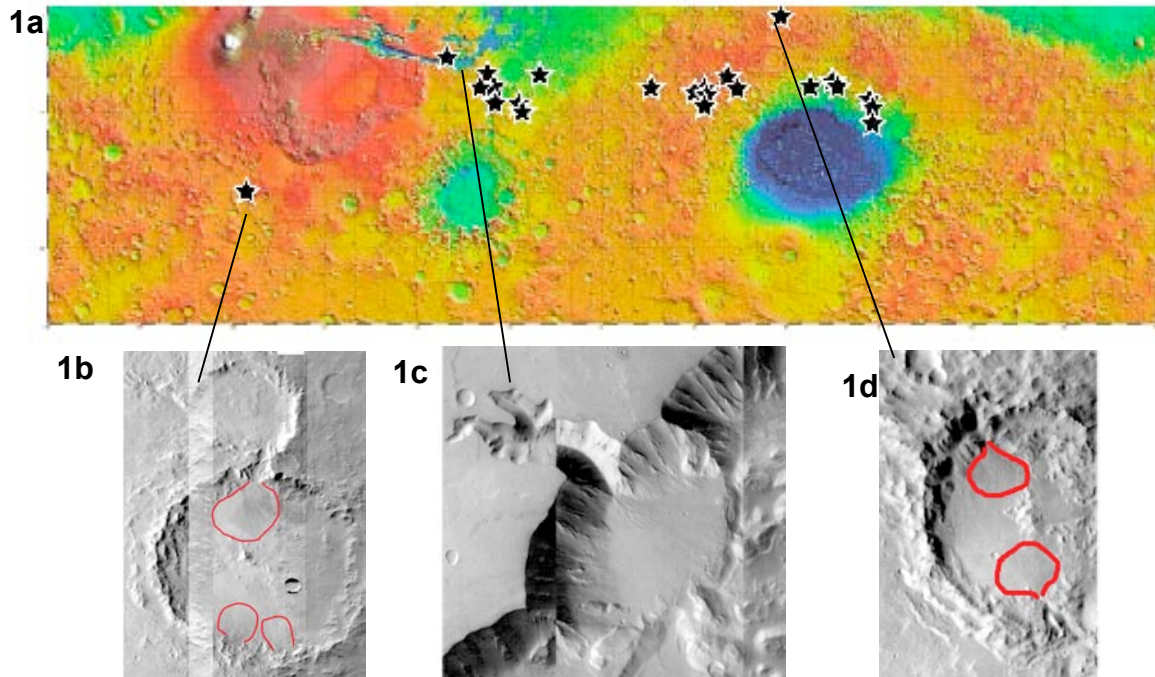


Fig. 1a shows the MOLA topography for 0S – 180S. Base image MOLA Science team. Fans are identified with a star symbol. 1b is Porter Crater, 50.7° S/113.71° W (100 km across) with fans outlined in red. The fan (13.6° S/51.7° W) in Capris Chasm (1c) is the only fan not originating from a crater rim. Fans have been found in small crater as well; 1d shows two fans in a 37 km diameter crater at 1.59° S/301.8° W.

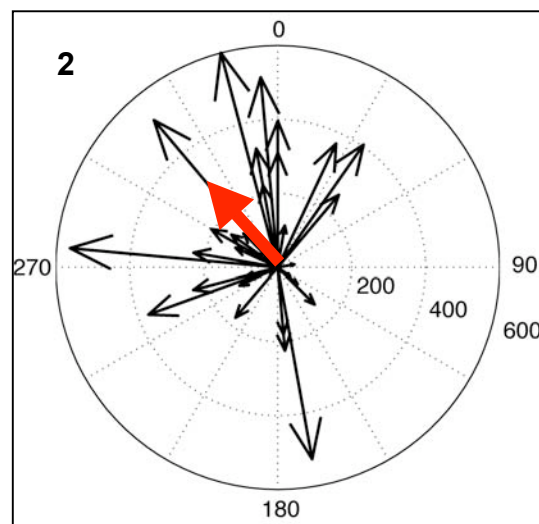


Fig. 2. Arrows point to the direction of emergence of the fan from the crater rim. Their length scales with area of the fan apron. North is up in all cases and area of fan is in km². The only fans included are those above MOLA topographic resolution (see [2]). Average fan is indicated in red. The average fan is 250 km² and originates from the northwest rim of the crater (300°), however there is a wide spread in the date. This is a preliminary plot and does not yet contain data for all of the fans identified, as data collection is still in process.

VENUSIAN IMPACT CRATERS

J. Raitala, M. Aittola, V.-P. Kostama and T. Törmänen

*Astronomy Division, Dept. of Physical Sciences, PO Box 3000, FIN-90014 University of Oulu, Finland.
jouko.raitala@oulu.fi, marko.aittola@oulu.fi, petri.kostama@oulu.fi, terhi.tormanen@oulu.fi*

1. INTRODUCTION

In the study of geologic processes, each of the planets will provide a limited insight of its own to a particular sequence of geologic events. This is also the case when considering impact event, formation of impact craters and impactites, and the subsequent modification and deformation of the impact crater and ejecta units. This is a limitation if the approach is concentrated to a single planet only, but – after related structures have been studied from a series of similar type planetary bodies together – it will, at its best, provide the required complementary details to our understanding of the geological process at hand.

Venus is a terrestrial planet, one of the inner Solar System planets with a solid rock surface, silicate composition and dense core. By size, it is a twin of the Earth with equatorial diameter of 12 104 km and the mean planetary radius of 6051.84 km. The total mass of the planet is 4.84×10^{24} kg, and the average density is 5.24 g/cm^3 . Venus' distance from the Sun is 0.7 AU and thus it is slightly closer to the Sun than Earth. The slow rotation period of Venus is 243 days which is longer than its orbital period of 225 days.

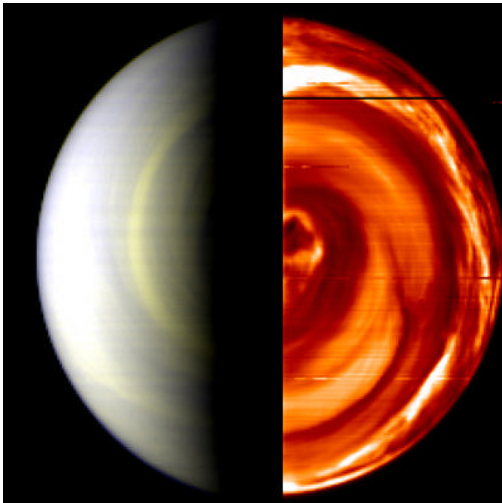


Fig. 1. The Venus Express VIRTIS instrument has revealed details of the wind-driven patterns in the upper levels of Venus' thick and complex atmosphere (http://www.esa.int/SPECIALS/Venus_Express/index).

html). Credit: ESA / INAF-IASF, Rome, Italy and Observatoire de Paris, France.

The most important Venus missions include Venera 9/10 (1975) and Venera 13/14 (1981) landers, and Pioneer Venus (1978), Venera 15/16 (1983) and Magellan (1989) radar orbiters. The most recent mission, Venus Express, was launched in fall 2005 to and reached the Venus' orbit in April 2006 (Fig. 1).

2. VENUSIAN ENVIRONMENT AND GEOLOGICAL PROCESSES

The surface environment is very hot and dry. The average temperature is $\sim 737\text{K}$ rising from 663.15K within the mountains to 763.15K in lowlands. The 95 bar dense CO_2 atmosphere and the thick cloud coverage are responsible for this runaway greenhouse effect. While wind velocities close to the surface are low ($<1\text{m/s}$) the winds get stronger with altitude [1-3; cf. also Fig. 1] with the implication that they may be more effective on mountain crests.



Figure 2. The Venera 13 panorama image reveals details of the Venusian surface with lithified rock layers and loose rock material.

Unlike the other terrestrial planets which all have a clear surface dichotomy, Venus displays a more monotone elevation distribution [4]. The radar data sets have shown that its vast volcanic plains cover most of the surface with elevation within ± 1 km of the mean planetary radius (MPR) while tessera highlands, domical areas and mountain belts rise a few to several kilometers above the MPR. The Venera lander panoramas revealed layered surface rocks which may consist of lithified sediments, lava flows or exfoliated lavas [Fig. 2; e.g. 5-9]. By composition, all the analyzed rock types are close to basalts [e.g. 10-16]. The vast lava plains cover lowlands and highland depressions, and indicate, together with numerous dome fields, larger volcanic edifices, rift zones and ridge belts that volcanism and tectonics have played a major role on Venus (cf. Fig. 3). Its exogenic

geological processes include eolian erosion, transportation and deposition (which is connected to the impact crater parabolas), atmosphere- and temperature-related chemical weathering, and impact crater formation.

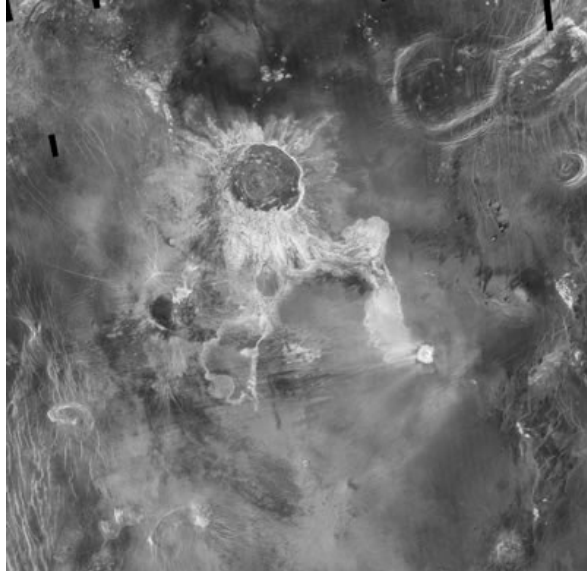


Fig. 3. The 175 kilometer diameter impact crater Isabella ($-29.9^{\circ}\text{S}/204.2^{\circ}\text{E}$) has a rather pristine-looking ejecta close to the crater rim. It is partially surrounded by younger lava plains and the floor was also covered by lavas. The lava plains show wrinkle ridges as a result of compressional tectonics. The lava-like outflow structures extend long distances away from within the ejecta. The wind-driven deposits from a later 20 km-size impact crater Cohn cover the southernmost tip of the outflow.

3. CHARACTERISTICS OF VENUSIAN IMPACT CRATERS

On the Earth, the small number (approximately 170) of positively identified impact craters is a consequence of the large water-covered areas and the effective exo- and endogenic re-surfacing processes. On the other hand, the smaller terrestrial planets (Mars, Mercury and the Moon) have had a much lower geologic activity and less-effective re-surfacing processes and this has allowed their impact craters to remain largely free from the destroying effects. Venus is somewhere in between: It has almost 1000 impact craters [17-20] but none of them date back to the Venusian early history [18]. This peculiar planetary environment and geologic history has resulted in several crater-related variations and detail, which, if studied and understood in details, may give additional new information of the crater-formation processes as well as of the history of Venus (cf. Fig. 3).

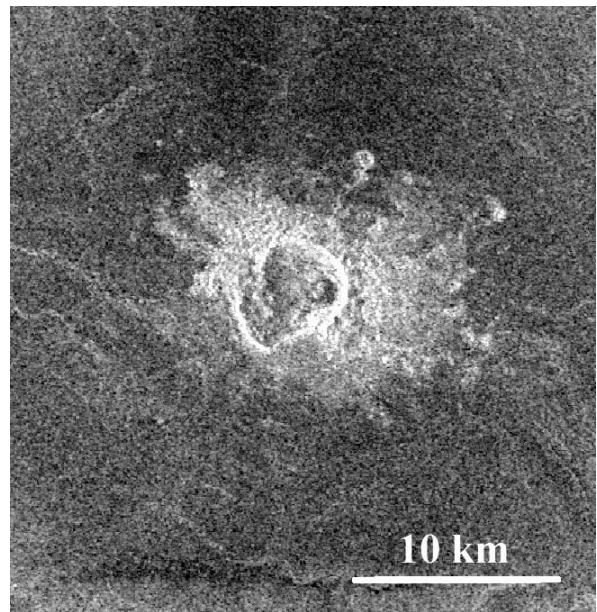
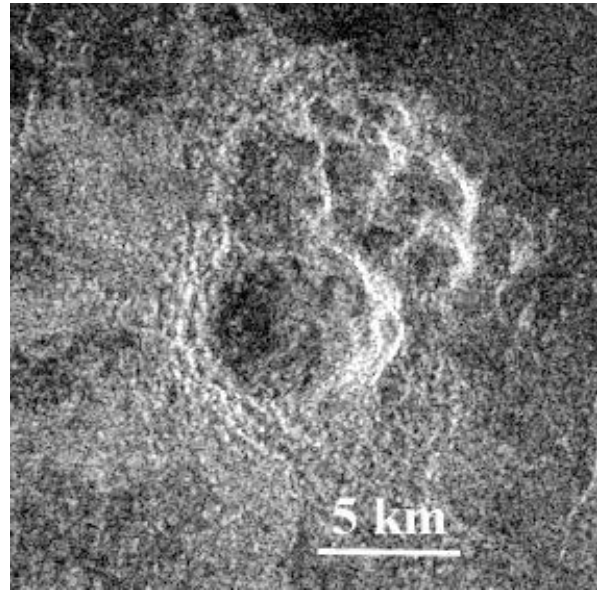


Fig. 4. On Venus, the shape of the impact crater correlates with the diameter. In general, the smallest impact craters (2-5 km) have multiple basin interiors (upper, Jutta crater centered at $0^{\circ}\text{N}/142.6^{\circ}\text{E}$) and the slightly larger impact craters (5-16 km) have irregular rim shapes (lower, Veta crater centered at $42.6^{\circ}\text{N}/349.5^{\circ}\text{E}$).

The size distribution of the Venusian impact craters shows that the smallest impact structures with a few kilometers in the size are not as plentiful as expected from the size-frequency distribution obtained from the other planets. The absence of impact craters less than 1.5 to 2 km in size, the complicate or multiple form of the impact craters a few kilometers in size [17, 21], and

the deficiency of craters smaller than 30 km in size indicate that the dense Venusian atmosphere has a strong effect to the smallest impacting bodies. The thick atmosphere prevents the smallest impactors from cratering the surface in an effective way either by eroding the smallest ones totally or breaking the slightly larger ones into pieces before their contact with the surface, and eroding the still larger ones partially during the entry phase [e.g. 21-24 cf. Fig. 4]. A study of the smallest craters would add to our information of the impactor type distribution as well as of the disruption and deceleration of the atmosphere-penetrating bodies.

The approximately 1000 craters of 1.5 – 280 km in diameter on the Venusian surface of $460 \times 10^6 \text{ km}^2$ are basically randomly distributed around the planet without any indications of such a clear tendency that is visible on Mars and shows a distinct dichotomy. Compared to Mars, the distribution of impact craters on Venus is random as expected from the stochastic nature of impact events. This implies that Venusian impact craters at large are not distorted by a major geologic process.

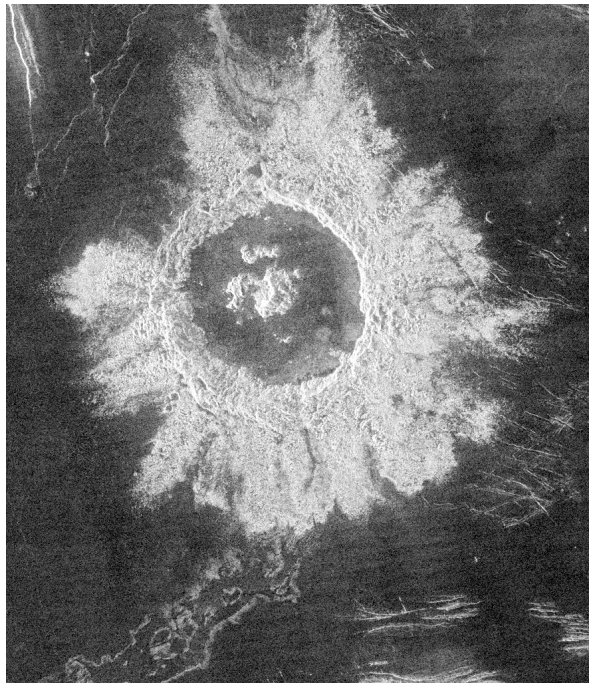


Fig. 5. The impact crater Danilova ($-26.4^\circ\text{S}/337.2^\circ\text{E}$) is 50 km in diameter. It has a central peak complex and a fresh-looking bright ejecta but its floor is flooded by lavas and outflows have changed its ejecta blanket.

Most impact craters on Venus display rather fresh-looking details [18,20,21; cf. Fig. 5]. Early analysis of Magellan radar data indicated that only a small

number of them appeared to be embayed by volcanic lavas (Fig. 6) or deformed tectonically (Fig. 7). There are no such old, heavily cratered terrains on Venus that are found on the Moon, Mercury and Mars. Most of surface of Venus was thus formed in rather late in the Venusian history during a relatively short geological time scale. The oldest impact craters have been connected with the peak phase of regional plains formation (cf. Fig. 6) perhaps by flood-basalt type volcanism with the following impact events contributing to the present random crater decoration on the Venusian surface.

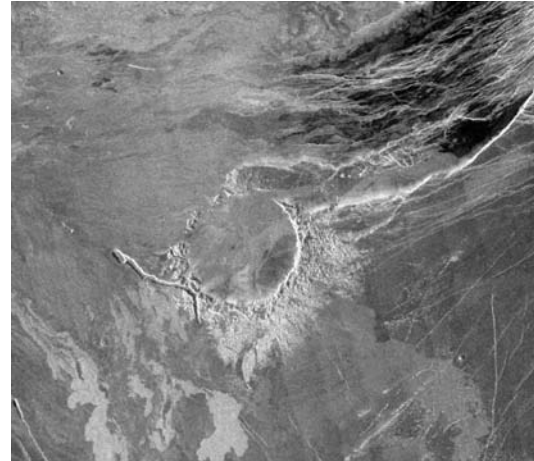


Fig. 6. A small part of the Venusian impact craters is this middle of the disappearing process as is the 60-km size crater Alcott ($-59.5^\circ\text{S}/354.4^\circ\text{E}$).

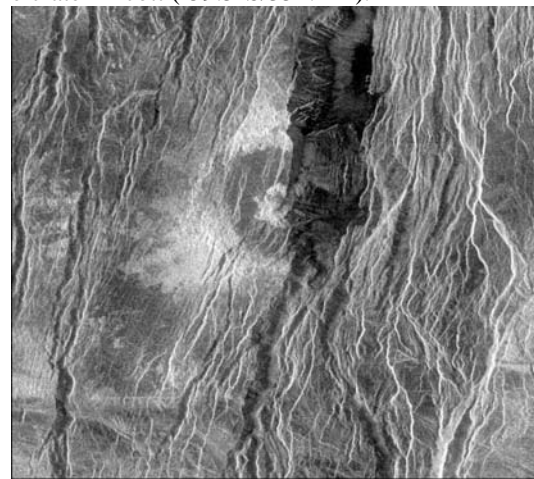


Fig. 7. The 37-km crater Balch ($29.9^\circ\text{N}/282.9^\circ\text{E}$) has been cut by a rift valley formation (Devana Chasma in northern Beta Regio). Prior to the rifting events, the crater floor was covered by lavas.

Morphology - and especially the shape - of an impact crater correlates well with its diameter. Many of the smallest craters ($< 5 \text{ km}$) are multiple and the slightly larger ones (~ 5 to $\sim 15 \text{ km}$) have irregular shapes [21,

25; cf. Fig. 4]. Transition from an impact crater cluster or field to a single crater takes place gradually when approaching this upper diameter. The impact craters above ~12 km in size are circular and the 10-30 km craters have a central peak which may be partly covered by lavas. The larger craters up to 60 km in size have flat floors and possible peak rings (Fig. 8) while the largest craters may have multiple rings [18].

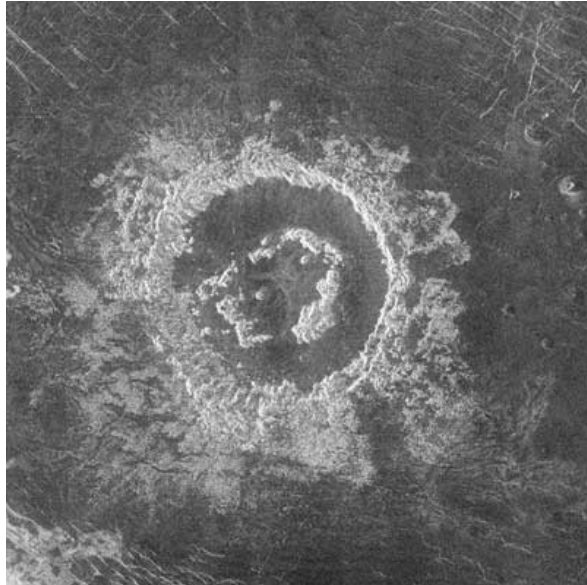


Fig. 8. The 54-km diameter Barton impact crater (27.4°N/337.5°E) possesses a discontinuous peak ring. The flat radar-dark floor of the crater is covered by lavas. The ejecta has been partially covered by lavas and modified by outflows. At least part of the outflows seem to be younger than the surrounding lava plains.

Most of the impact craters have been thought to be pristine ones. A smaller number of the craters would then have been deformed by tectonic structures and only 4% covered by volcanic materials [18]. This would allow the time period of geologic activity which formed majority of the landforms to be rather short. However, a significant fraction of craters appear to have experienced some volcanic modification. Features such as a dark halo, a parabola, and deep radar-bright floor may distinguish truly pristine craters [cf. 26]. Herrick [26] noted that actually many of the previously thought pristine craters may in fact be located lower than the very top in the stratigraphy, by showing evidence of complex post impact volcanic and tectonic events.

The ejecta blankets of Venusian impact craters are mostly blocky and radar-bright (Figs. 4 to 8). They extend on average approximately one crater diameter from the crater rim [e.g. 18]. Many craters show

significantly directed bright ejecta indicating oblique impact events [18,27; cf. Fig. 4, for example].

In addition to the traditional ballistic ejecta blankets many Venusian impact craters display outflows from or from within the radar-bright ejecta field [18,21,27,28; Figs. 3, 5, 8]. These outflow formations - predominantly found around large craters - have typical lava flow morphology and some flows show evidence of their small thickness. The outflows may extend several crater radii from continuous blocky ejecta. Their location may also correlate with the asymmetry of continuous ejecta which is supposed to be the result of the small impact angle [e.g. 27; Fig. 5]. The outflow formation may have taken place before, during or after the emplacement of the continuous ejecta. Basically all the models for the formation of this kind of feature include the idea that the flow mechanisms may have involved impact melt and vapor admixed with target rock fragments in an oblique impact [21,25,29-34; see also 35]. Fine-grained, turbulent, dense and hot impact melt vapor cloud behaved like a pyroclastic flow or the impact melt itself behaved like a volcanic lava flow. We also propose that the crushed impact ejecta that accumulated on the surface, may have acted as an insulation layer. It prevented the normal heat transport to the surface and the additional heating of fine-grained ejecta material resulted in later melting and outflow formation (Figs. 5, 8).

The impact crater interiors provide clues to the crater formation and deformation. Dark crater floors (Figs. 3, 5, 7, 8) have evidently been covered by a large amount of volcanic material or impact melt [36-39], because dark-floored craters are shallower than bright-floored craters [40] and there are systematic differences in floor brightness, elevation and diameter between dark-floored and bright-floored craters [38]. The bright-floored craters (Fig. 4) may then display either a more original fall-back ejecta, or lavas with a different viscosity and cooling, or altitude-related variations in impact chemistry. The blocky bright material is evident on the floors of young impact craters with a dark parabola. There are no young craters with dark floor deposits [41,42]. This allows a conclusion that the bright crater floors may in many cases be primary and that the dark crater floor filling is secondary. This also implies that there may be more Venusian impact craters, which have been influenced by volcanic modification after the impact event, than previously thought [e.g. 38,39].

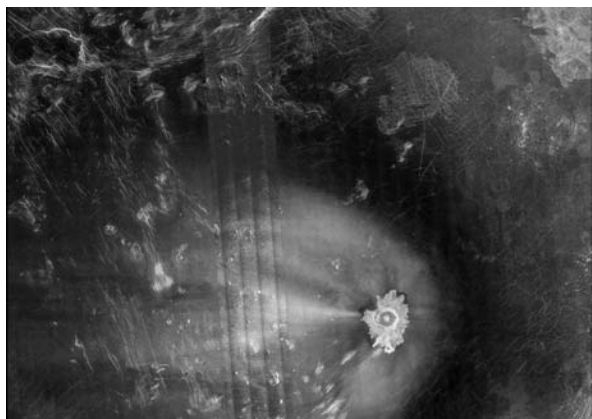


Fig. 9. The general east-to-west wind system on Venus moves high-rising ejecta particles to the western direction to form parabolic deposits as here in the case of the 30-km size crater Adivar ($8.9^{\circ}\text{N}/76.2^{\circ}\text{E}$).

4. IMPACT CRATERS AND AEOLIAN FEATURES

The Venusian impact craters are also connected to certain aeolian features. Approximately 6000 wind-related features have been identified on Venus [43-46]. Sometimes the wind streaks associate with impact craters, which are evident source of fine debris (cf. the crater Cohn in Fig. 3) but 68% of the wind streaks have no distinguishable association with an impact crater [45,46]. Along the time also the originally crater-related wind streaks may become separate from their source as the wind moves the material away. This is reflected by the typical diffuse lateral boundaries in the wind streaks.

The parabola deposits (Figs. 9, 10) provide an interesting group of crater- and atmosphere-related features. There are 55 craters larger than about 20 km in diameter, which have westward open radar-dark parabolas around them [17,18,21,41,47]. The zonal east-to-west winds move ejecta mainly to the western direction to form parabolic ejecta deposits of a few centimeters to a few meters thick [41,48,49]. This may resemble the air-fall deposition after a nuclear explosion or after an explosive volcanic eruption on the Earth [50].

There are also wind streaks (Type-P streaks, Fig. 9) associated with about 70% of the identified parabolic ejecta deposits [43,45,46]. The Type-P streaks may have been formed by the deposition of impact ejecta raised high enough into the atmosphere and transported downwind [44,46]. The idea of the role of high zonal winds in Type-P streak formation was tested by measuring all Venusian wind streaks and by

removing then the parabolic streaks. Downwind-directed parabolic Type-P streaks were found to indicate the high altitude westward winds while the non-parabolic streaks revealed totally different directions and aspects of the atmospheric circulation [46].

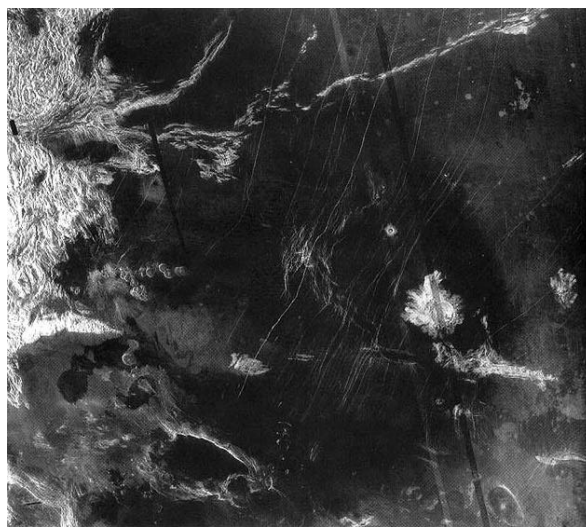


Fig. 10. The dark parabola covers lava plains around crater Stuart ($-30.8^{\circ}\text{S}/20.2^{\circ}\text{E}$) located to the east of Alpha Regio.

The parabolic ejecta deposits connected to the 55 impact localities indicate an effective long-distance material transport away from the impact craters they originated from (Figs. 9, 10). These deposits mix the surface rocks with a thin fine-grained layer that covers the original surface Venus-wide [50]. This material was proposed by Basilevsky et al. [50] to have been seen and analyzed on Venera landing sites (Fig. 2). The question is then if - and at what extent - this air-fall impact ejecta affected or even profoundly modified the rock analyses?

Many impact craters on Venus have surrounding halos visible in radar images (Figs. 9, 11, 12). Dark mantles are typical aeolian features connected to impact craters [18,21]. The impact crater halos have different sizes and forms around the impact crater and its ejecta field. It is concluded that the dark mantle is connected to the fine debris formed in impact event and it can be thus considered as a special facies of an impact crater ejecta deposit. The material did, however, settle down through the atmosphere and, as seen in freshest crater-associated radar-dark parabola, the deposition was strongly controlled by wind. This is a reason why the dark mantles have also to be considered aeolian [50-52]. Many dark mantles have already lost their strict contact to impact craters and they now occupy wind-shadow localities in local topography. There are also

transitions found from dark halo craters to dark spots or splotches with no crater in the center [18,20,21]. The impactor debris has been proposed [21] but the origin of the features may also be in the impact-induced atmosphere shock waves crushing the surface [21] or in supersonic winds cleaning-up the surface and leaving a radar-bright rubble around the site [53; cf. Figs. 11,13].

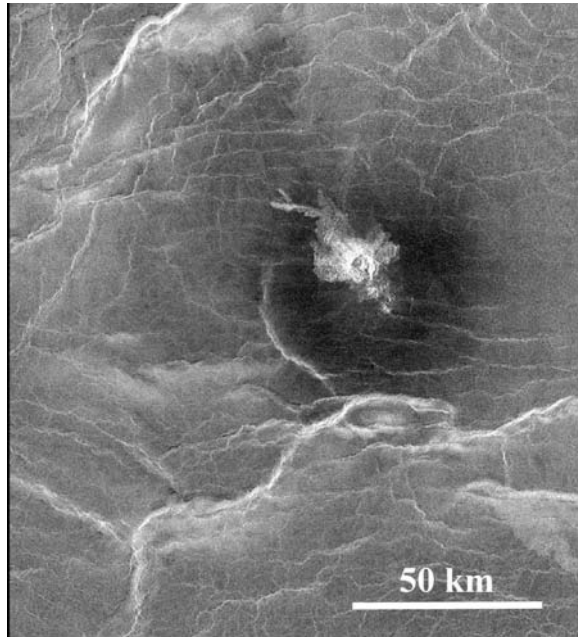


Fig. 11. Many fresh-looking impact craters on Venus have dark or bright halos surrounding their ejecta formations. The outflow and ejecta indicate an oblique impact from the southeast for the 6 km crater Rampyari (50.6°N/179.3°E).



Fig. 12. The 19-km diameter impact crater Jeanne (40.1°N/331.5°E) has two surrounding dark area

types. The very dark northern area resembles a fine-grained halo. The radar-dark area in the west has a fingered lava-like contact with the surrounding brighter flows. The actual ejecta is triangular in shape. If the outflow lobes were made by any direct impact-related process, the oblique impact came from SE.

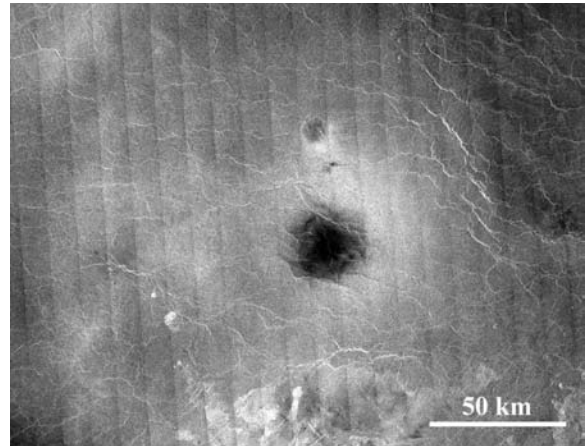


Fig. 13. The transition from dark halo craters (cf. Fig. 11) to dark splotches (the example at 8.7°N/333.5°E) without any crater in the center indicates that the smallest impacting bodies were destroyed in the atmosphere to send only a shock wave to effect the surface.

5. IMPACT CRATERS AND AGE DETERMINATION

In principle, the population of Venusian impact craters provides also a tool for age determination. The impact crater counting and surface age determination based on the crater density on the unit is currently the only available method to establish the ages and time durations of different geologic events and processes on planets we do not have any samples. There are several estimations of the average age of the Venus' surface: $288+311/-98 \times 10^6$ years [20], $400-800 \times 10^6$ years [17], $800+800/-400 \times 10^6$ years [54] and $750+250/-450 \times 10^6$ years [23]. Due to the statistical nature of crater density dating, it would need a large sample of impact craters. Low number of craters on areas covered by coronae or other small features (2 craters/ 10^6km^2 !) does not allow age estimations, which are statistically dependable and the obvious inaccuracy is too large [55]. The impact crater densities can not be used for absolute or relative age determination for a single Venusian structure or small unit. Impact craters provide tools for age determination for large areas or globally only. For small areas and single structures they can not be used and we have to determine relative ages only by geological relationships of units and structures.

6. IMPACT CRATERS AND RE-SURFACING

Some points of the re-surfacing history and the age of the surface of Venus can and have been made:

A) The resurfacing is thought to have been dominated by volcanism and/or tectonics.

B) Majority of craters are unaffected by the main volcanic and tectonic activity even if a part of them show a more complex history and may not locate – strictly speaking – on the highest top of the stratigraphic column [26, compare also with the dark-floor craters above and Fig. 14].

C) The spatial distribution of impact craters is statistically indistinguishable from random distribution, which leads to the hypothesis of a major resurfacing event approximately 300–1000 Ma ago [17,20,23; compare also with 18,56,57 and other references above]. If this is true, there appears to have been only limited geologic activity since that time (cf. with the following paragraph).

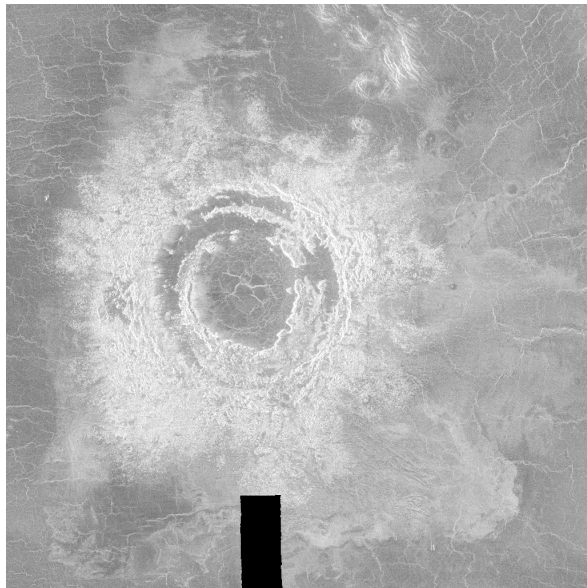


Fig. 14. The 79.4 km size impact crater Mona Lisa (25.6°N/25.1°E) indicates extended geologic activity and numerous crater modification features. It has a complex inner ring system but the rest of the floor has been covered by lava flows. The ejecta has been eroded and partly fluidized – evidently by post-impact events.

D) Recently, it was suggested that the impact crater population is not spatially random or the randomness is not necessarily destroyed by Venusian resurfacing, as large scale catastrophic events are not necessarily

needed to explain the magmatic activity of Venus [58]. If this is true, the re-surfacing could have extended over as much as 2.5 Gyr in time. This extended resurfacing may not have been catastrophic as proposed earlier and geologic activity may have occurred at more uniform rates over time [59] or the magmatic events may have been steadily decreasing in size during this time [58]. This increases the need to study the Venusian impact craters and related structures in a more detailed way.

7. DISCUSSION OF THE VENUSIAN GEOLOGIC HISTORY

There are still two models in Venusian re-surfacing:

1) The directional history model assumes that Venus has had a history with a series of epochs, each represented by a different volcanic or tectonic process on a global scale [60-62]. In the global stratigraphy this means that similar geological units were formed simultaneously. In this model, the youngest units that postdate the emplacement of regional plains consist of impact craters (of almost all of them), of aeolian material locating over the plains, and of dark parabola materials.

2) The non-directional history model [63,64] explains that Venus has had a complex history in which most geologic processes have operated in a non-directional fashion to a greater or lesser extent throughout the planet's history. The plains have been built up by lavas erupted in a number of different styles, each occurring throughout the history represented by the exposed stratigraphy of the planet. Non-directional history is supported by the fact that the coronae have formed throughout the Venusian history; some rifting occurred before and after the emplacement of the regional plains; in places, wrinkle ridges are formed due to regional stresses and both pre- and postdate the emplacement of the plains [65]; and – even if we do not know the absolute ages of the main bodies of the volcanic edifices – the latest lava flows from volcanoes are younger than the regional plains. Non-directional geology has operated on Venus at least locally and some regions are characterized by repeated episodes of volcanism and tectonics.

8. SUMMARY

The small number of Venusian impact craters reflects the relative young age of the surface formations. Based on the impact crater statistics, it is, however, not possible to draw a definitive conclusion of the absolute surface age nor of the directional or non-directional characteristics of the re-surfacing involved.

Even if a surface age of $750 \pm 250 / -450 \times 10^6$ years (crater retention age) is generally accepted, it may not cover all surface units and re-surfacing events. The proposed small deviation from the strict randomness in the spatial distribution of craters and the general decrease in magmatic activity along time may both point to the same direction.

The Venusian dense atmosphere is also partially responsible for the lower-than-expected number of small craters with diameters less than 30 kilometers. There is a clear relation between the crater size and type: The small-size craters tend to have irregular multiple depressions while slightly larger ones have irregular rims, and the circular crater shape is reached in craters still larger in their diameter. There are indications that the depth to diameter relation in Venusian impact crater population may not be the same than on other terrestrial planets. This may either reflect the atmospheric breaking effect or depend on the fact that rather many Venusian impact craters have dark floors due to lava or impact melt infilling.

Actually, a significant fraction of Venusian impact craters may have experienced some volcanic modification, and features such as a dark halo, a parabola, and deep radar-bright floor may distinguish truly pristine impact craters. The very smallest impacting bodies have totally broken up in the atmosphere, and the resulted high pressure wave event has created dark splotches on the surface without any indication of crater excavation. The splotches may also indicate sites of the youngest impact events because aeolian processes also tend to modify the impact features as seen from the parabola and wind streak distribution.

9. REFERENCES

1. Counselman C. C., et al., Wind Velocities on Venus: Vector Determination by Radio Interferometry, *SCIENCE*, Vol. 203, 805-806, 1979.
2. Counselman C. C., et al., Zonal and Meridional Circulation of the Lower Atmosphere of Venus Determined by Radio Interferometry, *J. GEOPHYS. RES.*, Vol. 85, 8026-8030, 1980.
3. Kerzhanovich V. V. and Marov M. I., The Atmospheric Dynamics of Venus According to Doppler Measurements by the Venera Entry Probes, *In: Venus*, Eds. Hunten D. M., et al., 766-778, Univ. of Arizona Press, Tucson, 1983.
4. Ford P. G. and Pettengill G. H., Venus Topography and Kilometer-Scale Slopes, *J. GEOPHYS. RES.*, Vol. 97, 13103-13114, 1992.

The most intriguing features of the Venusian impact craters are numerous lava-like outflows. They extend by several crater radii from the continuous blocky ejecta and are predominantly found around large craters. Their occurrence has been proposed to correlate with asymmetric ejecta and oblique angle of impact. The fine-grained, turbulent, dense and hot impact melt and vapor cloud may behave like a pyroclastic flow, and the impact melt itself may behave like volcanic lava flow during the impact event. In places, the outflows seem, however, to originate from within the ejecta deforming the ejecta formation. This indicates a post-impact process, possibly related to the fine-grained ejecta layer that isolates the underlying surface material perhaps allowing it to heat and later melt.

There are still unknown features in Venusian craters that deserve to be studied in detail. These include both strictly crater-related structures, but it is also possible to find new evidence and insights into the geology and development of the planet itself. Studies of the impact crater formation in the extreme Venusian environment may also reveal additional aspects in the more general crater formation process that are neglected when studying the more conventional impact craters on the Earth, Moon and Mars: Venus provides the necessary additional new window into this geologic phenomenon important all over in the history of the Solar System.

5. Florensky K. P., et al., Geomorphic Degradations on the Surface of Venus - an Analysis of Venera 9 and Venera 10 Data, *SCIENCE*, Vol. 196, 869-871, 1977.
6. Florensky C. P., et al., Venera 13 and Venera 14 - Sedimentary Rocks on Venus?, *SCIENCE*, Vol. 221, 57-59, 1983.
7. Basilevsky A. T., et al., Panoramas of the Venera-13 and Venera-14 Landing Sites /A Preliminary Analysis/, *SOL. SYS. RES.*, Vol. 16, 97-107, 1983.
8. Garvin J. B., et al., Venus - the Nature of the Surface from Venera Panoramas, *J. GEOPHYS. RES.*, Vol. 89, 3381-3399, 1984.
9. Basilevsky A. T., et al., The Surface of Venus as Revealed by the Venera Landings: Part II, *GEOL. SOC. AM. BULL.*, Vol. 96, 137-144, 1985.
10. Vinogradov A. P., et al., The Content of Uranium, Thorium, and Potassium in the Rocks of

- Venus as Measured by Venera 8, *ICARUS*, Vol. 20, 253-259, 1973.
11. Surkov Y. A., Geochemical Studies of Venus by Venera 9 and 10 Automatic Interplanetary Stations, *PROC. LUNAR PLANET. SCI. CONF. 8th*, Vol. 8, 2665-2689, 1977.
 12. Surkov Y. A., et al., Determination of the Elemental Composition of Rocks on Venus by Venera 13 and Venera 14 /Preliminary Results/, *J. GEOPHYS. RES. SUPPL.*, Vol. 88, 481-493, 1983.
 13. Surkov Y. A., et al., New Data on the Composition, Structure, and Properties of Venus Rock obtained by Venera 13 and Venera 14/, *J. GEOPHYS. RES. SUPPL.*, Vol. 89, 393-402, 1984.
 14. Surkov Y. A., et al., Venus Rock Composition at the VEGA 2 Landing Site, *J. GEOPHYS. RES. SUPPL.*, Vol. 91, 215-218, 1986.
 15. Surkov Y. A., et al., Uranium, Thorium, and Potassium in the Venusian Rocks at the Landing Sites of VEGA 1 and 2, *J. GEOPHYS. RES.*, Vol. 92, 537-540, 1987.
 16. Barsukov V. L., Venusian Igneous Rocks, *In: Venus Geology, Geochemistry, and Geophysics - Research Results from the USSR*, Eds. Barsukov V. L., et al., 165-176, Univ. Arizona Press, Tucson, 1992.
 17. Phillips R. J., et al., Impact Craters and Venus Resurfacing History, *J. GEOPHYS. RES.*, Vol. 97, 15923-15948, 1992.
 18. Schaber G. G., et al., Geology and Distribution of Impact Craters on Venus: What are they Telling Us?, *J. GEOPHYS. RES.*, Vol. 97, 13257-13301, 1992.
 19. Herrick R. R. and Phillips R. J., Implications of a Global Survey of Venusian Impact Craters, *ICARUS*, Vol. 111, 387-416, 1994.
 20. Strom R. G., et al., The Global Resurfacing of Venus, *J. GEOPHYS. RES.*, Vol. 99, 10899-10926, 1994.
 21. Phillips R. J., et al., Impact Craters on Venus - Initial Analysis from Magellan, *SCIENCE*, Vol. 252, 288-297, 1991.
 22. Herrick R. R. and Phillips R. J., Effects of the Venusian Atmosphere on Incoming Meteoroids and the Impact Crater Population, *ICARUS*, Vol. 112, 253-281, 1994.
 23. McKinnon W. B., et al., Cratering on Venus: Models and Observations, *In: Venus II - Geology, Geophysics, Atmosphere, and Solar Wind Environment*, Eds. Bougher S. W., et al., 969-1014, Univ. Arizona Press, Tucson, 1997.
 24. Cochrane C. G. and Ghail R. C., Topographic Constraints on Impact Crater Morphology on Venus from High-Resolution Stereo Synthetic Aperture Radar Digital Elevation Models, *J. GEOPHYS. RES.*, Vol. 111, DOI:10.1029/2005JE002570, 2006.
 25. Herrick R. R., et al., Morphology and Morphometry of Impact Craters, *In: Venus II: Geology, Geophysics, Atmosphere, and Solar Wind Environment*, Eds. Bougher S. W., et al., 1015-1046, Univ. Arizona Press, Tucson, 1997.
 26. Herrick R. R., Updates Regarding the Resurfacing of Venusian Impact Craters, *LUNAR PLANET. SCI. XXXVII*, #1588, 2006.
 27. Schultz P. H., Atmospheric Effects on Ejecta Emplacement and Crater Formation on Venus from Magellan, *J. GEOPHYS. RES.*, Vol. 97, 16183-16248, 1992.
 28. Asimow P. D. and Wood J. A., Fluid Outflows from Venus Impact Craters: Analysis from Magellan Data, *J. GEOPHYS. RES.*, Vol. 97, 13643-13666, 1992.
 29. Duval D. M. and Wood C. A., Impact Crater Flows on Venus: Morphological Evidence for Complex Ejection Dynamic, *LUNAR PLANET. SCI. XXIII*, 321-322, 1992.
 30. Edmunds M. S. and Sharpton V. L., Characterization of Ejecta Facies Around Large Venusian Craters: Implications for the Origin of Flow-Like Ejecta, *LUNAR PLANET. SCI. XXIII*, 329-330, 1992.
 31. Chadwick D. J. and Schaber G. G., Impact Crater Outflows on Venus: Morphology and Emplacement Mechanisms, *J. GEOPHYS. RES.*, Vol. 98, 20891-20902, 1993.
 32. Sugita S. and Schultz P. H., Impact Ejecta Vapor Cloud Interference Around Venus Craters, *LUNAR PLANET. SCI. XXV*, 1355-1356, 1994.
 33. Johnson J. R. and Gaddis L., Modeling of Fluidized Ejecta Emplacement Over Digital Topography on Venus, *J. GEOPHYS. RES.*, Vol. 101, 4673, 1996.
 34. Schaber G. G., et al., Venus Impact Craters and Ejecta: Relationships between Selected Morphologic Parameters, *LUNAR PLANET. SCI. XXVIII*, 1239-1240, 1997.
 35. Purdie P. and Petford N., Addams Crater, Venus: Outflow Analogous with a Submarine Debris Flow?, *LUNAR PLANET. SCI. XXXVI*, #1044, 2005.
 36. Sharpton V. L., Evidence from Magellan for Unexpectedly Deep Complex Craters on Venus, in *Large Meteorite Impacts and Planetary Evolution*, Eds.: Dressler B. O., et al., *SPEC. PAP. GEOL. SOC. AM.*, Vol. 293, 19-23, 1994.
 37. Grieve R. A. F. and Cintala M. J., Impact Melting on Venus: Some Considerations for the Nature of the Cratering Record, *ICARUS*, Vol. 114, 68-79, 1995.
 38. Wichman R. W., Internal Crater Modification on Venus: Recognizing Crater-Centered Volcanism by Changes in Floor Morphometry and Floor Brightness, *J. GEOPHYS. RES.*, Vol. 104, 21957-21978, DOI:10.1029/1997JE000428, 1999.

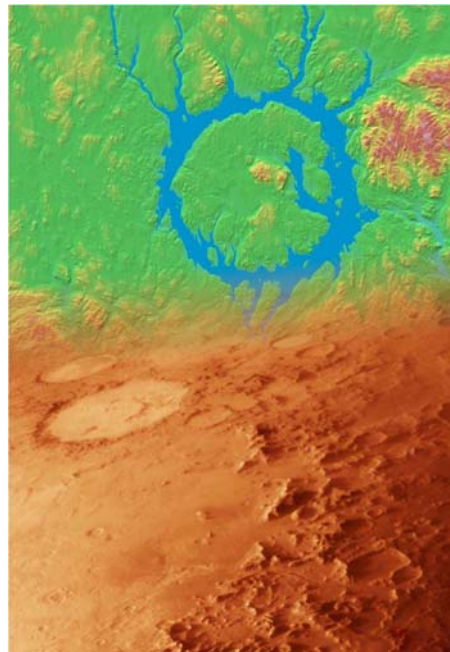
39. Herrick R. R. and Sharpton V. L., Implications from Stereo-Derived Topography of Venusian Impact Craters, *J. GEOPHYS. RES.*, Vol. 105, 20245-20262, DOI:10.1029/1999JE001225, 2000.
40. Herrick R. R. and Sharpton V. L., There are a Lot More Embayed Craters on Venus than Previously Thought, *LUNAR PLANET. SCI. XXX*, #1696, 1999.
41. Campbell D. B., et al., Magellan Observations of Extended Impact Crater Related Features on the Surface of Venus, *J. GEOPHYS. RES.*, Vol. 97, 16249-16277, 1992.
42. Izenberg N. R., et al., Impact Crater Degradation on Venusian Plains, *GEOPHYS. RES. LETT.*, Vol. 21, 289-292, 1994.
43. Greeley R., et al., Aeolian Features on Venus: Preliminary Magellan Results, *J. GEOPHYS. RES.*, Vol. 97, 13319-13346, 1992.
44. Greeley R., et al., Wind Streaks on Venus: Clues to Atmospheric Circulation, *SCIENCE*, Vol. 263, 358-361, 1994.
45. Greeley R., et al., Wind-Related Features and Processes on Venus: Summary of Magellan Results, *ICARUS*, Vol. 115, 399-420, 1995.
46. Greeley R., et al., Aeolian Processes and Features on Venus, In: *Venus II: Geology, Geophysics, Atmosphere, and Solar Wind Environment*, Eds. Bougher S. W., et al., 547-589, Univ. Arizona Press, Tucson, 1997.
47. Arvidson R. E., et al., Magellan - Initial Analysis of Venus Surface Modification, *SCIENCE*, Vol. 252, 270-275, 1991.
48. Vervack R. J. and Melosh H. J., Wind Interaction with Falling Ejecta - Origin of the Parabolic Features on Venus, *GEOPHYS. RES. LETT.*, Vol. 19, 525-528, 1992.
49. Schaller C. J. and Melosh H. J., Venusian Ejecta Parabolas: Comparing Theory with Observations, *ICARUS*, Vol. 131, 123-137, 1998.
50. Basilevsky A. T., et al., Impact Crater Air Fall Deposits on the Surface of Venus: Areal Distribution, Estimated Thickness, Recognition in Surface Panoramas, and Implications for Provenance of Sampled Surface Materials, *J. GEOPHYS. RES.*, Vol. 109, DOI:10.1029/2004JE002307, 2004.
51. Basilevsky A. T. and Head J. W., Venus: Analysis of the Degree of Impact Crater Deposit Degradation and Assessment of its use for Dating Geological Units and Features, *J. GEOPHYS. RES.*, Vol. 107, DOI:10.1029/2001JE001584, 2002.
52. Basilevsky A. T., et al., Venus: Estimation of Age of Impact Craters on the Basis of Degree of Preservation of Associated Radar-Dark Deposits, *GEOPHYS. RES. LETT.*, Vol. 30, DOI:10.1029/2003GL017504, 2003.
53. Zahnle K. J., Airburst Origin of Dark Shadows on Venus, *J. GEOPHYS. RES.*, Vol. 97, 10243-10256, 1992.
54. Zahnle K. and McKinnon W. B., Age of the Surface of Venus, *BULL. AM. ASTRON. SOC.*, Vol. 28, 1119, 1996.
55. Campbell B. A., Surface Formation Rates and Impact Crater Densities on Venus, *J. GEOPHYS. RES.*, Vol. 104, 21951-21956, DOI:10.1029/1998JE000607, 1999.
56. Turcotte D. L., An Episodic Hypothesis for Venusian Tectonics, *J. GEOPHYS. RES.*, Vol. 98, 17061-17068, 1993.
57. Herrick D. L. and Parmentier E. M., Episodic Large-Scale Overturn of Two-Layer Mantles in Terrestrial Planets, *J. GEOPHYS. RES.*, Vol. 99, 2053-2062, 1994.
58. Bond T. M. and Warner M. R., Dating Venus: Statistical Models of Magmatic Activity and Impact Cratering, *LUNAR PLANET. SCI. XXXVII*, #1957, 2006.
59. Ghail R. C., Catastrophe Not Required: A New Steady-State Model of Venus, *LUNAR PLANET. SCI. XXXVII*, #1269, 2006.
60. Basilevsky A. T. and Head J. W., Global Stratigraphy of Venus: Analysis of a Random Sample of Thirty-Six Test Areas, *EARTH, MOON, PLANETS*, Vol. 66, 285-336, 1995.
61. Basilevsky A. T. and Head J. W., Regional and Global Stratigraphy of Venus: A Preliminary Assessment and Implications for the Geological History of Venus, *PLANET. SPACE SCI.*, Vol. 43, 1523-1553, 1995.
62. Basilevsky A. T., et al., The Resurfacing History of Venus, In: *Venus II: Geology, Geophysics, Atmosphere, and Solar Wind Environment*, Eds. Bougher S. W., et al., 1047-1084, Univ. Arizona Press, Tucson, 1997.
63. Guest J. E. and Stofan E. R., A New View of the Stratigraphic History of Venus, *ICARUS*, Vol. 139, 55-66, 1999.
64. Stofan E. R., et al., Resurfacing Styles and Rates on Venus: Assessment of 18 Venusian Quadrangles, *ICARUS*, Vol. 173, 312-321, 2005.
65. McGill G. E., Tectonic and Stratigraphic Implications of the Relative Ages of Venusian Plains and Wrinkle Ridges, *ICARUS*, Vol. 172, 603-612, 2004.

Acknowledgements: This study was supported by the University of Oulu (JR, TT and VPK), Jenny and Antti Wihuri Foundation (MA), and Magnus Ehrnrooth Foundation (VPK and JR). Images were provided by Nordic Regional Planetary Image Facility.

Session S.05

Terrestrial Impact Craters and Impact Petrology

Chair: C. Koeberl



NON-IMPACT ORIGIN OF THE CRATER FIELD IN THE GILF KEBIR REGION (SW EGYPT)

M. Di Martino⁽¹⁾, L. Orti^(2,3), L. Matassoni^(2,3), M. Morelli^(2,3), R. Serra⁽⁴⁾, A. Buzzigoli⁽⁵⁾

⁽¹⁾ INAF – Osservatorio Astronomico di Torino, 10025 Pino Torinese (Italy)

⁽²⁾ Museo di Scienze Planetarie, via Galcianese 20/H, 59100 Prato (Italy)

⁽³⁾ Dipartimento di Scienze della Terra, Università di Firenze, via La Pira 4, 50121 Firenze (Italy)

⁽⁴⁾ Dipartimento di Fisica, Università di Bologna, via Irnerio 46, 40126 Bologna, (Italy)

⁽⁵⁾ Laboratorio di Geofisica Applicata–Dipartimento di Ingegneria Civile, Università di Firenze, Via S. Marta 3, 50139 Firenze, (Italy)

ABSTRACT

The present study is the result of the fieldwork carried out during a geologic expedition in the Gilf Kebir region (SW Egypt), where a large number of crater-like forms are present. It has been suggested that they could be the result of a meteoritic impact (impact breccia, shatter cones and planar fractures in quartz has been identified) or, as alternative hypothesis, a hydrothermal vent complex. From the data collected in the field and the results of the preliminary geological, petrographical and geophysical investigations, we can state that there are no evidences supporting the impact origin of the circular structures in Gilf Kebir region. As alternative hypothesis, an hydrothermal origin is suggested.

1. INTRODUCTION

In the South-Western Egyptian desert an impressive number of roughly circular, subordinatedly elliptical, structures is present, covering more than 30.000 km², East of Gilf Kebir plateau. They range from few tens of meters to more than 1 km in diameter. In 2004 [1] suggested that at least 13 of these structures, located between latitudes 23° 14' N - 23° 32' N and longitudes 23° 17' E – 27° 27' E, could be the result of a meteoritic impact. For this reason in November 2005 an Italian group of researchers has carried out an expedition in the Gilf Kebir region (Fig. 1).

The present study is an attempt to verify the impact hypothesis for the Gilf Kebir Crater Field by interpreting new field, petrographic, structural and geophysical data and possibly to suggest other kinds of origin.

In the eastern part of the Sahara region (Libya, Chad, Sudan and Egypt) several circular structures have been identified in satellite imagery, but only two (Oasis and BP) have been confirmed so far as impact craters. Five more structures (the Arkenu double “crater”, Kebira “crater” and two more large circular structures in northern Chad) need further *in situ* investigations.

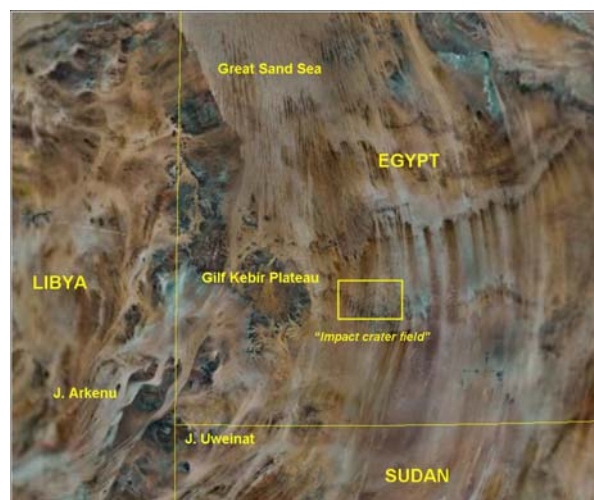


Fig. 1. Satellite image of the South-Western desert of Egypt and Gilf Kebir Crater Field area

2. GEOLOGY OF SOUTH-WESTERN EGYPT

The Gilf Kebir is a sandstone plateau about 1000 m-high (~300 m above the desert floor) larger than 8,000 km² located in the South-West corner of Egypt, near the Libya and Sudan borders. In the investigated area, located East of Gilf Kebir (Fig. 1), the outcropping rocks belongs mainly to the Sabaya Formation (Lower-Upper Cretaceous) with few outcrops ascribed to the Abu Ballas Formation (Lower Cretaceous). Both are mainly arenaceous formations: the former is made by flood-plain sandstones, with interbedded channel deposits and soil horizons; the latter by shallow nearshore marine to coastal siltstones and sandstones, with intercalations of fluviatile sandstones [2, 3].

The Precambrian-Lower Paleozoic intrusive and metamorphic rocks, outcropping in the Jebel Uweinat area and in the southern part of the Western Desert and representing the northern part of the African shield, form the basement over which deposition of clastic and carbonate sediments took place through most of the Phanerozoic. The highly-folded metamorphic complex

is intruded by undeformed plutonic bodies (forming the mountains of Jebel Uweinat and Jebel Arkenu in Libya), which, in turn, are penetrated by aplites and pegmatites [4, 3]. In the Jebel Uweinat and Western Gifl Kebir areas also Devonian-Carboniferous sandstones are present [2]; north of the Jebel Uweinat region, igneous rocks are interbedded within the sedimentary section. "Nubia Formation" (or Nubian Sandstones) is a term traditionally used in a broad range of stratigraphic and sedimentological connotations to designate continental sandstones, overlying the Paleozoic basement, of Paleozoic to Mesozoic age in Egypt and other Middle Eastern countries: it can be described as a heterochronous megafacies which can be correlated with different Upper Cretaceous-Lower Tertiary units exposed in the northern sector [4]. In south-western Egypt the Nubia Formation include several units, among which there are Sabaya Formation and Abu Ballas Formation. Volcanic rocks are represented by olivine basalts and dolerites are the most widespread igneous rocks in the area; they occur as plateau, cinder cones, dikes and sills. Their age range between the late Cretaceous and the early Oligocene [4]. Trachyte and phonolite plugs and cones represent much older volcanics (South of the Gifl Kebir area and North-East of Jebel Uweinat): these are probably associated with the late Paleozoic Hercynian movement.

3. THE CIRCULAR STRUCTURES OF EASTERN SAHARA

The eastern Sahara (in particular the Western Desert of Egypt, the eastern side of Libya, the northwestern Sudan and the northern Chad) shows the unusual presence of several circular features, with possible different origin. As already mentioned, the region surrounding the Gifl Kebir Plateau, and the top of the Plateau itself, are covered by an impressive number of crater-like forms, some of which associated with Tertiary basalts [2]. The craters interpreted as being originated by impact events by [1] belong to this large group of circular features. Also the plain between Jebel Uweinat and Gifl Kebir is covered by many volcanic crater-like features. Most of these craters have a sandstone rim and are filled with volcanic rocks (e.g. Clayton Craters [5, 6], located about 50 km North-East from Jebel Uweinat), while in some of these only the volcanic rocks are present without rims (e.g. Jebel Peter and Paul). The volcanics generally consist of trachyte and olivine basalts: the trachyte, associated with phonolites, rhyolites and microsyenites are believed to be associated with the Hercynian orogeny which affected the area during the late Paleozoic [7]. Some others of these crater-like features, which don't show volcanic rock exposures, were believed to be cryptoexplosion structures [7]. El-Baz crater (in Egypt), located about 320 km East of Kufra [5, 8], is another circular structure associated to

volcanic events. Also in northern Sudan a group of peculiar circular features (about 130 km East-Southeast of Jebel Uweinat) of unknown origin is present [7]. In the Eastern part of Libya 4 craters are present: Oasis (about 120 km North-Northeast of Kufra) and B.P. (about 80 km North of the Oasis crater), which impact origin has been confirmed [9], and the Arkenu double craters [10], which need further investigations. Moreover, the Kebira crater, on the Libya-Egypt border (about 170 km East-Northeast from Kufra): a 31 km circular structure identified by satellite imagery in March 2006 and suggested to be an impact crater and probably the source of the Libyan Desert Glass [11]; anyway, data collected during our expedition have failed to find any impact evidence in the Kebira crater area. Finally, two new possible impact structures in Chad, also detected by satellite imagery [12].

4. RESULTS OF THE INVESTIGATIONS

4.1 Study area and fieldwork

We visited 7 of the 13 structures indicated by [1] (GKCF1, 6, 7, 8, 11, 12 and 13) and some others ones in the surrounding areas (Fig. 2). On GKCF1 and 13 has been performed detailed geological survey. From four of these structures (GKCF 1, 7, 11, 13) has been collected rock samples on which petrographic studies has been performed. Geo-electromagnetic field anomalies has been measured using the Very Low Frequency (VLF) method at craters GKCF1 and 13.

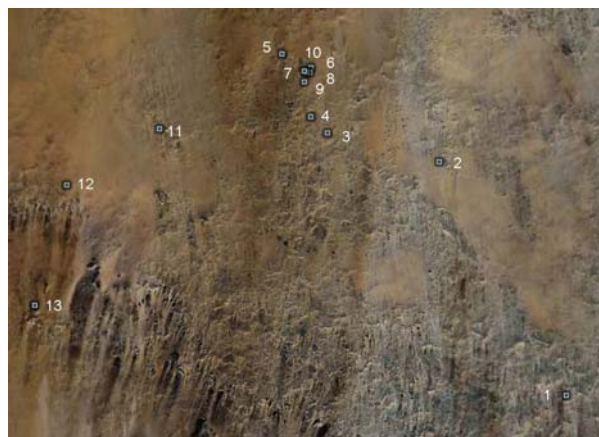


Fig. 2. The investigated area (numbers from 1 to 13 designate the supposed impact craters).

4.2 Local geological setting

In the investigated area, the outcropping lithotypes are made by medium- to coarse-grained, rarely fine-grained, moderately- to poor-sorted quartz-arenites with sub-rounded/sub-angular elements, mainly composed of quartz and minor sedimentary lithic grains (fine-grained

quartz-arenites) (Fig. 3a and 3b). The matrix, when not altered, is made by very fine quartz grains and phyllosilicates (mainly sericite); more commonly the matrix is partially or totally replaced by iron oxides/hydroxides cement and minor ferriferous carbonates. Zircon, tourmaline and muscovite are present as accessory minerals. Quartz grains sometimes show an undulose extinction and often micro-fracturing. Polycrystalline quartz is also present.

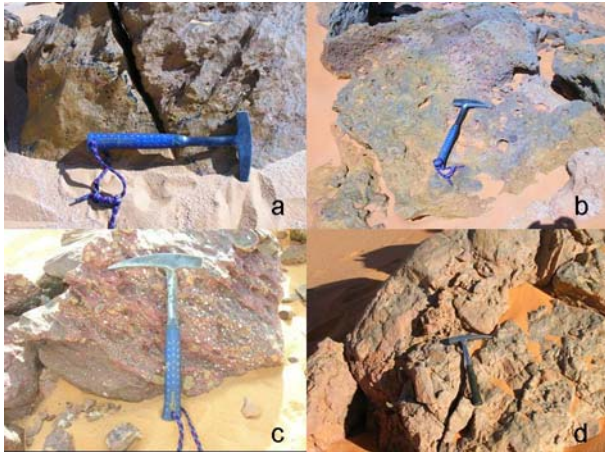


Fig. 3. Bedrock lithologies. a, b: Quartz-arenites; c: micro-conglomerates; d: intraformational breccia (Br1).

In some places the arenites grade to micro-conglomerates with rounded/sub-rounded quartz grains and sedimentary lithic clasts (fine grained quartz-arenites) mm- to cm-sized (Fig. 3c).

Intraformational sedimentary breccias (Br1) are also present; they are made by quartz-arenitic clasts, angular/sub-angular in shape, cm- to dm-sized, rarely up to 20-40 cm (Fig. 3d). Their stratigraphic position is not always clear but they seem to be intercalated with the quartz-arenites.

A different kind of breccias (Br2) outcrop in the inner part of the circular structures but also in the surroundings external parts (Fig. 4). They are made by sub-angular/sub-rounded quartz grains, mm- to cm-sized and by rock fragments (fine- to coarse-grained quartz-arenites and minor siltites), cm- to dm-sized and varying in shape from angular/sub-angular to sub-rounded. In Br2 rare boulders made of Br1 are included. When not altered, the matrix is composed of fine-grained quartz grains and phyllosilicates; often it's totally replaced by iron oxides/hydroxides cement and minor ferriferous carbonates. Zircon and tourmaline are present as accessory minerals. Quartz grains sometimes show an undulose extinction and often micro-fracturing. Polycrystalline quartz is rarely present. This second kind of breccia is often associated with fracture planes.

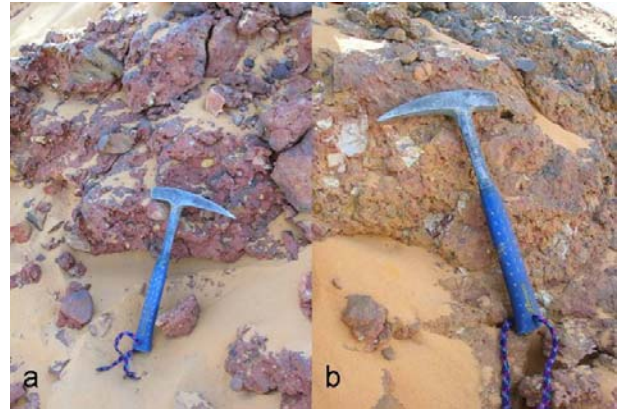


Fig. 4. Breccia Br2 from GKCF1.

As already mentioned, the craters have a roughly circular shape, in some cases very poorly evident (as in GKCF12 and 6). The bottom is covered by Quaternary aeolian sands and thus the inner part is not visible. The rim is made by tilted layers of sandstones (as in GKCF13 and 7) (Fig. 5a) or by arc-shaped nearly vertical fracture planes (Fig. 5b), as in GKCF1. These fracture planes characterize not only the “**supposed impact craters**” but are also in isolated structures in its surroundings (Fig. 5c). Iron-oxide mineralizations are often associated with the fracture zones and this is observable not only at the “crater-scale” but also at smaller scale (e.g. cm-sized fractures on the craters floor). Moreover, the fracture planes are frequently associated with breccia bodies (Br2), even though their relationships are not always clear (Fig. 5d). Linear fractures are also present, in and around the crater.

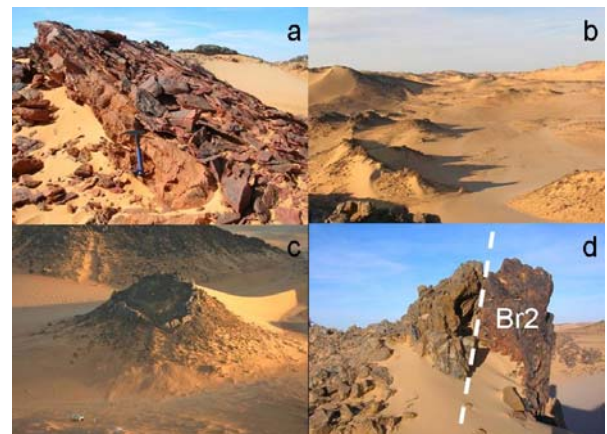


Fig. 5. a: Titled layers of sandstones, crater is on the right (GKCF7); b: Arc-shaped fracture planes (GKCF1); c: Circular structure 1 km S-SE from GKCF13, 50 m in diameter; d: Fracture plane associated with Br2 (crater is on the left) (GKCF1).

4.3 Pseudo-shatter cones

Shatter cones are conical striated fracture surfaces unequivocally indicative of meteoritic impacts on Earth. They are generally found in place in rocks below the crater floor, or in the central uplift if present, but they are also observed in isolated rock fragments in breccia units [13].

The surfaces of the outcropping rocks in the crater area are characterized by striations that, in some instances, resemble to shatter cones. From the data collected in the field, it's possible to note that the striations observed seem to be superficial and not pervasive and that they are not fracture surfaces but they occur only on the outcropping surfaces. Moreover, the same striations are visible also on the breccia surfaces (this evidence would be not compatible with an impact origin of the breccia) and on the surfaces of rocks out of the craters area (Fig. 6). Eventually, these features are characterized by directions varying always from N 20° to N 340°, in a rather consistent way with the main winds direction (from North and North-East at present, from North-West until the early Holocene [14]).

From this observations it's more appropriate to consider these pseudo-shatter cones as a result of the wind abrasion effect on the exposed rock surfaces.

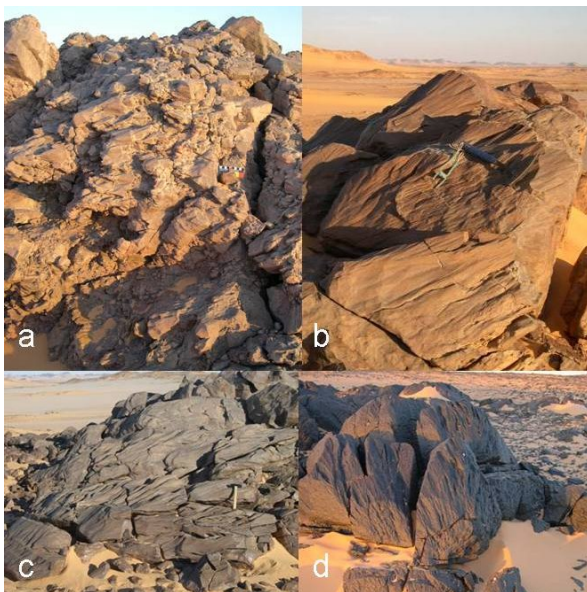


Fig. 6. Pseudo-shatter cones. a: GKCF13; b, c: GKCF1; d: El-Baz volcanic crater.

4.4 Geophysical survey

A geophysical survey has been carried out on GKCF1 and 13 to define the subsurface setting of these crater-like structures.

To know the relative thickness of the infilling deposits and then to reconstruct the morphology of the bedrock surface, we measured the geo-electromagnetic field

anomalies using the Very Low Frequency method (VLF) (e.g. [15]) with the ABEM WADI instrument. The electromagnetic anomalies in the inner part of impact craters change with a circular symmetry being the thickness of the infilling deposits different from the centre to the rim of the structures.

Both the investigated structures (GKCF1 and 13) reveal an irregular shape of the electromagnetic anomalies due both to an irregular variation of the thickness of the infill deposits and to the presence of iron-manganese oxide/hydroxide deposits in the basement rocks.

The electromagnetic anomalies measured at GKCF1 (Fig. 7) have a different trend respect to the expected ones: no circular shape anomalies are present and the higher values follow a linear distribution, locally aligned to the main fracture planes, associated with mineralizations.

The values variation measured are also due both to light topographic effects and to the presence of boulders and rock debris.

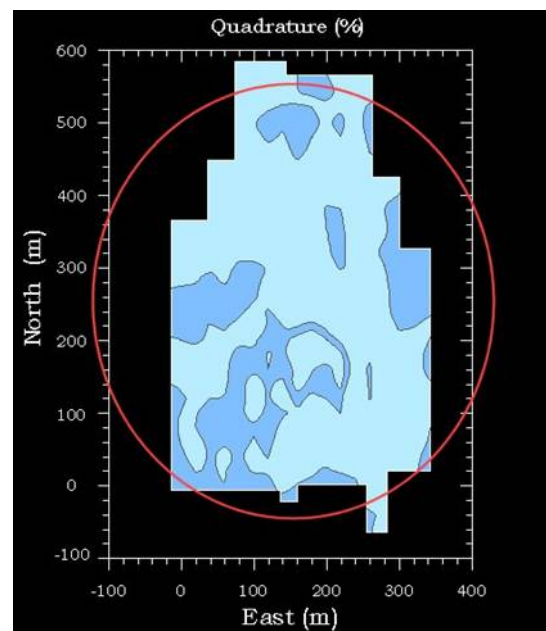


Fig. 7. Elaboration "In Quadrature" of the measured anomalies; dark blue = higher values

5. DISCUSSION

It has been suggested that the Gif Kebir crater field could be the result of a meteoritic impacts [1, 16]. The present study has been carried out in order to confirm or discount the impact origin of these structures, and possibly to suggest a different mechanism for their origin. For this reason this section is organized into topics concerning characteristics commonly used as diagnostic criteria to establish the impact origin of a structure. From the fieldwork and from the preliminary analysis, the following results can be summarized.

- *Target rocks*. They don't show any macroscopic or microscopic shock effects, in particular no planar deformation features (PDF's), no evidence of melting or glass. However, it is worth to note that, in porous sedimentary targets, the shock effects are not always well developed. It's also important to consider that impact structures in sedimentary (porous) targets result in different effects from that in non-porous crystalline targets, even if the same principal types of shock effects occur [17]. On the basis of the observations of shock effects on the Coconino Sandstones at Barringer Meteor Crater it's possible to see a progressive destruction of original texture: at the lowest pressure (< 5 GPa) the porosity is reduced to zero and the minerals are fractured and at moderate pressure (5-13 GPa) fractured quartz coexists with minor amounts of glass and coesite. That's not the case of "target rocks" in Gifl Kebir crater field: the porosity is still present, the quartz grains are only rarely fractured and never deformed, glass is absent.

For what concerns the shocked quartz, possibly identified in sandstones and breccias by [1, 16], it's important to say that the identification of PDF's based solely on petrographic techniques is now considered inadequate for positive identification of shock metamorphism. Visual identification of shock metamorphic features in the optical microscope can be somewhat ambiguous and controversial. SEM (or TEM) is the optimal tool for visual characterization and unequivocal identification of shock features. However, it's important to say that PDF's in porous target, compared to non-porous rocks, are generally rare [17]. Anyway the deformation features found in quartz grains in these rocks are significantly different from PDF's in impactites and possibly the result of "normal" tectonic processes.

Eventually, it's important to note that shocked quartz grains occur not only in parautochthonous target rocks of the crater floor, or in allochthonous lithologies, such as breccias or impact melt rocks, but also in various types of proximal and distal ejecta: the presence of shocked quartz grains in a clastic sedimentary rock (without any others impact evidence) can results from the erosion of a distant impact structure.

- *Breccias*. Interpreted as impact breccia by [1]. From the data collected in the field it's possible to say that there's the presence of two kind of breccia. Br1 is a sedimentary intraformational breccia; Br2, which has a more complex setting, a general discordant relationship with the bedrock and which is associated to the fracture planes on the craters rim, is likely genetically linked to the origin of the circular structures. They don't show any microscopic shock effects, no PDF's, no shock minerals, and no evidence of glass or melting. It's worthy to note that some impact breccias are melt-free

and with distinctive shock effects only rarely observed in the fragments ("impact lithic breccias"). This kind of breccia is often associated, horizontally and/or vertically, with units containing melts or shocked minerals and so the exact identification of the lithic breccia is possible. But that's not the case for Br2.

- *Pseudo-shatter cones*. The presence of shatter cones is considered an unequivocal fingerprints of meteoritic impacts on Earth. Other structures have similar morphology, for example natural percussion marks, slickensides, wind abrasion structures and cone-in-cone structures. As already mentioned, they are generally found in place in rocks below the crater floor, in the central uplift or in isolated rock fragments in breccia units [13]. The axes of shatter cones are generally described as pointing toward the shock wave source area but many cases of non-radial orientation are known [18]. From the analysis *in situ* and from the univocal direction of the striation, we can conclude that the pseudo-shatter cones are originated, very likely, by wind erosion.

- *Circular morphology*. The circular shape that is characteristic of the supposed impact craters is identifiable (both in the field and in satellite imagery) in many other structures in the surroundings. In the impact origin hypothesis these structures would be part of an impressive crater field made by thousands of craters with an extension of thousands of km². Moreover some of these structures are associated with basalts. The common morphology of all these structures and their huge numbers (together with the absence of impact evidences) lead to take into account the fact that all these features have a common origin and that a meteoritic impact is a very implausible hypothesis.

6. CONCLUSIONS

On the basis of our fieldwork and preliminary investigations, we can state that there are no clear and unequivocal evidence supporting the impact origin of the circular structures in Gifl Kebir region; until substantial evidence is provided, it's necessary to identify the origin of the craters in others endogenic geological processes.

The presence of such an extended field of circular structures, linked to a widespread volcanic activity in the surroundings and to the evidence of an intense fluid circulation in the craters, lead to take in consideration a hydrothermal origin for these structures (one of the hypotheses suggested also by [16]). The hydrothermal venting could account for the origin of such an extended field of nearly circular forms: what we actually see could be the result of an eroded hydrothermal vent complex. In this case the brecciation could be fluid-induced, probably for the fluctuations in pore fluids

pressure. These hydrothermal fluids could also have enriched with iron oxide during their way to the surface, crossing oxidized sediments or paleo-soils. The pre-existing sets of fractures planes could have driven partly the fluids circulation and also the development of the structures.

However, even this hypothesis is not fully satisfactory: probably these complex and peculiar features are the result of the interaction between different geological processes. At present, this hypothesis cannot be completely constrained: further investigations are necessary. Anyway, the lacking of clear evidences of a meteoritic impact and the geological framework of the investigated area, lead us to confirm the hydrothermal-volcanic hypothesis.

Eventually, as a general indication, it's important to emphasize that the analysis of satellite imagery is a fundamental tool for looking for impact craters, but has to be considered only as a preliminary step.

Acknowledgments

The authors would like to thank Vincenzo de Michele, Enrico Pandeli and Ali Barakat for constructive discussions, Benito Piacenza and Degussa Novara Technology for manufacturing the thin sections. They are also grateful to Maria Casini of the Italian Embassy in Cairo for her help in solving the bureaucratic procedures with the Egyptian authorities and Gabriella Losito of the University of Florence for providing the ABEM WADI instrument.

REFERENCES

1. Paillou Ph., et al. Discovery of the largest impact crater field on Earth in the Gilf Kebir region, Egypt, *C.R. Geoscience*, 336, 1491-1500, 2004.
2. Klitzsch E., et al. Geologic Map of Egypt 1:500000, The Egyptian General Petroleum Corporation, Cairo, Egypt, 1987.
3. Said R., *The Geology of Egypt*, A. A. Balkema Publishers, Rotterdam, Netherlands, 1990.
4. Issawi B., Geology of the southwestern desert of Egypt, in *Desert landforms of southwest Egypt: a basis for comparison with Mars*, 57-66, F. El-Baz and T.A. Maxwell Eds., National Air and Space Museum, Washington DC, 1982.
5. El-Baz F., The "Uweinat Deset" of Egypt, Libya and Sudan: a fertile field for planetary comparisons of crater forms, *Desert landforms of southwest Egypt: a basis for comparison with Mars*, 251-253, F. El-Baz and T.A. Maxwell Eds., National Air and Space Museum, Washington DC, 1982.
6. Clayton P.A., The western side of the Gilf Kebir, *Geographical J.*, 81, 254-259, 1933.
7. El-Baz F. and Issawi B., Crater forms in the Uweinat region, in *Desert landforms of southwest Egypt: a basis for comparison with Mars*, 79-89, F. El-Baz and T.A. Maxwell Eds., National Air and Space Museum, Washington DC, 1982.
8. Barakat A., El-Baz crater: basaltic intrusion versus meteoritic impact crater, *Annals of Geological Survey of Egypt*, XXIV, 167-177, 1994.
9. Abate B., et al., B.P. and Oasis impact structures, Libya: preliminary petrographic and geochemical studies, and relation to Libyan Desert Glass, *Conference Paper, 28th Annual Lunar and Planetary Science Conference*, 1997.
10. Paillou Ph., et al., Discovery of a double impact crater in Libya: The astrobleme of Arkenu, *C.R. Geoscience*, 335, 1059-1069, 2003.
11. El-Baz F. and Ghoneim E., Largest crater in the great Sahara discovered by Boston University scientists. <http://www.bu.edu/phpbin/news/releases/display.php?id=1073>.
12. González E. and Alonso S., Evidence of two new possible impact structures in Chad: separate impacts, binary asteroids or Aorounga impact chain?, *Lockne Workshop, Abstract Volume*, 2006.
13. French B.M., *Traces of catastrophe: a handbook of shock-metamorphic effects in terrestrial meteorite impact structures*, LPI Contribution N. 954, Lunar and Planetary Institute, Houston, 1998.
14. Brookes I.A., Geomorphic indicators of Holocene winds in Egypt's Western Desert, *Geomorphology*, 56, 155-166, 2003.
15. Reynolds J.M., *An Introduction to applied and environmental geophysics*, Ed. Wiley, New York 1997.
16. Paillou Ph., et al. An extended field of crater structures in Egypt: observations and hypotheses, *LPSC XXXVII*, Abs. #1286, 2006.
17. Grieve R.A.F., et al., Shock metamorphism of quartz in nature and experiment: II. Significance in geoscience, *Met. Plan. Sci.*, 31, 6-35, 1996.
18. Baratoux D. and Melosh H.J., The formation of shatter cones by shock wave interference during impacting, *Earth Plan. Sci.*, 216, 43-54, 2003.

THE METEOR CRATER, ARIZONA: A CENTURY OF EXPLORATION AND DEBATES

V. L. Masaitis

Karpinsky Russian Geological Research Institute, Sredny prospect 74

St-Petersburg, 199106, Russia

<victor_masaitis@vsegei.ru>

ABSTRACT

The scientific research of the Meteor (Barringer) Crater (also known as the Coon Butte) started more than a hundred years ago, but the ideas of its origin were contradictory. At the beginning of the XX century, mining engineer Mr. Daniel Moreau Barringer became interested in the search in this crater for a large mass of meteorite iron suitable for an economic extraction. For twenty-seven years he carried out prospecting works persisting in the idea that the crater was formed due to the collision of the Earth with a large meteorite, though some scientists attempted to explain its origin by the ordinary geological processes. The mining accompanied by exploration provided certain data on the crater's interior and on its impact origin; however, no iron body was ever found beneath the crater's floor.

The Meteor Crater was the first on the Earth that was studied purposefully over a long period. This study allowed to elaborate some criterions of impact origin of the geological objects, to reveal the mechanisms of their origin, and to compare them with the circular structures on the other planets. All these investigations are of great importance for the development of the generally recognized theory of impact cratering.

On December 5, 1905, at a session of the Academy of Natural Sciences, Philadelphia, USA, its president Mr. S. G. Dixon has announced that two members of the Academy, D. M. Barringer and B. C. Tilghman made a "...discovery that the crater of Coon Mountain or Coon Butte... is an impact crater and not a crater produced by a steam explosion, as has been supposed since the examination made of it by members of the United States Geological Survey. They have proved," he continued, "that the large crater and elevation known as Coon Mountain is the result of a collision with the Earth of a very large meteorite or possibly of a small asteroid, fragments of which are well known to the scientific world by name of the Canyon Diablo siderites... Mr. Barringer and Mr. Tilghman have presented to the Academy for publication two comprehensive papers in which they set forth in full their reasons for the above statements" [1].

The peculiar depression surrounded by a rim (Coon Butte, or Coon Mountain) as well as numerous fragments of iron, which were scattered on the surface in its vicinity, were well known to the Native Americans long before the arrival of the Europeans. Some naturalists who had visited this area at the end of the XIX century mentioned it too. However, only

the reports, which were published at the beginning of the 1906 [2, 3] gave strong impulse to the investigation of this unusual site and to the debates regarding its origin, which continued for several decades.

The data regarding the findings of numerous iron meteorites in Arizona dispersed around deep depression have attracted the attention of G. K. Gilbert, Chief Geologist of the USA Geological Survey. A. E. Foot, who had found some tiny diamonds in the meteorite sample [4], provided this information to him. Some years earlier G. K. Gilbert had studied the Moon's surface and had an idea of meteoritic origin of lunar craters [5]. At first, G. K. Gilbert supposed that Coon Butte was of impact origin too, and this scar could be the result of a collision with the Earth of a large iron meteorite, which is buried under the crater's floor, and if that is the case, it can produce a strong magnetic anomaly. The subsequent examination of this suggestion did not prove it right and later Gilbert renounced his point of view and concluded that the crater originated due to some volcanic activity. For a long time this opinion remained an official position of the US Geological Survey. It is no wonder that Barringer's and Tilghman's statements provoked a sharp discussion on the origin of the Coon Butte.

According to the modern data [6], the Meteor Crater (35° 03' N, 111° 02' W) was formed about 50,000 years ago. The diameter of a round-shaped depression is 1,220 m, its depth – 180 m. The surrounding rim is made of ejected rock fragments. The target consists of the sedimentary Permian (Coconino, Toroweap, and Kaibab formations), and Triassic (Moenkopi formation) rocks. The layers of these formations are uplifted, and dissected by faults at the crater's wall. The depression is filled with breccia, which is made up of blocks and fragments of the target rocks, and is about 200 m thick. The breccia lens is covered with lacustrine deposits of Pleistocene age. Iron fragments of the Canyon Diablo meteorite are scattered on surface around the crater and occur inside the breccia. Tiny diamonds, which are present in this octahedrite (IAB), originated after the graphite, which was transformed into high-pressure phase due to the shock compression.

Because numerous fragments of iron were found around the crater, D. M. Barringer, mining engineer and entrepreneur from Philadelphia, became interested in the prospecting for a large mass of meteoritic iron suitable for an economic mining. He first learned about the Coon Butte on the Colorado plateau and the observations and first suggestions of

G. K. Gilbert in 1902. D. M. Barringer took into account Gilbert's idea that a large iron mass may be found under the crater's floor and had founded the Standard Iron Company even before he visited the site. The purpose of this enterprise was a commercial use of a large iron body presumably lying under the crater's bottom that also contained nickel, platinum, iridium, and diamonds. D. M. Barringer was sure that a huge meteorite, which produced the crater, penetrated deep into the country rocks and has remained there under their fragments. The mining company has soon started to drive prospecting shafts, holes, and mines. This was the first case in the history of mining, when the purpose of prospecting was the search for a cosmic body.

Observations carried out by D. M. Barringer driven by the desire to confirm his assumptions, have allowed to reveal various features of morphology and internal structure of the crater, and to make a number of important finds. For example, he has found the sandstones transformed into a rock flour, particles of the oxidized iron embedded into breccia, established the inverted stratigraphic sequence in rock fragments on the crater's rim etc. Once D. M. Barringer and B. C. Tilghman obtained all these data, they have found it fitting and necessary in the autumn of 1905 to declare about the impact origin of the Coon Butte crater that they had established. However, although the reasons in favor of the impact origin of the Coon Butte were rather serious (many of them still keep the value as criteria of impact origin of circular geological structures) the United States Geological Survey chose to ignore them.

After Barringer's and Tilghman's publications there appeared a number of articles in which the idea about the meteoric nature of the crater has undergone doubts and criticism. The history of a long discussion about the crater's origin and the opportunity of detection of the meteoric iron under its bottom have been described in detail by W. G. Hoyt [7]. Following G. K. Gilbert's opinion, a significant number of the American geologists rejected the idea about the extraterrestrial origin of the Coon Butte, though some of them carrying out personal observations recognized its validity and the absence of any attributes of the volcanic phenomena within the limits of the crater.

One of the first geologists who have visited the Coon Butte was H. L. Fairchild who supported Barringer's opinion and suggested to rename the area into the "Meteor Crater" in the name of the nearest postal station [8]. One of the employees of the United States Geological Survey G. P. Merrill has also visited this place following Barringer's invitation. Merrill has shown that the varieties of the altered sandstone found by D. M. Barringer mark the successive phases of progressive transformations caused by a powerful impulse of pressure that acted over a very short time-interval and was accompanied by sharp heating. Merrill recognized that there is no alternative explanation of the crater's formation other than the one suggested by Barringer and Tilghman. In addition, he has pointed out the possibility of

evaporation of a great volume of the collided body that would explain the absence of a large iron mass at the crater's depth [9, 10]. Merrill's conclusions concerning shock metamorphism have played an important role in further discussions of the nature of the Meteor Crater; in essence they begun the development of ideas about the transformations of rocks that underwent the impact of the cosmic body. The conclusions made by Merrill compelled Barringer to get into dispute not only with the opponents of the idea of the impact origin, but also with those supporters that agreed with the impact origin idea, but objected to the idea that a significant part of the cosmic substance remains preserved inside the crater.

After several years of prospecting and observations, D. M. Barringer has presented a detailed report that contained his objections against the volcanic theory of crater's formation [11]. He categorically declared "...the further discussion about formation of the crater is a waste of time" (p.17). Yet, various hypotheses connecting the crater's origin with a karst sinkhole, magmatic stoping, or even volcanic explosion initiated with the impact of a meteorite continued to appear in the press. D. M. Barringer sharply objected to such theories. His correspondence shows that he was not indulgent to his opponents and did not show tolerance to the persisting supporters of the idea of the volcanic origin of the crater.

On the other hand, a number of geologists and especially astronomers supported D. M. Barringer's arguments and some of them pointed out to the similarity between the Meteor Crater and the craters on the Moon. At the beginning of the XX century, the statements about the meteoritic nature of the craters on its surface have been expressed repeatedly. The idea that the impact is a fundamental process in the formation and the evolution of the Solar system and that not only the Moon, but also other planets as well undergone such impacts was expressed by an astronomer T. See [12], however, outside of any link with the Meteor Crater discussion. Many other astronomers and geologists at that time took part in the discussion about the origin of the lunar craters as well.

While continuing to drill and to sink mines in the search of an iron deposit, D. M. Barringer actively corresponded with many scientists. When at the depth of 419 m the drill hole came across something very hard, he explained the breakage, which occurred by suggesting that the bit had entered into the iron mass. D. M. Barringer insisted that the impact crater could form without any explosion and that a huge meteorite still exists somewhere underneath its bottom [13].

In mid 20th, somewhat transformed mining company began to experience significant difficulties in attracting investors and finding the means to carry out further work. There were mining related problems as well. At this time, many astronomers emphasized a high probability that the main part of the iron meteorite has been evaporated at the time of

explosion, which caused the formation of the crater. Based on calculations that dealt with energies necessary to eject shattered bedrocks the astronomer F. R. Moulton estimated the possible size of the meteorite, which formed the crater. He pointed out that the initial mass of the collided body did not exceed 500,000 tons and that its significant portion must have been dispersed during the impact and the explosion. These estimates (they have not been published) finally destroyed hopes for the detection of large iron bodies inside the crater. F. R. Moulton has sent his conclusions to the president of the mining company at the end of November 1929. D. M. Barringer died of a heart attack on November 30, 1929, shortly after.

In spite of a variety of additional arguments in favor of an extraterrestrial origin of the Meteor Crater, which were published in different editions, only a small number of researchers have recognized the impact theory up until the end of the 1940th. During this period, only astronomers almost unconditionally recognized the meteoric nature of the crater, especially in connection with further development of the theory of the formation of the lunar craters and the publication of the book by R. Baldwin [14], where this theory was substantiated in detail.

A serious blow to some attempts to explain the crater's origin by essentially terrestrial processes that continued to appear in the press was delivered by a long-term work of H. H. Nininger [15]. In the vicinity of the crater and on its rim he discovered numerous particles of slag formed by fusion of various local rocks that contained magnetite spheroids enriched with cobalt and nickel. The latter could occur only from fusion or condensation and oxidation of the material of the collided body. Particles of glass slag were named impactites, in accordance with the meaning of this term offered by G. B. Shtenzel and for the first time applied to products of impact fusion by V. Barns [16].

The renewal of interest to further research of the Meteor Crater in the middle of the last century has been indirectly connected with the study of sites of the underground nuclear tests made in the USA, and also with the beginning of the epoch of the space exploration. This interest has been realized by G. M. Shoemaker, who has seen in the simultaneous geological study of the Meteor Crater and the hollows of the underground explosions an opportunity to explore in greater detail the nature of the lunar craters. He sent several samples of shocked sandstones from the Meteor Crater for research to the mineralogist E. Chao, and very soon, the coesite has been found [17]. A short time previously this mineral was synthesized by the compression of quartz at over 15 thousand atmospheres. The other high-pressure phase of SiO_2 – stishovite, has been found in these samples as well [18]. These two finds have finished long discussions about the origin of the Meteor Crater and about the formation of the other similar terrestrial objects.

The detailed analysis of the mechanism of the Meteor Crater formation undertaken by G. M. Shoemaker showed that its formation (as well as other impact craters, including lunar) is connected, mainly, with the effect of a shock wave, instead of being a direct result of the "explosion" of the collided body [19, 20]. A little bit earlier G. M. Shoemaker took part in one of the projects on remote studying of the Moon and then begun to organize the Department of Astrogeology of the USA Geological Survey in Flagstaff, Arizona. Actually, this meant the recognition of an impact origin of the Meteor Crater by Geological Survey. G. M. Shoemaker was the participant in the Apollo program in the beginning and the middle of the 1960th at which time he together with other astronaut candidates repeatedly visited the Meteor Crater that was chosen as a training ground by the NASA. Among G. M. Shoemaker's geology students were the first astronauts who have landed on the Moon [21, 22].

Special geological and other research proceeded in the Meteor Crater in the next decades; the intentions of these studies were specification of its morphology and structure, comparison with other impact objects on the Earth and with craters of the underground nuclear explosions [23, 24], the in-depth study of the transformations of the shocked rocks [25, 26], and also modeling of the cratering processes [27, 28]. G. K. Gilbert's idea about the extraterrestrial nature of the Coon Butte, which he had prematurely rejected, has born plentiful fruits many decades later.

Strange as it may seem, but D. M. Barringer who devoted the better part of his life to the exploration of the Coon Butte inadvertently worked on his scientific opponent who was one of the first to suggest the impact origin of the lunar craters. Paradoxical as it may also seem, but it was the elaboration and the substantiation of the hypothesis of the meteoric impact defended by D. M. Barringer that was further developed and worked out in detail by scientists specializing in the field of astronomy that at the end lead his mining company to its financial demise. At the same time, various works carried out in the Meteor Crater by D. M. Barringer and later by many other researchers revealed numerous important facts regarding its interior structure and shed light on the conditions of its formation.

The value of D. M. Barringer's contribution to the creation of the basis for the geological exploration of the impact structures may have even exceeded the supposed profits, which he hoped to achieve by mining the iron mass that was never found. In recognition of Mr. D. M. Barringer's contribution to the exploration of the Meteor Crater, in 1946 the crater itself was renamed in his honor [29].

The results acquired during the research of the Meteor Crater exerted great influence on the evolution of ideas regarding mechanisms of the impact cratering, and on the elaboration of various criteria of impact origin of structures similar to this crater, including structures modified by some other geological processes. One of the main results was the identification of various mineralogical and

petrographical features of shock metamorphism, which received comprehensive theoretical and experimental substantiation. In many respects due to the use of such mineralogical and petrographical criteria, the nature of a number of so-called «cryptovolcanic» or «cryptoexplosive» structures that were long a subject of debates was finally reliably determined. In the middle of the 1960th, because of the specialized research in a number of regions of the world, mainly in Europe and the Northern America, it has been shown, that some circular geological structures are in fact eroded impact craters. At the suggestion of R. Dietz, they were named «astroblemes» [30]. Further development of the geological research in this field in combination with the analysis of the remote sensing and the geophysical surveys data led to the discovery of numerous ancient impact structures on the Earth's surface, the combined number of which is now approaching two hundred. The Meteor Crater was in essence the first impact structure where the purposeful geological works accompanied by geophysical observations, drilling, and prospecting for economic minerals took place. In the second half of the last century, this arsenal of various methods of exploration of such objects, though further improved, was widely used in different regions of the world.

The first partially systematized results of such studies were widely presented at a special conference in 1966 [31]. The study of the Meteor Crater and the accompanying discussion appreciably promoted the development of separate branches of the doctrine about the impact cratering and also contributed to its formation into a new field of natural science that combined data from astronomy, meteoritics, physics of solid bodies, comparative planetology, and from various other branches of geology. The study of the Canyon Diablo meteorite also had great value; it allowed to establish abundance of some elements in space, and to develop standards of parities of isotopes of sulfur in cosmic bodies. In the middle of the 1950th, fragments of this meteorite were used to achieve first reliable estimates of the ages for the Solar System and the planet Earth.

Research carried out at the end of the last century have shown that economic mineral deposits, which were found within some impact structures, are connected with processes that had occurred in the target rocks either before the shock event, during the cratering, or at some point in a long period after formation of the impact structure [32, 33]. In a number of impact structures various ores (copper, nickel, iron, uranium, gold, basic metals), nonmetallic raw materials (technical diamonds, evaporites, combustible slates), and liquid and gaseous hydrocarbons are now found. Therefore, almost eighty years later D. M. Barringer's dreams about a possibility of discovery of economic mineral resources inside impact craters have come to fruition, although mineral deposits found in such structures have nothing to do with the remains of the meteoric substance that are found in small size craters and only as small fragments.

Widespread exploration executed during the last several decades showed that round-shaped depressions bordered with rims (they reflect the changes of morphology of their solid surfaces in the exact sense of the term «impact cratering») that form at the sites of the high-speed collisions of cosmic bodies are only one of the results of such interactions. In addition, they are also accompanied by considerable changes of the geological structure at the impact site, and by appearance of a wide spectrum of newly formed and transformed rocks – impactites and impact breccias. If the colliding body falls into the gaseous or liquid environment it produces only a short-term disturbance of these environments as was seen for example during the collision of the comet Shoemaker-Levi fragments with the outer shell of the planet Jupiter in 1994 [22]. In connection with this, in terms of etymology an earlier suggested term «coptogenesis» more precisely corresponds to the general character of the transformations that occur at such collisions [34, 35].

The ideas about the character and the consequences of cosmic collisions during the evolution of the system of bodies rotating around the Sun are now universally recognized. Impact interactions are considered a major factor of transformation of surfaces of the solid cosmic bodies (especially devoid of outer gaseous shell), and with reference to the Earth as a fundamental geological process [36], which played an essential role at an early stages of the formation of the Earth's crust and which during the subsequent epochs sporadically influenced external shells of our planet, and the evolution of biota [37, 38, 39].

Over a hundred years long history of the Meteor Crater exploration and the accompanying debates may serve as an example of the vicissitudes of scientific hypothesis that little by little was converted into the well-grounded and generally recognized theory, which became the basis of one of the fundamental lines of investigation of the Earth's and space science [40]. This history confirms once again that only firmly established and concordant observation results may reject some hypothesis, or confirm and transform it into the finalized theory. Exactly such approach allowed, on the one hand, to reject the assumptions regarding the possibility of discovery of an iron mass beneath the crater's floor, and on the other to prove the crater's extraterrestrial origin.

REFERENCES

1. Dixon S.G. (1905.) Coon Mountains and its Crater. President's statement. *Proceedings of the Academy of Natural Science of Philadelphia*, December, 5.
2. Barringer D.M. (1906.) Coon Mountain and its Crater. *Proceedings of the Academy of Natural Science of Philadelphia*, 57, pp.861-886. American

- Journal of Science, vol. XXI, May 1906, pp. 347-355.
3. Tilghman B.C. (1906.) Coon Butte, Arizona. *Proceedings of the Academy of Natural Science of Philadelphia*, 57, pp.887-914.
 4. Foot A.E. (1891.) A new locality for the meteoritic iron with a preliminary notice of the discovery of diamonds in the iron. *Am. Journ. of Science*, 3rd ser., v.42, pp.413-417.
 5. Gilbert G.K. (1893) The Moon's face: a study of the origin of its features. *Bull. of the Philosophical Society of Washington*, 12, pp.241-292.
 6. Shoemaker E.M. and Kieffer S.W. (1974.) *Guidebook to the geology of Meteor crater*. Meteoritical Society, Center for Meteorite Studies, Arizona State Univ., Tempe, Arizona, USA. 66p.
 7. Hoyt W.G. (1987.) *Coon Mountain controversies. Meteor crater and the development of impact theory*. Tuscon. The University of Arizona Press, 423p.
 8. Fairchild H.L. (1907.) Origin of Meteor crater (Coon Butte), Arizona. *Bull. of the Geological Society of America*, 18, pp.493-504.
 9. Merrill G.P. (1907). On a peculiar form of metamorphism in silicious sandstone. *Proc. US Nat. Museum*, vol. xxxii, pp.547-550.
 10. Merrill G.P. (1908.) The Meteor crater of Canyon Diablo, Arizona; its history, origin and associated meteoritic irons. Smithsonian Misl. Collections, v.50, p.4, pp.461-498; pls. 61-75.
 11. Barringer D.M. (1909.) *Meteor crater (formerly called Coon Mountain or Coon Butte) in northern central Arizona*. Paper read before the Natural Academy of Sciences in the autumn meeting at Princeton University, November 16, 1909. 24 pp. +18 plates.
 12. See T.J.J. (1910) The origin of so-called craters on the Moon by the impact of satellites, and the relation of these satellite indentations to the obliquities of the planets. *Popular Astronomy*, 18, pp.137-144.
 13. Barringer D.M. (1924) A discussion of the origin of the craters and other features of the Lunar surface. *Scientific American*, 131, pp. 10-11, 62-63, 102, 104.
 14. Baldwin R.B. (1949.) *The face of the moon*. Chicago, Univ. of Chicago Press. Pp.66-113
 15. Nininger H.H. (1954.) Impactite slag at Barringer crater. *Am. Journ of Science*, v.252, no 5. pp.277-290.
 16. Barnes V.E. (1940). *North American tektites*. Univ. Texas Publ., Houston. No 3945, p.477-582.
 17. Chao E.C.T., Shoemaker E.M., Madsen B.M. (1960.) First natural occurrence of coesite. *Science*, v.132, p.220-222.
 18. Chao E.C.T., Fahey J.J., Littler J., and Milton D.J. (1962.) Stishovite, SiO_2 , a very high pressure new mineral from Meteor crater, Arizona. *Journ. Geophys. Research*, v.67, pp.419-421.
 19. Shoemaker E.M. (1960.) Penetration mechanics of high velocity meteorites, illustrated by Meteor crater, Arizona. *International Geological Congress*, 21 sess. pp.418-434.
 20. Shoemaker E.M. (1963.) Impact mechanics at Meteor crater Arizona. In: Middlehurst B.M., Kuiper G.P. (eds.) *The Moon, meteorites and comets*, University Chicago Press, Chicago, pp.301-336.
 21. Wilhelms D. E. (1993.) *To a rocky Moon*. The University of Arizona Press, Tuscon and London. 477p.
 22. Levy D.H. (2000.) *Shoemaker by Levy. The man who made an impact*. Princeton University Press, Princeton, New Jersey. 303 p.
 23. Roddy D.J. (1978.) Pre-impact geologic conditions, physical properties, energy calculations, meteorite and initial crater dimensions and orientation of joints, faults, and walls of Meteor Crater, Arizona. *Proceedings, Lunar and Planetary Science Conference*, 9-th. New York, Pergamon Press, pp.3891-3930.
 24. Roddy D.J., et al. (1975) Meteor crater, Arizona, rim drilling with thickness, structural uplift, diameter, depth, volume, and mass balance calculations. *Proceedings, Lunar and Planetary Science Conference*, 6-th. New York, Pergamon Press, pp.2621-2644.
 25. Kieffer S.W. (1971). Shock metamorphism of the Coconino sandstone at Meteor Crater, Arizona. *J. Geophys. Res.* 76, pp.5449-5473.
 26. Hörz F., et al. (2002.) Petrographic studies of the impact melts from Meteor Crater, Arizona, USA. *Meteoritics and Planetary Science*, v.37, pp.501-531.
 27. Bryan J.B. et al. (1978). A two-dimensional computer simulation of hypervelocity impact cratering: some preliminary results for Meteor crater, Arizona. *Proc. Lunar Planet. Sci. Conf.* 9th, pp.3931-3964.
 28. Schmidt R.M. (1980.) Meteor crater. Energy of formation – implication of centrifuge scaling. *Proceedings, Lunar Planet. Sci. Conf.* 11th, pp 2099-2128/
 29. Marvin U.B. (1993). The Meteoritical Society: 1933 to 1933. *Meteoritics*. 28, pp.261-314.
 30. Dietz R.S. (1963.) Astroblemes: Ancient meteorite-impact structures on the Earth. In: Middlehurst B.M. and Kuiper G. P. (eds.) *The Moon, meteorites and comets*. University Chicago Press, Chicago. pp. 285-300.
 31. French B.M., Short N.M. (eds.) (1968.) *Shock metamorphism of natural materials*. Baltimore. Mono Book Corp. 644p.
 32. Grieve R. A. F., Masaitis V. L. (1994.) The economic potential of terrestrial impact craters. *International Geological Review*, 36, pp.105-151.
 33. Reimold W.U., et al. (2005.) Economic mineral deposits in impact structures: a review. In: Koeberl C., Henkel H. (eds.) *Impact tectonics*. Springer, Berlin-Heidelberg-New York. pp.479-552.
 34. Masaitis V.L. (1984). Impact reworking of the Earth's crust. *International Geological Congress*, 27 session, Sect.19, Comparative planetology, p.74-80 (in Russian).
 35. Masaitis V.L. (2005). Morphological, structural and lithological records of terrestrial impacts: an overview. *Australian Journal of Earth Sciences*, #5 p.509-528.

36. Melosh H.J. (1989). *Impact cratering. A geological process*. Oxford University Press, New York, Clarendon Press, Oxford. 245 p..
37. Grieve R. A. F. (1980.) Impact bombardment and its role in protocontinental growth on the early Earth. *Precambrian research*, 10, pp.217-247.
38. Glikson A. Y. (2001.) The astronomical connection of terrestrial evolution: crustal effects of post 3.8 Ga mega-impact clusters and evidence for major 3.2 ± 0.1 Ga bombardment of the Earth-Moon system. *Journal of Geodynamics*, 32, pp. 205-229.
39. Montanari A., Koeberl C. (2000). *Impact stratigraphy. The Italian record*. Lecture notes in Earth Sciences 93. Springer-Verlag, Heidelberg, 364 pp.
40. French B. M. (2004.) The importance of being cratered: the new role of meteorite impact as a normal geological process. *Meteoritics and Planetary Science*, 39, pp.169-198.

THE GEOLOGICAL RECORD OF METEORITE IMPACTS

Gordon R. Osinski

Canadian Space Agency, 6767 Route de l'Aéroport, St-Hubert, QC J3Y 8Y9 Canada,
Email: gordon.osinski@space.gc.ca

ABSTRACT

Meteorite impact structures are found on all planetary bodies in the Solar System with a solid surface. On the Moon, Mercury, and much of Mars, impact craters are the dominant landform. On Earth, 174 impact sites have been recognized, with several more new craters being discovered each year. The terrestrial impact cratering record is critical for our understanding of impacts as it currently provides the only ground-truth data on which to base interpretations of the cratering record of other planets and moons. In this contribution, I summarize the processes and products of impact cratering and provide an up-to-date assessment of the geological record of meteorite impacts.

1. INTRODUCTION

It is now widely recognized that impact cratering is a ubiquitous geological process that affects all planetary objects with a solid surface (e.g., [1]). One only has to look up on a clear night to see that impact structures are the dominant landform on the Moon. The same can be said of all the rocky and icy bodies in the solar system that have retained portions of their earliest crust. On Earth, however, erosion, volcanic resurfacing, and tectonic activity are continually erasing impact craters from the rock record. Despite this, 174 confirmed impact structures have been documented to date with several more 'new' sites being recognized each year (Fig. 1) [2].

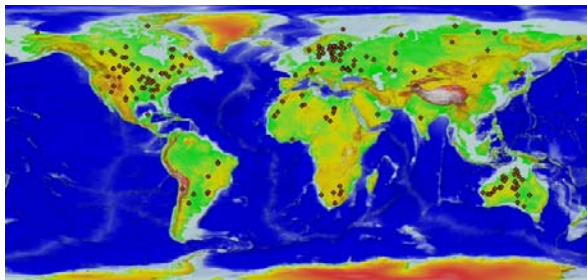


Fig. 1. Location of the 174 recognized terrestrial impact structures superimposed on a digital elevation map of the Earth. Location of structures from the Earth Impact Database [2] (see Appendix 1).

2. FORMATION OF METEORITE IMPACT STRUCTURES

The formation of hypervelocity impact craters has been divided, somewhat arbitrarily, into three main stages [3] (Fig. 2): (1) contact and compression, (2) excavation, and (3) modification. A further stage of "hydrothermal and chemical alteration" is also considered as a separate, final stage in the cratering process (e.g., [4]), and is also described below.

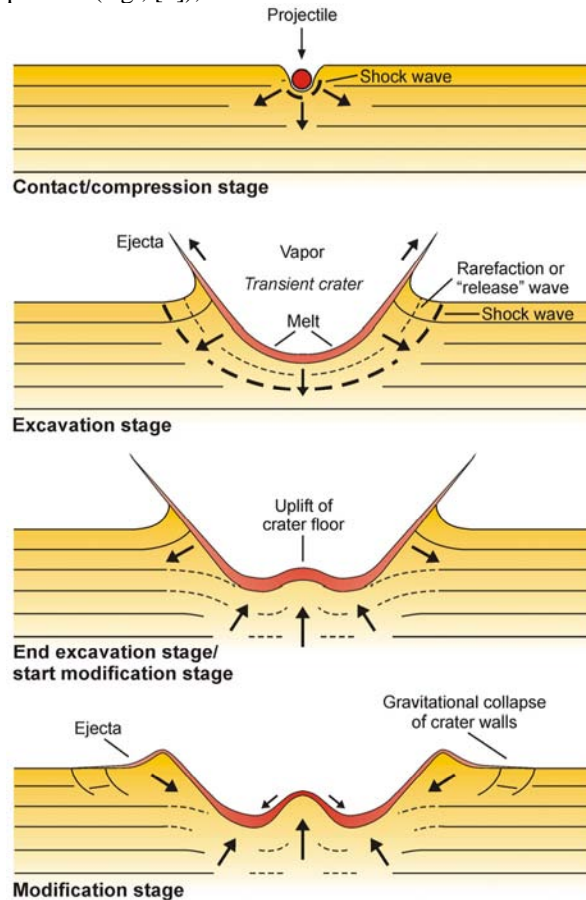


Fig. 2. Series of schematic cross sections depicting the formation of a terrestrial complex impact structure (i.e., diameter >2–4 km). From [5].

2.1. Contact and compression

The first stage of an impact event begins when the projectile, either an asteroid or comet, contacts the surface of the target (Fig. 2). The projectile penetrates no more than 1–2 times its diameter [4], before transferring its kinetic energy into the target in the form of shock waves that are created at the boundary between the compressed and uncompressed target material [6]. These shock waves subsequently propagate both into the target sequence and back into the projectile itself. When the reflected shock wave reaches the ‘free’ upper surface of the projectile, it is reflected back into the projectile as a rarefaction, or tensional wave [7]. The passage of this rarefaction wave through the projectile causes it to unload from high shock pressures, resulting in the complete melting and/or vaporization of the projectile itself [3, 6]. The increase in internal energy accompanying compression and subsequent rarefaction results in the virtually instantaneous melting and/or vaporization of a volume of target material close to the point of impact, producing characteristic impact melt rocks and glass-bearing breccias that form the crater-fill impactites in many terrestrial impact craters [7, 8].

For impact craters formed in crystalline targets, these crater-fill impact melt rocks display characteristic igneous textures and features (e.g., columnar jointing; Fig. 3). In contrast, the crater-fill impactites in craters developed in sedimentary or mixed crystalline–sedimentary targets, do not display such obvious characteristics (e.g., Fig. 4), which has led to many uncertainties regarding the importance of impact melting in volatile-rich sedimentary target rocks [5]. However, recent work has shown that impact melting is an important process during impacts into sedimentary targets [9–12] (Fig. 4).



Fig. 3. Impact melt rocks at the ~28 km diameter, ~36 Ma Mistastin impact structure, Canada. Notice the well-developed columnar jointing on the ~80 m high cliff face. Photo courtesy of D. Wilton.



Fig. 4. Crater-fill impactites at the Houghton impact structure, Canada, interpreted as carbonate-rich impact melt breccias [12].

The point at which the projectile is completely unloaded is generally taken as the end of the contact and compression stage [6]. The duration of this initial stage depends on the projectile’s size, composition, and impact velocity; however, it lasts no more than a few seconds for all but the largest basin-forming impacts [6].

2.2. Excavation stage

The transition from the initial contact and compression stage, into the excavation stage is a continuum. It is during this stage that the actual impact crater is opened up by complex interactions between the expanding shock wave and the original ground surface [6]. During the excavation stage, the roughly hemispherical shock wave propagates out into the target sequence (Fig. 2). This causes target material to be set in motion, with an outward radial trajectory. At the same time, shock waves that initially travelled upwards intersect the ground surface and generate rarefaction waves that propagate back downwards into the target sequence [6]. The combination of the outward-directed shock waves and the downward-directed rarefaction waves produces an ‘excavation flow’ and generates a so-called ‘transient cavity’ (Figs. 2, 3) [13, 14]. The different trajectories of material in different regions of the excavation flow field result in the partitioning of the transient cavity into an upper ‘excavated zone’ and a lower ‘displaced zone’ (Fig. 5). Material in the excavated zone is ejected beyond the transient cavity rim, while material in the displaced zone remains within the transient cavity [15]. It is notable that the excavation flow lines transect the hemispherical pressure contours, so that ejecta will contain material from a range of different shock levels, including shock-melted target lithologies.

A portion of the melt and rock debris that originates beneath the point of impact remains in the transient cavity [8]. This material forms the crater-fill impactites in terrestrial impact craters (Figs. 3, 4). Eventually, a point is reached at which the shock and rarefaction waves can no longer excavate or displace

target rock and melt [16]. At the end of the excavation stage, a mixture of melt and rock debris forms a lining to the transient cavity. Calculations suggest that the excavation stage for a 200 km diameter crater requires ~ 90 s [6].

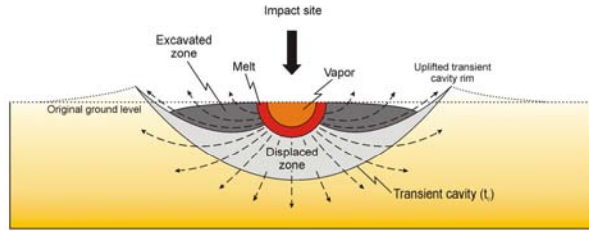


Fig. 5. Theoretical cross section through a transient cavity showing the locations of impact metamorphosed target lithologies. Excavation flow lines (dashed lines) open up the crater and result in excavation of material from the upper one-third to one-half the depth of the transient cavity. Modified after Grieve [17] and Melosh [6].

2.3. Modification stage

The effects of the modification stage are governed by the size of the transient cavity and the properties of the target rock lithologies [18]. For crater diameters $< 2\text{--}4$ km on Earth, the transient cavity undergoes only minor modification resulting in the formation of a simple bowl-shaped crater (Figs. 6a, 7). However, above a certain size threshold (generally quoted as $> 2\text{--}4$ km diameter on Earth, but see discussion in section 3), the transient cavity is unstable and undergoes modification by gravitational forces, producing a so-called complex impact crater (Figs. 2, 6b,c, 8) [19]. Uplift of the transient crater floor occurs leading to the development of a central uplift (Figs. 2, 6b). Subsequently, the initially steep walls of the transient crater collapse under gravitational forces (Fig. 2). Numerical models suggest that the maximum depth of the transient cavity is attained before the maximum diameter is reached (e.g., [20]). Thus, uplift of the crater floor may commence before the maximum diameter has been reached. As French [16] notes, the modification stage has no clearly marked end. Processes that are intimately related to complex crater formation, such as the uplift of the crater floor and collapse of the walls, merge into normal geological processes such as mass movement, erosion, etc.

2.4. Post-impact hydrothermal activity

Impact events generate pressures and temperatures that can melt and/or heat substantial volumes of

target material. Interaction of these hot rocks with groundwaters and surface water can lead to the development of an impact-generated hydrothermal system [21]. Recent studies suggest that impact-induced hydrothermal activity will occur following the majority of impact events, with some exceptions for small craters or those formed in arid environments [22, 23]. The circulation of hydrothermal fluids through impact craters can lead to substantial alteration and mineralization of impactites and target rocks. Thus, the recognition of impact-associated hydrothermal deposits is important in understanding the evolution of impact craters through time.

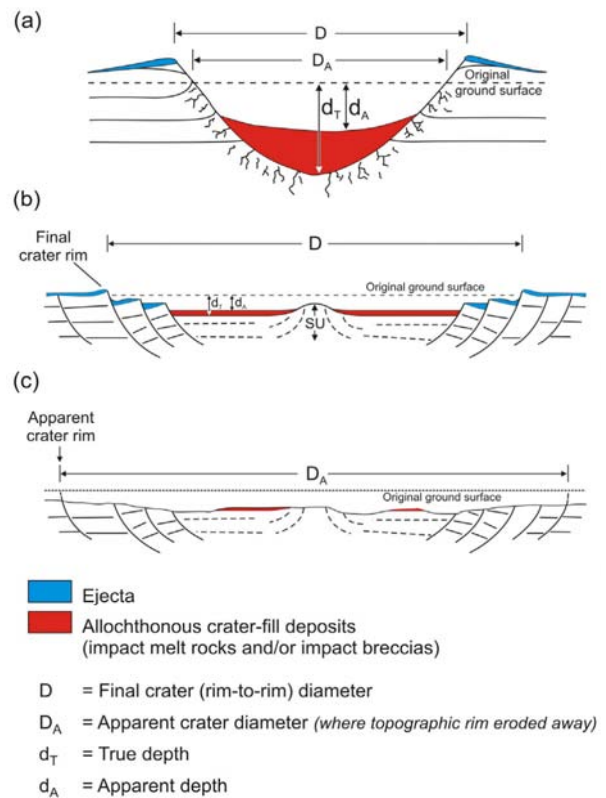


Fig. 6. Series of schematic cross sections through a simple (a) and complex (b, c) impact structure. This figure also illustrates the various diameters and depths associated with hypervelocity impact craters (see Turtle et al. [24] for a detailed review and discussion of the different connotations associated with "crater diameter"). It is important to note that for the majority of terrestrial impact structures, which are eroded, the apparent crater diameter (D_A) will be the only value obtainable. This is not the same metric quoted in numerical modeling studies, where the final crater (rim-to-rim) diameter (D) is typically used. Modified after Turtle et al. [24].

3. MORPHOLOGY OF IMPACT CRATERS

Impact craters are subdivided into two main groups based on morphology: simple and complex. Simple craters comprise a bowl-shaped depression that is similar in shape to the initial transient cavity (Figs. 6a, 7). Complex impact structures generally have a structurally complicated rim, a down-faulted annular trough, and an uplifted central area (Fig. 6b). These features form as a result of gravitational adjustments of the initial crater during the modification stage of impact crater formation (see section 2.3).



Fig. 7. Oblique aerial view of the 1.2 km diameter Meteor Crater, Arizona. Photo courtesy of T. Bunch.

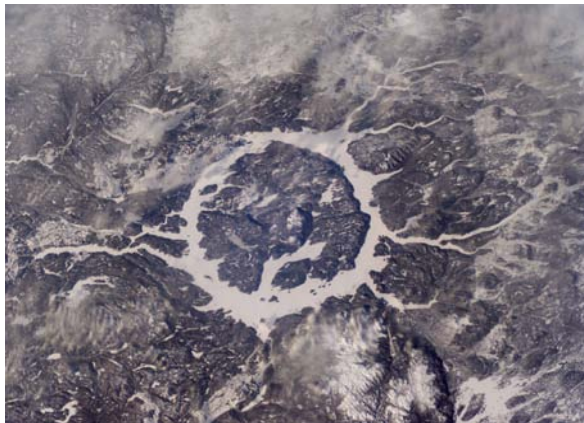


Fig. 8. View from the Space Shuttle of the ~100 km diameter Manicouagan impact structure, Canada. Image courtesy of Earth Sciences and Image Analysis Laboratory, NASA Johnson Space Center. ISS012 Roll: E Frame: 15880.

It is widely cited that the transition from simple to complex craters on Earth occurs at a smaller diameter in sedimentary (2 km) as opposed to crystalline targets (4 km). This dates back to the work of Dence [25] who based this observation on a compilation of the 50 known impact structures at that

time. Figure 9 shows that this inference may require updating, given the current impact cratering record. In particular, it is apparent that the simple-to-complex transition for craters developed in crystalline and mixed sedimentary-crystalline targets occurs over a range of diameters (~3–4 km). For sedimentary targets, the average transition diameter does appear to be at a slightly lower value of ~3 km, but the difference between craters developed in different target rocks is not as pronounced as previously noted. In addition, there is also the notable exception of the ~5 km diameter Goat Paddock impact structure, Australia, which appears to be a simple crater but with features transitional to the complex morphology [26]. It should be noted that Figure 8 was compiled using those craters where the diameter was deemed reliable by the author. However, this relies on the accurateness of the literature. In addition, there are also complications due to differing erosion levels and differences in opinion as to what crater diameter actually means (e.g., apparent versus final crater diameter; Fig. 6), which is often not clear in the literature (see Turtle [24] for a review).

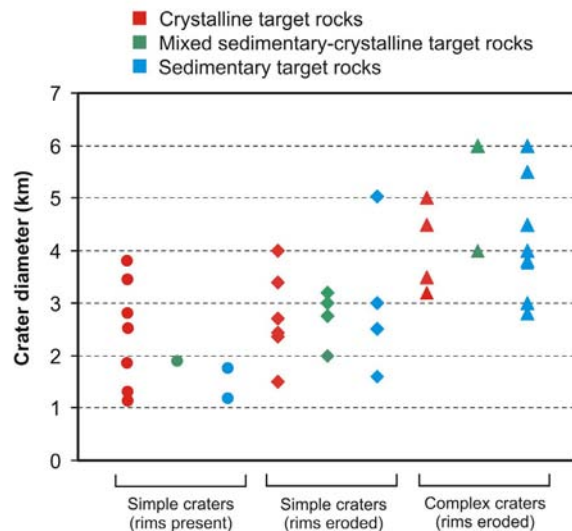


Fig. 9. Classification of all known impact structures 1–6 km in diameter with reliable metrics.

4. IMPACT CRATERING v. ENDOGENOUS GEOLOGICAL PROCESSES

Meteorite impact events differ in several ways from more familiar endogenous geological processes such as earthquakes and volcanic eruptions. In the past, there has been much confusion and controversy surrounding impacts, in part, due to their rarity, even over geological timescales. Unlike large earthquakes, volcanic explosions, or tsunamis, there have been no historical examples of crater-forming impact events

[16]. Major differences between impact events and other geological processes include: (1) the extreme physical conditions (Fig. 10); (2) the concentrated nature of the energy release at a single point on the Earth's surface; (3) the virtually instantaneous nature of the impact process; and (4) the high strain rates involved ($\sim 10^4 \text{ s}^{-1}$ to 10^6 s^{-1} for impacts versus 10^{-3} s^{-1} to 10^{-6} s^{-1} for endogenous tectonic and metamorphic processes) [16]. Impact events are, therefore, unlike any other geological process.

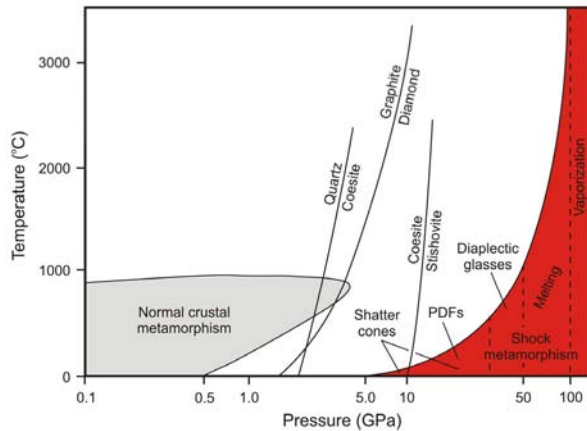


Fig. 10. Pressure–temperature (P–T) plot showing comparative conditions for shock metamorphism and ‘normal’ crustal metamorphism. The approximate P–T conditions needed to produce specific shock effects are indicated by vertical dashed lines below the exponential curve that encompasses the field of shock metamorphism. Modified from French [16].

5. THE RECOGNITION OF METEORITE IMPACT STRUCTURES

Several criteria may be used to identify hypervelocity impact structures, including the presence of a crater form and/or unusual rocks, such as breccias, melt rocks, and pseudotachylite; however, on their own, these indicators do not provide definitive evidence for a meteorite impact structure. The general consensus within the impact community is that unequivocal evidence for hypervelocity impact takes the form of shock metamorphic indicators, either megascopic (e.g., shatter cones Fig. 11) or microscopic (e.g., planar deformation features, Fig. 12; diaplectic glass, Fig. 13), and the presence of high-pressure polymorphs (e.g., coesite, stishovite). Unfortunately, this requires investigation and preservation of suitable rocks within a suspected structure. However, this is often not possible for eroded and/or buried structures and/or structures presently in the marine environment (e.g., the Eltanin structure in the South Pacific), even though there is strong evidence for an impact origin.

A prime example is the controversy surrounding the Silverpit structure in the North Sea. Stewart and Allen [27] originally proposed that this structure was an impact crater based on high-resolution 3D seismic data and despite some opposition (e.g., [28]), most impact workers accept this; however, without drilling to retrieve samples, this structure is currently relegated to the list of “possible” impact structures. This is unfortunate as the seismic dataset for this structure surpasses that available for any known impact structure and may provide important insights into complex crater formation [27]. In order to try and address this issue, Stewart [29] proposed a framework for the identification of impact structures based on 3D seismic data, but this has received little attention to date within the impact community.



Fig. 11. Shatter cones developed in fine-grained limestones of the central uplift of the Haughton impact structure, Canada. The height of the image is 18 cm.

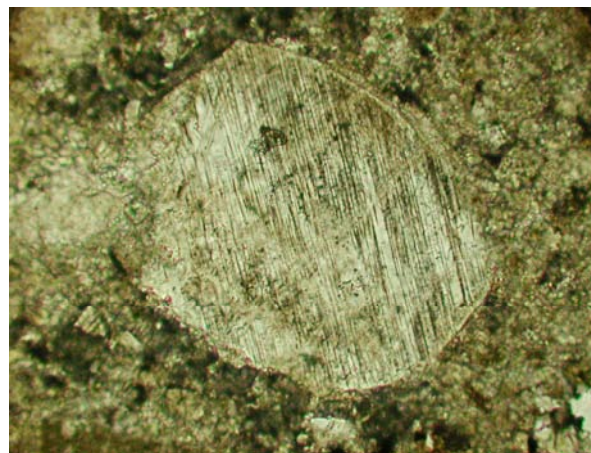


Fig. 12. Quartz grain displaying planar deformation features from the crater-fill impact melt breccias of the Haughton impact structure, Canada. Plane polarized light photomicrograph. Field of view is 2 mm.

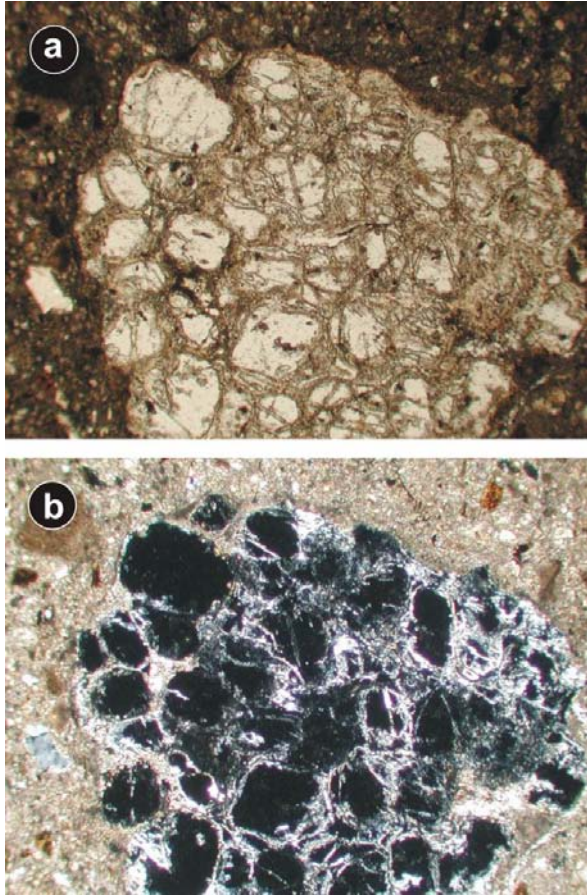


Fig. 13. Sandstone clast features from the crater-fill impact melt breccias of the Haughton impact structure, Canada. Comparison of Plane (a) and cross (b) polarized light photomicrographs reveals that the majority of the quartz grains have been transformed to diaplectic glass. Field of view is 4 mm.

6. THE TERRESTRIAL IMPACT CRATERING RECORD

It has been 100 years since D. Barringer published his landmark paper outlining the evidence for the impact origin of Meteor Crater, Arizona [30]. Since then, the inventory of known terrestrial impact structures has grown steadily through time (Fig. 14), with a current average detection rate of ~3–5 impact sites per year. Systematic field and remote sensing campaigns in Scandinavia [31] and Australia [32] have been particularly successful in the detection of new impact sites. Currently, there are 174 recognized terrestrial impact structures (Fig. 15) (i.e., structures where characteristic shock metamorphic criteria have been recognized) listed in the Earth Impact Database [2], hosted and updated by the University of New Brunswick, Canada.

Notwithstanding the problems surrounding the recognition of meteorite impact structures (see

section 5), the potential for finding new impact sites and/or confirming suspected sites remains high, as exemplified by the recent compilation of Suspected Earth Impact Sites (SEIS) by D. Rajmon and published online at <http://web.eps.utk.edu/ifsg.htm>.

6.1. Spatial distribution of terrestrial impact structures

Despite the recognition of 174 terrestrial impact sites, the record is notably incomplete. There are still few impact sites in South America, Central Africa and large parts of Asia. Important questions remain as to whether this is due to the regional geology of these regions (e.g., lack of ancient, stable cratons), or if the scarcity of impact sites is due to a lack of detailed field and remote sensing studies and/or other factors, such as vegetation coverage or erosion.

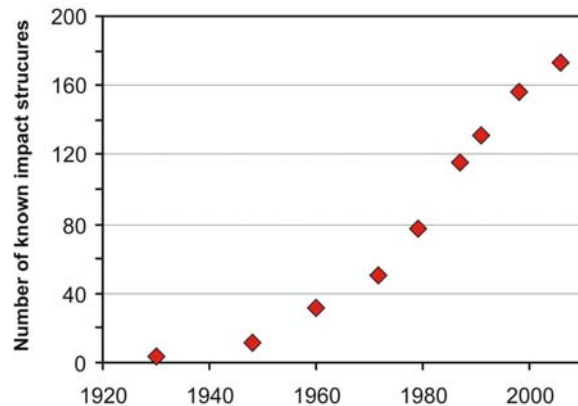


Fig. 14. Variation through time of the number of confirmed terrestrial impact structures. Note the increase in detection rate of impact structures in the 1970's, which is due to the recognition of shock metamorphic criteria (i.e., [33]).

6.2. Distribution of terrestrial impact structures with respect to target composition and setting

Figure 15 shows the distribution of impact structures with respect to the composition of the target rocks. Over two-thirds (96) of terrestrial craters formed, at least in part, in sedimentary target rocks. This is notable given the outstanding questions concerning the processes and products of impacts into volatile-rich, porous, layered sedimentary rocks (e.g., see the discussion in section 2.1 regarding impact melting in sedimentary target rocks).

The majority of the recognized impact sites also occur on land, although recent advances have been made in the recognition of impact events that occurred in the shallow marine environment. Dypvik

and Jansa [34] recognized 16 marine impact structures and bathypelagic ejecta (Eltanin, South Pacific), 6 of which are still currently in the marine environment. However, besides Eltanin that occurred

in ~4700 m of water, the other marine impact sites all occurred in <500 m of water, with most at depths of <200 m [34].

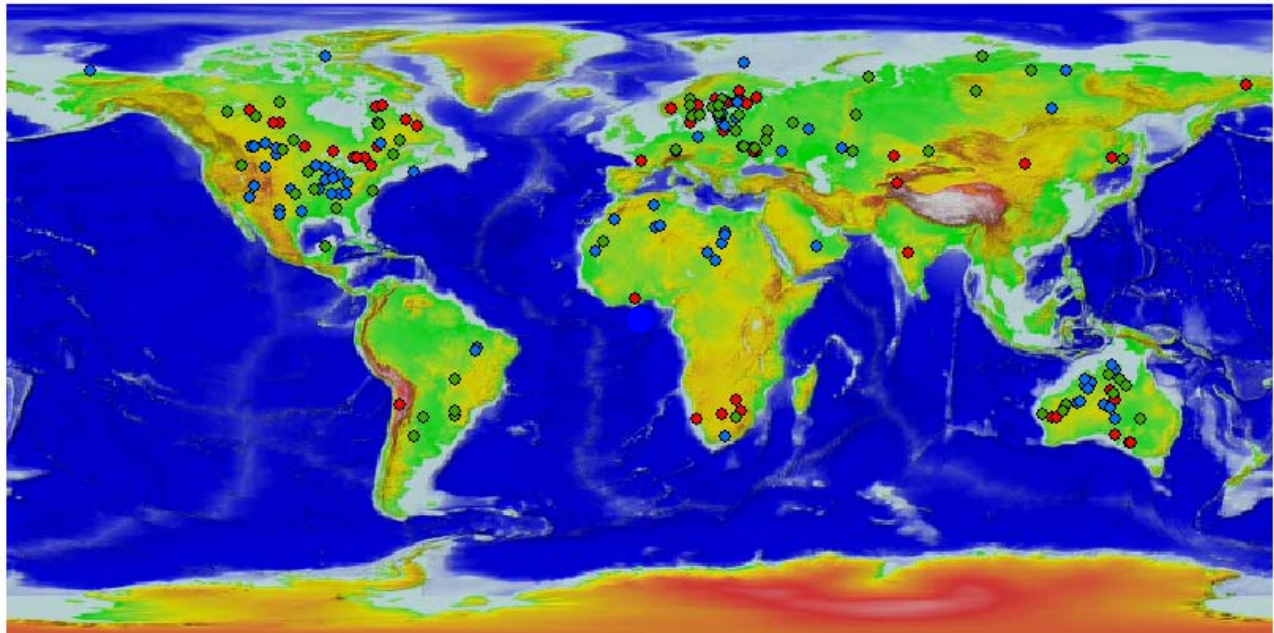


Fig. 15. Distribution of the 174 recognized terrestrial impact structures superimposed on a digital elevation map of the Earth. The red dots represent structures formed entirely in crystalline target rocks; blue dots represent structures formed entirely in sedimentary target rocks; and green dots represent mixed crystalline-sedimentary targets. Location of structures from the Earth Impact Database [2] (see Appendix 1).

6.2. Age distribution of terrestrial impact structures

There is a clear bias in the ages of terrestrial impact structures, with over half of the known structures being <200 Ma. Questions remain as to whether the cratering record has been falling off smoothly since the end of the Late Heavy Bombardment, or if there are periods of enhanced flux. Caution should be exercised given the incompleteness of the terrestrial cratering record; however, it is interesting to note the large number of Ordovician craters (Fig. 16), the majority of which are in Northern Europe [35], which also coincides with a proposed rain of ordinary chondritic meteorites [36]. The age distribution of young (<50 Ma) craters is also noticeably asymmetric (Fig. 16). In particular, there is evidence for an increased flux during the Late Eocene (Fig. 16), with several well-dated large impact craters and evidence for enhanced flux of interplanetary dust. Recent re-dating of the Haughton structure also raises the possibility of two periods of increased flux during the Eocene [37], one around 35 Ma (Popigai, Russia; Chesapeake, USA) and 39 Ma (Haughton, Wanapitei, Mistastin, Canada).

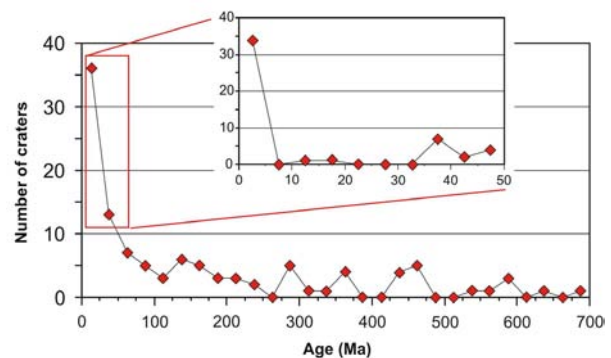


Fig. 16. Frequency plot showing known crater ages ($n = 125$). Note that only craters with reliable radiometric or stratigraphic ages are plotted.

7. ACKNOWLEDGEMENTS

This paper is based, in part, on Chapter 1 of the author's Ph.D. thesis. John Spray is thanked for providing and upkeeping the Earth Impact Database. This paper benefited from discussions with Richard Grieve.

8. REFERENCES

1. French, B.M., The importance of being cratered: The new role of meteorite impact as a normal geological process, *Meteoritics & Planetary Science* Vol. 39 169-197, 2004.
2. Earth Impact Database,
<<http://www.unb.ca/passc/ImpactDatabase/>>
Accessed: 25th June.2006.
3. Gault, D.E., Quaide, W.L., Oberbeck, V.R., Impact cratering mechanics and structures, in: B.M. French, N.M. Short, (Eds), *Shock Metamorphism of Natural Materials*, Mono Book Corp., Baltimore, 1968, pp. 87-99.
4. Kieffer, S.W., Simonds, C.H., The role of volatiles and lithology in the impact cratering process, *Reviews of Geophysics and Space Physics* Vol. 18 143-181, 1980.
5. Osinski, G.R., *Hypervelocity impacts into sedimentary targets: Processes and products*, PhD Thesis, University of New Brunswick, 2004.
6. Melosh, H.J., *Impact Cratering: A Geologic Process*, Oxford University Press, New York, 1989.
7. Ahrens, T.J., O'Keefe, J.D., Shock melting and vaporization of Lunar rocks and minerals, *Moon* Vol. 4 214-249, 1972.
8. Grieve, R.A.F., Dence, M.R., Robertson, P.B., Cratering processes: As interpreted from the occurrence of impact melts, in: D.J. Roddy, R.O. Pepin, R.B. Merrill, (Eds), *Impact and Explosion Cratering*, Pergamon Press, New York, 1977, pp. 791-814.
9. Graup, G., Carbonate-silicate liquid immiscibility upon impact melting: Ries Crater, Germany, *Meteoritics & Planetary Science* Vol. 34 425-438, 1999.
10. Jones, A.P., Claes, P., Heuschkel, S., Impact melting of carbonates from the Chicxulub Crater, in: I. Gilmour, C. Koeberl, (Eds), *Impacts and the Early Earth, Lecture Notes in Earth Sciences 91*, Springer-Verlag, Berlin, 2000, pp. 343-361.
11. Osinski, G.R., Spray, J.G., Impact-generated carbonate melts: Evidence from the Haughton Structure, Canada, *Earth and Planetary Science Letters* Vol. 194 17-29, 2001.
12. Osinski, G.R., Spray, J.G., Lee, P., Impactites of the Haughton impact structure, Devon Island, Canadian High Arctic, *Meteoritics & Planetary Science* Vol. 40 1789-1812, 2005.
13. Dence, M.R., Shock zoning at Canadian Craters: Petrography and structural implications, in: B.M. French, N.M. Short, (Eds), *Shock Metamorphism of Natural Materials*, Mono Book Corp., Baltimore, 1968, pp. 169-184.
14. Grieve, R.A.F., Cintala, M.J., A method for estimating the initial impact conditions of terrestrial cratering events, exemplified by its application to Brent crater, Ontario, *Proceedings of the Lunar and Planetary Science Conference* Vol. 12B 1607-1621, 1981.
15. Stöffler, D., Gault, D.E., Wedekind, J., Polkowski, G., Experimental hypervelocity impact into quartz sand: Distribution and shock metamorphism of ejecta, *Journal of Geophysical Research* Vol. 80 4062-4077, 1975.
16. French, B.M., *Traces of Catastrophe. Handbook of Shock-Metamorphic Effects in Terrestrial Meteorite Impact Structures*, Lunar and Planetary Institute, Houston, 1998.
17. Grieve, R.A.F., Terrestrial impact structures, *Annual Review of Earth and Planetary Science* Vol. 15 245-270, 1987.
18. Melosh, H.J., Ivanov, B.A., Impact crater collapse, *Annual Review of Earth and Planetary Science* Vol. 27 385-415, 1999.
19. Dence, M.R., The extraterrestrial origin of Canadian craters, *Annals of the New York Academy of Science* Vol. 123 941-969, 1965.
20. Kenkmann, T., Ivanov, B.A., Stöffler, D., Identification of ancient impact structures: Low-angle faults and related geological features of crater basements, in: I. Gilmour, C. Koeberl, (Eds), *Impacts and the Early Earth, Lecture Notes in Earth Sciences 91*, Springer-Verlag, Berlin, 2000, pp. 279-309.
21. Newsom, H.E., Hydrothermal alteration of impact melt sheets with implications for Mars, *Icarus* Vol. 44 207-216, 1980.
22. Osinski, G.R., Lee, P., Parnell, J., Spray, J.G., Baron, M., A case study of impact-induced hydrothermal activity: The Haughton impact structure, Devon Island, Canadian High Arctic, *Meteoritics & Planetary Science* Vol. 40 1859-1878, 2005.
23. Naumov, M.V., Principal features of impact-generated hydrothermal circulation systems: mineralogical and geochemical evidence, *Geofluids* Vol. 5 165-184, 2005.
24. Turtle, E.P., Pierazzo, E., Collins, G.S., Osinski, G.R., Melosh, H.J., Morgan, J.V., Reimold, W.U., Impact structures: What does crater diameter mean? in: T. Kenkmann, F. Hörz, A. Deutsch, (Eds), *Large meteorite impacts III: Geological Society of America Special Paper 384*, Geological Society of America, Boulder, 2005, pp. 1-24.
25. Dence, M.R., The nature and significance of terrestrial impact structures, *International Geological Congress Proceedings* Vol. 24th 77-89, 1972.
26. Milton, D.J., Macdonald, F.A., Goat Paddock, Western Australia: an impact crater near the simplecomplex transition, *Australian Journal of Earth Sciences* Vol. 52 689-697, 2005.
27. Stewart, S.A., Allen, P.J., A 20-km-diameter multi-ringed impact structure in the North Sea, *Nature* Vol. 418 520-523, 2002.

28. Underhill, J.R., Earth science An alternative origin for the "Silverpit crater", *Nature* Vol. 428 doi: 10.1038/nature02476, 2004.
29. Stewart, S.A., How will we recognize buried impact craters in terrestrial sedimentary basins? *Geology* Vol. 31 929-932, 2003.
30. Barringer, D.M., *Proc. Acad. Natl. Sci. Philos.* Vol. 66 861-886, 1905.
31. Puura, V., Plado, J., Settings of meteorite impact structures in the Svecofennia crustal domain, in: C. Koeberl, H. Henkel, (Eds), *Impact Tectonics*, Impact Studies Series, Volume 6, Springer-Verlag, Berlin, 2005, pp. 211-245.
32. Haines, P.W., Impact cratering and distal ejecta: the Australian record, *Australian Journal of Earth Sciences* Vol. 52 481-507, 2005.
33. French, B.M., Short, N.M., *Shock Metamorphism of Natural Materials*, Mono Book Corp., Baltimore, 1968.
34. Dypvik, H., Jansa, L.F., Sedimentary signatures and processes during marine bolide impacts: a review, *Sedimentary Geology* Vol. 161 309-337, 2003.
35. Lindström, M., Puura, V., Floden, T., Bruun, A., Ordovician impacts at sea in Baltoscandia, *International Conference on Large Meteorite Impacts and Planetary Evolution*, Lunar and Planetary Institute, 1992, p. 47.
36. Schmitz, B., Tassinari, M., Peucker-Ehrenbrink, B., A rain of ordinary chondritic meteorites in the early Ordovician, *Earth and Planetary Science Letters* Vol. 194 1-15, 2001.
37. Sherlock, S.C., Kelley, S.P., Parnell, J., Green, P., Lee, P., Osinski, G.R., Cockell, C.S., Re-evaluating the age of Houghton impact event, *Meteoritics & Planetary Science* Vol. 40 1777-1787, 2005.

Appendix 1. List of confirmed terrestrial impact structures with their important attributes (data from the Earth Impact Database, 2006) and a summary of the target stratigraphy (this study).

Crater name	Location	Latitude	Longitude	Age (Ma)	Diameter (km)	Target rock ¹
Acraman	Australia	S 32° 1'	E 135° 27'	~590	90	C
Ames	U.S.A.	N 36° 15'	W 98° 12'	470 ± 30	16	M
Amelia Creek	Australia	S 20° 55'	E 134 ° 50'	1640– 600	~20	M
Anguid	Algeria	N 26° 5'	E 4° 23'	< 0.1	0.45	S
Aorounga	Chad	N 19° 6'	E 19° 15'	< 345	12.6	S
Aouelloul	Mauritania	N 20° 15'	W 12° 41'	3.0 ± 0.3	0.39	S
Araguainha	Brazil	S 16° 47'	W 52° 59'	244.40 ± 3.25	40	M
Arkenu 1	Libya	N 22° 4'	E 23° 45'	< 140	6.8	S
Arkenu 2	Libya	N 22° 4'	E 23° 45'	< 140	10	S
Avak	U.S.A.	N 71° 15'	W 156° 38'	3-95	12	S
B.P. Structure	Libya	N 25° 19'	E 24° 20'	< 120	2	S
Barringer	U.S.A.	N 35° 2'	W 111° 1'	0.049 ± 0.003	1.186	S
Beaverhead	U.S.A.	N 44° 36'	W 113° 0'	~ 600	60	M
Beyenchime-Salaatin	Russia	N 71° 0'	E 121° 40'	40 ± 20	8	S
Bigach	Kazakhstan	N 48° 34'	E 82° 1'	5 ± 3	8	M
Boltysh	Ukraine	N 48° 45'	E 32° 10'	65.17 ± 0.64	24	C
Bosumtwi	Ghana	N 6° 30'	W 1° 25'	1.07	10.5	C-Ms
Boxhole	Australia	S 22° 37'	E 135° 12'	0.0540 ± 0.0015	0.17	C
Brent	Canada	N 46° 5'	W 78° 29'	396 ± 20	3.8	C
Calvin	USA	N 41° 50'	W 85° 57'	450 ± 10	8.5	S
Campo Del Cielo	Argentina	S 27° 38'	W 61° 42'	< 0.004	0.05	M
Carswell	Canada	N 58° 27'	W 109° 30'	115 ± 10	39	M
Charlevoix	Canada	N 47° 32'	W 70° 18'	342 ± 15	54	M
Chesapeake Bay	U.S.A.	N 37° 17'	W 76° 1'	35.5 ± 0.3	90	M
Chicxulub	Mexico	N 21° 20'	W 89° 30'	64.98 ± 0.05	170	M
Chiyli	Kazakhstan	N 49° 10'	E 57° 51'	46 ± 7	5.5	S
Chukcha	Russia	N 75° 42'	E 97° 48'	< 70	6	M
Clearwater East	Canada	N 56° 5'	W 74° 7'	290 ± 20	26	M
Clearwater West	Canada	N 56° 13'	W 74° 30'	290 ± 20	36	M
Cloud Creek	U.S.A.	N 43° 7'	W 106° 45'	190 ± 30 Ma	7	S
Connolly Basin	Australia	S 23° 32'	E 124° 45'	< 60	9	S

Crater name	Location	Latitude	Longitude	Age (Ma)	Diameter (km)	Target rock ¹
Couture	Canada	N 60° 8'	W 75° 20'	430 ± 25	8	C
Crawford	Australia	S 34° 43'	E 139° 2'	> 35	8.5	C-Ms
Crooked Creek	U.S.A.	N 37° 50'	W 91° 23'	320 ± 80	7	S
Dalgaranga	Australia	S 27° 38'	E 117° 17'	~ 0.27	0.024	C
Decaturville	U.S.A.	N 37° 54'	W 92° 43'	< 300	6	M
Deep Bay	Canada	N 56° 24'	W 102° 59'	99 ± 4	13	C
Dellen	Sweden	N 61° 48'	E 16° 48'	89.0 ± 2.7	19	C
Des Plaines	U.S.A.	N 42° 3'	W 87° 52'	< 280	8	S
Dobele	Latvia	N 56° 35'	E 23° 15'	290 ± 35	4.5	S
Eagle Butte	Canada	N 49° 42'	W 110° 30'	< 65	10	S
Elbow	Canada	N 50° 59'	W 106° 43'	395 ± 25	8	S
El'gygytgyn	Russia	N 67° 30'	E 172° 5'	3.5 ± 0.5	18	C
Flaxman	Australia	S 34° 37'	E 139° 4'	> 35	10	C-Ms
Flynn Creek	U.S.A.	N 36° 17'	W 85° 40'	360 ± 20	3.8	S
Foelsche	Australia	S 16° 40'	E 136° 47'	> 545	6	M
Gardnos	Norway	N 60° 39'	E 9° 0'	500 ± 10	5	C
Glasford	U.S.A.	N 40° 36'	W 89° 47'	< 430	4	S
Glikson	Australia	S 23° 59'	E 121° 34'	< 508	~19	M
Glover Bluff	U.S.A.	N 43° 58'	W 89° 32'	< 500	8	S
Goat Paddock	Australia	S 18° 20'	E 126° 40'	< 50	5.1	S
Gosses Bluff	Australia	S 23° 49'	E 132° 19'	142.5 ± 0.8	22	S
Gow	Canada	N 56° 27'	W 104° 29'	< 250	5	C
Goyder	Australia	S 13° 9'	E 135° 2'	< 1400	3	S
Granby	Sweden	N 58° 25'	E 14° 56'	~ 470	3	M
Gusev	Russia	N 48° 26'	E 40° 32'	49.0 ± 0.2	3	S
Gweni-Fada	Africa	N 17° 25'	E 21° 45'	< 345	14	S
Haughton	Canada	N 75° 22'	W 89° 41'	39 ± 2	23	S
Haviland	U.S.A.	N 37° 35'	W 99° 10'	< 0.001	0.015	S
Henbury	Australia	S 24° 34'	E 133° 8'	.0042 ± 0.0019	0.157	S
Holleford	Canada	N 44° 28'	W 76° 38'	550 ± 100	2.35	C
Ile Rouleau	Canada	N 50° 41'	W 73° 53'	< 300	4	S
Ilumetsä	Estonia	N 57° 58'	E 27° 25'	> 0.002	0.08	S
Ilyinets	Ukraine	N 49° 7'	E 29° 6'	378 ± 5	8.5	M
Iso-Naakkima	Finland	N 62° 11'	E 27° 9'	> 1000	3	S
Jänisjärvi	Russia	N 61° 58'	E 30° 55'	700 ± 5	14	C-Ms
Kaalijärv	Estonia	N 58° 24'	E 22° 40'	0.004 ± 0.001	0.11	S
Kalkkop	South Africa	S 32° 43'	E 24° 34'	< 1.8	0.64	S
Kaluga	Russia	N 54° 30'	E 36° 12'	380 ± 5	15	M
Kamensk	Russia	N 48° 21'	E 40° 30'	49.0 ± 0.2	25	S
Kara	Russia	N 69° 6'	E 64° 9'	70.3 ± 2.2	65	M
Kara-Kul	Tajikistan	N 39° 1'	E 73° 27'	< 5	52	C
Kärdla	Estonia	N 59° 1'	E 22° 46'	~ 455	4	M
Karikkoselkä	Finland	N 62° 13'	E 25° 15'	< 1.88	1.5	C
Karla	Russia	N 54° 55'	E 48° 2'	5 ± 1	10	S
Kelly West	Australia	S 19° 56'	E 133° 57'	> 550	10	C-Ms
Kentland	U.S.A.	N 40° 45'	W 87° 24'	< 97	13	S
Keurusselkä	Finland	N 62° 8'	E 24° 36'	<1800	30	C
Kgagodi	Botswana	S 22° 29'	E 27° 35'	< 180	3.5	C
Kursk	Russia	N 51° 42'	E 36° 0'	250 ± 80	6	M
La Moinerie	Canada	N 57° 26'	W 66° 37'	400 ± 50	8	C
Lappajärvi	Finland	N 63° 12'	E 23° 42'	73.3 ± 5.3	23	M
Lawn Hill	Australia	S 18° 40'	E 138° 39'	> 515	18	M
Liverpool	Australia	S 12° 24'	E 134° 3'	150 ± 70	1.6	S
Lockne	Sweden	N 63° 0'	E 14° 49'	455	7.5	M
Logancha	Russia	N 65° 31'	E 95° 56'	40 ± 20	20	M
Logoisk	Belarus	N 54° 12'	E 27° 48'	42.3 ± 1.1	15	M

Crater name	Location	Latitude	Longitude	Age (Ma)	Diameter (km)	Target rock ¹
Lonar	India	N 19° 58'	E 76° 31'	0.052 ± 0.006	1.83	C
Lumparn	Finland	N 60° 9'	E 20° 6'	~ 1000	9	M
Macha	Russia	N 60° 6'	E 117° 35'	< 0.007	0.3	S
Manicouagan	Canada	N 51° 23'	W 68° 42'	214 ± 1	100	M
Manson	Iowa, U.S.A.	N 42° 35'	W 94° 33'	73.8 ± 0.3	35	M
Maple Creek	Canada	N 49° 48'	W 109° 6'	< 75	6	S
Marquez	U.S.A.	N 31° 17'	W 96° 18'	58 ± 2	12.7	S
Middlesboro	U.S.A.	N 36° 37'	W 83° 44'	< 300	6	S
Mien	Sweden	N 56° 25'	E 14° 52'	121.0 ± 2.3	9	C
Mishina Gora	Russia	N 58° 43'	E 28° 3'	300 ± 50	4	M
Mistastin	Canada	N 55° 53'	W 63° 18'	36.4 ± 4	28	C
Mizarai	Lithuania	N 54° 1'	E 23° 54'	500 ± 20	5	C
Mjølnir	Norway	N 73° 48'	E 29° 40'	142.0 ± 2.6	40	S
Montagnais	Canada	N 42° 53'	W 64° 13'	50.50 ± 0.76	45	S
Monturaqui	Chile	S 23° 56'	W 68° 17'	< 1	0.46	C
Morasko	Poland	N 52° 29'	E 16° 54'	< 0.01	0.1	S
Morokweng	South Africa	S 26° 28'	E 23° 32'	145.0 ± 0.8	70	C
Mount Toondina	South Australia	S 27° 57'	E 135° 22'	< 110	4	S
Neugrund	Estonia	N 59° 20'	E 23° 40'	~ 470	8	S
New Quebec	Canada	N 61° 17'	W 73° 40'	1.4 ± 0.1	3.44	C
Newporte	U.S.A.	N 48° 58'	W 101° 58'	< 500	3.2	M
Nicholson	Canada	N 62° 40'	W 102° 41'	< 400	12.5	M
Oasis	Libya	N 24° 35'	E 24° 24'	< 120	18	S
Obolon	Ukraine	N 49° 35'	E 32° 55'	169 ± 7	20	M
Odessa	U.S.A.	N 31° 45'	W 102° 29'	< 0.05	0.168	S
Ouarkziz	Algeria	N 29° 0'	W 7° 33'	< 70	3.5	S
Paasselkä	Finland	N 62° 2'	E 29° 5'	< 1800	10	
Piccaninny	Australia	S 17° 32'	E 128° 25'	< 360	7	S
Pilot	Canada	N 60° 17'	W 111° 1'	445 ± 2	6	C
Popigai	Russia	N 71° 39'	E 111° 11'	35.7 ± 0.2	100	M
Presqu'île	Canada	N 49° 43'	W 74° 48'	< 500	24	C
Puchezh-Katunki	Russia	N 56° 58'	E 43° 43'	167 ± 3	80	M
Ragozinka	Russia	N 58° 44'	E 61° 48'	46 ± 3	9	M
Red Wing	U.S.A.	N 47° 36'	W 103° 33'	200 ± 25	9	S
Riachao Ring	Brazil	S 7° 43'	W 46° 39'	< 200	4.5	S
Ries	Germany	N 48° 53'	E 10° 37'	15.1 ± 0.1	24	M
Rio Cuarto	Argentina	S 32° 52'	W 64° 14'	< 0.1	1 by 4.5	M
Rochechouart	France	N 45° 50'	E 0° 56'	214 ± 8	23	C
Rock Elm	U.S.A.	N 44° 43'	W 92° 14'	< 505	6	S
Roter Kamm	Namibia	S 27° 46'	E 16° 18'	3.7 ± 0.3	2.5	C
Rotmistrovka	Ukraine	N 49° 0'	E 32° 0'	120 ± 10	2.7	C
Sääksjärvi	Finland	N 61° 24'	E 22° 24'	~ 560	6	M
Saarijärvi	Finland	N 65° 17'	E 28° 23'	> 600	1.5	C
Saint Martin	Canada	N 51° 47'	W 98° 32'	220 ± 32	40	M
Serpent Mound	Ohio, U.S.A.	N 39° 2'	W 83° 24'	< 320	8	S
Serra da Cangalha	Brazil	S 8° 5'	W 46° 52'	< 300	12	S
Shoemaker (formerly Teague Ring)	Australia	S 25° 52'	E 120° 53'	1630 ± 5	30	M
Shunak	Kazakhstan	N 47° 12'	E 72° 42'	45 ± 10	2.8	C
Sierra Madera	U.S.A.	N 30° 36'	W 102° 55'	< 100	13	S
Sikhote Alin	Russia	N 46° 7'	E 134° 40'	0.000055	0.027	C
Siljan	Sweden	N 61° 2'	E 14° 52'	361.0 ± 1.1	52	M
Slate Islands	Canada	N 48° 40'	W 87° 0'	~ 450	30	C
Sobolev	Russia	N 46° 18'	E 137° 52'	< 0.001	0.053	M

Crater name	Location	Latitude	Longitude	Age (Ma)	Diameter (km)	Target rock ¹
Söderfjärden	Finland	N 63° 2'	E 21° 35'	~ 600	5.5	C
Spider	Australia	S 16° 44'	E 126° 5'	> 570	13	S
Steen River	Canada	N 59° 30'	W 117° 38'	91 ± 7	25	M
Steinheim	Germany	N 48° 41'	E 10° 4'	15 ± 1	3.8	S
Strangways	Australia	S 15° 12'	E 133° 35'	646 ± 42	25	M
Suavjärvi	Russia	N 63° 7'	E 33° 23'	~ 2400	16	C-Ms
Sudbury	Canada	N 46° 36'	W 81° 11'	1850 ± 3	250	C
Suvasvesi N	Finland	N 62° 42'	E 28° 10'	< 1000	4	C
Tabun-Khara-Obo	Mongolia	N 44° 6'	E 109° 36'	150 ± 20	1.3	C
Talemzane	Algeria	N 33° 19'	E 4° 2'	< 3	1.75	S
Tenoumer	Mauritania	N 22° 55'	W 10° 24'	0.0214 ± 0.0097	1.9	M
Ternovka	Ukraine	N 48° 08'	E 33° 31'	280 ± 10	11	C
Tin Bider	Algeria	N 27° 36'	E 5° 7'	< 70	6	S
Tookoonooka	Australia	S 27° 7'	E 142° 50'	128 ± 5	55	M
Tswaing (formerly Pretoria Saltpan)	South Africa	S 25° 24'	E 28° 5'	0.220 ± 0.052	1.13	C
Tvären	Sweden	N 58° 46'	E 17° 25'	~ 455	2	M
Upheaval Dome	U.S.A.	N 38° 26'	W 109° 54'	< 170	10	S
Vargeao Dome	Brazil	S 26° 50'	W 52° 7'	< 70	12	M
Veevers	Australia	S 22° 58'	E 125° 22'	< 1	0.08	S
Vepriai	Lithuania	N 55° 5'	E 24° 35'	> 160 ± 10	8	S
Viewfield	Canada	N 49° 35'	W 103° 4'	190 ± 20	2.5	S
Vista Alegre	Brazil	S 25° 57'	W 52° 41'	< 65	9.5	
Vredefort	South Africa	S 27° 0'	E 27° 30'	2023 ± 4	300	M
Wabar	Saudi Arabia	N 21° 30'	E 50° 28'	0.00014	0.116	S
Wanapitei	Canada	N 46° 45'	W 80° 45'	37.2 ± 1.2	7.5	C
Wells Creek	U.S.A.	N 36° 23'	W 87° 40'	200 ± 100	12	S
West Hawk	Canada	N 49° 46'	W 95° 11'	351 ± 20	2.44	C
Wetumpka	U.S.A.	N 32° 31'	W 86° 10'	81.0 ± 1.5	6.5	M
Wolfe Creek	Australia	S 19° 10'	E 127° 48'	< 0.3	0.875	S
Woodleigh	Australia	S 26° 3'	E 114° 39'	364 ± 8	40	M
Yarrabubba	Australia	S 27° 10'	E 118° 50'	~ 2000	30	C
Zapadnaya	Ukraine	N 49° 44'	E 29° 0'	165 ± 5	3.2	C
Zelenv Gai	Ukraine	N 48° 4'	E 32° 45'	80 ± 20	2.5	C
Zhamanshin	Kazakhstan	N 48° 24'	E 60° 58'	0.9 ± 0.1	14	M

¹Abbreviations: C = crystalline target; C-Ms = metasedimentary target; M = mixed target (i.e., sedimentary strata overlying crystalline basement); S = sedimentary target (i.e., no crystalline rocks affected by the impact event);

CHARACTERISATION OF A SMALL CRATER-LIKE STRUCTURE IN SE BAVARIA, GERMANY

W. Rösler⁽¹⁾, A. Patzelt⁽²⁾, V. Hoffmann⁽¹⁾, B. Raeymaekers⁽³⁾

⁽¹⁾*Institute for Geoscience, University Tübingen, Sigwartstr. 10, D-72076 Tübingen (Germany),*

Email: wolfgang.roesler@uni-tuebingen.de, viktor.hoffmann@uni-tuebingen.de

⁽²⁾*Terrana Geophysik Zeppelinstr. 15, D-72116 Mössingen (Germany), Email: ap@terrana-geophysik.de*

⁽³⁾*Infraserv Gendorf, D-84504 Burgkirchen (Germany), Email: Bert.Raeymaekers@Gendorf.de*

ABSTRACT

A small scale crater-like structure, where fused country rocks had been found, was studied in detail. The heated cobbles show a variety of extreme heat effects, but no clear indications for shock metamorphism could be found. For a non-destructive characterisation and for resolving the depth structure, geophysical field methods were used. Magnetic mapping reveals a large number of individual, small scale dipole anomalies associated with the heated crater walls and a negative anomaly in the center of the crater. Ground penetrating radar profiles indicate a continuation of the crater wall morphology into depths of several meters. The crater floor is characterised by strong reflections, indicating significantly different physical properties of the crater floor material compared to the surrounding. The age of the structure is definitely pre-industrial and the signatures can hardly be explained by primitive industrial human activities. At present, an interpretation in terms of a meteoritic or cometary impact is highly speculative and needs more, reliable, data.

1. INTRODUCTION

A large number of small, circular, bowl shaped, depressions is found in Holocene and Quaternary glacial and fluvial gravel beds in SE Bavaria, covering large areas of the Alpine foreland, stretching northward, approximately 50 km to the Inn river. Many of these structures with diameters of a few meters to several tens of meters have been described as features of glacial landscape morphology like buried ice or moraine features [1] or as archaeological structures with ambiguous origin [2]. In a large forest area along the Alz river, between the towns Altötting and Burghausen, north of the maximum extent of glaciation, numerous circular depressions have been described [3]. The crater-like structures attracted our attention when carrying out regional studies on magnetic properties of surface soils for mapping industrial pollution [4] and trace elements in bee honey [5], which both showed anomalous signatures in this area. A brief inspection of some of the suspected crater-like structures could not establish a direct link between the observed anomalous magnetic signatures

of top soils or trace elements in bee honey with the circular structures in general. However, at one of the inspected depressions, located at approx. 48°13'N, 12°45'E, considerable amounts of suspicious, fused, cobbles with slag-like appearance, associated with a strong magnetic signal, were found and prompted us to a more detailed characterisation of the structure using macroscopic, microscopic, mineralogical, and geophysical methods. First systematic studies on a few other structures nearby have been undertaken by other investigators but could not yet clarify their origin [6].



Fig. 1. Crater-like structure in beech forest

2. GEOLOGICAL SETTING

The landscape surrounding the investigated structure is characterised by late glacial to Early Holocene fluvial deposits, consisting of unconsolidated glacial gravel and cobble beds, intercalated with fine grained sand and clays, which were deposited at the end of the last, Würm, glaciation period (ca. 12.000 years BP) by rivers draining the melting Salzach and Inn glaciers [7]. The cobble beds are dominated by alpinotype rocks from Northern Alps and crystalline rocks from the Tauern and Engadin window metamorphic series. Typical lithologies are limestones, dolomites, marls, silicatic limestones, quartz and quartzite, gneisses, granitoides, greenstones, amphibolites from the central Alps, clastites, sandstones and others [1]. Soils are of Holocene age, the soil type near the investigated

structure is a para-brown earth with a thickness of ca. 10 cm.

3. MORPHOLOGY

The investigated structure is found on a gentle NW-SE dipping slope of a terrace of the Alz river, in old beech forest (Fig. 1). Trees growing on the structure and dead tree trunks indicate a minimum formation age of more than hundred years, a maximum formation age is given by the deposition of the gravel beds ca. 12.000 years BP. The depression represents an almost perfectly circular, crater-like, structure with a pronounced crater rim with a rim to rim diameter of ca. 11 m and a depth of ca. 1,2 m. At the hill side, the crater rim morphologically merges into the slope and is probably even covered by sediment material transported down the slope. The other parts of the crater rim show almost no sediment or soil cover and form a crater wall with a gently rounded profile.

4. EVIDENCE FOR EXTREME HEAT

The rocks of the crater walls appear to have suffered from extreme temperatures. Throughout the crater walls, except the hill side which is covered with finer grained material, the country rocks show a variety of heat effects, ranging from fused, glazed cobble surfaces, partial or complete melting of minerals and thermoplastic deformation of cobbles, to signs of volatilisation of certain mineral phases (Figs. 2&3). Due to extreme metamorphic effects and a wide variety of source rock lithologies, a secure identification of the source rocks from slag-like thermally altered products is hardly possible. At some granite type rocks, the quartz fraction seems to have survived whereas the feldspar fraction is completely molten. Other rock types show lava- or pumice-like appearance with signs of volatilisation of single mineral phases or of the whole rock from one side. At many places, the cobbles are thermo-plastically deformed, indented into each other, and cemented by a brown, silicatic, melt to a solid mass, indicating that the wall structure has been heated as a whole and cannot be explained as a slag deposit. Temperatures exceeding 900 °C are indicated by the lack of carbonaceous rocks, which account for about half of all rocks of the surrounding, in the thermally altered material. Thin sections of selected rocks have been inspected for planar deformation features (PDFs) or high pressure mineral phases but no evidence of shock metamorphism could be observed [8]. X-ray diffraction analysis of quartz phases reveal that a part of the quartz fraction has been transformed to the high temperature polymorphs tridymite (870-1470 °C) and cristobalite (1470-1725 °C; Fig. 4) In fused crusts of a few cobbles, iron silicon crystals and carbon spherules [9] can be observed (Fig. 5), indicating temperatures close to 2000 °C [10].



Fig. 2. Thermally altered cobbles, indented into each other and cemented by silicate melt



Fig. 3. Thermally altered cobble, cut in slices, pumice-like structure with signs of volatilisation

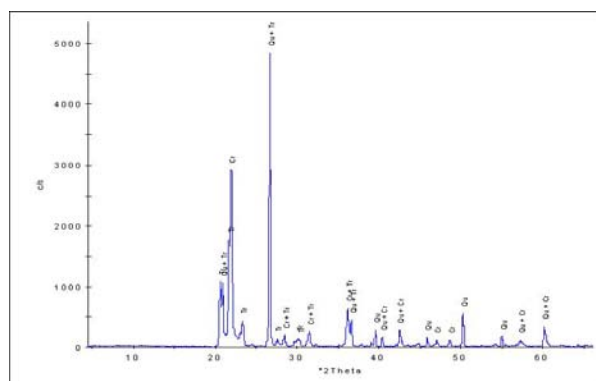


Fig. 4. X-ray diffraction diagram of a thermally altered quartz-type rock fragment. High temperature phases of quartz (Qu; $T < 870$ °C), tridymite (Tr: 870-1470 °C), and cristobalite (Cr; 1470-1725 °C) can be assigned

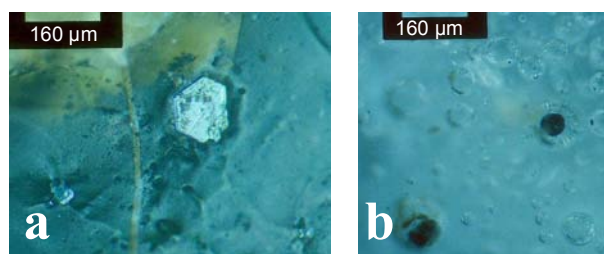


Fig. 5. a: Iron silicon crystal in fused cobble surface
b: Carbon spherules in fused cobble surface

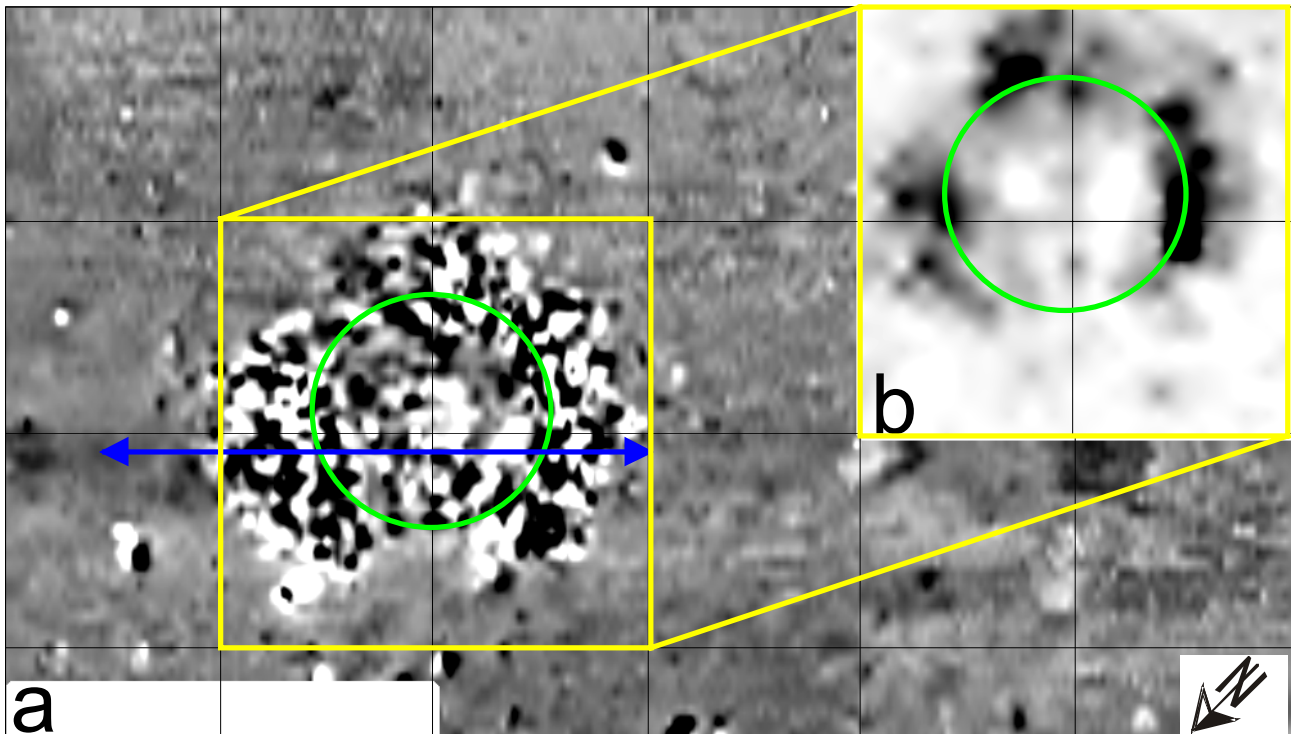


Fig. 6. Magnetic mapping.

- a: Gradient of the Earth magnetic field Z component, sampling interval 0.25 m x 0.5 m, dynamics -10 nT (white)/ $+10$ nT (black), 256 greyscales, 10 m grid overlay. The green circle indicates the position of the crater rim, the yellow box the area mapped for magnetic susceptibility, the blue line represents the GPR profile displayed in Fig. 7.
- b: Volume specific magnetic susceptibility of the soil surface, sampling interval 1 m x 1 m, dynamics 10^{-4} SI (white) to 10^{-3} SI (black), 256 greyscales

5. MAGNETIC SURVEY

For a non-invasive characterisation of the crater-like structure, several geophysical field methods have been applied. The observed heat-induced mineralogical changes should also lead to changes in magnetic properties and in magnetization. Moreover, the possible presence of archaeological materials such as tools or meteoritic materials should lead to magnetic anomalies or characteristic patterns. Magnetometry was carried out using a FM36 handheld fluxgate gradiometer (Geoscan Research, UK), a standard system designed for near-surface archaeological applications with a sensor separation of 50 cm, measurement position ca. 30 cm above ground, and a resolution of 0.1 nT in Earth magnetic field Z component gradient. The surrounding of the crater-like structure was mapped in an area larger than 40 m by 30 m with a sampling interval of 0.5 m x 0.25 m. The grey scale plot (Fig. 6a) reveals a calm background with dynamics of generally less than 1 nT in the surrounding of the crater-like structure, indicating generally weakly magnetic country rocks, with a few occasional interspersed dipole anomalies (scrap or highly magnetic individual rocks). The thermally altered crater wall material is characterised by a large

number of strong, small scale dipole anomalies, probably representing individual, near surface, re-magnetized, thermally altered country rock cobbles. At the inner crater slopes and at the hill (NW) side of the crater wall, such individual, strong dipole anomalies are partly missing, indicating probably a considerable cover with less magnetic material or the erosion of the strongly magnetised material at some places. Altogether, the resulting image of the gradiometer survey indicates that an area with a diameter of ca. 20 m had been subjected to substantial re-magnetisation. In the centre of the crater-like structure, a negative magnetic anomaly with a diameter of ca. 3 m is visible. Mapping of the volume specific magnetic susceptibility, using a Bartington M2-D loop sensor (Fig. 6b), reveals extremely enhanced magnetic susceptibility values, up to more than $350 \cdot 10^{-5}$ SI associated with the heated crater wall material in contrast to the low background values of less than $10 \cdot 10^{-5}$ SI. Here it is suspected that the increased magnetic susceptibility values may be associated with newly formed highly magnetic mineral phases, such as magnetite or iron silicon phases (Fig. 5a).

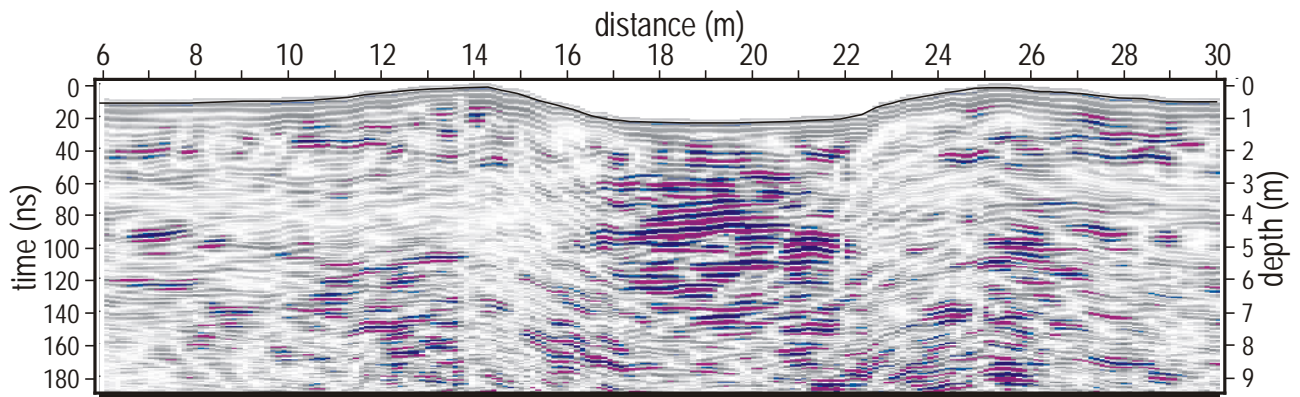


Fig. 7. radargram, 200 MHz antenna

6. GROUND PENETRATING RADAR

Ground penetrating radar (GPR) measurements were performed with a RAMAC GPR CU II (Mala Geosciences, Sweden) and an unshielded 200 MHz antenna on lines with 1m separation parallel to the profiles of the magnetic survey. Along a profile every 0.1 m a trace was recorded. Fig. 7 shows exemplarily a radargram across the centre of the crater-like structure. The position of the radar profile can be seen from Fig. 6a. In this profile and the other radar profiles as well, no significant reflections occur outside the crater. The morphology of the crater wall seems to continue into depths of several meters. Within the crater, strong reflection amplitudes can be observed, indicating significant changes in the physical property ϵ , the dielectrical constant. Strong reflections start in a depth below ground level of about 2.7 m and last until about 7.5 m. However, the lower limit is not very well constraint, as the maximum penetration depth of the selected antenna is somewhere in that depth range. The shape of the anomaly is not indicative for a larger single body in the subsurface, but points towards a broader zone of massive physical changes.

7. DISCUSSION

The main characteristics of the investigated structure can be summarised as follows:

- Crater-like morphology
- Extreme heat effects on crater wall rocks
- No shock indicators yet
- Depth structure of crater walls and fill

^{14}C data from other nearby craters [6] and preliminary own data from the investigated structure indicate a date of around 2000 BP, which falls into Roman time. A Roman villa is known nearby, and a possible origin or use of the structure as lime kiln, fire place, or furnace place could be debated. However, the heat effects documented in this study are unparalleled by any pre-industrial or early industrial process. Nevertheless, the

structure seems to have parallels to some “vitrified forts” in Scotland or other parts of Europe, but the origin and the purpose of some of such vitrified forts itself is debated ever since their discovery [11]. Unlike at other vitrified forts, no wood remnants or wood casts were found on or between the fused stones. Moreover, a fortification of an 11 m diameter object at a slope, erected with considerable effort, would not make any sense. Until industrial times, ca. 100 years ago, it was extremely difficult to generate temperatures exceeding 1000 °C. Kilns or furnaces for such high temperature applications were generally small and had a distinct morphology. Such temperatures could not be reached using a wood fire, even with ventilation. Early ore smelters used charcoal and could probably reach ca. 1300 °C, typically had diameters of less than 1 m, and produced slags which were usually thrown on a slag heap nearby. From size and morphology the investigated crater-like structure cannot be interpreted as a smelter. Other early furnaces like lime kilns could reach only considerably lower temperatures (ca. 900 °C – 1000 °C) and the observed effects can be hardly explained by a lime kiln gone out of control.

For nearby crater-like structures of similar size without any heat signatures, possible formation mechanisms by meteoritic impacts or human activity have been discussed [6] and an anthropogenic origin has been excluded. The European-wide and regional presence of suspicious carbon materials in soils [9], at a few crater-like structures in considerable quantities, requires a large carbon source and may indicate a carbon rich impactor, probably a comet. The Earth impact record is lacking cometary impacts. It is a paradigm that due to its high velocity and low mechanical strength, a cometary impactor would fractionate in atmosphere and completely vaporise. But there is a lack of data on the nature of cometary matter (dirty snow-ball or snowy dirt ball) and even more on its behaviour during atmospheric entry. Nevertheless, for a few impact events like the Tunguska event [12], carbon anomalies can be found and cometary impacts are taken into

account. In order to generate a strewn field of impact craters, exhibiting different effects and stages of shock metamorphism, a progressive break-up of a heterogeneous body, combined with explosive break-up events, could be imagined. Modeling crater sizes and shock effects [13], an impactor of 30-50 cm diameter - irrespective whether ice, stone, or metal - and a velocity of > 12 km/s would be necessary to create a crater with the observed dimensions, melt, and vaporisation.

8. INTERPRETATION AND OUTLOOK

The studied crater-like structure seems to have suffered from extreme temperatures which seem unlikely to have been produced by human activity. The regional context with structures of similar shape and size, but without melt may either indicate an yet unknown human use of the structure, or a strewn field of craters with significantly different formation conditions at individual craters. Here the existing data base on different local crater-like structures, on signatures of cometary matter, on break-up of heterogeneous, weak bodies during atmospheric entry, and on the interaction of a cometary gas cloud in the shock front of a bolide are largely unknown and interpretations are highly speculative. Unless accepted signatures for an impact like PDFs or high pressure mineral phases can be found, a careful study of the crater-like structures, also focusing on carbon materials, is proposed.

9. ACKNOWLEDGMENTS

Part of this study was carried out under the 5th framework EU RTD project MagProx [4] (EVK2-CT-1999-00019) 2000-2004. The administrative and financial support by the Landratsamt Altötting is gratefully acknowledged.

10. REFERENCES

1. *Geologische Übersichtskarte von Bayern 1:500.000, Mit Erläuterungsheft*. 4th impression, Munich, 1996.
2. Weber, F., *Die vorgeschichtlichen Denkmale des Königreiches Bayern*, Vol. 1., Munich, 1909.
3. Stechele, K., *Vor- und Frühgeschichtliches aus dem Heimatbezirke*, Burghausen, 1911.
4. "MAGPROX" *Screening and monitoring of anthropogenic pollution over central Europe by using MAGnetic PROXies*, EU 5th Framework RTD project (EVK2-CT-1999-00019) 2000-2004.
http://cordis.europa.eu/data/MSS_PROJ_CZ_FP5/ACTIOneqDndSESSIONeq17571200595ndDOCeqlndTBLeqEN_PROJ.htm
5. Raeymaekers, B., A prospective biomonitoring campaign with honey bees in a district of Upper Bavaria (Germany), *Environmental Monitoring and Assessment*, Vol. 116, 233-243, 2006.
6. Fehr, K.T. et al., A meteorite impact crater field in eastern Bavaria? A preliminary report, *Meteoritics & Planetary Science* 40, Nr.2, 187-194, 2005.
7. Grimm, W.-D. et. al. *Quartärgeologische Untersuchungen im Nordwestteil des Salzachvorlandgletschers (Oberbayern)*. – In: Schlüchter, Ch. (Ed.) *Moraines and Varves*: 101-114, Rotterdam, 1979.
8. Langenhorst, F., personal communication, 2004.
9. Rösler, W. et al., Diamonds in Carbon Spherules - Evidence for a Cosmic Impact?, *Meteoritics & Planetary Science Abs.* 40.5114R, 2005.
10. Sheffer, A. A. et al., Reduction of silicates at high temperature: fulgurites and thermodynamic modelling, *Lunar and Planetary Science Conference XXXV*, Abs. #1467, 2003.
11. Williams, J. *An Account of some Remarkable Ancient Ruins*, 1777.
12. Kolesnikov, E. M. et al., Finding of probable Tunguska cosmic body material: isotopic anomalies of carbon and hydrogen in peat, *Planetary and Space Science*, Vol. 47, 905-916, 1999.
13. Holsapple, K. A. The cratering database: making code honest, *Lunar and Planetary Science XXXV*, Abs. 1779, 2004.
<http://keith.aa.washington.edu/craterdata/scaling/index.htm>

GEOLOGIC SETTING, PROPERTIES, AND CLASSIFICATION OF TERRESTRIAL IMPACT FORMATIONS

Dieter Stöffler⁽¹⁾ and Wolf Uwe Reimold⁽¹⁾

⁽¹⁾ Museum für Naturkunde (Mineralogie), Humboldt Universität zu Berlin, Invalidenstrasse 43, 10115 Berlin, Germany. dieter.stoeffler@rz.hu-berlin.de

ABSTRACT

Terrestrial impact formations (impactites) provide the undisputed ground truth for the process and the products of hypervelocity impacts on planetary surfaces. According to [1], *impactites* which are *proximal* to the parent crater, are subdivided into *shocked rocks*, *impact breccias* and *impact melt rocks*. There are 3 types of impact breccias: *monomict breccia*, *suevite* and *lithic breccia*. *Distal impactites* comprise (*micro*)*tektites* and *global air fall beds*. Based on their geological setting proximal impactites form either allochthonous layered deposits of the crater fill and the continuous ejecta blanket, or appear as (par)autochthonous massive units in the crater basement or as dikes, veins, and vein networks in the basement or in displaced megablocks.

1. INTRODUCTION

Terrestrial impact structures and their associated regional or global deposits provide the fundamental and indispensable data for the interpretation of impact formations on the surfaces of solid planetary bodies, if properly corrected for differences in gravity, target composition (including presence or lack of water), and density of the atmosphere of the various planets or moons. This review deals with all rock types collectively termed “impactites”, which are formed by hypervelocity impacts on Earth, and extends this classification to planetary bodies without an atmosphere. It is based on a yet unpublished proposal [1] by the Subcommittee on the Systematics of Metamorphic Rocks (SCMR) of the International Union of Geological Sciences (IUGS).

2. BASIC FACTS AND CAVEATS ABOUT TERRESTRIAL IMPACT CRATERS AND IMPACT FORMATIONS

Some of the most relevant facts resulting from the study of terrestrial and planetary impact structures in the past 50 years can be briefly summarised as follows:

(1) Most of the record of terrestrial impact craters has been lost by erosion and other geological processes (plate tectonics, volcanism); in particular the early

Archaean record is lacking but can be inferred indirectly from the moon’s cratering record.

(2) Although the original morphology and the surficial impact formations of individual craters are rarely preserved, the morphological and structural type of a crater changes distinctly with increasing crater diameter in the following sequence: (a) simple bowl-shaped, (b) complex with central uplift, (c) complex with peak ring, and (d) complex with multi-rings (?). This is in clear analogy to what can be recognised on other planetary surfaces except for multi-ring basins for which no undisputed examples exist on Earth.

(3) The crater-forming process on Earth is often complicated by the complexity of the target stratigraphies and target rock compositions and by the presence of a hydrosphere and atmosphere.

(4) Due to the effects of erosion the invaluable advantage of terrestrial craters is that they are accessible at different erosional levels and therefore allow a true three-dimensional analysis unlike craters on other planets and moons.

(5) Comparative studies of craters of the same size class but different target stratigraphy/composition provide an excellent insight into the crater-forming process if properly accompanied by the most-advanced computer code calculation techniques.

3. PRINCIPAL APPROACH FOR THE ANALYSIS OF IMPACT FORMATIONS

The analytical approach to study craters and impactites should be as comprehensive and multi-disciplinary as possible and should include the following steps:

(1) Field mapping and identification/sampling of the different types of impact formations, and assessment of their regional distribution and geological/structural setting.

(2) Petrographic and chemical analyses with respect to texture, modal/chemical composition, and shock metamorphism including radiometric age dating of the appropriate type of impactite (crystallised impact melt rock or impact glass).

(3) Geophysical surveys including seismic, gravity, magnetic and geoelectric analyses to assess the

(4) Exploration by drilling and drill core analyses using methods listed under (2) and (3). Meaningful verification of the regional geophysical signatures and a full understanding of the structural and lithological characteristics of a crater needs focused drilling at several critical sites such as the centre of crater, rim zone, inner ring (peak ring), and ejecta blanket if present. This means that at least 3 drill sites are required for complex craters.

4. WORKING HYPOTHESES FOR THE FORMATION OF CRATERS AND IMPACTITES

Impactites are formed during a complex but very short sequence of processes (Fig. 1): Shock compression of the target rocks (compression stage), decompression and material transport (excavation stage), and material deposition upon ballistic or ground-surfing transport and upon collapse of the central ejecta plume (Fig. 2). The first two phases constitute the first of two fundamental working hypotheses in impact cratering: the so-called *transient cavity*, which independently of the size of the crater, has a nearly parabolic shape [2] and collapses to a final crater (modification stage) that becomes more complex (central uplift and ring formation) and less deep with increasing final crater diameter [2]. Although all phases of the cratering process are transitional and partially simultaneous, it is helpful to consider the formation, evolution and collapse of the central *vapour plume* [2] separately in the context of a second working hypothesis.

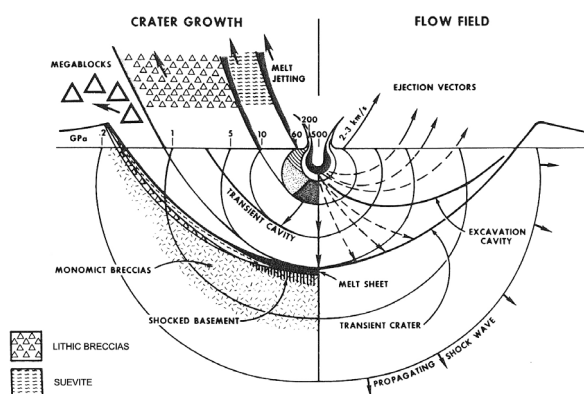


Fig. 1: Shock wave propagation, crater growth and formation of a transient cavity following a hyper-velocity impact (from [1]).

The concept of a *transient cavity* (Fig. 1; [2]) includes products formed by highly dynamic transport and by a mixing process driving material (type 1) downward into the growing crater floor (breccia lens formed by ground surging) and ejecting material (type 2) ballistically outside of the cavity forming the ballistically emplaced continuous ejecta blanket. In all craters type 1 material consists of impact melt, shocked lithic clasts, and unshocked lithic clasts from relatively deep levels of the target stratigraphy. As far as we know from the few craters with preserved ejecta blankets, the type 2 material - defined here as material not engulfed in the vapour plume (see below) - appears

to include predominantly unshocked lithic clasts, shocked lithic clasts of relatively low degree of shock and no or only rare melt particles. This material originates from relatively shallow levels of the target stratigraphy. Both types of displaced materials are highly polymict except for the type 2 material (ejecta blanket) of small simple craters which may display a layered, inverted stratigraphy.

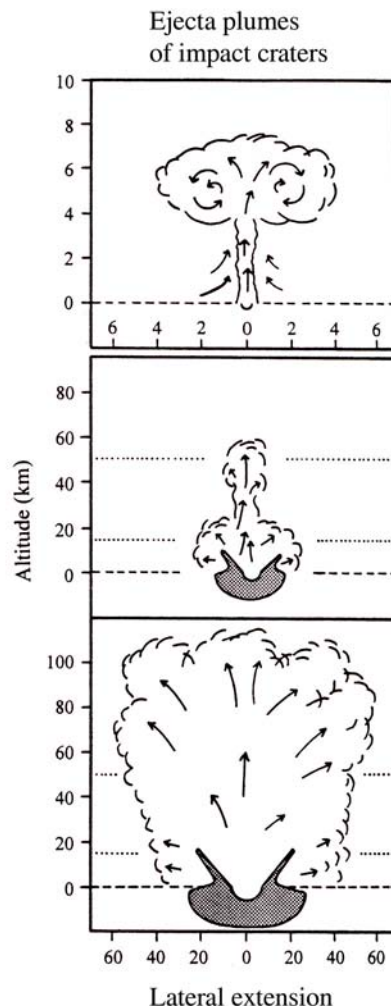


Fig. 2: Expansion of a vapour plume at impact craters of different size (from [25]).

The concept of the *vapour plume* (or *ejecta plume*) considers products resulting from vaporisation, melting, and comminution of target material located in the central part of the target below the penetrating impactor [2]. This material is ejected at very high velocities and is turbulently mixed within the expanding vapour plume that eventually collapses and forms fallback deposits (suevitic polymict breccias) inside the crater and - as we know it from the Ries and Chicxulub craters - also on top of the continuous ejecta blanket. It appears that the tektite and microtektite strewn fields observed at some young impact craters are also part of the vapour plume forming process. Depending on the size of the crater the vapour plume may rise well above the Earth's stratosphere and consequently may distribute material globally. The deposits from the vapour plume are expected to contain condensates of vaporised rocks.

5. CLASSIFICATION AND NOMENCLATURE OF IMPACTITES

The term "*impactite*" is defined as a collective term for all rocks being affected by one or several impact(s) resulting from collision(s) of planetary bodies. A classification scheme is proposed for products of single and multiple impacts ([1], Table 1, Figs. 3 and 4). It is applicable to both terrestrial and extraterrestrial rocks such as lunar rocks and meteorites of asteroidal, lunar, and Martian provenance. The basic classification criteria are based on texture, degree of shock metamorphism, and the type(s) of lithological components.

Table 1: Classification of impactites formed by single and multiple impacts; from [1]

1. Impactites from single impacts
1.1. Proximal impactites
1.1.1. Shocked rocks*
1.1.2. Impact melt rocks ¹
1.1.2.1. clast-rich
1.1.2.2. clast-poor
1.1.2.3. clast-free
1.1.3. Impact breccias
1.1.3.1. Monomict breccia
1.1.3.2. Lithic breccia (without melt particles) ²
1.1.3.3. Suevite (with melt particles) ²
1.2. Distal impactites
1.2.1. Consolidated
1.2.1.1. Tektite ³
1.2.1.2. Microtektite ³
1.2.2. Unconsolidated
1.2.2.1. Air fall bed ⁴
2. Impactites from multiple impacts
2.1. Unconsolidated clastic impact debris
2.1.1. Impact regolith ⁵
2.2. Consolidated clastic impact debris
2.2.1. Shock-lithified impact regolith ⁵
2.2.1.1. Regolith breccia ⁵ (breccia with in-situ formed matrix melt and melt particles)
2.2.1.2. Lithic breccia ⁵ (breccia without matrix melt and melt particles)

*see Tables 2-4 for further subclassification of some common rocks; for other rocks and sediments see [1]

¹ may be subclassified into glassy, hypocrystalline, and holocrystalline varieties, ² generally polymict but can be monomict in a single lithology target, ³ impact melt (generally glassy) with admixed shocked and unshocked clasts, ⁴ pelitic sediment with melt spherules, shocked and unshocked clasts, ⁵ generally polymict but can be monomict in a single lithology target.

Impactites from a single impact are classified into 3 major groups irrespective of their geological setting: *shocked rocks* (Tables 2-4), *impact melt rocks*, and *impact breccias*. The latter fall into three subgroups (monomict breccia, lithic breccia, suevite) according to the degree of mixing of various target lithologies and their content of melt particles. *Impact melt rocks* that have a crystalline to glassy matrix, and *lithic breccias* and *suevites* which have a fine-grained particulate matrix, are generally polymict breccias, except for single-lithology targets.

Impactites from multiple impacts, as known from the Moon [3] and from the meteorite parent bodies [4],

are subdivided into two main groups: *Impact regolith* and *shock lithified impact regolith*. This group is subclassified into *regolith breccias* (with in-situ formed matrix melt and individual melt particles) and *lithic breccias* (without matrix melt and melt particles). The term lithic breccia is synonymous to the traditional term "fragmental breccia", which has been used also for lunar rocks and meteorites [3, 4].

An important extension of the first-order classification, which is based essentially on texture, modal composition, and shock metamorphism, is achieved if the geological or structural setting of impactites is taken into account (Fig. 4). Structurally, three types of formations have been recognised: (a) Parautochthonous massive *monomict breccias* and *shocked rocks* of the crater basement, (b) *layered impact formations* such as *impact melt rocks* and *impact breccias*, and (c) *dyke breccias*. The latter two types occur as proximal impactites both inside the crater and outside as part of the continuous ejecta blanket extending outward for some 2 to 3 crater radii.

6. GEOLOGIC SETTING AND PROPERTIES OF THE MAIN TYPES OF IMPACTITES

The geological setting of the various textural types of impactites (Table 1) is rather variable ([1], Figs. 3 and 4):

Impact melt lithologies [1, 5] occur as (1) allochthonous coherent melt sheets, (2) inclusions in polymict impact breccias (suevite), (3) dykes and veins in the autochthonous crater basement, in displaced shocked rock fragments and in displaced (unshocked) megablocks, (4) individual melt particles on top of the ejecta blanket, glassy or crystallised spheres in global air fall beds, and (5) glassy tektites. Coherent melt sheets in large craters and the related hydrothermal processes may produce extensive ore deposits [6]. *Shocked rocks and minerals* (~5–50 GPa) are found as allochthonous clasts within polymict impact breccias, impact melt rocks and air-fall beds, and as (par)autochthonous material of the crater basement [1, 7].

Monomict breccias (< ca. 5 GPa) formed during shock compression and dilation are characteristic of the crater basement but are also common constituents of polymict breccias [1, 7, 8]. Displaced megablocks within the continuous ejecta blanket are usually monomictly brecciated.

Dyke breccias can be related to all major phases of the crater formation process and up to 4 generations of dykes have been observed [8, 9]. *Melt veins* or *shock veins* and *vein networks* [4, 10, 11, 12] described from many terrestrial impact sites [11] and from asteroidal, lunar and Martian meteorites [4, 10, 13] are clearly formed during the early compression stage, as they often occur as clasts within later-formed breccia dykes and sometimes contain high-pressure polymorphs. The category "*Dykes, veins and vein networks*" (Fig. 4) includes also formations that in the past have been collectively labelled "*pseudotachylite*". This term should be avoided as it includes a variety of formations of melt and purely clastic breccia as well as friction-generated bona fide pseudotachylite [11]. The injection

Table 4: Classification of shocked sandstone; modified after [23 and 24]; ranges of pressure estimates are given in parentheses; post-shock temperature are relative to an ambient temperature of 0°C

Shock stage	Equilibration shock pressure, GPa	Post-shock temperature, °C	Shock effects
0	0.2-0.9	~25	Undeformed sandstone
1a	~3.0 (2.2-4.5)	~250	Compacted sandstone with remnant porosity
1b	~5.5 (3.6-13)	~350	Compacted sandstone compressed to zero porosity
2	~13	~950	Dense (non-porous) sandstone with 2-5% coesite, 3-10% glass and 80-95% quartz
3	~30	>1000	Dense (non-porous) sandstone with 15-35% coesite, traces of stishovite, 0-20% glass and 45-80% quartz
4			Dense (non-porous) sandstone with 10-30% coesite, 20-75% glass and 15-45% quartz
5			Vesicular (pumiceous) rock with 0-5% coesite, 80-100% glass (lechatelierite) and 0-15% quartz

modification stage while the transient crater collapses with development of an extensional regime; large-scale faulting may take place during this phase.

The time for the formation of impactites ranges from seconds to hours [2, 14] and is extremely short compared to any other geological process. Despite of this, distinct superposition contacts between layered impact formations or contacts at discordant impact breccia dykes are quite common; e.g. sharp contacts of coherent sheets of impact melt to monomictly brecciated, unshocked or mildly shocked crater basement, or contacts between the continuous ejecta deposits (polymict lithic breccias) and the overlaying suevite are characteristic.

7. OPEN QUESTIONS AND FUTURE PERSPECTIVES

In our view some of the most burning *open questions* in terrestrial impact crater research are:

1. What is the role of target composition and target structure for the cratering process? To answer this question we need more comparative studies of craters of similar size but of different target composition and target stratigraphy. Such studies should be performed in close interaction with numerical modeling of the cratering process.
2. How does the formation and collapse of the vapour (ejecta) plume take place and how does it change as a function of crater size? To make progress in this

area one needs more focused analyses of the products of ejecta plumes, in particular suevite breccias, at craters of different size and different target composition. These studies, again, should be accompanied by numerical modeling which should include modeling of the global effects in the case of large impact event such as that at Chicxulub.

3. What is the distribution and state of impactor material in impactites? In a first step the data base should be substantially enlarged, i.e. we need to know the type of impactor for much more craters than we have so far. This requires a comprehensive research effort using platin group elements (PGE) analyses of those impactites which were “contaminated” by projectile material during crater formation, namely impact melt rocks and suevites. This requires that also the data base of the known types of meteorites must be improved substantially. In a second step an attempt should be made to better understand the process of mixing of impactor and target material during the crater-forming process. Such studies may eventually yield a better understanding of the variation of the Earth-crossing impactor flux as a function of time since the formation of the Earth-moon system, if the analysis of melt rocks from the lunar highlands (Apollo samples and meteorites) is included.
4. What are the exact absolute ages of the known terrestrial impact craters? There is a strong need for more high-precision radiometric dating of impact melts in terrestrial craters, as only a fraction of the currently known terrestrial impact structures have been dated at reasonable precision (< 5 Ma error). This is also mandatory with regard to question 3.

Regarding *future strategies* for impact crater research there are certainly conflicting views about the best approach to future research. We do not argue against any effort to discover and describe new craters. However, it is not extremely helpful to produce more “bits and pieces” from unknown or poorly studied craters. There are good arguments for promoting comprehensive and multidisciplinary studies on well documented and well accessible craters in the context of the major issues of cratering mechanics. In this approach any possible effort should be made to favor comparative studies of craters of different size classes and of different target compositions. In any case, a better interaction of field, laboratory, and modeling studies for any crater in question is highly recommendable. In view of the general importance of impact cratering for the geological, climatological and biological evolution of planets and moons in the Solar System, a strong research focus on large complex terrestrial craters such as Vredefort, Sudbury, and Chicxulub is highly promising as such studies do have clear and far-reaching planetary implications. Last not least, a special interdisciplinary effort for learning more about the Achaean cratering record on Earth should be made. In particular, the search for distal ejecta layers (so-called *spherule beds*; [15]) in the Archaean and Proterozoic has the potential to extend the current terrestrial impact record which is strongly skewed to impact ages < 500 Ma.

Classification of impactites from single impacts according to geological setting, composition, texture, and degree of shock metamorphism (see text for details)

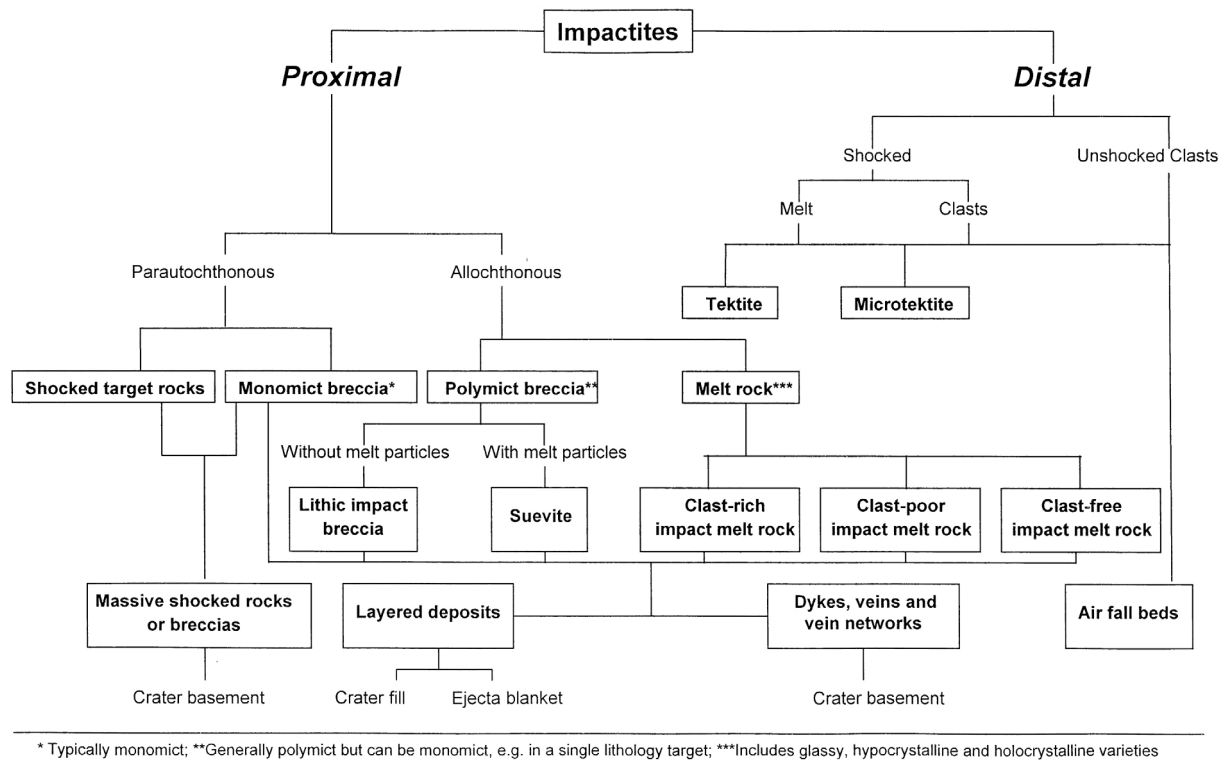


Fig. 4: Classification of impactites and their geological setting (from [1]).

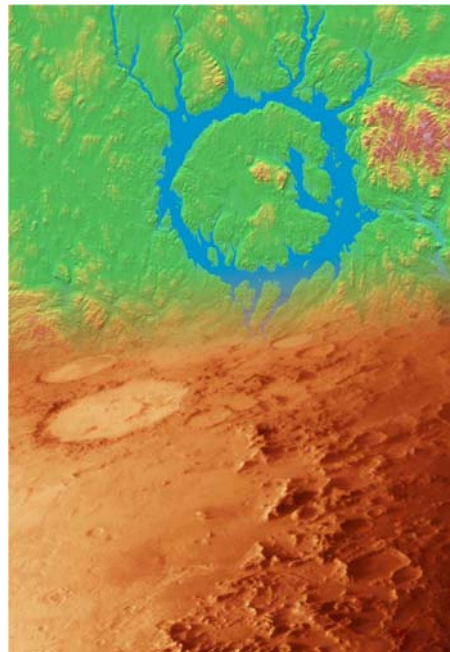
8. REFERENCES

- [1] Stöffler D. and Grieve R. A. F., *Towards a unified nomenclature of metamorphic petrology. Chapter 11: Impactites, A proposal on behalf of the IUGS Subcommission on the Systematics of Metamorphic Rocks*, IUGS Blackwell Publishers, in press, 2006. [2] Melosh H. J., *Impact Cratering: A Geologic Process*, Oxford University Press, New York, 245p., 1989. [3] Stöffler D. et al., in J. J. Papike and R. B. Merrill (eds.) *Proc. Conf. Lunar Highland Crust*, 51-70, Pergamon Press, New York, 1980. [4] Bischoff A. and Stöffler D., *Eur. J. Mineral.* 4, 707-755, 1992. [5] Dressler B. O. and Reimold W. U., *Earth-Sci. Rev.* 56, 205-284, 2001. [6] Reimold W. U. et al., in Koeberl, C. and Henkel, H. (eds.) *Impact Tectonics*, 479-552, Springer-Verlag, Berlin, 2005. [7] Stöffler D., *J. Non-Crystalline Solids* 67, 465-502, 1984. [8] Stöffler D. et al., in Boden A. and Eriksson K. G. (eds.) *Deep Drilling in Crystalline Bedrock*, 277 – 297, Springer Verlag, Berlin, 1988. [9] Lambert P., *Proc. Lunar Planet. Sci. 12A*, 59-78, Pergamon, New York, 1981. [10] Stöffler D. et al., *Geochim. Cosmochim. Acta* 55, 3845-3867, 1991. [11] Reimold W.U. and Gibson R.L., in Koeberl, C. and Henkel, H. (eds.) *Impact Tectonics*, 1-53, Springer Verlag, Berlin, 2005. [12] Dressler B. O. and Reimold W. U., *Earth-Sci. Rev.* 67, 1-60, 2004. [13] Nyquist L. E. et al., in Kallenbach R. et al. (eds.), *Chronology and Evolution of Mars*, Space Science Series of ISSI, Kluwer Academic Publishers, Dordrecht, Space Science Reviews 96, 105-164, 2001. [14] Ivanov B. A. and Artemieva N. A., *Geol. Soc. Amer. Spec. Paper* 356, 619-630, 2002. [15] Simonson B. M. and Glass B. P., *Annual Reviews of Earth and Planetary Science* 32, 329-361, 2004. [16] Stöffler D., *J. Geophys. Res.* 76, 5541-5551, 1971. [17] Kieffer S. W. et al., *Proc. Lunar Planet. Sci. Conf.* 7th, 1391-1412, 1976; [18] Schaal R. B. and Hörz F., *Proc. Lunar Planet. Sci. Conf.* 8th, 1977. [19] James O. B., *Science* 116, 1615-1620, 1969. [20] Ostertag R., *Proc. Lunar Planet. Sci. Conf.* 14th, *J. Geophys. Res.* 88, B364-B376, 1983. [21] Stöffler D. et al., *Geochim. Cosmochim. Acta* 50, 1986. [22] Raikes S. A. and Ahrens T. J., *J. Royal Astron. Soc.* 58, 717-747, (1979); [23] Kieffer S. W., *J. Geophys. Res.* 76, 5449-5473, 1971. [24] Kieffer S. W. et al., *Contrib. Mineral. Petrol.* 59, 41-93, 1976. [25] Kring et al., *Earth Planet. Sci. Letters* 140, 201-212, 1996.

Session S.07

Chicxulub: New Geophysical Studies

Chair: G. Osinski



CHICXULUB, ANATOMY OF A LARGE IMPACT STRUCTURE: FROM IMPACTITE TO EJECTA DISTRIBUTION

Philippe Claeys

Dept. of Geology, Vrije Universiteit Brussel, Pleinlaan 2, B-1050, Brussels, Belgium, E-mail: phclaeys@vub.ac.be

ABSTRACT

The impactites from the Cretaceous-Tertiary boundary Chicxulub crater in Yucatan are described. Chicxulub is one of the largest and best-preserved terrestrial craters. It is thus one of the only places where cratering process and distribution of ejecta on rocky planets with an atmosphere can be directly documented. The Chicxulub impactites originated from a series of wells ranging from the crater center to outside the rim. The impactites were emplaced by either ground surge transport on the crater floor or settled out of the vapor cloud; for the last debris to fall back sorting through the air or water occurred. The possible existence of suevite in outcrops in Yucatan and southern Mexico indicate that the vapor cloud probably had a very wide geographic extension.

1. INTRODUCTION

The Cretaceous-Tertiary (KT) boundary Chicxulub crater buried under the Yucatan peninsula in Mexico is one of the largest impact structures on Earth. This crater is now accepted as the cause of the KT boundary mass extinction that led to the demise of the dinosaurs and 50 to 60 % of the fauna and flora on Earth. Another major scientific significance of Chicxulub lies in the fact that it is a young and well preserved, large impact structure. It is the only pristine crater in the size range > 150 km on Earth (Table 1). After formation, the crater was rapidly buried under Cenozoic sediments, which limited erosion and hampered major modifications of the original morphology. Moreover, little tectonic activity affected the Yucatan peninsula during the Cenozoic.

Currently, the Chicxulub structure is interpreted either as a peak-ring or a multi-ring basin between 180 and 200 km in diameter [1;2;3;4;5]. It was formed some ~ 65 million years ago, by the impact of either an asteroid or a comet between 10 and 12 km in diameter. The recovery, at the KT boundary in a Pacific Ocean deep-sea core, of a small piece of carbonaceous chondrite, inferred to derive from the Chicxulub projectile, favors perhaps an asteroidal origin [6]. The impact occurred on a shallow water carbonate platform with interlayered evaporites overlying a Pan African basement, probably essentially gneissic or granitic in composition [7].

Buried under ~ 1 km of Cenozoic sediments, the crater is not directly accessible and must be investigated using geophysical methods and deep drilling. Seismic

data and impact-modeling indicate that the crater transient cavity was between 80 and 110 km in size, reached at least 30 km in depth and excavated the Yucatan crust down to ~ 15 km [3;5;8;9;10]. Although, several geophysical surveys led to major progresses during the last decade, key questions remain open concerning the formation, structure and exact dimensions of the Chicxulub crater. The difficulties in constraining its diameter are in part semantic and related to the precise concept of crater size and crater rim [see discussion in 11].

Table 1: Comparison of the 3 largest terrestrial craters

	Vredefort	Sudbury	Chicxulub
Age (Ma)	2023 ± 4	1850 ± 3	65.0 ± 0.1
Method	U/Pb, zircons	U/Pb, zircon	Ar-Ar, impact melt
Diameter in km	~ 300	~ 250	~ 180
Position	surface	surface	buried
State of preservation	eroded to sub-crater basement	crater basement to sediments	quickly buried, presumably v. good
Impact melt sheet	relics only dikes, bronzite-granophyre	> 2.5 km, differentiated, SIC	exact size unknow
Target rock	crystalline basement + metasediments?	crystalline basement + metasediments	carbonate evaporite + crystalline basement
Ejecta blanket	eroded	unknown	continuous
Distant ejecta	unknown	Gunflint-Rove Fm	worldwide KTB
Effects	unknown	unknown	mass extinction

The ejecta material produced by this impact spread worldwide and is relatively easy to find as it marks the KT stratigraphic boundary [12]. At this point ejecta have been identified at more than hundred KT boundary sites worldwide, in depositional settings ranging from deep marine to continental [13]. Starting at the crater margin, the continuous ejecta blanket extends over the Yucatan platform all the way to Belize, more than 400 km from the rim [14]. In the Gulf of Mexico region, impact glass and ejecta-spherules are associated with high-energy

sedimentation induced by the collapse of the Yucatan platform margin [15] and the production of giant tsunami-waves [12;16]. This ballistic ejecta deposition stretches to the continental sites in the US Western Interior, forming a double ejecta layer [17;18]. At more distal locations worldwide, the products of the Chicxulub vapor plume, which covered the whole planet, are concentrated in the fine KT layer. They mainly consist of shocked materials, Ni-rich spinels and the now classic enrichment in platinum group elements (known as the *positive Ir anomaly*) [12]. The detailed study of Chicxulub provides a unique view of the processes leading to the formation of a complex impact structure and the production and distribution of ejecta debris on a rocky planet with an atmosphere.

2. IMPLICATIONS FOR CRATERING ON OTHER PLANETS

Impact craters occur on most solar system bodies and attest of the importance of collisions in planetary evolution [see 19 for a discussion of crater terminology]. However, despite several decades of multidisciplinary efforts, the process of crater formation is far from being fully understood, in particular for large complex structures. The formation of complex crater releases so much energy that the fundamental properties of a sizeable volume of the target rock are modified. These lithologies become capable of flowing, and large volume of rocks can be displaced in various directions. The final crater morphology is the result of complex interactions between the propagation of shock waves, strength and viscosity of the target rock, and gravity. Terrestrial craters are so far the only place where the relationships between crater size and morphology on the one side and subsurface structure and lithology on the other side can be established. On planetary bodies, craters show, with increasing size, a drastic change in morphologies, essentially marked by trend towards flatter structures of higher internal complexity [19]. The trend is best documented from the Moon, which thanks to its lack of geological activity ideally preserves crater morphologies (Fig. 1). Good examples are also known from Venus and Mars.

On the Moon, small structures display a simple bowl-shaped morphology. With size, the crater evolves into a central-peak crater, characterized by a flat central zone marked by a central protuberance. As size continues to augment, this central peak transforms into an almost circular peak-ring surrounding an inner basin (Fig. 1). A succession of concentric uplifted rings, and down-faulted grabbens, appears in the largest craters, forming what is characterized as a multi-ring basin morphology. The “bulls-eyes” structure of the 900 km in diameter Mare Orientale basin is a classic example of a multi-ring basin.

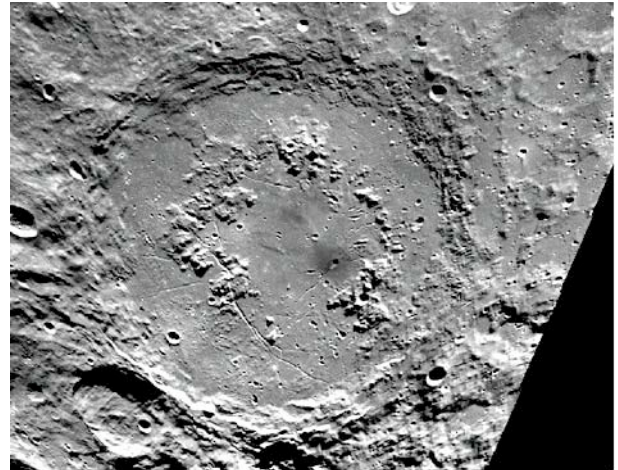


Fig. 1 Schrodinger central peak-ring crater on the Moon (320 km in diameter)

About 170 impact craters are known on Earth. Geological activities bias their distribution towards young craters (< 200 Ma). On average, small size structures are underrepresented because quickly eroded. It is difficult to establish clear size limits for the different crater morphologies. Depending on the composition of the target rock, structures less than 2 to 4 km display a bowl-shaped morphology such as Barringer crater (1.1 km) in Arizona. Central peak craters do form between 2 and 20 km, such as Sierra Madera, (13 km) in Texas. Above ~25 to 30 km, the craters develop a peak-ring morphology, as shown by the Ries (25 km) in Southern Germany, Mjølneir (40 km) in the Barents Sea, Clearwater West (36 km) in Canada [20]. The presence of multi-ring basins on Venus indicates that such huge impact basins should also exist on Earth [4]. In this size range (>> ~ 100 km), the lack of understanding of the ring formation process, coupled with erosion and post-impact deformations renders the determination of morphology of the largest terrestrial crater more difficult and in some cases rather controversial. In multi-ring basins, the post-impact movements of the target rock affecting the transient crater are far more complex and extensive than in smaller structures [19;20].

Only three recognized complex structures > 150 km in diameter are known on Earth. These 3 large craters are Vredefort in South Africa, 203 Ma old and estimated between 250 to 300 km in size; Sudbury in Canada, 1850 Ma old and estimated to be 250 km in size, and Chicxulub, 65 Ma, between 180 and 200 km in size. Table 1 compares the 3 structures. At Vredefort, erosion has removed the original features down to a depth between 5 and 11 km, preserving only the deeper inner structure [21]. On top of 1.8 billion years of erosion, the shape of Sudbury has been severely distorted by post-impact tectonic activity. The exact morphology and size of these two ancient craters is thus difficult to reconstruct. The well-preserved

Chicxulub crater probably represents an ideal candidate for a terrestrial multi-ring basin [2;3]. The rings could be marked by small topographic elevations recognized on the Yucatan platform [22], which seem to correlate with concentric highs of the target lithology, detected by seismic reflection profiling (Fig. 2) [4]. However, the case is far from being settled and major discussions remain [see 5;11;23].

3. DRILLING IN THE CHICXULUB CRATER

Several drilling campaigns took place within or at the margin of the Chicxulub crater (Fig. 3). Several decades ago, PEMEX, the Mexican oil company, drilled Chicxulub as a petroleum exploration target. Three holes penetrated the structure and another 5 were set outside the rim. Some information from the ditch

cuttings and logging data are still available and a few pieces of cores have been preserved mainly from well Yucatan 6 (Y6), and to a much lesser extend Chicxulub 1 (C1). The holes Sacapuc 1 (no core preserved) and C1 were drilled in the central peak-ring of the crater, and Y6 on the flank of the uplifted central zone. In 1994, the Universidad Nacional Autonoma de Mexico (UNAM) started a shallow drilling campaign outward from the crater margin [24]. Three holes intersected the impactite lithologies, UNAM 5, 6 and 7. In 2002, the International Continental Scientific Drilling Project (ICDP) drilled the hole Yaxcopoil 1 (Yax1) in the structural low zone, between the inner peak-ring and the crater rim [25].

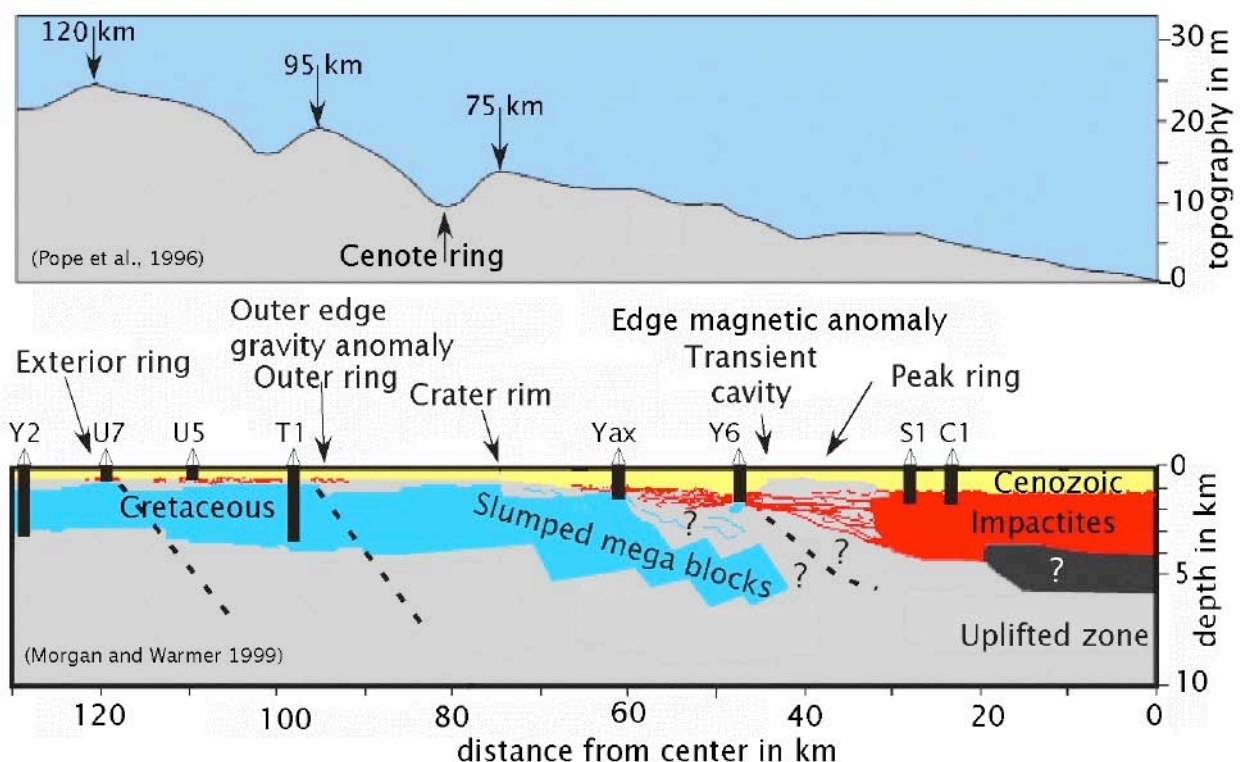


Fig 2 Above: topography of the Yucatan Peninsula showing local elevations, possibly reflecting the ring structure from the underlying Chicxulub crater. The aligned cenotes are most likely also related to the intense fracturing of the crater lithologies. Below: projection of the onshore wells on a crater model based on the offshore seismic line. The advocated expansion of the impact melt-rock outside the peak ring central depression is indicated (modified after [11]). As documented in Yax1 and Y6, layers of melt breccia settled on the flank of the peak ring and became very thin in the annular trough

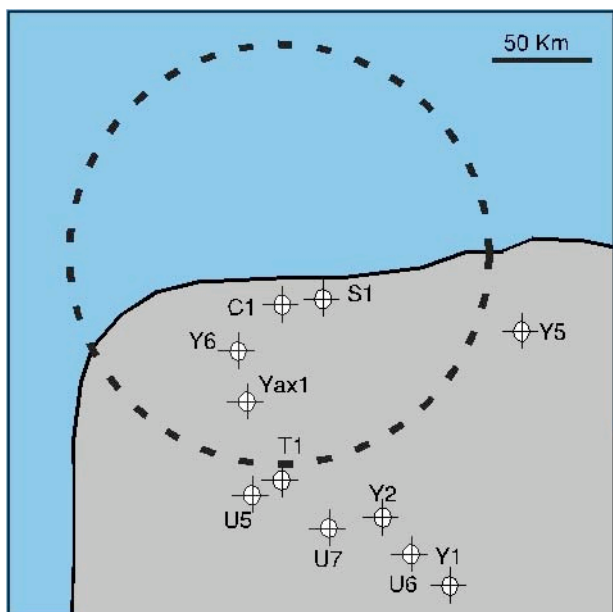


Fig. 3 Location of the existing wells in Chicxulub

4. THE PEMEX CORES: CHICXULUB 1 AND YUCATAN 6

Fig. 4 shows the stratigraphy of the impactites and the samples available from wells C1 and Y6. Near the center of the peak-ring, the Chicxulub-1 well seems to have reached the melt-rock around 1250 m. The only two preserved samples (C1-N9 and C1-N10 around 1400 m) show a classic melt-rock texture with an abundant millimeter sized melt-fragments floating in a rather coarse matrix (Fig. 5). All the clasts show various degree of melting and the majority is clearly digested in the matrix. The clasts are composed of plagioclase and pyroxene and their original composition cannot be identified. The matrix contains small (0.5 mm) augitic pyroxene and lath-shaped plagioclase grains, which calcic core is often surrounded by albite. Slightly larger K-feldspar crystals are also present. Less abundant minerals are epidote, magnetite, sphene, pyrite and Fe – Mg - alumino-silicates. Calcite and anhydrite are rare, and when present clearly form a secondary replacement phase. The presence of albite rim around plagioclases indicates some hydrothermal alteration of this locally porous matrix. However, this alteration appears less intense compared to the samples from Y6 or Yax1 (see below). This is supported by the $^{40}\text{Ar}/^{39}\text{Ar}$ dating of the C1 samples that produced flat Ar release spectra and yielded reliable KT boundary ages [26].

In C1, the melted material is derived from the deep basement part of the target rock, with little contribution from the overlying sedimentary rocks. The absence of unmelted fragments and the coarse-grained matrix support a rather slow cooling process within the inner part of a probably thick melt-sheet. The Chicxulub C1 melt-rock resembles the thick melt sheets described at

other large (> 100 km) craters such as Manicouagan and Sudbury. C1 is so far the only site within the Chicxulub crater where real impact melt-rock has been recovered.

More samples are available from well Y6 (Fig. 4). Despite their sporadic distribution, the sequence of impactite can be reconstructed. Below the Cenozoic sequence, suevite is encountered at ~ 1100 m, its thickness is estimated around 170 m. Three different types of suevitic lithologies have been described in details by [13].

A fine-grained carbonate-rich suevite occurs at the very top of the impactite (upper suevite, 1100-1103 m). This unit is dominated by small size (~ 0.5 mm) solid and formerly molten fragments of the carbonate layers forming the upper part of the Yucatan target. Some solid fragments still display fossils, while others are characterized by feathery textures supporting the existence of carbonate melt [13]. Melted basement clasts, most of them altered to phyllosilicates are also present. Carbonate globule are closely associated with the silicate melt. These clasts are embedded in a porous, matrix composed mainly of small (~10 to 30 μm) crystals of calcite, feldspar, and quartz.

The underlying unit is a coarser and more clast-rich suevite (middle suevite, 1208-1211 m). The clasts are distinctively larger and more distinct than in the overlying unit. The proportion of unmelted basement (mm to cm in sizes) and altered silicate melt increases while the carbonate clasts clearly decrease. The silicate clasts reflect the composition of the deep Yucatan basement (gneiss and quartzite) and show a high degree of shock metamorphism (several sets of PDF and mosaics in quartz). The clasts are floating in much more compacted but still very calcite-rich (~ 40 wt%) matrix. Rare anhydrite clasts are present. This unit resembles the “classic” fall-back suevite described at the Ries crater for example.

The last unit of the sequence is an annealed suevite (thermometamorphic or lower suevite, 1253-1256 m). It contains essentially shocked basement clasts and silicate-melt fragments. Carbonates, both as clasts or in the matrix are much less abundant in this unit. The matrix is dense, recrystallized and composed of intergrown feldspar and pyroxene grains. Locally, anhydrite fragments are present, but most likely as a secondary replacement, as are the calcite veins running through parts of the rock. This unit lies on top of several hundred meters of impact melt breccia (Fig. 4). The clastic matrix was probably thermometamorphosed and recrystallized at the contact on the hot underlying unit.

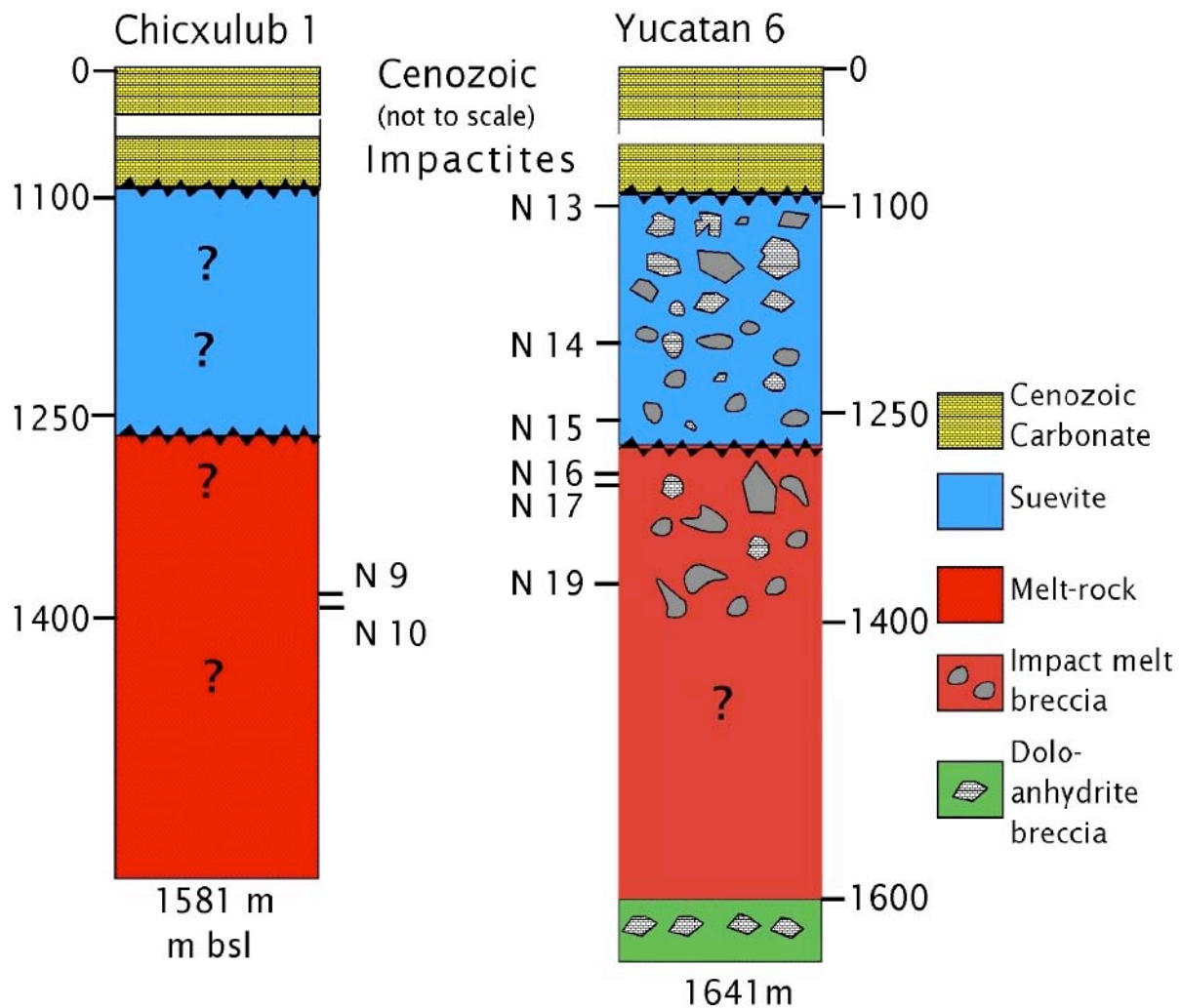


Fig 4 Schematic representation of the impactite lithologies encountered in the PEMEX cores C1 (peak ring) and Y6 (flank of peak ring), the depth of the preserved core fragments in indicated. In Y6, carbonate content decreases with depth.

The Y6 suevite, despite the lack of continuity in the available samples, is clearly stratified. Carbonates from the upper part of the Yucatan target rock noticeably dominate the composition of the top of the suevite. With increasing depth, it is replaced by a more basement-derived composition. In terms of bulk chemistry, SiO_2 is negatively correlated with both CaO and MgO . Evaporite clasts are underrepresented compared to their proportion ($\sim 1/3$) in the upper part of the Yucatan target rock.

Below $\sim 1260 - 1270$ m (?), the suevite is replaced by an impact melt-breccia, which seem to extend down to a depth of more than 1600 m. According to the ancient PEMEX logging reports, Y6 bottomed in a dolomite-anhydrite breccia at ~ 1641 m. The thickness of the impact melt-breccia is about 330 m, but unfortunately, only its upper part has been sampled. It is composed of solid and melted basement clasts, a few mm in size dispersed in a fine matrix. Some gneiss clasts can be recognized, but the majority is composed of

recrystallized quartz and feldspar. The silicate basement clasts display clear evidence of PDF. The fragments are well distinct in the matrix and often are surrounded by a corona of pyroxene. Other clasts are assimilated in the matrix but to a much lesser extend than in C1. The matrix is abundant (70% of the rock) and composed of microcrystals ($< 10 \mu\text{m}$) of pyroxene and plagioclase embedded in a loose cryptocrystalline groundmass. Carbonate and anhydrite are not common in this unit. Locally veins of anhydrite occur but clearly representing secondary hydrothermal processes. The upper part of this unit down to ~ 1400 m (Fig. 4) appears rather homogeneous in terms of clast and matrix composition.

The Y6 impact melt-breccia is clearly finer grained and significantly, more altered than the impact melt material described in C1. It differs also from the “classic” melt-rocks known at other large craters. In terms of bulk chemistry, the Y6 impact melt-breccia is similar to the lower suevite unit and is more carbonate-

rich than the C1 melt-rock. Based on its fine texture and undigested clasts, it crystallized more rapidly, probably from a thinner melt pool than its C1 counterpart. The components are clearly derived from the shock melting of the deep Yucatan target rock, with limited contribution from the overlying sedimentary units.

Little is known about the dolomite / anhydrite breccia reported to occur at the bottom of Y6. This well is located in or near the rim of the collapsed transient cavity [3;4;5]. This is most likely, a rather complex structural zone. One simple explanation is that this breccia represents the top of a series of mega-blocks of the stratified Yucatan target rock, as in Yaxcopoil 1 (see below). However, this remains to be confirmed, as the mega-blocks could also have been scraped off and slumped away from this very zone. The breccia would then represent deeper lithologies. The offshore seismic profiles do not permit to clarify this question. This polymict breccia constrains the thickness of the melt material to ~ 360 m. The Y6 impact melt breccia probably formed a tongue of melt material spilled over from the central zone and emplaced on the flank of the central peak-ring (Fig. 2).

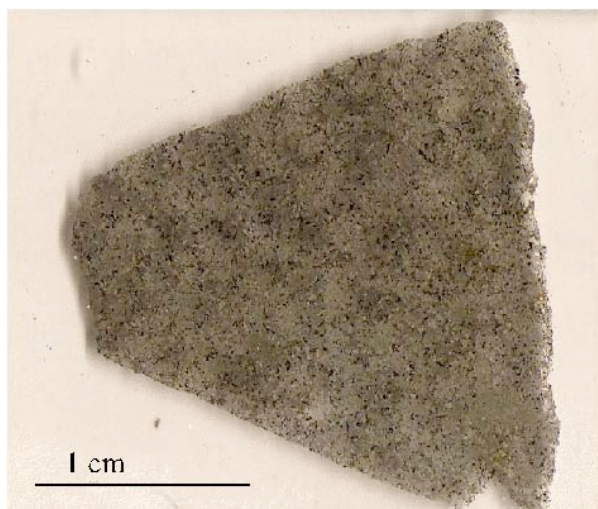


Fig. 5 Chicxulub coarse grained impact melt-rock from well C1. This sample originates from the top of a thick impact melt sheet (photograph of a thin section).

5. THE ICDP YAXCOPOIL-1 (YAX1) CORE

The ICDP drilling at Hacienda Yaxcopoil took place between December 2001 and March 2002 and reached a depth of 1511 m. The well was located some 62 km south from the center of the Chicxulub crater, and ~15 km south of previously described well Y6 (Fig. 3). In terms of the crater structure, this location corresponds to the depression zone between the inner peak-ring and the crater rim.

Post-impact Cenozoic sediments form the top 795 m of the encountered lithologies (cored only from 495 to 795 m). They overlie 100 m of allochthonous polymict

breccia (794.63 to 894.94 m) characterized as suevites according to [27]. Below, a 616-m thick sequence of Mesozoic carbonate and anhydrite layers occurs from a depth of 895 m all the way to the bottom of the well (1511 m).

The thin impactites sequence has been described by several authors and subdivided in 6 units [23]. Only, [28] preferred to group to upper two units (sorted suevite), what appears reasonable considering that they form a continuous fining upward sequence. Bulk rock chemical analyses of these units are given by [28].

In general, the Yax1 suevites are rich in melt particles, mostly derived from the silicate basement. They are clast supported and the percentage of matrix varies significantly throughout the sequence. Carbonates form a major component of the matrix and occur as solid clasts. These characteristics were also reported for Y6 and in general distinguish Chicxulub from the suevites described at other craters [13]. In the suevite units, basement fragments contain indications of shock metamorphism, mainly in the form of quartz grains displaying 2 or 3 sets of PDF. There is no marked increase in shock metamorphism with depth. Some of the shock features were perhaps recrystallized in unit 5, but unit 6 seems to contain fewer shocked grains than the overlying units. Yax1 is more affected than Y6 by hydrothermal alteration that has transformed most of the formerly melt or glass components in phyllosilicates or has caused the precipitation of secondary K-feldspars [23]. Within the matrix, calcite often appears recrystallized. The nomenclature of the Yax1 suevite given below follows that of [23]. It is the most consistent with the one used for Y6 [13], facilitating the comparison and correlation between the two wells.

1) Unit 1 (upper sorted suevite) occurs between 794.63 m and 807.75 m. This homogeneously fine grained (1 to 2 mm), and in part, laminated unit is composed of greenish to brownish melt particles mixed with carbonates and a lesser proportion of basement fragments. It is clearly clast supported. The matrix, composed of fine calcite and some silicates occurs only as local patches between the clasts. Shocked minerals are rare, and there is no traces of former calcite melt as in the Y6 upper suevite, except perhaps as small inclusions in altered silicate melt particles.

Unit 2 (lower sorted suevite) is found between 807.75 m and 823.25 m. It is similar in terms of components and matrix to the overlying suevite. This unit is coarser grained, with some clasts reaching several centimeters. In general, the sorting is not as good, as in unit 1. There is a clear decrease in grain size upward from unit 2 to unit 1 [28]. This supports a continuous deposition in a relatively quiet environment with sorting of the grains during settling through the air or the water column. The sorted suevites in Yax1 share many similarities with the upper suevite of Y6. Both

resulted from the same sedimentation process: an air fall deposition with possible aquatic interactions [13;23].

Unit 3 (upper suevite) occurring between 823.25 m and 846.09 m is noticeably distinct from the overlying units. In this unit, also rich in shard-like melt particles, basement clasts are floating in a clearly clastic matrix, representing more than 50% of the rock. The matrix is essentially composed of calcite, lithic particles and phyllosilicates. Among the clasts, the silicate basement dominates over carbonates. The melt particles show fluidal texture and often contain vesicles and carbonate inclusions aligned parallel to the direction of flow. Anhydrite occurs but it is difficult to say if it is as clasts or most probably as a secondary replacement.

Unit 4 (middle suevite) is comprised between 846.09 m and 861.06 m. It resembles unit 3, except that the clasts and melt particles are more variable in colors and have somewhat larger sizes. The amount of matrix is also significantly lower (<30 %). These last two units are genetically linked and can be correlated with the middle suevite in Y6. A fall-back process deposited them as the vapor cloud rising on top of crater collapsed.

Unit 5 (brecciated impact melt-rock), occurring between 861.06 m and 884.92 m is not a suevite *sensu stricto*. It can be considered an impact-melt breccia, although it differs from that underlying the suevite units in Y6. Basement and carbonate clasts commonly occur in this unit but they are always less abundant than the melt particles. Some of the clasts and melt particles display rather large sizes (> 20 cm). The non-clastic matrix is composed of recrystallized plagioclase and pyroxene, mixed with calcite and phyllosilicates. It represents less than 10% of the rock. This unit can perhaps be considered as a reworked and more carbonate-rich equivalent (both as clast and matrix) to the much thicker impact melt-breccia at Y6.

Unit 6 (lower suevite) occurs between 884.96 m and 894.94 m and is rather different from the overlying sequence. It consists essentially of melt particles and clasts dispersed in a very carbonate-rich groundmass. The solid clasts are mostly limestone and dolomite and often are completely integrated and assimilated in this groundmass. A few rather large (10 cm) silicate basement clasts are present. This unit has no known equivalent in Y6. It appears to be a mixture of the material forming the overlying impact melt-breccia, diluted in a poorly sorted carbonate breccia. The underlying thick sequence of carbonates and evaporitic sediment is interpreted as tilted mega-blocks, displaced during the excavation process. They are cut by a series of impact-related dikes containing suevite, impact-melt and monomict breccias [29]. The carbonates are composed of alternating layers of limestone and dolomite. Locally, some organic-rich and oil-bearing

layers are present (1410 to 1455 m). The anhydrite layers vary in thickness from a few cm to more than 12 m and represent between 25 and 30 % of the mega-block sequence. They display textural characteristics indicative of deposition in shallow-water restricted environment, such as sebkha. The 616 m of underlying Mesozoic sediments have so far not been studied in details, except for the small intervals cut by impact related dikes. An in depth biostratigraphic study of these Mesozoic sedimentary units is urgently needed to document the pre-impact position, source and amount of displacement of the mega-blocks.

6. THE UNAM SHALLOW CORES OUTSIDE THE CRATER RIM

Below Cenozoic carbonates, well UNAM 5, located some 105 km south of the crater center, (Fig. 2) encountered a polymict impact breccia from a depth of ~ 332 m all the way to the bottom at 504 m [24]. This ~ 172 m thick breccia contains melt particles and qualifies as fall-out suevite according to the definition of [27]. The whole sequence appears rather homogenous and composed of various proportions of melt particles, some of them with a well preserved glassy textures, carbonate and anhydrite fragments as well as basement clasts. These fragments are floating in a clastic carbonate-rich matrix. The proportion of clast versus matrix varies significantly. Clasts of anhydrite and dolomite are much more widespread than in the suevite contained within the crater.

Well UNAM 7 is located some 125 km from the crater center [24]. This same suevite unit as in UNAM 5 is encountered, below the Cenozoic carbonates, from a depth of 222.20 m to 348.40 m. A polymict chaotic breccia, with no or only very rare melt fragments occurs below. The clasts are composed of carbonates (limestone and dolomite) and numerous evaporite fragments. The well bottoms in stratified layers alternating between carbonates and evaporites.

Well UNAM 6, some 150 km from the crater center contains no suevite unit. The basal polymict breccia of UNAM 7, containing clasts of limestone, dolomite and evaporite occurs from a depth of 282.80 m below the Cenozoic sediments. The stratified carbonate and evaporite layers appear around 540.50 m. Either the fall-out suevite was eroded from this location before the deposition of the overlying carbonates or it was not deposited.

The observed succession of polymict breccia topped by suevite is similar to the Bunte breccia – fall-out suevite units seen outside the Ries crater. At this point, it remains rather difficult to correlate the fall-out suevite with the units found within the crater in either Yax1 or Y6 and to invoke similarity in their depositional processes. The fall-out suevite is much richer in sedimentary clasts in particular anhydrite and dolomite than its crater counterpart. It also contains no

indication of carbonate melt. This must be viewed as an indication that the fall-out suevite sampled another part - perhaps towards the outside - of the vapor cloud, enriched in these sedimentary components.

7. EXPANSION OF THE FALL-OUT SUEVITE

Several elements may indicate a greater geographic distribution of the deposition of the fall-out suevite outside the crater rim. The continuous ejecta blanket extends over Yucatan and reaches Central Belize, some 360 km from the crater [14]. This unit is essentially composed of autochthonous small and large blocks of dolomite, eroded from the underlying layers and transported over relatively short distances. A finer groundmass of highly crushed carbonates rims the blocks, which size reach several meters. This unit is still about 15 m thick near the Mexican-Belize border. If fall-out suevite ever covered this part of the ejecta blanket, it has now been completely eroded. However, within the top of this is diamictite-like breccia, meter-size clasts composed of greenish to brownish clay material occur (Fig. 6). Small (< cm) fragments of the Yucatan basement can be extracted from these large clasts. They could perhaps represent highly altered suevite debris, lofted from the crater and incorporated in the upper part of ejecta blanket as it was spreading over the Peninsula.

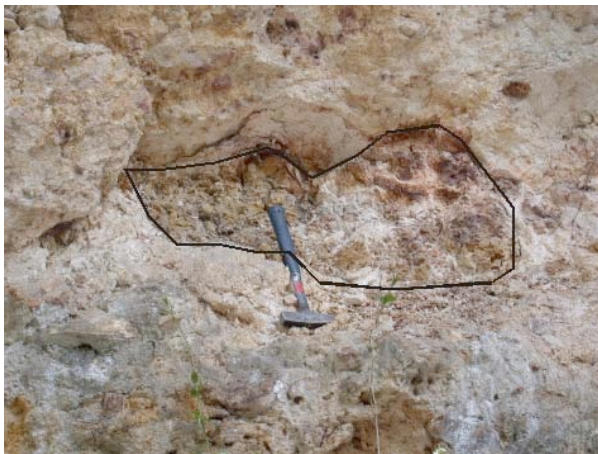


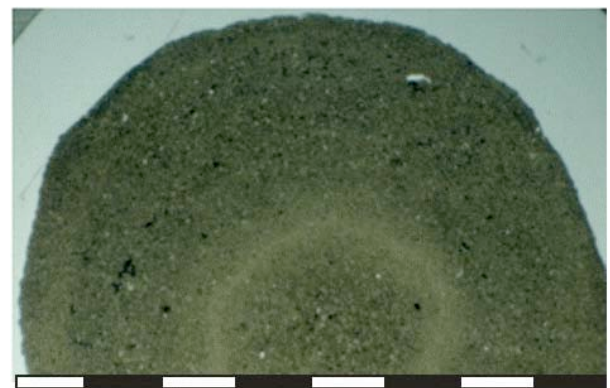
Fig. 6 Diamictite-like ejecta blanket made of autochthonous blocks of dolomite and finely crushed carbonate. This unit crops out in Yucatan, Quintana Roo and Belize [14]. A clay-aggregate is outlined; it could represent what remains of a suevite fragment incorporated in the top of the ejecta blanket as it was deposited all over the Yucatan peninsula. Basement clasts probably originating from the crater can be extracted from such sample.

Further away, in the zone extending today from Campeche to the Northern part of the Chiapas region, the deep-water setting KT boundary is characterized by thick carbonate breccias formed by the collapse of the margin of the Yucatan platform [15]. In El Guayal

(State of Tabasco), some 650 km from the crater, the breccia is covered by a ~ 9 m thick succession of calcareous sands and silts rich in impact material. The same succession has been reported from the oil wells offshore in the Campeche area [15]. The grain size fines upward and the ejecta are essentially composed of altered glass particles, basement clasts, shocked quartz and carbonate fragments. Microfacies analyses indicate that these carbonate fragments formed on a shallow water carbonate platform, such as that covering Yucatan. This unit also contains an 80 cm-thick layer with accretionary lapillis (~ 2 cm, Fig. 7).



Fig. 7 A. Lapilli unit found ~ 2 m below the KT clay containing the platinum group anomaly in El Guayal (Tabasco). The lapillis are up to 2 cm in size and composed of aggregated small grains of calcite and silicates. They are interpreted to be part of a distal fall-out suevite and to have formed in the turbulent part of the vapor cloud.



B. Cross section of lapilli showing the concentric structure. The rings formed by accreted submillimetric grains of calcite, quartz and melt particles can be distinguished.

The lapillis are composed of concentric laminations of accreted carbonates, melted particles and shocked grains, less than a few hundred microns in size. This unit is separated from the Ir-enriched KT boundary

clay by a < 2 m thick, poorly consolidated siltstone, rich in ejecta. Similar lapillis, but significantly smaller, are known in the Ries crater suevite [30]. Although, highly altered this whole succession is interpreted as fall-out suevite. Its mineralogical composition clearly links it to the turbulent vapor and debris cloud that expanded from the crater. Its deposition in the El Guayal area attests of the lateral extension and magnitude of the cloud. A very similar unit, displaying a succession of carbonate breccia, topped by possible fall-out suevite with accretionary lapillis has been reported from Central Cuba [31].

8. EMPLACEMENT OF THE IMPACTITES IN CHICXULUB (FIG. 8)

In the light of the current Chicxulub situation, it is possible to propose scenarios explaining the emplacement of the impactites. So far, most of the seismic lines are located offshore while the core data come from onshore wells. By projecting the well locations on the existing seismic lines, a transversal sequence of crater locations is established (Fig. 2). This projection of course implies a perfect symmetry of the crater, which is unlikely to be the case. The wells spread from the central peak ring area (C1) to the flank of the central peak ring (Y6) to the annular through outward from the peak ring (Yax1) to the outside crater margin (UNAM 5, 6, 7 wells). Considering the fragmented aspect of the information provides by C1 and Y6, this sequence is far from ideal, nevertheless interesting observations can be made (Fig. 8)

Based on seismic data and the rare samples from C1, it is clear that an impact melt sheet lies within the central part of the peak-ring area. This coherent melt sheet cooled off slowly and must be rather thick (Fig. 2). Based on its chemical composition (highest $\text{SiO}_2/(\text{CaO}+\text{MgO})$ of all the analyzed units) it is essentially derived from the melting of the deep silicate basement under Yucatan. The contribution of the overlying carbonate and evaporite target lithologies was minor. The offshore seismic data coupled with modeling results support the presence of a coherent impact melt sheet, 3 to 4 km thick. The transition with the underlying uplifted deep crustal lithologies remains to be clarified [5;10;32].

Some of this impact melt escaped the central depression and accumulated on the flank of the peak ring forming the impact melt-breccia encountered in Y6 (Fig. 2;8). This tongue of impact melt was deposited on top of a polymict breccia of dolomite and evaporite. The structural relationships of this breccia remain to be clarified. It is certainly related to the excavation of the transient cavity, and the outward displacement of mega-blocks from the target lithologies. The tongue of impact melt-breccia extended further out- and downward, cooling down, thinning and in part solidifying. The presence of

brecciated clasts indicates that it was already solid as the reworking took place. As it propagated on a carbonate-rich substrate, it picked up more and more clasts. When this ground surge reached the lower zone of the annular trough, its base was laden with solid and melted carbonate fragments of various sizes. It forms the “lower suevite” identified at Yax1. The same type of mass flow transport is responsible for the emplacement of the overlying unit, with reworked consolidated melt fragments but less carbonates. This ground-surge unit was still hot, when fall-back suevite landed on top of it, as documented by the recrystallization of the matrix in the lower suevite unit in Y6 [13]. The melt-rich fall-back suevite described in Y6 and Yax1 share enough similarities to be both explained by the collapse within the crater of the vapor and debris plume. The observed variation in composition and proportion of the different melt components and clasts can be attributed to different thermal regimes of the plume, and/or a sorting effect during sedimentation.

Later, the fining upward suevite settled, through interaction and sorting by the atmosphere. It is unclear if water effectively rushed back in the crater shortly after the impact [33]. In both Yax-1 and Y6, there is evidence for fine scale laminations, which could be interpreted to indicate gentle settling through the water column [13]. This unit is clearly derived from the hottest zone most likely in the upper and central part of the plume that was rich in carbonate (both as melt and solid) and silicate melts, but depleted in solid basement clasts.

The fall-out suevite deposited on top of the ejecta blanket outside the crater rim is probably derived from a different part of the vapor cloud. Based on the Mesozoic Yucatan stratigraphy [7] and field observation over the Yucatan peninsula, it appears plausible that the dolomite and evaporite clasts were lofted from a more superficial part of the target rock, outward from the excavation zone. The possible wide extension (> 500 km) of the fall-out suevite deposition seems to indicate that the vapor cloud also had a considerable lateral expansion. The presence of accretionary lapillis in the region of Tabasco and in Central Cuba [31], which in the late Cretaceous was located somewhere to the southwest of Yucatan, attest of the lateral magnitude of the cloud. A more in detailed study of these outcrops in term of ejecta transport and deposition is required.

9. PERSPECTIVES

The scenario proposed here is preliminary and schematic as it based on limited impactite samples. It could be improved by a better correlation with the offshore seismic lines, and of course by obtaining more continuous cores in Chicxulub as planned by the ICDP/IODP drilling project [34]. Stratigraphic and

biostratigraphic studies of the sedimentary Mesozoic sequence underlying the impactite in Yax1 will shed light on the original position and the amount of displacement of the mega-blocks away from the transient cavity zone. In these mega-blocks, evaporites represent between 25 and 30 % of the upper 3 km of the sedimentary target rock. This resolves in part the controversy as to the amount of sulfate involved in the cratering process and eventually vaporized [13]. The relative absence of evaporite clasts in the crater's suevite can then be interpreted to reflect the (almost) complete vaporization of the evaporitic layers in the

upper part of the target rock. It is likely that the amount of released SO_x reached the saturation effect in the climate forcing advocated by [35]. The association of impactite studies with numerical modeling as developed by [23] for the Yax1 well certainly deserves to be applied to the whole crater. Numerical models could also document the amount of lateral expansion of the vapor cloud, and test if it is compatible with suevite deposition at more than 500 km from the crater rim.

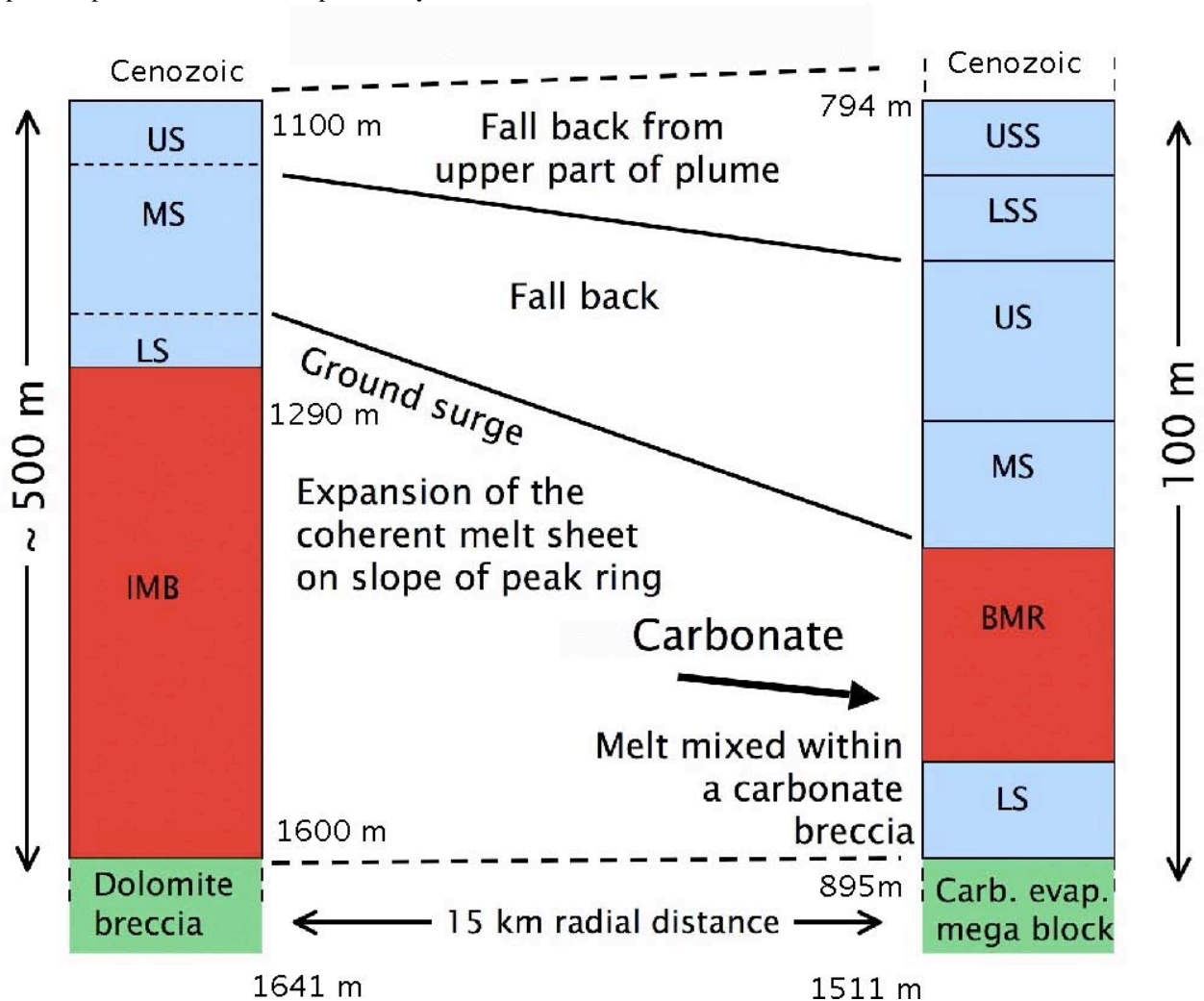


Fig. 8 correlation of the impactite lithologies encountered in Y6 and Yax1, with the three major emplacement processes, ground hugging transport of the basal units, classic fall-back suevite and fall-back with a sorting agent such as air or water for the upper part of the sequence. (Y6: US=upper suevite, MS=middle suevite, LS=lower suevite, IMB=impact melt breccia; Yax1: USS=upper sorted suevite, LSS=lower sorted suevite, US=upper suevite, MS=middle suevite, BMR=brecciated melt rock, LS=lower suevite) [13;23].

ACKNOWLEDGMENTS

Thanks to ICDP and UNAM for access to the Chicxulub samples. This work was supported by a grant from the FWO-research foundation – Flanders. This paper summarizes a keynote presentation given at the 40th ESLAB Symposium: “First international conference on impact cratering in the solar system” 08-12 May 2006.

REFERENCES

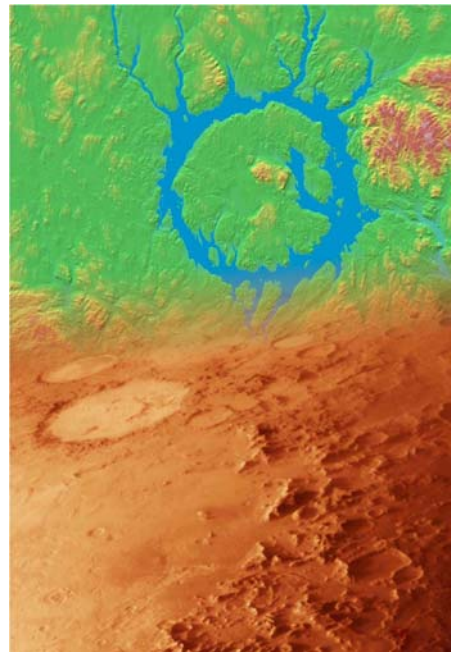
1. A.R. Hildebrand, et al., Chicxulub crater: a possible Cretaceous/Tertiary boundary impact crater on the Yucatán Peninsula, Mexico, *Geology* 19, 867-871, 1991.
2. V.L. Sharpton, et al., Chicxulub multiring impact basin; size and other characteristics derived from gravity analysis, *Science* 261, 1564-1567, 1993.
3. J. Morgan, et al., Size and Morphology of the Chicxulub impact crater, *Nature* 390 472-476, 1997.
4. J.V. Morgan and M. Warner, Chicxulub: The third dimension of a multi-ring impact basin, *Geology* 27, 407-410, 1999.
5. J.V. Morgan, et al., Geophysical constraints on the size and structure of the Chicxulub impact crater, *Geological Society of America Special Paper*, 356, 39-46, 2002.
6. F.T. Kyte, A meteorite from the Cretaceous/Tertiary boundary, *Nature* 396, 237-239, 1998.
7. E. López Ramos, Geological summary of the Yucatán Peninsula, in: *The gulf of Mexico and the Caribbean*, pp. 257-282, Plenum, New York, 1975.
8. E. Pierazzo and H.J. Melosh, Hydrocode modeling of Chicxulub as an oblique impact event, *Earth and Planetary Science Letters*, 163-176, 1999.
9. E. Pierazzo, et al., Hydrocode simulation of the Chicxulub impact event and the production of climatically active gases, *Journal of Geophysical Research* 103(E12), 28607-28625, 1998.
10. J.V. Morgan, et al., Peak-ring formation in large impact craters : Geophysical constraints from Chicxulub, *Earth and Planetary Science Letters* 183, 347-354, 2000.
11. E.P. Turtle, et al., Impact structures: What does crater diameter mean? *Geological Society of America Special Papers* 384, pp. 1-24, 2005.
12. J. Smit, The global stratigraphy of the Cretaceous-Tertiary boundary impact ejecta, *Annual Review of Earth and Planetary Sciences* 27, 75-113, 1999.
13. P. Claeys, et al., Distribution of Chicxulub ejecta at the Cretaceous-Tertiary Boundary, *Geological Society of America Special Paper* 356, pp. 55-69, 2002.
14. A.C. Ocampo, et al., Ejecta blanket deposits of the Chicxulub crater from Albion island, Belize, *Special Paper Special Paper* 307, pp. 75-88, 1996.
15. J.M. Grajales-Nishimura, et al., Chicxulub impact: The origin of reservoir and seal facies in the southeastern Mexico oil fields, *Geology* 28, 307-310, 2000.
16. J. Bourgeois, T.A. et al., A tsunami deposit at the Cretaceous-Tertiary boundary in Texas, *Science* 241, 567-570, 1988.
17. W. Alvarez, et al., Emplacement of Cretaceous-Tertiary Boundary Shocked Quartz from Chicxulub Crater, *Science* 269, 930-935, 1995.
18. B.F. Bohor and B.P. Glass, Origin and diagenesis of K/T impact spherules—From Haiti to Wyoming and beyond, *Meteoritics* 30, 182-198, 1995.
19. H.J. Melosh, *Impact cratering: A geologic process*, 245 pp., Oxford University Press, New-York, 1989.
20. B.M. French, *Traces of catastrophe*, 120 pp., Lunar and Planetary Institute, Houston, 1998.
21. R. Grieve and A. Theriault, Vredefort, Sudbury, Chicxulub : Three of a kind?, *Annual Review Earth Planetary Science* 28, 305-38, 2000.
22. K.O. Pope, et al., Surface expression of the Chicxulub crater, *Geology* 24, 527-530, 1996.
23. D. Stöffler, et al., Origin and emplacement of the impact formations at Chicxulub, Mexico, as revealed by the ICDP deep drilling at Yaxcopoil-1 and by numerical modeling, *Meteoritics & Planetary Science* 39, 1035-1067, 2004.
24. J. Urrutia-Fucugauchi, et al., UNAM Scientific drilling program of Chicxulub impact structure - Evidence for a 300 kilometer crater diameter, *Geophysical Research Letters* 23, 1565-1568, 1996.
25. J. Urrutia-Fucugauchi, et al., The Chicxulub scientific drilling project (CSDP), *Meteoritics and Planetary Science* 39, 787-790, 2004.
26. C.C. Swisher, et al., Coeval ⁴⁰Ar/³⁹Ar ages of 65.0 million years ago from Chicxulub crater melt rock and Cretaceous-Tertiary boundary tektites, *Science* 257, 954-958, 1992.
27. D. Stöffler and R.A.F. Grieve, Classification and nomenclature of impact metamorphic rocks, *Lunar and Planetary Science Conference XXV*, 1347-1348, 1994.
28. M.G. Tuchscherer, et al., Major and trace element characteristics of impactites from the Yaxcopoil-1 borehole, Chicxulub structure, Mexico, *Meteoritics and Planetary Science* 39, 955-978, 2004.
29. A. Wittmann, T. et al., Impact-related dike breccia lithologies in the ICDP drill core Yaxcopoil-1, Chicxulub impact structure, Mexico, *Meteoritics & Planetary Science* 39, 931-954, 2004.
30. G. Graup, Terrestrial chondrules, glass spherules and accretionary lapilli from the suevite, Ries crater Germany, *Earth and Planetary Science Letters* 55, 407-418, 1981.
31. L. Alegret, et al., Cretaceous-Paleogene boundary deposits at Loma Capiro, central Cuba: Evidence for the Chicxulub impact, *Geology* 33, 721-724, 2005.

- 32 . J. Ebbing, et al., 3D gravity modelling of the Chicxulub impact structure, *Planetary and Space Science* 49, 599-609, 2001.
33. K. Goto, et al., Evidence for ocean water invasion into the Chicxulub crater at the Cretaceous/Tertiary boundary, *Meteoritics & Planetary Science* 39, 1233-1247, 2004.
34. J. Morgan, et al., Chicxulub Crater Seismic Survey Prepares Way for Future Drilling, *EOS* 86(36), 325-332, 2005.
35. E. Pierazzo, et al., Chicxulub and climate: Radiative perturbations of impact-produced S-bearing gases, *Astrobiology* 3, 99-118, 2003.

Session S.08

Physics and Chemistry of Impact Cratering

Chair: N. Artemieva



SHATTER CONES OF THE HAUGHTON IMPACT STRUCTURE, CANADA

Gordon R. Osinski⁽¹⁾ and John G. Spray⁽²⁾

⁽¹⁾Canadian Space Agency, 6767 Route de l'Aéroport, St-Hubert, QC J3Y 8Y9 Canada,
Email: gordon.osinski@space.gc.ca:

⁽²⁾Planetary and Space Science Centre, Department of Geology, University of New Brunswick, 2 Bailey Drive,
Fredericton, NB E3B 5A3, Canada, Email: jgs@unb.ca

ABSTRACT

Despite being one of the most distinctive products of hypervelocity impact events, shatter cones remain enigmatic. Several contrasting models for their formation have been presented, none of which appear to account for all of the observations. In this preliminary study, we present an overview of the distribution and characteristics of shatter cones at the Haughton impact structure, one of the best preserved and best exposed terrestrial impact sites. Shatter cones are abundant and well developed at Haughton, due in part to the abundance of fine-grained carbonates in the target sequence. They occur in three main settings: within the central uplift, within megablocks of the ballistic ejecta blanket; and within clasts in allochthonous crater-fill impact melt breccias. Examples of shatter cones within impact breccias are rare in the terrestrial impact cratering record, yet their characteristics at Haughton provide some important insights in to the mechanism of shatter cone formation.

1. INTRODUCTION

Shatter cones are one of the most characteristic products of hypervelocity impact events and are the only shock metamorphic effect that develop on a megascopic (i.e., hand specimen to outcrop) scale [1-3]. Despite the recognition of shatter cones in dozens of terrestrial impact structures, there is still considerable uncertainty concerning their mechanism(s) of formation.

In this study, we present the preliminary results of a study of shatter cones from the Haughton impact structure, Canada. These observations are discussed with respect to the various models proposed for the formation of shatter cones.

2. FORMATION OF SHATTER CONES

Several models have been put forward for the formation of shatter cones. Johnson and Talbot [4] suggested that shatter cones form due to interaction between a propagating shock wave and heterogeneities within the target rocks. Other

workers suggested that shatter cones are tensile fractures that form due to interference between the incident shock wave and reflected stress waves [5]. Two new models have also been proposed. The first model by Baratoux and Melosh [6] builds upon earlier suggestions [4] invoking heterogeneities in rocks as initiation points for shatter cone formation. These authors suggest that the interference of a scattered elastic wave by heterogeneities results in tensional stresses, which produces conical fractures. In contrast, Sagy et al. [7, 8], favour a model in which shatter cones are fractures produced by nonlinear waves that propagate along a fracture front.

3. GEOLOGICAL SETTING OF THE HAUGHTON IMPACT STRUCTURE

Haughton is a well preserved and well exposed 23 km diameter, 39 Ma complex impact structure situated on Devon Island in the Canadian Arctic Archipelago (Fig. 1) (see Osinski et al. [9] for an overview). The target sequence comprises a ~1880 m thick series of Lower Paleozoic sedimentary rocks (predominantly dolomite and limestone, with subordinate evaporate horizons and minor shales and sandstones) overlying Precambrian metamorphic basement of the Canadian Shield.

Allochthonous crater-fill impact melt breccias form a virtually continuous ~54 km² unit in the central area of the structure (Fig. 1) [10]. These pale grey impactites comprise variably shocked mineral and lithic clasts set within a groundmass of calcite + silicate glass ± anhydrite [10]. The groundmass phases represent a series of impact-generated melts derived from the sedimentary target sequence. The lithic clasts are typically angular and are predominantly limestone and dolomite, with subordinate sandstones, shales, and gneisses. Interaction of groundwaters with these hot impact melt breccias led to the development of a hydrothermal system within the crater following the impact event [11, 12]. This resulted in the deposition of a series of alteration products within cavities and fractures in the impact melt breccias, central uplift, and around the faulted crater rim [11, 12].

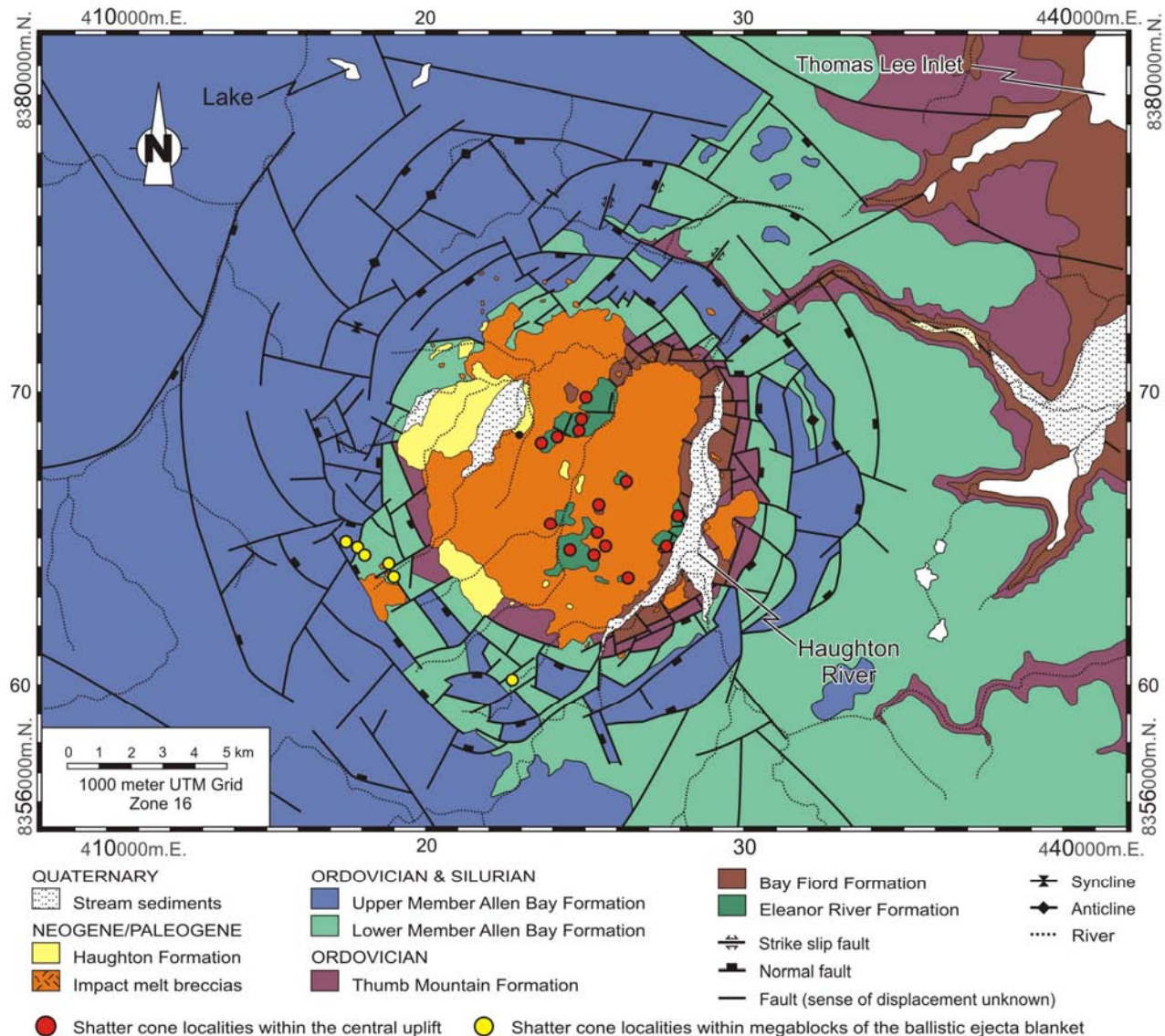


Fig. 1. Simplified geological map of the Haughton impact structure, Devon Island, Canada. Shatter cone localities within the central uplift and ballistic ejecta blanket are highlighted. Note that shatter cones are found throughout the crater-fill impact melt breccias so these localities are not shown. Modified after Osinski [13].

4. SHATTER CONES OF THE HAUGHTON IMPACT STRUCTURE

Shatter cones are common and extremely well developed at Haughton. They were first recognized by Robertson and Mason[14] and are best developed in fine-grained carbonate lithologies. The excellent preservation state and exposure at Haughton allow a detailed study of the shatter cone distribution and morphology to be conducted. Detailed mapping carried out by GRO over the course of 7 field expeditions reveals that shatter cones occur in three main settings at Haughton (Fig. 1): (1) within

uplifted and rotated strata of the central uplift (Fig. 2); (2) within megablocks of the ballistic ejecta blanket (Fig. 3); and (3) within clasts in allochthonous crater-fill impact melt breccias (Figs. 4, 5). The latter are the main focus of this preliminary study.

4.1 Observations

Carbonate clasts within the allochthonous crater-fill impact melt breccias at Haughton show abundant and well-developed shatter cones (Fig. 4). Point counting of clasts at 4 separate locations showed that 50–60 % displayed shatter cones. Weathering in the prevailing

polar desert environment tends to break down the fine-grained groundmass of the impact melt breccias so that the more resistant clasts are available for study on talus slopes. This affords an exceptional opportunity to study the 3-D nature of shatter cones.

The important results of our observations of shatter cones from the Haughton structure are summarized below:

- Apical angles range up to 120° .
- While many shatter cones display curved, oblate, spoon-like surfaces (cf., [7]), many are also conical (Figs. 5a, b).
- Apices often point in opposite directions (Figs. 5b–d).
- Complete cones are present in ~5–10 % of the samples studied (Figs. 5a,b).



Fig. 2. Shatter cones developed in fine-grained limestones of the central uplift of the Haughton impact structure, Canada. The height of the image is 18 cm.



Fig. 3. Field photograph of shatter cones in a limestone megablock from the ballistic ejecta blanket, near the eroded southern rim of the Haughton structure. 35 cm long rock hammer for scale.



Fig. 4. Field photograph of a large carbonate clast (above 6 cm diameter lens cap) with well-developed shatter cones included within crater-fill impact melt breccias. All the clasts in this image are carbonates.

5. DISCUSSION

Shatter cones within central uplifts have been documented at many complex terrestrial impact structures, and have been studied in detail at a few sites (e.g., Beaverhead, USA [15]; Kentland, USA [7]; Sudbury, Canada [16]; Vredefort, South Africa [17]). In this study, we have presented the first detailed observations of shatter cones from allochthonous crater-fill deposits at a terrestrial impact site. These results have some important implications for the currently proposed models for the origin of shatter cones.

The Haughton shatter cones display many of the characteristics typical of shatter cones from other impact sites (e.g., striated surfaces, horsetail structures). The formation of such features can be explained by the models of Baratoux and Melosh [6] and Sagy et al. [7, 8]. However, the presence of shatter cones with complete cones and apices pointing in opposite directions is not explained by the model of Sagy et al. [7] in which shatter cones are "branched, rapid fractures formed by shock impact". These authors also concluded that shatter cones "are intrinsically not conical", which is at odds with our observations from Haughton.

In the model of Baratoux and Melosh [6], conical, complete cones result from conical tensile fractures that are produced by the interference of a scattered elastic wave by heterogeneities in the target rock. However, shatter cones with apices pointing in different directions, as noted at Haughton (this study) and Vredefort [17] were not produced in the numerical simulations of Baratoux and Melosh [6]. This may, however, be due to the simplified nature of the target in these numerical models. Thus, neither of the currently proposed models for shatter cone

formation can explain all the features of shatter cones from terrestrial impact structures.

The abundance of shatter cones within the crater-fill deposits at Haughton is also interesting. Shatter cones form a plane of weakness along which a rock may break apart. The presence of shatter cones within crater-fill deposits at Haughton also indicates that they form early in the cratering process

(i.e., during the contact and compression stage). Thus, the target will be pervaded by shatter cones during the opening up of the transient cavity during the subsequent excavation stage. We suggest that shatter cones may, therefore, play a role in weakening the target prior to collapse during the modification stage, which appears to be necessary to form complex impact structures [18].

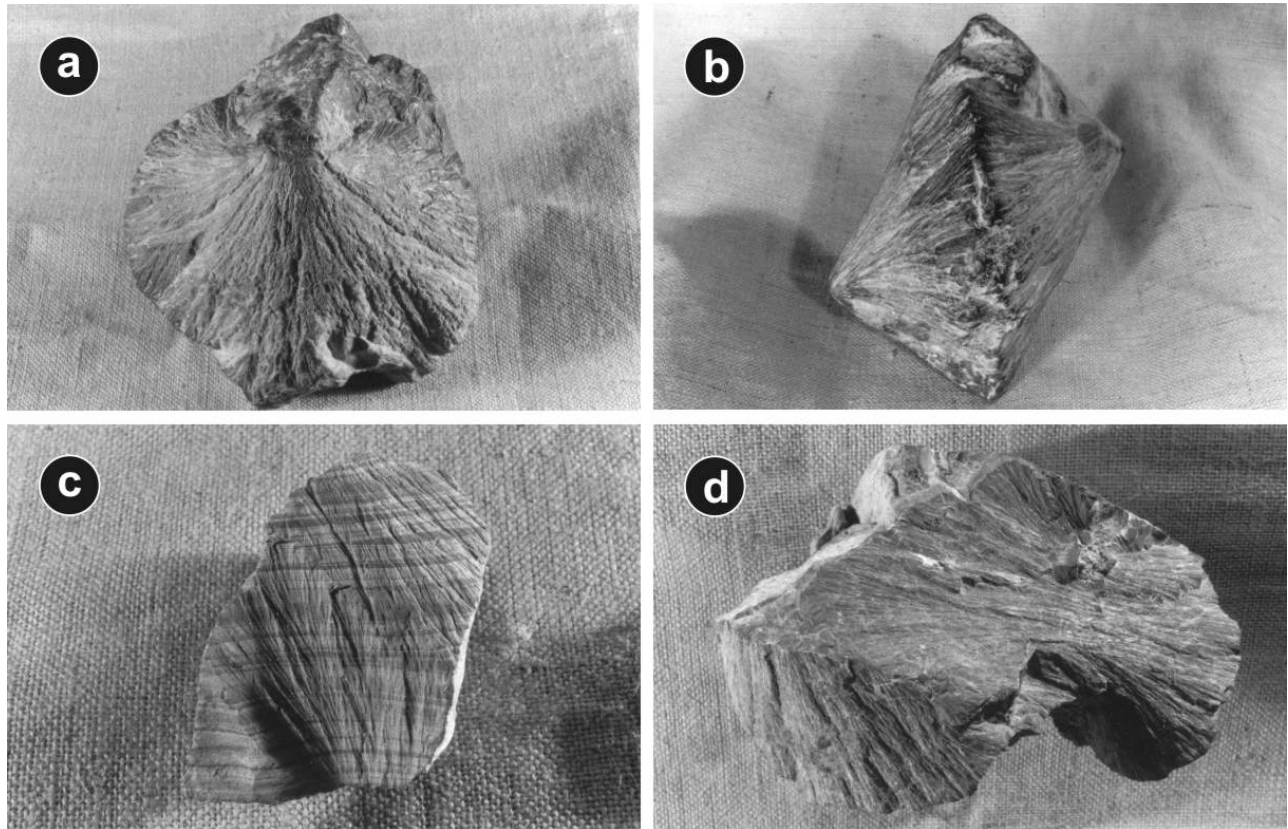


Fig. 5. Hand specimen photographs of carbonate clasts with well-developed shatter cones from the Haughton impact structure. (a) A well-developed shatter cone ~14 cm in diameter. (b) Two complete cones pointing in opposite directions. The specimen is ~13 cm across. (c) Shatter cones with apices pointing in opposite directions. Note the faint horizontal bedding. Specimen is ~6 cm across. (d) Several shatter cones are present in this clast. Note that the striations on the large face converge and then diverge (i.e., these are two shatter cones whose apices meet).

6. ACKNOWLEDGEMENTS

GRO and was funded by the Natural Sciences and Engineering Research Council of Canada (NSERC) through research grants to JGS. Field studies were conducted under the auspices of the Haughton–Mars Project. We are grateful to the Polar Continental Shelf Project (Natural Resources Canada), the Nunavut Research Institute, and the Communities of Grise Fiord and Resolute Bay for their support. We thank Alain Berinstain, Colleen Lenahan, Samson

Ootoovak, Nesha Trenholm and everyone involved in the Haughton–Mars Project for assistance during the HMP 1999–2004 field seasons.

7. REFERENCES

1. Dietz, R.S., Shatter cones in cryptoexplosion craters, in: B.M. French, N.M. Short, (Eds), *Shock metamorphism of natural materials*, Mono Book Corp., Baltimore, 1968, pp. 267–285.

2. French, B.M., *Traces of Catastrophe. Handbook of Shock-Metamorphic Effects in Terrestrial Meteorite Impact Structures*, Lunar and Planetary Institute, Houston, 1998.
3. Milton, D.J., Shatter cones - An outstanding problem in shock mechanics, in: D.J. Roddy, R.O. Pepin, R.B. Merrill, (Eds), *Impact and Explosion Cratering*, Pergamon Press, New York, 1977, pp. 703-714.
4. Johnson, G.P., Talbot, R.J., A theoretical study of the shock wave origin of shatter cones, *Air Force Institute of Technology*, 1964.
5. Gash, P.J.S., Dynamic mechanism for the formation of shatter cones, *Nature* Vol. 230 32-35, 1971.
6. Baratoux, D., Melosh, H.J., The formation of shatter cones by shock wave interference during impacting, *Earth and Planetary Science Letters* Vol. 216 43-54, 2003.
7. Sagy, A., Fineberg, J., Reches, Z., Shatter cones: Branched, rapid fractures formed by shock impact, *Journal of Geophysical Research* Vol. 109 doi:10.1029/2004JB003016, 2004.
8. Sagy, A., Reches, Z., Fineberg, J., Dynamic fracture by large extraterrestrial impacts as the origin of shatter cones, *Nature* Vol. 418 310-313, 2002.
9. Osinski, G.R., Lee, P., Spray, J.G., Parnell, J., Lim, D.S.S., Bunch, T.E., Cockell, C.S., Glass, B.J., Geological overview and cratering model for the Haughton impact structure, Devon Island, Canadian High Arctic, *Meteoritics & Planetary Science* Vol. 40 1759-1776, 2005.
10. Osinski, G.R., Spray, J.G., Lee, P., Impactites of the Haughton impact structure, Devon Island, Canadian High Arctic, *Meteoritics & Planetary Science* Vol. 40 1789-1812, 2005.
11. Osinski, G.R., Lee, P., Parnell, J., Spray, J.G., Baron, M., A case study of impact-induced hydrothermal activity: The Haughton impact structure, Devon Island, Canadian High Arctic, *Meteoritics & Planetary Science* Vol. 40 1859-1878, 2005.
12. Osinski, G.R., Spray, J.G., Lee, P., Impact-induced hydrothermal activity within the Haughton impact structure, Arctic Canada; generation of a transient, warm, wet oasis, *Meteoritics & Planetary Science* Vol. 36 731-745, 2001.
13. Osinski, G.R., Geological map, Haughton impact structure, Devon Island, Nunavut, Canada, *Meteoritics & Planetary Science* Vol. 40, 2005.
14. Robertson, P.B., Mason, G.D., Shatter cones from Haughton Dome, Devon Island, Canada, *Nature* Vol. 255 393, 1975.
15. Hargraves, R.B., Cullicott, C.E., Deffeyes, K.S., Houghton, S., Christianson, P.P., Fiske, P.S., Shatter cones and shocked rocks in southwestern Montana: The Beaverhead impact structure, *Geology* Vol. 18 832-834, 1990.
16. Gibson, H.M., Spray, J.G., Shock-induced melting and vaporization of shatter cone surfaces: Evidence from the Sudbury impact structure, *Meteoritics & Planetary Science* Vol. 33 329-336, 1998.
17. Wieland, F., Gibson, R.L., Reimold, W.U., Structural analysis of the collar of the Vredefort Dome, South Africa—Significance for impact-related deformation and central uplift formation, *Meteoritics & Planetary Science* Vol. 40 1537-1554, 2005.
18. Melosh, H.J., Ivanov, B.A., Impact crater collapse, *Annual Review of Earth and Planetary Science* Vol. 27 385-415, 1999.

DIRECT OBSERVATION OF TRANSIENT CRATER GROWTH

Satoru Yamamoto⁽¹⁾, Olivier S. Barnouin-Jha⁽²⁾, Takashi Toriumi⁽¹⁾, Seiji Sugita⁽¹⁾, Takafumi Matsui⁽¹⁾

⁽¹⁾Graduate School of Frontier Sciences, University of Tokyo, Kashiwanoha 5-1-5, Kashiwa, 277-8561, Japan, yamachan@impact.k.u-tokyo.ac.jp

⁽²⁾The Johns Hopkins University, Applied Physics Laboratory, MD, USA

ABSTRACT

We observed the formation and collapse processes of transient crater using the laser method. Polycarbonate projectiles, which were accelerated by a single-stage light-gas gun, were impacted vertically into soda-lime glass sphere targets with different material properties. We found that the increase in crater diameter during the excavation stage does not follow a simple power-law relation and its increase rate depends on target material properties. We also showed that the transient crater collapses owing to the gravity, resulting in increase in diameter and decrease in depth. The degree of collapse also depends on target material properties. These results suggest reconsideration of scaling relations on impact cratering.

1. INTRODUCTION

Scaling relations on impact cratering in the gravity regime have been studied for many years, based on explosion and impact experiments for granular targets [e.g., 1, 2, 3, 4]. However, even for the gravity regime, the impact cratering may be affected by target material properties [e.g., 5, 6, 7]. Thus we need to take into account the effects of target material properties on scaling relations in the gravity regime. However, little is known as to how the scaling relations are related to target material properties. This is because the previous scaling relations were formulated based on the data of final craters. In order to investigate this issue, we need to study the relation between transient crater growth (i.e. formation and collapse processes of transient craters) and target material properties. In this case, direct observation of transient crater growth is necessary.

In the previous works, the quarter-space technique has been used for direct observation of transient crater growth [e.g., 3, 7, 8, 9]. In this method, a granular target or sand target is set in a sample box with a transparent window, and a projectile is impacted into the target along the transparent window, through which we can observe the cross sectional view of transient crater growth. However, the presence of the transparent window may affect transient crater growth. Indeed, it has been reported that the crater diameters of final craters measured in the quarter-space technique are

smaller than those in the half space experiment [e.g., 8]. Thus, for the quantitative study of transient crater growth, we need to develop another way of direct observation without any physical interference with targets.

We have recently developed a new technique of the direct observation using a laser sheet [10] (we call this method the laser method and describe in detail hereafter). This allows us to observe the transient crater growth without any physical interference with targets. In this study, using the laser method, we did the direct observations of transient crater growth for different target materials, and studied the relation between transient crater growth and target material properties.

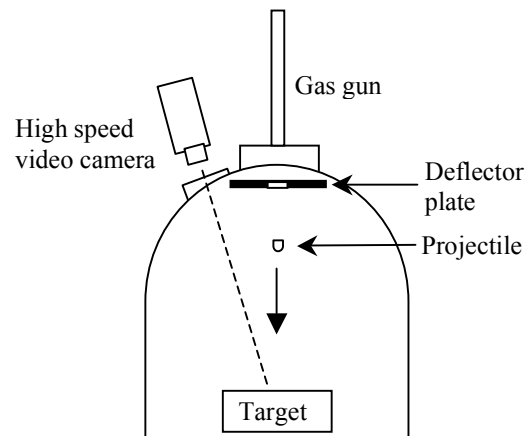


Fig. 1: Schematic diagram (side view) of the experimental apparatus.

2. EXPERIMENTAL SETUP

A schematic diagram of the experimental apparatus is shown in Fig. 1. We used a polycarbonate cylinder with a hemispherical front as projectile (10 mm diameter, 8 mm length, and mass of 0.49 g). The projectile was accelerated by a single-stage light-gas gun. The impact velocities ranged from 93 to 236 m/s (Table 1). The impact angle was vertical to the target surface. We prepared soda-lime glass spheres as targets, whose mean diameters are 36 and 220 μm , respectively; these are referred as TA and TC targets hereafter. In Table 2 we list the target properties such as porosity and the angle of repose. Although the target materials

are the same, their target material properties are different between TA and TC targets, because the mean diameters are different (the porosity and the angle of repose depend on the mean grain size [7]). A stainless basin (40 cm diameter and 15 cm depth) filled with the glass spheres was placed in the vacuum chamber (1 m diameter and ~ 1.3 m height)(Fig. 1). All the experiments were conducted under the condition with the ambient pressure < 50 Pa. In order to prevent the propellant gas (helium) from perturbing the impact cratering, a deflector plate (with a hole 18 mm in diameter for the passage of projectiles) was set at a projectile inlet of the experimental chamber (Fig. 1). Experimental conditions are summarized in Table 1.

Table 1: Experimental condition.

Shot No.	Target	Impact velocity [m/s]
604091	TA	189
604092	TA	236
604093	TA	100
604114	TA	216
604117	TA	205
6041110	TA	96
604051	TC	98
604052	TC	205
604053	TC	93
604054	TC	160
604055	TC	216

Table 2: Material properties of the glass sphere targets.

Target	TA	TC
Mean diameter	36 μ m	220 μ m
Porosity	40 %	36 %
Angle of repose	33 deg	25 deg

3. LASER METHOD

Fig. 2 shows a schematic diagram of the laser method. A vertical laser-sheet formed by a 3mW He-Ne laser through a cylindrical lens was used to illuminate the impact site of a projectile. The temporal change of the laser line formed on the target surface during the transient crater growth can be observed by using a high-speed video camera set above the target (Fig. 2). Example images taken by the camera are shown in Fig. 3. This is the case for impact velocity of 216 m/s into TC target. Before impact (Fig. 3a), we see a straight laser line on the target surface. After impact, the shape of the laser line changes with the expansion of the crater cavity (Fig. 3b). Transient crater was formed by $t=0.108$ s, because the crater rims can be seen by this time step (white arrows in Fig. 3c). Then, the transient crater started to collapse and the crater shape began to

change again. Finally, the collapse halts and then the final crater was formed (Fig. 3d).

Analyzing images taken by the camera (the detailed analytical procedure is described in [10]), we obtained the profile of the crater cavity for each image (Fig. 4). From these profiles, we can determine the apparent diameter and depth of the crater cavity for each time step.

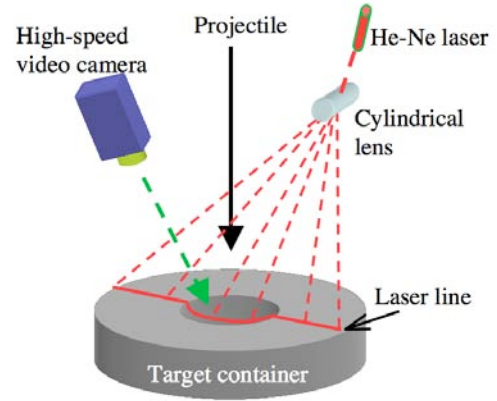


Fig. 2: Schematic illustration of the laser method.

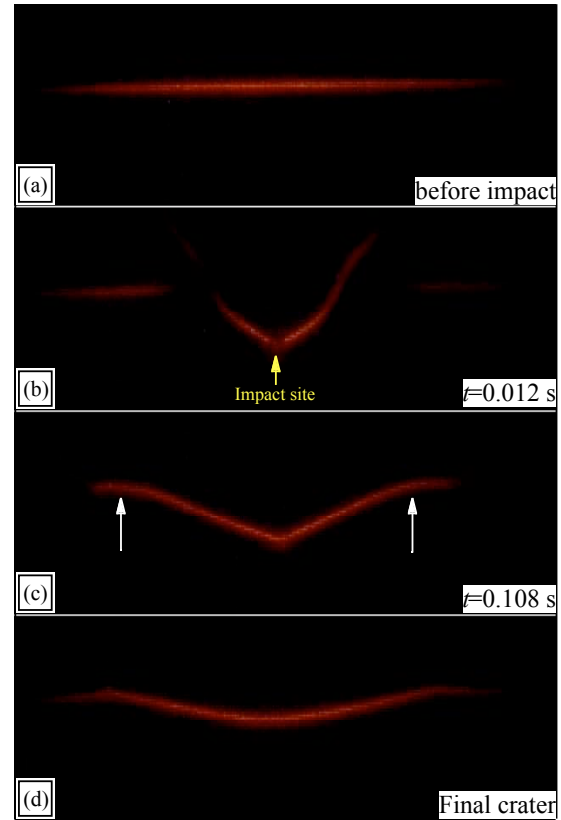


Fig. 3: Example images taken by the camera. t is the time after impact. This is the case for impact velocity of 216 m/s into TC target (Shot 604055).

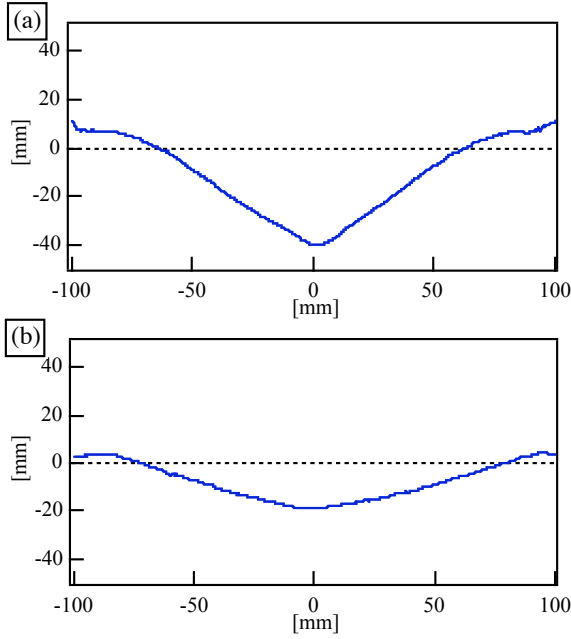


Fig. 4: Example profiles of the crater cavities at (a) $t=0.108$ s and (b) $t=0.264$ s, respectively. This is the case for impact velocity of 216 m/s into TC target (Shot 604055). The broken line corresponds to the original target surface before impact.

4. RESULTS: TEMPORAL CHANGES IN DIAMETER AND DEPTH

Using the laser method, we can observe the temporal changes in diameter and depth for various impact velocities for TA and TC targets. Fig. 5 shows the temporal changes in diameter (red solid circles) and depth (blue solid circles) for the case of the impact with velocity of 216 m/s into TC target. As shown clearly in this figure, the diameter increases with increasing time t after impact. We consider that the transient crater is formed by $t \sim 0.108$ s, because the crater rim is formed by this time step (Fig. 3c). In this case, the diameter of transient crater is 129 mm. The increase rate in crater diameter appears to become slow but after formation of transient crater, the diameter starts to increase again owing to the collapse of the crater wall and rims. The increase in diameter stops at around $t \sim 0.2$ s, and we consider that the final crater was formed at this time step, that is, the diameter does not change further. The final crater diameter is 152 mm in this case.

As shown in Fig. 5 the depth (blue circles) rapidly increases until about $t=0.008$ s after impact. However, the increase in depth becomes slow after this time step and stops at around $t \sim 0.012$ s. Then the depth becomes to decrease slightly and to be nearly constant until $t \sim 0.1$ s, which is nearly equal to the formation time of transient crater. After $t \sim 0.1$ s, the depth starts to

decrease largely owing to the collapse of the crater. Finally, the collapse halts by $t \sim 0.3$ s, because the depth does not change further after this time step. The depth of final crater is 19 mm.

Note that the increase rate in diameter does not follow a power-law relation, as shown in Fig. 5; the increase rate gradually decreases with increasing t even during the formation processes of transient crater ($t < 0.1$ s). This feature such as the gradual increase in diameter is different from the previous result observed by the quarter-space technique [e.g., 3], in which the increase rate in diameter during the early stages ($t < 0.004$ s) of formation process of transient craters was shown to follow a simple power-law relation ([3] did not show the features for $t > 0.004$ s). The reason for this discrepancy is uncertain, but may be due to the difference between the early and late stages of formation process of transient craters. In any case, the present results may suggest that we need to take into account this feature (the gradual increase) when we consider the scaling relations on crater diameters.

Furthermore, as shown in Fig. 5, the increase in diameter continues after the increase in depth stops at $t \sim 0.012$ s, which means that the radial expansion process continues after the vertical expansion process stops. It is therefore suggested that the shape of the crater cavity changes with time: the expansion of the crater cavity does not follow a self-similar way.

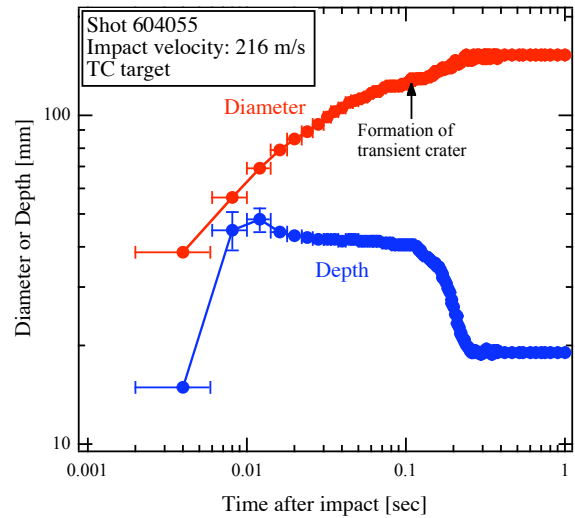


Fig. 5: Temporal changes in diameter and depth for impact velocity of 216 m/s into TC target.

5. EFFECTS OF TARGET MATERIAL PROPERTIES ON TRANSIENT CRATER GROWTH

5.1 Formation process

In order to investigate how the formation process of transient craters depends on the target material properties, we first compared the results of TA and TC targets for the same impact velocity. In Fig. 6, the diameter of crater cavity is plotted against the time after impact for TA and TC targets (the impact velocities for both cases are 205 m/s). At the early stage ($t < \sim 0.008$ s), we cannot see any significant differences in diameter between TA and TC targets. This may suggest that the effects of target material properties are not important during this stage. On the other hand, at later stages ($t > \sim 0.008$ s) we can see the difference between TA and TC targets; the diameters for TC target are larger than those for TA target for $t > \sim 0.008$ s, and this difference increases with increasing t . It is therefore suggested that the formation process of transient craters depends on target material properties at the later stage.

This might be interpreted as follows: During the early stage of the formation processes ($t < \sim 0.008$ s), the dynamic pressure of the excavation flow was high enough to dominate over the effects of target material properties. Therefore, the formation process does not depend on target material properties at the early stage. On the other hand, the dynamic pressure of the excavation flow becomes to be low at the later stage of the formation processes, and as a result the excavation flow during the later stage was affected by the material properties such as internal friction or cohesion among glass spheres.

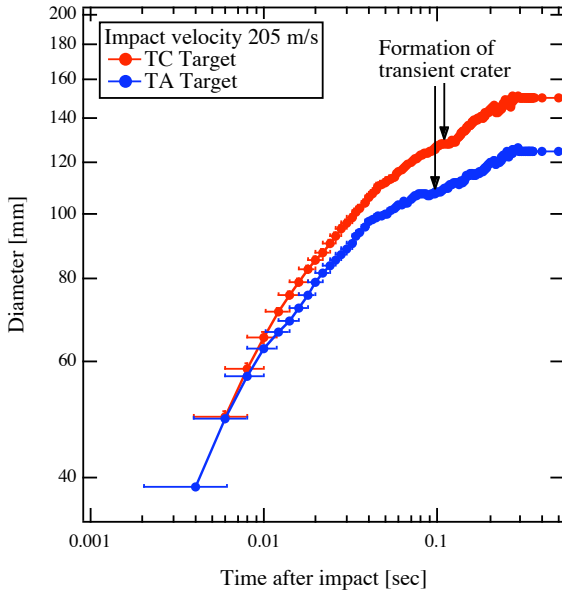


Fig. 6: Diameter growth for TA and TC targets (Shots 604117 and 604052 for TA and TC targets, respectively). The impact velocities for both cases are the same (205 m/s).

5.2 Collapse process

In order to investigate how the collapse process depends on target material properties, we next estimate the degree of collapse. We use the diameter ratio of final to transient craters as the estimate of the degree of collapse. In Fig. 7, the degrees of collapse are plotted against the impact velocity for TA and TC targets. We can see that the degrees of collapse for TC target are larger than those for TA target; the average values for TC and TA targets are 1.17 ± 0.02 and 1.12 ± 0.01 , respectively. It is therefore suggested that the degree of collapse depends on target material properties.

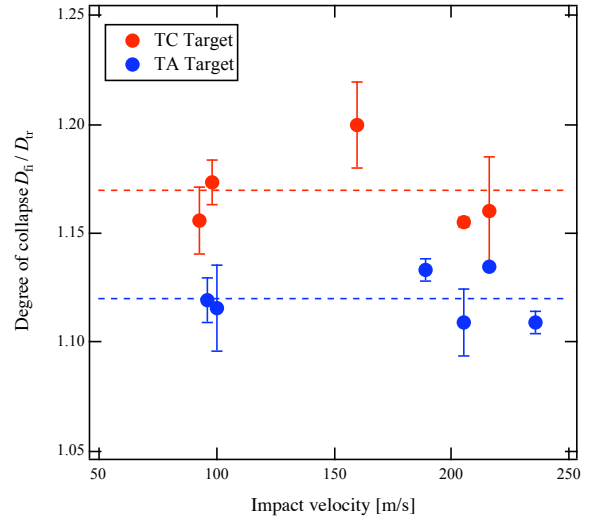


Fig. 7: The diameter ratio of D_{fi} to D_{tr} (the degree of collapse) is plotted against the impact velocity for TA and TC targets, where D_{fi} and D_{tr} are the diameters of final and transient craters, respectively. The broken lines indicate the average values: 1.12 and 1.17 for TA and TC targets, respectively.

5.3 Crater shape: depth-diameter ratio

Next we study the relation between the depth and diameter (depth-diameter ratio) of transient and final craters. In Fig. 8 the depth-diameter ratios of transient and final craters are plotted against the impact velocity for TA and TC targets. We cannot see any systematic difference in the depth-diameter ratio of transient craters (filled circles) between TA and TC targets. On the other hand, it is clear that the depth-diameter ratios of final craters for TA target (blue open circles) are larger than those for TC target (red open circles). The average values of final craters for TA and TC targets are estimated to be about 0.17 ± 0.01 and 0.13 ± 0.01 , respectively. Therefore, we may suggest that the crater shape (depth-diameter ratio) of final craters depends on target material properties, while the crater shape of transient craters does not. This may suggest that the

shape of final craters is mainly controlled by the collapse process.

6. SUMMARY

We observed the formation and collapse processes of transient crater using the laser method. We found that the increase rate in diameter of crater cavity does not follow a simple power-law relation; the increase rate during the formation process of transient craters decreases with increasing time, and depends on target material properties. In addition, the radial expansion process continues after the vertical expansion process stops, suggesting that the shape of the crater cavity changes with time. We also showed that the transient crater collapses owing to gravity, resulting in increase in diameter and decrease in depth. The degree of collapse was also shown to depend on target material properties. Furthermore, the crater shape (depth-diameter ratio) for final craters showed target material property dependence, while that for transient craters did not. These features may need to be considered, when we consider the effects of target material properties on the scaling relations.

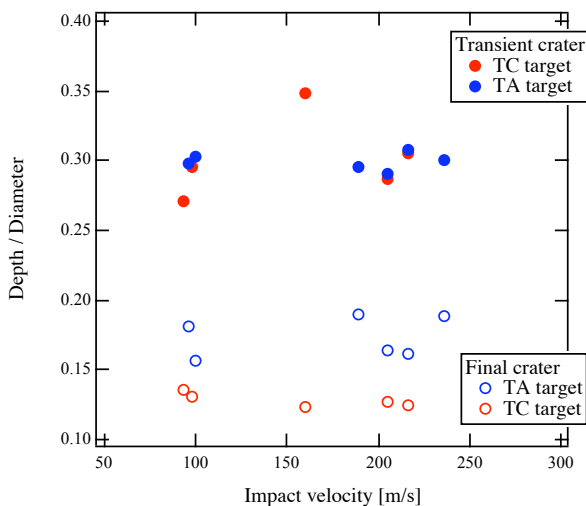


Fig. 8: Depth-diameter ratio of transient (solid circles) and final craters (open circles) for TA and TC targets.

REFERENCES

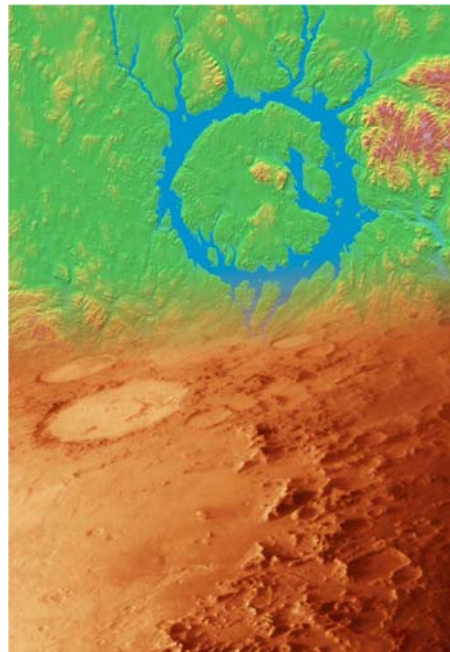
1. Housen K.R. et al., Crater ejecta scaling laws: Fundamental forms based on dimensional analysis, *J. Geophys. Res.* 88, 2485, 1983
2. Mizutani H. et al., Cratering experiments in sands and a trial for general scaling law, *J. Geophys. Res.* 88 (Suppl.), A835, 1983.

3. Schmidt R.M. and Housen K.R., Some recent advances in the scaling of impact and explosion cratering, *Int. J. impact Eng.* 5, 1987.
4. Holsapple K.A., The scaling of impact processes in planetary sciences, *Ann. Rev. of Earth and Planet. Sci.* 21, 333, 1993.
5. Schmidt R.M., Meteor crater: Energy of formation- Implications of centrifuge scaling, *Proc. Lunar Planet. Sci. Conf.* 11, 2099, 1980.
6. Melosh H.J., *Impact cratering*, Oxford Univ. Press, New York, 1989.
7. Yamamoto S. et al., Transient crater growth in granular targets: An experimental study of low velocity impacts into glass sphere targets, *ICARUS* 183, 215, 2006.
8. Schmidt R.M. and Piekutowski A.J., *Lunar Planet. Sci. Conf.* 14 Abs. 668, 1983.
9. Schultz, P.H., Transient crater growth in low density targets. *Lunar Planet. Sci. Conf.* 36, Abs. 206, 2003.
10. Barnouin-Jha O.S. et al., submitted to *ICARUS*, 2006.

Session S.09

Computer Simulations

Chair: M. Gerasimov



EVALUATION OF PLANETARY IMPACTS USING NUMERICAL AND EXPERIMENTAL TECHNIQUES

E. C. Baldwin⁽¹⁾, E. A. Taylor⁽²⁾, M. J. Burchell⁽³⁾, D. J. Milner⁽³⁾, I. A. Crawford⁽¹⁾, L. Vocablo⁽¹⁾, A. P. Jones⁽¹⁾

⁽¹⁾ UCL-Birkbeck Research School of Earth Sciences, University College London, Gower Street, London WC1E 6BT, Email: e.baldwin@ucl.ac.uk

⁽²⁾ Department of Physics and Astronomy, The Open University, Walton Hall, Milton Keynes MK6 7AA, Email: E.A.Taylor@open.ac.uk

⁽³⁾ Centre of Astrophysics and Planetary Science, School of Physical Sciences, University of Kent, Canterbury, Kent CT2 7NH. Email: M.J.Burchell@kent.ac.uk

ABSTRACT

Numerical modelling is an important facet of impact cratering research, offering a means for examining various stages of the impact event that cannot be investigated by other methods, particularly for large planetary impacts. Experimental techniques, such as light gas gun impacts, are important to understand cratering processes at smaller scales. In this study the 2D AUTODYN hydrocode [1] is used to demonstrate the capabilities of simulations in replicating large planetary impact events. We highlight some common issues arising from modelling planetary impacts, and relate laboratory results attained from light gas gun impacts to our modelled output, in order to further our understanding of cratering processes at all scales.

1. USING CHICXULUB TO EVALUATE STRENGTH MODELS

Chicxulub crater is a complex crater with interpreted diameters ranging from ~150 [2] to 300km for a proposed multi-ringed basin [3]. Typical estimates for the transient cavity lie between 85km [4] and 100km [e.g. 2] for the diameter and 33km [2] for the depth. Our models were initialised with a three layer stratigraphy comprising 3km sediments (calcite), 27km granite (westerly granite) and mantle (dunite) [e.g. after 5]. The materials indicated in brackets are those selected from the AUTODYN library to represent each layer. We model the impact of a 10km diameter dunite projectile striking at 20km/s.

As part of a series of fundamental parameter tests into the sensitivity of output to material model input, initial models vary only the yield strength of the materials. This sensitivity study is further motivated by the observation that data available in the literature for any particular material can cover a wide range, sometimes over several orders of magnitude. We subsequently find that the output yielded by numerical simulations is extremely dependent on these input values (Table 1). When varying only the yield strength from 0.1MPa to a

few hundred MPa the crater depth is found to vary from 5 – 33km and crater diameter from 144 – 72km respectively. Neglecting yield strength altogether intuitively results in a flat surface.

Yield strength values for the materials used in the Chicxulub impact event are quoted by [6] as 344MPa for the crust and 619MPa for dunite (which is chosen to model both the mantle and the projectile). This produces a crater of 72km by 33km, comparable to published data for the transient cavity [e.g. 2]. However, it is the lower yield strength values that yield the most favourable final crater dimensions, for the initial conditions stated. This implies that, as concurred by [e.g. 7], standard strength models used in hydrocodes are not successful for describing crater collapse. Indeed, when the rock is initialised with its static strength properties, we observe that the crater does not collapse significantly, if at all.

The dynamic behaviour of crater collapse and relaxation can be described by the acoustic fluidisation model [8], which allows for the ephemeral fluidisation of rock. It is based on the premise that acoustic vibrations within a granular material become violent enough to temporarily relieve the overburden pressure, and therefore reduce the internal friction resistance of the material. Consequently, the material will behave as a fluid. However, this fluidisation is short lived, or else the end result would be a flat surface.

Target Yield Stress	Final Diameter, D (km)	Final depth, d (km)	Depth to Diameter Ratio (d/D)
Crust: 344MPa Mantle: 619MPa	72	33	0.46
10MPa	117	13	0.11
0.1MPa	144	5	0.03

Table 1: Effect of target yield stress on final crater dimensions. For the first line of data, the crust (to a depth of 30km) and mantle are assigned different values [after 6], as indicated.

Crater collapse is evidently a very complicated, non-linear process that is not easily described by a numerical code. Indeed, acoustic fluidisation is not implicitly included in our models, although adjustment of the yield strength may prove a suitable approach to reproduce these effects. It is therefore with some caution that material models and parameters can be applied in hydrocodes if the desired output is to accommodate transient cavity collapse into a complex crater.

2. METEOR CRATER

Meteor Crater is an excellent example of a well-preserved simple crater, with a text-book bowl shaped morphology of diameter 1.2km and depth 180m below the pre-impact surface, that formed simply by the relatively straightforward collapse of the transient crater to the angle of repose. An additional 200m deep lens of brecciated material lies beneath the crater floor [9].

2.1 A numerical approach to investigate projectile size and angle of impact.

Preliminary efforts to model this impact event used a single layered target of sandstone defined with standard shock equation of state (EoS) data [10]. We are currently using the Drucker-Prager strength and P-min failure models [1]. Further work will implement the P-alpha [1] and eventually epsilon-alpha equation of states for sandstone, which enables a more realistic approach to modelling porous materials [e.g. 11].

Data books [e.g. 12] state that yield strength values for various sandstones range from 2-360MPa, with Coconino Sandstone (the predominant material at the Meteor Crater site) exhibiting a yield strength of approximately 70MPa. We also investigate experimentally the yield strength of sandstone, the outcome and implications of which are discussed in section 2.2.

As highlighted in the previous section, high target yield strengths have resulted in simulations producing typical transient sized cavities; this was also the case for a Meteor Crater sized event when quoted yield strengths were applied to the models. For subsequent simulations we therefore chose to reduce the yield strength, initially to 10MPa. We subsequently varied only the projectile diameter from 50m to 25m; all other parameters remained the same. Simulations running at the time of submission are investigating lower yield strengths, given the outcome of the Chicxulub style simulations described in the previous section.

Our preliminary best fit crater diameter of 1112m was achieved with a 35m projectile impacting at 12km/s, producing a depth of 462m for these initial conditions. This depth is obviously more comparable to the 'true' crater depth, which is measured to the base of the brecciated zone. Indeed, our models do not account for the brecciated lens below the crater floor, or even any significant fall-back of ejecta. However, it is not unusual for simulations to overestimate crater depth. For example, this phenomenon has also been observed by [13], whereby an overestimate of 300m is calculated using SALEB and SOVA codes for an observed crater depth of 550m. This apparent overestimate can obviously be in part attributed to the material strength values assigned to the materials within the simulation, as discussed previously.

An additional but no less important factor lies in the implicit assumption by 2D simulations of a vertical (90 degree) impact, whereas the most likely angle of impact will be 45 degrees [14]. Indeed, [15] show that, at laboratory scale, crater depth and excavated mass start to decrease immediately when non-normal incidence occurs. This effect is also illustrated through the Earth Impact Effects Program [16] whereby the crater depth decreases by ~100-200m with increasing obliquity for a Meteor Crater type event, using our preferred 35m diameter projectile (Fig. 1). It is therefore reasonable to assume that our 2D simulations are overestimating the depth of the crater by a similar amount, therefore putting our crater depth at a value closer to that observed. It is envisaged that oblique simulations using 3D AUTODYN will further support this dependence of impact angle on crater dimensions.

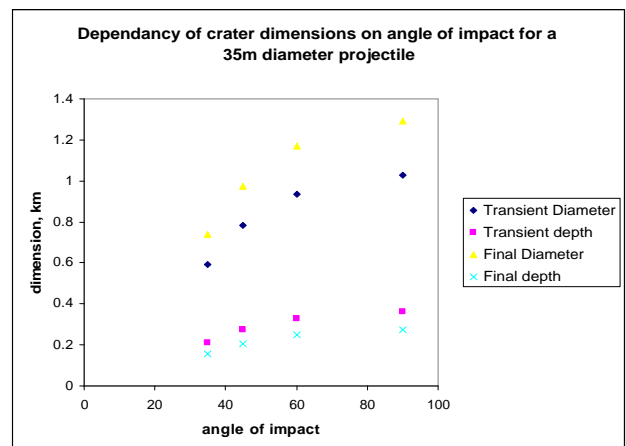


Fig. 1. The dependency of crater dimensions on impact angle, as demonstrated by the Earth Impact Effects Program [16] for a Meteor Crater type event.

2.2 An experimental approach to investigate the effect of local target conditions

The predominant material at the Meteor Crater impact site is the porous (~23%) Coconino Sandstone. In addition [17] suggest that this material may have in part been saturated, due to the influence of a local water table. Experiments [e.g. 11, 18] have shown that at a lab scale, it requires more energy to produce craters of the same size in porous targets than in non-porous targets, due to the additional energy required to collapse the pore spaces. In addition, studies have shown that the brittle strength of a rock is reduced in the presence of water [e.g. 19] and that water reduces the compressibility of porous materials [20]. Moreover, particularly at large scales, the target is mechanically disrupted by expanding steam after the passage of the shock wave, which increases the volume and enhances cavity growth in comparison to dry rocks [20].

In order to assess the influence of target saturation and porosity on crater dimensions we perform light gas gun impacts into wet and dry sandstone targets of differing porosity. Porosity was determined using standard laboratory techniques based on volume differences between wet and dry samples. In addition, the yield strengths of wet and dry core samples were also determined in the lab, using the Servo-Controlled 200KN universal load equipment at UCL. Our lab-characterised data is shown in Table 2. The wet core sample was determined to have approximately half the strength of the dry core sample.

Light gas gun impacts were carried out at the University of Kent. Impact conditions were set at 5km/s +/- 0.2km/s and used a 1mm diameter stainless steel projectile. While we are comparing two materials with only 6% difference in porosity, we still observe differences in crater dimensions. Initial results indicate that a higher porosity sandstone allows a crater with a larger diameter but smaller depth to form than in a lower porosity sandstone (Fig. 2). We find that the higher porosity wet target yields a wider and deeper crater than the lower porosity wet target (Fig. 3).

We also find that a wet target allows a greater volume of material to be excavated than in a dry target (Fig. 4), consistent with pilot studies by [20]. However, while we find that a wet target yields a deeper crater than a dry target, [20] observe a shallower depth in their wet target. This may largely be due to differences in experimental setup and target heterogeneities. It may be of interest to note that the experiments conducted by [20] use centimeter sized projectiles, whereas we use millimeter sized projectiles; perhaps the outcome of the two experiments is in part attributed to scale differences. The grain size of the materials may also be responsible for this observation; our Pilot Test Sandstone has a grain size of <0.4mm which is comparable to the difference in crater depth between the two sandstones (Figs. 2 & 3), and may also be analogous to large-scale ‘mega-block’ type failure.

3. SIMULATING LABORATORY RESULTS WITH AUTODYN

In order to represent porosity in our simulations, we first attempt to simulate our light gas gun impacts. Current models implement standard shock EoS data [10], which precludes explicit consideration of porosity. Our sandstone model therefore is representative of a non-porous sandstone. We use the yield strength attained in the lab for the dry pilot test sandstone (90MPa), defined within the Drucker-Prager strength model. Our output (Fig. 5) is consistent with the observation of [18] that more impact energy is required to produce a similar sized crater in a porous material than non-porous. Although the morphology of the craters are different, the profiles show that the dimensions are in fact very similar. This observation, along with the laboratory results, could be used to suggest that porosity effects morphology more than crater dimensions. Future efforts will focus on implementing, testing and applying both the P-alpha [1] and epsilon-alpha [11] equation of states, along with our own experimentally derived data [20, 21].

Sample	Grain size, mm	Dry Density, g cm ⁻³	Wet Density, g cm ⁻³	Porosity	Dry Yield Strength, MPa	Wet Yield Strength, MPa
Pilot Test	<0.40	2.20	2.35	17%	90	43
Coconino	<0.15	1.80	2.00	23%	tbd	tbd

Table 2. Parameters characterised in the laboratory for two sandstone samples.

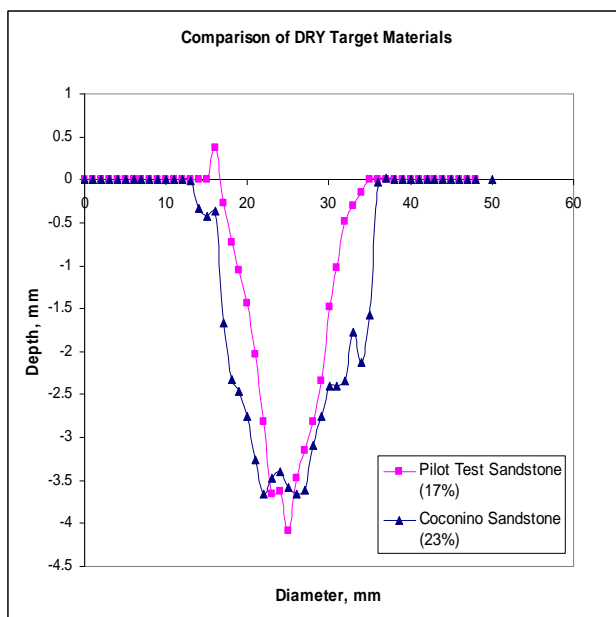


Fig. 2. Comparison of craters in dry target materials. Note the main difference is morphology; the depth of the two craters are essentially identical, especially when the grain size (<0.4mm) is taken into consideration.

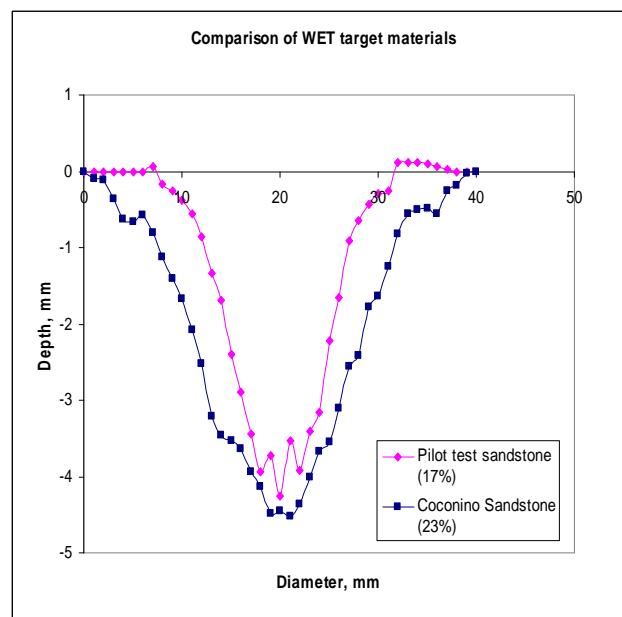


Fig. 3. Comparison of craters in wet target materials.

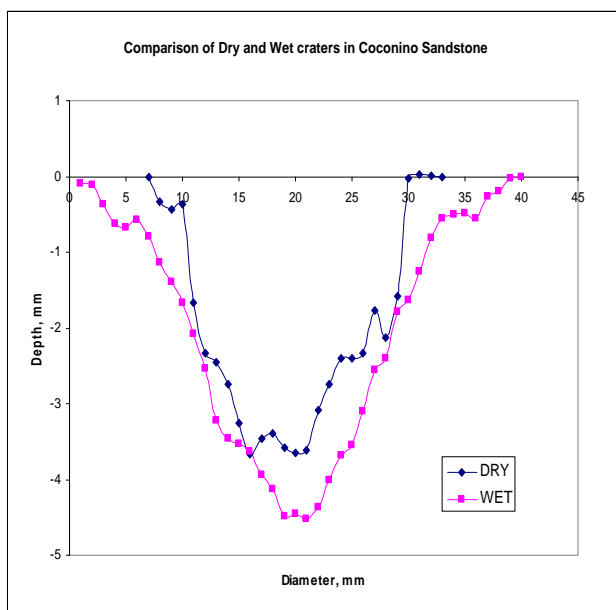


Fig. 4. Comparison of craters in dry and wet Coconino Sandstone

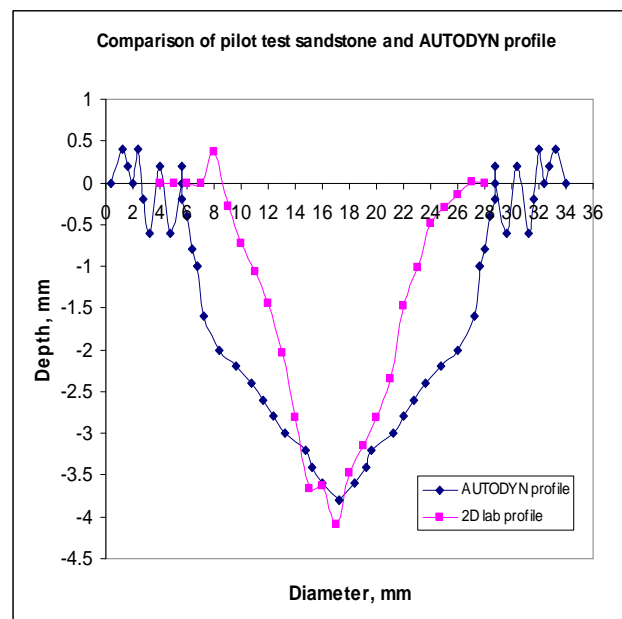


Fig. 5. Comparison of experimental crater with simulation output.

4. SUMMARY

We find that the output yielded by numerical simulations is only as effective as the material models that are applied. For a realistic model to be successful we require input data concerning equation of state parameters, strength and failure models (i.e. mechanical and elastic properties such as yield strength, shear modulus and ultimate tensile strength). It is also important to consider local conditions such as the influence of water or porosity.

Although it is imperative to choose strength models at a laboratory scale, it is the material weakening mechanism, along with crater collapse under gravity, which is important at large planetary scales. At this large scale we have shown that the material must behave as a strength-less material in order to reach the observed crater dimensions. This is obviously not the case for small-scale lab impacts, where the strength regime is the controlling factor, and in general, only the transient cavities of the crater are recorded.

Simulations of our normal incidence light gas gun hypervelocity impacts into sandstone illustrate the need for consideration of factors such as porosity and saturation when attempting to reconstruct laboratory impact events via modelling; therefore these factors are presumably also important for planetary scaled impacts. We are currently implementing into our models experimentally derived data, including revised equation of state data for geological materials that will include consideration of porosity for sandstone [21, 22].

REFERENCES

- [1] Century Dynamics Inc (2005) *AUTODYN v.6.0 Theory Manual*. [2] Collins, G. et al. (2002) *Icarus* 157 24-33. [3] Sharpton et al. (1996) *GSA Special Paper* 307 55-74. [4] Morgan, J. et al. (1997) *Nature* 390 472-476. [5] Pierrazo, E., et al. (1998) *JGR* 103 E12 28,607-28,625. [6] Saito, T. et al. (2005) *HVIS 2005*. [7] Melosh, H. J. and Ivanov, B. A. (1999) *Annu. Rev. Earth Planet Sci.* 27:385-415. [8] Melosh, H. J. (1979) *JGR* 84 7513-7520. [9] Shoemaker, E. M. and Kieffer, S. W. (1974) *Guidebook to the Geology of Meteor Crater, Arizona*. [10] Ahrens T. J. (ed) (1995) *AGU Reference Shelf 3: Rock Physics and Phase Relations, A Handbook of Physical Constants*. [11] Wunnemann, K., et al. (2006) *Icarus* 180 514-527. [12] Lama, R. D. and Vutukuri, V. S. (1978) *Handbook on Mechanical Properties of Rocks* (Trans Tech Publications). [13] Artemieva, N. et al. (2004) *Geochemistry Geophysics Geosystems* 5 DOI:10.1029/2004GC000733. [14] Shoemaker, E. M. (1962) in *Physics and Astronomy of the Moon* p283-359. [15] Burchell, M. J. and Whitehorn, L. *Mon. Not. R. Astron. Soc.* 341 192-198. [16] Collins, G. S. et al (2005) *MAPS* 40 (6) 817-840. [17] Kieffer, S. et al (1976) *Cont. to Mineralogy and Petrology* 59, 41-93. [18] Love, S. G. et al. (1993) *Icarus* 105, 216-224. [19] Baud et al. (2000) *JGR* 105 B7 16,371-16,389. [20] Kenkmann, T. et al (2006) *LPSCXXXVII* abstr. 1587. [21] Taylor, E. A. et al. (2006) *ESLAB 40th* abstr. 296109. [22] Church, P. et al. (2006) *ESLAB 40th* abstr. 295760.

NUMERICAL MODELING OF IMPACT CRATERING

Elisabetta Pierazzo

Planetary Science Institute, 1700 E. Ft. Lowell Rd., Suite 106, Tucson AZ 85719, U.S.A, Email: betty@psi.edu

ABSTRACT

Numerical modelling is a fundamental tool for understanding the dynamics of impact cratering, in particular at planetary scales. Impacts have influenced the formation and evolution of nearly every planetary surface in the solar system, yet we can only observe the scars left by past events. Detailed computer modeling of the physics of the impact process provide the possibility of studying the dynamics of impact cratering at all scales, becoming an invaluable tool that connects and complements geologic and remote sensing observations, and small scale laboratory experiments. The main requirements for computer modelling are a good understanding of the physics and chemistry of the process and enough computer power to model the part of the impact process we are interested in.

1. INTRODUCTION

Impacts of asteroid and comets have affected the formation and evolution of nearly every solid planetary surface of the solar system. They produce impact craters of all sizes, which are easily observed both remotely (on various planetary surfaces) and in-situ (on Earth). Experimentally, laboratory tests can produce small-scale analogues of large impacts; the largest man-made experiments, high explosive/nuclear tests and the most recent Deep Impact cratering mission, can only create structures that are comparable to the smallest observed planetary impact craters. In particular, processes like shock melting and vaporization in large impacts, which involve extreme pressures and temperatures, cannot be easily reproduced in the laboratory, while the influence of planetary gravity in the late stages of crater formation makes it difficult to extrapolate small-scale laboratory collapse experiments to planetary impact cratering. Computer simulations provide the only feasible method for studying the physics of the impact cratering process connecting and complementing planetary-scale geologic and remote sensing observations to small-scale laboratory experiments. Moreover, they provide detailed temporal and spatial information of various variables of interest, in a controlled environment, in a sense making them the best instrumented experiment [1]. The main requirements for computer models are a

good understanding of the physics of the process and enough computer power to model the part of the impact process we are interested in.

This paper will provide a brief overview of the most important aspects of numerical modelling of impact cratering, including recent progress made in the field and future developments. For more information see also [2].

2. THE THEORY BEHIND MODELING

The continuum dynamics of impact cratering and relative hydrodynamics and solid state deformations are well understood and implemented in the computer programs used to model impacts, usually referred to as hydrocodes. A high speed impact causes a sudden compression of projectile and target materials at the impact point, generating a shock wave that propagates through both projectile and target. As the shock passes, the material's initial thermodynamic state changes rapidly and irreversibly to a shocked state. As the shock wave reaches the projectile's rear end, or the target surface, it is reflected back as a rarefaction wave that adiabatically releases the material from the shock state. The speed of the rarefaction wave is usually higher than that of the shock wave and ultimately the shock wave becomes a thin shell sandwiched between the shock front and the rarefaction wave. Behind the shell, some residual particle velocity remains in the target with a tangential component (due to the presence of the target's free surface) that initiate the excavation of the crater.

The physics required to describe large meteorite impacts consists essentially of the classical Newtonian mechanics ($F=ma$ plus conservation equations) supplemented by classical thermodynamics [3].

Newton's Laws of motion are implemented in hydrocodes as a set of differential equations, first derived by P.H. Hugoniot from the principles of conservation of mass, momentum and energy across the shock discontinuity. The Hugoniot equations are entirely general, regardless of the phase of medium through which the shock wave propagates.

The thermodynamics of impacts is not as straightforward as Newtonian mechanics. Thermodynamics is implemented through the response of materials to the shock, and it is represented in the model by material equations of state. The combination

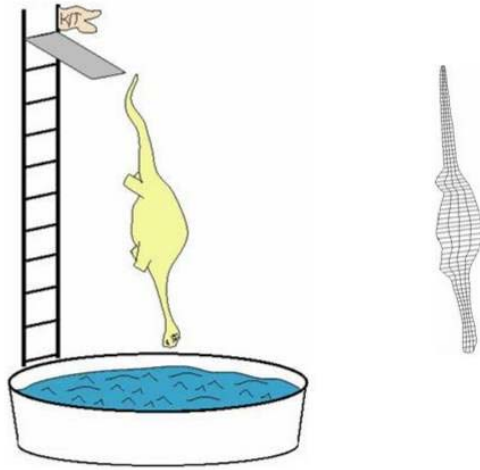


Fig. 1: Numerical modeling of any impact event begins with a discretization process. Projectile and target are divided into discrete blocks, or cells, each with associated individual sets of physical parameters. (Image courtesy of Gareth Collins).

of the Hugoniot equations and the equation of state completely specify the conditions on either side of the shock. In addition, material strength is crucial in the late stages of an impact event. To date, few good equations of state and strength models exist for geologic materials, such as rock and ice.

Material modelling is further complicated by porosity that can affect the partition of energy in the impact process and the overall response of material to an impact event. Finally, it must be kept in mind that the composition of planetary crusts is rarely homogeneous, both microscopically and macroscopically. The mixing of materials of different impedances in the target affects the distribution of the shock wave, causes shock reverberations at material boundaries, and overall modifies the final thermodynamic state of the various materials. In turn, this affects material melting, vaporization and ejection, and the final crater morphology.

3. FROM THE THEORY TO THE NUMERIC CODE

The implementation of the continuum dynamics of impact cratering into a numerical code occurs through a discretization process that consists of dividing space and time into discrete blocks, or cells. The total number of cells, i.e., the mesh of the simulation, can vary and is ultimately limited by the computer's physical memory and the amount of time available for the computation. The combination of the total number of cells possible and the total mesh required for the simulation determines the spatial and temporal resolution of the simulation. The choice of resolution in space and time is important when modelling impact

events. On one hand, any simulation's resolution should be high enough to resolve all the important flow variations in space and time. On the other hand, we are limited by the available computer power and time allowed to complete the simulation. For example, a spatial resolution of 100m in the modelling of a 100 km diameter impact crater requires around 10^{10} cells in a 3D simulation, yet 100m resolution is too coarse to distinguish small, meter scale features, that can be observed in the field by a geologist. Modelling the entire impact process to the final 100 km crater may require a timescale around 500s that corresponds to around 500,000 time steps if the temporal resolution is around 10^{-3} s. However, 10^{-3} s may not be good enough to clearly distinguish the early development and propagation of the shock wave in the target and projectile and that may introduce instabilities in the integration process. This is usually avoided by introducing a stability condition (Courant-Friedrichs-Lewy stability condition), which requires that no signal (e.g., the shock wave) can propagate across the shortest dimension of a cell in a single time-step [1]. Resolution problems can be mitigated somewhat by better solution algorithms, such as those employing smooth particle hydrodynamics (SPH; [4]) or adaptive mesh refinement (AMS; [5]). Finally, the total computer storage needed to record the important parameters in an impact simulation depends on the total number of parameters recorded, the total number of cells in the simulation and the total number of time steps required to complete the simulations. Thus computer hardware can severely limit the comprehensiveness of a simulation.

3.1 Resolution Effects

Computer power may limit the maximum number of cells that can be used to cover the spatial mesh required for any particular impact simulation. This is particularly true in the case of 3D simulations. However, much care must be exerted to make sure that the desired results of impact simulations (e.g., mass of rock melted, maximum shock pressure, mass and speed

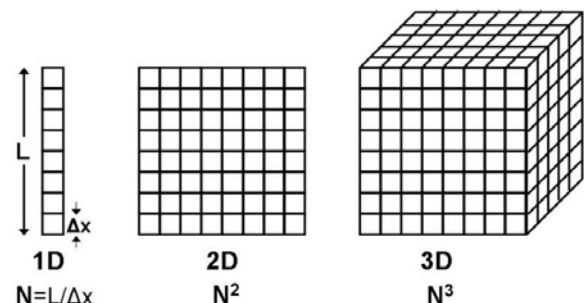


Fig. 2: Schematic of the number of cells involved in a numeric simulations for 1- 2- and 3-dimensions. L is the spatial scale of the simulation, Δx is the desired spatial resolution and N is the number of cell in any direction.

of ejecta, etc.) do not depend on the simulation resolution and mesh chosen.

The danger of using inadequate mesh resolutions can be illustrated by two simple examples (Fig. 3), dealing with a) the determination of target melt/vapour volumes in 2D simulations and b) the estimate of maximum shock pressure in 3D simulations.

Melt/vapour volumes from impacts into a crystalline rock target were estimated for several 2D simulations at different resolutions [6]. The upper panel of Fig. 3 shows the results of planetary-scale simulations for four different resolutions: 5, 10, 20 and 40 cells-per-projectile-radius, or cppr. The lowest resolutions, 5 and 10 cppr, are similar to resolutions used in early modelling work, while the higher resolution, 40 cppr, is rather typical of today's 2D simulations. The figure shows the clear deterioration of melt/vapour estimates with decreasing resolution. The resolution effects are strongest (low melt production) for simulations with impact velocities that are typical of asteroidal impacts on Earth ($v \leq 30$ km/s), resulting in artificially small estimates of melt/vapour production by as much as a factor of 2.

Estimates of maximum shock pressure in a crystalline rock target were obtained for a series of 3D hydrocode

simulations at different resolutions. The simulations indicate that low resolution affects the results of the simulations by reducing the intensity of the recorded shock (recorded shock parameters are averaged over the volume of the cell: the smaller the cell the sharper the shock), as shown in the lower panel of Fig. 3. This affects the final estimates of melting/vaporization volumes. In particular, even at typical resolutions currently used in 3D runs (given computer availability), i.e., 18-20 cppr, the volumes associated with high shock pressures may still be underestimated. Overall, in the simulations with CTH there is a loss of about 20% in melt-volume when the mesh resolution is degraded from 18 to 8 cppr. This result is similar to studies done with similar 3D hydrocodes [7].

3.2 Eulerian versus Lagrangian Treatment

The solution of the equations describing the shock event can be approached in two ways: using a coordinate system moving with the material, known as the Lagrangian approach, or fixed in space, known as the Eulerian approach. [1].

In the Lagrangian approach the mesh is fixed with the material. The mesh is generated by assigning a single material to each cell. No material flows in or out of a cell, so mass in the cell is a constant and it is possible to record the evolution of material in each individual cell. Any variation of density inside the cell is due to changes in the cell's volume during the simulation. With this approach, free surfaces and contact surfaces between different materials are easily determined and remain distinct throughout the calculation. This is an important advantage over the Eulerian approach, in which the mesh is fixed in space and material flows through it. In this case it is the cell's volume that stays constant and any change in density within the cell is due to variation in the cell's mass during the simulation. In this approach material interfaces are quickly blurred with the introduction of "mixed cells", thus making boundaries less sharp. This problem can be partly obviated by using high resolutions, but at the price of a longer simulation run.

The major limitation of the Lagrangian approach is the inaccuracy in the solution of the shock equations when the cells are significantly distorted; an extreme case is a computed negative cell volume occurring when a cell folds over itself. A way to overcome the extreme grid distortion problem is to stop the simulation, carefully rezone the computational grid by overlaying a new, undistorted grid, on the old distorted mesh and restart the run. This process may have to be repeated many times when strong distortions are involved, making it a highly unfeasible approach for modeling the early stages of impact cratering. The problem does not exist or Eulerian codes, which can easily handle flows with large distortion, and are thus ideal to simulate the early

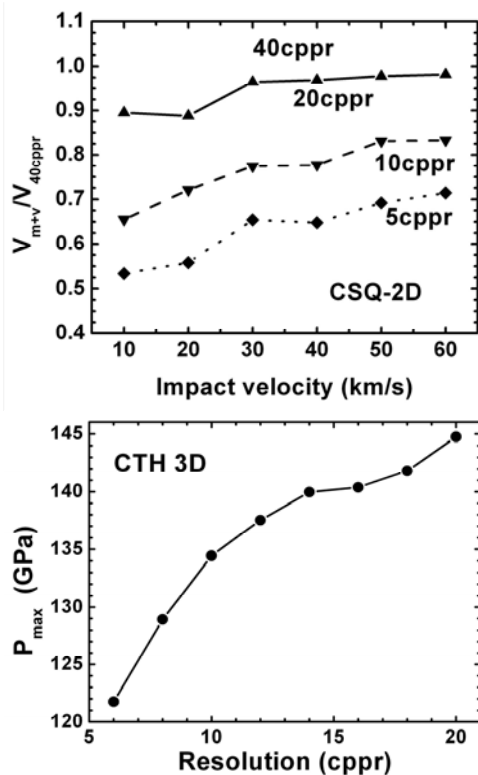


Fig. 3: *Upper:* Resolution effects in estimates of melt volumes for 2D simulations (using the hydrocode CSQ). From [6]. *Lower:* resolution effects in estimates of target's maximum shock pressures for 3D simulations (using the hydrocode CTH) [7].

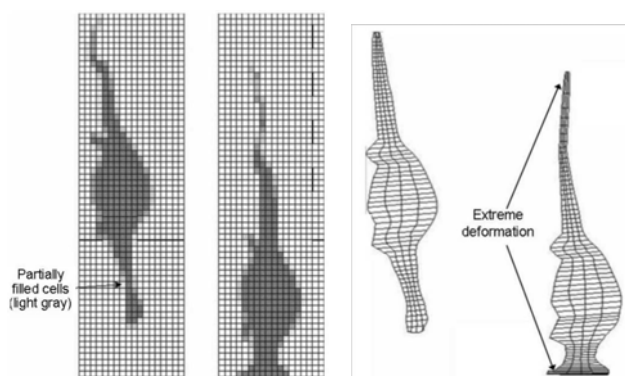


Fig. 4: Eulerian (*left*) versus Lagrangian (*right*) approach For numerical modeling. (Image courtesy of Gareth Collins).

stages of the impact process and the evolution of the expansion plume.

An alternative approach to typical Eulerian and Lagrangian “cell-codes” is the Smoothed Particle Hydrodynamics (SPH) approach, routinely used in the study of astrophysical fluid dynamics [4]. In the SPH approach material is represented by individual nodes with mass associated with them so that they can be considered and treated as physical fluid particles. Each node represents an average of its immediate area and its characteristics are determined as weighted sums over its neighboring node’s values. One advantage of the SPH approach is that it is not subject to boundary conditions because it is not bound to a fixed grid, typical of “cell-codes”. Among the main limitations of the SPH approach are resolution problems (it is intrinsically a low-resolution approach when compared to typical cell-based hydrocodes) and problems with material models, in particular with the implementation of strength models.

3.2 Material Models

Specific material properties govern the response of materials to stress, resulting in different behaviours of different materials for nominally the same impact conditions. The changes in a material’s density and internal energy with pressure are described by the *equation of state* (EOS). This relation is critical in the early stages of an impact event, when material strength is negligible compared to the pressure involved. The relation between stress and the strain (distortion) that produced it is given by the *constitutive equation*. This relation is fundamental for modelling the late stages of impact cratering, when material strength determines the final shape and characteristics of the crater.

The EOS is a necessary complement to the Hugoniot equations as to completely describe the conditions on either side of the shock. Thanks to the EOS it is then possible to specify the final thermodynamic state of shocked materials, usually represented graphically in

pressure-volume, or in shock velocity-particle velocity plots.

Equations of state depend on the complexities of a material’s atomic, molecular and crystalline structure and are unique for each material. In impact modeling studies they must describe the material’s thermodynamic behavior over a wide range of pressures, temperatures and specific volumes (or densities). The famous Tillotson EOS [8], specifically built for and widely used in impact modeling, is an analytical EOS which can describe the material below or above vaporization. However, it provides an incomplete description of a material’s thermodynamic properties as it cannot model two-phase regions nor it provides any information on how to compute the temperature or entropy of the material.

More complete equations of state consist in sophisticated computer codes that use different physical approximations in different thermodynamic regions. A widely used example of such codes is ANEOS [9], which uses Helmholtz free energy to obtain thermodynamically consistent estimates of properties like pressure, temperature, density, entropy. Material specific properties are provided through a series of parameters. ANEOS offers a (limited) treatment of phase changes, which is especially important when they interfere with the shock state. An updated version of ANEOS [10] expands the vapor phase treatment from simply monoatomic to biatomic species, improving the treatment of the vapor phase.

An important limitation of ANEOS is that it does not allow us to simultaneously treat solid-solid and solid-liquid phase changes. As a result, for complex materials, such as many minerals of geologic interest, a choice must be made between the two types of phase changes, depending on their influence on the material’s Hugoniot shock curve. A proper reproduction of the Hugoniot shock state has been the main drive to treat the solid-solid phase transition (in compression) in the development of ANEOS EOSs for geologic materials [e.g., 6]. The price for this capability, however, is an oversimplified description of the solid-liquid (melting) transition and unrealistic values of the heat expansion coefficients (too large for low-pressure solid phases). This generally does not affect strongly the early stages of impact cratering, especially when the determinations of average melt/vapor volumes are based on experimentally determined estimates of shock pressures for incipient and complete melting (assuming that the material always reaches ambient pressure after release from the shock state). On the other hand, the lack of an explicit treatment of melting as a gradual transition from a solid to a liquid state may cause severe errors in estimating the energy balance in the impact, especially when the latent heat of fusion may affect the P-T path of the material’s thermodynamic evolution. For example, in very large impacts (>300

km in diameter; [11,12]) large amounts of material may be compressed above incipient melting shock pressures at some depth below the surface, unloading to non-ambient pressure where they could be strongly heated but not completely melted.

Failing to correctly account the utilization of impact energy for (partial) melting, and the correct status of the material upon unloading from the shock state will strongly affect the subsequent modeling of important impact processes such as material ejection and crater collapse.

4. ADVANTAGES OF IMPACT MODELS

Hydrocode modeling is the only approach that can describe the dynamic of the impact process, including crater excavation, material ejection, melting/vaporization, crater collapse, ejecta launch and deposition. Throughout the simulation it can provide detailed information regarding all variables of interest which can ultimately be tested against observations. In this respect, numerical modeling is a crucial and unique approach in the study of impact cratering.

Historically, there has been a separation between early and late stage modeling of impact cratering. Each stage is modeled separately from the other, and often using different codes. This approach allows us to maximize the scientific return of numerical simulations. Early stage studies, usually carried out using Eulerian codes, focus on evaluating shock states in the target and projectile and require simulations with high temporal resolution and high spatial resolution near the impact point. Late stage studies focus on the process of crater collapse and the formation of the final impact structure. They require long integration times, not necessarily with high temporal resolutions, and a large spatial mesh that can be accompanied by a lower spatial resolution. Reasonable deformations in the cells during the late stage of impact cratering permits the use of Lagrangian codes, which in turn have the advantage of a better control over the material boundaries and material properties. Detailed studies of both impact stages in a single, continuous numerical simulation are becoming a possibility today with the aid of increasingly more powerful computers.

5. LIMITATIONS OF IMPACT MODELS

The colorful and spectacular images and animations generated by impact models may instill the notion that impact models can tell us anything about the impact process from microscopic (e.g., fragment sizes in impact melt breccia) to macroscopic levels (e.g., final ejection and deposition of materials in different shock states around the crater). However, spatial and temporal resolutions combined with computer

hardware limitations place severe constraints on what can be investigated in any individual simulation. In particular, numerical simulations cannot model processes that fall below the resolution limit of the model used. As described in section 3.1, accurate testing must be done before and after numerical studies, to ensure that the results are not affected by numerical limitations.

Furthermore, numerical simulations can only model processes that have been (correctly) implemented in the numeric code. Thus, limitations in material models, described in section 3.2 will limit the usefulness of the simulations. Other processes of interest may not be described in the code. For example, at this time no current hydrocode can model the chemistry that occurs inside the expansion plume. This does not mean that such process is untreatable, only that the correct implementation of the process of interest in the numeric code has not been developed yet. In some instances, the implementation cannot be carried out until we have a better understanding of the process, i.e., the physics and thermodynamics that govern it.

6. UNDERSTANDING IMPACT CRATERING THROUGH MODELING

Hydrocodes offer a means for studying various aspects of the impact process that cannot be investigated by other methods. Two obvious examples are the role of hydrocode simulations in constraining the amount and distribution of impact melt and vapor production and in characterizing the evolution of complex morphologies observed in large craters.

6.1 Melt Production and Ejecta

The amount of melt and vapor produced in an impact

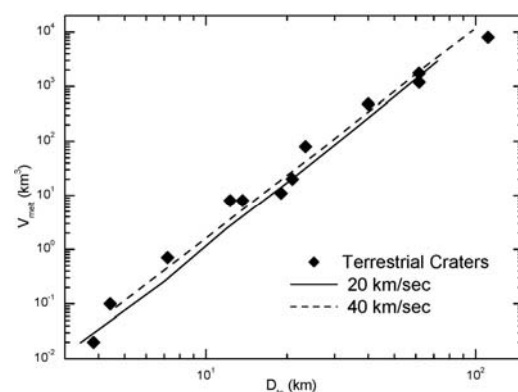


Fig. 5: Numerically estimated impact melt volumes versus transient crater diameter (solid and dashed lines) compared with terrestrial data on crystalline targets (diamonds) compiled by [12]. Simulations are for dunite projectiles on dunite targets at 20 and 40 km/s in 2D. From [6].

influences various aspects of the impact cratering event and its effects, from heat deposition to the development and composition of the vapor plume, to crater shape and impact lithology. In an impact event, melting and vaporization is an early stage phenomenon, governed by the thermodynamics of shock compression and release. Melt production cannot be reproduced in laboratory experiments (due to limitations in impact energy associated with experiments). Numerical modeling is thus the only approach that provides a handle on estimating melt/vapor production in impact events. This requires, however, accurate material equations of state, as well as realistic target compositions, where material mixing can occur at all spatial scales.

Numerical estimates of melt production in crystalline targets suggest that melt volumes increase linearly with increasing impact energy [6,13]. This result, holds for

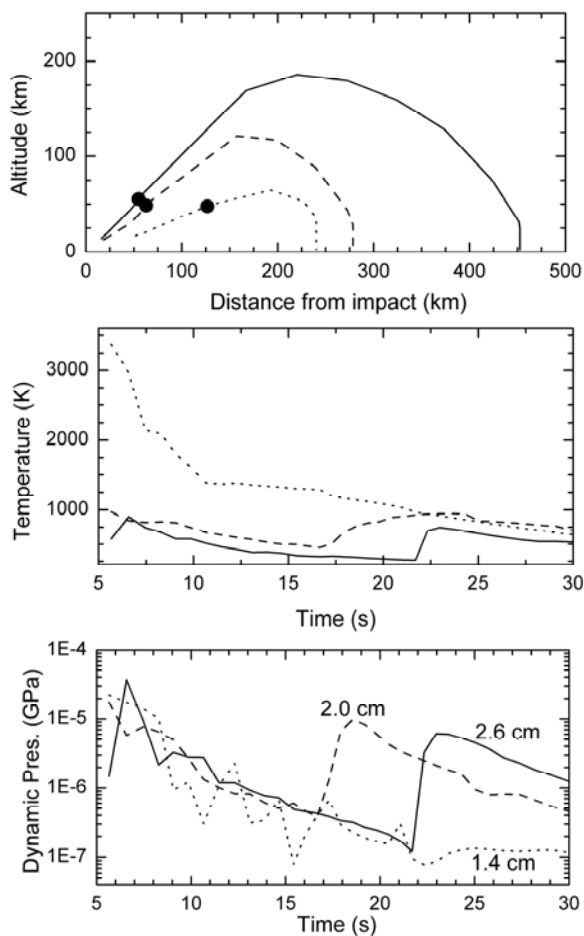


Fig. 6: Trajectories (*upper*), temperatures (*intermediate*), and dynamic pressure (*lower*) versus time for a few tektite-type particle of different sizes. The solid line represents a tektite 1.3 cm in diameter, dashed line a tektite 1.0 cm in diameter, and dotted line a tektite 0.7 cm in diameter. Solid circles in the upper panel mark the end of the hydrodynamic simulations (~30 seconds after the impact). From that point on the trajectories represent the motion of particles in an undisturbed atmosphere. From [16].

all but the lowermost impact angles ($\leq 15^\circ$, measured from the impact surface). Fig. 5 from [6] shows that numerical estimates of melt volumes appear to be in good agreement with available observational data from terrestrial structures [14]. For oblique impacts a rough direct relationship seems to hold between melt production and transient crater volumes for all but the lowermost impact angles [15].

Accurate numerical studies of melt production in impact events have helped in understanding the production of a unique kind of impact ejecta that has fascinated and puzzled scientists for many years: tektites. As recently as the 1960s, O'Keefe argued strenuously that tektites originated on the Moon; however, geochemical comparison between tektites and lunar rocks returned by the Apollo program made it clear that they are in fact of terrestrial origin. Tektites are naturally occurring glasses, usually not more than few centimeters in diameter. Today they are grouped into four distinct strewn fields: central European, Ivory Coast, North American and Australasian, all but one (Australasian) associated by spatial and geochemical characteristics to an impact crater (European: Ries, Ivory Coast: Bosumtwi, North American: Chesapeake Bay). Tektites have very low extraterrestrial component, with a maximum of about 0.06 wt% in Ivory Coast tektites. Water content, cosmogenic nuclides and chemical and physical homogeneity indicate that tektites originate from high-temperature melting of the uppermost few tens of meters of terrestrial rocks during impact cratering. Numerical modeling of the formation moldavites [16], Ivory Coast tektites [17] and Popigai distal ejecta [18] has indicated that tektites arise from a restricted area inside the growing crater in the very uppermost layer of the target rocks. During their flight in a post-impact plume they are not subjected to high pressures and cool slowly, as shown in Fig. 6, thus allowing for the time necessary to lose water/volatiles and obtain their hydrodynamic shape [16]. No special conditions are required to produce tektites: the study presented in [16-19] shows that the deficiency of tektite strewn fields (4 against ~180 impact structures) can be easily explained by the need of relatively large impact events (final crater diameter > 10 km) and by the quick degradation of natural glasses under weathering (natural glasses are normally < 50 Myr old).

3.2 Crater Collapse

Impact crater collapse is controlled by the competition between the gravitational forces tending to close the excavated cavity and the inherent material strength properties of the post-shock target. Thus, accurate simulations of crater collapse require a realistic constitutive model to represent the target material, and a good understanding of the fundamentals of dynamic

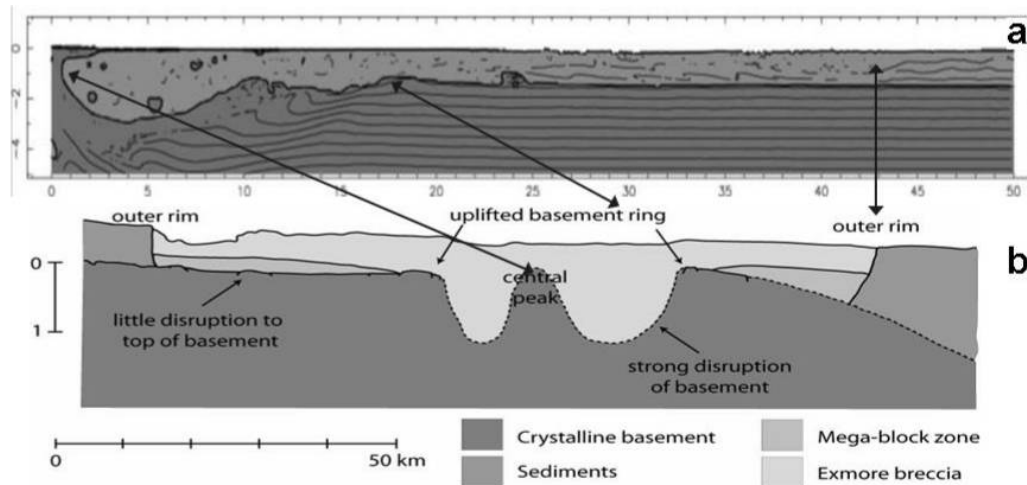


Fig. 7: Comparison between **a)** the crater collapse model result of Chesapeake Bay crater [24] and **b)** the schematic cross-section of the structure based on interpretations of seismic data and drill cores [22,23]. Double-headed lines show the correspondence in central peak uplift, inner rim, and outer deformation zone. From [24].

rock failure. It has been found that to reproduce the observed morphologies of complex crater collapse requires significant, but temporary, weakening of the target material beneath the crater floor. Suggested mechanisms for such a temporary strength-weakening effect include acoustic fluidization [20] and strain localization and thermal softening [21]. Both mechanisms seem to significantly improve the hydrocodes' ability to model crater collapse (i.e., the collapse of a geometrically simple, bowl-shaped "transient crater" during the late phase of crater formation); however, the relative importance of each mechanism is still poorly constrained.

A good example of the usefulness of crater collapse modelling is shown by the investigation of the Chesapeake Bay structure [22] in Virginia, United States. Late Eocene in age (35.2-36.0 Ma), the Chesapeake Bay impact occurred in a shallow marine environment, with a crystalline basement overlain by close to 1km of sediments and few hundred meters of water. Schematically, the crater has the morphology of an inverted sombrero, with a deep inner basin surrounded by a shallower brim (Fig. 7b), typical of marine impacts on Earth. Its surface morphology, however, is almost entirely flat, due to the presence of an unusually thick crater fill deposit, the Exmore breccia. The morphology of the Chesapeake Bay structure is quite different from similar-sized subaerial structures on Earth, or large craters on other planets, making it difficult to estimate the size of the impacting object, comet or asteroid, that formed it. This causes problems in evaluating the energy involved in the impact event and consequently the overall environmental consequences of the impact event. Early investigations suggested the edge of the shallow brim as the outer rim of the crater, analogous to the outer rim of complex craters while the inner basin edge was

compared to the peak ring of complex extraterrestrial craters [23].

Recent numerical studies of the Chesapeake Bay impact event [24] provide a different interpretation. The model results, Fig. 7a, indicate that the morphology of the crater was strongly affected by the particularities of the target rocks. The water-saturated sedimentary layer of low density and strength (modelled as wet tuff) was strongly mobilized during crater collapse. The water column also played an important role in aiding the mobilization of the underlying sediments. As a result, the initial opening cavity process which excavated the crystalline basement and created the inner basin was followed by a prolonged collapse phase in which impact ejecta landing outside the opening cavity disrupt the sedimentary unit to a radius of about 40 km. The final distribution includes a large fraction of the disrupted sediments moving back into the inner basin, filling it up (Exmore breccia). The resulting picture, shown in Fig. 7, is that of a flat crater, with a sombrero-like shape, just as observed at Chesapeake,.

While current impact simulations have produced a consistent paradigm for how large craters might collapse to form the final complex form, they still do not provide a complete explanation for why large impact craters collapse in this manner. A full mechanical understanding of large impact crater formation requires further testing and refining of numerical crater collapse models, supported by geological observation, geophysical data and drill cores.

7. SUMMARY AND FUTURE TASKS

There are still many important and difficult problems that computer modeling can help investigate. At this

time, material models are still the weakest component of impact modelling and require further improvement so that other important open questions can be addressed. Some of these questions deal with the role of complex targets in the cratering process, from porous (i.e. sediments) to mixed targets, such as ice/rock mixing in the Martian crust that may be responsible for the formation of rampart craters. The evolution of the expansion plume is another important area of impact studies, from target/projectile degassing to the thermodynamic evolution of ejecta (i.e., tektites and or ejecta blankets), to the chemical evolution of expansion plumes.

8. ACKNOWLEDGMENTS

The author is indebted to Natasha Artemieva, Gareth Collins, Boris Ivanov, Jay Melosh, Kai Wünnemann for the useful discussions and for providing some of the figures in this paper. This work is supported by NASA Grant NAG5-13429.

9. REFERENCES

1. Anderson C.E., An overview of the theory of hydrocodes, *Int. J. Impact Eng.*, Vol. 5, 33-59, 1987.
2. Pierazzo E. and Collins G., A brief introduction to hydrocode modeling of impact cratering, in (H.. Dypvik, M. Burchell, and P. Claeys, Eds.) *Cratering in Marine Environments and on Ice*, Impact Studies Series, Springer, Heidelberg, 323-340, 2004.
3. Melosh H.J., *Impact Cratering: A Geologic Process*, Oxford Univ. Press, New York, NY, 245 pp, 1989.
4. Monaghan J.J., Smoothed particle hydrodynamics. *Ann. Rev. Astron Astroph.*, Vol. 30, 543-574, 1992.
5. Berger M.J. and Colella P., Local adaptive mesh refinement for shock hydrodynamics, *J. Comput. Phys.*, Vol. 82, 64-84, 1989.
6. Pierazzo E., et al., A re-evaluation of impact melt production, *Icarus*, Vol. 127, 408-423, 1997.
7. Pierazzo E., et al., The Ries impact event: A tale of two hydrocodes. *ESF-IMPACT 5 Workshop*, Granada, Spain, 2001.
8. Tillotson J.H., *Metallic equation of state for hypervelocity impact*, Tec. Rep. GA-3216, General Atomic Report, 1962.
9. Thompson S.L. and Lauson H.S., *Improvements in the chart-D radiation-hydrodynamic code III: Revised analytical equation of state*, Tech. Rep. SC-RR-61 0714, Sandia National Labs., 1972.
10. Melosh H.J., A new and improved equation of state for impact computations, *31st Lunar Planet. Sci. Conf.*, Abst. #1903, 2000.
11. Ivanov, B.A. and Melosh, H.J., Impacts do not initiate volcanic eruptions: Eruptions close to the crater. *Geology*, Vol. 31, 869-872, 2003.
12. Ivanov B.A., Modeling of largest terrestrial impact craters. *Solar Sys. Res.*, Vol. 39, 381-409, 2005.
13. O'Keefe J.D. and Ahrens T.J., Impact-induced energy partitioning, melting and vaporization on terrestrial planets, *Proc. Lunar Sci. Conf.*, Vol. 8, 3357-3374, 1977.
14. Grieve R.A.F. and Cintala M.J., An analysis of differential impact melt-crater scaling and implications for the terrestrial impact record, *Meteoritics*, Vol. 27, 526-538, 1992.
15. Pierazzo E. and Melosh H.J., Melt production in oblique impacts, *Icarus*, Vol. 145, 252-261, 2000.
16. Stöffler et al., Modeling the Ries-Steinheim impact event and the formation of the Moldavite strewn field. *Met. Planet. Sci.*, Vol. 37, 1893-1908, 2002.
17. Artemieva et al., Investigating the Lake Bosumtwi impact structure: Insight from numerical modeling, *Geochem. Geophys. Geosyst.*, 5, 2004. Q11016, doi:10.1029/2004GC000733.
18. Ivanov et al., Popigai Impact Structure Modeling: Morphology and Worldwide Ejecta. *35th Lunar Planet. Sci. Conf.*, Abst.#1240, 2004.
19. Artemieva N.A., Tektite origin in oblique impact: numerical modeling. *Lecture Notes in Earth Physics*, Springer Verlag, Berlin, 257-276, 2002.
20. Melosh H.J. and Ivanov B.A., Impact crater collapse, *Ann. Rev. Earth Planet. Sci.*, Vol. 27, 385-415, 1999.
21. O'Keefe J.D. and Ahrens T.J., Complex craters: Relationship of stratigraphy and rings to impact conditions, *J. Geophys. Res.*, Vol. 104, 27091-27104, 1999.
22. Poag C.W., Koeberl C. and Reimold W.U., *The Chesapeake Bay crater – Geology and geophysics of a late Eocene submarine impact structure*, Impact Studies Series, Springer, Heidelberg, 522p.
23. Poag C.W., Structural outer rim of Chesapeake Bay impact crater: Seismic and borehole evidence, *Met. Planet. Sci.*, Vol. 31, 218-226, 1996.
24. Collins G.S. and Wünnemann K., How big was the Chesapeake Bay impact? Insight from numerical modeling, *Geology*, Vol. 33, 925-928, 2005.

GEOLOGICAL ASPECTS OF TERRESTRIAL IMPACT CRATERING RATES; SIMULATING THE PROCESSES AND EFFECT OF CRATER REMOVAL. S. N. D. Thackrey¹, G. M. Walkden¹, G. Dunn²

¹Department of geology and Petroleum Geology, University of Aberdeen, AB24 3UE Aberdeen, Scotland, U.K.

²Department of Physics, University of Aberdeen, AB24 3UE Aberdeen, Scotland, U.K. s.thackrey@abdn.ac.uk

ABSTRACT

Regression impact flux models have been accepted by many to be the best way of representing flux trends for quite some time. However, through the creation of these models, key factors have been overlooked that play a vital role in impact flux trends. These factors are associated with geological and astronomical processes. To develop a new flux model, regression trends have to be replaced by computer simulations as to develop higher accuracies and flexibility.

INTRODUCTION

Impact cratering has been an area of keen interest for a number of decades and is now well established as an important geological process. Research developed by various workers such as [2] provided an impact flux model where it could be established that a crater of diameter X should occur every Y years somewhere on the Earth's surface.

When considering these well established models, a number of problems are immediately recognizable. Primarily the influence of geological or rather Earth surface processes has been poorly represented. Furthermore, the concentrations of impacts will inevitably vary as a function of Latitude; the affects of these two fundamental factors form the basis of this paper.

THE IMPACT FLUX

The impact flux is the frequency at which impactors (Asteroids and Comets) of a given diameter collide with Earth. Establishing when the next large impact is going to occur on the Earth's surface has long since been hailed as the "Holy Grail" of impact related studies. The impact flux was initially very high. This period is known as the "heavy bombardment period" [4]. The heavy bombardment period was a time when the solar system was still somewhat chaotic, large asteroids were common forming some of the very large craters seen on the Moon. However from about 3.8Ga, the impact flux greatly reduced by about a factor of five, and since c. 1Ga, has remained relatively constant.

[2] were the first to try and quantify Earth's impact flux. The methodology mainly involved studying the terrestrial and lunar record. The lunar impact record was seen to be the most complete due to the fact that there have been no significant

surface processes influencing the craters. The only mechanism influencing craters on the moon is the subsequent reworking by other impacts. By calculating the age and diameter of craters and also their surface concentrations, a LOG regression trend model can quickly be established. The latest version of the model by [2] can be seen in Eq.1, where C is the concentration per Km^2 and D is the diameter of the crater in Km.

$$\text{Log } \Phi_c = - (11.67 \pm 0.21) - (2.01 \pm 0.13) \text{ Log } D \quad (1)$$

There are three fundamental weaknesses with the regression trend approach. Firstly, the model produced is only as reliable as the limited data used. Secondly, it does not take into consideration latitudinal variations in impact concentrations. Thirdly, it does not recognize and take account of model the effects of geological processes.

The latest version of the model produced by [3] does attempt to take into consideration the effects of geological processes. However, in doing so the available database used becomes severely restricted. The rationale was that craters between the diameters of 19-45Km, younger than 105Ma and occurring in stable cratonic areas were seen to represent the crater concentration expected even with the influence of Geological processes. By focusing the criteria down to this level, it only left six craters to base the new model on. This in turn only served to exaggerate the already inherent inaccuracies with the regression models.

GEOLOGICAL AND ASTRONOMICAL EFFECTS.

To create a holistic model, every possible aspect that influences crater preservation, formation and distribution must be fully integrated. This information can be derived through knowledge of both planetary surface processes (geology) and orbital/geometric processes (Astronomy). Three key geological processes that contribute to the deletion of craters are: - Tectonics \rightarrow Erosion \rightarrow Burial / Sedimentation. These are hierarchically inter-linked, with plate tectonics having the most effect on crater preservation

Geological processes not only affect Earth. Many other planets show evidence that geological processes play or once played an important role in developing a planet's surface. Earth and Venus are perhaps the best examples in our solar system of planets with well established active geological

systems. Mars also shows good evidence of volcanism and plate tectonics, but these processes now seem to be dormant with only Aeolian erosional processes actively affecting the cratering record. There is also evidence of relic fluvial erosion. These geological systems act to both mask and erase the impact record of a planet which in turn leads to difficulties when attempting to derive an impact flux model from a database of impact craters.

On Earth, oceans occupy over 70% and of this oceanic crust the oldest is c.185Ma. That means that plate tectonics (crustal recycling through subduction) has removed over 2/3 of the entire impact record spanning in excess of 3Ga.

The terrestrial cratering record seems to be restricted to the cratonic areas of continental crust Fig. 1.

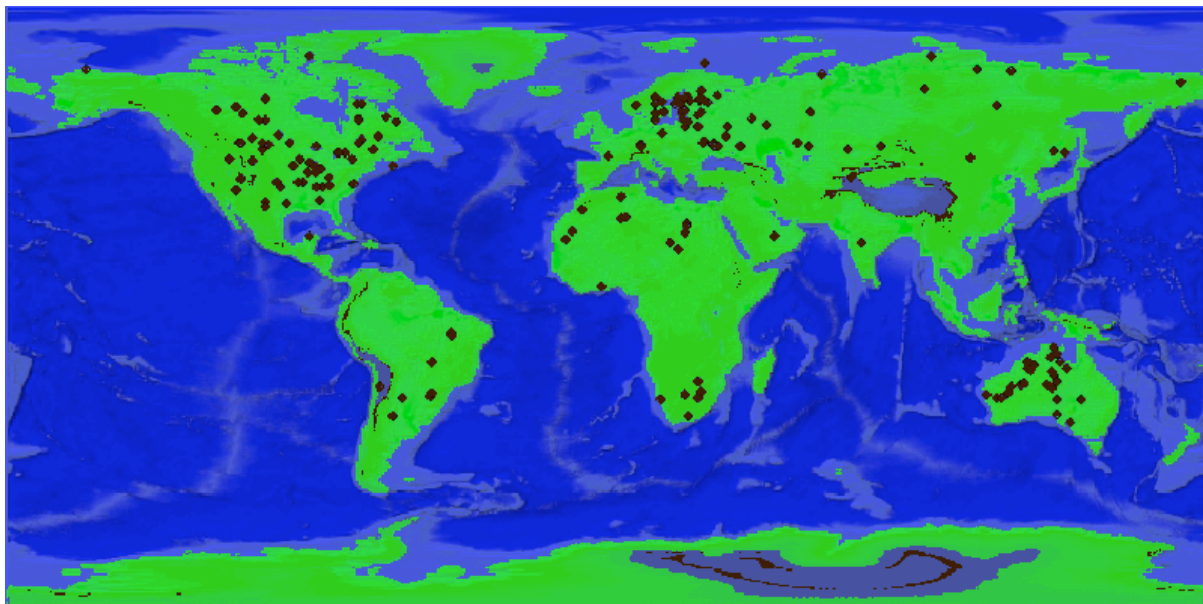


Fig. 1. Global distribution of impact craters. DEM image from ESRI

These cratonic areas have been exposed for much longer periods of time and hence more craters can be observed. Nonetheless, even within cratonic areas there is a bias towards well populated or well researched regions such as Western Europe, North America and Australia. This bias probably reflects the distribution of researchers and accessible field areas as much as it reflects the distribution of craters.

Erosion produces vast amounts of sediment in various forms and also at various rates depending on topography and climate. The sediment generated from erosion can rapidly bury an impact crater beyond detection. A secondary effect of erosion and burial is the misinterpretation of impact crater diameter. Manicouagan is an excellent example where workers have suggested pre-erosional

diameters of 64Km to 120Km. This uncertainty in crater diameter directly influences the impact database that regression models are based upon. Crustal deformation and volcanism also contribute to the deletion of craters from the record.

A particular feature of the terrestrial cratering record is that the distribution of impact craters that we see today is not the primary distribution. Plate tectonic movements have radically altered the positions of continents and consequently the position of impact craters. Craters that are older than c.20Ma are likely to have been moved from their original positions. Fig. 2. shows the latitudinal distribution of all known craters corrected back to their original latitude at time of impact (This was achieved by using palaeocontinental data [5]).

What is immediately apparent in Fig. 2. is the variation in crater distribution patterns through time.

Zone 1. Shows the Polar Regions devoid of preserved impact craters. During these time periods, there were comparatively small areas of continental crust around the poles. There is also an astronomical factor that concentrates impacts to the equatorial belt, but this will be covered when discussing *zone 4*.

Zone2. The equatorial concentration observed during pre-Triassic periods is not continuous. *Zone 2* illustrates a marked decrease in preserved impact craters. The equatorial regions during this time had a very low coverage of continental crust. Marine craters only make up about 7% of the entire cratering record, for this reason, we find very little craters preserved in this zone. Furthermore, Equatorial regions, due to the climate, exhibit elevated erosional rates through rock decomposition (particularly in feldspar rich rocks).

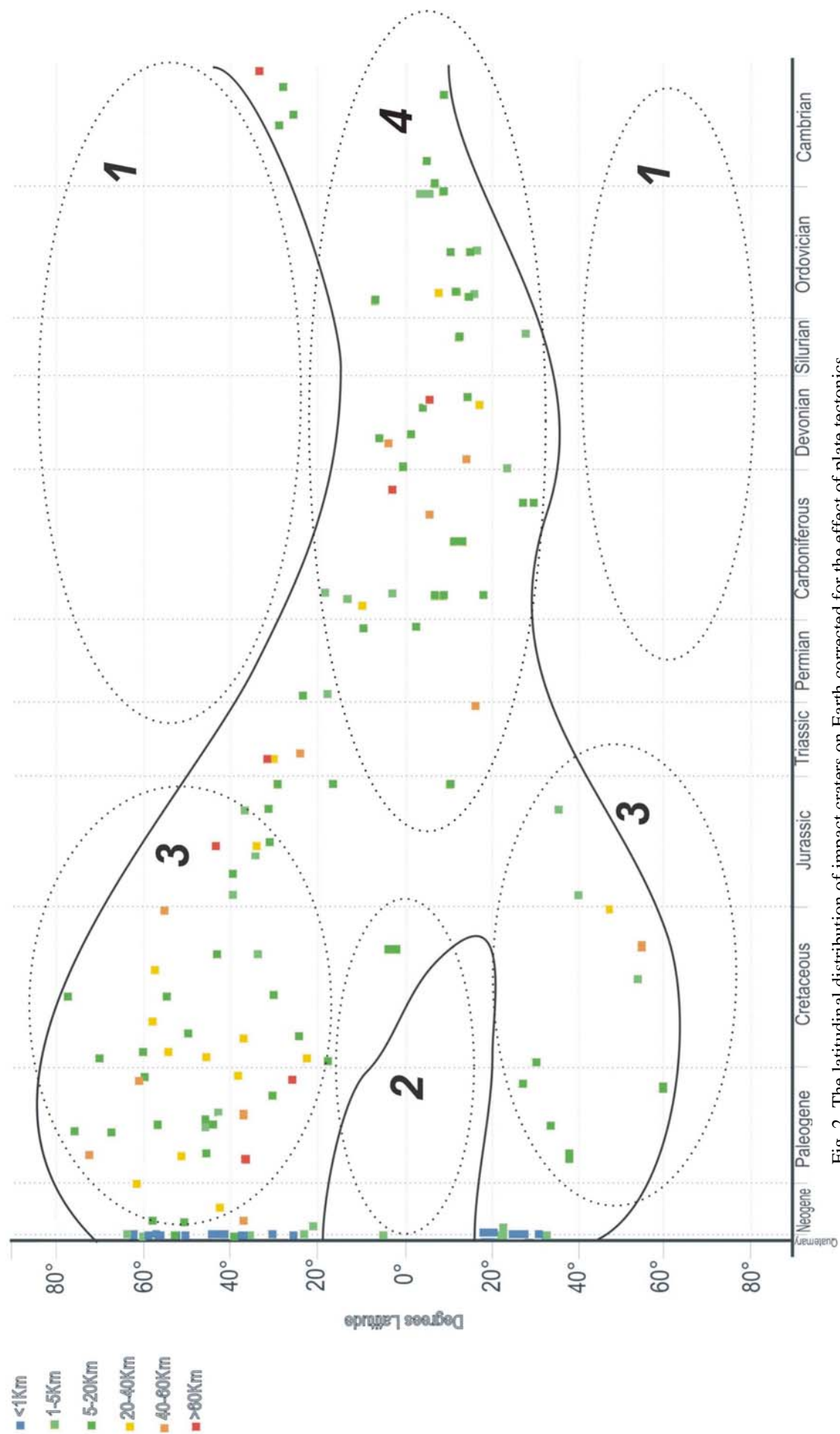


Fig. 2. The latitudinal distribution of impact craters on Earth corrected for the effect of plate tectonics.

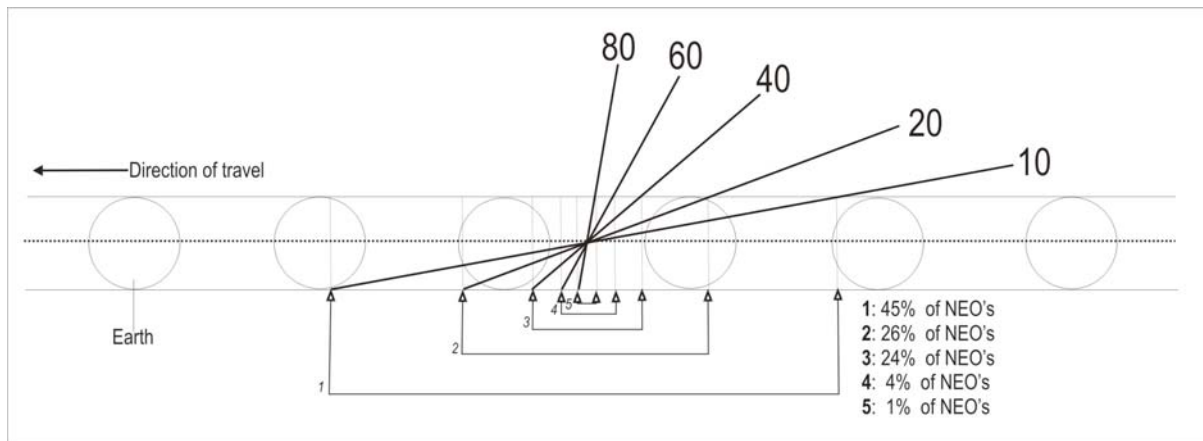


Fig. 3. NEO orbital inclination density with respect to the ecliptic.

Zone 3. Shows a significant number of preserved impact craters in the mid latitudes both in the northern and southern hemisphere (Note that polar latitudes have no preserved craters). These impacts are still preserved due to the locations of continental crust. Here the opposite is true of *Zone 2*, whereby craters are preserved where there are sufficient areas of continental crust. Quaternary and late Neogene impacts are quite plentiful; this is due to the fact that geological processes have had very little time to act upon them.

Zone 4. This zone covers a broad span of time that seems to highlight a natural tendency for craters to be concentrated across the equatorial latitudes. It does however reflect the equatorial distribution of continental crust during this time. With the continental crust occupying large areas of the equator, a large number of craters can be preserved.

An equatorial concentration is, however, to be expected. This is an astronomical feature that is influenced by two key factors; orbital inclination of impactors and impact obliquity. Potential impactors, in the form of asteroids and comets, have three sources: - the asteroid belt (which resides in the orbit between Mars and Jupiter), the Kuiper belt (which resides in the orbits of the outer solar system) and the Oort cloud. These objects can be perturbed from their original orbits into potential Earth crossing orbits. These objects are classified as Near Earth Objects (NEO's). Over 3000 NEO's have been identified to date along with their attributes, such as orbital properties. Fig. 3. is a representation of all the current NEO's orbital inclination. Over 70% of all NEO's lay in the 0- 20° inclination range (with respect to the ecliptic). In analogy of the sun's radiation as it strikes the Earth, the Polar Regions present a larger surface area. This means that less energy is delivered per Km^2 at the poles compared to the equator. This can be applied to the NEO populations where the exact same is true whereby a large percentage of NEO's orbits follow close to the ecliptic. For this reason, there is a

considerably higher concentration of impact craters at the equator compared to the poles. Fig.4. is an impact probability plot using current NEO orbital data. The simulation also integrates the effect of the Earth's rotational axis "wobble" and differences in the impact trajectory aspect (i.e. the simulation does not assume that all NEO's are aiming directly towards the centre of the Earth). When analyzing the model, it can be seen that there is generally a 2:1 ratio of probability when comparing the equator with the poles. This equatorial concentration could also be a further reason why the polar gaps are observed in *zone 1* Fig. 2.. Furthermore, the Polar Regions present impactors with a more oblique impact trajectory that may result impact craters being smaller due to prolonged re-entry times and a reduced energy release during impact.

DEVELOPING A NEW MODEL

With the identification of the significance of both Astronomical and Geological factors, how can a new model for impact flux be developed? To answer this, the techniques of developing regression models must first of all be established. With regression models there must first of all be a good reliable database to deduce trends. Once there is a reliable database, then a reliable trend model can be produced. In the case of modelling impact flux, this complete database does not exist. The best alternative to a regression model would be a simulation that approaches the problem from a different stance. Instead of relying on the observed, geological processes could be simulated to establish a rate at which impact craters disappear. From this the flux can be established, for once the correct flux is attained then direct comparisons can be made to the known.

To develop a holistic model we have been developing a simulation that will not only model Astronomical and Geological processes but can also integrate already well established equations for re-entry effects, crater diameter, and effect of impact obliquity such as [1]. This provides a far more accurate way of producing a new model. Our

simulation, although still in its basic development stages, is already modelling continental drift and the effects of erosion.

With the simulation complete we will be able to test current models and also develop a new alternative model based on more factors than ever before. Furthermore, the results of the simulation could be applied to other studies and aid in our understanding of other planets.

CONCLUSIONS

Impact flux models based upon regression trend LOG functions were initially seen to be the best way of representing impact flux. However, there are some major factors that have either been overlooked or poorly represented.

As the regression models rely on a database of craters, then producing a model based upon Earth's preserved craters would provide an inaccurate model. This is due to the fact that geological processes (Tectonism, Erosion, and Burial respectively) have removed a vast amount of craters from the Earth's surface. Some attempts have been

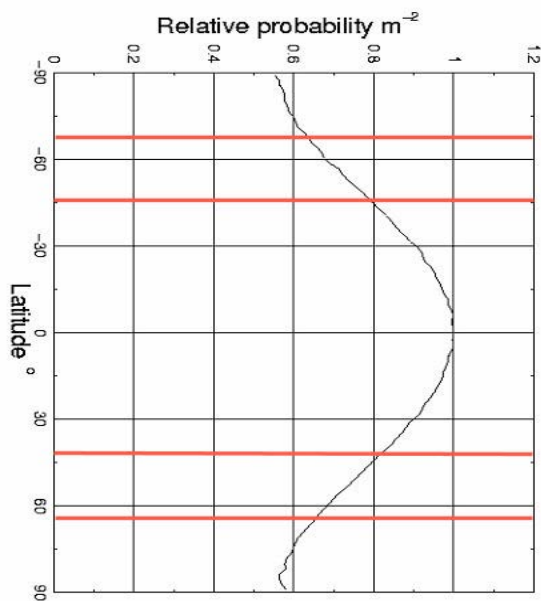


Fig. 4. Impact probability plot using NEO orbital data.

made to integrate a geological aspect into these models [3]. The problem with integrating a geological aspect into a regression model is that the database resolution becomes severely reduced to the point that the model becomes unreliable.

Furthermore, current regression models are expressed in the form of: - A crater of diameter D will occur every X years per 1Km^2 somewhere on the Earth's surface. The problem here is the "somewhere on Earth's surface". It has been proved by our probability simulations that there is a definite equatorial bias of impact crater concentrations. The ratio of concentration between the poles and the equator is about 2:1. This is quite a significant difference and highlights that current regression models cannot be applied accurately to planetary studies.

We regard the best way to develop a new impact flux model would be to produce a simulation that encapsulates all aspects of impacts. By approaching the problem from an alternative perspective, the new model will be far more accurate and furthermore, as the science of impacts develops, so can the simulation.

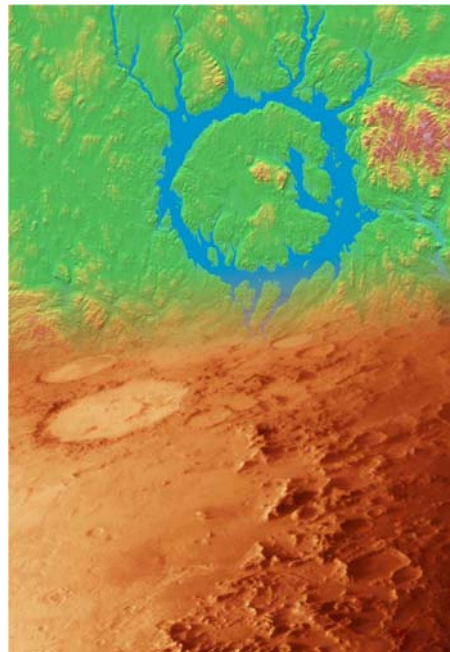
References:

- [1] Chyba C. F. Owen T. C. Ip W. (1994) in; *Hazard due to comets and Asteroids*, ed. Gehrels T. Univ. Arizona Press, 9-59
- [2] Grieve R. A. F. & Shoemaker E. M. (1994), in; *Hazards due to Comets and Asteroids*, ed. T. Gehrels. Univ. Arizona Press, 417-462.
- [3] D. W. Hughes (1999), *Jl. Brit. Interplanet. Soc.* 52, 83-9
- [4] Shoemaker E. (1983), *ann. Rev. Earth Planet. Sci.* 11, 461-494.
- [5] Smith A. G. & Briden J. C. (1981), *Phanerozoic palaeocontinental world maps. Camb. Earth Science series.*

Session S.10

Laboratory Experiments

Chair: E. Pierazzo



IMPACT EXPERIMENTS ON DRY AND WET SANDSTONE

F. Schaefer⁽¹⁾, K. Thoma⁽¹⁾, T. Behner⁽¹⁾, S. Nau⁽¹⁾, T. Kenkmann⁽²⁾, K. Wünnemann⁽²⁾, Alex Deutsch⁽³⁾, and the MEMIN-Team⁽⁴⁾

⁽¹⁾ Fraunhofer-Institute for High-Speed Dynamics (Ernst-Mach-Institut, EMI), Eckerstr. 4, 79104 Freiburg, Germany, Email: schaefer@emi.fhg.de, thoma@emi.fhg.de, behner@emi.fhg.de, nau@emi.fhg.de

⁽²⁾ Museum für Naturkunde, Humboldt-Universität Berlin, Invalidenstraße 43, 10115 Berlin, Germany, Email: thomas.kenkmann@museum.hu-berlin.de, kai.wuennemann@museum.hu-berlin.de

⁽³⁾ Institut fuer Planetologie, Westfaelische Wilhelms-Universitaet Muenster, Wilhelm-Klemm-Str. 10, 48149 Muenster, Germany, Email: deutsca@uni-muenster.de ⁽⁴⁾ see Acknowledgement below

ABSTRACT

The availability of a new powerful light-gas gun accelerator at the Fraunhofer-Institute for High-Speed Dynamics, Ernst-Mach-Institute (EMI), has triggered a study that investigates the dynamics of impact processes in sandstone. Using this accelerator, crater sizes in the decimetre-range can be obtained, narrowing further the gap between crater sizes obtainable in laboratory and geological impact craters: The smallest impact craters detected on the earth's surface differ in size by roughly two to three orders of magnitude with regards to what can be achieved with the new facility. Hence, the new experimental capabilities enable a more realistic laboratory simulation of geological impact processes.

Two impact cratering experiments on dry and wet sandstone have been performed. This paper provides a description of these impact experiments and the measurements performed including crater size analysis, pressure curve recordings, and high-speed shadowgraphs. The impact cratering experiments reported here are designed to support the comprehensive understanding of the dynamics of impact processes and the quantification of the properties of impact-damaged sandstone. These investigations are performed in the framework of a *Multidisciplinary Experimental and Modeling Impact* crater research Network (*MEMIN*), which was recently established and combines the expertise of geologists, geophysicists, engineers, and modellers [1].

1. TARGET DESCRIPTION

The targets were blocks ($1.0 \times 1.0 \times 0.5 \text{ m}^3$) of sandstone ("Seeberger Sandstein", Fig. 1), which had a distinct stratified structure (Fig. 2). Its average density amounted to 2.2 g/cm^3 . The target material has an average grain size of 0.17 mm and $\sim 18 \%$ porosity (Fig. 3). One of the blocks was put in a water basin for four months and reached a water saturation of $44 \text{ vol. } \%$ (Fig. 4).



Fig. 1. Sandstone target blocks

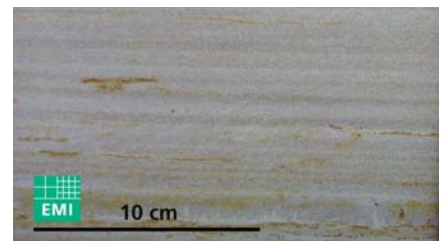


Fig. 2. Stratified target structure



Fig. 3. Microscopic picture of target material, showing sand particles and voids (black)



Fig. 4. Watered sandstone block

The strength and elastic modulus are $62.4 \pm 2.8 \text{ MPa}$ and $14.8 \pm 1.4 \text{ GPa}$ respectively for the dry sandstone and $47.0 \pm 3.7 \text{ MPa}$ and $12.1 \pm 1.0 \text{ GPa}$ for the highly water saturated equivalent.

2. HYPERVELOCITY IMPACT FACILITY

2.1 Working Principle

The accelerator system is based on the two stage light gas gun principle.



Fig. 5. Working principle of a two-stage light-gas gun

A schematic sketch of the working principle is shown in Fig. 5. The expanding gases of the combusting gun powder drive a plastic piston in the pump tube. The pump tube is filled with a light-weight gas, either Helium (He) or Hydrogen (H). The piston compresses the gas between its leading surface and a thin metal diaphragm located in the high pressure section, which is the joining point between the two gun barrels. This diaphragm prevents the light weight gas in the pump tube from escaping into the launch tube until the gas is compressed to a specific pressure at which the diaphragm is ruptured. Behind the diaphragm is the projectile, embedded in a plastic cylinder (sabot),

which is launched by the escaping light-weight gas from the pump tube.

After the projectile exits the launch tube, it enters the blast tank, where the sabot separates from the projectile under action of the residual atmosphere. Before the projectile enters the target chamber, a laser light barrier measurement system determines the velocity of the projectile. Immediately after the velocity measurement, the sabot parts are captured, allowing only the projectile to enter the target chamber. In the target chamber, a high speed framing camera has been integrated to capture shadowgraph images of the impact process. Such guns are used for spacecraft protection applications [2,3] and research related to hypervelocity impacts on geological matter [4].

2.2 Facility description

The facility and the gun are shown in Fig. 6 [5]. The gun is modular, offering a large variety of gun configurations enabling application of launch and pump tubes with different lengths and diameters. The largest gun configuration consists of a 22 m long pump tube, with a caliber of 150 mm, in combination with a 12 m long launch tube of caliber 50 mm. All of the following experimental results refer to this configuration. For an accelerated mass of 150 gr. (sabot + projectile), the current maximum velocity of the gun exceeds 6 km/s. The facility can be operated at atmospheric pressure or evacuated to forevacuum pressures.

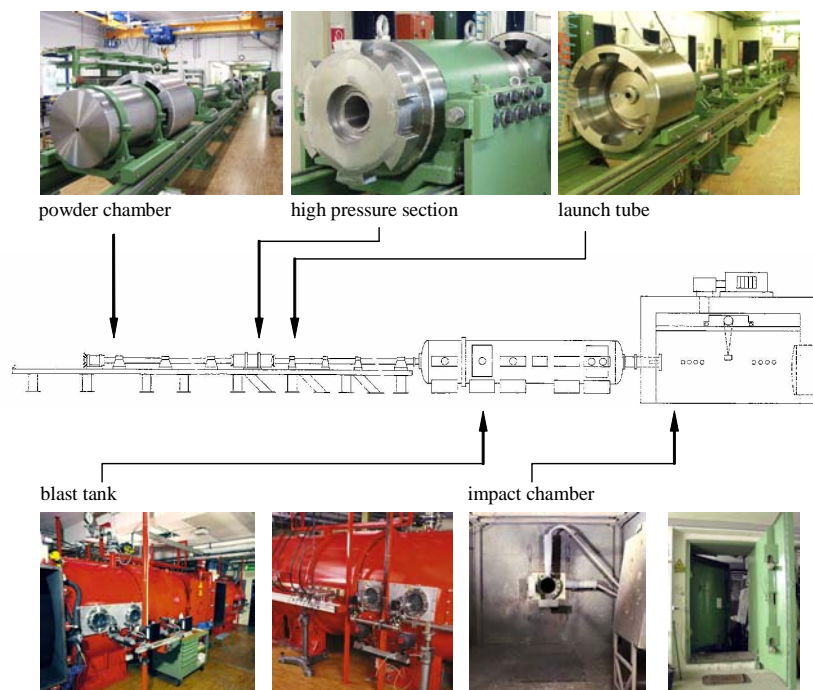


Fig. 6. EMI's two stage light gas gun at proving ground Efringen-Kirchen, south of Freiburg. The upper row shows the launcher system, the lower row the blast tank and the impact chamber with its double access door

3. SET-UP

The set-up is shown in Fig. 7. The blocks were positioned vertically to simulate a vertical impact on flat lying sediments. The target was enclosed in a steel casing, with only the target surface designated for impact left uncovered. Uprange ejecta catchers consisted of fiber boards with an area of 1 m² and a 10 cm hole for allowing the projectile to pass. The catchers were placed about 55 cm in front of the target surface. Carbon resistor- and SMD (Surface Mounted Device) resistor shock pressure gauges, manufactured at EMI, were emplaced within the sandstone blocks at a depth of 6 cm beneath the sandstone surface. Two gauges were placed at each lateral side of the target block, and four sensors were placed at the rear side. A 16 channel High Speed Digital Camera was used to image the ejection process in a shadowgraph imaging technique. The camera was placed perpendicular to the shot direction, in the plane of the front target surface. Camera, flash, and transient recorder for the shock pressure gauges were triggered by a trigger foil that was electrically shorted by the impacting projectile during the first tens of nanoseconds of the penetration phase. The shots were performed with the target chamber pre-conditioned to reduced pressure of ca. 0.5 bar.

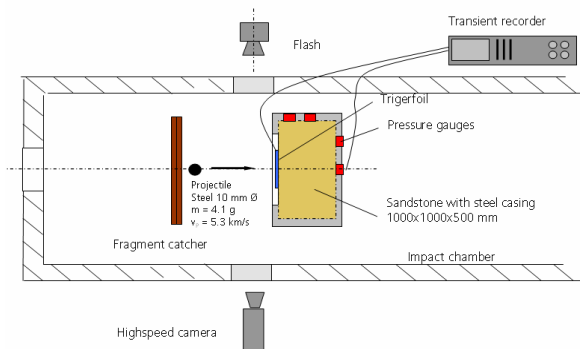


Fig. 7. Experimental set-up



Fig. 8. Target set-up: left: fragment catcher, right: sandstone block



Fig. 9. Right: side of the target block, showing the steel casing and two of the integrated pressure gauges; Left: rear side of the target with 4 gauges integrated

4. IMPACT EXPERIMENTS

Two impact crater experiments were performed with a dry and a water saturated sandstone, respectively. In both cases, the projectile was a 10 mm diameter steel sphere with a mass of 4.1 g. The material specification of the steel was: AISI 4130 Steel, German Industry Standard material number DIN 1.7218. The sabot mass was established at 113 gr., which is relatively high compared to the projectile mass, in order to ensure safe acceleration of the projectile. The impact velocities were ca. 5.3 km/s in both impact experiments (Table 1). In future experiment campaigns, savings on the sabot mass through optimized design can be realized, permitting higher velocities to be attained with the same gun loading parameters.

Table 1 Impact parameters

	dry sandstone (Exp. 2808)	wet sandstone (Exp. 2809)
projectile	Steel 10 mm, 4.1 gr.	Steel, 10 mm, 4.1 gr.
impact velocity	5.34 km/s	5.27 km/s

5. EXPERIMENTAL RESULTS

5.1 Impact Damage

The impact craters were funnel shaped (Fig. 10). The crater in the dry sandstone (Exp. 2808) had an average diameter of 24.3 cm and a depth of 5.6 cm, whereas in the wet sandstone (Exp. 2809) the crater diameter amounted to 28.7 cm and the depth to 4.5 cm (Fig. 11). Volumetrical analyses of the craters based on 3D-scans determined 715 and 1099 cm³ of excavated material in the dry and wet case, respectively [1]. These results show that the presence of fluid has influenced significantly the cratering process. A wider spall zone

and a shallower crater depth characterize the wet target compared to the dry sandstone.



Fig. 10. Impact crater in wet sandstone - perspective

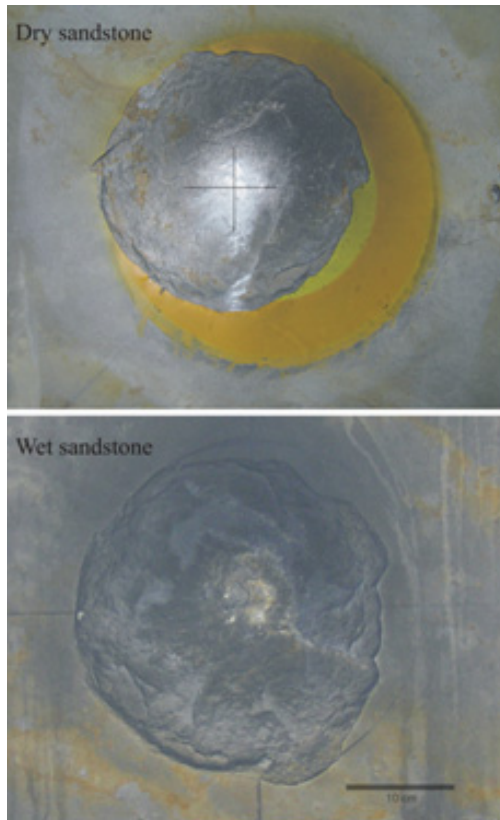


Fig. 11. Impact craters - top view

The uprange ejecta from both targets comprised a wide spectrum of fragment sizes from below $160\ \mu\text{m}$ to above 3 cm. The size distribution had a maximum in the size interval $160\text{--}310\ \mu\text{m}$ corresponding to the initial grain size of the sandstone, and in the size range

exceeding 2.5 cm, which corresponds to spall fragments. The uprange ejecta caused just minor impact damage in the fragment catcher (Fig. 12), ranging from minor surface erosion to shallow craters with a maximum size of about 1 cm. The main portion of craters produced by the ejecta were located in an area with an outer diameter of about 810 mm (Exp. 2808) and 790 mm (Exp. 2809).

In the impact experiment on the dry sandstone, a single large remnant of the projectile having 69% of the steel projectile mass was recovered from its position in the uprange fragment catcher, at a radial distance of just about 10 cm from the shot-axis. In the impact experiment on the wet sandstone no larger projectile remnants were found, which was most likely due to it passing right through the hole in the fragment catcher.



Fig. 12. Damage from uprange ejecta in fragment catcher in Exp. 2809 (wet sandstone)

5.2 Ejecta velocities

Ejecta velocities were determined from the high-speed shadowgraphs during a time frame of ca. 1.2 ms, shown in Fig. 17 for Exp. 2808 (dry sandstone) and Exp. 2809 (wet sandstone). The shutter time was 180 ns. From the high-speed shadowgraphs it is obvious that most of the ejected matter is concentrated both in the central portion of the cloud and the cone. Further, the digital images suggest higher ejection velocities for the wet sandstone compared to the dry sandstone. The ejecta velocities were determined from the projection of the expanding cone fragments in a plane perpendicular to the target surface, schematically shown in Fig. 13. Thus, the values supplied below refer to the normal components of the ejection velocities. The actual expansion velocities along the cone can be obtained by dividing the supplied values by $\cos \alpha$.

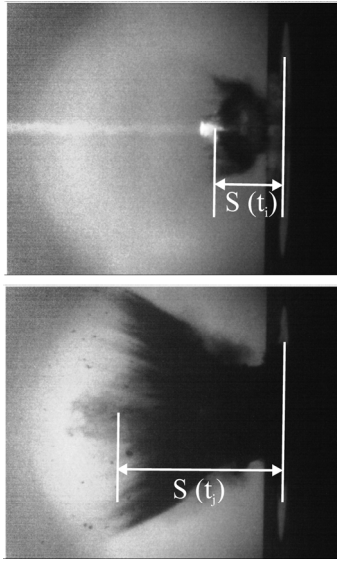


Fig. 13. Determination of ejecta velocities

The mean ejecta velocity perpendicular to the target surface as plotted in Fig. 14 decreases from 2.3-2.4 km s⁻¹ in a time frame between projectile encounter and 20 μ s afterwards to 0.2-0.3 km s⁻¹ after 230-470 μ s. On average, the velocities of the ejecta from the wet sandstone are up to 50 % higher than for the dry sandstone. The reason for this behaviour is under investigation. It is believed that the vaporization of the water in the wet sandstone may serve as an additional source of acceleration for the ejecta.

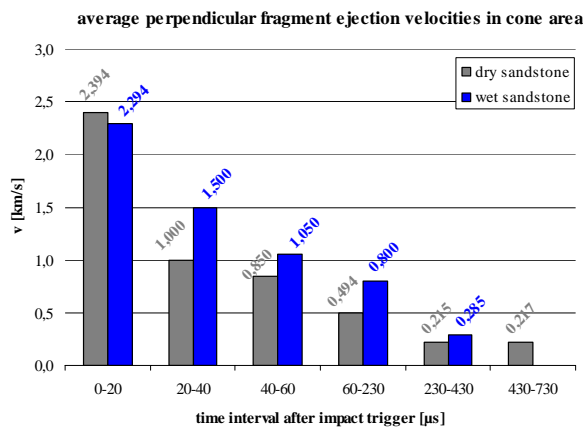


Fig. 14. Average perpendicular fragment ejection velocities for both shots

Ejecta cone angles recorded with high speed cameras are 69.8° and 58° after 1.23 msec in the dry and wet experiments [1].

5.3 Pressure gauge records

Pressure-time profiles recorded with the gauges integrated in the rear side of the target block (K13 for dry sandstone, S4 for wet sandstone, see Fig. 15) have

been analyzed. The pressure-time signals are plotted in Fig. 16, where the reference time 0 μ s corresponds to the impact trigger, the same as was used for the high-speed shadowgraphs. The signal curves are normalized to the maximum pressure signals recorded, because the pressure gauges are currently under calibration at EMI. Thus, only preliminary magnitudes for the peak pressures can presently be provided.

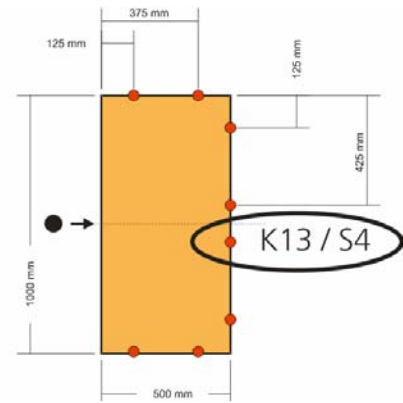


Fig. 15. Pressure gauge locations

As can be seen from Fig. 16, the shape of the signal time curves in both experiments is similar. In both experiments the arrival of the compression wave at the gauge locations occurs about 150 μ s after impact trigger. The strong pressure peak is followed by a release wave caused by the reflection of the wave at the rear surface of the target block, starting at ca. 180 μ s, and continuing for several 100 microseconds. The preliminary evaluation of the signal amplitudes indicate that the peak pressures measured in the dry sandstone block reach a magnitude of about 5 MPa at about 45 cm from the impact location, while the peak pressures measured in the wet sandstone are about one order of magnitude lower. The reasons for this massive difference are under investigation.

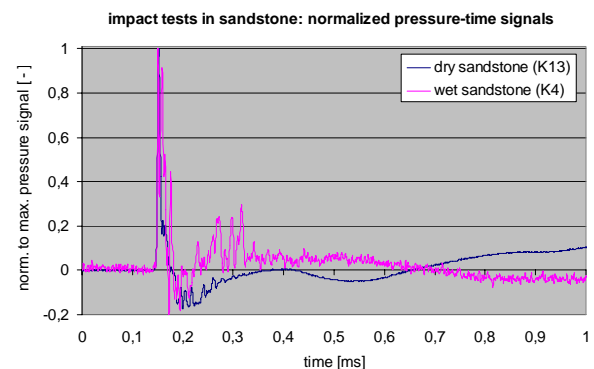


Fig. 16. Normalized pressure-time signals recorded at the rear side of the target blocks, see Fig. 15 (K13: Exp. 2808, S4: Exp. 2809)

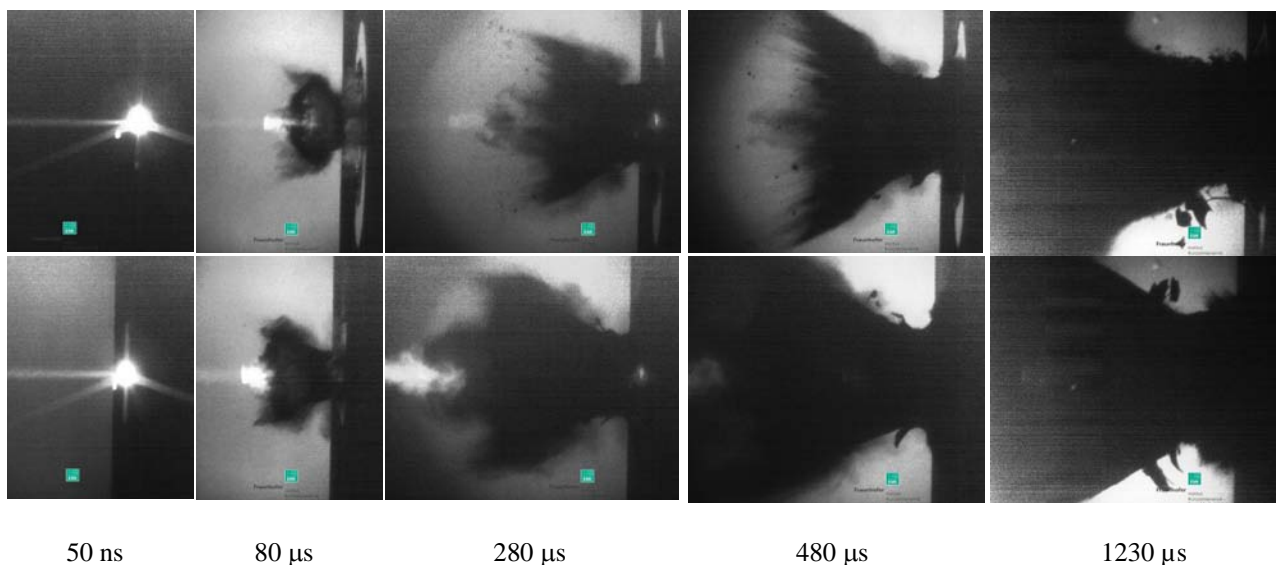


Fig. 17. Impact experiment on 0.5 m³ dry (Exp. 2808, top row) and wet (Exp. 2809, bottom row) sandstone target with a 4.1 g Steel Projectile at 5.3 km/s; High-Speed Digital Shadowgraphs of ejecta cone evolution during initial 1230 μs after impactor encounter with sandstone target.

6. SUMMARY

Ernst-Mach-Institute now possesses a new powerful Light Gas Gun accelerator that is able to generate decimetre-size craters in a sandstone target. The availability of this accelerator offers more realistic opportunities for laboratory simulation of geological impact processes. In this project, which is part of the MEMIN program, the influence of the water content in porous rock vs. dry rock on cratering, shock wave amplitudes, and fragment ejection processes was investigated. It was found that impact into water-saturated sandstone results in shallower but wider craters with larger volumes. It also causes higher ejection velocities of the ejecta. The pressure gauge recordings indicate that the peak pressures at the rear of the sandstone targets are about one order of magnitude lower for the wet sandstone than for the dry sandstone. Analysis of the results is ongoing.

7. ACKNOWLEDGEMENT

The authors would like to acknowledge the contributions of the other members of the MEMIN team to this paper, especially for the mechanical and physical target properties: W. U. Reimold, R.T. Schmitt, L. Hecht (Museum für Naturkunde, Humboldt-Universität Berlin, Germany); U. Yaramanci, S. Mayr, (Abteilung Angewandte Geophysik, Technische Universität Berlin, Germany); C. Grosse (Institut für Werkstoffe im Bauwesen,

Universität Stuttgart, Germany); G. Dresen (Projektbereich 3.2, GeoForschungsZentrum Potsdam, Germany); J. Kuder (Fraunhofer EMI, Efringen-Kirchen proving ground)

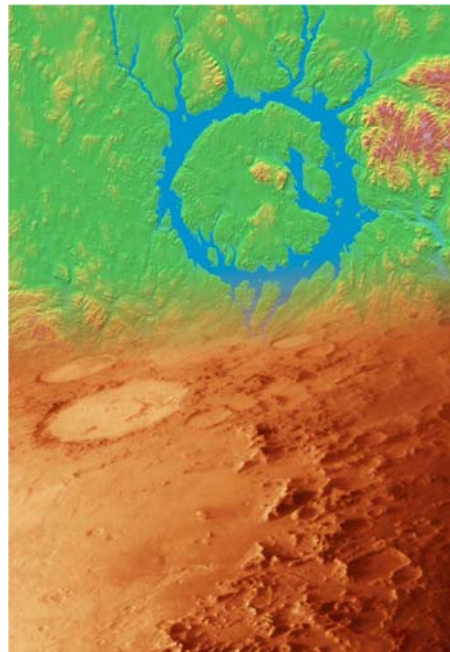
8. REFERENCES

1. Kenkmann T., et al., *LPSC XXXVII*, Abs. # 1587, 2006.
2. Schneider E. and Schaefer F., Hypervelocity impact research - acceleration technology and applications *Advances in Space Research*, 28 (2001) pp. 1417-1424
3. Schaefer F., Geyer T., Schneider E., Rott M., and Igenbergs E., Degradation and Destruction of Optical Surfaces by Hypervelocity Impact, *Int. J. Impact Engng.* Vol. 26, 2001, pp 683 - 698
4. Thoma K., Hornemann U., Sauer M., Schneider E., Shock waves - Phenomenology, experimental, and numerical simulation, *Meteoritics & Planetary Science* 40, Nr. 9/10, 1283-1298, 2005
5. Junginger M., Schmolinske E., Performance Tests of a new Two Stage Light Gas Gun at the Ernst-Mach-Institut, Proc. 53rd Meeting of the Aeroballistic Range Association, October 21-25, 2002, Sendai, Japan

Session S.12

Catastrophes and Extinctions

Chair: A. Rossi



LARGE BOLIDE IMPACTS - IS IT ONLY SIZE THAT COUNTS?

G. Walkden¹ and J. Parker¹.

Kings College, University of Aberdeen, AB24 3UE, UK. g.walkden@abdn.ac.uk

ABSTRACT

Just one well documented large terrestrial impact, the end Cretaceous Chicxulub event, can be linked to a mass extinction. Other well-constrained large impacts, evidenced by craters in the region of 100km or more, have been implicated in extinction but either their exact timing or the independent biodiversity data fail to clinch the link. By breaking down impact events into their component effects and separately assessing their biotic damage we can get nearer to a true risk assessment. We conclude that a major reason for some large impacts being apparently "safe" relates as much to where they struck, what they struck and when, as to how large the events were as revealed by crater size.

1. INTRODUCTION

In estimating the biotic effects of large impacts great reliance is usually placed on apparent crater size. Raup's [1] definitive "Kill Curve" explicitly linked crater diameter with extinction numbers, and later modifications by Jansa et al [2] and Poag [3] sought to determine just what size of impact, implied by crater size, was necessary to be catastrophic for the planet as a whole (Fig. 1). However, the model is based on a very small statistical sample (only one well known Phanerozoic impact has been credited with substantial and immediate biotic effects) and apparent crater diameter alone is an unreliable proxy for the environmental and biotic consequences of an impact. Risk of extinction stems from a number of factors (Fig.2) and having regard for crater diameter alone ignores variables such as location (environment, plate tectonic setting, site geology ("Where" in Fig. 2) and timing in relation to biological and geological evolution ("When" in Fig. 2).

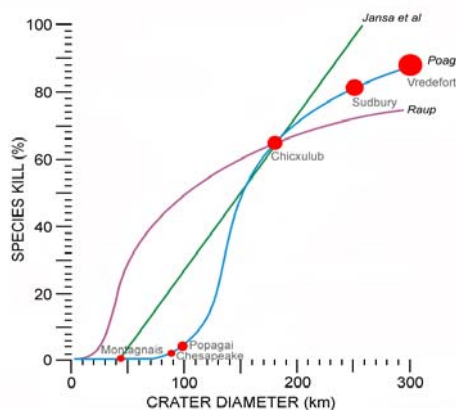


Fig. 1. The Raup Kill Curve (labeled) with subsequent modifications by Poag.

2. SIZE VERSUS LOCATION AND TIMING

There are around 170 well constrained and documented terrestrial craters larger than 1km, only one of which, the c.170km end Cretaceous Chicxulub crater in Mexico, has been justifiably linked to a major extinction. Crater diameter is usually the only information we have upon which to estimate the scale of an impact and uncertainty is increased through the effects of erosion, deposition or tectonism that have deleted large parts of the record.

Size is broadly related to bolide mass, velocity and impact angle ("What" and "How"; Fig. 2), but the location of an impact can also affect size. For example, a substantial depth of water can reduce apparent crater diameter (many terrestrial impacts must have been marine), whilst the architecture and rheology of shallow site geology can cause an increase in apparent size through the development of collapse structures.

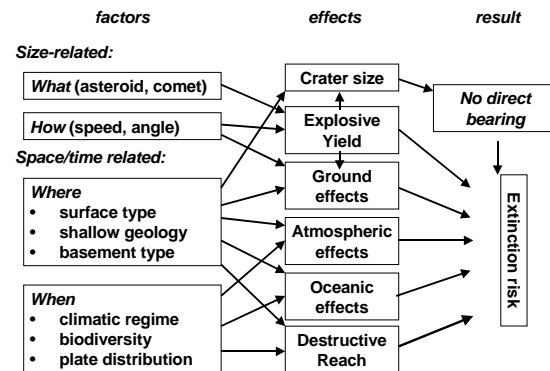


Fig. 2. Factors contributing to risk of Extinction.

We propose that in the critical size range of consideration by Raup (say, 30 to 300km), two strong determinants on the extinction potential of an impact are where it struck and when (Fig. 2). To test this, we have looked in some detail at our two best - documented large terrestrial craters. These are the c.170km end Cretaceous Chicxulub impact structure, Mexico (linked to a major extinction), the c.100km late Triassic Manicouagan structure, NE Canada (negligible extinction).

Both craters point up the complexity of the key piece of data upon which the Kill Curve depends - namely the accurate determination of the final crater diameter. Chicxulub is now completely obscured. It was excavated through an unstable carbonate platform into a subsiding (and also potentially unstable)

continental margin. It is now buried by up to 1km of post Cretaceous sediment. Manicouagan, on the other hand, was formed in a thick high- strength ancient continental interior. Exposed since the Triassic, the original crater morphology and all proximal ejecta have been lost to erosion, together with >1km of the underlying crust. The structure is now eroded down to c.65% of an original 100km diameter.

More usefully, Chicxulub and Manicouagan provide locational and environmental extremes. Although they both struck the planet at between 20°N and 25°N, Chicxulub zeroed on a humid subtropical marine embayment next to wide expanses of high biodiversity continent and ocean, whilst Manicouagan struck well within the arid interior of the massive Pangean supercontinent, well away from oceans and forest. The Manicouagan impact also caught the planet at a time of relatively low world-wide biodiversity. It might be said that whilst the late Cretaceous sub tropical belt was a highly vulnerable target, the late Triassic continental interior was already the sort of barren extreme that a large impact might create. It therefore is of little surprise that, independent of their actual size, the Chicxulub and Manicouagan events had such contrasting biotic effects.

3. MODELLING AND REVERSE-MODELLING CHICXULUB AND MANICOUAGAN

We have modelled some of the probable effects of the Chicxulub and Manicouagan using a combination of existing mathematical models [4-14] to arrive at a link between crater diameter and potentially lethal distal effects such as radiation, firestorms, pressure, wind and dust fallout. The mathematics are adopted as published and are incorporated into an holistic spreadsheet without further critical review. The spreadsheet presently permits two calculations to be run simultaneously and side-by-side (Fig. 3) and is easily modified and extended.

The calculations derived in this way have been used to inform a semi quantitative table (Fig.4) that lists the principal hazards associated with the respective impacts from the local scale to the global.

These hazards are briefly detailed as follows:

Cratering

The bolide strikes at between 11 and 72 km/s; rock bolides being in the lower part of this range. Kinetic energy release vaporises, melts and pulverises rocks at ground zero, excavating a crater up to 20x the diameter of the impactor. The crater partly refills through return of ejecta and slumping of sides. Local obliteration of biota is guaranteed.

	BOLIDE A	BOLIDE B
Impactor diameter m	9000	15000
Impactor density kg/m3	2750	2750
Impactor velocity km/s	20	20
Kinetic Energy J	2.09937E+23	9.7193E+23
Entry Angle	75	75
Water thickness m	0	0
Target density	2750	2750
Transient Water Crater (m)	0	0
Transient Rock Crater (m)	59579	88758
Crater "rim-to-rim" final (km)	102	160
Avg Rim-to-Floor depth (km)	1.60	1.83
Melt Volume km3)	1801	8345
Melt thickness in crater (m)	646	1349
Fireball radius (m)	118787	198031
Max pulse seconds after impact (s)	6	10
Location Distance (km)	2000	2000
Irradiation duration (s)	1544	2573
Thermal exposure at location (J)	0	0
Trees Burn from plume radiation?	NO	NO
Siesmic Effect (Richter Scale)	4.2	4.6
Arrival time (s)	400	400
Ejecta Thickness (mm)	14.1	69.3
Peak overpressure Pa	32196.1	66423.1
Peak wind velocity MPH @	150	280
Summary	Background A	Background B
	Background C	Background D

Fig. 3. Sample section from spreadsheet used to calculate and compare the distal effects of two different impactors at a range of possible impact site conditions (equations used are derived from numerous authors and are acknowledged in text). This run models a Manicouagan - scale and a Chicxulub - scale impact at the Manicouagan site. The distance from impact chosen here represents that of the distal impact deposit from Manicouagan reported by Walkden et al.[]

Shock/Blastwave

An atmospheric pressure pulse of c.4-psi centred on the impact site is followed by winds of >250 km/h. Blast radiates and blows off the atmosphere between 140° and tangentially to the curvature of the Earth. Regional devastation of biota takes place.

Ejecta curtain

A corona of gaseous and molten ejecta rises and expands on a ballistic trajectory. This leaves a thick melt sheet proximally and a torrent of condensing glass droplets distally (microtektites). Local obliteration and regional devastation of biota are assured.

Fireball and Plume

A plume of ejecta erupts from the cratering process beyond the level of the earth's atmosphere. Material enters orbital and suborbital paths re-entering proximally to distally (perhaps antipodally) with associated IR radiative effects. No direct plume-related deleterious effects on biota.

Atmospheric surge

Atmosphere is sheared away locally by the expanding blast. Compression and displacement of atmospheric gases outwards is replaced by a counterflow. Supercanes occur proximally, atmospheric destratification is general. Damage to biota is related to regional hypervelocity winds and local atmospheric depletion.

4a. "Actual"	Chicxulub		Manicouagan	
<i>Bolide: rock</i>	c. 15km		c. 10km	
<i>Crater diameter</i>	c. 170km -		c. 100km	
<i>Latitude</i>	20-25°N		20-25°N	
<i>shallow geology</i>	unstable carbonate shelf		thin Palaeozoic cover	
<i>deep geology</i>	subsiding plate margin		stable high-strength craton	
<i>Continent configuration</i>	dispersed E-W		assembled N-S	
<i>Surface type</i>	marginal marine		continental dryland	
<i>Climate</i>	sub tropical humid		sub tropical arid	
<i>Regional biodiversity</i>	high		low	
<i>Global biodiversity</i>	high		moderate	
EFFECT		Approx. biotic damage		Approx. biotic damage
Cratering	LOCAL	V	LOCAL	V
Shockwave		IV		III
Ejecta curtain		IV		III
Plume/ Fireball		I		I
Atmospheric surge	REGIONAL	II	REGIONAL	II
Seismic wave series		II		I
Tsunami		III		
Shelf wasting		III		
Plume fallout	GLOBAL	I	GLOBAL	I
IR radiation		III		I
Suspended dust		III		II
Wildfires		III		
Wildfire soot		III		
CO/CO ₂		III		I
SO ₂		II		
NO ₂		II		I
CH ₃		II		

4b. Reversed	Chicxulub		Manicouagan	
<i>Bolide: rock</i>	c. 9km		c.15km	
<i>Crater diameter</i>	c.100km -		c.170km	
<i>Latitude</i>	20-25°N		20-25.8°N	
<i>shallow geology</i>	unstable carbonate shelf		Thin Palaeozoic cover	
<i>deep geology</i>	subsiding plate margin		stable high-strength craton	
<i>Continent configuration</i>	dispersed E-W		assembled N-S	
<i>Surface type</i>	marginal marine		continental dryland	
<i>Climate</i>	sub tropical humid		sub tropical arid	
<i>Regional biodiversity</i>	high		low	
<i>Global biodiversity</i>	high		moderate	
EFFECT		Approx. biotic damage		Approx. biotic damage
Cratering	LOCAL	V	LOCAL	V
Shockwave		IV		IV
Ejecta curtain		III		IV
Plume/ Fireball		I		I
Atmospheric surge	REGIONAL	II	REGIONAL	II
Seismic wave series		I		I
Tsunami		II		?
Shelf wasting		II		?
Plume fallout	GLOBAL	I	GLOBAL	I
IR radiation		II		II
Suspended dust		II		III?
Wildfires		II		I
Wildfire soot		I		I
CO/CO ₂		II		I
SO ₂		II		
NO ₂		I		I
CH ₃		I		?

Fig. 4. Modelling biotic damage arising from the effects of the Chicxulub and Manicouagan impacts.

4a: Probable biotic damage based upon actual crater diameter, target structure, target composition, continental massing, ambient biodiversity and environmental conditions at the time and location of the two impacts (toned columns; these reflect an estimate of damage arising from each effect between 0 and V with 5 high. Colour density is arranged accordingly).

4b: Modelled biotic damage based upon interchanged energy output of the impacts (blue highlight). Other parameters remain as in 4a. Note that even under reversed modelling, where the smaller impactor strikes at Chicxulub and the larger impactor strikes at Manicouagan, Chicxulub marginally remains the more lethal event.

Seismic waves

Ground zero earthquake exceeds force 10 by orders of magnitude and spreads across the globe. Secondary earthquakes and tsunamis are triggered. Biotic depletion almost anywhere.

Tsunami

Marine impacts generate giant primary Tsunami. Secondary ones follow crater refilling and waves oscillate across oceans. Oceanic circulation can break down. Biotic devastation takes place on shelves and coastal plains.

Shelf wasting

Cratering, tsunami and seismic shaking produce mass wasting of shelves and release of shelf gas hydrates. Severe biotic effects from resuspension, slumping and mass flow. Benthic zones affected and as far as 100's km from ground zero.

Plume fallout

The rising plume of vapour, melt and pulverised rock collapses, returning groundwards to produce pyroclastic flows, dust storms and debris flows. Biotic effects are limited to areas already affected by other devastation.

IR radiation

Frictional heating of re-entering ejecta produces infra-red radiation. Ground surface heats to 200-300° C. Biotic damage limited to dessiccation (see below for wildfires) but might be sub global. Devastation is dependent on ejecta volume and dynamics.

Wildfires

The landfall of hot re-entered ejecta on IR-desiccated flora can ignite ravaging wildfires. Severe biotic effects sub-globally, but mostly limited to areas of desiccation.

Dust

Suspended dust can remain in the atmosphere for weeks or months. Severe light and heat reduction are implicit. Biotic effects are dependent on duration, potentially affecting whole food chains worldwide.

Soot

Large volumes can be thermally lofted from forest and grassland wildfires. Widespread dispersal is by winds and atmospheric circulation. Temperature effects are disputed and uncertain. Biotic damage takes place through disruption of atmospheric heat budgets, low light levels and changes to weather and climatic patterns.

H₂O (not modelled)

Marine impacts eject large volumes of water into the atmosphere. Long term residence in the upper atmosphere will have greenhouse and general climatic effects, but worldwide rainout of soot and dust is likely. Biotic effects are unpredictable.

CO₂ / CO

CO₂ from dissociation of carbonates is possible. CO₂ from wildfire combustion is likely. Biotic effects stem from resultant greenhouse warming.

SO₂

Sulphur dioxide from evaporites in the impact site rock column could be produced in large volumes. Oxidised, and coupled with water in the upper atmosphere, this creates sulphuric acid, then acid

rain. Severe biotic effects have been claimed for both terrestrial and marine areas worldwide.

NO₂

Shock heating of outer atmosphere by re-entering material can produce Nitric Acid. Biotic effects similar to SO₂ and are dependent on volume.

CH₃

Oceanic disturbances (including tsunami, slumps, and temperature change) can destabilise gas hydrates and release large volumes of methane. This is a greenhouse gas and reacts to create ozone that can become toxic in large quantities.

Useful discussions of most of these effects can be found in [16-18].

Informed by numerical modelling in the spreadsheet (eg. Fig 3) we go on to analyse each effect noted above for its potential biotic damage (Fig. 4). Severity is scored on a subjective scale of 0-5(V) with 5 high. These estimates are tone-coded for direct visual comparison from low (light) to high (dense). At the moment some significant effects noted in the tables are only approximations informed by the nearest factor in the spreadsheet. Continued development of the spreadsheet (Fig. 3) should achieve better correspondence between this and the assessments of hazard (Fig. 4). At that stage we intend to make the spreadsheet available on the internet.

We first model Chicxulub and Manicouagan using values to match their apparent actual crater diameters (Fig. 4a). Then, to test the influence of location, we have reversed the craters, showing the effects of a Chicxulub - scale impact at Manicouagan and a Manicouagan - scale impact at Chicxulub (Fig. 4b). Although the diameters of the two craters are arguably in the same order of magnitude, the energy release at Chicxulub was as much as five times that at Manicouagan (Fig.3). Nonetheless, there are substantial differences between the two events relating to location and timing that strongly influence the modelling. These include target structure, target composition, massing of continents, ambient biodiversity, and environmental conditions (noted in Fig. 4). These locational and timing factors lead to a strong contrast in predicted biotic effects from the two impacts (Fig. 4a). However, after reversing the craters and despite their size difference the modelling suggests that, instead of completely reversing the biotic effects, there would have been very little difference between them in terms of biotic effects (Fig 4b). What emerges from this is that, to the extent that the Chicxulub event was "unlucky" through its location and timing, Manicouagan was "lucky". The following factors served to reduce the biotic effects of the Manicouagan event and probably saved it from becoming a planetary disaster:

- lower general and local biodiversity in the Trias

- the high crustal strength and stability of the Manicouagan site
- the lack of a substantial thickness of rocks at the impact site capable of generating potentially lethal volatiles (eg. CO, CO₂, SO₂)
- the location of the impact in a climatically inert arid continental belt.
- the pre-adaptation of the animal and plant population in this belt to a climatic extreme comparable to post-impact conditions
- the location of the impact at the centre of a supercontinent well remote from oceans and seaways
- the massing of continents in a N-S direction so that the east-west smearing of re-entering fallout mainly dissipated over ocean.
- the position of the antipodal site (the location of any antipodal re-entry of ejecta, eg. [19]). over ocean.
- Westward smearing from the above mainly affecting the southern continental arid belt.
- the lack of ignitable Triassic forest ecosystems in mid latitude regions where the main fallout and re-entry effects were concentrated.

4. CONCLUSIONS AND RECOMMENDATIONS

Impact site variables such as geological structure of the target, composition of the target rocks, the position of a target in plate tectonic terms, the massing of continents at the time of the impact, regional paleoclimatic conditions, ambient biodiversity, trophic structure and the local paleoenvironment at the time of the impact have a strong influence on the "kill potential" of an impact event. Size of an impact alone is not a reliable indicator of biotic effects.

Two of our best known and age-constrained craters, The 100km late Triassic Manicouagan crater and the c.170km end Cretaceous Chicxulub crater were both large and potentially lethal environmental traumas. They represent extremes in terms of the impact site variables noted and they were extremes in terms of their biotic effects. Chicxulub has been implicated in an extinction event that depleted species by c. 65%, whilst a convincing extinction effect is yet to be demonstrated with respect to Manicouagan.

The modelling procedures we have employed require further refinement before they can be applied rigorously and predictively. What we have shown is that, by combining the output of existing mathematical models for predicting proximal and distal effects of an impact with a systematic assessment of an impact event factor by factor, an holistic picture of the biotic effects of an impact will emerge. This is, effectively, an early stage in the

development of a systematic risk assessment procedure for ancient impacts.

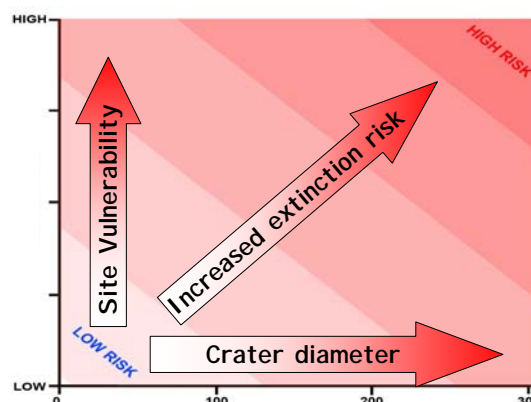


Fig. 5 New "Risk" diagram, with size plotted against environmental and/ or locational factors ("vulnerability").

Our modelling exercise confirms that location and timing of an impact are significant variables with potentially strongly determinant effects on biotic consequences. Size alone is an insufficient measure of the likely biotic effects of a bolide impact event and few extinction specialists would continue to support the simple Kill Curve approach. Ultimately, it reflects only superficial data and cannot be used analytically or predictively. Instead, we are developing a more sophisticated means of diagrammatically expressing "kill potential" in terms of an expression of risk, related both to size and site vulnerability (Fig 5). This, together with an extended analysis of some large impact events will be published elsewhere.

5. REFERENCES

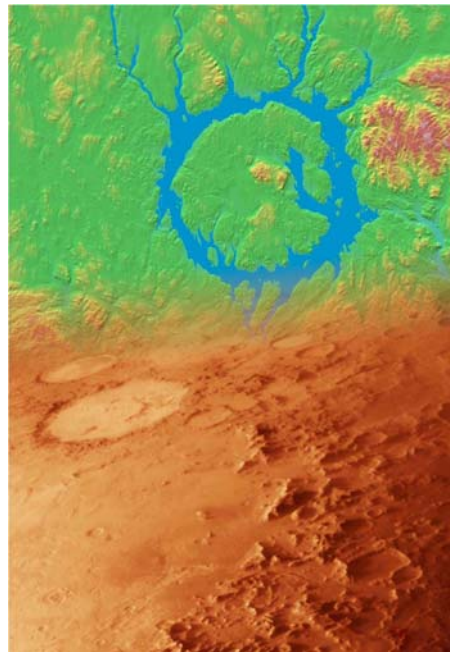
- [1] Raup DM, Large - body impact and extinction in the Phanerozoic: *Paleobiology* 18, 80-88, 1992
- [2] Jansa LF, Cometary impacts into ocean: their recognition and the threshold constraint for biological extinctions. *Palaeogeography, Palaeoclimatology, Palaeoecology*, 104: 271-286, 1993
- [3] Poag CW, Roadblocks on the Kill Curve: testing the Raup Hypothesis: *Palios* 12, 582-590, 1997
- [4] Barnouin-Jha, O.S. and Schultz, P.H., Ejecta entrainment by impact-generated ring vortices: theory and experiments, *Journal of Geophysical Research*. 101, 21099-21115, 1996
- [5] Collins, G.S. and Melosh, H.J. and Marcus, R.A. Earth Impact Effects Program: A Web-based computer program for calculating the regional environmental consequences of a meteoroid impact on Earth, *Meteoritics and Planetary Science*, 40, 6, 817-840, 2005
- [6] Collins, G.S. and Melosh, H.J. and Morgan, J.V., et al, Hydrocode simulations of Chicxulub crater collapse and peak- ring formation, *Icarus*, 157, 24-33, 2002
- [7] Lorenz, R.D., Microtektites on Mars : Texture and Volume of Distal Impact Ejecta Deposits, *Icarus*, 144, 353-366, 2000

- [8] McGetchin, T.R. and Settle, M. and Head, J. W, Radial thickness variation in impact crater ejecta: Implications for lunar basin deposits ,*Earth Planetary Science Letters*, 20, 1973
- [9] Luder, T. and Benz, W. and Stoker, T.F. A model for long-term climatic effects of impacts, *Journal of Geophysical Research*, 108, E7, 5074, 10, 1-16, 2003
- [10] McKinnon, W.B. and Schenk, P.M. and Moore, J.M., Goldilocks and the Three Complex Crater Scaling Laws, Impact Cratering: Bridging the Gap Between Modeling and Observations, LPI Contribution No. 1155. Houston, TX: Lunar and Planetary Institute, p.48 February 7-9, 2003
- [11] Newman, W.L. and Symon, E.M.D. and Ahrens, T.J. and Jones, E.M., Impact erosion of planetary atmospheres: Some surprising results, *Icarus*, 138, 224– 240, 1999
- [12] O’Keefe, J.D. and Stewart, S.T. and Lainhart, M.E. and Ahrens, T.J. Damage and rock-volatile mixture effects on impact crater formation. *International Journal of Impact Engineering* 26: 543-553, 2001
- [13] Stoffler, D. and Gault, D.E. and Wedekind, J. and Polkowski, G., Experimental hypervelocity impact into quartz sand: Distribution and shock metamorphism of ejecta, *Journal of geophysical Research*, 80, 29, 1975
- [14] Turtle, E.P. and Pierazzo, E. and Collins, G.S. et al, Impact structures: what does crater diameter mean?, In: Kenkmann T, Horz F, Deutsch A, editor, Large Meteorite Impacts III, Boulder CO, *Geological Society of America*, 2005, Pages: 1-24,
- [15] Walkden, G.M and Parker, J. and Kelley, S., A Late Triassic Impact Ejecta Layer in Southwestern Britain, *Science*, 298, 2185– 2188. 2002
- [16] Toon, O.B. and Turco, R.P. and Covey, C. Environmental perturbations caused by the impacts of asteroids and comets, *Reviews of Geophysics*, 35, 1, 41-78, February 1997
- [17] Pierazzo E. and Hahmann, A.N. and Sloan L.C., Chicxulub and Climate: Effects of stratospheric injections of impact-produced S-bearing gases, *Astrobiology* 3, 99-118, 2003
- [18] Claeys, P. and Kiessling, W. and Alvarez, W.: Distribution of Chicxulub ejecta at the Cretaceous-Tertiary boundary. *Geological Society of America Special Paper* 356: 55–68. 2002
- [19] Kring, D. A., and D. D. Durda. Trajectories and distribution of material ejected from the Chicxulub impact crater: Implications for postimpact wildfires. *Journal of Geophysical Research* 107:6-1 - 6-22. . 2002.

Session S.14

Impacts and Habitability of Terrestrial Planets

Chair: C. Cockell



THE PROCESSING OF ORGANIC MATTER IN IMPACT CRATERS: IMPLICATIONS FOR THE EXPLORATION FOR LIFE

John Parnell, Paula Lindgren

Department of Geology and Petroleum Geology, University of Aberdeen, Aberdeen AB24 3UE, U.K.

Email: J.Parnell@abdn.ac.uk

ABSTRACT

The study of organic matter in impact craters is important to understanding the relationships between impact events and the origin and preservation of biologically relevant materials on Earth and other planets. Case studies show the effects of moderate heating (maturation), strong heating (melting), and interaction with irradiation on organic matter.

Moderate heating in craters can be assessed using biomarker distribution. Measurements in the 24km diameter Haughton Crater, Canada, show that most organic matter at these moderate-sized impact sites may survive, including biomolecules, fossilized remains, and even extant microbial life. Stronger heating in crater centres should cause melting of carbon. Melt fragments in the Gardnos Crater, Norway, preserve abundant carbon, showing that despite high-temperature processing it may be available for reworking into biologically relevant organic molecules. Irradiation can cause the polymerization of simple organic molecules, causing an increase in complexity and the concentration of carbon, exemplified in the Lockne Crater, Sweden.

1. INTRODUCTION

Numerous impact craters contain organic matter, sometimes abundantly, suggesting that impact events can have a significant role in hydrocarbon generation and concentration [1,2]. The survival of organic matter following hypervelocity impacts is also of high interest because impact craters are viewed as possible sites for the establishment and evolution of primitive life on Earth and other planets such as Mars [3,4,5]. Impact craters have a further role in planetary exploration in providing a potential window through the surface zone of irradiation and oxidation in which most organic molecules may be destroyed [3].

2. ORGANIC MATTER IN IMPACT CRATERS

Carbonaceous matter in impact craters has been identified as particularly deserving of study [6]. A wide range of carbon forms is created at impact sites, including graphite, diamonds, silicon carbide, and

fullerenes [7]. However, this documentation of mineralogical phases places an emphasis on high-temperature/high-pressure refractory forms, which are limited to the very centre of a crater. Over almost all of the crater volume, the response of organic matter is likely to be less extreme. Issues that deserve research include:

- (i) Whether organic matter is entirely carbonized (i.e. all hydrogen lost), or if identifiable organic molecules survive.
- (ii) Whether gradients in thermal alteration can be determined across a crater, and can be interpreted in a quantitative way.
- (iii) Whether other processes pertinent to the impact environment affect the organic matter.

Addressing these issues will help us to predict the degree to which we might seek biosignatures within impact crater systems on Mars.

3. MODERATE HEATING

Moderate heating in craters can be assessed using biomolecules whose distribution is dependent upon thermal maturity. The 24km diameter Haughton Impact Structure, Canada, formed in rocks which contained pre-existing liquid hydrocarbons. Biomarker ratios in the hydrocarbons show a consistent pattern of variation in degree of heating across the structure (Fig. 1). The heating reached a maximum at the crater centre, and is attributed to hydrothermal activity following impact. Kinetic modelling, using absolute temperatures from fluid inclusion data, suggests a time scale of about 5000 years for the heating, at a maximum temperature of 210 °C [8]. The short time scale suggests that in moderate-sized craters, which are abundant on Mars, heating may have been short-lived in terms of organic evolution, but concomitantly did not present such an extensive source of heat that existing organic matter was obliterated. Most organic matter at these moderate-sized impact sites may have survived, including biomolecules, fossilized remains, and even extant microbial life.

Studies of impact melt breccias within the Haughton crater have shown that biomarkers are even preserved within clasts of bedrock suspended within the melt matrix [9]. This is despite a probable original

superheated melt temperature of 2000+ °C and a melt crystallization temperature of 600+ °C [10]. Clasts falling into the melt would have experienced a minimum contact temperature of the crystallization temperature, but although the organic matter within them has been thermally altered from brown to black

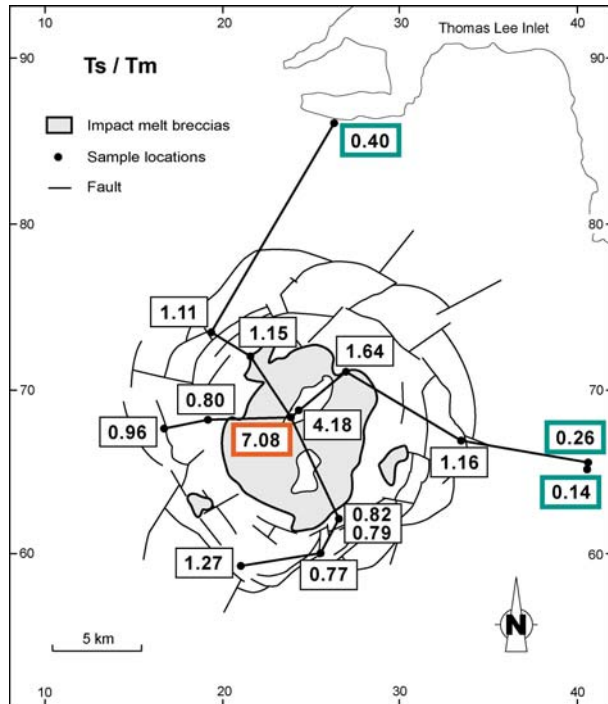


Fig. 1. Variations in biomarker ratio T_s/T_m , which increases with thermal maturity, across Haughton Crater, Canadian Arctic. Maximum maturity recorded at Crater centre, minimum maturity outside crater limits. From [8].



Fig. 2. Clasts of organic-rich target rock, Haughton Crater, Canadian Arctic. Upper row from bedrock coloured brown, reflecting moderate thermal maturity; Lower row from melt breccia coloured black, reflecting severe thermal alteration. Pen scale 15cm.

colour (Fig. 2) because of carbonization, organic molecules can still be extracted. Lower ratios of melt volume to transient crater volume on Mars, consequent of lower gravity, mean that the clast content of Martian impact melts should be greater than on Earth [11], so clasts may be an important target for biosignatures on Mars.

4. STRONG HEATING

Stronger heating in crater centres should cause melting of carbon. Melt fragments in melt breccias from the Gardnos Crater, Norway, contain abundant carbon. The carbon is ultimately derived from an organic-rich shale source, which is almost certainly the Cambrian Alum Shale as no other source has the requisite amount of carbon to explain the amount preserved in the melt fragments. A high proportion of the carbon present in the original melt was preserved, located at the boundary between two immiscible silicate phases in melt fragments (Fig. 3). The silicates represent alteration products from immiscible glasses in the original melt [12]. The stripping of hydrogen from carbon during melting prevents later hydrocarbon formation, hence the carbon is fixed in place rather than volatilized. Underlying lithic breccias that were not melted record hydrocarbon generation as a response to less extreme heating. Despite the high temperature history of the melt, the carbon is highly disordered as determined by Raman spectroscopy, rather than ordered crystalline graphite, and in this respect is comparable with carbon in chondrite chondrules. Hence carbon preserved through impact or other melting processes may be available for reworking into biologically relevant organic molecules.

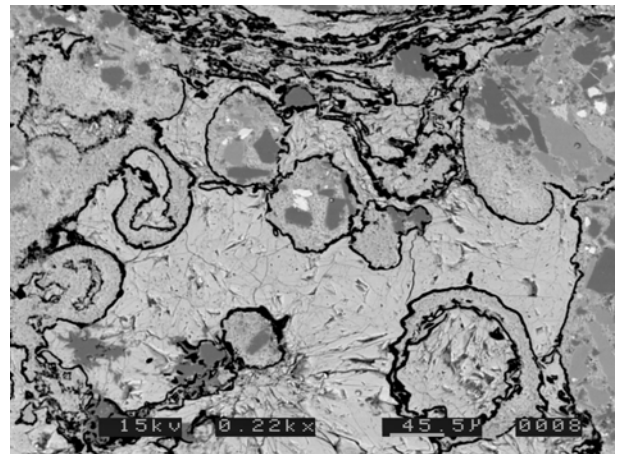


Fig. 3. Backscattered electron micrograph of melt fragment from Gardnos Crater suevite, showing immiscible fabric of two silicate phases separated by carbonaceous film (black). Scale bar 45.5 microns.

The response of hydrocarbon source rocks to flash heating will show a gradation with intensity of heating. With decreasing intensity the response will range through vaporization, melting, carbonization (graphitization), hydrocarbon generation, and lesser degrees of thermal maturation. These effects will be evident in different parts of a crater system. In the Gardnos crater, the products are carbon-rich melt and hydrocarbons. While the melt is generated almost instantaneously by the impact, the generation of hydrocarbons is kinetically-controlled and will occur during post-impact hydrothermal activity.

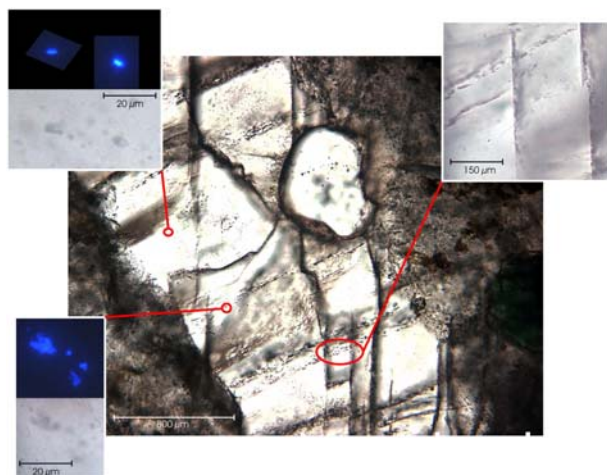


Fig. 4. Fluid inclusions in quartz vein in suevite, Gardnos crater. Fluorescing inclusions are liquid hydrocarbons; non-fluorescing inclusions contain aqueous fluid. (Photo courtesy D. Mark).

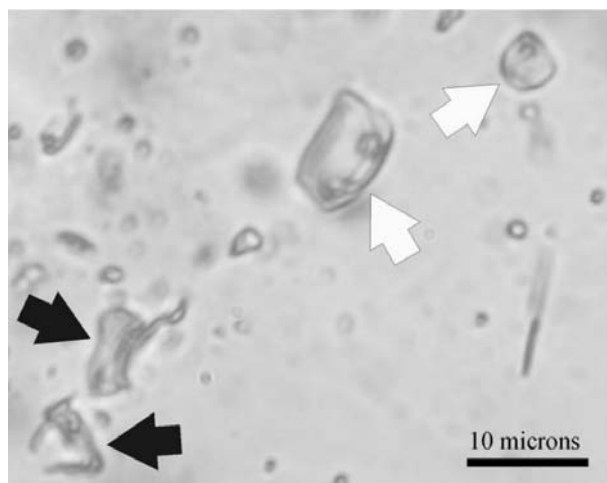


Fig. 5. Fluid inclusions in shocked quartzite, Gardnos Crater. Aqueous inclusions (white arrows) coexist with methane inclusions (black arrows).

In the suevite, cross-cutting quartz veinlets contain fluid inclusions with liquid hydrocarbons (Fig. 4). Beneath

the melt-bearing rocks, shocked quartzite in lithic breccias contains traces of graphite, and methane sealed in fluid inclusions [13] (Fig. 5). They represent products of the hydrocarbon generation under less extreme heating.

5. IRRADIATION

Irradiation can cause the polymerization of simple organic molecules, causing an increase in complexity and the concentration of carbon. This has been suggested as a mechanism that could have occurred on the early Earth, involving irradiation from radioactive minerals [14]. Could this process occur in hydrothermal systems in impact craters, which have been suggested as sites for prebiotic chemistry and primitive evolution? In terrestrial craters, it is difficult to assess if complex organic molecules can be created from abiogenic compounds because abundant biogenic materials are already present, but we can assess if (i) crater environments can support concentration of carbon by radioactive minerals, albeit from biogenic sources, (ii) carbon concentration can occur in both target rock and crater-fill sediments, and (iii) carbon is concentrated where it would otherwise be undetectable.

These ideas were tested in the Lockne Crater, Sweden [15], where organic matter occurs in both impact brecciated granite and in resurge deposits, but is most common in the impact brecciated granite. The organic matter is present as migrated hydrocarbons and carbon-rich shale fragments. Samples were taken at several localities across the crater, including impact-brecciated granite from a drill core, then prepared as polished blocks of ca 1 x 2 cm for investigation by electron microscopy. Petrographic studies show that carbonaceous polymers have precipitated around radioactive minerals in both granitic and impact breccia matrix (Fig. 6). Uranium/thorium-rich carbonaceous nodules were detected in 17 of 20 crater samples investigated (Fig. 7). No nodules were detected outside the crater, where 5 samples of granitic basement and 5 samples of Caledonian fault brecciated granite were examined. The size of the nodules varies between ca 50 to 200 µm. They are usually rounded, lobate and sometimes exhibit crenulated margins, indicative of replacement (Fig.6). The U/Th phase often occurs as small inclusions in the bitumen, which implies digestion of a pre-existing mineral (Fig.6). Sometimes a rim of carbonaceous matter is observed around a U/Th silicate crystal, suggesting that the mineral is indigenous to the granite and was later coated by the carbon. The distribution data suggests that the carbonaceous nodules are associated with an impact-related process. The deposition of the hydrocarbon could be a result of fracture-controlled fluid flow at any time after impact, including hydrothermal fluid circulating in the crater

after impact. The impact event would have increased the fracture permeability in the target rocks. These results show that where radioactive minerals are present in the target rocks for craters, they are a preferred site both for carbon concentration, and for our detection of organic molecules.

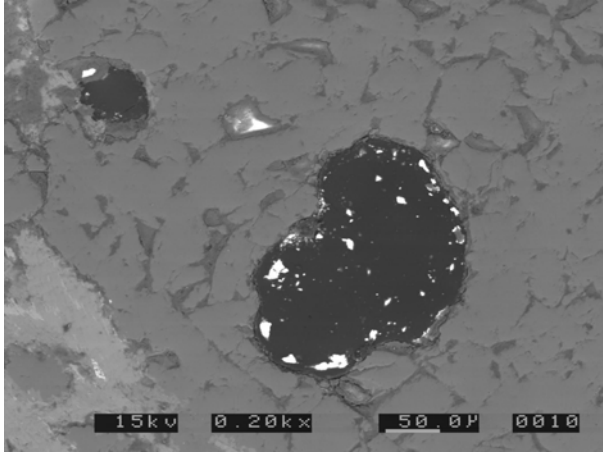


Fig. 6. Carbonaceous nodule (dark) containing uranium mineral inclusions (bright) in granitic quartzose clast, Lockne Crater. Scale bar 50 microns.

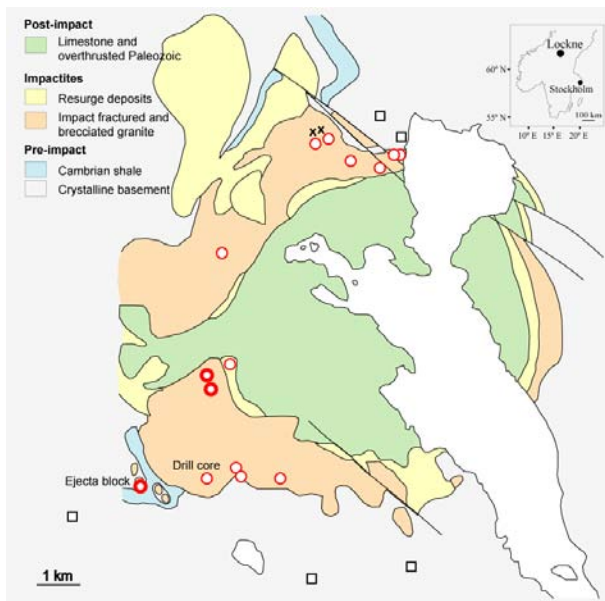


Fig. 7 Map of Lockne impact crater, Sweden, (simplified after [15]) showing the distribution of carbonaceous nodules.

White circles with red rims represent samples from impactites where U/Th- rich carbonaceous nodules have been detected. Nodules were detected in 17 of 20 crater rocks. The circles with a thinner red rim represent samples where 1-4 nodules in each thin section of ca 1x2 cm have been detected. The circles with a thicker

red rim represent samples where 8-12 nodules have been found in a single thin section. From the drill core (see map), 3 of 4 samples investigated contained nodules. Crosses represent the other two samples investigated where nodules were not detected in the crater rocks, and occur in an unusual overturned granite flap. White squares represent samples of granite from outside the crater where no nodules have been detected.

6. PLANETARY EXPLORATION FOR BIOMARKERS

The relationships discussed above have implications for the search for organic molecules during planetary exploration. The survival of biomarkers despite impact heating means that sampling from a crater central uplift, impact ejecta blanket or melt breccia on Mars could allow detection of any fossil biomarkers present in the impact target rocks. In addition, impact-generated hydrothermal systems might well be a focus for any extant life (Fig. 8). An overwhelming advantage of sampling such materials in a relatively young crater is that the impact will have excavated them from beneath the depth at which irradiation/oxidation would have destroyed the majority of organic molecules [3]. Estimates using amino acid stabilities suggest that for surface samples older than 100-500 Ma, this depth of destruction reaches about 2-3m [16]. For younger samples, the accumulated irradiation dose is less and there is a better chance of organic molecules being preserved. Thus in a younger crater, ejecta and other breccias, and the newly exposed central uplift, offer this chance of preservation of fossil biomarkers. Any subsurface life in the same bedrocks, extant at the time of impact, could also leave a biomarker record. As the samples may be excavated from a depth below the liquid water isotherm, this need not be psychrophilic life. Contemporary life could become focussed in hydrothermal systems induced by impact activity. If there is any subsequent extant life, the fractured nature of the bedrock and ejecta, and shocked clasts in melt breccias, provide it with a habitat for colonization (Fig. 8), which has been demonstrated in the Haughton crater [17, 18, 19].

We can estimate an approximate minimum crater size required to sample ejecta from below the alteration depth. For relatively small craters, with a diameter/depth ratio of about 5:1 and ejecta derived mostly from the top third of the crater [20, 21], a crater of 300+m diameter gives a high level of confidence that a single ejecta block derives from below a 2m alteration depth (Fig. 9). In a young crater, this strategy would allow sampling of material that has been protected during burial from surficial alteration, but will not be exposed for long enough after ejection from the crater to be strongly affected. Evidence through thermal inertia

data of hydrated minerals in impact ejecta within Noachian terrain on Mars [22] suggests that this could

be a promising strategy in future exploration for organic remains from early in Mars' history.

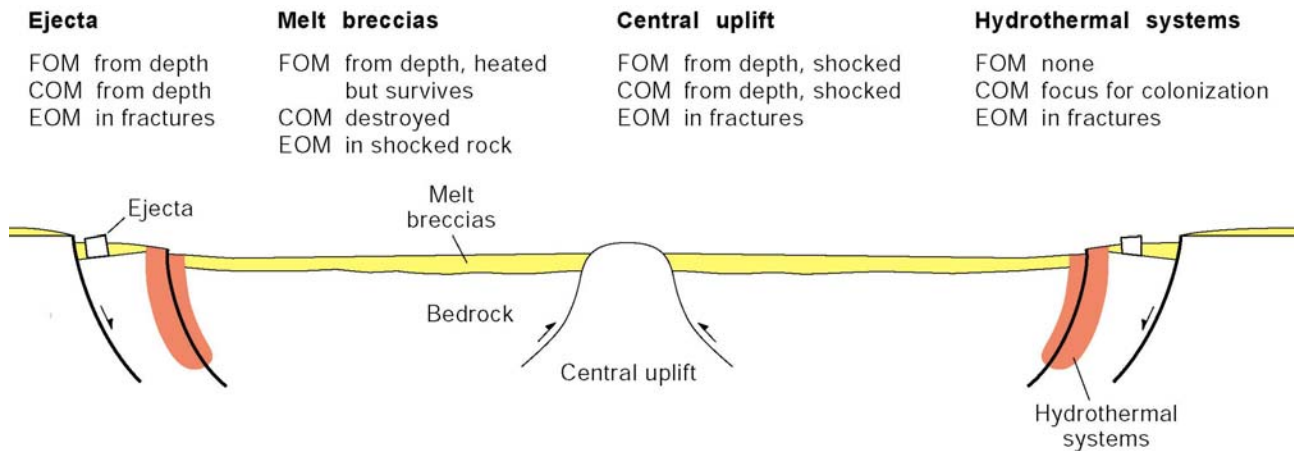


Fig. 8. Schematic cross-section of impact crater, showing four settings for sampling of organic matter (pre-existing fossil organic matter FOM, contemporaneous organic matter COM alive at time of impact, subsequent extant organic matter EOM).

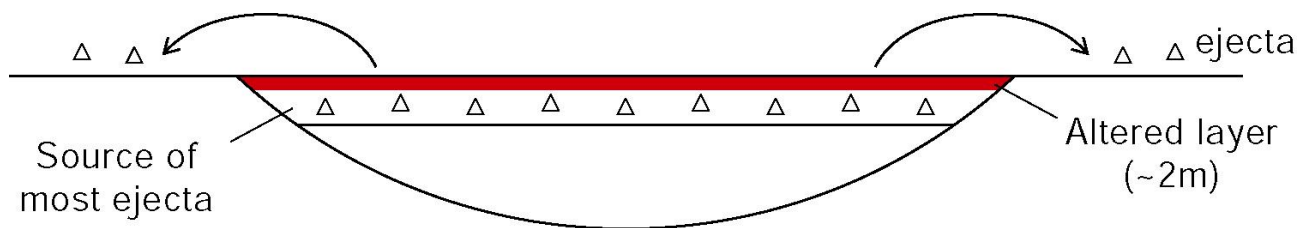


Fig. 9. Schematic cross-section of typical small crater with diameter-depth ratio of 5:1, and excavation of top third to form ejecta [20, 21]. Given a depth of alteration (irradiation, oxidation) of about 2m, the probability of an ejecta sample originating from below the altered layer is high for craters of >300+m diameter.

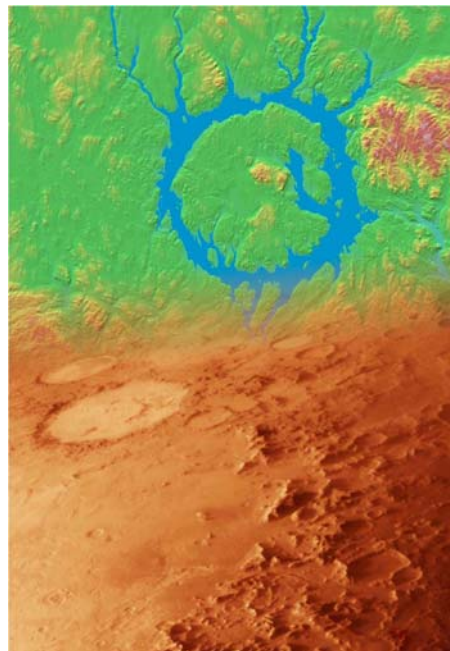
7. REFERENCES

1. Grieve R.A.F. and Masaitis V.L., The economic potential of terrestrial impact craters, *INTERNATIONAL GEOLOGY REVIEW*, Vol. 36, 105-151, 1994.
2. Grieve R.A.F., Terrestrial impact structures: Basic characteristics and economic significance, with emphasis on hydrocarbon production, *OKLAHOMA GEOLOGICAL SURVEY CIRCULAR*, Vol. 100, 3-16, 1997.
3. Newsom H.E., et al. Location and sampling of aqueous and hydrothermal deposits in Martian impact craters, *ASTROBIOLOGY*, Vol. 1, 71-88, 2001.
4. Farmer J.D., Hydrothermal systems: Doorways to early biosphere evolution, *GSA TODAY*, Vol. 10, No. 7, 1-9, 2000.
5. Kring D.A., et al. Impact events and their effect on the origin, evolution and distribution of life, *GSA TODAY*, Vol. 10, No. 8, 1-7, 2000.
6. French B.M., The importance of being cratered: The new role of meteorite impact as a normal geological process, *METEORITICS & PLANETARY SCIENCE*, Vol. 39, 169-197, 2004.
7. Hough R.M., et al. Diamond and silicon-carbide in impact melt rock from the Ries impact crater, *NATURE*, Vol. 378, 41-44, 1995.

8. Parnell J., et al. Thermal alteration of organic matter in an impact crater and the duration of postimpact heating, *GEOLOGY*, Vol. 33, 373-376, 2005.
9. Lindgren P., et al. Preservation of biological signature within impact melt breccias, Haughton Impact Structure, *LUNAR AND PLANETARY SCIENCE*, Vol. XXXVII, abstract 1028, 2006.
10. Osinski, G.R. and Spray, J.G., Impact-generated carbonate melts: evidence from the Haughton structure, Canada, *EARTH AND PLANETARY SCIENCE LETTERS*, Vol. 194, 17-29, 2001.
11. Pope K.O., et al. Impact melt sheet formation on Mars and its implication for hydrothermal systems and exobiology, *ICARUS*, in press, 2006.
12. Lindgren P., et al. Liquid immiscibility in suevite melt, Gardnos impact crater, *LUNAR AND PLANETARY SCIENCE*, Vol. XXXVI, abstract 1629, 2005.
13. Andersen T. and Burke E.A.J., Methane inclusions in shocked quartz from the Gardnos impact breccia, South Norway, *EUROPEAN JOURNAL OF MINERALOGY*, Vol. 8, 927-936, 1996.
14. Parnell J., Mineral radioactivity in sands as a mechanism for fixation of organic carbon on the early Earth, *ORIGINS OF LIFE AND EVOLUTION OF THE BIOSPHERE*, Vol. 34, 533-547, 2004.
15. Lindstrom M., et al. The Lockne Crater: Revision and Reassessment of Structure and Impact Stratigraphy, In Koeberl C. and Henkel H. (eds) *Impact Tectonics*, Springer, Berlin, 357-388, 2005.
16. Kminek G. and Bada J.L., The effect of ionizing radiation on the preservation of amino acids on Mars, *EARTH AND PLANETARY LETTERS*, Vol. XX, in press, 2006.
17. Cockell C.S., et al. Impact-induced microbial endolithic habitats, *METEORITICS & PLANETARY SCIENCE*, Vol. 37, 1287-1298, 2002.
18. Cockell C.S., et al. Effect of asteroid and comet impacts on habitats for lithophytic organisms – A synthesis, *METEORITICS & PLANETARY SCIENCE*, Vol. 40, 1901-1914, 2005.
19. Parnell J., et al. Microbial colonization in impact-generated hydrothermal sulphate deposits, Haughton impact structure, and implications for sulphates on Mars, *INTERNATIONAL JOURNAL OF ASTROBIOLOGY*, Vol. 3, 247-256, 2004.
20. Melosh H.J., *Impact Cratering*, Oxford University Press, New York, 1989.
21. Grier J.A. and Hartmann W.K. Rayed craters as probes of the upper surface of Ma'adim Vallis and Elysium Planitia: Images from Mars Global Surveyor, *LUNAR AND PLANETARY SCIENCE*, Vol. XXXI, abstract 1478, 2000.
22. Costard F., et al. Detection of hydrated minerals on fluidized ejecta lobes from Omega observations; Implications in the history of Mars, *LUNAR AND PLANETARY SCIENCE*, Vol. XXXVII, abstract 1288, 2006.

Poster Session 1

Tuesday, 9 May 2006



40th ESLAB Proceedings
First International Conference on Impact Cratering in the Solar System

COLLISIONS HISTORY IN THE MAIN-BELT BY SPECTROSCOPIC METHODS

Mirel Birlan¹ and Alin Nedelcu²

¹Institut de Mécanique Céleste et de Calculs des Ephémérides 77 av Denfert-Rochereau 75014 Paris cedex, France

²Astronomical Institute of the Romanian Academy, str Cutitul de Argint nr 5, Bucharest 4, Romania

²Institut de Mécanique Céleste et de Calculs des Ephémérides 77 av Denfert-Rochereau 75014 Paris cedex, France.

ABSTRACT

New results concerning binary or multiple asteroids (Marchis et al (2005), Michałowski et al (2004), Margot et al (2002), Behrend et al (2006)) as well as those concerning the young families (Nesvorný & Bottke (2004)) bring forth the history of the main-belt on which mutual collisions play the major role.

Investigating the nature of the surface of fragments by spectroscopic methods is necessary for refining several aspects, namely: mineralogical homogeneity of the whole surface of object, degree of space weathering, homogeneity of the parent body, mineralogy of family members, and the balance between the space weathering and the astrophysical timescale for a given object. The spectroscopic results in the 0.8-2.5 μm spectral range for 809 Lunda and 832 Karin will be presented, and some generalizations will be pointed out.

Key words: asteroids, spectroscopy, mineralogy.

1. INTRODUCTION

The last decade was marked by several discoveries of complexes of bodies among asteroids of the main belt as well as to near-earth ones. The binary or multiple structures of asteroids, hypothesized around 1980 (Zappala et al (1980), Leone et al (1984)), were accessible for observing later thanks to the large aperture telescopes and innovative techniques (adaptive optics, correlated observations photometry/radar, ...).

When the components of a double object have comparable sizes, the generic term of *binary object* is commonly used. Particular geometries of the system will allow observations from the ground where

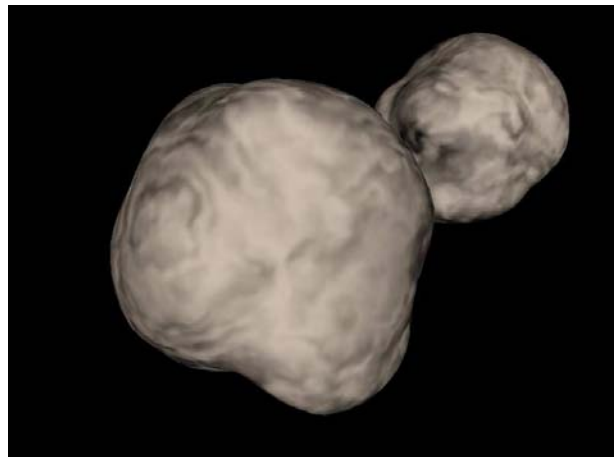


Figure 1. Example of synthetic binary object and the beginning of the mutual event

the components will be mutually occulted. Recording these events by photometric techniques will allow the obtention of the lightcurve, and further, modeling several physical and dynamical parameters such as dimensions, shape, bulk density and dynamical parameters of binary system.

The occultation of a component by its pair in a binary asteroid (Figure 1) represent an important event which allows to investigate its mineralogical structure and to discriminate between the homogeneity/heterogeneity of components, thus tracing a most probable history of the system. The low-resolution spectroscopy in the visible and the near-infrared regions will be involved in this kind of studies. The correspondent lightcurve has particular behaviors, exhibiting several profiles and depths in magnitude decreasing, associated to mutual event.

Spectroscopic techniques might be also used in studying the young families of asteroids in the main-belt. The asteroids are considered a population dy-

namically relaxed, characterized by rare mutual collisions. Recent work (Nesvorný et al (2003); Nesvorný & Bottke (2004); Farley et al (2006)) reveal young families of asteroids resulted from relative recent breakups and re-accretion of fragments of the parent bodies (in the order of tenths of millions of years). Some of them (e.g. Karin, Veritas families) could be related to the solar system dust bands or dust showers. The study of young families allows to refine our knowledge concerning the spreading mechanisms of orbital elements of families members by small, but long term effects such is the Yarkovsky effect (Nesvorný & Bottke (2004)).

Sophisticated numerical codes have been also used also recently (Michel et al (2002, 2004)) in order to study the formation of asteroid families by both fragmentation and gravitational re-accumulation. The post-collision phase reveal a re-accumulation of fragments in aggregates commonly named *rubble piles*, held together by small gravitation field, by little (or zero) tensile strength. This implies a structure of the surface very unstable on the external conditions (planetary perturbations, gravitations instabilities,...). This scenario favours the fresh surface of rubble pile asteroids, less affected by the *space weathering* effects.

Since the discovery of its young family, the asteroid 832 Karin was the subject of a systematic campaigns of observations using both photometric and spectroscopic techniques. Near-IR spectroscopy (Sasaki et al (2004)) revealed spectra with quite distinct trends, corresponding to different surfaces of the asteroid. The authors conclusion is that 832 Karin presents surface variations corresponding to different ages of minerals (i.e. experiencing several degrees of space weathering).

The enlargement of the available observing timescale to do spectroscopy in the solar system has increased the sample of asteroids with well defined spectral characteristics, also widening the asteroid period coverage having spectra taken at different rotation phases. If any difference is to be find, discriminating the real, intrinsic variation from more spurious instrumental induced artifacts (Gaffey et al (2002)) is a necessary step before advancing a surface inhomogeneity explanation

Laboratory studies are also emphasized in order to combine both spectra obtained through astronomical observations with spectra of irradiated minerals, in order to simulate the space weathering. One important aspect of this promising work is the establishment/correlation of the surface status (astrophysical age) with the amount of irradiation experienced by this surface.

The asteroid 809 Lundia was reported as a V type asteroid by Florczak et al (2002) based on the spectroscopic observations in the visible region. As long

as its orbital elements are far enough from Vesta family, the authors suggested 809 Lundia to be a V-type non-member of Vesta family. Carruba et al (2005) have investigated also the possibility of 809 Lundia as a member of Vesta family to whom the orbital elements drifted mainly by non-gravitational effects, and the object being captured by the ζ_2 resonance. Last but not least, photometric observations of this asteroid allow (Kryszczyńska et al (2005)) to conclude that 809 Lundia is a binary system spinning with a period roughly estimated of 15.4 hours.

The main purpose of this article is to present the results of observational campaigns in near-IR of two asteroids: the binary asteroid 809 Lundia and the asteroid 832 Karin. The article describes the observing technique, data reduction procedures, and the main aspects which occur in discrimination between various sources of noise and the intrinsic signal obtained from the asteroid.

Both asteroids may be related to catastrophic disruptions occurred at different moments in the history of the main belt. The variation in mineralogy of these bodies could be evidence of the degree of melting of chemical elements and the degree of segregation experienced by the parent body. Also, the variation in mineralogy can be correlate with the freshness of various parts on the surface of them.

2. OBSERVATIONS

Both objects were observed in the 0.8-2.5 μm spectral region. The observations were carried out using the SpeX instrument mounted on the IRTF, located on Mauna Kea, Hawaii. Remote observing technique was used from CODAM -Paris Observatory (Birlan et al (2004)), 12,000 km away from the telescope. The time lag between Paris and Hawaii allows day light remote observations. A versatile schedule together with the remote observing facilities of IRTF allow short, punctual observations which could not be predicted long time in advance. This is the case of the asteroid 809 Lundia, who was announced as a binary object in October 2005, and for which it is important to have coordinated photometric and spectroscopic observations in order to predict with accuracy the moment of mutual events of the system.

The asteroids 809 Lundia and 832 Karin were observed in circumstances described in Table 1. In the case of 809 Lundia, the observation time was limited for two time intervals of one hour each, during the technical time of the telescope, for two distinct configurations of the binary system. The lightcurves of the asteroid 809 Lundia, obtained just before the run allowed observations to be planned around the time corresponding to one of the minima of the lightcurve and the plateau, respectively.

SpeX was used in Low resolution Prism mode, with a 0.8×15 arcsec slit oriented North-South. Spectra of the asteroids and solar analogs were obtained alternatively on two distinct location on the slit (referred to as A and B beam).

832 Karin was observed as close as possible to the zenith, while 809 Lunda was observed at different airmasses, function of the desired configuration. The solar analogs were chosen as close as possible to the asteroids.

3. RESULTS AND DISCUSSION

Data reduction was carried out by means of standard procedures for near-IR spectral range. The median flat-field for each night was constructed. The A-B pairs of images were subtracted in order to eliminate the sky influence. The result was the addition of these images. The final images were flat-fielded, and collapsed to a two dimensional pixel-flux matrix. Finally, the calibration in wavelength, using the Argon lamp lines was performed.

The same steps were performed for solar analogs. This paper presents the spectral reflectances of the asteroids with respect to the solar analogs, normalized to $1.25 \mu\text{m}$ (value of the maximum in J filter).

As long as accurate results are required, a cautious analysis has to be carried out. We can identify several sources of errors who can hide the intrinsic properties of the asteroid. Several sources of errors could be identified, namely: 1) the atmospheric influence, 2) the spectral variations of solar analog, 3) the intrinsic anomalies in instrument recording.

The atmospheric influence is presented mainly by the amount of water vapours in the atmosphere column, which could exhibit variations between the time interval of the asteroid integration and those of the standard star. Its influence could be minimized by the atmospheric modelling during the procedure of data reduction. Another manifestation of atmospheric influence could be the different extinction coefficient depending upon the azimuthal angle of observations (Gaffey et al (2002)). This error could be minimized if the solar analog is chosen as closely as possible to the asteroid target.

The spectral analog variations in time must also be taken into account as a possible element which could impede the results. Thus, the solution must be the choice of reliable solar analogs, (i.e. stars with the same spectral class, well studied in the near-IR spectral region). These analogs could be observed several times during the night.

By the intrinsic anomalies in instrument recording we define all the functionality of the instrument

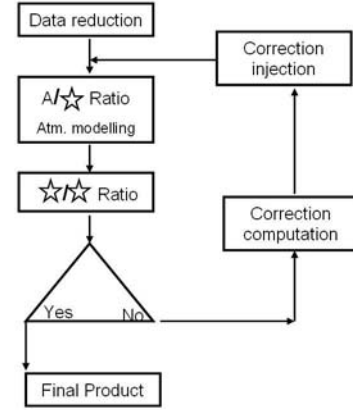


Figure 2. Diagram explaining the data reduction procedure applied for obtaining spectra of the asteroid 832 Karin.

(spectrograph) which may change the signatures of the asteroid final spectrum. In our case, the observations were performed in two consecutive nights. Tests concerning the signal analysis for the standard stars must be done to study possible exchanges in the spectral trend of the standard star spectrum between the nights.

For the high quality spectra of the asteroids, not only the high S/N ratio, but also the error-bars in the flux and their propagation in the final product must be taken into account. Furthermore, these spectra will be the input for particular studies linked to the mineralogy of the surface.

In our case, we experiment several steps, iteratively. The data reduction procedure is synthetized in Figure 2. The diagram provides good results in a few steps.

3.1. 832 Karin

The data reduction process is described in Figure 2. A pipeline Image Reduction and Analysis Facility (IRAF) was used at several stages, the data reduction steps being largely described by Rivkin et al (2004), Rivkin et al (2005), and Binzel et al (2006), which act like a wrapper over the real IRAF set of instructions. Based on some assumptions on the file names, the script groups together the flat fields, calibration, and science images having the advantage that the reduction procedure should be run only once for the entire data gathered in one night of observations. At the first step the pipeline extracts from the entire frame the region containing the spectrum. Then, a bad pixels map and a master flat frame to apply the corrections is computed. Images in A and B positions of the slit are then paired and subtracted

Table 1. Observational circumstances occurred during the observations of 809 Lundia and 832 Karin. Date, exposure time, airmass, seeing and humidity are presented for both asteroids and solar analogs.

Date (UT)	Object	Texp	Itime (s)	Cycles	Airmass	Seeing (")	Humidity (%)
Nov, 4, 2003, 6h 16m	832 Karin	32 min	120	8	1.21	1.0	28
Nov, 4, 2003, 5h 18m	SA 113-276	4 min	40	3	1.06	1.0	28
Nov, 5, 2003, 5h 35m	832 Karin	24 min	120	6	1.17	0.7	23
Nov, 5, 2003, 6h 35m	SA 113-276	128 s	8	8	1.14	0.7	23
Dec, 21, 2005, 7h 16m	809 Lundia	16 min	120	4	1.04	0.6	18
Dec, 21, 2005, 7h 30m	HD 16018	11.0	25.0	12	1.05	0.6	18
Dec, 22, 2005, 9h 26m	809 Lundia	20 min	120	5	1.52	0.56	14
Dec, 22, 2005, 10h 04m	HD 16018	2s	0.5	2	1.53	0.56	14

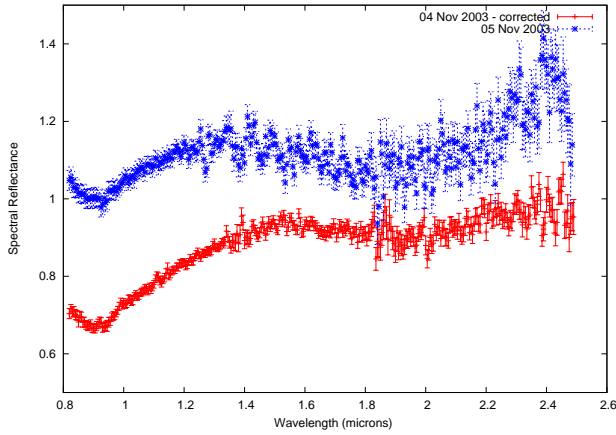


Figure 3. Spectra of 832 Karin obtained in November 4 and November 5, 2003, obtained with respect to the standard star SA 113-276. These spectra are corrected by the star influence in the region 0.8-1.3 and the error-bars are also estimated. The spectra presents similar trends, but they are clearly distinct, outside the error-bars. This may support the hypothesis of surfaces which have been experienced different degrees of space weathering.

to minimize the sky background and the telescope influence. One-dimensional spectra are extracted from the newly obtained images containing both a negative and a positive spectrum, and wavelength calibration using an Argon lamp spectrum is done.

After comparing wavelength scales for A and B beams and computing the average shift between the two, the images are trimmed, so only the positive half of them is retained and scaled to achieve peak data value. User defined groups of asteroids and reference stars taken at similar airmasses are combined, then single one-dimensional spectra are extracted for each of the groups. Applying the wavelength calibration to all groups spectra concludes the first step of the reduction procedure.

The second step of the reduction rely on IDL procedures making use of the ATRAN model (Lord

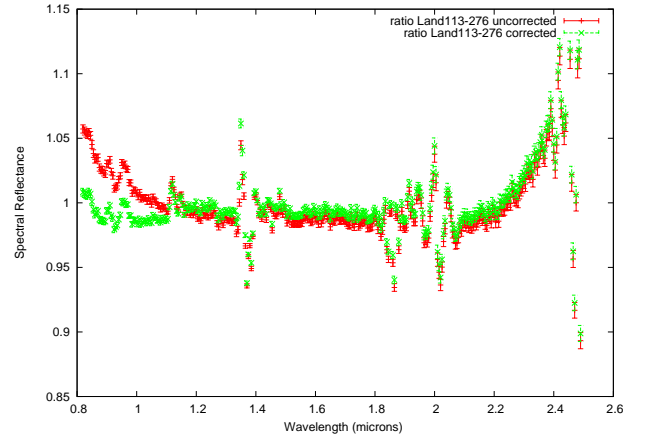


Figure 4. The standard star SA 113-276 spectrum of November 4 was divided by the one of November 5, 2003 (red color). The region 0.8-1.3 μm presents a negative slope which was modeled and corrected (green color) in order to erase this spectral influence in the final spectra of 832 Karin. The error-bars are also represented in the figure

(1992)) to correct for telluric absorption. Final spectra obtained for each group in the previous step are paired with values of zenith angles, each asteroid spectrum being divided by each reference star spectrum to obtain the final normalized reflectance spectrum.

Additionally cross division of the reference stars spectra should be checked for any important slope variation in the normalized reflectance spectrum that could artificially induce spectral variation in asteroid spectra taken in different times. As it can be seen in Figure 3 the comparison between two different series of the solar analog SA 113-276 obtained in two different nights exhibits a non-neutral trend in the wavelength region 0.8-1.3 μm . This affects the mineralogic interpretation of Karins' spectra, the region being the subject of major signature of minerals typically associated with silicates. A correction factor was introduced for this spectral region, then the

data reduction was performed in order to verify the quality of this correction. While the correction has given satisfactory results (i.e. constant values for the ratio of two series for the solar analog) it was injected into the asteroid spectra.

The final results are presented in Figure 4. The correction applied decreases the difference between the spectra, however the spectra remain distinct, the errorbars of reflectances at the same wavelength cannot be superimposed. The global trend of both spectra are similar, with absorption bands around $1\ \mu\text{m}$ and a shallow absorption band around $2\ \mu\text{m}$, which corresponds to silicate minerals. The difference in spectra could be associated to material which have experienced different irradiation (space weathering).

The spectra data of 832 Karin were correlated with its corresponding surface, by taking into account the lightcurve deduced by Yoshida et al (2004). The spectrum obtained in December 4, corresponds to a rotational phase of 0.95, quite close to one of maxima, while the that of December 5 was obtained to a rotational phase of 0.21. The distinct trend in the spectra, corroborated with the information deduced from the composite lightcurve in the hypothesis of a *pole-on* geometry of the asteroid may conclude to a spectral variation of two distinct parts of its surface.

At this stage, the science concerning the asteroid 832 Karin will be oriented toward a precise/qualitative analysis of its mineralogy, by taking into account both the visible and the near-IR spectral intervals. The possibility of heterogeneous regions of the asteroid surface will be also taken into consideration. Finally, the approach with reflection spectra obtained in the laboratory from terrestrial minerals and meteoritic material will be investigated.

3.2. 809 Lundia

The asteroid data reduction was performed using the Spextool package (Cushing et al (2004)). 809 Lundia analysis was performed with respect to the HD 16018 solar analog. The spectra of the asteroid, normalized to $1.25\ \mu\text{m}$ and presented in Figure 5 are the first obtained in peculiar conditions of a spectroscopic study of a binary system in coordination with photometrical observations. The planning of observations was made in order to observe spectroscopically at least a minima of the lightcurve. This occurred in December 22, 2005, at 11h50m UT when one of component was occultated by the other. The blue color spectrum in Figure 5 corresponds to a moment very close to this minimum. As the magnitude 809 Lundia drops with more than an unit, this effect could be observed also in terms of error bars of the spectrum comparing with the one obtained in December 21, 2005 in the conditions of similars integration time and a minor difference in atmospheric extinction.

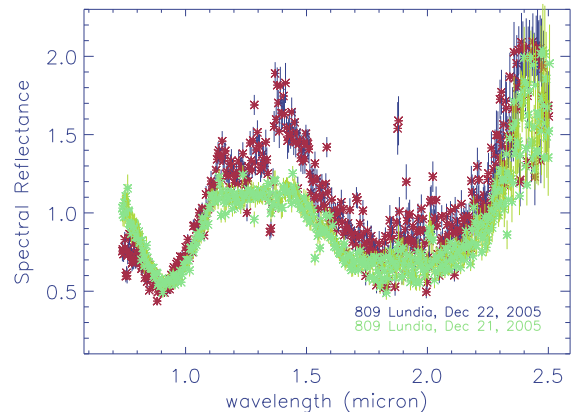


Figure 5. Spectra of 809 Lundia obtained in December 21 and 22, 2005, obtained with respect to the standard star HD 16018. The spectrum of December 22 corresponds to a position in the lightcurve on which one component is occulted by the other one, while the spectrum of December 21 corresponds to the plateau of the lightcurve (contribution of both components).

In December 21, 2005, the spectrum cooresponded almost to the plateau of the lightcurve (i.e. the collected flux is the contribution of both components, in almost equal proportions).

The eye-made preliminary analysis conclude for 809 Lundia a typical V-type spectrum in the near-IR region, with large absorption bands around 1 and $2\ \mu\text{m}$ for both spectra. Our data support the classification proposed by Florczak et al (2002). The visible part of the spectrum, combined with the present one can be easily designed, allowing to obtain the entire absorption band with the minimum one around $1\ \mu\text{m}$.

The differences between spectra are included in the error-bar, which may conclude to a binary system with homogeneous components in terms of mineralogy of theirs surfaces. The dichotomy between spectra are mainly in the region $1.2-1.45\ \mu\text{m}$. As weel as this region contains telluric bands, a deep and carefully analysis will be done (i.e. atmospheric modelling).

In the case of a binary system, in order to have the highest contrast between spectra components, the ideal geometry of observations would be to record two consecutive mutual events (central, if possible) for which the contribution in the flux belongs to each component. Future opportunities for observing such configurations will be analyzed.

4. CONCLUSIONS

The space weathering has been proposed for long time as one of the principal mechanisms who

partially explain the paradox asteroids-meteorites. Near-IR spectroscopy could be used as a tracer of this alteration for some objects of the main-belt, namely objects issued for relatively recent collisions, and complex ones.

In the case of the asteroid 832 Karin, we can conclude a relative difference between spectra which could be explained by regions on the asteroid surface experiencing different degree of maturity.

For the binary object 809 Lundia, the spectra obtained in two distinct geometries exhibit similar features, however more studies are under work in order to confirm a possible/probable homogeneity of this complex.

ACKNOWLEDGMENTS

The work of Alin Nedelcu was supported by the ESA grant RES-H/3006. This article is based on IRTF/Spex observations performed in remote observing mode from CODAM - Paris Observatory.

REFERENCES

- Behrend R., et al 2006, A&A 466, 3, p 1177-1184
- Binzel R.P., Thomas C. et al, 2006, LPSC, abs 1491
- Birlan M., Barucci M.A. et al, 2004, AN 6-8, p. 571-573
- Carruba V., Michtchenko T.A., et al, 2005, A&A 441, 2, p. 819-829
- Cushing M., et al 2004, PASP 116, p. 262
- Farley K.A., Vokrouhlický, D., et al 2006, Nature 439, 7074, p 295-297
- Florczak M., Lazzaro D., et al 2002, Icarus 159, p. 178-182
- Gaffey M., Cloutis Z.A., et al in ASTEROIDS III (Eds W. Bottke, A. Cellino, P. Paolicchi, R.P. Binzel) University of Arizona Press, 2002
- Kryszczyńska A., Kwiatkowski T. et al, 2005, CBET 239.
- Leone G., Paolicchi P., et al 1984, A&A 140, p 265-272
- Lord S.D. 1992, NASA Technical Memor. 103957
- Marchis F., Descamps P., et al 2005, Nature 436, 7052, p. 822-824
- Margot J. L., Nolan M. C., et al 2002, Science 296, 5572, p. 1445-1448
- Michałowski T., Bartczak P. et al 2004, A&A 423, p. 1159-1168
- Michel P., Benz W., et al. 2002, Icarus 160, p. 10-23
- Michel P., Benz W., Richardson D.C. 2004, PSS 52, p. 1109-1117
- Nesvorný D., Bottke W.F., et al 2003, AJ 591, 1, p 486-497
- Nesvorný D., Bottke W.F. 2004, Icarus 170, p 324-342
- Rivkin A., Binzel R.P, et al 2004, Icarus 172, 2, p 408-414
- Rivkin A., Binzel R.P, et al 2005, Icarus 175, 1, p 175-180
- Sasaki T, Sasaki S., et al 2004, AJ 615, 2, L161-L164
- Zappala V., Scaltriti F. et al. 1980, MP 22, p 152-163
- Yoshida F., Dermawan B. et al. 2004, PASJ 56, 6, p. 1105-1113

21 LUTETIA AS A POSSIBLE BINARY SYSTEM AFTER PHOTOMETRIC, FREQUENCY AND SPECTRAL INVESTIGATIONS

V. V. Busarev⁽¹⁾, V. V. Prokof'eva⁽²⁾ and V. V. Bochkov⁽²⁾

⁽¹⁾*Sternberg Astronomical Institute (SAI), Moscow University, Universitetskij pr., 13, Moscow, 119992 Russia, busarev@sai.msu.ru;*

⁽²⁾*Research Institute Crimean Astrophysical Observatory, p/o Nauchnyi, Crimea, 334413 Ukraine, prok@crao.crimea.ua*

ABSTRACT

We have analyzed spectra (0.4-0.9 μm) of 21 Lutetia, a target of the ROSETTA space mission, and discovered periodic splitting of them on three nights (4/5, 5/6 and 7/8) in November 2004. The effect was confirmed by us on 3/4 March 2006 at a twice aspect angle. We suggested that the asteroid is a close binary system. Extraction of its component reflectance spectra showed considerable variations in their shapes corresponding to C-S-type bodies. It may point to changes in matter content from carbonaceous-chondritic to silicate-metallic materials. This contradicts classification of Lutetia as an M-type asteroid.

The frequency and colorimetric analysis of Lutetia's *BVR*-data obtained in August-November 2000 and November 2004 led us also to conclusions that 21 Lutetia is a close binary system consisting of a pair of similar in size bodies orbiting with the period of $\sim 17^{\text{h}}$ around a common center of masses. Also, the components probably are in rotation with periods of ~ 3 -4 hours. From the conception it follows that previously determined period of Lutetia's rotation ($8^{\text{h}}172$) may be actually a half of the supposed period of revolution of its components.

1. SPECTROPHOTOMETRIC AND PHOTOMETRIC DATA

Spectrophotometric (0.37 - 0.74 μm) and photometric (*B*, *V*, *R*) observations of 21 Lutetia were carried out in the Crimean Astrophysical Observatory with a 0.5-m meniscus telescope MTM-500 by Bochkov. The system included a digital television facility equipped with an LI804 superisocon television camera tube with an electron-optical preamplifier stage. The analog signal was digitized and summarized on a personal computer. Usually, the information from several hundreds of television pictures was summarized.

A slitless spectrograph with two exchangeable transparent gratings which provided a resolution capability of 40 or 30 \AA was used for the spectrophotometric observations [1]. The observations

were continued for 14 nights from August 31 to November 20, 2000. For the whole observation period it was obtained 186 original spectra of 21 Lutetia. Its phase angle changed from 2.7° to 23° ; the magnitude in the *V*-band, from $9^{\text{m}}.27$ to 11.02 ; and the aspect angle, from 62° to 68° . A solar analog star, HD10307 [2], was also observed for calculation of the approximate asteroid reflectance spectra. The extra-atmospheric synthetic magnitudes *B*, *V* and *R* of the asteroid were calculated from the averaged spectra taken out of the atmosphere. The resulting values were recalculated for a unit distance from the Sun and the Earth to the asteroid and for zero phase angle.

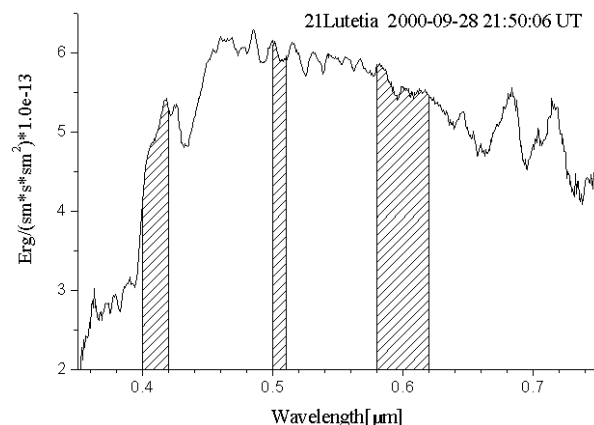


Fig. 1. Positions of three artificial photometric bands in the out-atmosphere spectrum of Lutetia obtained on 28 September 2000 in $21^{\text{h}} 50^{\text{m}} 06^{\text{s}}$ UT.

To estimate variations in intensity of an absorption band centered at 0.43 μm in the asteroid reflectance spectrum [3-4] characteristic of hydrated silicates [5] we calculated the equivalent width of the absorption band [6] according to the formula (1):

$$W = \sum_{i=1}^N (1 - r(\lambda_i)) \Delta \lambda, \quad (1)$$

where W is the equivalent width, $\Delta \lambda$ is the spectral step, $r(\lambda_i)$ are the residual intensities in the spectrum, and N is the number of points in the band. Additionally, to describe an overall shape of Lutetia's

blue-visible reflectance spectrum with asteroid rotation we selected artificial bands 0.40-42 μm (1), 0.50-51 μm (2) and 0.58-0.62 μm (3) (Fig. 1) and calculated the synthetic color indexes as Δm_{1-2} , and Δm_{1-3} .

Photometric observations of Lutetia in November 2004 were performed with the same telescope and television facility, but a technique of simultaneous registration of light fluxes in *B*-, *V*- and *R*-bands was used. About 1000 measurements of the asteroid brightness in the bands were made on 3-11 November 2004. For the period, the phase angle of Lutetia changed from 1.6° to 4.9°; and the aspect angle, from 42.85° to 43.18°. The data were taken out of the atmosphere and reduced to a unit distance from the Sun and the Earth to the asteroid and to zero phase angle.

2. FREQUENCY ANALYSIS

Numerous photometric observations showed previously irregular variations in Lutetia's brightness with amplitudes ranging from 0.^m1 to 0.^m25 [7-11].

To elucidate a nature of Lutetia's brightness changes with rotation we analyzed the synthetic (after observations of August-November 2000) and usual (after observations of November 2004) values of *V* and color indexes *B*–*V* and *V*–*R* by four methods of frequency analysis (the Breger, Lafler–Kinman, Jurkewich, and Deeming ones) [12]. From the first set of data the frequency analysis of the synthetic values *V*(1, 0) (52 measurements) confirmed a known rotational period of Lutetia 0.^d3405 (8.^h172) [11] and showed a two-humped light curve with a maximal amplitude of 0.^m25. However, the synthetic color indexes *B*–*V* (51 measurements) and *V*–*R* (50 measurements) revealed no noticeable variations with the period [6].

A more precise frequency analysis of a considerably larger second set of *BVR*-data of 2004 year confirmed also absence of the known rotational period of Lutetia in the *B*–*V* and *V*–*R* color indexes. Averaging the data over five measurements provided accuracies $\pm 0.^m008$ in the values of asteroid brightness and $\pm 0.^m005$ in the values of the asteroid color indexes. At the same time, it was found presence of other periods in the *V*-data at a high confidence level of 7-10 σ (the accuracy of the estimated value is taken as 1 σ). Whitening the most pronounced frequencies in the row of *V*-data allowed to refine periods corresponding to the frequencies as $P_1 = 0.^d70 (16.^h8) \pm 0.^d01$ and $P_2 = 3.^d25 \pm 0.^d05$. Both periods yielded a two-hump convolutions with *V*-data at amplitudes 0.^m10 (P_1) and 0.^m12 (P_2). Similar curves were obtained with the periods for *B*–*V* and *V*–*R* color indexes (Figs 2 and 3).

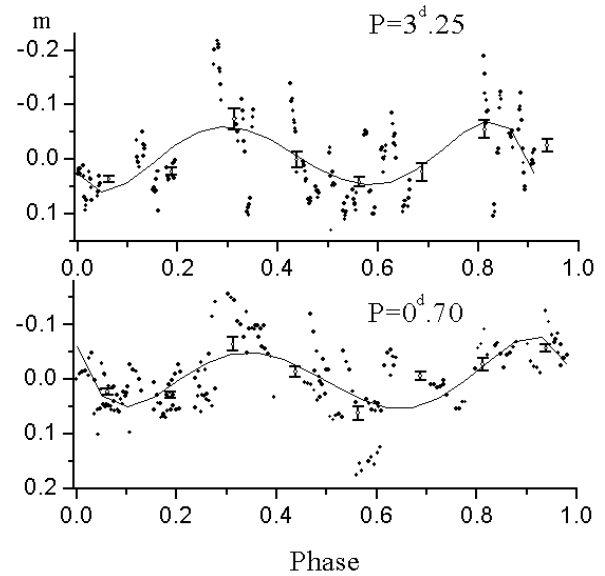


Fig. 2. Light-curves (convolutions) of Lutetia's *V*-values drawn with obtained periods 3.^d25 (the top curve) and 0.^d70 (the bottom curve). Zero-phase is JD2453313^d.4232. Points with vertical bars indicate the average brightness in centers of eight phase regions and their accuracy (the curve is a polynomial of 5th degree).

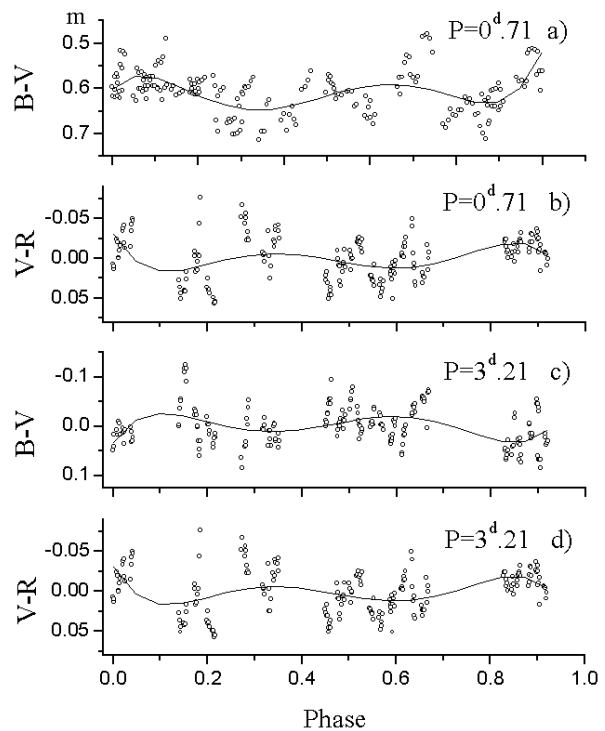


Fig. 3 (a, b, c, d). Phase diagrams (convolutions) of color indexes *B*–*V* and *V*–*R* drawn with periods found in the process of whitening. Values of the periods are shown in the pictures.

The *B*–*V* color indexes of 21 Lutetia (of 2004 year) were also analyzed in the high-frequency range. Two

conjugated periods 8.17 c/d ($2^{\text{h}}.94$) and 9.17 c/d ($2^{\text{h}}.62$) were found. A $2^{\text{h}}.94$ -period convolution of the $B-V$ color indexes is shown in Fig. 4. It has one maximum, and its amplitude is $0^{\text{m}}.05$. Whitening low frequencies in the data led to ratio of its amplitude to its accuracy equal about 7. This indicates a high confidence level of the period existence.

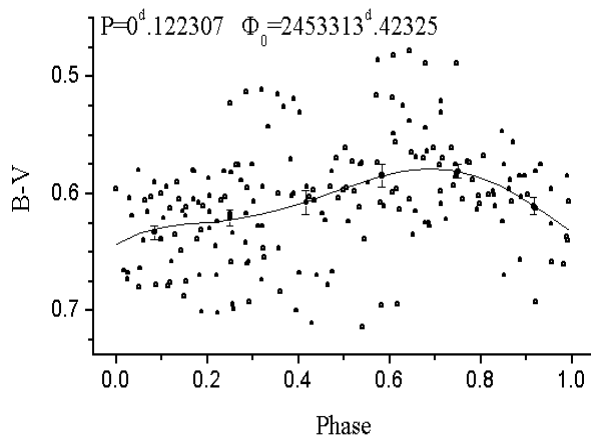


Fig. 4. Phase diagrams (convolutions) of color indexes $B-V$ drawn with period $P=0^{\text{d}}.12231$ ($2^{\text{h}}.94$). Zero-phase is $\text{JD}2453313^{\text{d}}.42325$. The approximate curve is a polynomial of 5th degree.

It is interesting that frequencies greater of 5.5 c/d were not found in analyzed $V-R$ color indexes. After three times of whitening in the low frequency range, only a $0^{\text{m}}.02$ -amplitude period of $1^{\text{h}}.8$ was found at a low confidence level.

Additionally, we performed the frequency analysis of 40 measurements of the equivalent width of a $0.43\text{-}\mu\text{m}$ absorption band of hydrated silicates in the first set of spectrophotometric data (of 2000 year). It was found eight significant periodic oscillations with frequencies from 6 to 31 c/d. The most pronounced frequencies turned out to be in the range from 11 to 14 c/d [6] and may characterize distribution of phyllosilicate spots on the asteroid surface.

The frequency analysis of the synthetic color indexes Δm_{1-3} and Δm_{1-2} calculated also on the first set of data of 2000 year gave periods $P_{1-3}=0^{\text{d}}.718$ and $P_{1-2}=0^{\text{d}}.717$ corresponding to the most pronounced variations. The periods are close to each other and to $0^{\text{d}}.70$ -period found from the frequency analysis of BVR -data. Whitening frequencies corresponding to the periods from the Δm_{1-2} - and Δm_{1-3} -data allowed to refine oscillations with a shorter period of $0^{\text{d}}.1238$ ($2^{\text{h}}.97$) in the both series of the synthetic color indexes. (Fig. 5). Convolutions of the synthetic color indexes Δm_{1-3} with periods of $0^{\text{d}}.718$ and $0^{\text{d}}.12375$ are presented in Fig. 5. Similar convolutions of the synthetic color indexes Δm_{1-2} with periods of $0^{\text{d}}.717$ and $0^{\text{d}}.124$ were obtained.

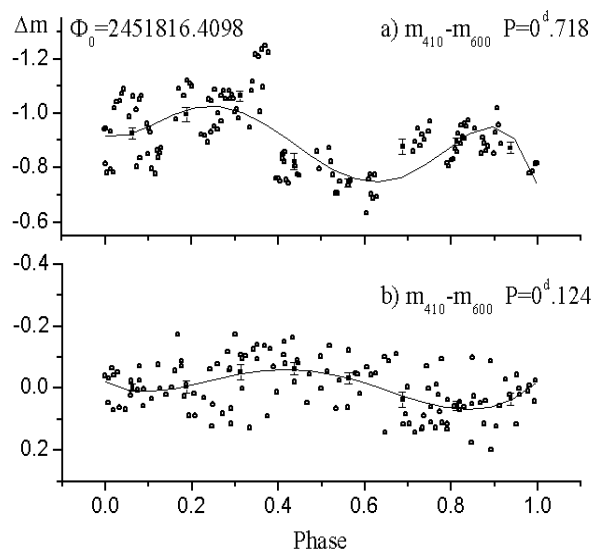


Fig. 5 (a, b). Convolutions of the synthetic color indexes $\Delta m_{1-3} = m_{410} - m_{600}$ with periods of $0^{\text{d}}.718$ (a) and $0^{\text{d}}.12375$ (b) obtained in the process of whitening of the data.

At the same time, the frequency analysis of Δm_{1-2} and Δm_{1-3} synthetic color indexes not confirmed a period equal $3^{\text{d}}.20$ found in the BVR -data.

SPECTRAL DATA

Spectral observations of 21 Lutetia were performed by Busarev on 31 August 2000 and 4-8 November 2004 with a spectrograph and ST-6 SBIG CCD mounted on the 1.25-m telescope of the SAI Crimean observatory. The data were reduced in a standard way. “Blue-visible” ($0.40\text{-}0.68\text{ }\mu\text{m}$) and “visible-red” ($0.63\text{-}0.90\text{ }\mu\text{m}$) parts of the spectra were observed separately at no more than a ten-minute interval. Relative statistical errors of the spectra do not exceed 1-2% within the $0.45\text{-}0.80\text{ }\mu\text{m}$ wavelength range and grow up to 8% and 3% at “blue” and “red” ends. A solar analog star, 16 Cyg B [13], was also observed for calculation of the approximate asteroid reflectance spectra. The original reflectance spectra with the spectral dispersion of about $8\text{ }\text{\AA}/\text{pix}$ were smoothed with a 5-point running box average and normalized to unity at $0.55\text{ }\mu\text{m}$. The weather conditions in November 2004 were not perfect but better on 5/6 November. The spectra obtained on 5/6 and 7/8 November at favorably small aspect ($\sim 43^\circ$) and phase ($\sim 3^\circ$) angles of the asteroid are shown in Figs. 6-10.

The observations of Lutetia on 4-8 November 2004 became a sensation. It was discovered a subtle splitting of the asteroid spectra into two at about 1-2-hour interval. The effect was registered on three nights in November 2004 (4/5, 5/6 and 7/8) and confirmed on 4/5 March 2006 at a considerably bigger aspect angle

($\sim 83^\circ$) in a longer interval of time. This means that images of two close objects instead of one were observed at the moments on the spectrograph slit. We suppose that no other instrumental, atmospheric or celestial factors could cause the periodic splitting of Lutetia's spectrum. We have made an assumption that the asteroid is a close binary system probably consisting of about similar in size components.

Examples of the most clear splitting of Lutetia's spectra on 5/6 and 7/8 November 2004 in the 0.40-0.68 μm and 0.63-0.90 μm regions and the line profiles of the spectra at several wavelengths are shown in Fig. 6.

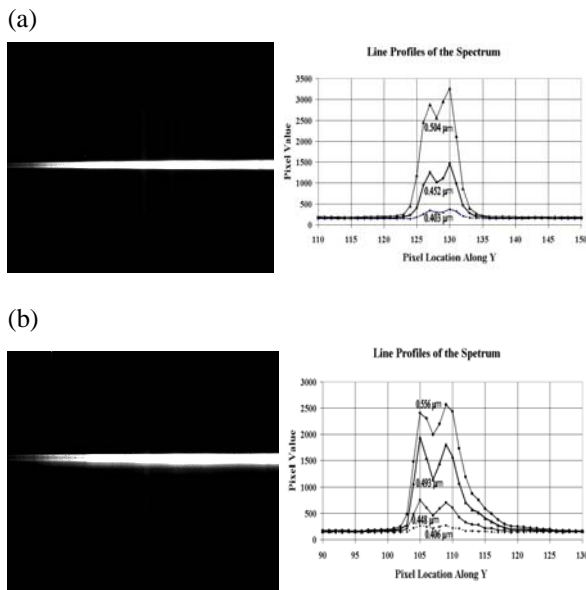


Fig. 6 (a, b). Examples of splitting of Lutetia's spectra obtained on 5/6 November 2004 and 7/8 November 2004: (a) the blue-visible spectrum of Lutetia obtained on 5/6 November 2004 (01:05:33 UT) and its line profiles along Y axis at 0.403, 0.452 and 0.504 μm ; (b) the blue-visible spectrum of Lutetia obtained on 7/8 November 2004 (22:40:36 UT) and its line profiles along Y axis at 0.406, 0.448, 0.493 and 0.556 μm .

From seeing conditions on the nights (~ 2 -3 arc seconds and, hence, the same width of a single spectrum) we estimated splitting of Lutetia's spectra as $< 1''$. From the line profiles (Fig. 6), the level of splitting is relatively far from the background and may correspond to a 3-4 times lesser arc distance between the asteroid components than the width of a single spectrum.

Table 1. Time (UT) of spectral observations (Figs 7-10).

N of spectrum	Date	Time (UT, hms)
21	5 November 2004	01 00 00
21-1	5 November 2004	01 05 33
21-2	5 November 2004	01 05 33
21-1-1	5 November 2004	01 05 33
21-1-2	5 November 2004	01 12 30
21-2-1	5 November 2004	01 05 33
21-2-2	5 November 2004	01 12 30
21-1-1	7 November 2004	22 21 38
21-1-2	7 November 2004	22 27 56
21-1-3	7 November 2004	22 34 36
21-1-4	7 November 2004	22 40 36
21-2-1	7 November 2004	22 21 38
21-2-2	7 November 2004	22 27 56
21-2-3	7 November 2004	22 34 36
21-2-4	7 November 2004	22 40 36

Note: The time corresponds to the middle of each exposition (300s).

We have preliminary designated a slightly brighter (and possibly bigger) component as 21-1 and a fainter (and possibly smaller) one as 21-2. From the forked spectra of Lutetia (Table 1) we extracted spectra of both components and calculated the reflectance spectra presented in Figs 7-10. As seen from the figs, shape of the reflectance spectra is changing quickly with time (and with rotation of the components) and is similar to bodies of C- or S-types at different moments. Interestingly, when the spectral splitting was not observed, Lutetia's integral reflectance spectrum was similar to that of an M-asteroid (curve 21, Fig. 7).

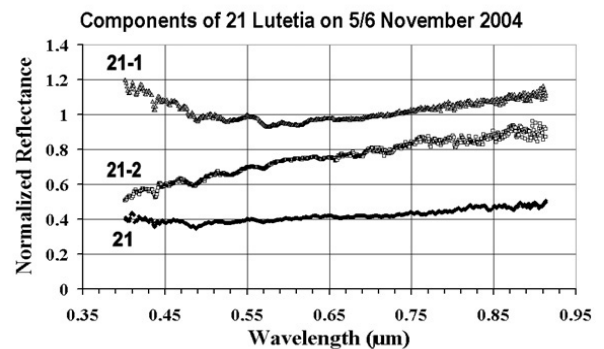


Fig. 7. Reflectance spectra of components of 21 Lutetia (21-1 – a brighter (bigger?) one; 21-2 – a fainter (smaller?) one on 5/6 November 2004. The spectra are normalized to unity at 0.55 μm and shifted on the vertical axis for clarity. Curve 21 is an integral reflectance spectrum of Lutetia when the splitting was not observed.

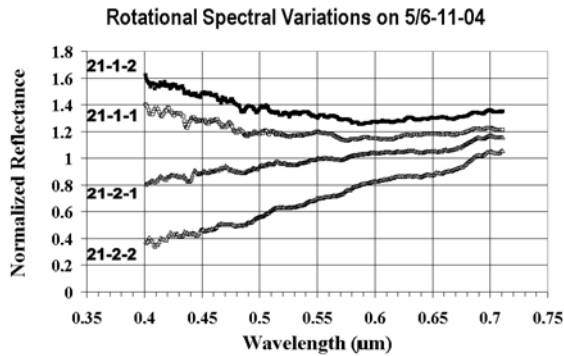


Fig. 8. Reflectance spectra of the components of 21 Lutetia in the blue-visible region obtained at the 10-minute intervals on 5/6 November 2004 (21-1-1 and 21-1-2 – a brighter (bigger?) one; 21-2-1 and 21-2-2 – a fainter (smaller?) one).

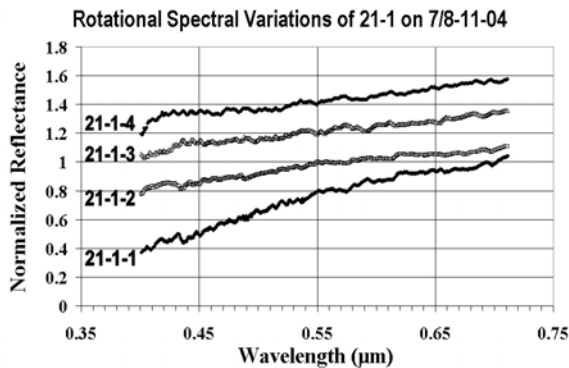


Fig. 9. Consecutive reflectance spectra of a brighter (bigger?) component of 21 Lutetia in the blue-visible region obtained at the 10-minute intervals on 7/8 November 2004.

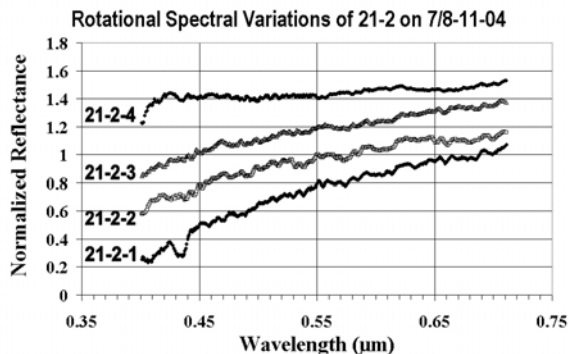


Fig. 10. Consecutive reflectance spectra of a fainter (smaller?) component of 21 Lutetia in the blue-visible region obtained at the 10-minute intervals on 7/8 November 2004.

3. DISCUSSION AND CONCLUSIONS

We have paid a special attention to 21 Lutetia for unusual photometric and spectral properties. For the present, it is considered as an M-type asteroid

according to well-known taxonomic classifications [14]. Relying on relatively high albedo (0.22) [15] and a shape of integral spectrum of the asteroid, we have concluded previously [4] about its M-type. From our data obtained in 2000, the synthetic $B-V$ color indexes range from $0.^m63$ to $0.^m80$; their mean value of $0.^m715$ is rather close to the value $0.^m73$, typical of the M asteroid spectral type. At the same time, the synthetic $V-R$ color indexes range from $0.^m02$ to $0.^m27$ with a mean value of $0.^m17$, while a value calculated from an average M-type asteroid spectrum [14] is $0.^m23$. This more low value agrees with our finds in Lutetia's reflectance spectra absorption bands characteristic of hydrated silicates of a serpentine-chlorite-type [4]. Frequency analysis allowed us to establish uneven distribution of the silicates on the asteroid surface. We estimated a typical size of hydrosilicate spots on the asteroid surface as 30–40 km (taking into account a known 96–100-km size of the asteroid [15]).

Binarity of 21 Lutetia was first suggested on the basis of the frequency analysis of its BVR -data of November 2004 [16]. According to the analysis, the most pronounced periods of variations in the V -, $B-V$ - and $V-R$ -values are $0.^d70$ ($16.^h8$) and $3.^d20$. We consider the first one as an orbital period of the asteroid components around the common center of masses whereas the second as a period of precession of the system. From these suppositions we came to a conclusion that the previously known period of $0.^d3405$ ($8.^h172$) was taken by mistake for a rotational period of Lutetia, and it is actually a half of the found orbital period of the asteroid components $0.^d70$ ($16.^h8$). As mentioned before, the $8.^h172$ -period is not confirmed by our $B-V$ and $V-R$ color data. If we take into consideration the conception, a periodic 1-2-hour splitting of Lutetia's reflectance spectrum could be explained as a result of synchronous rotation of irregular in shape asteroid components with a period of 3-4 hours. This may happen when the line connecting centers of the bodies is perpendicular to the line of sight. Probably, the interpretation is confirmed by the found $0.^d1238$ ($2.^h97$) period of oscillations in the synthetic color indexes $\Delta m_{1,2}$ and $\Delta m_{1,3}$ characterizing changes in the asteroid reflectance spectrum and by a close $0.^d1223$ ($2.^h94$) period in the $B-V$ color indexes. The discovered $<1''$ splitting of the asteroid spectra may correspond to <1000 -km distance between its components (at semi-major axis $a = 2,4369$ AU of Lutetia's orbit). However, we understand that the estimated distance was restricted by our seeing conditions. Actually, the distance may be several times lesser.

Further, from the obtained reflectance spectra of Lutetia's components (Figs. 7-10) we found that their shape changes quickly with rotation of the bodies and

is similar to those of C-S type asteroids at different moments. It is possible that the components are conglomerates of materials with very different content (from hydrated silicates, the main component of carbonaceous chondrites, to igneous silicates and/or metals [17]).

In the framework of the current paradigm about nature of M- and S-type asteroids (e. g., [18]), 21 Lutetia may be a nucleus (or an internal part) of a differentiated parent body disrupted under strong collisions with other objects. For instance, those might have been bodies with a more primitive content ejected by Jupiter from its growth zone [19]. Such scenario could explain the co-existence of non-uniform materials in Lutetia's system. A non-monolithic internal structure of the asteroid also follows from the possible asteroid shock origin. In case of strong subsequent collision(s) the asteroid could have experienced fragmentation and separation into two or more parts presently observed.

Thus, we suggest that 21 Lutetia is a close binary system. Taking into account a similar intensity of its components' spectra (Fig. 6), the bodies may have approximately equal size (probably, ~60-70-km diameter basing on the radiometric diameter 96-100 km of the asteroid of [15]) and orbit around a common center of masses with a period of $\sim 17^h$. At the same time, the components are probably seen always in a visual contact under observations from the earth. For the reason, we could not observe more considerable changes in the integral brightness of the system than $0.^m25$, even in the case of mutual eclipses of the components. Probably, a periodic splitting Lutetia's reflectance spectrum points to the fact of physical separation of the components and their irregular shape changing the extent of the visual contact with their rotation. From our frequency analysis, the both components probably are in rotation with periods of ~3-4 hours. On the whole, the system may have a precession with the period of $\sim 3^d$.

We would recommend to investigate thoroughly Lutetia's system for instance with the Hubble Space Telescope since there is a possibility of existence in the system of smaller bodies having sizes lower of resolution of the earth-based telescopes. The smaller bodies may be hazardous to the ROSETTA spacecraft at the moment of its close approach to the asteroid in 2010 year.

4. REFERENCES

[1] Bochkov V.V., et al., Spectrophotometric observations of M-, S- and E- asteroids in the Sternberg Astronomical Institute and the Crimean

Astrophysical Observatory, *ASTRON. ASTROPHYS. TRANS.*, Vol. 22, 621–624, 2003. [2] Busarev V.V., Spectrophotometry of atmosphereless celestial bodies of the solar system, *SOLAR SYS. RES.*, Vol. 33, 120–129, 1999. [3] Busarev V. V., Oxidized and hydrated silicates on M- and S- asteroids: spectral indications, *Lunar Planet. Sci. Conf. XXXII*, abstr. #1927, 2001. [4] Busarev V. V., et al., Characterizing 21 Lutetia with its reflectance spectra, in *The new ROSETTA targets* /L. Colangeli et al., eds., Kluwer Acad. Publishers, 79–83, 2004. [5] Busarev V. V., et al., Possible spectral signs of serpentines and chlorites in reflectance spectra of celestial solid bodies, *Vernadsky Inst. - Brown Univ. Microsimp. 40th.*, Moscow, abstr. #15, 2004. [6] Prokof'eva V. V., et al., The surface structure of the M-type asteroid 21 Lutetia: Spectral and frequency analysis, *SOLAR SYS. RES.*, Vol. 39, 410–420, 2005. [7] Lupishko D.F. and Velichko F.P., The direction of rotation of asteroids 21, 63, 216, and 349, *KINEMATIKA FIZ. NEBESNYKH TEL*, Vol. 3, No. 1, 57–65, 1987. [8] Lupishko D.F., et al., The pole coordinates and the phase dependence of brightness for asteroid 21 Lutetia, *KINEMATIKA FIZ. NEBESNYKH TEL*, Vol. 3, No. 5, 36–38, 1987. [9] Dotto E., et al., M-type asteroids: Rotational properties of 16 objects, *ASTRON. ASTROPHYS. SUPPL. SER.*, Vol. 95, 195–211, 1992. [10] Michalowski T., Poles, shapes, senses of rotation, and sidereal periods of asteroids, *ICARUS*, Vol. 106, 563–572, 1993. [11] Michalowski T., Pole and shape determination for 12 asteroids, *ICARUS*, Vol. 123, 456–462, 1996. [12] Prokof'eva, V.V., et al., Satellites of asteroids, *PHYS.-USP.*, Vol. 38, 623–649, 1995. [13] Hardorp J., The Sun among the Stars, *ASTRON. & ASTROPH.*, Vol. 91, 221–232, 1980. [14] Tolen D. J. and Barucci M. A., Asteroid taxonomy, in *Asteroids II* /R. P. Binzel et al., eds, Univ. of Arizona Press, Tucson, 298–315, 1989. [15] Tedesco E. F., et al., Three parameter asteroid taxonomy classification, in *Asteroids II* /R. P. Binzel et al., eds, Univ. of Arizona Press, Tucson, 1151–1161, 1989. [16] Prokof'eva V. V., et al., About possible binarity of asteroid 21 Lutetia by analysis of the simultaneous observations in the BVR-bands, *SOLAR SYS. RES.*, Vol. 40, 2006, in press. [17] Gaffey M. J., et al., Reflectance spectroscopy and asteroid surface mineralogy, in *Asteroids II* /R. P. Binzel et al., eds, Tucson: Univ. of Arizona Press, 98–127, 1989. [18] Bell J.F., et al., Asteroids: The big picture, in *Asteroids II* /R. P. Binzel, et al., eds, Tucson, Univ. of Arizona Press, 921–945, 1989. [19] Busarev V. V., Hydrated silicates on M-, S-, and E-type asteroids as possible traces of collisions with bodies from the Jupiter growth zone, *SOLAR SYS. RES.*, Vol. 36, 39–47, 2002.

PREPARATION DEVELOPMENT AND PRELIMINARY APPLICATION OF NOVEL EQUATIONS OF STATE FOR GEOLOGICAL MATERIALS AND ICE

Principal Author P Church⁽¹⁾, D Porter⁽²⁾, I Cullis⁽¹⁾, R Townlsey⁽¹⁾, D Fishpool⁽¹⁾, E Taylor⁽³⁾

⁽¹⁾*QinetiQ, Fort Halstead, Sevenoaks, Kent TN 14 7BP, United Kingdom Email:pdchurch@qinetiq.com*

⁽²⁾*QinetiQ, Farnborough, Hampshire, GU14 0LX, United Kingdom Email:dporter@qinetiq.com*

⁽³⁾*Open University, Dept of Physics & Astronomy, Walton Hall, Milton Keynes, MK7 6AA, United Kingdom Email:e.a.taylor@open.ac.uk*

ABSTRACT

This paper describes the use of Quantitative Structure/Property Modelling (QSPM) to derive physically-based equations of state directly, from knowledge of the constituents of the material. For geological materials this is based on an implicit assumption that many geological materials are a derivative of different crystal forms of silica (i.e. cristobalite, coesite, α -quartz, and stishovite) based around packing of the Si-O tetrahedra. This approach is validated by predicting shock Hugoniot data for various materials. These crystal forms are present in craters after impact, but the link to each phase during the impact process is largely unknown. Equations of state have been developed for each of these forms and simulations have been performed in the QinetiQ GRIM Eulerian hydrocode to investigate their effect on the initial cratering phase. These have been compared to standard geological models in GRIM and AUTODYN SPH. The QSPM approach has also been used to investigate the equation of state for ice in its various forms and compared to published experimental data.

1. INTRODUCTION

There are an abundance of planetary and asteroid type bodies in the solar system which consist of either geological materials or ice or a mixture of both. This can cause a great disparity in the behaviour of these objects when subject to a significant impact leading to crater formation in terms of crater dimensions, ejecta and subsequent momentum transfer to the body. Given this uncertainty it is important to understand the effect of the material composing the body on the cratering process. Modelling combined with precise experimentation is the key to providing this understanding. This requires the development of physically based models where the constants are either measured or derived.

This paper describes the use of Quantitative Structural Property Modelling (QSPM) in deriving physically based equations of state directly, from knowledge of the constituents of the material. For geological

materials this is based on an implicit assumption that many geological materials are a derivative of different crystal forms of silica (i.e. cristobalite, coesite, α -quartz, stishovite). Equations of state have been developed for each of these forms and simulations have been performed to investigate their effect on the initial cratering phase.

2. QUANTITATIVE STRUCTURE/PROPERTY MODELLING OF SILICA

Silica is a molecule which exhibits 4 main crystal forms. These are in ascending order of density: cristobalite, quartz, coesite and stishovite and their molecular structure is illustrated in Fig 1. CASTEP [1] reproduced the minimum energy structures of the different polymorphs of silica with the specified space group of the crystal forms and predicted their correct density values. However, CASTEP was unable to simulate changes in the crystal structure of silica with different boundary conditions such as pressure or volume imposed. The practical consequence of this problem was that the predicted bulk elastic modulus of all four polymorphs was identical, with a value of about 100 GPa.

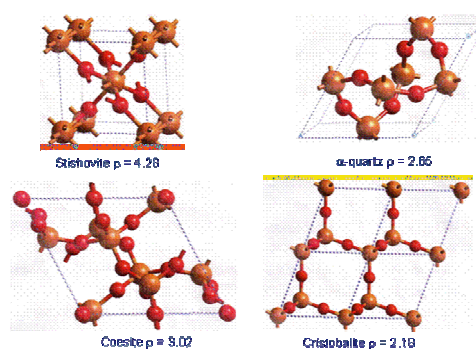


Fig 1 – Different crystal forms of silica

Most quantum mechanics programs try to change the length or angle of a chemical bond to simulate a change in structure, since the energy associated with these changes is large. However, the Si-O bond is very

mobile and can rotate easily around relatively rigid chemical bonds with very small changes in energy. Thus, changes in crystal structure or dimensional changes in silica are dominated by rotation of torsional bond angles that are very difficult to reproduce with programs such as CASTEP, unless a crystal structure is specified in advance to direct the calculations.

The failure of molecular mechanics or quantum mechanics to predict the volumetric properties of silica polymorphs requires a different modelling technique that can predict properties associated with the relatively small changes in energy associated with physical (van der Waal's) bonding between atoms that are not chemically bonded in a structure. This type of bonding dominates the properties of polymers, since the preferred mode of deformation is through the weak van der Waal's bonding normal to the chemical bonding in the chain axis of the polymer macromolecules.

2.1 Potential Function Method

A modelling technique has been developed by the author to predict the structural properties of polymers, called Group Interaction Modelling, GIM [2]. This technique has been used to predict equations of state for polymer based materials [3]. The technique uses an empirical equation to describe the relationship between energy and separation distance between adjacent (but not chemically bonded) groups of atoms in a molecular structure. Fortunately, a very simple power-law function called the Lennard-Jones function works very well for most polymers that are based upon carbon or silicon lattices. To a first approximation, the method assumes that chemical bonds do not deform significantly, relative to the weak physical bonds, due to electronic interactions between atoms or molecules. Note that, although the potential function here is an empirical relation for simplicity, all the fundamental contributions to bond energy are embodied in that function, and a potential function can be constructed from 'first principles' by a series of quantum mechanics simulations.

Fig 2 shows the general form of a potential energy well for Van der Waal's bonding. Energy, E, is expressed relative to the depth of the potential energy well, E₀, and dimensions are given as volume, V, relative to the volume at the absolute depth of the potential energy well, V₀. Note that energies for bonding are negative.

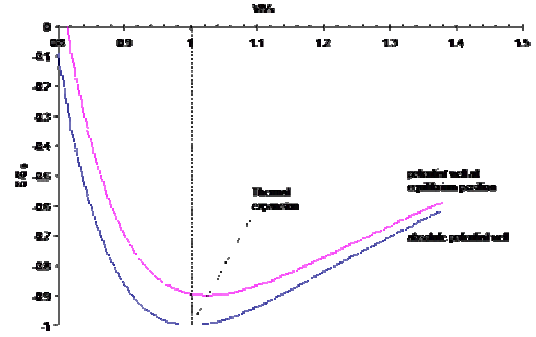


Fig 2 - A potential well for intermolecular energy

As positive energy (such as thermal energy, HT) is increased, the interaction dimensions move away from the minimum energy position to two possible values on either side of the minimum. Generally, the potential well is asymmetric, such that the equilibrium mean position of the new well minimum moves to higher volumes to cause thermal expansion in a material.

The energy E can be expressed either as a Lennard-Jones power function in separation distance, r, (or volume proportional to r³) or in terms of the positive and negative contributions to total energy

$$E_T = E_0 \left(\left(\frac{r_0}{r} \right)^{12} - 2 \left(\frac{r_0}{r} \right)^6 \right) = E_0 \left(\left(\frac{V_0}{V} \right)^4 - 2 \left(\frac{V_0}{V} \right)^2 \right) = -E_0 + H_T + H_c \quad (1)$$

where H_c is the configurational energy due to metastable non-zero energy configurations in the chains of atoms (a sort of entropy term) and E_T is the energy at a temperature T. If we take the new equilibrium function at T to have the same mathematical form as the absolute zero-point potential function with a new minimum energy E_T at a position V_T

$$E = E_T \left(\left(\frac{V_T}{V} \right)^4 - 2 \left(\frac{V_T}{V} \right)^2 \right) \quad (2)$$

then we can express pressure as a function of volume through the highly non-linear relation

$$P = \frac{dE}{dV} = \frac{4 E_T}{V} \left(\left(\frac{V_T}{V} \right)^2 - \left(\frac{V_T}{V} \right)^4 \right) = \frac{6 E_T}{V_T} \left(\left(\frac{V_T}{V} \right)^3 - \left(\frac{V_T}{V} \right)^5 \right) \quad (3)$$

The potential function relation of equation (3) for pressure as a function of volume requires two reference parameters of energy and volume that can be calculated in terms of chemical composition, crystal structure, and temperature for any polymer-like material such as

silica. Equation (3) for pressure can be used to predict the bulk modulus

$$B = -V \frac{dP}{dV} = \frac{6 E_T}{V_T} \left(3 \left(\frac{V_T}{V} \right)^3 - 5 \left(\frac{V_T}{V} \right)^5 \right) = \frac{12 E_T}{V_T} \quad (4)$$

at $V_t = T$

Since the required model predictions are for high rate properties that are conventionally expressed as Hugoniot parameters from impact experiments, we need expressions for the particle and shock velocities U_p and U_s in terms of pressure and volume

$$U_p = \sqrt{\frac{P(1 - V/V_T)}{\rho_T}} \quad (5)$$

$$U_s = \sqrt{\frac{P}{(1 - V/V_T)\rho_T}} \quad (6)$$

2.2 Application of Model to Geological Materials

On close inspection, the parameters show a qualitative trend that the reference parameter of volume for the different silica forms scales with the inverse of the density of the polymorphs and the energy parameter stay remarkably constant. The conclusion from this observation is that the many polymorphs of silica can be modelled as a single material in terms of a single adjustable parameter of volume at zero pressure, V_T , and two absolute reference parameters of energy and molar volume of an underlying polymeric form of silica, E_r and V_r respectively. The key point is that each polymorph adopts a crystal structure as if it were constrained by an energy or pressure, P_r , of configuration associated with the non-zero energy of each particular set of metastable chemical bond angles in the polymorph structure.

The remarkably simple conclusion from the pressure-volume relations for silica can be translated into a single predictive equation for any given silica polymorph of the following form

$$P = 0.34 \left(\left(\frac{V_r}{V} \right)^3 - \left(\frac{V_r}{V} \right)^5 - \left(\frac{V_r}{V_T} \right)^3 + \left(\frac{V_r}{V_T} \right)^5 \right) \quad (7)$$

This implies that the only variable required to predict the equation of state is the initial density of the material. The prediction using this approach for the pressure/volume relationship for each of the crystal

forms compared to experimental data is shown in Fig 3.

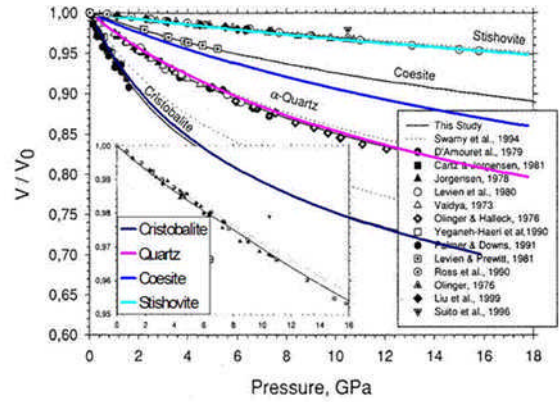


Fig 3 - Comparison of predicted pressure/volume relationship compared with experimental data for different crystal forms.

An interesting feature of the model is the radical difference in shock velocity versus particle velocity as shown in Fig 4. This has quite significant implications for the impact behaviour of the materials as discussed later. In addition the approach is also capable of predicting tensile states up to the point of failure.

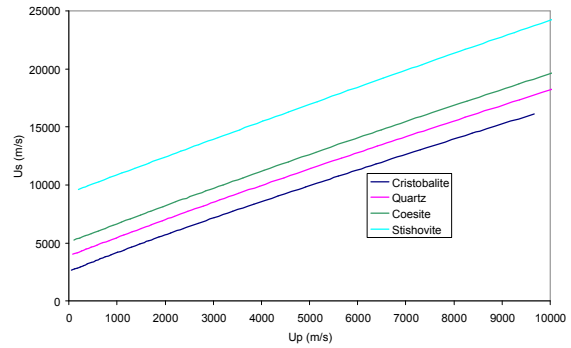


Fig 4 – Predicted Shock velocity versus particle velocity for different crystal forms

The model has also been used to predict shock Hugoniot data for a range of geological materials as shown in Fig 5

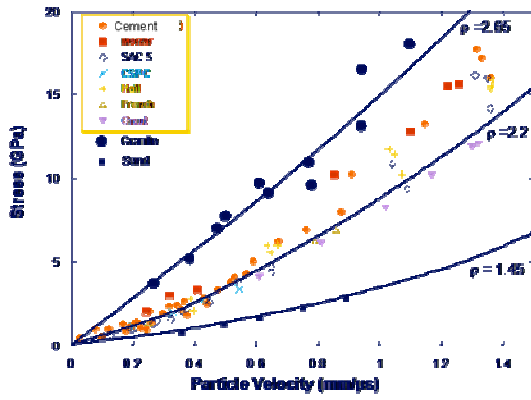


Fig 5 – Comparison of model with experiment

At present this approach generates a SESAME type equation of state format in terms of P, V, T and is used in combination with an existing constitutive relation, such as the Johnson-Holmquist model for brittle materials [4]. The model is referred to as the QinetiQ Porter-Gould Equation of State (EOS).

3. APPLICATION OF MODEL APPROACH TO ICE

The case of ice presents a novel problem, since it is a solid material consisting of hydrogen-bonded small molecules, which can adopt a wide range of different molecular structures, with a commensurate range of different physical properties such as density and elastic modulus. If we assume that water/ice behaves as a simple solid, with intermolecular interactions represented by a Lennard-Jones function, and positive energy terms H_T and H_C that are the thermal energy of molecular vibrations and energy of configuration (zero point energy) respectively.

$$E = E_o \left(\left(\frac{V_o}{V} \right)^4 - 2 \left(\frac{V_o}{V} \right)^2 \right) = -E_o + H_T + H_C \quad (8)$$

where E_o is the depth of the potential energy well at a volume V_o . Pressure is then the differential, with E_o and V_o now at a specified temperature.

$$P = -\frac{dP}{dV} = 4 \frac{E_o}{V} \left(\left(\frac{V_o}{V} \right)^5 - \left(\frac{V_o}{V} \right)^3 \right) \quad (9)$$

The cohesive energy for water/ice is simply the dispersion energy for oxygen (6300 J/mol) plus any hydrogen bonding, with 10,000 J/mol for each hydrogen bond per molecule. For liquid water or any

dynamic form of the H_2O molecule, we assume that the hydrogen bonds are not active, and for solid ice we assume that there are generally two hydrogen bonds per molecule. This suggests two values of cohesive energy: 6300 and 26300 J/mol for liquid and solid H_2O respectively.

Let us take the melting point of ice as the transition point, where an energy instability occurs as $d^2E/dV^2 = 0$ at $E = 0.84 E_{coh}$ and $V = 1.29 V_o$ on the absolute potential well. This suggests a value of $V_o \approx 14$ cc/mol using the density of water as 1 g/cc and $V = 18$ cc/mol.

The review by Stewart and Ahrens [5] shows that ice is a complex material with many different structural forms. At its most simple we reduce these to porous and compacted ice. Porous ice is composed of water molecules that are arranged in the attractive multitude of different H-O hydrogen bonding structures, which are also seen as pentagons and hexagons in materials such as clathrates that encapsulate methane under the sea. We take this porous form to be the Ih form with a density 0.93g/cc or specific volume 1.08cc/g. The compact form should have a density approximately $M/V_o \approx 18/14 = 1.3$ g/cc, which is approximately that of the VI and VII forms with densities of 1.3 and 1.46 respectively.

Table 1 suggests the parameters required to predict P-V relations for the specified three different ice forms, and also suggests a transition form of ice where the structures are compacting from Ih to the compacted structures and the hydrogen bonds are not active in the real part of the complex cohesive energy (effectively a 'yield' state). These predictions are performed using the QinetiQ Porter-Gould EOS.

Ice Type	Density (g/cc)	Sp. Gravity (cc/g)	E_o (J/mol)	V_o (cc/mol)	$4 E_o/V_o$ (GPa)
Ih	0.93	1.08	25600	19.4	5.28
VI	1.3	0.769	25600	13.8	7.39
VII	1.46	0.685	25600	12.3	8.29
Transition	0.93	1.08	4800	19.4	1.00

Table 1 – Predicted parameters for ice

The prediction for the shock velocity v particle velocity for the different ice forms compared to experimental data is shown in Fig 6 and PV data in Fig 7.

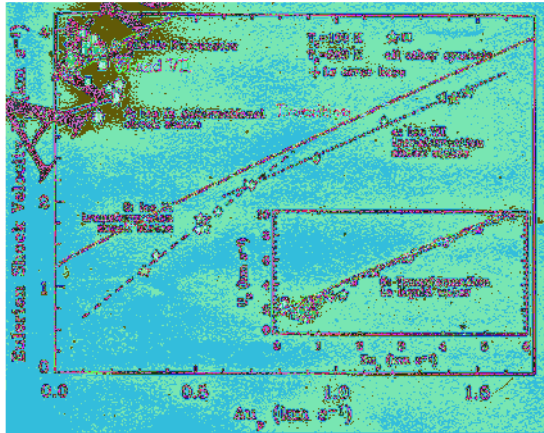


Fig 6 – Comparison of prediction (red) with experimental Hugoniot data

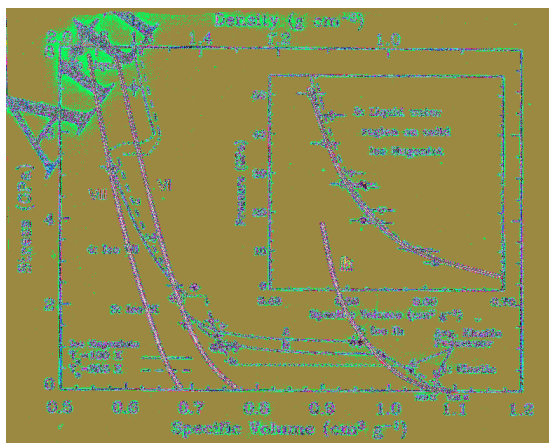


Fig 7 – Comparison of prediction (red) with experimental PV data

4. SIMULATIONS

The main purpose of the simulations was to perform scoping studies for initial crater formation using the new silica models compared to standard models for concrete. The crater formation was simulated using the QinetiQ Eulerian hydrocode GRIM which is capable of multi-material analysis and is 3rd order accurate in the transport of material variables (advection) through the mesh. In addition the AUTODYN Smooth Particle Hydrodynamics (SPH) model was used using a Johnson-Holmquist concrete model.

The simulations comprised a 1500kg aluminium sphere normally impacting a semi-infinite target at 10km/s. The models used were the QinetiQ Porter-Gould EOS for the different silica forms combined with a Johnson-Holmquist type model for concrete. The standard model for concrete was a tabulated EOS combined with the same constitutive model. Thus the only

difference between the simulations was the EOS. The simulations were run to a maximum of 10ms after impact to investigate the initial crater formation. In addition the runs were performed without a failure model, other than a simple volumetric strain cut-off so as not to confuse the spallation effects with the basic crater dimensions. The crater formation for coesite is illustrated in Fig 8 after 10ms, which shows a zoomed in plot of the crater interface. It was established that the target was large enough such that reflections from the boundaries did not significantly affect the results.



Fig 8 – Crater formation using GRIM for Coesite 10ms after impact

The results for the crater dimensions after 10ms are given in Table 2. These show the surprising result that the lower density crystal form (i.e. cristobalite) results in the least penetration. The prediction of the crater dimensions is also shown on the universal cratering curve [6] and fits quite well as shown in Fig 9.

	Depth (m)	Diameter (m)
Cristobalite	3.07	7.4
Quartz	3.85	7.2
Coesite	3.95	7.3
Stishovite	4.08	7.3
Concrete	3.47	6.2

Table 2 - Predicted Crater Depth and Diameters 10ms after impact for impact of 1500kg al sphere at 10km/s

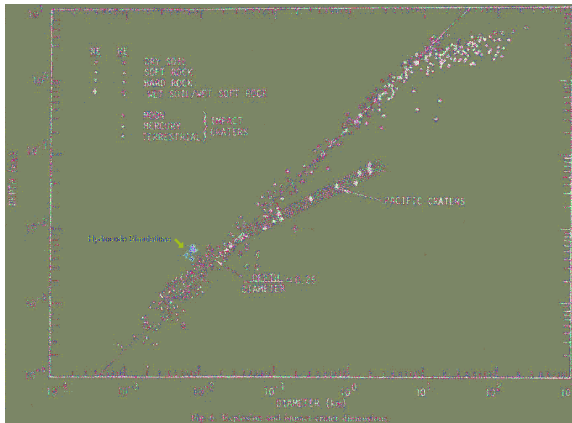


Fig 9 – Position of simulation results on the Universal cratering curve

After extensive analysis there was no evidence of the model causing errors in the GRIM hydrocode or of wave reflections from the edge of the mesh influencing the results. On closer inspection there are potentially some complex mechanisms operating in the crater formation. This is illustrated in Fig 10, which shows a data point (station) indicating the penetration as a function of time and the cumulative pdv work input into the target.

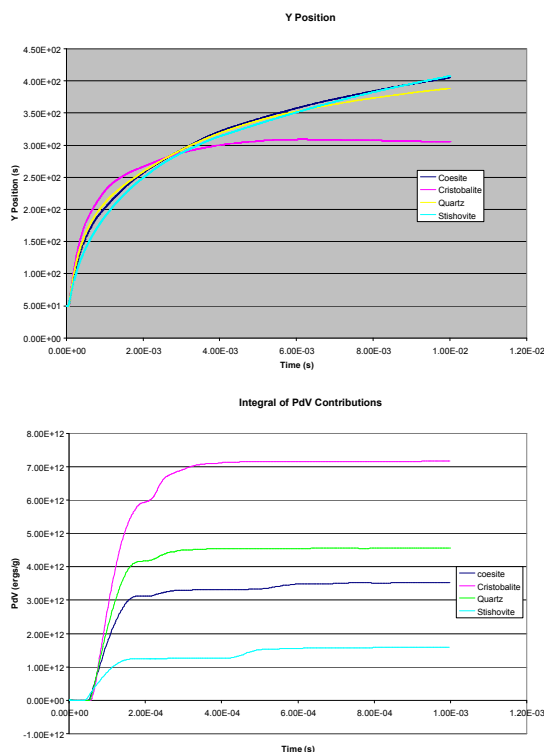


Fig 10 – predicted penetration v time (top) and cumulative pdv work (bottom) for each crystal form

It is very interesting that in the penetration v time curve the order for maximum penetration corresponds with that for maximum density. However, the order reverses after about 3ms. For the cumulative pdv work the stishovite starts off with the maximum, but again the trend reverses and the cristobalite has by far the largest pdv work. This could be an indication that the cristobalite is absorbing more energy from the impact and therefore deforming less resulting in a lower penetration depth. However, these results need more analysis.

It is also important to note that there will be solid-solid phase transitions during the impact. In particular the quartz will transition to stishovite at about 20GPa and thus the behaviour may be completely different. Development of a hybrid EOS is the subject of ongoing work and has recently been completed for concrete. Another very important factor is that the energy contribution leading to melt has not been explicitly accounted for these models. However, understanding the role of each crystal form is important since they can exist at different points in the crater away from the initial impact.

It is also interesting that the model prediction for quartz is very similar to that of concrete for both GRIM and AUTODYN, as would be expected. This indicates that the numerical scheme for this aspect of cratering is not particularly crucial, although it may have an effect at later times and for spallation effects.

5. CONCLUSIONS

A new approach using Quantitative Structure/Property Modelling (QSPM) has been described, which is capable of predicting shock Hugoniots for different crystal forms of silica. The approach has also been applied to various forms of ice and comparisons with available experimental data are highly encouraging.

The models have been applied in the QinetiQ Eulerian hydrocode GRIM to investigate the initial cratering phase. The results, which require further analysis, indicate that energy absorption in the material is critical in determining the final crater shape. Future studies will investigate the effect of phase transitions, particularly from quartz to stishovite on the cratering process.

6. REFERENCES

1. www.Accelrys.com
2. Porter D, *Group Interaction Modelling of Polymer Properties*, Marcel Dekker Inc, New York (1995)

3. Porter D, Gould P, Multiscale Modelling for Equations of State, *Jnl de Phys IV*, DYMAT 2003
4. Johnson G, Holmquist T; A computational model for brittle materials subjected to large strains, high strain rates and high pressures, *14th Int Symp Ballistics*, 1983, pp591-600
5. Stewart S, Ahrens T; Shock Properties of H₂O Ice, *Jrnl of Geophysical Research*, Vol 110, March 2005
6. Cooper H, A Summary of Explosion Cratering Phenomena relevant to Meteor Impact Events, *Impact and Explosion Cratering*, Pergamon Press, pp11-44, 1976.

INVESTIGATION OF IMPACT CRATERING PROCESSES INTO POROUS TARGETS THROUGH HYPERVELOCITY EXPERIMENT AND SIMULATIONS.

C. Giacomuzzo⁽¹⁾, F. Ferri⁽¹⁾, E. Toson⁽¹⁾, A. Bettella⁽¹⁾, D. Pavarin⁽¹⁾, A. Francesconi⁽¹⁾, E. Flamini⁽²⁾, F. Angrilli⁽¹⁾

⁽¹⁾ CISAS, University of Padova, via Venezia 15, 35131 Padova, Italy, Email: cinzia.giacomuzzo@unipd.it

⁽²⁾ ASI, Viale Liegi, 26, 00198 Roma, Italy

ABSTRACT

The goal of these studies is to obtain a better comprehension of the impact processes on solid body surface (specifically asteroids, comets, icy satellites of giant planets, Kuiper belt objects) and for the data interpretation of remote sensing observations.

We focus on the study of impact processes on porous targets both by experimental and theoretical approach in order to complement and extend the available data to ranges of velocity and physical conditions not yet explored.

Dedicated hypervelocity impact experiments into low density materials and numerical simulations by using Smooth Particle Hydrodynamics technique have been performed and results are presented in this paper.

1. INTRODUCTION

The surface of the solid bodies of the Solar System is exposed to impacts of cosmic objects of different dimensions and composition.

A better understanding of impact processes is needed to further our understanding of the surface evolution of the solid bodies in the Solar System and to allow remote sensing data from forthcoming missions as Smart1, MarsExpress, VenusExpress, BepiColombo, Cassini/Huygens, Rosetta to be correctly interpreted.

New data from observations of asteroids and spacecraft encounters revolutionized our understanding of asteroid bulk density [1]. Most asteroids appear to have bulk densities that are well below the grain density of their likely meteorite analogs [4]. This indicates that many asteroids have significant porosity. High porosity attenuates shock propagation, strongly affecting the nature of cratering and greatly lengthening the collisional lifetimes of porous asteroids.

A peculiar example is the C-type, main-belt asteroid 253 Mathilde recently imaged by the Near Earth Asteroids Rendezvous (NEAR) spacecraft. The NEAR determination of a bulk density of 1.3 ± 0.2 g cm⁻³ for Mathilde [13] and the presence of several giant craters larger than conventionally accepted crater size limit for disruption [2] suggests that this asteroid has

significant porosity and this porosity must dampen the shock wave propagation waves in the interior of the asteroid. Another more recent example is the asteroid Itokawa, target of the Japanese mission Hayabusa, which shows a typical rubble pile structure [5].

Porosity is an important physical characteristic of the minor bodies, affecting their behaviour during cratering and catastrophic disruption.

Kawakami et al. (1991) [9] performed impact experiments on a gypsum target simulating Phobos and studied the impact origin of grooves radially growing from a central large crater; they concluded that fracture mode was highly dependent on target material properties, in particular on porosity, and that the low shock impedance of the gypsum target induced rapid attenuation of shock pressure during propagation. Love et al (1993) [10] have shown that it requires more projectile energy to produce the same cratering effect in a porous target than in a nonporous target.

Porous targets are likely to have sound velocity lower than those of nonporous targets composed of same material and compaction of initially porous materials can produce rapid attenuation of the shock, thus affecting energy propagation during collisions.

Similar results have been obtained during our hypervelocity tests campaign aimed at analysing hypervelocity impact effects on porous target. Tests descriptions and results are presented in this paper.

2. HYPERVELOCITY EXPERIMENTS

Dedicated hypervelocity impact experiments into low density materials have been performed by using a two-stage light-gas gun (see Fig. 1) of the hypervelocity impact facility at CISAS “G. Colombo” of the University of Padova, Italy [11].

These tests have been performed by shooting aluminium and nylon projectiles from 1 to 4.72mm at velocities of 1600-5500 m/s on targets of several dimensions and materials, i.e. glass ceramic foams, pumices with densities from 0.35 to 1.07 g/cm³.

Physical properties of the impacted materials are analysed by visual and photographic investigation

before, during (when possible) and after the event by means of the diagnostic instrumentation available at the impact facility. After the impact, targets are analysed in order to evaluate crater morphology, volume, depth-diameter ratio and ejected mass-projectile mass ratio.

In Tab. 1 some physical properties, density and crushing strength, for the tested materials are reported, while

Tab. 2 presents shots parameters, target characteristics and crater depth of cratering experiments performed at CISAS for this campaign.

Examples of craterization on ceramic glass foam, natural pumices and limestone (Vicenza stone) samples are presented in Fig. 2, Fig. 3 and Fig. 4 respectively.

All figures report shot parameters and craters morphology, thus from a first tentative of comparison it can be argued that natural pumices, which have the lowest density, present small and deep craters.

Craterization has been also provided of photographic proofs of impact event inside impact chamber: the detection of flash generated by the impact of projectile onto the target (see Fig. 4) and shadowgraphies (see Fig. 2) a sequence of four shadow images taken with a

mean time delay of 15 μ s obtained by using a system of flashes to detect impact event and to monitor ejecta.

Tab. 1 Type of employed samples. Density, crushing strength and sample shape are reported for each material.

Material	Density ρ (g/cm ³)	Crushing Strength (MPa)	Shape
Glass Ceramic Foam	0.92	15-20	Geode
Natural Pumice	0.5-0.7	--	Irregular Sphere
Limestone (Vicenza stone)	2.01	23	Cube
Natural Marble (Rosso Trento)	2.6	137	Cube
Refractory blocks	0.5	--	Cube

Tab. 2 Summary of shots aimed at craterization performed by using LGG at CISAS. ρ_T is the target density in g/cm³, D_p is the projectile diameter in mm, V_p represents projectile velocity in m/s and Depth p in mm is the crater depth.

Shot No.	Target	ρ_T (g/cm ³)	Target dimensions (mm)	Projectile	D_p (mm)	V_p (m/s)	Depth p (mm)
6320	Ceramic foam geode	0.73	Ø 80	Al sphere	1.5	3288	13.3
6322	Ceramic foam geode 1	0.73	Ø 80	Al sphere	1.5	4430	9.2
6326	Ceramic foam geode 1	0.73	Ø 80	Nylon Cylinder	1.5	1170	14.8
6327	Ceramic foam geode 1	0.73	Ø 80	Nylon Cylinder	4.72	2400	15.9
6457	Ceramic foam geode 3	1.067	Ø 70.5	Al sphere	0.8	2483	3.0
6458	Ceramic foam geode 3	1.067	Ø 70.5	Al sphere	1	2189	4.0
6459	Ceramic foam geode 3	1.067	Ø 70.5	Al sphere	1.5	1899	4.0
6460	Ceramic foam geode 3	1.067	Ø 70.5	Nylon Cylinder	2.3	1997	5.0
6667	Refractory block R1 white	0.850	60x60x60	Polycarbonate	4.72	4923	2.0
6668	Refractory block R1 white	0.850	60x60x60	Al sphere	1.5	5100	1.07
6672	Refractory block R1R red	0.500	57x64x56	Al sphere	1.5	4770	1.1
6679	Refractory block R2R red	0.500	56x64x55	Al sphere	1.5	4800	1.1
6692	Refractory block R2R red	0.500	56x64x55	Al sphere	1.5	5156	1.26
7467	pumice1	0.676	Ø 73	Al sphere	1	4100	5.0
7559	pumice2	0.543	Ø 55	Al sphere	1	1644	5.5
7560	pumice2	0.543	Ø 55	Al sphere	1	4180	5.7
7561	pumice2	0.543	Ø 55	Al sphere	1.5	4111	10.3
7603	pumice3	0.600	Ø 62	Al sphere	1	4881	5.0
7605	pumice3	0.600	Ø 62	Al sphere	1.9	5016	6.8
7881	Marble1	2.6	70x70x70	Al sphere	1.0	4916	1.5
7882	Marble1	2.6	70x70x70	Al sphere	1.9	5192	4.5
7883	Limestone1	2.01	70x70x70	Al sphere	1.0	5000	2.0
7884	Limestone1	2.01	70x70x70	Al sphere	1.9	5000	4.7
7886	Marble1	2.6	70x70x70	Al sphere	1.0	5085	1.8
7887	Marble1	2.6	70x70x70	Al sphere	1.5	5085	2.4



Fig. 1 The two stage light gas gun, the hypervelocity facility at CISAS (left), and the recovery box for targets in the vacuum chamber (right).

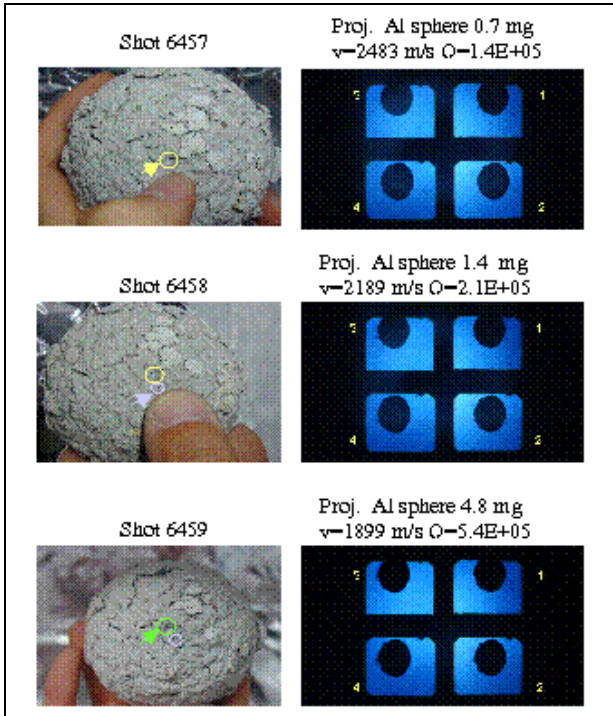


Fig. 2 Examples of tests on glass ceramic foam: in the images on the left pictures of the targets after impact are reported with evidence of crater formation, while on the right the shadowgraphies of the event are presented.

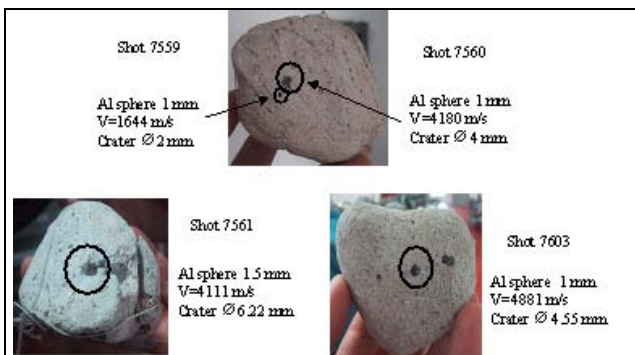


Fig. 3 Examples of craterization impact results on natural pumice.

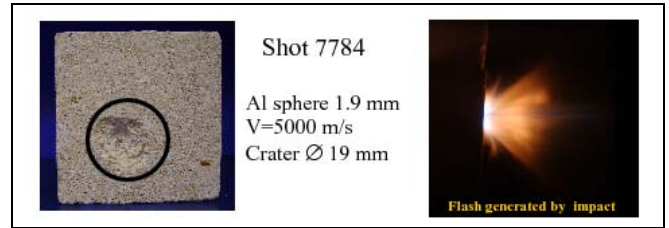


Fig. 4 Craterization results of hypervelocity impacts on limestone target (Vicenza stone) and image of detection of flash generated by projectile impact.

Craterization as function of impact energy has been investigated. Crater dimensions have been then related to impact conditions, and thus compared to published results [7,8].

Crater diameter with respect to projectile diameter, has been studied as function of impact velocity by comparing our experimental results with those obtained by Ishibashi by shooting 7mm nylon projectiles at 0.4-4.3 km/s on polystyrene targets ($\rho=0.011-0.079 \text{ g/cm}^3$). our results follow Ishibashi's empirical distribution (see Fig. 5), except for refractory blocks results. This may be due to the great uncertainty in crater morphology determination for this kind of material. As observed by Kadono [8] with various types of porous material, the penetration of a dense projectile into these porous target produces a carrot-spindle shaped cavity with a maximum cavity diameter larger than the entrance hole diameter.

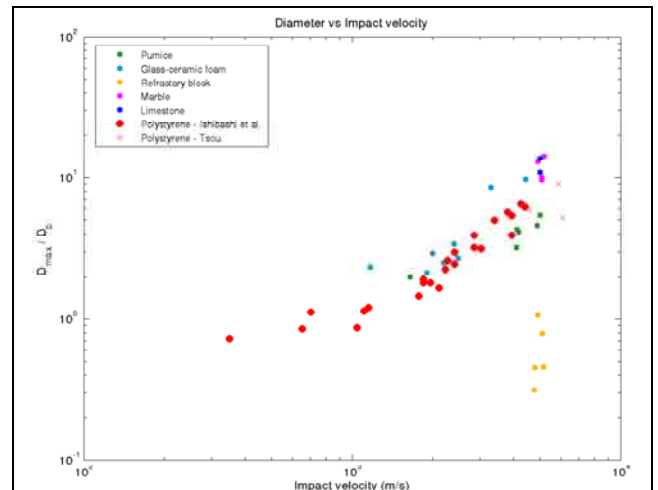


Fig. 5 Crater diameter normalised to projectile diameter vs. Impact velocity: comparison between experimental data obtained at CISAS and Ishibashi et al. (1990) results [5].

Furthermore, the relation between crater depth (penetration p) with respect to crater diameter has been

investigated as function of density ratio between projectile and target. Also in this case our results (see Fig. 6) are in good agreement with other experimental data on porous targets.

In particular, they lay within the uncertainty range of the empirical distribution obtained by Kadono [8] described by Eq. 1.

$$p_{\max} / D_p = 10^{0.33 \pm 0.31} (\rho_p / \rho_t)^{1.07 \pm 0.17} \quad (1)$$

The visual inspection of the impacted targets revealed that the effect of the impacts resulted in the compaction of target material as observed by Housen & Holsapple [6].

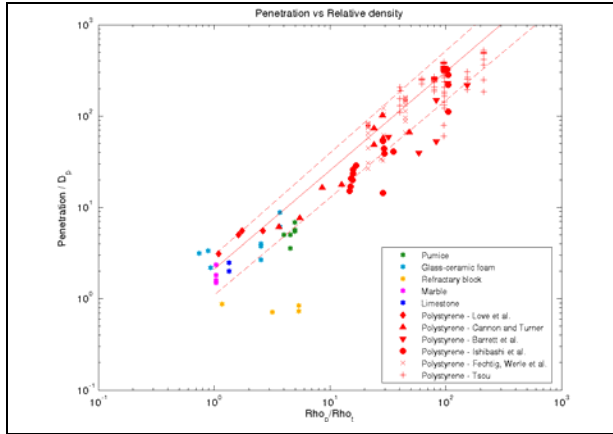


Fig. 6 Penetration as function of relative density: comparison between our experimental values and Kadono results obtained by comparing polystyrene experimental data from literature[8].

3. NUMERICAL SIMULATIONS

Numerical modelling is a fundamental tool for understanding of the dynamics of impact cratering, especially at planetary scales [12].

In particular, processes like melting/vaporization and crater collapse, typical of planetary-scale impacts, are not reproduced in the laboratory, and can only be investigated by numerical modelling. The continuum dynamics of impact cratering events is fairly well understood and implemented in numerical codes; however, the response of materials to shocks is governed by specific material properties. Accurate material models are thus crucial for realistic simulation of impact cratering, and still represent one of the major problems associated with numerical modelling of impacts.

In order to validate the experimental data we have performed preliminary numerical simulations by applying Smooth Particle hydrodynamics (SPH)

technique, by using Software Autodyn 2D by Century Dynamics.

The code combines finite difference, finite volume, and finite element techniques; meshing is performed by considering each material as composed by spherical particles whose interactions are based on the laws of conservation of mass, momentum and energy.

Our simulations are aimed at investigating the propagation of the shock wave into the targets, the variation of the material physical properties and energy partition. Targets of different materials (concrete, concrete 35MPa, rock, quartz), porosity and dimensions have been considered and impacts of different velocities and different projectile to target diameter ratios have been simulated.

In Fig. 7 simulation results for different materials at the same impact conditions are reported. By comparing quartz or rock samples to more porous samples, as ones made of porous concrete, it can be inferred that the first are more affected by wave propagation reflection, with generation of compression waves which can cause the detachment of big fragments.

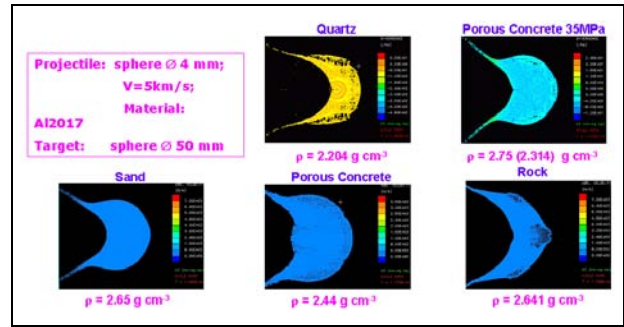


Fig. 7 Comparison between numerical simulations performed by using Smooth Particle Hydrodynamics (SPH) technique in the case of an aluminum projectile of 4mm diameter impinging at 5km/s on a spherical target made of quartz, porous concrete 35MPa, sand, concrete and rock.

In order to estimate scaling effect, projectile dimensions variations with respect to target were studied also by using two different techniques: SPH and Lagrangian mesh; results of the simulations at 1.8e-02 ms in the case of a porous concrete target are reported in Fig. 8. An impact of an Aluminum projectile onto a target of porous concrete at a velocity of 5km/s has been studied; projectile to target diameter ratios of 0.02, 0.04 and 0.08 have been simulated.

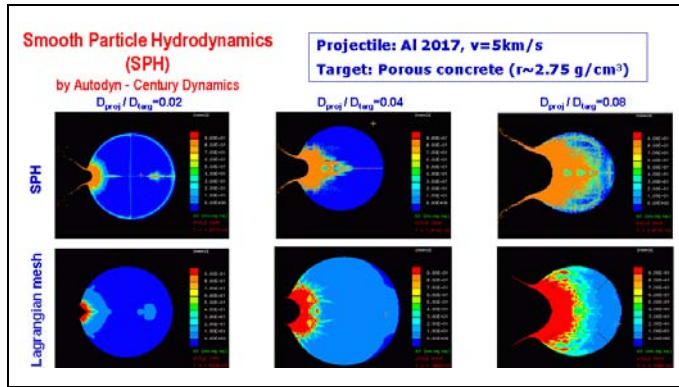


Fig. 8 Comparison between SPH and Lagrangian technique by simulating impacts of different projectile dimensions on the same target at 5km/s. Diameter ratio of 0.02, 0.04, 0.08 were considered.

SPH technique seems to better simulate this kind of hypervelocity impacts as damage and crater shape seems to be quite similar to experimental cases, more than Lagrangian mesh.

Simulations of small projectile impact on porous targets, in particular those using SPH technique, showed a damaged zone quite similar to the carrot shaped cavity produced by hypervelocity impact observed by Kadono [8] and confirmed during our experiments.

4. CONCLUSIONS

In order to obtain a better comprehension of the impact processes on solid body surface and for the data interpretation of remote sensing observations we studied impact processes on porous targets both by experimental and theoretical approach simulating ranges of velocity and physical conditions not yet explored.

Dedicated hypervelocity impact experiments into low density materials have been performed by using a two stage Light Gas Gun facility at CISAS "G.Colombo". About 25 impact experiments only aimed at craterization have been conducted on several porous material: glass ceramic foam, porous natural pumices, limestone, marble and refractory blocks.

Projectiles with diameter of 0.8 up to 2 mm with a velocity of 2-5 km/s have been used.

The visual inspection of impacted samples revealed on porous targets a carrot shaped cavity, as observed by Kadono et al. 1990 [8], and the effect of the impacts resulted in the compaction of target material as observed by Housen & Holsapple [6].

Crater morphology has then been analysed and results compared to published results, as and Ishibashi et al. (1990) [7] and Kadono et al. (1999) [8] data.

In particular crater diameter normalised to projectile dimensions, for all our shots, has been related to impact velocity and results seem to follow Ishibashi's empirical distribution. Furthermore the distribution of penetration as function of projectile-target density ratio given by our data agree with the empirical distribution obtained by Kadono [8].

In order to validate experimental results and to infer scale effects, some preliminary numerical simulations by using hydrocodes, in particular the Smooth Particle Hydrodynamics technique, have been performed.

Tests revealed that SPH technique seems to be more suitable than Lagrangian mesh as crater shape and dimensions are quite similar to experimental results.

In conclusion it can be inferred that porous targets revealed to have sound velocity lower than those of non porous target as compaction of initial porous material produces rapid attenuation of the shock, thus affecting energy propagation.

5. REFERENCES

1. Britt, D. T.; Yeomans, D.; Housen, K.; Consolmagno, G., Asteroid Density, Porosity, and Structure, in *Asteroids III*, W. F. Bottke Jr., A. Cellino, P. Paolicchi, and R. P. Binzel (eds), University of Arizona Press, Tucson, p.485-500, 2002.
2. Chapman C., Merline W., P. Thomas, and the NEAR MSINIS Team, Cratering of the C-type asteroid Mathilde, *Meteor. Planet. Scie.* 33, A30, 1998.
3. Durda, D. et al., The formation of asteroid satellites in large impacts: results from numerical simulations, *Icarus*, 167, pp.382-396, 2004.
4. Flynn, G. J., Moore L. B. and Klock W., Density and Porosity of Stone Meteorites: Implications for the Density, Porosity, Cratering, and Collisional Disruption of Asteroids, *Icarus* 142, 97-105, 1999.
5. Fujiwara A, Kawaguchi J, Yeomans DK, Abe M, Mukai T, Okada T, Saito J, Yano H, Yoshikawa M, Scheeres DJ, Barnouin-Jha O, Cheng AF, Demura H, Gaskell RW, Hirata N, Ikeda H, Kominato T, Miyamoto H, Nakamura AM, Nakamura R, Sasaki S, Uesugi K, The rubble-pile asteroid Itokawa as observed by Hayabusa, *Science*, 312(5778):1330-4, 2006 Jun 2.
6. Housen, K. R., & K. A. Holsapple, Impact Cratering on Porous Asteroids, *Icarus* 163, 102-119, 2003.
7. Ishibashi, T., A. Fujiwara, N. Fujii, Penetration of Hypervelocity Projectile into Foamed Polystyrene, *Jpn. Journal Appl. Phys.* 29, 2543-2549, 1990.
8. Kadono, T., Hypervelocity impact into low density material and cometary outburst, *Planetary and Space Science* 47, 395-318, 1999.
9. Kawakami, S. et al., An experimental study of impact fracturing of small planetary bodies in the solar system

- with an application to PHOBOS, *Astron. Astrophys.* **241**, 233–242, 1991.
10. Love, S.G., F. Horz, and D.E. Brownlee, Target Porosity Effects in Impact Cratering and Collisional Disruption, *Icarus* **105**, 216–224, 1993.
 11. Pavarin, D. and Francesconi, A., Improvement of the CISAS High-Shot-Frequency Light-Gas Gun *J.Impact Eng.* **29**, 549–562, 2003.
 12. Pierazzo E., Collins G., in Henning D., Burchell, M., Claeys P. (eds.), A brief introduction to hydrocode modeling of impact cratering, *Cratering in Marine Environments and on Ice* (Springer, New York), 323–340, 2003.
 13. Yeomans, D.K., et al., Estimating the Mass of Asteroid 253 Mathilde from Tracking Data During the NEAR Flyby, *Science* **278**, 2106–2109, 1997.

LABORATORY IMPACT CRATERING ON ICE-SILICATE MIXTURE TARGETS

K. Hiraoka⁽¹⁾, M. Arakawa⁽²⁾, M. Seto⁽¹⁾, A. M. Nakamura⁽¹⁾

⁽¹⁾Kobe University, 1-1 Rokko-dai, Nada, Kobe, Hyogo, 657-8501, Japan, Email: kensuke@kobe-u.ac.jp

⁽²⁾Nagoya University, Furou-cho, Chikusa, Nagoya, Aichi, 464-8601, Japan

ABSTRACT

We performed impact experiments on ice-silicate mixture targets and measured target compressive and tensile strength at low strain rate ($\sim 10^{-3}\text{s}^{-1}$) by uniaxial compression and Brazilian tests at 263K. The crater volume decreases with increasing silicate content. Both compressive and tensile strength increase with silicate content, however, tensile strength is more sensitive over wide range of silicate content. We found that the crater depth and the crater diameter are well scaled by the compressive and the tensile strength of the target, respectively. As crater size decreases, the fraction of material ejected by spallation increases. Thus increase of the tensile strength with silicate content is probably the main reason why the crater volume decreases with silicate content.

1. INTRODUCTION

There are many objects with surfaces consisting of water ice in the solar system such as icy satellites and comets. Water ice in the solar system is not pure ice, but mixed with other material (e.g., silicate, NH_3 and CO_2). This is why understanding the impact process of mixtures of ice and other materials is important. In this study, we focus on impact cratering on ice-silicate mixtures.

Previous studies suggest that a crater size decreases with increasing silicate content[1][2]. Reference [2] performed impact cratering experiments on ice-silicate mixture targets. They changed silicate content of target from 5 to 20wt% and impact velocity from about 1km/s to 10km/s. They found the crater volume decreased with increasing silicate content (see Fig. 9 in [2]). Because the data of crater volume of 5wt% silicate content was very scattered, they decided this tendency with the results of 0, 10 and 20wt%. The reason of this tendency is not understood. Reference [3] estimated the dynamic tensile strength of ice and ice-silicate mixture at high strain rates of about 10^4s^{-1} . They concluded that ice had a tensile strength of about 17MPa, and ice-silicate mixtures with 5 and 30wt% silicate content had strengths of about 20 and 22MPa, respectively. From this study we qualitatively expect that increase of target strength with silicate content

explains why the crater volume decreases with silicate content. However, the strength of ice-silicate mixtures would depend on the particle size and the kind of silicate, and other experimental conditions. Thus it is necessary to measure the strength of the target used in impact cratering.

We performed impact experiments on ice-silicate mixtures and measured the target strength. Silicate content of the targets was varied from 0 to 50wt%.

2. EXPERIMENTS

2.1 Impact cratering on ice-silicate mixture targets

The experiments were performed in a cold room (263K) at Institute of Low-Temperature, Hokkaido University, Japan. Cylindrical projectiles (pure ice, 15mm in diameter, 10mm in height and 1.6g in weight) were used for gas gun and corn shaped projectiles (nylon, 1mm and 2mm in diameter, 2.5mm in height and 7mg in weight) for the two-stage light-gas gun. The range of impact velocity was from 299 to 657m/s and from 1,480 to 3,684 m/s, respectively. The silicate content was changed from 0 to 50wt%. The powder of serpentine was used. The porosity of our target was estimated to be about 10%. The diameter of serpentine was several μm in most of the experiments. In order to investigate the effect of the difference of size of silicate powder, we made three targets of 50wt% silicate content with powders of about 200-500 μm in diameter. No difference due to the diameter of silicate grain was found for any results. Detail of our impact experiments is described in our previous paper[4].

2.1 Measurement of target strength

The cratering in the strength regime continues until the target strength becomes higher than stress caused by impact, which propagates from impact site with attenuation. A compressive wave caused by impact excavates the target, and this process makes a central pit. Thus, a crater depth would depend on compressive strength. The compressive wave reflects as a tensile wave at the target surface, which detaches the surface and it is called “spallation”. Spallation determines crater diameter. Thus, a crater volume probably depends on both compressive and tensile strength.

Accordingly, we measured the target compressive and tensile strength at low strain rate ($\sim 10^{-3}\text{s}^{-1}$) by uniaxial compression and Brazilian test[5]. We performed the experiments in the cold room (263K) in the Institute of Low-Temperature, Hokkaido University. Ice-silicate mixture samples were prepared in cylindrical sample cases by following the same steps of the procedure in the impact experiments[4]. The porosity of samples was estimated to be about 10%. The silicate content of most of the samples was serpentine powders with typical diameter of several μm similar to the powder used in cratering experiments. We used two other kinds of powders for comparison that were coarse serpentine and dunite powders. These powders were about 200-500 μm in diameter. The test specimens were 32mm in diameter and 43-48mm in height for uniaxial compression test, and 20-35mm in height for Brazilian test, respectively. The silicate content of the samples using fine serpentine powder was changed from 0 to 50wt% for both tests. For the coarse powder samples, only 50wt% silicate content specimens were prepared. Each strength test was repeated more than three times for the same type of specimens.

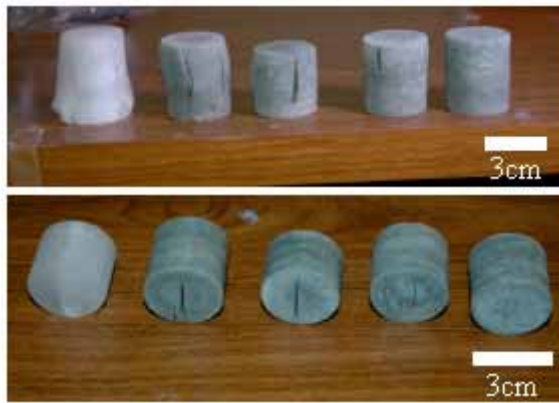


Fig. 1. Samples after uniaxial compression (upper) and Brazilian test (lower). From the left silicate content is 0, 12.5, 25, 37.5 and 50wt%, respectively.

3. RESULTS

3.1 Impact cratering

The crater volume was calculated by dividing the crater weight by the target density. The crater weight was determined by a subtraction of the weight of the post-impacted target from the weight of the pre-impacted target. The crater volume decreases with increasing silicate content. Especially, this tendency is clear for the results of two-stage light-gas gun (Fig. 2). In the range of this kinetic energy, the crater volume is more sensitive to the silicate content than the kinetic energy. The plots of 100wt% in Fig. 2 are the results of serpentine block. The crater volume of 50wt% target is especially smaller than those of the other silicate

content. More detail results are described in our previous paper[4].

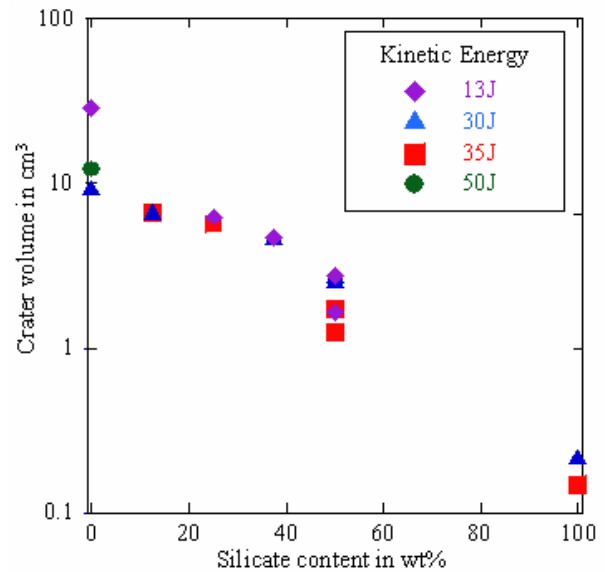


Fig. 2. The relation between the silicate content and the crater volume for the data of the shots by two-stage light-gas gun. The symbols show the kinetic energy of the projectiles.

3.2 Target strength

The results of uniaxial compression and Brazilian test were shown in Fig.3. Both strengths increase with silicate content, although the gradient of increase was steeper for the tensile strength. The compressive strength did not differ among the samples of fine, coarse serpentine, and dunite particles. It drastically increased when a small amount of silicate (less than 12.5wt%) was included and, then, it gradually increased for the wide range of silicate content from 12.5 to 50wt% except for 37.5wt%. The compressive strength of the 37.5wt% silicate content was lower than expected. An irregular deformation was observed for the other silicate content samples and probably related to the scatter in the measured values. The compressive strength of pure ice at 263K[6] was 6.6MPa at lower strain rate (10^{-4}s^{-1}). This pure ice sample was made by bubble free, which would explain why its compressive strength was higher than those of our samples.

The tensile strength increased differently with silicate content from the compressive strength. In Brazilian test, the amount of plastic deformation of ice-silicate mixture samples increases with increasing silicate content. Accordingly, the tensile strength of the specimens with higher silicate content might not be measured precisely. Tensile strength of dunite coarse 50wt% samples was smaller than the serpentine fine 50wt%, while the 50wt% coarse serpentine samples continued plastic deformation without fracture. The

present results are lower than the tensile strength of ice at higher strain rate ($1s^{-1}$), which was found 1.6MPa[3], and those of ice-silicate mixtures at much higher strain rate ($\sim 10^4s^{-1}$), which were 17, 20 and 22 MPa for 0, 5 and 30wt% silicate[3], respectively. This discrepancy is probably due to the higher strain rate.

In general, the ratio of compressive to tensile strength for a brittle material is from about 8 to 20. Thus the present values of the tensile strength were not strange. However, because flat plates were used as loading plates, accurate tensile strength might not be measured[5].

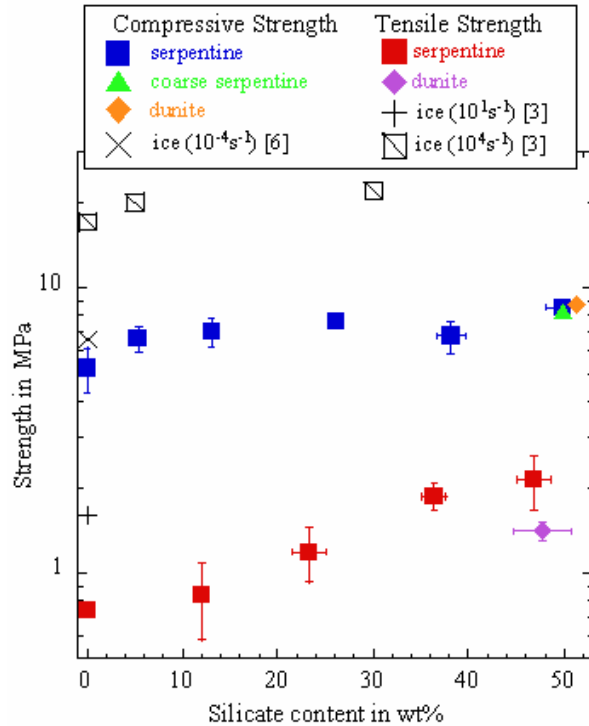


Fig. 3. The relation between the silicate content and the compressive and tensile strength.

4. DISCUSSION

4.1 Crater depth

The initial peak pressure for the mixture targets was calculated[7] using Hugoniot data of ice[8] and serpentine[9]. A value of 6.6MPa[11] is adopted as the compressive strength of the ice specimens.

The crater depth is better scaled by initial peak pressure normalized by the compressive strength than by the tensile strength. However the slope in log-log plot (Fig. 4) becomes shallower at higher peak pressure. This is probably due to higher shock attenuation rate at higher peak pressure[10]. The crater depth found in impact experiments with projectiles of aluminium and polycarbonate[11] are larger than our results and the results of ice-on-ice impact. This is probably caused by the difference of projectile materials.

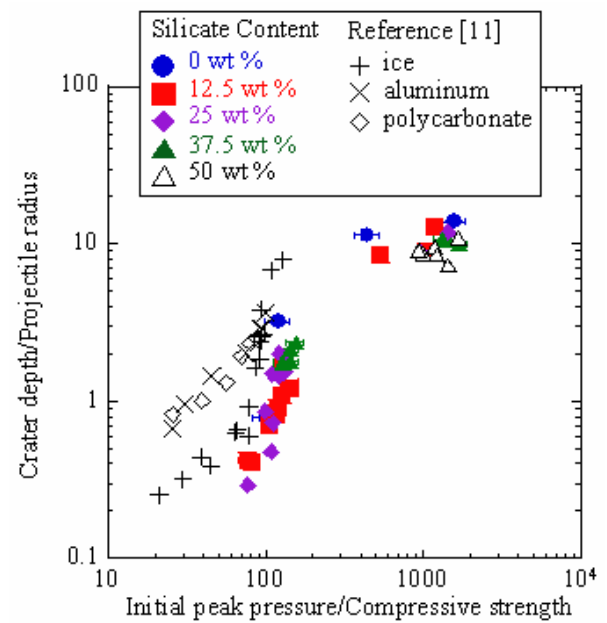


Fig. 4. The relation between normalized initial peak pressure and normalized crater depth. The projectile material of the previous study[11] is shown by different symbols.

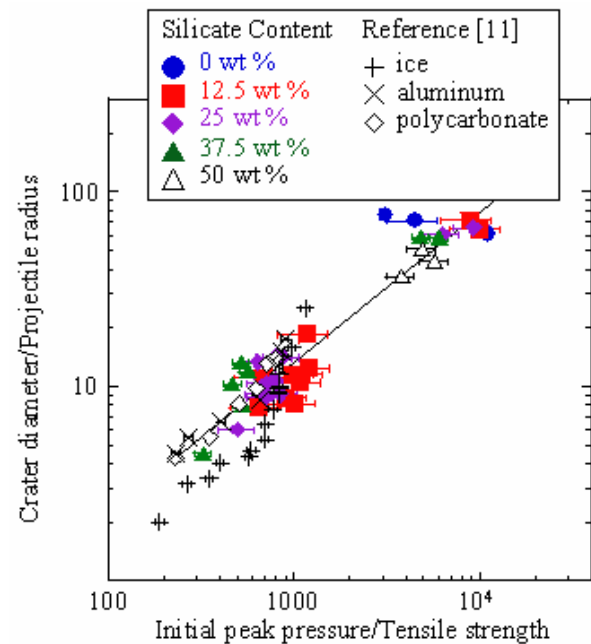


Fig. 5. The relation between normalized initial peak pressure and normalized crater diameter. The projectile material of the previous study[11] is shown by different symbols.

4.2 Crater diameter

The crater diameter is well scaled by initial peak pressure normalized by tensile strength. A least squares fit in Fig. 5 gives

$$\frac{D_c}{a_p} = 0.063 \pm 0.003 \left(\frac{P_i}{Y_T} \right)^{0.78 \pm 0.04} \quad (1)$$

where D_c is the crater diameter, a_p is the projectile radius, P_i is the initial peak pressure and Y_T is the tensile strength.

Although the slope in log-log plot of the crater depth becomes shallower at higher peak pressure, the slope of the crater diameter seems almost constant. This probably indicates that the shock attenuation rate in horizontal direction is not sensitive to the initial peak pressure.

4.3 Crater volume

The crater volume is well scaled by initial peak pressure normalized by tensile strength. A least squares fit in Fig. 6 gives,

$$\frac{C_v}{a_p^3} = (1.5 \pm 0.9) \times 10^{-5} \left(\frac{P_i}{Y_T} \right)^{2.3 \pm 0.1} \quad (2)$$

where C_v is the crater volume. As crater size decreases, the fraction of material ejected by spallation increases. Thus the crater volume depends on the crater diameter and is controlled by the tensile strength. It is consistent that the slope in Fig. 6 seems constant like the plot of the crater diameter. Increase of the tensile strength with silicate content is probably the main reason why the crater volume decreases with silicate content.

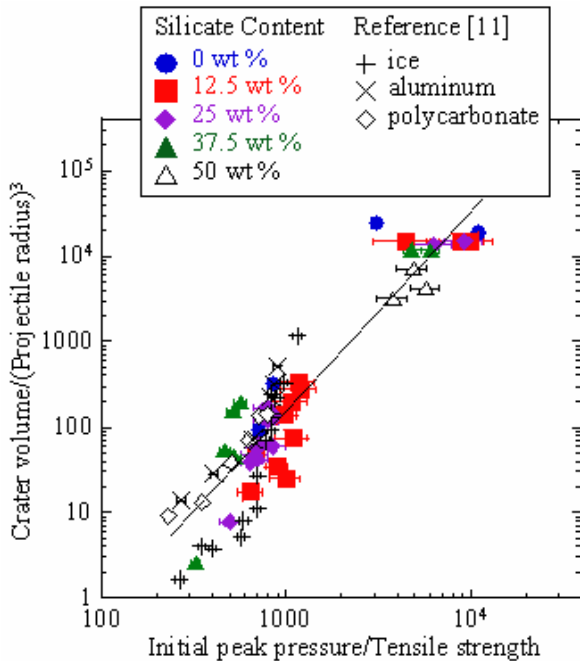


Fig. 6. The relation between normalized initial peak pressure and normalized crater volume. The projectile material of the previous study[11] is shown by different symbols.

5. SUMMARY

We performed impact experiments on ice-silicate mixtures and measured compressive and tensile strength of the targets at low strain rate ($\sim 10^{-3} \text{ s}^{-1}$). The crater volume decreases with increasing silicate content. We confirm that the tendency, which was also suggested by previous work, continues until 50wt% of silicate content. The compressive and tensile strengths increase with silicate content, although the gradient of increase was different. The compressive strength drastically increased when a small amount of silicate was included and, then, it gradually increased for the wide range of silicate content from 12.5 to 50wt%. The tensile strength increased with almost constant gradient. When we apply these strengths to the results of impact cratering, the crater depth and the crater diameter are well scaled by the compressive and the tensile strength of the target, respectively. The crater volume is well scaled by the target tensile strength. Increase of the tensile strength with silicate content is probably the main reason why the crater volume decreases with silicate content.

6. REFERENCES

1. Lange M.A. and Ahrens T.J., Impact Cratering in Ice- and Ice-Silicate Targets: an Experimental Assessment, *Lunar and Planetary Sci. XIII*, 415-416, 1982.
2. Koschny D. and Grün E., Impact into Ice-Silicate Mixtures: Crater Morphologies, Volumes, Depth-to-Diameter Ratios, and Yield, *ICARUS*, Vol. 154, 391-401, 2001.
3. Lange M.A. and Ahrens T.J., The Dynamic Tensile Strength of Ice and Ice-Silicate Mixtures, *J. of Geophys. Res.*, Vol. 88, 1197-1208, 1983.
4. Hiraoka K., et al. Laboratory Experiments of Crater Formation on Ice-Silicate Mixture Targets, *Advances in Space Res.*, in press, 2005.
5. Mellor M. and Hawks I., Measurement of Tensile Strength by Diametral Compression of Discs and Annuli, *Eng. Geol.*, Vol. 5, 173-225, 1971.
6. Arakawa M. and Maeno N., Mechanical Strength of Ice under Uniaxial Compression, *Cold Regions Sci. and Tech.*, Vol. 26, 215-229, 1997.
7. Kani K., et al. Hugoniot of Eight Meteorites, *Proce. of 18th Int. Symp. on Shock Waves*, 447-452, 1991.
8. Stewart T.S. and Ahrens T.J., Shock Hugoniot of H₂O Ice, *Geophys. Res. Lett.* Vol. 30(6), 1332, 2003.
9. Marsh S.P., *LASL shock Hugoniot data*, Univ. of California Press, London, 1980.
10. Holsapple K., The Scaling of Impact Processes in Planetary Sciences, *Annu. Rev. Earth Planet Sci.*, Vol. 21, 333-373, 1993.
11. Kato M., et al. Ice-on-Ice Impact Experiments, *ICARUS*, Vol.133, 423-441, 1995.

SHOCK EFFECTS AND PETROLOGICAL FEATURES OF THE OHABA CHONDRITE

G. O. Iancu⁽¹⁾, Y. Miura⁽²⁾, G. Kurat⁽³⁾, F. Brandtstaetter⁽³⁾

¹*Dept. of Geology and Geochemistry, University "Al. I. Cuza" of Iasi, B-dul Carol I 20A, 700505 Iasi, Romania,
Email: ogiancu@uaic.ro*

²*Dept. of Earth Sciences, Yamaguchi University, Yoshida, Yamaguchi, 753-8512, Japan,
Email: dfb30@yamaguchi-u.ac.jp*

³*Naturhistorisches Museum, Postfach 417, A-1014, Vienna, Austria, Email: franz.brandtstaetter@NHM-WIEN.AC.AT*

ABSTRACT

The Ohaba meteorite, which fell on October 11, 1857, in Transylvania (Alba District, Romania) has been classified in this study as an H5 chondrite based on the petrologic features and the chemical composition of olivine and pyroxene. By studying the shock effects in silicates and metallic phases we estimate the shock degree of this meteorite as S-3.

INTRODUCTION

The Ohaba meteorite fell in October 11, 1857, in Transylvania (Alba District, Romania). After appearance of a fireball, followed by detonations, a stone of 16.25 kg was found by a priest [1,2,5,7,9]. The fragments recovered are kept in 16 museums from 11 countries. The Museum of Natural History from Vienna is the repository of the main mass (15.73 kg). The samples of the Ohaba chondrite are kept in 16 foreign museums from 11 countries.

The meteorite was previously classified as an H5 veined ordinary chondrite, based on olivine composition – Fa₂₀, as in [4].

SAMPLES AND ANALYTICAL METHODS

Two polished thin sections representing the Ohaba chondrite were studied under the microscope in both transmitted and reflected light. In order to determine the shock degree of this chondrite the mineral grains were examined with 20x- or 40x- objectives as in [10] and with the electron microprobe. Quantitative chemical analyses of the constituent minerals were obtained on the carbon-coated, polished thin sections by using a JEOL JSM-6400 scanning electron microscope at the Museum of Natural History from Vienna. The instrument was operated at an accelerated voltage of 15 kV, a 38.5 nA beam current and 39 mm working distance. About 30 points of both olivine and orthopyroxene were measured on each thin section.

PETROLOGIC TYPE OF THE KAKOWA METEORITE

The microscopic study in thin sections revealed the presence of the following types of chondrules in the

Ohaba chondrite: readily distinguished PO – porphyritic olivine (Fig. 1), RP – radial pyroxene, BO – barred olivine (sometimes polysomatic; Fig. 2) and GOP – granular olivine-pyroxene chondrules, ranging in size from 300 µm to up 1200 µm. The matrix is recrystallized, the feldspar (An₁₅Or₃) occurs in grains smaller than 50 µm and the igneous glass is absent. Pyroxenes are mainly orthopyroxenes but less than 10% of the grains are clinopyroxenes with Wo₃₇ (mole percentage), which is similar to diopside composition. Other minerals identified in polished thin sections are kamacite (Fig.3), troilite, taenite, plessite, chromite and magnetite.

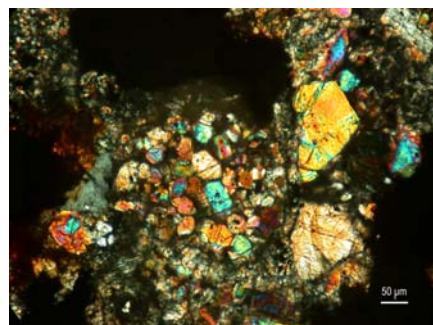


Fig. 1. Readily distinguished PO chondrule, 2N

Based on petrographic data, the Ohaba chondrite is classified as petrologic type 5, consistent with the data printed in [1]. Reference [6] reported a density of 3.38 g/cm³ for Ohaba which is close to the bulk density found by [11] for the H group: 3.44 ± 0.19 g/cm³.

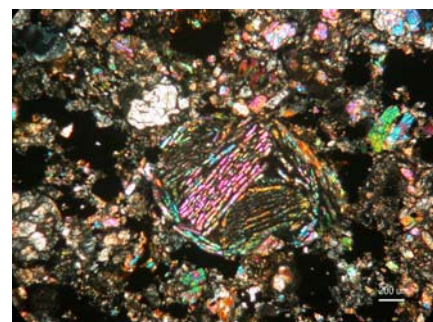


Fig. 2. Readily distinguished BO chondrule, 2N

Analysis of 15 olivine grains from two thin sections shows a variation in composition from Fa₁₄ to Fa₁₅

mole% fayalite (avg. Fa_{15} ; PMD 2.2%). Twelve orthopyroxene grains from thin sections show a range in composition from Fs_{13} to Fs_{16} mole % ferrosilite (avg. Fs_{14} ; PMD 6.06%).

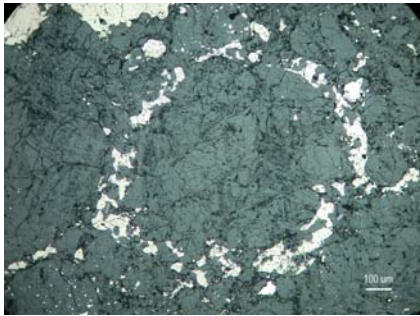


Fig. 3. Rim of kamacite bordering a BO chondrule (RL), 1N

Taking into account the iron-content of olivine plotted against iron-content of orthopyroxene [3], Ohaba meteorite may be considered as an ordinary chondrite – H₅, belonging to the primitive meteorites class (Fig. 4), consistent as well with the data published by [1].

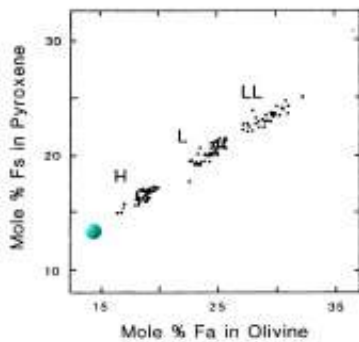


Fig. 4 - Iron-content of olivine plotted against iron-content of orthopyroxene as in [3]

SHOCK EFFECTS

The shock effects in ordinary chondrites vary with increasing shock intensity such that a progression of characteristic stages of shock metamorphism can be recognized and arranged on a relative scale of increasing degree of deformation and alteration of the constituent mineral phases. Therefore, a particular ordinary chondrite sample can be assigned to a specific "shock stage" or to a "shock facies" [10]. The shock effects in chondritic silicates for which an accurate shock pressure calibration is available include the following major deformation and transformation phenomena in olivine, oligoclase, and pyroxene observable in the petrographic microscope:

1) Mechanical deformations - a) undulatory extinction in olivine, pyroxene and plagioclase; b) planar fractures and planar deformation features in olivine and planar deformation features in plagioclase; c) mechanical

twinning in pyroxene and d) mosaicism in olivine, pyroxene and plagioclase.

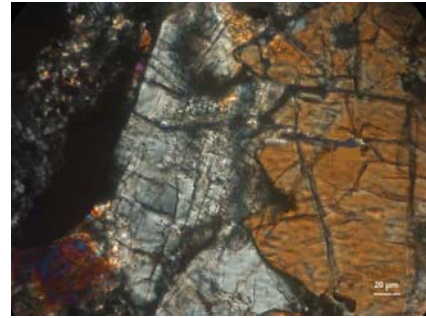


Fig. 5. Planar fractures and undulatory extinction in olivine, 2N

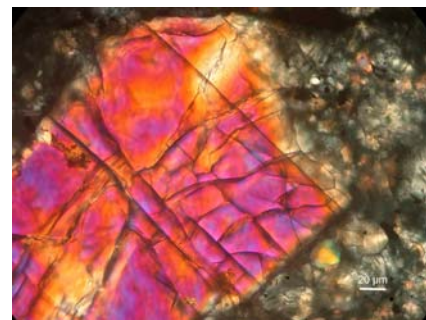


Fig. 6. Olivine with one set of parallel planar fractures, 2N

2) Phase transformations - a) transformation of plagioclase into diaplectic glass (maskelynite); b) melting of plagioclase and formation of (normal) glass; c) solid state recrystallization of olivine; d) melting of olivine and formation of fine-grained polycrystalline olivine and e) transformation of olivine and pyroxene into ringwoodite and majorite, respectively, and / or dissociation of olivine into several crystalline or glassy phases.

Reference [8] stated that in addition to shock events in olivine, plagioclase, orthopyroxene and Ca-pyroxene, petrographic shock indicators in equilibrated ordinary chondrites (OC) include chromite veinlets, chromite-plagioclase assemblages, polycrystalline troilite, metallic Cu, irregularly shaped troilite grains within metallic Fe-Ni, rapidly solidified metal-sulfide intergrowths, melting of metal (and troilite), martensite and various types of plessite, metal-sulfide veins, large metal and/or sulfide nodules, silicate melt veins, silicate darkening, low-Ca clinopyroxene, silicate melt pockets, and large regions of silicate melt. The presence of some of these indicators in every petrologic type-4 to -6 ordinary chondrite demonstrates that collisional events caused all equilibrated OC to reach shock stages S3-S6. From the above features, in the Ohaba chondrite we observed olivine with undulatory extinction, irregular fractures (Fig. 5) and planar fractures (Fig. 6),

plagioclase with undulatory extinction and metal-sulfide melt drops along planar fractures in olivine (Fig. 7). The shock degree of this chondrite may be estimated as S-3 (weakly shocked).

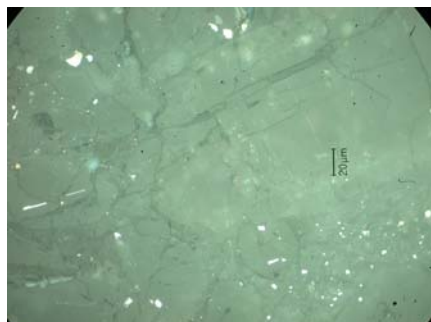


Fig. 7. Metal-sulfide melt drops and troilite along planar fractures in olivine (RL), 1N

CONCLUSIONS

The results of this study are summarized as follows:

1. Based on electron probe microanalyses and optical microscope study, the Ohaba meteorite is a typical H5 chondrite. The result is consistent with the classification of this chondrite made by [4].
2. The degree of shock metamorphism reached by Ohaba meteorite during its evolution in space is S-3 (weakly shocked).

ACKNOWLEDGMENTS

We are grateful to Professor dr. Corina Ionescu and dr. Dana Pop from the Mineralogical Museum of Babes-Bolyai University, Cluj-Napoca, Romania.

This work was mainly supported by the Romanian Ministry of Education and Research (CNCSIS grants no. 547/2002 and 90/2003).

REFERENCES

1. Graham, A.L., Bevan, A.W.R., Hutchison R., Catalogue of meteorites; with special reference to those represented in the collection of the British Museum (Natural History), 4th ed., *British Museum (Natural History)*, London, 460, 1985.
2. Hörnes M., Über den Meteorsteinfall bei Ohaba im Blasendorfer Bezirke in Siebenbürgen, in der Nacht zwischen dem 10. Und 11. October 1857, *Sitzungsberichte der Akademie der Wissenschaften*, Wien, 79-85, 1858.
3. Keil K., Fredriksson K., The iron, magnesium and calcium distribution in coexisting olivines and rhombic pyroxenes in chondrites. *J. Geophys. Res.*, 64, 3487-3515, 1964.
4. Mason B., Olivine composition in chondrites. *Geochimica et Cosmochimica Acta*, 27, 1011-1023, 1963.
5. Maxim I. A., Meteoriti și materiale meteoritice din România, *Studia Univ. Babeș-Bolyai, Ser. Geol. - Geogr.*, 1, Cluj-Napoca, 3-6, 1968.
6. Moșiu A., Neșțianu T., Romanescu D., Relații între proprietățile fizice și compoziția mineralogică a meteoritelor din România și aspecte comparative cu unii meteoriti din alte țări, *St. Cerc. Geol., Geofiz., Geogr., Geofizică*, 18, București, 11-24, 1980.
7. Neugeboren J.L., Meteorsteinfall in der Nacht zwischen dem 10. Und 11. October d. J. Bei Ohaba im Blasendorfer Bezirke nach amtlich eingegangenen Berichte, *Verhandlungen und Mitteilungen des siebenbürgischen Vereins für Naturwissenschaften*, 8, Sibiu, 229-230, 1857.
8. Rubin A.E., Postshock annealing and postannealing shock in equilibrated ordinary chondrites: Implications for the thermal and shock histories of chondritic asteroids. *Geochimica et Cosmochimica Acta*, 68, 673-689, 2004.
9. Stanciu V., Stoicovici E., Meteoriti din România, *Rev. Muz. Mineral. Geol. al Univ. din Cluj la Timișoara*, VII/1-2, 2-34, 1943.
10. Stöffler D., Keil K., Scott E.R.D., Shock metamorphism of ordinary chondrites, *Geochim. Cosmochim. Acta*, 55, Pergamon Press, 3845-3867, 1991.
11. Wilkison S.L., Robinson M.S., Bulk density of ordinary chondrite meteorites and implications for asteroidal internal structure. *Meteoritics & Planetary Science*, 35, 1203-1213, 2000.

IMPACT SIMULATION WITH FRACTURE AND POROSITY

Martin Jutzi and Willy Benz

Physikalisches Institut, University of Bern, Siedlerstrasse 5, 3012 Bern, Switzerland

ABSTRACT

Our Smooth Particle Hydrodynamics (SPH) impact code can be used to model impact and collisions in the strength- and gravity-dominated regime (Benz & Asphaug, 1994). Here we describe the extension of this numerical tool with a porosity model. The model is based on the so called $P - \alpha$ model which is adapted for implementation in our code. We are now capable of performing SPH simulations including fracture and porosity and report some very encouraging results.

Key words: SPH, impact physics, porosity.

1. INTRODUCTION

Spacecraft missions and ground based observations are providing increasing evidence that many or even most asteroids are porous (Housen & Holsapple, 2003). Also comets are thought to have highly porous structures. Porosity may also play an important role in the formation of planets as the dissipative properties of porous media will enhance the collisional sticking mechanism required to build planetesimals. In order to study the effects of porosity in impacts and collisions, we have developed a numerical model suitable for the calculation of shock dynamics and fracture in porous media.

2. NUMERICAL METHOD

Our numerical tool is based on the Smooth Particle Hydrodynamic (SPH) method. In order to simulate solids, standard SPH was extended to include (Benz & Asphaug, 1994):

- elastic-perfectly plastic strength model
- fracture model based on the Weibull distribution of flaws

Therefore, our impact code can be used to model impacts and collisions involving solid bodies in the strength- and gravity-dominated regime. This was successfully tested at different scales.

2.1. Tests of our method

At small scales, the method was validated by simulating laboratory impacts. Our model predicts shapes, locations and velocities of the largest fragment with high accuracy (Benz & Asphaug, 1994).

A natural laboratory for studying collision physics at larger scales is provided by the twenty or more asteroid families identified in the asteroid belt. By simulating classes of collisions, our model was able to reproduce the main characteristics of such families (Michel et al., 2003).

2.2. Extension of our numerical method: Including a porosity model

While porosity at large scales can be modelled explicitly by introducing macroscopic voids, porosity on a scale much smaller than the numerical resolution has to be modelled through a different approach. Our porosity model is based on the so called $P - \alpha$ model (Herrmann, 1969). The model provides a description of microscopic porosity with pore-sizes beneath the spatial resolution of our method.

According to the $P - \alpha$ model, the distention α is defined as

$$\alpha = \frac{\rho_s}{\rho} \quad (1)$$

where ρ_s and ρ are the density of the solid (matrix excluding the pores) and the bulk density (including the pores), respectively. Porosity is related to distention as $1 - 1/\alpha$. We use the variable α to extend the following equations/models of our method (Jutzi, 2004).

$$P \rightarrow P(\alpha) \quad (2)$$

$$S^{ij} \rightarrow S^{ij}(\alpha) \quad (3)$$

$$D \rightarrow D(\alpha) \quad (4)$$

where P is the hydrostatic pressure, S^{ij} the deviatoric stress tensor and D the variable damage. The time evolution of the distention α is given by

$$\dot{\alpha} = f(\alpha, \rho, E, \dot{\rho}, \dot{E}) \quad (5)$$

where E is the specific energy.

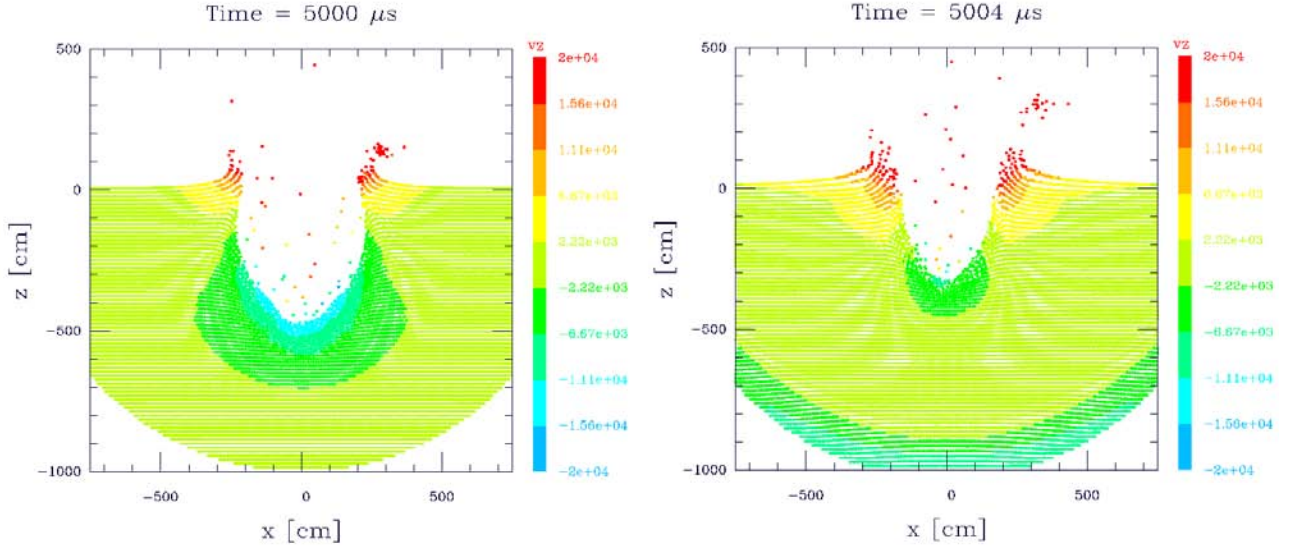


Figure 1. Comparison between simulation of an impact in porous ice (left) and nonporous ice (right)

All parameters used by our porosity model are material parameters which can in principle be measured; most of them quite easily (e.g. the so called crushcurve) even though this is rarely done in practice. Others such as Weibull parameters, shear strength etc. are more difficult to measure.

3. PRELIMINARY RESULTS

In porous material, the stress wave produced in a impact is attenuated due to the energy expense needed to collapse the pores. Furthermore, crater and ejecta blanket formation is different in porous material. In contradiction to solid material, there is only a small amount of ejecta and the crater volume is primarily formed by compaction.

Using our model, this behavior of porous material can be reproduced as it is shown in this section. Moreover, simulations of laboratory impacts show a good agreement between the shape of craters obtained by the simulation and the experiment.

3.1. Impact in porous ice

To demonstrate the described behavior of porous material we compare an impact in porous ice ($\alpha_0=1.5$) and an otherwise identical impact in nonporous ice. The impact velocity is 10 km/s. The simulations are shown in figure 1 where the colors label the vertical velocity of the particles (positive values indicate ejection).

As it can be seen, there is much less material ejected in the case with porous ice (left) than with nonporous ice (right). Obviously, the crater in the porous material is

formed primarily by compaction of the material. A measure of the compaction is provided by the actual value of the distention α which is shown in figure 2.

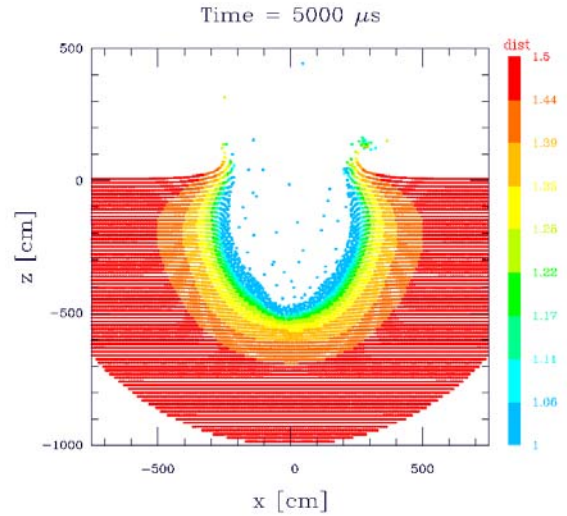


Figure 2. Impact in porous ice. The initial distention of $\alpha_0=1.5$ is decreased to $\alpha=1$ in a small zone around the crater. With increasing distance from the crater, distention increases until $\alpha = \alpha_0$.

3.2. Laboratory impact

In order to test our model we simulate laboratory impacts in porous material performed by Housen & Holsapple (2003). In these experiments, a mixture of sand, perlite, fly ash and water was used to obtain a highly porous ma-

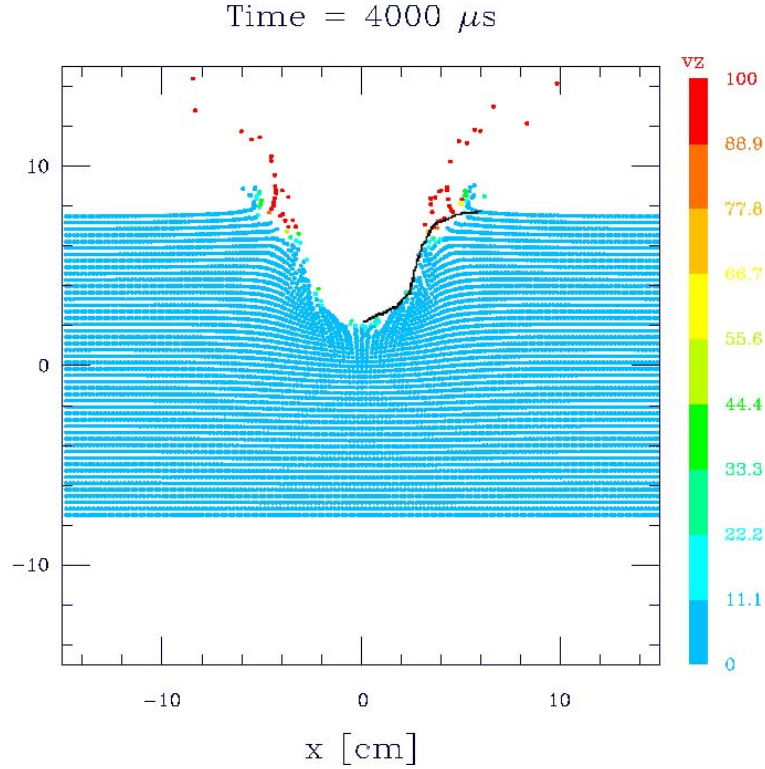


Figure 3. Simulation of a laboratory impact in porous material ($\alpha_0=3.3$). The colors label the z -component of the velocity, the black line represents the experiment.

terial ($\alpha_0=3.3$). As impactor served a polyethylene bullet of 1.3g with an impact velocity of 1.9 km/s. Figure 3 shows the simulation of this impact. Taking into consideration that particles with positive velocity (red) will be ejected, the agreement with the experiment (black line) is reasonable. However, not all necessary material parameters were measured and some reasonable values were chosen for the missing ones.

4. CONCLUSION

Using our extended numerical method including porosity for the simulation of impacts in porous material, we get reasonable results. The expected effects of porosity are reproduced as well as the shape of craters generated in laboratory impacts. However, to validate our model, comparisons to appropriate experiments are needed where all necessary material parameters can be measured.

5. ACKNOWLEDGEMENT

The authors gratefully acknowledge partial support from the Swiss National Science Foundation.

REFERENCES

- Benz W., Asphaug E., 1994, ICARUS 107, 98
- Herrmann W., 1969, J. Appl. Phys., 40, 2490-2499
- Housen K.R., Holsapple K.A., 2003, Icarus, 163, 102-119
- Jutzi M., 2004, Diploma thesis, University of Bern.
- Michel P., Benz W., Richardson D.C., 2003, Nature, 421, 608-611

FLOOR-FRACTURED CRATERS ON THE TERRESTRIAL PLANETS – THE MARTIAN PERSPECTIVE

J. Kortenienmi⁽¹⁾, M. Aittola⁽¹⁾, T. Öhman^(1,2), J. Raitala⁽¹⁾

⁽¹⁾ *Astronomy, Physical Sciences, P.O. Box 3000, 90014 University of Oulu, Finland, Email: JarmoKortenienmi@oulu.fi*

⁽²⁾ *Department of Geosciences, Division of Geology, P.O. Box 3000, FI-90014 University of Oulu, Finland.*

ABSTRACT

Floor-fractured craters appear to occur on all the cratered terrestrial planets. Their floors are typically raised as a whole, or they are cut into large elevated blocks. The floors exhibit radial, concentric and/or polygonal fractures, occasionally mixed with volcanic features. The craters occur almost always next to large regional volcanic provinces, indicating an intimate relationship with endogenic activity. This paper reviews shortly the multitude of past work done on the floor-fractured craters in the inner Solar System. We also provide the preliminary results of a new survey done on Martian floor-fractured (and related) craters.

1. INTRODUCTION

Fractured floors are a type of anomalous features which can be found in impact structures. Instead of ‘regular’ flat floors with just peak rings, pits or occasional slumps from the walls, they exhibit intense modification of the crater interiors, including fracturing and uplifting [1]. They occur near large regional volcanic provinces, indicating an intimate relationship with them. Floor fractures occur only in some impact craters (FF craters) but not in most. Thus they are representations of endogenic processes, which emerge into view only through impact structures and special conditions. This is probably caused by the combination of the undercrater environment, e.g. the subcrater fracture zone, and its occurrence just in the “right” place and time.

2. DESCRIPTIONS AND CLASSIFICATIONS

FF craters are a diverse group, which can be classified using several properties. Although generally similar from planet to planet, they do occur in slightly varying forms, indicating the environment they reside in.

2.1. Basic types

Much of the fundamental observational data on the FF craters have been gathered from the Moon [e.g. 1-5]. The idealized floor-fractured impact crater exhibits both concentric and radial crevasses/troughs, with an

additional circumferential moat near the crater rim. [1] found that the FF craters are generally clearly shallower and tend to often have 2-3 times smaller rim to peak ring elevation differences than unmodified craters in the same region, indicating that the FF crater floors have been uplifted by some process. There are, of course, several deviations from the basic form, and classifications can be used to categorize the features.

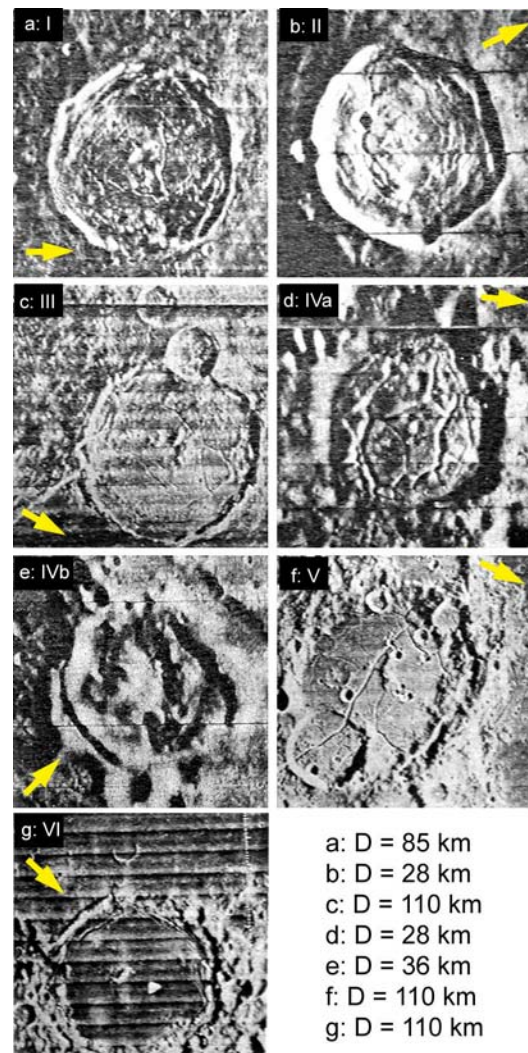


Fig. 1. Examples of fractured-floor crater classes I-VI (see text). Yellow arrows show rough estimation of Sun direction. Modified from [1].

Classification by [1] puts the Lunar FF craters into six types, representing degrees of modification, initial appearance and size, and possible different crater origins. In short, they are (see Fig. 1 for reference):

- I) 16 fresh-looking deep large craters (D ~50-120 km); central peaks and concentric/radial fracture patterns; elongate pits and dark mantle deposits in fractures near the wall; typically near shallow maria, only two individuals in the highlands.
- II) 23 shallow small craters (D ~20-40 km); hummocky floors and fractures; near/within maria.
- III) 37 shallow small craters (D ~20-100 km); wide U-shaped moats next to crater wall; a symmetric ridge borders the raised floor plate; cones and fissures are common; near maria.
- IV) 92 small craters (D ~20-30 km); narrow V-shaped moats with a ridge bordering it; ridge can be higher than the crater rim (class IVb; 7 craters). Situated mostly at great distances from the maria.
- V) 25 medium-size craters (D ~70 km); relatively unmodified; polygonal/concentric fractures; deep or shallow depending on post-impact modification stage prior to fracturing; near the maria.
- VI) 13 craters (D ~20-120 km); fractured mare or mare-like plains; fractures polygonal, radial or concentric; some low-relief hummocks.

Many Lunar floor-fractured craters also exhibit dark mantling, cone structures placed on and immediately next to the fractures, and occasionally fresh floor units overlying the older fractured terrain; these have been interpreted as volcanic units [e.g. 1,2,6,7].

2.2. Martian deviances

On Mars, the basic FF crater form is the same as on the Moon (Fig. 2a), though some exhibit properties not found elsewhere. [8-10] showed that these craters have a more extensive and wider system of fractures (Fig. 2b), which they interpreted as volatile-induced enhancement of the fracture formation. Additionally, the Martian craters exhibit more often a polygonal fracture system, indicating repeated periods of floor uplift and subsidence [8].

Additionally, two other crater types found on Mars should be mentioned here, as they are related to the FF craters. Firstly, craters with chaotic floors (CF craters) occur in the same regions (see chapter 3 for details on the distribution). These crater floors are so heavily dissected that instead of fractures, they rather exhibit deep floors with only remnant mesas and knobs inside (Fig. 2c). Often the “craters” themselves are so highly modified that they can only be interpreted as ancient remains of impact craters, as they have no rim or ejecta blanket. The chaotic regions are described and discussed in detail e.g. in [11 and references therein]. Together with the FFs, the CFs have been interpreted

to create a sequence of crater modification stages [12]. Smallest FF fractures and moats seemingly develop and larger concentric and radial fissures of the fully grown FF craters. Continuing this deformation, they cut the crater floor into pieces; in the end this results in a CF crater-like circular depression with a chaotically dissected floor, which often ends up with partly collapsed or totally destroyed walls [e.g. 11,13].

Secondly, regions harbouring FF craters also exhibit crater floors with irregular depressions (ID craters, see Fig. 2d) [14-16]. These depressions have typical depths of 50-300 m, and are mostly small compared to the parent crater (cover usually <20% of crater diameter). The depression walls exhibit layers, indicating a sedimentary origin of the surrounding material; usually the craters with IDs are rather shallow compared to average fresh craters. This is seen as evidence for crater filling by deposited materials. However, these depressions are typically not found outside impact craters. The ID craters are usually not connected with any fluvial or major tectonic features directly capable of explaining the depressions. The ID craters often occur on the outskirts of the FF crater clusters, and ostensibly continue the FF-CF sequence. However, it must be emphasized that this proposed sequence does not necessarily represent a proven developmental continuum.

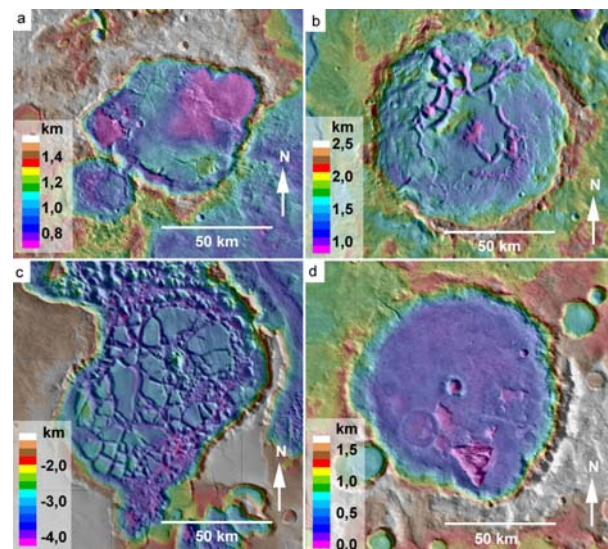


Fig. 2. Martian FF craters shown in Viking MDIM2 detail with MOLA colors. **a)** Narrow concentric / radial crevasses along the border of an uplifted central plate (16°N, 56°E); note the southern edge moat. **b)** Wider fissures (3°N, 53°E) common only to Mars. **c)** This chaotically fractured crater pair (3°N, 331°E) has a broken northern rim and a connection to nearby fluvial channel. The fracture patterns still retain the crater shapes. **d)** 3-part irregular depression complex (32°S, 41°E); a triangle-shaped S portion and two shallower irregular depressions NE and NW from it.

Although irregular and very diverse as a group, directional patterns do emerge from the depressions; many of the depression walls are straight. These ID walls are usually either 1) radial or concentric to the parent crater, or 2) straight and parallel to each other within a cluster of ID craters in particular regions [17]. This may indicate that the ID formation is controlled, enhanced or enabled in the first case by the crater structure itself, similar to the radial and concentric FF fractures. In the second case they appear to be controlled by a regional trend - the main direction was radial to the nearby Hellas region [17]. Similar regional patterns are also observed e.g. in the distribution of polygonal crater wall directions [18,19].

3. FRACTURED CRATER DISTRIBUTIONS

3.1. Moon

On the Moon 206 craters have been recognized to be floor-fractured [1]. They are situated on a relative narrow region on the highlands, surrounding the mare regions. Mainly those belonging to class IV are additionally spread around farther away from the maria. The distribution differs considerably from that of the global crater population, inferring their close relationship with the mare development [1].

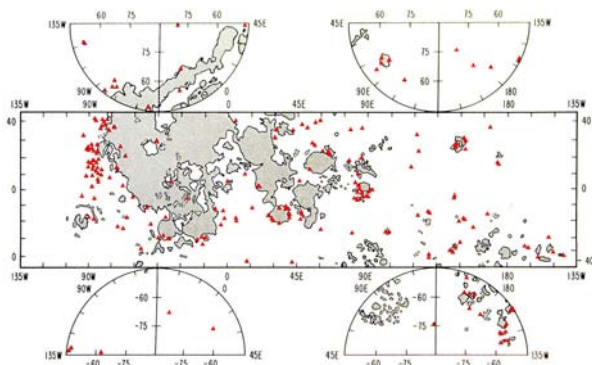


Fig. 3. Distribution of floor-fractured craters (red triangles) on the Moon relative to the maria (grey) and the highlands (white). Note the dense clusters near some of the large basins. Modified from [1].

3.2. Mars

Martian floor-fractured craters are mostly distributed along a narrow band south of the dichotomy boundary in Arabia Terra (0-45 °N, -15-120 °E) and at the mouths of Valles Marineris and the adjacent outflow channels (-20-10 °N, 305-355 °E). 80 FF craters were found and categorized using Mariner 9 and preliminary Viking data [8]. A newer search, using standardized Viking MDIM2 and MGS MOLA data, revealed a total of 111 FF craters [15,16], strengthening the same

regional trend as found before (Fig. 4). At the same time, additional 69 CF craters were recognized to lie at the northern sides of the regional FF clusters - generally directly on the dichotomy boundary.

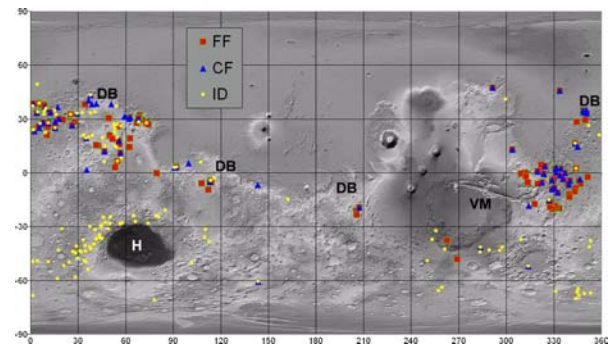


Fig. 4. Distribution of Martian craters with floor-fractures (red boxes), chaotic floors (blue triangles) and floors with irregular depressions (yellow circles). The main concentration of FF, CF and some ID craters is near the dichotomy boundary (DB) and the mouth of Valles Marineris (VM), and the separate cluster of IDs near the Hellas basin (H). Data from [16].

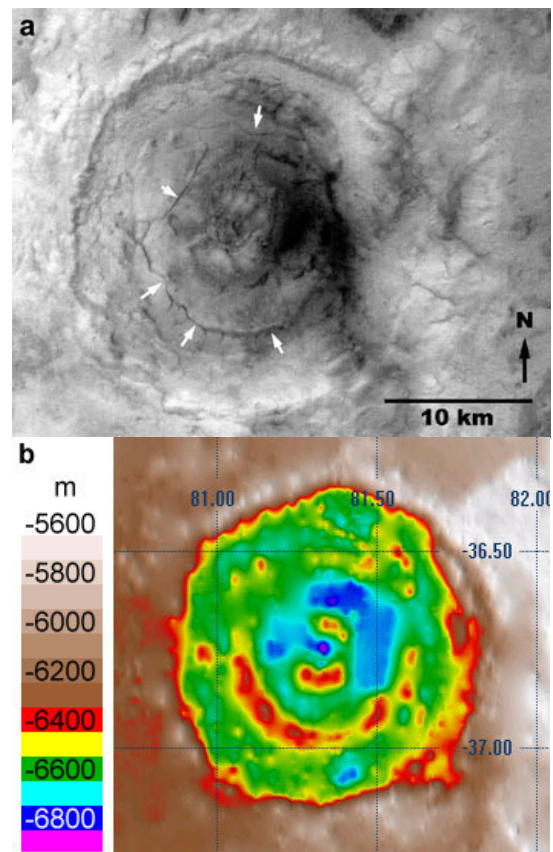


Fig. 5. a) Newly found 52-km Martian floor-fractured crater (36.7 °S, 81.2 °E); arrows show the concentric fracture system with radial branches. HRSC orbit 49, modified from [21]. **b)** MOLA topography; noted fractures lie on the concentric >200 m high ridge top.

Additional 129 ID craters were identified; roughly 1/3 of which are situated in or immediately adjacent to the Arabia Terra FF clusters, while 2/3 lie in a separate distinct faction north and west the Hellas basin with a 'tail' in Noachis Terra thinning out towards Argyre [14-17,20-23]. Continuing this work, one FF crater was identified (and a few proposed) on the floor of the southern Hellas impact basin (Fig. 5) [16,21], perhaps indicating that also the Hellas floor has been volcanically active and not just flooded with lavas from nearby volcanic centers, Hesperia and Malea Plana.

3.3. Other planets

Mercury has been imaged only partly, and with a rather poor ~1 km pixel resolution. Because of this, no definite floor-fractured craters have yet been identified there. However, [24] found several good candidates searching for intracrater dark haloes or other color variations indicating post-impact emplacement of mafic materials onto the floor. They did find several crater floors with contrasting deposits, and additionally a few rimmed moat-like depressions (see Fig. 6). However, all the found structures are either ambiguous or just at the edge of resolution. Thus, more detailed data is needed for proof of Mercurian FF craters.

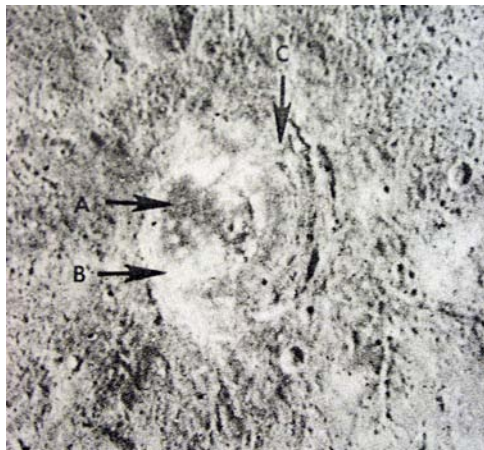


Fig. 6. (left) The Mercurian 120-km crater Zeami (2°S, 148°W) shows dark (A) and bright (B) regions on its floor. C shows a possible rimmed moat, similar to those of the Lunar FF craters. Modified from [24].

Both **Venus'** and Earth's geologic records have been cut off by the intense resurfacing phenomena reworking the planets. Thus, the most ancient and cratered surfaces are mostly wiped out on both planets. However, according to the online databases, over 942 craters remain on Venus [25,26]. Out of these, only a few probable FF craters have been recognized [27-29].

Earth has preserved only 174 impact structures recognized (proven) so far [30], but still two large

terrestrial craters exhibit features which can be interpreted as being result of the floor-fracturing processes. [31] proposed that the 55 km central floor of the Manicouagan structure was uplifted by a post-impact tabular magmatic body leaving behind the circular moat we see today. They also state that the outer ring structure of Manicouagan was produced by a ring dike intrusion originating from that magma. However, the authors do admit that their idea is not entirely airtight.

The Sudbury structure has offset dikes, which have been taken by [32] to represent post-impact magma injections. They continue to state that the dike pattern may reflect the flexural uplift of the crater floor during its post-formation isostatic movement, showing resemblance to Lunar floor-fractured craters. They also acknowledge that the source is probably not an independent endogenic intrusion; instead it is an independent injection from the impact melt sheet body. [33] indeed recognize that the dikes are genetically related to the igneous complex in the impact crater. However, they conclude that it was caused by the collapse of the transient cavity and subsequent back-injection of impact-caused melting or by peak ring formation during rebound.

4. FORMATION MODELS FOR THE FRACTURED FLOORS

The morphology of the FF craters suggests that they have undoubtedly been modified by an endogenic process uplifting the crater floor [e.g. 1]. Judging from their distribution, this is apparently related to regional volcanism, but the mechanism is under some debate.

Classically there are two models, which have been used to explain the floor-fracturing of some craters; 1) laccolith intrusions traversing along subcrater fracture patterns and 2) viscous relaxation of the crater floor over time. Both mechanisms can explain the development of the observed features in individual floor-fractured craters, but they have distinctly different implications for the nature of local crustal conditions during crater modification. Below we summarize the model ideas but do not go deep into model implications. These models have been studied and compared thoroughly in [34,35].

4.1. Intrusion model

In the intrusion model, laccolith protrudes through the fractured undercrater zone directly or indirectly into the subcrater brecciated region. This causes a small magma chamber to form into the subcrater brecciated region (inside the transient crater). Subsequently the floor is uplifted *en bloc* and fractures occur on the floor surface. If the volcanism reaches the surface, some

flooding of the crater floor may occur. Thus the FF craters indicate sites of individual intrusions, in a region / time when large subsurface magma chambers and/or surface mare /lava plains units are emplaced [1,2,34,36].

4.2. Relaxation model

The elastic or “elastoviscoplastic” relaxation model requires the crustal viscosity to be quite low at depth. This in turn would enable the impact crater to search a new equilibrium state after its formation, and create the features seen today. This model requires that the crustal viscosity scheme is somehow altered either locally or regionally near the affected craters. This is thought to occur at time periods of active (mare) volcanism, and thus the floor-fractured craters would reflect the extent and intensity of regional heating [37,38]. The fractured crater floor is at the roughly same elevation as the exterior mare elevation, suggesting isostatic adjustment. This scheme has later been modelled [34,35,39] and proven to be unsatisfactory in explaining all the FF features [35]. Not all impact craters of similar size, age or location are affected by this modification process. Thus it is felt that internal magma plumbing, rather than isostatic adjustment, controlled the crater modification [24].

4.3. Enhancement by volatiles

The wider Martian FFs and chaotic crater floors are generally thought to be the result of volcano-ice/water interaction [8-11,13]. In this scenario, water (or possibly CO₂?) trapped in the subsurface reacts to the raised temperatures induced by the magmatic intrusion. It is melted, and either flows through subsurface drainage systems [see 11 for details], evaporates into the atmosphere or escapes through fluvial channels on the surface. The craters with the widest floor-fractures are indeed sometimes connected to small or medium-sized fluvial outlets, and the CF craters are the usual starting points of major outflow channels.

If the craters with irregular depressions found on Mars indeed are related to FF craters, the occurrence of a major ID cluster around Hellas basin can be explained. In our view, this also requires the presence of volatiles in the sediments filling the parent crater. The proposed sequence is as follows. 1) A crater forms, and later becomes partly filled with volatile-laden sediments. 2) A laccolith injection occurs, forming a magma chamber beneath the crater floor, raising it and its general temperature. 3) The volatiles in the sediments warm up and become mobile; they are either pumped out through a subsurface drainage system (as no surface tracks are visible), or they vaporize straight into the atmosphere. 4) The volume

left by the removed volatiles is collapsed, where applicable, controlled by regional /local stress patterns.

5. DISCUSSION

As for Mars, the discovery of a floor-fractured crater inside the giant Hellas impact basin may indicate that the region is or at least has been more active volcanically than has previously been believed. This is further supported by the interpretation that the ID craters, abundant in the region, may in fact be a continuation of the FF-CF sequence [15]. Additionally, the thorough analysis of one ID crater pair on the Hellas rim [22] showed at least a possibility of long distance dikes propagating and penetrating into the crater floor. The floor of the Hellas basin is often covered by dense cloud layers and dust in the atmosphere – it has only recently been imaged thoroughly with a good resolution by the HRSC, THEMIS and MOC cameras. Thus, a more detailed search of the Hellas rim and floor craters for signs of fracturing (as well as other possible volcanic features) will provide new insight to both 1) the large scale modification of the crust by a Hellas size impact, and 2) regional interaction between volcanism and volatile-rich subsurface.

The eminent search for floor-fractured craters on all terrestrial planets, their categorization and interpretation done in the 1970's and early 80's [1-5, 8-10, 24, 31, 37-38] is an extremely good basis for work using new data and new methods at hand today. As recently acquired data has shown [21], not all floor-fractured craters have previously been recognized, e.g. due to resolution constraints. The apparent absence of terrestrial FF craters may provide interesting clues to the crater formation and later modification – why do no FF craters appear to occur on Earth? Would the best place to create such a crater be a tectonic plate border with abundant volcanism, and if so, how quickly is the crater destroyed? The datasets accumulated on our own impact structures should be looked into carefully, to see if some of the modified craters may in fact have been floor-fractured. This applies to all terrestrial planets; new space probes have recently imaged the Mars and Moon with unprecedented spectral and spatial resolutions, and in a few years several missions will extend our knowledge of both Mercurian and Venusian surfaces.

Whatever the mechanism, the FF crater formation is intimately related to regional volcanism, possibly magmatic intrusions. They are found on all terrestrial planets in one form or another. Thus, they can be used as indicators and study tools of deep-seated regional endogenic activity. Furthermore, as the crater floor is uplifted and fractured, more detailed studies of e.g. the fractures and moats themselves will reveal also much

more information, being natural cross-sections through the stratigraphy of the crater floor.

6. ACKNOWLEDGEMENTS

We acknowledge the Magnus Ehrnrooths foundation and the Finnish graduate school of Geology for funding parts of this research.

7. REFERENCES

- Schultz, P. H., Floor-fractured Lunar craters, *The Moon*, Vol. 15, pp. 241-273, 1976A.
- Young R. A., Lunar volcanism: fracture patterns and rilles in marginal premare craters, *Apollo 16 preliminary science report*, NASA SP-315, pp. 29-89, 1972.
- Cameron W. S. and Padgett J. L., Possible Lunar ring dikes, *The Moon*, Vol. 9, pp. 249-294, 1974.
- Brennan W. J., Modification of premare impact craters by volcanism and tectonism, *The Moon*, Vol. 12, pp. 449-461, 1975.
- Schultz P. H., *Moon Morphology - interpretations based on Lunar orbiter photography*, Univ. of Texas Press, USA, 641 p., 1976.
- Zisk, S. H., Campbell B. C., Pettengill G. H. and Brockelman R., Alphonsus crater: floor fracture and dark-mantle deposit distribution from new 3.0 cm radar images, *Geophysical Research Letters*, Vol. 18, 11, pp. 2137-2140, 1991.
- Head J. W. III, Wilson L. and Pieters C. M., Pyroclastic eruptions associated with the floor-fractured Lunar farside crater Oppenheimer in the South pole - Aitken basin, *Lunar and Planetary Science Conf.*, 31, Houston, TX, USA, abstract 1280, 2000.
- Schultz P. H., Martian intrusions: possible sites and implications, *Geophysical Research Letters*, Vol. 5, 6, pp. 457-460, 1978.
- Schultz P. H. and Orphal D. L., Floor-fractured craters on the Moon and Mars, *Meteoritics*, Vol. 13, pp. 622-625, 1978.
- Schultz P. H., Glicken H. and McGetchin T. R., Intrusive melting of water/ice on Mars, *Lunar and Planetary Science Conference*, 10, Houston, TX, USA, pp. 1075-1077, 1979.
- Rodriguez J. A. P., Sasaki S., Kuzmin R. O., Dohm J. M., Tanaka K. L., Miyamoto H., Kurita K., Komatsu G., Fairém A. G., and Ferris J. C., Outflow channel sources, reactivation, and chaos formation, Xanthe Terra, Mars, *Icarus*, Vol. 175, pp. 36-57, 2005.
- Newsom, H. E., Central Remnant Craters on Mars -- Localization of Hydrothermal Alteration at the Edge of Crater Floors?, *Lunar and Planetary Science Conference*, 32, Houston, USA, abstr. 1402, 2001.
- Sato H. and Kurita K., Circular collapsed features related to the chaotic terrain formation on Mars, *Lunar and Planetary Science Conference*, 36, Houston, TX, USA, abstract 2248, 2005.
- Korteniemi J., Collapses and depressions post-dating crater formation in Martian impact structures – distribution and consequences, *3rd International Conference on Large Meteorite Impacts*, Nördlingen, Germany, abstract 4091, 2003.
- Korteniemi J., Aittola M., Lahtela H., Öhman T. and Raitala J., Martian floor-fractured craters vs. craters with irregular depressions, *Lunar and Planetary Science Conference*, 37, Houston, TX, USA, abstract 2145, 2006.
- Database of Martian crater depressions*, J. Korteniemi, <www oulu.fi/astronomy/planetology/mars_depressions> (Accessed 30/June/2006).
- Korteniemi J., Kostama V.-P. and Raitala J., Post-impact depressions on Martian crater floors: preliminary results and a case study of the greater Hellas region, *Vernadsky-Brown Microsymposium*, 38, Moscow, Russia, abstract 38, 2003.
- Öhman T., Aittola M., Kostama V.-P. and Raitala J., The preliminary analysis of polygonal impact craters within greater Hellas region, Mars, in: *Impact tectonics*, Koeberl C. & Henkel H. (eds.), Springer, Berlin, Germany, pp. 131–160, 2005.
- Öhman T., Aittola M., Kostama V.-P. and Raitala J., Preliminary geological analysis of polygonal impact crater data from Argyre region, Mars, *Lunar and Planetary Science Conference*, 37, Houston, TX, USA, abstract 1236, 2006.
- Aittola M., Öhman T., Kostama V.-P. and Raitala J., Impact craters establish geological diversity within Hellas region, *Lunar and Planetary Science Conference*, 32, Houston, USA, abstr. 1485, 2002.
- Korteniemi J., Lahtela H., Raitala J., Neukum G. and the HRSC Co-Investigator Team, Anomalous depressions on the circum-Hellas crater floors as seen in the first year MEX HRSC images, *Lunar and Planetary Science Conference*, 36, Houston, TX, USA, abstract 1669, 2005A.
- Korteniemi J., Kostama V.-P., Törmänen T., Aittola M., Öhman T., Lahtela H., Raitala J. and Neukum G., Complex geology of two large impact craters in Tyrrhena Terra, Mars: detailed analysis using MEX HRSC camera data, *Journal of Geophysical Research*, Vol. 110, E12S18, doi:10.1029/2005JE002427, 2005B.
- Moore J. M. and Howard A. D., Layered deposits and pitted terrain in the circum Hellas region, *Lunar and Planetary Science Conference*, 36, HOUSTON, TX, USA, abstract 1512, 2005.
- Schultz P. H., Endogenic modification of impact craters on Mercury, *Physics of the Earth and Planetary Interiors*, Vol. 15, pp. 202-219, 1977.
- Herrick R. R., Sharpton V. L., Malin M. C., Lyons S. N., and Feely K., Morphology and Morphometry of Impact Craters, *Venus II*, S. W. Bougher, D. M. Hunten, and R. J. Phillips (eds.), University of Arizona Press, Arizona, USA, pp. 1015-1046, 1997.
- Venus Crater Database*, 2002, Rev. 2, Lunar and Planet. Inst. <www.lpi.usra.edu/resources/vc/vchome.htm> (Accessed: 30/June/2006).
- Wichman R. W. and Schultz P. H., Floor-fractured crater models for igneous crater modification on Venus, *International colloquium on Venus*, LPI contribution #789, pp. 131-132, 1992.
- Wichman R. W. and Schultz P. H., Large floor-fractured craters and isostatic crater modification: implications for lithospheric thickness on Venus, *Lunar and Planetary Science Conference*, 24, Houston, TX, USA, pp. 1515-1516, 1993.
- Wichman R. W. and Schultz P. H., Floor-fractured impact craters on Venus: implications for igneous crater modification and local magmatism, *Journal of Geophysical Research*, Vol. 100, E2, pp. 3233-3244, 1995A.
- Earth Impact Database*, 2006. <www.unb.ca/passc/ImpactDatabase/> (Accessed: 30/June/2006).
- Orphal D. L. and Schultz P. H., An alternative model for the Manicouagan impact structure, *Proceedings of the Lunar and Planetary Science Conference*, 9, p. 2695-2712, 1978.
- Wichman R. W. and Schultz P. H., Floor-fractured crater models of the Sudbury structure, Canada: implications for initial crater size and crater modification, *Meteoritics*, Vol. 28, pp. 222-231, 1993.
- Wood C. R., and Spray J. G., Origin and emplacement of offset dykes in the Sudbury impact structure: constraints from Hess, *Meteoritics and Planetary Science*, Vol. 33, 2, pp. 337-347, 1998.
- Wichman R. W. and Schultz P. H., Floor-fractured craters in Mare Smythii and west of Oceanus Procellarum: Implications of crater modification by viscous relaxation and igneous intrusion models, *Journal of Geophysical Research*, Vol. 100, E10, pp. 21201-21218, 1995B.
- Wichman R. W. and Schultz P. H., Igneous intrusion models for floor fracturing in Lunar craters, *Lunar and Planetary Science Conference*, 22, Houston, TX, USA, p. 1501-1502, 1991.
- Dombard A. J. and Gillis J. J., Testing the viability of topographic relaxation as a mechanism for the formation of Lunar floor-fractured craters, *Journal of Geophysical Research*, Vol. 106, E11, pp. 27901-27909, 2001.
- Hall J. L. and Solomon S. C., Lunar floor-fractured craters: the relative importance of isostatic relaxation and uplift by volcanic intrusion, *Lunar and Planetary Science Conference*, 11, Houston, TX, USA, pp. 385-387, 1980.
- Hall J. L. and Solomon S. C., Evidence for viscous relaxation of crater topography, *Lunar and Planetary Science Conference*, 12, Houston, TX, USA, pp. 389-391, 1981.
- Dombard A. J. and Gillis J. J., Simulating the formation of Lunar floor-fracture craters using elastoviscoplastic relaxation, *Workshop on new views on the Moon 2: understanding the Moon through the integration of diverse datasets*, Flagstaff, Arizona, USA, p. 10, abstract 8044, 1999.

A TIME ESTIMATE FOR CONSOLIDATION AND DISINTEGRATION OF AN ASTEROID – RUBBLE PILE. THE SIMPLEST MODEL. A PRELIMINARY ANALYSIS.

G.A. Leikin, A.N. Sanovich

Sternberg State Astronomical Institute

Universitetsky Prosp. 13, Moscow 119992, Russia

E-mail: san@sai.msu.ru

Abstract

The existence of asteroids - rubble piles is significant for estimation analysis of asteroidal danger to the Earth, because, as is shown in the present work, in the evolution of such asteroids there is a long period during which the asteroid is a dissipating (or consolidating) cluster of fragments. The vector of evolution is determined by the dynamic characteristics of the asteroid fragments. The effective cross-section of interaction of the Earth with such a cluster is much larger than for the interaction with individual fragments or consolidated asteroids.

The analysis of the simplest model shows that an asteroid – rubble pile evolves, depending on the parameter V^2d (where V is the average velocity of fragments and d is the average distance between fragments), either as a conglomerate of "independent mutually gravitating clusters" (when $V^2d < fm$, where f is the gravitational constant and m is the average mass of a fragment) or as a "receding cluster" (when $V^2d > fm$). In the latter case the recession energy is drawn from the gravitational energy of the cluster. Within the framework of the model considered, the characteristic consolidation time in the first ("elliptical") case is

estimated to be within \sim ten million years; in the second ("hyperbolic") case, the doubling time for the average distance between the asteroid fragments lies within the limits of several hundred thousand to several million years. It should be noted that the actual consolidation time in the first case may be considerably smaller due to the presence of diffuse matter increasing kinetic energy loss. In the second case, the presence of diffuse matter will result in accelerated exchange of gravitational and kinetic energies and consequently in accelerated "recession" of the cluster of fragments. Thus the mechanism considered enables an asteroid – rubble pile to survive for a long time, and on the other hand, even without tidal effects, it prevents the transformation of the whole Asteroid belt into a structureless "cloud".

Leikin and Sanovich (2002, 2003) showed that a typical asteroid – rubble pile (ARP) within $10^7 - 10^8$ s after its formation loses the fragments whose velocities about its center-of-mass are greater than ~ 10 m/s.

In this paper, the time of consolidation or disintegration of an ARP due to energy dissipation of

its fragments is estimated using the simplest model. The model is not intended to be precise; its aim is to determine the direction of evolution of asteroids – rubble piles and to give a very rough estimate of the temporal scale of their evolution.

We consider an ARP to be a cluster of n identical bodies of radius r distributed at random in volume W with the average distance between the bodies equal to d ($d \approx (W/n)^{1/3}$). The bodies are assumed to be of mass m and density ρ and to have within the cluster velocities V with equal magnitudes and random orientations.

In this model, it is easy to estimate the free path length $\lambda \approx d^3/(4\pi^2)$ and the time between collisions $\tau = \lambda/V$. Obviously, if the free path length is greater than the characteristic cluster diameter, the model is not applicable, – collisions are negligible, – but in that case an ARP will actually disintegrate approaching a planet for the first time due to tidal dissipation.

In modelling the collision process, the following considerations were used.

A body in a collision is perfectly elastic with respect to the normal velocity and completely inelastic with respect to the tangential (shearing) velocity. If the speed of propagation of longitudinal oscillations in the body is c , the duration of the collision is determined as $\tau_c = 2r/c$ (discharge time). The depth of the deformation zone over this period is $h = V_n \tau_c$, – or $h = (1/3) \cdot (2r/c) \cdot V$, as in the model under consideration we have $V_n = V/3$, – and the radius of the deformation zone is $r_c = 2r(V_n/c)^{1/2}$,

as $V_n \ll c$; so the volume of the deformed spherical cap is $W_d = 2\pi r_c h/3$ or $W_d = (2\pi/9) \cdot (2r/c) \cdot V \cdot [(2r/c) \cdot (V/3)]^2 = (16/81) \cdot r^3 (V/c)^3$, with the mass $m_d = (16/81) \pi r^3 \rho (V/c)^3$.

In this situation, V_t (the tangential velocity) is equal to $(2/3)V$, and the deformed mass is given energy $m_d \times (2V/3)^2/2$, that is, $(2/9)m_d V^2$, or around $0,2 \times 10^6$ erg/g for $V \ll 10$ m/s, which for the heat capacity of rock equal to $\sim 10^7$ erg/(g·K) corresponds to the increase of the temperature by fractions of a degree and is unlikely to cause destruction of the rock unless the rock is weakened by jointing.

Thus the kinetic energy loss in a single collision is $\Delta K = (16/81) \pi r^3 \rho (V/c)^3 (2/9) V^2 =$

$= [(16 \cdot 2 \cdot \pi) / (81 \cdot 9)] \cdot [(r^3 \rho V^5 / c^3)]$. The number of such collisions in a unit of time is $(1/\tau) = [d^3 / (4\pi^2 V)]^{-1}$, hence the derivative of the kinetic energy and the parameters of the model are related by the following differential equation:

$$\frac{dK}{dt} = \frac{32 \cdot 4 \cdot \pi^2}{81 \cdot 9} \cdot \frac{r^5 \cdot \rho \cdot V^6}{c^3 \cdot d^3} \quad (A)$$

As the sound velocity in a solid is considerably greater than the velocity of the fragments, dK/dt is quite small compared to the kinetic energy of a fragment, which is mainly due to the short duration of the collision.

Because of the slow change of K with time we can use the virial theorem as the 2nd equation relating the velocity V and the distance d between fragments through gravitational forces. Here the virial theorem should be regarded as an osculating approximation. For

our model, the simplest form of the virial theorem is $V^2d=2fm$, where f is the gravitational constant.

Taking this relation into account in the case $V^2d>2fm$ (hyperbolic motion) leads to the conclusion that the mutual distance between fragments grows with time. Then the collisional "transparency" of the cluster of fragments also grows, which increases the loss of high-velocity fragments. However, it should be noted that, depending on the spatial distribution of fragments in the cluster, the motion in the outer part of the cluster may become "elliptical", and for some time the cluster may have a rarefied "corona", which will be lost when approaching planets due to tidal effects.

It should be noted, however, that the presence of a diffuse component in the volume occupied by an ARP radically changes the situation. If during some time a fragment sweeps away an amount of matter comparable to its mass, its kinetic energy roughly halves in that time. Note however that the above considerations are only valid as long as the gravitational interaction between the particles doesn't make their orbits "elliptical" with the major axes less than d . In this case the contact interaction will take place within a dense group of gravitating fragments and will recur with the frequency corresponding to the gravitational period. It should be noted that this process, especially in the presence of a diffuse component, facilitates the consolidation of massive objects and may play a significant role in the consolidation of large objects, for example in the Kuiper Belt.

The analysis of the model shows that an asteroid – rubble pile evolves, depending on the parameter V^2d , either as a conglomerate of "independent mutually gravitating clusters" (when $V^2d<fm$) or as a "receding cluster" (when $V^2d>fm$). In the latter case the recession energy is drawn from the gravitational energy of the cluster. Within the framework of the model considered, the characteristic consolidation time in the first case (see Table 1) is estimated to be within ~ ten million years; in the second case, the doubling time for the average distance between the asteroid fragments (see Table 1) lies within the limits of several hundred thousand to several million years. It should be noted that the actual consolidation time in the first case may be considerably smaller due to the presence of diffuse matter increasing kinetic energy loss. In the second case, the presence of diffuse matter will result in accelerated exchange of gravitational and kinetic energies and consequently in accelerated "recession" of the cluster of fragments. Thus the mechanism considered enables an asteroid – rubble pile to survive for a long time, and on the other hand, even without tidal effects, it prevents the transformation of the whole Asteroid belt into a structureless "cloud".

The important point is that the process described makes an ARP's lifetime long enough for the asteroid to be observed in the ARP phase, and at the same time explains the possibility of multiple asteroids such as Ida.

Analysing the asteroid danger problem it must be kept in mind, that the asteroid can be not a single

object, but a cluster of objects, thus hindered seriously the solving of the problem.

References

1. Leikin G. A. and Sanovich A. N. Some problems of the evolution of asteroid – rubble pile // ACM, 2002. P. 741-742.

2. Leikin G. A. and Sanovich A. N. Some problems of the dynamical evolution of asteroid – rubble pile // Abstr. pap. of Vernadsky – Brown 38, 2003. MS059.

Table 1. The parameters of the model and the characteristic evolution time of an ARP

m (grams)	ρ (g/cm ³)	c (cm/s)	V (m/s)	d (km)	T (years)
"elliptical" case					
$1,003 \times 10^{16} -$ $-2,836 \times 10^{19}$	1 – 8	$1,0 \times 10^5 -$ $.5,1 \times 10^5$	1 – 10	1,340 – – 37,840	$\sim 10^7$
"hyperbolic" case					
$3,75 \times 10^{17} -$ $-2,40 \times 10^{19}$	1 - 8	$1,0 \times 10^5 -$ $-5,1 \times 10^5$	1	20 – 40	$\sim 10^5 -$ 10^6

m – the average mass of a fragment, ρ – the average density of a fragment, c – the speed of longitudinal wave in the body of the fragment, V – the root-mean-square

velocity of a fragment. Table 1 also shows T – the characteristic doubling time d (hyperbolic case) and T – the characteristic consolidation time (elliptical case).

MODELLING CRATER SHAPES WITH GAUSSIAN RANDOM SPHERES

Tatjana Tchumatchenko⁽¹⁾⁽²⁾, Karri Muinonen⁽³⁾, SMART1 AMIE Science Team

⁽¹⁾ TU Darmstadt, Institute for Applied Physics, Schlossgartenstr. 7, 64289 Darmstadt, Germany

Email: tatjana.tchumatchenko@physik.tu-darmstadt.de

⁽²⁾ Observatory, P.O. Box 14, FI-00014, University of Helsinki, Finland, Email: tchumat@astro.helsinki.fi

⁽³⁾ Observatory, P.O. Box 14, FI-00014, University of Helsinki, Finland, Email: muinonen@cc.helsinki.fi

ABSTRACT

Impact cratering is an important geological process which affects the majority of the terrestrial planets, moons and asteroids. The size and shape of the craters are determined by the velocity of the impactor and the soil conditions of the target material. The conditions present at the moment of the impact as well as the surface properties can be therefore estimated from the crater shape. Simple crater shapes were modeled so far with hemispheres, or are fitted with polynomials [1]. In this paper we present a novel statistical two-parameter model, which allows both symmetrical and asymmetrical shapes.

1. INTRODUCTION

We take a statistical approach, assuming that each crater is a representation of a Gaussian random hemisphere. This is motivated by the fact that the majority of simple craters on planetary bodies resemble hemispheres. So hemispheres are a good first-order approximation [6], but they do not take into account the irregularities of the craters. We therefore take the hemispheres as a starting point and introduce a Gaussian distortion.

Each shape is unique, but the craters resulting from similar impact events should have similar statistical parameters. We therefore assume that craters which were formed during approximately the same time period in the same region of a planetary body should have similar statistical parameters. In this paper we introduce a way of estimating the statistical parameters of craters from the form of the rim.

We begin this paper by introducing the mathematical formalism of Gaussian random spheres and by showing how it can be used to model crater shapes. We then describe the method we used to extract the rim profile from the nadir viewing images and how the statistical

parameters can be estimated from the parameterized rim profile. We then give an outlook on the application of this method to study light scattering inside craters with potential implications for clinometry, and how the crater shapes on different planetary bodies can be statistically compared.

2. GAUSSIAN RANDOM SPHERES

The Gaussian random sphere given by the radial distance $r(\theta, \varphi)$ introduced in [2] and [8] is a lognormally distributed isotropic random field defined on the unit sphere. It can be described by the mean radial distance and the covariance function of the logarithmic radial distance.

$$r(\theta, \varphi) = a \cdot \exp(s(\theta, \varphi) - \frac{1}{2} \beta^2) \quad (1)$$

$$s(\theta, \varphi) = \sum_{l=0}^{\infty} \sum_{m=-l}^l s_{lm} Y_{lm}(\theta, \varphi) \quad (2)$$

The radius as given by Eq. 1 is determined by the spherical harmonics coefficients of the logradius.

The quantity $s(\theta, \varphi)$ is called "logradius" and has zero mean and a standard deviation β . The radius $r(\theta, \varphi)$ has the mean value a and the standard deviation σ determined by the Eq. (3):

$$\sigma = \sqrt{\exp(\beta^2) - 1} \quad (3)$$

The coefficients s_{lm} of the spherical harmonics Y_{lm} have to fulfill several requirements: Their mean value must be zero and they have to be independent variables with the variances given as by Eq. 5 and Eq. 6:

$$s_{l,-m} = (-1)^m \cdot s_{lm}^* \quad (4)$$

$$\text{Var}(\text{Re}(s_{lm})) = (1 + \delta_{m0}) \cdot \frac{2\pi}{2l+1} C_l \quad (5)$$

$$\text{Var}(\text{Im}(s_{lm})) = (1 - \delta_{m0}) \cdot \frac{2\pi}{2l+1} C_l \quad (6)$$

δ_{m0} denotes the Kronecker delta function and C_l the Legendre coefficients of the correlation function. The covariance function for an isotropic random field defined on a unit sphere is given in the Eq. 7:

$$k_s(\gamma) = \beta^2 \cdot C_s(\gamma) = \sum_{l=0}^{\infty} C_l P_l(\cos(\gamma)) \quad (7)$$

The angle γ is the difference between two solid angles on the unit sphere. The coefficients C_l of the covariance function for the unit sphere have to fulfill the Eq. 8.

$$\sum_{l=0}^{\infty} C_l = \beta^2 \quad (8)$$

The covariance function for an isotropic random field defined on the unit circle is given in Eq. 9:

$$k_s(\gamma) = \sum_{k=0}^{\infty} \delta_k^2 \cos(k \cdot \gamma) \quad (9)$$

Starting with the Legendre expansion one can define the correlation angle Γ as

$$\Gamma = 2 \arcsin \left(\frac{1}{2 \cdot \sqrt{-C_s^{(2)}(0)}} \right) \quad (10)$$

$C_s^{(2)}(0)$ is the second derivative of the correlation function $C_s(\gamma)$ taken at the position 0.

The correlation angle and the radial standard deviation are important quantities of a random sphere. For the numerical generation of sample surfaces, one starts with a correlation function $C_s(\gamma)$.

Typically, one chooses $C_s(\gamma)$ to follow a power law or a Gaussian. The correlation function determines the variances of the spherical-harmonics coefficients and allows to calculate the two characteristic quantities σ and Γ . The spherical harmonics coefficients are generated using random variables, which have the variances as defined by the correlation function in Eq. 5 and Eq. 6.

Sample spheres generated by a power law correlation function are shown in Fig. 1. These sample shapes show that lower power-law index weights the spectrum

towards higher-degree spherical harmonics and the shapes have more hills per solid angle. The increase in variance enhances the hills radially.

The Gaussian shapes were already used to model the forms of asteroids [2] and in this paper we want to apply this formalism to crater shapes.

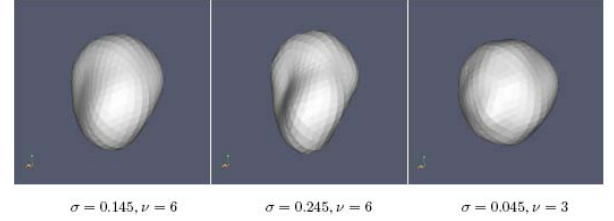


Fig. 1. These sample shapes are generated using a power law correlation function; the standard deviation of radius σ and the power law index ν are given.

3. GAUSSIAN HEMISPHERES

According to [3], the diameter-to-depth ratio of simple lunar craters is 5, therefore we model the craters with a hemisphere which is cut by a plane, in the way that the diameter-to-depth ratio is matched. For lunar craters it corresponds to the height value $z = 0.7241$ for unit sphere. This value fulfills Eq. 11.

$$\left(\frac{2 \cdot \sin(\arccos(z))}{1 - z} \right) = 5 \quad (11)$$

Fig. 2. shows sample crater shapes with the diameter-to-depth ratio =5 which are generated using a power-law correlation function.

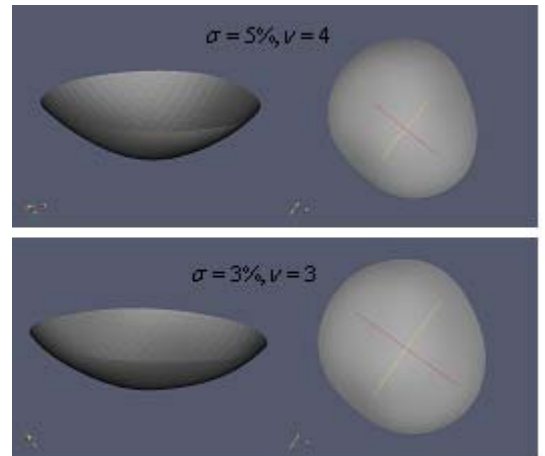


Fig. 2. The nadir view of the sample crater is shown in the right; in the left are the craters as seen from the side. The standard deviation of radius σ and the power-law index ν for each crater are given.

4. RIM PROFILE EXTRACTION

To extract the rim profiles, we used nadir view images and extracted the rim form using active contours. These are curves that are defined within an image and can move under the influence of internal and external forces. The forces are defined in such a way, that the active contour will conform to an object boundary. There are different ways of defining the external and internal forces of the active contours; the most popular is GVF (Gradient Vector Flow) which is described in [4].

On a given image $I(x, y)$ an edge map $f(x, y)$ is defined. Starting with $u = \nabla f$ one iterates Eq. 12 to find the equilibrium solution.

$$u_t = \mu \nabla^2 u + |\nabla f|^2 (u - \nabla f) \quad (12)$$

The equilibrium solution V is then used to determine the shape of the active contour. This is done by iterating Eq. 13. The right hand side of Eq. 13 is zero for the stationary solution. This solution is typically reached after 120 steps.

$$x_t(s, t) = \alpha x''(s, t) - \beta x''''(s, t) + V \quad (13)$$

The contour is given as a function of s and t . $s \in [0, 1]$ is the parameterisation of the contour curve and t is the time parameter indicating the iteration step. x' is the derivative with respect to s .

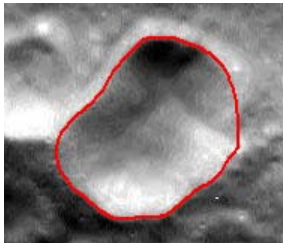


Fig. 3: A sample crater as determined by the active contour method.

The sample crater image shown in Fig. 3 was delivered by the AMIE camera on board of SMART1 satellite. We successfully extrapolated the shapes of craters in the mare and highland region of the Moon. All crater shapes which had more than 150 pixel diameter were extrapolated using the same parameters α, β etc., which determine the convergence of the active contour.

5. EXTRACTION OF STATISTICAL PARAMETERS

To estimate the radial standard deviation σ and the power law coefficient ν , the rim profile as determined by the active contour fitting needs to be equidistantly gridded in the angular direction. The estimation of the statistical parameters is then done by comparing the set of the rim profiles belonging to the same group to the sample sets of shapes with known power law coefficient and known standard deviation.

The quality of the agreement between the retrieved shapes and the sample shapes is characterized by comparing the χ_{red}^2 value, the agreement is the better the lower χ_{red}^2 .

To compute the χ_{red}^2 , we define a rotationally invariant azimuth angle by equidistantly dividing the length of the curve into a given number of cells. We then compute the angles of the normals of two points along the curve which are an angular distance φ apart and then move along the curve an angle Φ further and calculate the normals again. This procedure is repeated for each of the sample curves n times, the agreement of both sample sets is tested with χ_{red}^2 [5].

The sample shapes can be compared either to a set of Gaussian circles or to Gaussian spheres, the correlation function is the given by Eq. 9 and Eq. 7 respectively.

When estimating the parameters of the corresponding random Gaussian sphere, one needs to take into account that the extrapolated rim circle corresponds to a cross-section at a given height value of the random sphere, which is not the equator of the random sphere.

6. LIGHT SCATTERING INSIDE CRATERS

We implemented a ray tracing procedure to study the light scattering inside the sample Gaussian shapes. We assumed the Lommel Seeliger scattering law as given in Eq. 14

$$S_{LS} = \frac{\varpi \cdot p(\alpha)}{4\pi} \cdot \frac{1}{\cos(\theta_{in}) + \cos(\theta_{out})} \quad (14)$$

In this equation, ϖ is the single scattering albedo, $p(\alpha)$ is the single particle phase function and the angles θ_{in} and θ_{out} are the angle of incidence and the angle of emergence respectively.

The irradiance L_{direct} received by a cell with an area A_1 from direct radiation is given by the Eq. 15

$$L_{direct} = \cos(\theta_{in}) \cdot A_1 \quad (15)$$

We assume a unidirectional incident flux of $1 \frac{W}{m^2}$.

As there is no compact mathematical relationship to find out whether a cell is directly illuminated or not, we determined this by tracing a ray from the cell center in the inverse direction of the incident illumination, and determined whether the ray would escape the crater. If this was the case, the cell was considered to be directly illuminated.

Though the local incidence and emergence angles change, the phase angle remains the same for all cells for fixed viewing conditions. We therefore used a constant to approximate the phase function $\varpi \cdot p(\alpha) = const$. This is a multiplicative constant, which varies depending on the angle of emergence and incidence. Varying this constant does not change the spatial scattering distribution; this distribution is only determined by the local angle of incidence.

We did not consider second level scattering, because the effect resulted in a deviation of less than 1% of the emitted radiance values and was found to be much more CPU time consuming.

Using Eq. 14 with the assumptions above, we could determine the radiance emitted by each cell in the viewing direction. To determine, whether the emitted ray could escape the crater, we used the same method as for determining whether or not a cell is illuminated. The results of this study are shown in Fig. 4.. it shows the spatial light distribution inside a sample crater with a diameter-to-depth ratio of 5, $\sigma = 6\%$ and $\nu = 3$. The light enters the crater along the x-axis (red) with an inclination of 45° and the observer is looking parallel to the incoming light. To generate the plot in Fig. 4 we used $\varpi \cdot p(\alpha) = 0.03$. The maximum value emitted by a cell in this example is $1.6 \cdot 10^{-6}$ Watt, the minimum is zero due to the shadowed regions.

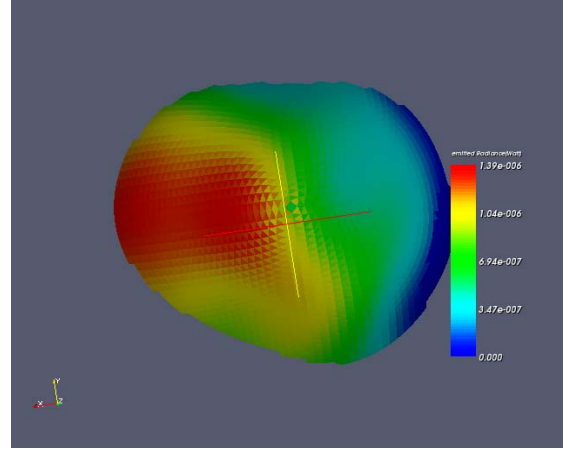


Fig. 4: Colour-coded emitted radiance in the direction of the observer. The maximum values are denoted in red, the minimum values in blue.

7. RESULTS AND DISCUSSION

The two parameter statistical model presented in this paper has the advantage of offering a compact description for a variety of crater shapes. The advantage of the two statistical parameters compared to a fit with Zernike polynomials [7] is the low number of parameters and the direct physical interpretation of them.

Using our method, we studied the crater shapes of the mare and highland regions on the Moon, and found that the radial deviation σ is typically 3 to 5 %, and the power law coefficient ν is approximately 3 to 4. The number of the extrapolated sample crater rims was 24 in this study. We plan to extend this to higher number of sample shapes and to study the statistical parameters of different regions.

The first results suggest that the total integrated brightness of more deformed craters can be up to 5% higher or lower compared to the integrated brightness of a homogenous sphere with the same diameter-to-depth ratio.

8. OUTLOOK

The compact two parameter statistical model is a powerful tool for characterizing the crater shapes as well as the crater rim profiles. Several questions are interesting: Do the statistical parameters depend on the planetary body, the soil material and the angle of impact? How can we qualitatively and quantitatively access this dependence? How much influence does the shape have on the integrated brightness of the crater?

9. ACKNOWLEDGEMENTS

We gratefully acknowledge the support of the German National Academic Foundation, the Muehlfehl Foundation, and the Physics Faculty of the TU Darmstadt.

10. REFERENCES

- [1] C. J. Solomon et al., *Automated compact parametric representation of impact craters*, Int. J. Impact Engineering Vol. 21, No.10, p. 895-904, 1998.
- [2] K. Muinonen and J.S.V. Lagerros, *Inversion of shape statistics for small solar systems bodies*, A&A 333, 753-761, 1998
- [3] Pike et al., *Size-dependence in the shape of fresh impact craters on the moon* in Eds., Impact and explosion cratering. Pergamon Press, New York, 489-509, 1977
- [4] C. Xu, J. L. Prince, *Snakes, Shapes, and Gradient Vector Flow* IEEE Transactions on image processing, Vol. 7, No. 3, March 1998
- [5] Muinonen, K. (2006). *Inversion of small-particle silhouettes for Gaussian-sphere parameters*, Proceedings of the 9th Conference on Electromagnetic and Light Scattering by Nonspherical Particles: Theory, Measurements, and Applications, St. Petersburg, Russia, June 5-9, 2006, 4 pp., in press.
- [6] A.P. Ingersol et al., *Stability of Polar Frosts in Spherical Bowl-Shaped Craters of Moon, Mercury, and Mars*, Icarus 100, 40-47 1992
- [7] D.Wallis, C.J. Solomon, and N. McBride., *Modelling radially symmetric impact craters with orthogonal functions*, Int. J. Impact Engineering, 2000
- [8] L. Lamberg et al, *Spectral estimation of Gaussian random circles and spheres*, Journal of Computational and Applied Mathematics 136 (2001) 109–121

HIGH ACCURACY MATCHING OF PLANETARY IMAGES

Giuseppe Vacanti and Ernst-Jan Buis

cosine Science & Computing BV, Niels Bohrweg 11, 2333 CA, Leiden, The Netherlands

ABSTRACT

We address the question of to what accuracy remote sensing images of the surface of planets can be matched, so that the possible displacement of features on the surface can be accurately measured. This is relevant in the context of the libration experiment aboard the European Space Agency's BepiColombo mission to Mercury. We focus here only on the algorithmic aspects of the problem, and disregard all other sources of error (spacecraft position, calibration uncertainties, *etc.*) that would have to be taken into account. We conclude that for a wide range of illumination conditions, translations between images can be recovered to about one tenth of a pixel *r.m.s.*

Key words: pattern matching; BepiColombo; libration.

1. INTRODUCTION

One of the goals of the European Space Agency's Bepi-Colombo mission to Mercury is the measurement of the amplitude of the libration of Mercury. In order to do this images of the same surface areas will be taken at different times during the libration cycle and compared. When all other effects—spacecraft position, Mercury's rotation, spacecraft attitude, *etc.*—are taken into account, any remaining discrepancy between the positions of features on the surface must be due to the libration of the crust of the planet.

Here we address the question of to what accuracy images can be matched, and we focus only on the algorithmic aspects of the problem, disregarding all other sources of error that would have to be taken into account to solve the scientific problem. We shall show that by using a shape-based matching algorithm images taken under a wide range of illumination conditions can be matched to one tenth of a pixel root-mean-square. Based on this we conclude that the accuracy of the pattern matching algorithm is not the limiting factor in the ultimate accuracy that can be achieved by the libration experiment on Bepi-Colombo.

2. PATTERN MATCHING

The pattern matching algorithms to be used in this study will have to deal with images that may appear to be drastically different from one another, still they refer to the same region. Consider for example the images shown in figure 1. To the human eye it is clear that the images refer to the same region, but any algorithm that relied on the presence of identical features in the images would have great difficulty concluding that the images are related at all.

What is clear by visual inspection is that a number of edges—sharp changes in the level of illumination between contiguous pixels—are common between images. These edges appear where sharp changes in the altimetric profile occur. It is also clear that not all edges appear in all images, owing to the complex interplay between the position of the Sun, and the orientation and slope of the features on the ground.

Compare for instance images *b* and *d* in figure 1: the left rim of the crater is bright in one image, and dark in the other. No similar change is observed on the right rim of the crater.

Take now images *a* and *c*. Here the left rim of the crater appears almost to be the same, but the extent of the shadow cast by the right rim is dramatically different.

The ideal algorithm must be able to identify the edges in the two images, must be robust against local, non-linear changes in illumination conditions, and it must be able to operate by identifying a subset of features that are common to the pair of images being compared. Finally, based on the common features identified, the algorithm must be able to recover a possible translation between the two images.

Algorithms that try to minimize the difference between the two, possibly scaled, images are clearly not going to be suited for the task, unless the images to be compared are taken under very similar illumination conditions. While this is possible, it would be a very strong constraint on the operations of a mission.

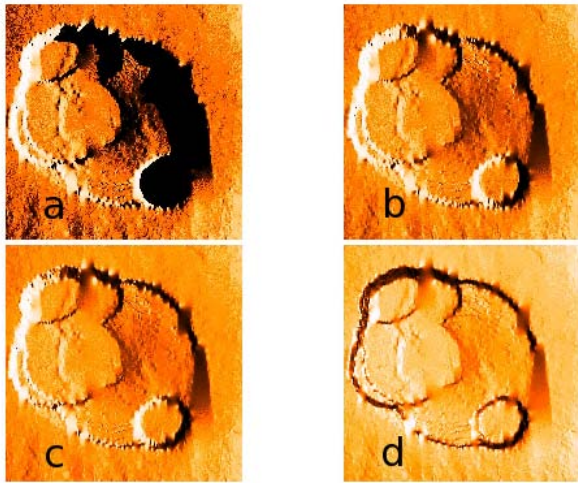


Figure 1. A digital elevation model of Olympus Mons viewed by an imaging camera under different illumination conditions: (a) The Sun is at 5° elevation; (b) The Sun is at 25° elevation; (c) The Sun is at 50° elevation; (d) The Sun is at 85° elevation. In all cases the Sun's azimuth is 0° (to the right).

Based on the considerations above, we have chosen to make use of the image matching algorithms available in the HALCON software library (Ref. 1). This is a commercial product used in image vision and image recognition applications.

One particular technique available in the HALCON library is the so-called *shape-based matching* (Ref. 2). This technique is based on an algorithm that identifies the shape of patterns in images, and can be instructed to find in a comparison image the shape identified in a reference image.

2.1. Shape-Based Pattern Matching

The detailed description of the algorithm can be found in the HALCON documentation (Ref. 2) and has been submitted as part of a European Patent Application (Ref. 3).

The algorithm proceeds through the following steps:

1. A so-called *region of interest* is identified in the reference image. This is a region of the image where edges will be looked for. The region of interest must be selected to be fully contained in both images. This step is done by hand, based on some *a priori* knowledge, or visual inspection of the images. In our case, where the simulated translations amount to a few pixels along either or both the X and Y axes (see § 5), the region of interest is the whole reference image, minus a few pixels around the edges. In the case of two partially overlapping images of the same region one would choose the intersection of the two images.
2. Features are identified in the comparison image with an edge detection algorithm. Pixels identified by the edge detection algorithm are part of the *reference pattern*.
3. The edge detection algorithm is run on the comparison image. This results in a second collection of pixels, the *search pattern*.
4. The algorithm now overlays the reference pattern on the search pattern. The reference pattern is stepped over the search pattern in an attempt to maximize the number of overlapping pixels. In doing so the algorithm is allowed to reduce the number of pixels in the reference pattern. The maximum fraction of the search pattern that can be discarded in the process can be set by the user. In our application the reference and search patterns can differ vastly. Therefore we have allowed the algorithm to throw away up to 70 % of the pixels. In trying to maximize the overlap between the two patterns, the algorithm can be instructed to allow for a rotation and a scaling factor.
5. The algorithm reports the recovered translations and the fraction of the pixels in the reference pattern that was used to find a match. The latter is called the *score*. Within the parameters given by the user, the algorithm always chooses the match with the highest score.

2.1.1. The Meaning of the Score

The HALCON score is the normalized sum of the cross product between the vectors describing the position of the pixels in the reference pattern and those describing the pixels in the search pattern. If the two patterns are identical, it is clear that the score will be equal to one. When pixels have to be dropped from the reference pattern, the score will decrease.

In the actual algorithm, the sum of the cross products of the pixels used in the match is slightly modified to take into account the possibility of non-linear changes in the illumination conditions, either locally, around certain features, or globally, across the entire image (Ref. 3).

It is tempting to interpret the HALCON score as a quality factor for the goodness of the translation parameters found. However this would be wrong on two counts.

First of all, it is clear that often only a subset of the pattern to be looked for is to be found in the search pattern. (Refer back to the examples shown in figure 1.) In this case the search algorithm must discard some of the pixels in the reference pattern in order to find a good matching sub-pattern. How many pixels are left in the sub-pattern has nothing to do with whether the match is good or not.

Second, the notion of *goodness of match* implies that the matched pattern can be compared to an expected result,

or true pattern, or that the algorithm proceeds through the optimization of an objective function. But the only measure of how well the algorithm has performed, is how close the recovered translation is to the values injected in the simulation. This means that the accuracy of the algorithm can only be judged through an extensive set of Monte Carlo simulations. Only by repeatedly comparing two images in multiple realizations of the same detection and matching process, is it possible to gauge the statistical errors in the results, and therefore establish to what accuracy and under what conditions the algorithm can be effectively employed.

3. APPROACH

The following steps were identified.

1. Render a digital elevation model of the surface of a planet, by choosing the position of the Sun and of the spacecraft. We have used **povray** (Ref. 4) for this task.
2. Create two images, the reference image and the comparison image. The latter is possibly translated along one or both of the image axes.
3. Convert the rendered images to instrument count images of a given signal-to-noise ratio.
4. Recover translation parameters between the two images using a shape-based pattern matching algorithm.
5. Study the accuracy with which the parameters are recovered, and derive information on the range of illumination conditions for which the parameters can be successfully recovered.

4. DIGITAL ELEVATION MODELS

Four digital elevation models have been used in this study. These are shown in figure 2¹.

5. SIMULATION RUNS

After some preliminary simulations used to determine a useful sampling scheme of the parameter space, the bulk of the simulations were carried out with the following parameters values:

- Translations: 100 meter in X, in Y, and in X and Y.
- Sun elevation angles: 10°, 30°, 60°, 90°.

¹The Olympus Mons digital elevation model was kindly provided to us by the Mars Express Team.

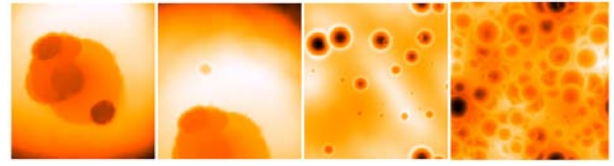


Figure 2. The four digital elevation models used in this study. From left: The Olympus Mons caldera; a bowl-shaped crater close to the Olympus Mons caldera; a synthetic landscape with several bowl-shaped craters; another synthetic landscape containing approximately 5000 craters. (An image of Mercury taken from an height of 400 km might contain a few thousands of craters with a diameter larger than a few tens of meters.) Darker colors represent lower elevations.

- Nominal spacecraft height 1500 km².
- Sun azimuth angle: several (the same azimuth angle for reference and comparison images). For one model a difference in azimuth of 30° between the two images was introduced.
- Four digital elevation models rendered with a signal-to-noise ratio of 50. The signal-to-noise ratio is determined when the Sun is at the zenith.

6. RESULTS

For each digital elevation model used, several thousand data points have been calculated. Each data point refers to a particular combination of Sun elevation and azimuth for the reference and comparison images, and a translation along one or both of the image axes. For each combination of parameters, the same number of simulation runs (ten) was carried out.

In the following we use Δ_x and Δ_y to indicate the difference between the amplitude of the translation recovered by the algorithm and the amplitude of the translation used in the simulation. Therefore the expectation value of Δ_x and Δ_y is always 0, and the width of their distributions is a measure of the statistical error in the reconstruction.

In table 1 we give a summary of how successful the algorithm has been. For each digital elevation model we give the number of realizations (all Sun angles and all translations), how many times the algorithm failed to return a match, and how many times the returned result was more than 2 pixels away from the expected result. The latter figure has no special meaning, but is meant to give an idea of the global behavior of the algorithm.

One thing is immediately apparent: for the synthetic digital elevation model the algorithm always returned a

²The actual height of the camera above the surface is not important for the results of this study, at least as long as the images recorded from different heights show the same level of detail.

DEM	Total	No match	$\Delta_x > 2$ or $\Delta_y > 2$
A	9878	2.8%	2.3%
B	7300	3.2%	4.2%
C	6254	0%	12.6%

Table 1. Global success statistics for the simulation runs. For each digital elevation model (DEM) the following data are reported: the total number of independent realizations; the fraction of realizations for which the algorithm was not able to find any match; the fraction of realizations for which either $|\Delta_x|$ or $|\Delta_y|$ were larger than two pixels. DEM keys: A = Olympus Mons, B = bowl crater, C = synthetic.

match, but a larger fraction of the returned answers was significantly wrong. Because the synthetic model is significantly more regular than the other two — in particular the craters are identical but for a scale factor, the algorithm has an easier job at finding some matching pattern, although relatively more often the pattern found is not the good one.

Based on these observations, we present the results for the synthetic model separately. However, we will be able to show that the same conclusions on the accuracy of the algorithm can be reached for all digital elevation models by applying the same selection criteria on the illumination conditions.

In the following sections we use the following notation:

- θ_{cut} refers to the following selection: $\theta_{sun} > 10^\circ$ and $\theta_{sun} \neq 90^\circ$, where θ_{sun} is the Sun elevation angle in the reference or the comparison image.
- ϕ_{cut} refers to the following selection: $|\phi_{sun} - n \times 90^\circ| > 20$ for $n \in 0, 1, 2, 3, 4$, where ϕ_{sun} is the Sun azimuth — this is the same in both the reference and the comparison images.

6.1. The Olympus Mons Models

Most of the high-deviation points come from images where the Sun elevation is equal to 90° , or images where the Sun elevation is lower than 10° (θ_{cut}). This is shown in figure 3.

In figure 4 we plot the data with θ_{cut} applied versus the Sun azimuth. We observe that the mean of Δ_x and Δ_y vary with ϕ_{sun} in a quasi-periodic fashion. What we observe is that the deviation is larger when the Sun azimuth is orthogonal to one of the image axes. Namely, the largest deviations for Δ_x are observed when $\phi_{sun} \approx 90^\circ$ or 270° , whereas the largest deviations for Δ_y are observed when $\phi_{sun} \approx 0^\circ$ and 180° . The direction defined by the Sun azimuth appears to be a preferential direction: translations along this direction can be more accurately recovered, because the features on the terrain create sharper shadows along the direction to the Sun.

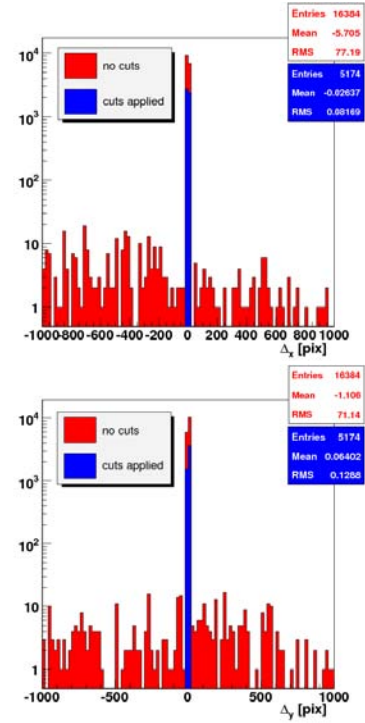


Figure 3. The effect of the Sun elevation cut on the distribution of Δ_x (top) and Δ_y (bottom) for the Olympus Mons data.

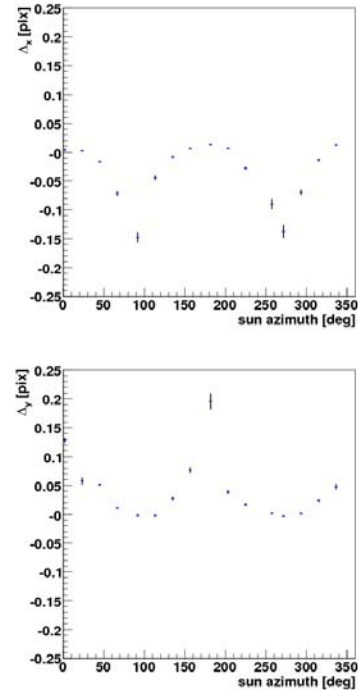


Figure 4. The average Δ_x and Δ_y versus the Sun azimuth for the Olympus Mons data. The error bar on each point represents the root-mean-square.

Based on the data in figure 4 we can devise a selection criterion for the Sun azimuth, so that translations along both axes can be recovered with comparable accuracy. The selection criterion is that the Sun azimuth must be more than 20° away from both image axes. The distributions of Δ_x and Δ_y when both θ_{cut} and ϕ_{cut} are applied are shown in figure 5.

Figure 5 represents the end point of our analysis. We observe that the two distributions are centered on 0, and have a width of ≈ 0.1 pixel root-mean-square. The two distributions have a tail in the direction of the translation applied in the simulations (-100 m along the X axis, and +100 m along the Y axis). The nature of this slight asymmetry is not understood at present.

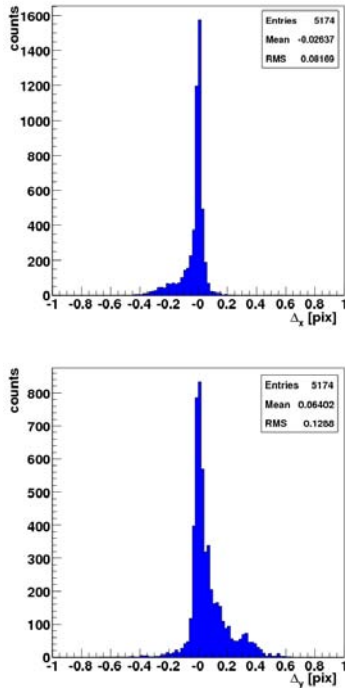


Figure 5. The distribution of Δ_x and Δ_y for the Olympus Mons data, once both the Sun cuts are applied.

6.1.1. Changing the Sun Azimuth

The bulk of the simulation runs was carried out with the same Sun azimuth for both the reference and comparison images. We however also made a set of simulation runs where the azimuth of the Sun in the comparison image was 30° away from the azimuth used in the reference image; only a translation of 100 meters along the X axis was applied. The results are shown in figure 6. Even in this case the algorithm is able to recover the injected translation with an accuracy of ≈ 0.1 pixel root-mean-square.

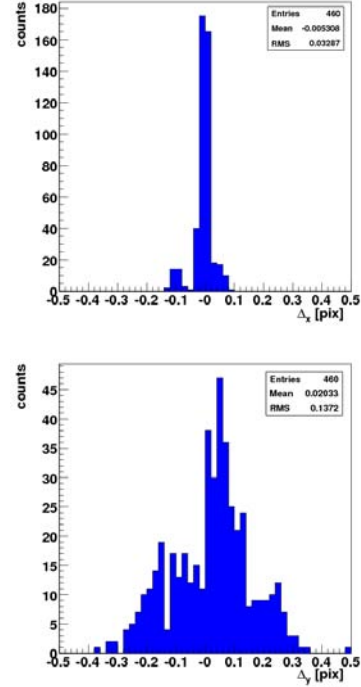


Figure 6. The distribution of Δ_x (top) and Δ_y (bottom) for the Olympus Mons data for date where the Sun azimuth of the comparison and reference images differ by 30° .

6.2. The Synthetic Model

As already hinted to, the results based on the synthetic digital elevation model give a slightly different picture, although the main conclusions do not change.

The θ_{cut} criterion is still effective in rejecting data points that return a large deviation from the expectation.

A point of discrepancy with respect to the Olympus Mons data is the behavior of the recovered translations as a function of Sun azimuth. Figure 7 shows that the effect observed for the Olympus Mons models is almost not observed here. After the θ_{cut} criterion is applied, any remaining offset is smaller than 0.05 pixel.

Finally, figure 8 shows the distribution for Δ_x and Δ_y . Again, the translation is recovered with an accuracy of ≈ 0.1 pixel root-mean-square, but the details of the distributions differ from what was observed before.

7. CONCLUSIONS

We have performed a study of the accuracy with which a shape-based pattern matching algorithm can identify translations between remote sensing images of the same planetary features. We have applied the algorithms in a Monte Carlo fashion to digital elevation models (both real

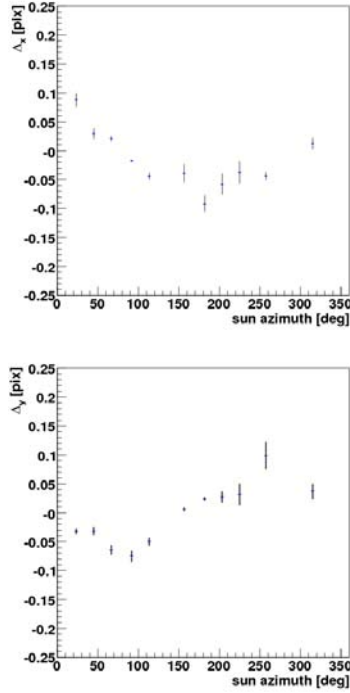


Figure 7. The average Δ_x (top) and Δ_y (bottom) versus the Sun azimuth for the Synthetic Model data. The error bar on each point represents the root-mean-square.

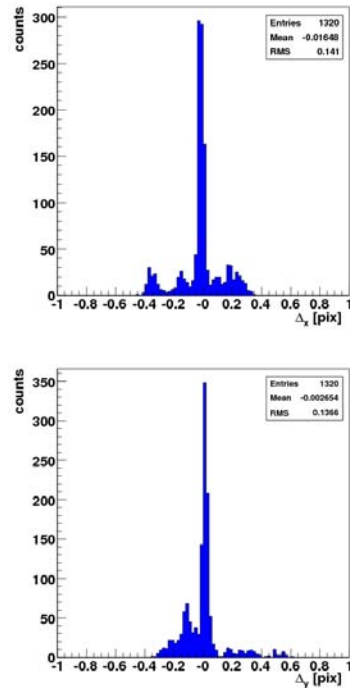


Figure 8. The distribution of Δ_x (top) and Δ_y (bottom) for the Synthetic Model data, once both the Sun cuts are applied.

and synthetic) in order to investigate the statistical performance of the procedure.

We find that for a broad range of illumination conditions translations between images can be recovered with an accuracy of 0.1 pixel *r.m.s.*

The algorithm performs best for translations along the projected direction to the Sun on the image plane. This study shows that translations along both image axes at the same time can be recovered with the same accuracy of 0.1 pixel as long as the projected direction to the Sun lies more than $\approx 20^\circ$ away from the same image axes.

Finally, this study demonstrates that the images to be compared need not be taken under the very same illumination conditions in order to be effectively matched. For a given Sun azimuth, any pair of images taken with Sun elevation angles larger than 10° can be used; images taken when the Sun is at the zenith must also be avoided. The range of useful illumination conditions is further broadened because this study concludes that differences in Sun azimuth of at least 30° do not affect the accuracy of the matching algorithm.

The error contributed by the matching algorithm is but one of the several error contributions to be taken into account during the analysis of the data pertaining to the measurement of the possible libration of the surface of Mercury. This study shows that the accuracy of the pattern matching algorithm is not a limiting factor in the ultimate accuracy of the libration experiment aboard the BepiColombo mission to Mercury.

ACKNOWLEDGMENTS

This study was carried out under ESA contract ESTEC 18624.

REFERENCES

1. *HALCON Documentation*.
<http://www.mvtec.com/halcon/>.
2. *HALCON Manual*.
<http://www.mvtec.com/download/documentation/>.
3. EP1193642, April 2002.
<http://www.espacenet.com/>.
4. Persistence Of Vision Raytracer.
<http://www.povray.org/>.

SEDIMENTARY AND PALEOCLIMATIC RESEARCH ON THE PROMETHEI BASIN IN THE SOUTH POLAR CAP OF MARS.

E. Velasco Domínguez⁽¹⁾⁽²⁾, F. Anguita Virella⁽¹⁾⁽³⁾, A. Carrasco Castro⁽¹⁾⁽⁴⁾, R. Gras Peña⁽¹⁾⁽⁵⁾, J. Martín Chivelet⁽¹⁾⁽⁶⁾, I. Iribarren Rodríguez⁽¹⁾⁽⁷⁾. ⁽¹⁾*Seminario de Ciencias Planetarias, Facultad de Ciencias Geológicas, Universidad Complutense de Madrid, Spain*
 Emails: ⁽²⁾ estherveldom@hotmail.com, ⁽³⁾ anguita@geo.ucm.es, ⁽⁴⁾ angelurico@gmail.com, ⁽⁵⁾ athosgras@hotmail.com, ⁽⁶⁾ j.m.chivelet@geo.ucm.es, ⁽⁷⁾ ilazkeitor@hotmail.com

INTRODUCTION:

Impact cratering is one of the most important planetary geological processes in the forming of relief in terrestrial planets. On Mars, many impact craters and basins are probable candidates for sedimentary basins.

Impacts form an uplifted rim as well as a lower basin, creating this way a suitable area for the study of sedimentary processes. Even on *Viking* imagery, a number of eroded sedimentary series have been identified on the craters of Mars' highlands.

Promethei Basin, a half crescentic depression at the border of Planum Australe, is probably the best example of a Martian sediment trap, since its 900 km wide original impact basin could harbor sedimentary layers several kilometres deep.

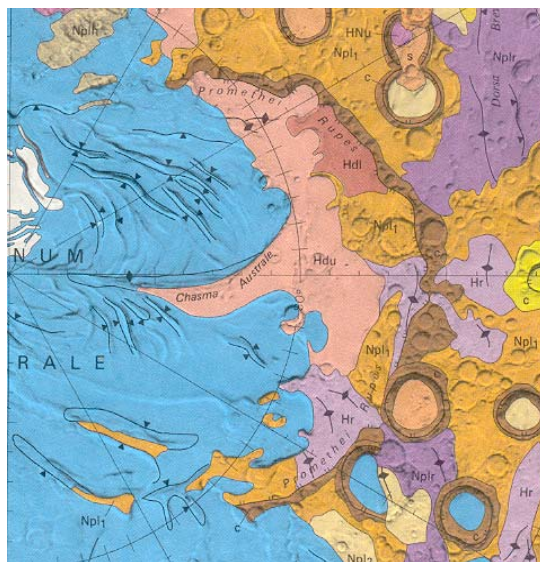


Fig. 1: Geological map of the Promethei Basin. Amazonian sediments appear in white and blue (Apl, Api), those with Hesperian age in pink (Hdu), medium brown (Hdl), and purple (Hr). Finally, Npl1 (in yellow) and Promethei Rupes (dark brown) are Noachian units. [9]

This basin has been selected because it is located in an area with some specific characteristics which may yield relevant conclusions on the geological and climatic

history of Mars. It possesses a most complete geological history as it contains layers whose ages range from Noachian to Amazonian. (Fig. 1)

These sediments come mainly from Chasma Australe, which was carved in Amazonian times [1] providing us therefore with an insight into the recent geological history. The basin was also filled through channels coming from the western edge of Dorsa Argentea [7], with sediments which possibly contain older rock succession. (Fig. 2)

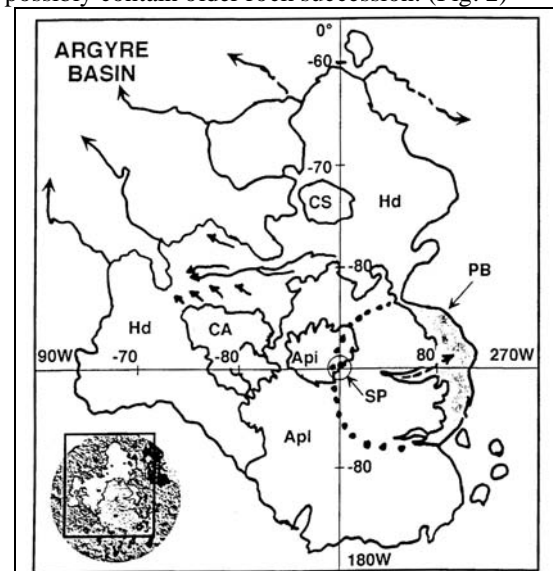


Fig. 2: Sketch map showing the location of the channels leading from the western edge of the Dorsa Argentea Formation to the surrounding lowlands and into the Argyre Basin. The distribution of Api, Apl, Hd, and HNu and features associated with the south polar deposits are also shown. SP, south pole; PB, Promethei Basin; dotted line shows extension under polar cap; dashed line shows Chasma Australe; CA, Cavi Angusti; CS, Cavi Sisyphi; arrows within Hd are Dorsa Argentea esker-like ridges, and arrows outside Hd are channels interpreted to be draining Hd. [7]

The Promethei Basin is located close to the south pole of Mars (75°-85° South and 45°-135°East). Fishbaugh and Head [3] follow hypotheses according to which Mars' climate changes from cold and wet to colder and dry could be due to changes in the planet's obliquity. If this has been the case, then, the

most outstanding climate changes would have taken place simultaneously in both polar caps, and therefore it should be possible to find evidence of these changes in the sedimentary record of both hemispheres.

If this however proved not to be the case, other possible causes for the climatic change can be proposed [3]. Among them, we should mention local subcap volcanic eruptions, a higher geothermal heat flux in the past, a much thicker cap, outgassing of volatiles and/or variations in solar luminosity, polar wander, cap compositional differences, and, finally, frictional heating due to basal sliding.

After a first analysis, using *Themis* context images, we have concluded that the basin fill has taken place through fluvial-alluvial, glacial, aeolian and gravitational processes. The alternation of alluvial and glacial sediments should be an indication of Mars climatic changes because these deposits are formed in very different environmental contexts. At present, it is highly improbable that water liquid can flow over the Mars surface, because in case that it happened, it would directly sublimate, due to the low atmospheric pressure. Nevertheless, the presence of fluvial deposits and paleochannels proves that liquid melting water did flow through this area.

EVOLUTION OF THE SEDIMENTARY FILL AT PROMETHEI BASIN

In this note, a preliminary geomorphological map based in *Themis* context images is presented. It includes the main morphological features and sedimentary units of paleoclimatological interest. Subsequent research will improve this preliminary map.

From the base to the top of the sequence (figure 3), we find:

1. Recessional front moraines, shaped as sinuous strings. They overlie the cratered terrain outside the basin as well. They record the first great glaciation, and the biggest one of which we have evidence. These materials are the most cratered, and therefore the oldest sediments in this area.
2. Alluvial deposits. They are also highly cratered, but most of them (and therefore also the bigger ones) are eroded. We have found braided drainage networks, which are visible in at least one place near the basin rim.
3. Sheet-flow deposits. These deposits are characterized by the lack of big craters. We have found in this area, near the mouth of Chasma Australe, an exhumed relief

including ridges with the same direction as unit 1. Although this terrain is not the only one that contains pedestal craters, this morphology appears frequently.

4. Base of slope deposits. This unit is composed by materials very similar to unit 2, with most of the bigger craters eroded. In this area we have found both gravitational slope deposits as well as fluvial processes as gullies
5. Frontal moraines unit. Similar to 1, though it drapes all but the youngest terrains. It covers units 2,3 and 4.
6. Alluvial fans.
7. Upper glacial unit. It unconformably overlies units 1 and 5, and is in turn overlain by the PLD. Here we have found esker structures.
8. Polar Layered Deposits (PLD). They are very young deposits, since they do present very few craters. Here, we find several deep valleys or chasmata, the deepest and biggest of them being Chasma Australe. It is interesting to note that we haven't found any trace of sedimentary remains near its mouth.
9. Barkhanoid dunes present on the bottom of chasmas. We consider them to be recent formations, as they cover all other materials.

Altogether, the sedimentary fill bears the trace of at least four glacier advances and recessions. Further geomorphologic analyses will surely bring to light an even more complicated palaeoclimatic history.

PENDING QUESTIONS:

- Where are the sediments eroded from Chasma Australe? Even supposing that most PLD materials were ices, one would expect to find well-defined deposits draping the mouth of the chasma, from which at least $30 \cdot 10^6 \text{ km}^3$ have been eroded.
- Why eskers are limited to only a small part of the basin?
- To discuss the range of transport mechanisms of Chasma Australe and the other re-entrants.
- Has there been only one glacial period which formed moraines in all the Basin areas, even outside the basin? Or have there been two glacial periods, one at older terrains and another glacial advance on more recent terrains?

PENDING TASKS:

- To use HRSC images to improve the mapping of the geomorphologic units. For instance,
 - To clear the relations between fluvial and glacier processes at the number 7 area [see map]
 - To study in detail the possible dendritic network at area 2.
 - To delve in the apparent tectonic control of the deposits inside the craters outside Promethei Basin included at unit 4.
 - To study in detail the minor re-entrants at unit impact 5.
 - To map the different alluvial sediment units.
 - To analyse the Dorsa Argentea erosive network [7]

REFERENCES:

1. Anguita, F., Babin, R., Benito, G., Gomez, D., Collado, A., and Rice, J. 2000. Chasma Australe, Mars: Structural framework for a catastrophic outflow origin. *Icarus* 144, 302–312.
2. Clifford, S.M., Doran, P.T., Fisher, D., and Herd, C., 2005. Third Mar polar science special issue: Key questions, needed observations, and recommended investigations. *Icarus* 174, 291-293.
3. Fishbaugh, K., and Head, J.W., 2001. Comparison of the north and south polar caps of Mars: New observations from MOLA data and discussion of some outstanding questions. *Icarus* 154, 145-161.
4. Kolb, E.J., Tanaka, K. L., 2006. Accumulation and erosion of south polar layered deposits in the Promethei Lingula region, Planum Australe, Mars.
5. Mangold, N., 2005. High latitude patterned grounds on Mars: Classification, distribution and climatic control. *Icarus* 174, 336-359
6. Márquez, A., Fernández, C., Anguita, F., Farelo, A., Anguita, J., De la Casa, M., 2004. New evidence for a volcanically, tectonically, and climatically active Mars. *Icarus* 172, 573-578.
7. Milkovich S., Head, J.W., and Pratt, S., 2001. Melt of Hesperian-aged ice-rich deposits near the south pole of Mars: Evidence for drainage channels and Lakes. *Journal of Geophysical Research*, 107. doi: 10.1029/2001JE001802.
8. M., Pondrelli, A. Baliva, S. Di Lorenzo, L. Marinangeli and A.P. Rossi, 2004. Complex evolution of paleolacustrine systems on Mars: an example from the Holden Crater. *L.P.S.C. XXXV*.
9. Tanaka, K. L., and Scott, D. H., 1987. Geologic Map of the Polar Regions of Mars, MAP I-1802-C, 1:15.000.000, USGS

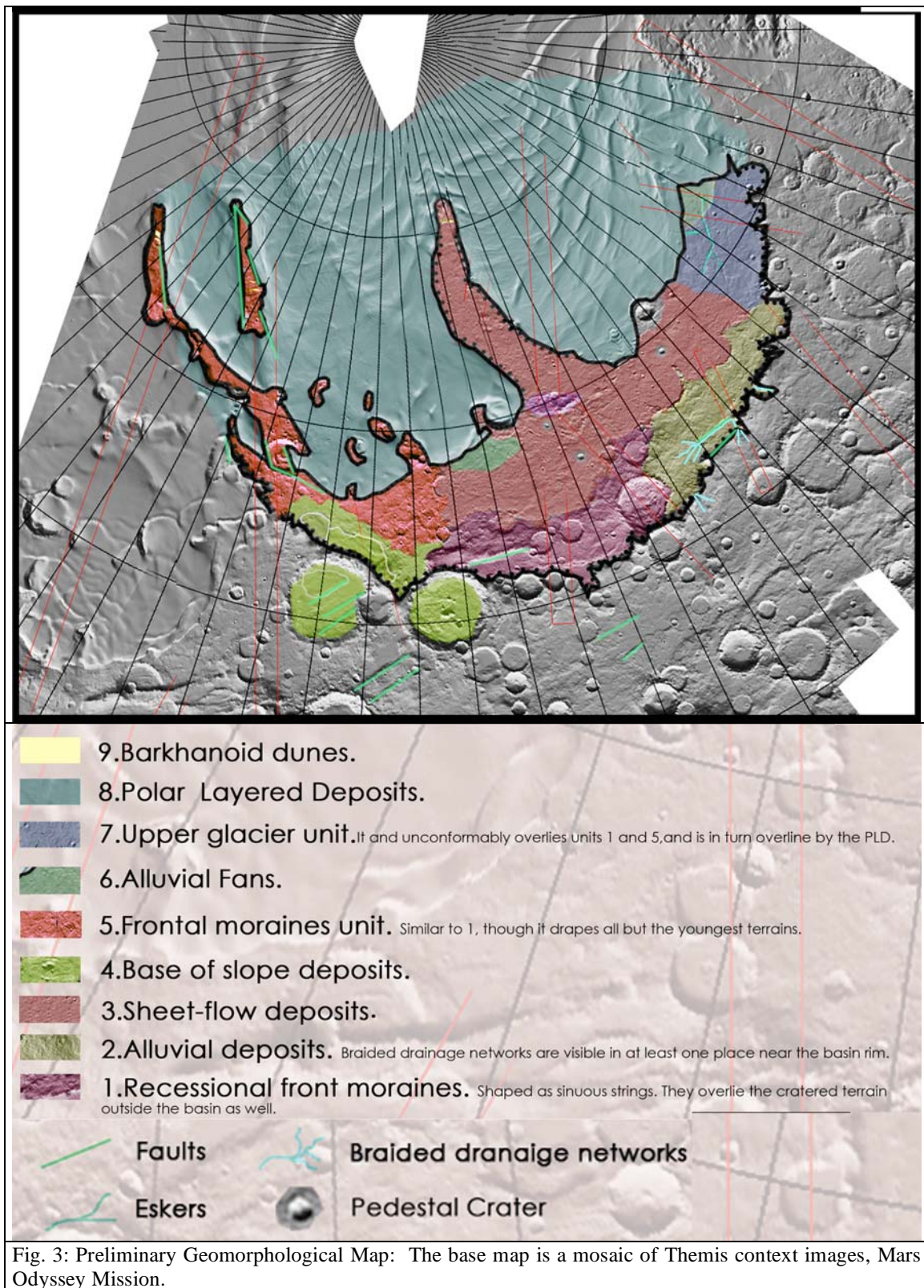
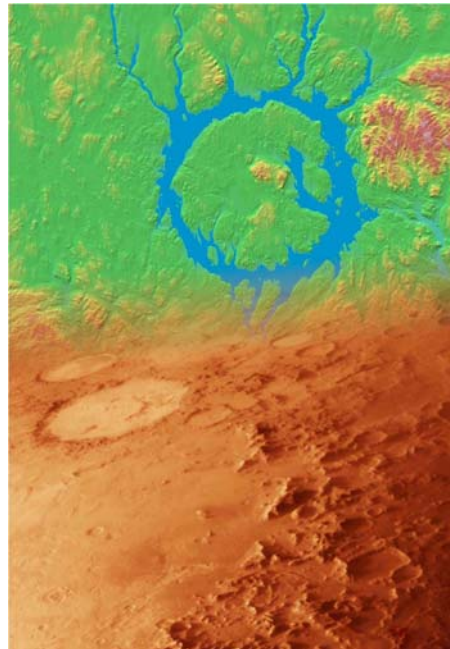


Fig. 3: Preliminary Geomorphological Map: The base map is a mosaic of Themis context images, Mars Odyssey Mission.

Poster Session 2

Thursday, 11 May 2006



40th ESLAB Proceedings
First International Conference on Impact Cratering in the Solar System

THE TELLURIC CONDUCTIVITY ANOMALY AT MAGYARMECSKE: IS IT A BURIED IMPACT CRATER?

Tamás Bodoky^(1,3), Márta Kis⁽¹⁾, István Kummer⁽¹⁾, György Don⁽²⁾

⁽¹⁾Eötvös Lorand Geophysical Institute of Hungary, H-1145 Budapest, Columbus str. 17-23, Hungary, Email: bodoky@elgi.hu, mkis@elgi.hu, kummer@elgi.hu

⁽²⁾Geological Institute of Hungary, H-1443 Budapest, P.O. Box 106, Hungary, Email: dongy@mafi.hu

⁽³⁾University of Miskolc, Dept. of Geophysics, H-3511 Miskolc-Egyetemváros, Hungary, Email: bodoky@elgi.hu

ABSTRACT

In the fifties an approximately round shaped high amplitude telluric conductivity anomaly was found at MagyarMEcske, in South-West Hungary (Fig. 1, [1]). Though attempts were made to interpret it as a highly conductive coal bearing Carboniferous sequence (Fig. 2, [2]) some questions have been left open:

- The Carboniferous sequence covered an area much more extended than the anomaly itself, why did the anomaly appear only on a restricted part of it ([3])?
- Old seismic data indicated a low velocity zone in the refracting basement coinciding roughly with the telluric anomaly ([2]), why?
- Deep DC soundings carried out in the area detected an extraordinary deepening of the high resistivity basement on the same location ([2]). What could cause such an approximately round deepening of the basement?

The authors reinvestigated all available geophysical data measured in the area and based on them came to the conclusion, that the conductivity anomaly might indicate a buried impact crater of a big meteorite ([4]).

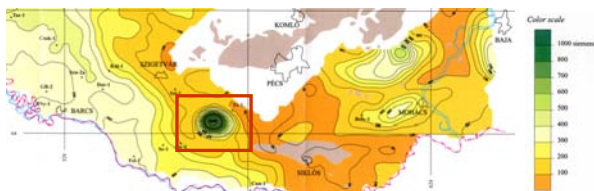


Fig. 1. The telluric conductivity anomaly at MagyarMEcske, Hungary, on the Telluric Conductance Map of Transdanubia ([2])

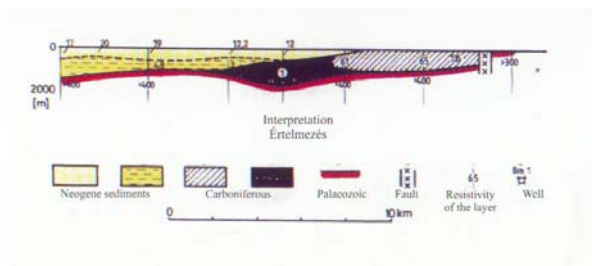


Fig. 2. The MagyarMEcske region ([2])

1. GEOPHYSICAL SIGNATURES OF AN IMPACT CRATER

Pilkington and Grieve gave a summary of the geophysical signature of known terrestrial impact craters in 1992 [5]. Following their paper we briefly summarise the expected geophysical signature of an impact crater (Fig. 3).

- **Gravity signature:** The density of crater fills consisting of the breccia lens and covering postimpact sediments is usually much lower than that of the target rocks. The fractured zone around and below craters has decreased density as well. Consequently craters are characterized by a deficiency of mass compared to the preimpact status which means that they are characterized by a *negative gravity anomaly*.

Maximum values of gravity anomalies due to craters lie between 1 and 10 mgal depending on the diameter of the crater. Horizontally the gravity low extends generally to the crater rim. Since the effect is small it is practical to use residual anomaly maps.

- **Magnetic signature:** Target rocks might have characteristic preimpact magnetic properties indicated by characteristic anomaly trends. Heating up and melting of rocks due to an impact wipe out earlier magnetic properties and postimpact cooling down may result in development of new ones. In this way impacts may confuse preimpact magnetic trends of the target area if there were any. However, the magnetic field is more complex than the gravity field and the magnetic properties of rocks are far more diverse than the gravity ones, thus there is not a one-to-one correlation of the character of the magnetic anomaly and the crater morphology, or by other words impact craters have *no characteristic magnetic signature*.

- **Electrical signature:** The porosity of a breccia lens and a fractured zone is generally higher than that of the unaffected target rocks. Higher porosity results in higher fluid content and that again in higher conductivity. So craters are characterized generally by *high conductivity anomalies*.

- **Seismic signature:** In rocks the velocity of seismic wave propagation depends very much on the

compaction of rocks. Breccia lenses and fractured zones are less compact than corresponding target rocks, consequently *seismic velocities are smaller and the attenuation of seismic energy is higher* in them if compared to the unaffected target rocks.

The list of geophysical signatures has to be completed by an important possibility of geophysics, i.e. by the geophysical imaging of subsurface morphology. Impact craters have characteristic morphologic features. As long as they are located on the surface of the Earth those features can be recognised on images of the Earth surface like maps or satellite images. However, if old crater structures are covered by postimpact geologic formations then they are hidden from direct observations. In such cases geophysical methods, electric, electromagnetic and seismic refraction and reflection measurements are to be used to get their morphologic images.

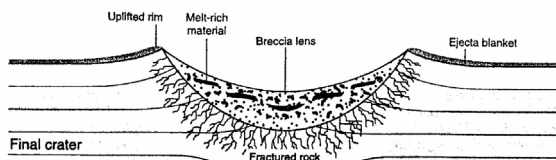


Fig. 3. The final crater (after [6])

2. GEOPHYSICAL RESULTS OF THE MAGYARMECSKE REGION

In the case of the MagyarMECSKE conductivity anomaly on the surface there are young sediments and the area is entirely flat, no any special morphology can be seen. Old data of magnetotelluric and deep DC soundings indicate that the highly conductive formations are located below the young sediments. Thus if the conductivity anomaly is regarded as the electric signature of an ancient meteorite impact crater then it is buried under younger formations (Fig. 4).

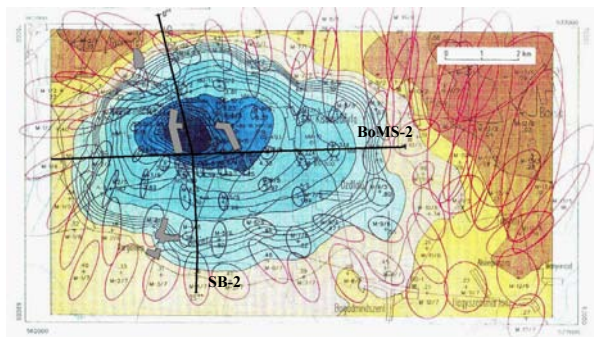


Fig. 4. Detailed map of the conductivity anomaly with the location of seismic reflection lines, and telluric ellipses

In the Bouguer anomaly map a gravity minimum with a peak value of -2 mgal can be found almost on the same location, it is similar in size and extension, however, its centre is slightly shifted westwards from that of the telluric anomaly (Fig. 5).

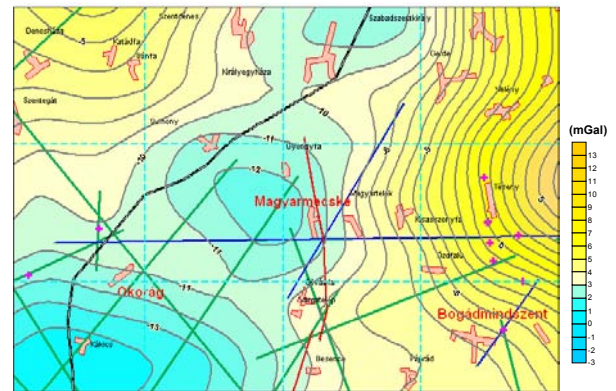


Fig. 5. Gravity Bouguer-anomaly map of the MagyarMECSKE area

Again on the same location a seismic refraction velocity anomaly of the refracting high velocity basement has been known from the time of the extensive seismic refraction surveys of the fifties. Here the anomaly means a 20 % decrease of the seismic refraction velocities (Fig. 6).

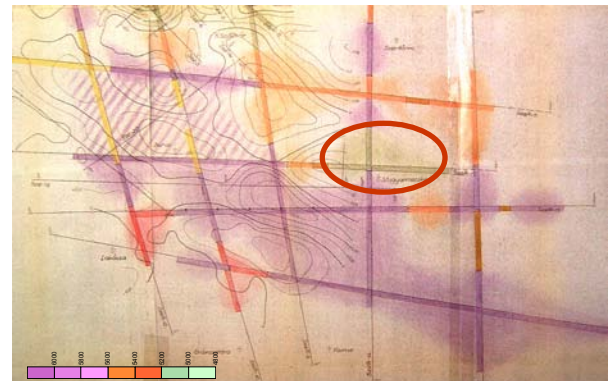


Fig. 6. Seismic refraction basement velocity map in the MagyarMECSKE area

An old, low coverage, seismic reflection profile crosses the centre of the conductivity anomaly in W-E direction. It was recorded by analogue technique in 1971 and today is available only in paper version (Fig. 7). It shows a structure dipping strongly from East to West. On its deeper western part one side of a crater like structure can be recognised below the young sediments which are at the western rim approximately 900 m thick. On the uplifted eastern part the other side of the structure seems to be rather much eroded and the remnants of the assumed eastern rim underlies sedimentary layers of no more than a 100 m thickness. Maybe, the uplifted and eroded eastern part of the

structure is the reason of the asymmetry in the gravity as well as the conductivity images.

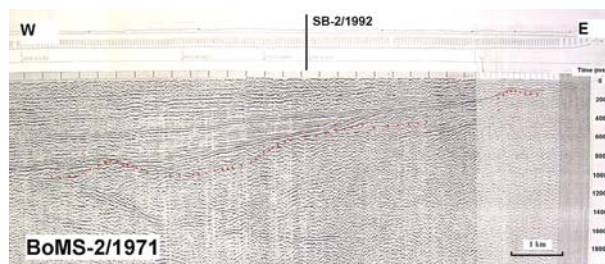


Fig. 7. The BoMS-2/1971 seismic reflection profile

Another seismic reflection profile recorded by up-to-date digital technique in the early nineties crosses the area in N-S direction also just in the centre of the telluric anomaly. It shows remarkable features similar to the cross-section of a one-ring impact crater just below the Neogene sediments (Fig. 8). The northern rim can be found in a depth of approximately 450 m, the southern rim at 550 m whereas the peak of the central uplift at 650 m, respectively. The southern side of the structure shows the traces of postimpact tectonic events, the profile crosses a fault line here with a throw of about 100 m.

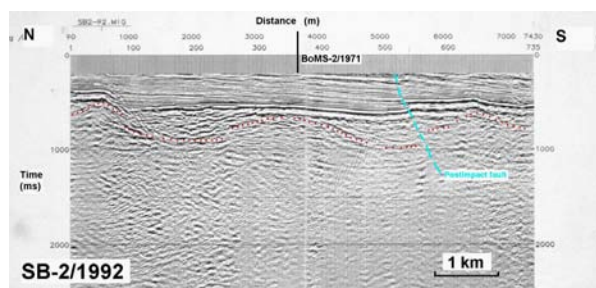


Fig. 8. The SB-2 migrated seismic reflection profile

3. CONCLUSIONS

Based on the geophysical signatures of the area described above, the authors came to the conclusion, that the Magyarmecske conductivity anomaly might indicate a buried impact crater of a big meteorite.

The impact happened probably sometimes after the Carboniferous on an area where the Carboniferous sedimentary rocks were on the surface that time, and it created a complex crater with central uplift in them. The structure had a crater diameter of approximately 6-8 km. The surface of the target rocks was either oblique by the time of the impact or became tilted soon after that. The western part of the structure had been or got under sea-level and was covered by sediments meanwhile the eastern part fell on mainland and suffered erosion for a while. Later the whole structure has been buried and underwent tectonic effects. We think, that the above described process resulted in the

complex structure which is known today as the "Magyarmecske telluric anomaly".

4. REFERENCES

1. Ádám A., Verő J., Results of the regional telluric measurements in Hungary (in German), *Acta Technica*, Vol. 47, 63-77, 1964.
2. Nemesi L. et al., Telluric map of Transdanubia, *Geophysical Transactions*, Vol. 43, 169-204, 2000.
3. Majoros Gy., A few reflections on the telluric conductance map of Transdanubia, *Geophysical Transactions*, Vol. 43, 291-296, 2000.
4. Bodoky, T. et al., A magyarmecskei tellurikus vezetőképesség anomália: eltemetett meteoritkráter? (in Hungarian with English abstract), *Magyar Geofizika*, Vol. 45, 96-101, 2004.
5. Pilkington, M., Grieve, R.A.F., The Geophysical Signature of Terrestrial Impact Craters, *Reviews of Geophysics*, Vol. 30, 161-168, 1992.
6. French, B. M., *Traces of Catastrophe: a Handbook of Shock-Metamorphic Effects in Terrestrial Meteorite Impact Structures*. LPI Contribution No. 945, Lunar and Planetary Institute, Houston, 1998.

EXCAVATION EFFICIENCIES IN THREE-DIMENSIONAL SIMULATIONS OF THE CHICXULUB METEOR IMPACT

G. R. Gisler⁽¹⁾, R. P. Weaver⁽²⁾, M. L. Gittings⁽³⁾

⁽¹⁾*Physics of Geological Processes, University of Oslo, PO Box 1048 Blindern, 0316 Oslo, NORWAY
Email: galen.gisler@fys.uio.no*

⁽²⁾*Los Alamos National Laboratory, MS T087, Los Alamos, NM 87545 USA, Email: rpw@lanl.gov*

⁽³⁾*Science Applications International, MS T087, Los Alamos NM 87545 USA, Email: gittings@lanl.gov*

ABSTRACT

Simulations of the meteor impact at Chicxulub with the Los Alamos hydrocode SAGE are presented here for four angles of impact. We describe the code and its validation, including a comparison of simulation results with measurements at the crater from the Sedan underground nuclear test. We investigate energy partitioning and excavation efficiency as a function of impact angle, and discuss implications for the consequent distribution of ejected material. We find that the impact angle must be fairly steep to account for the worldwide distribution of shocked quartz.

1. INTRODUCTION

We have performed several three-dimensional simulations of the meteor impact at Chicxulub, Mexico with the Continuous Adaptive Mesh Refinement Eulerian hydrocode SAGE. The Chicxulub impact, which occurred 65 million years ago, is widely believed to be associated with the mass-extinction event at the end of the Cretaceous period and may have caused this extinction by a combination of widespread wildfires, high atmospheric opacity, atmospheric toxicity, and severe climate excursions. The worldwide distribution of shocked quartz, platinum-group elements, tektites, and soot in the Cretaceous/Tertiary (K/T) boundary layer can provide important diagnostics of the dynamics of the impact and the mechanisms of extinction [1]. Studies of the energy partitions and excavation efficiencies among simulations at various angles of impact and projectile characteristics are useful in elucidating the relation between the impact event, the distributed evidence in the K/T boundary layer, and the extinction mechanism.

2. SAGE

The SAGE code is a fully-compressible multiphase multifluid hydrocode using a Godunov scheme for second-order accuracy. It has been jointly developed by the Los Alamos National Laboratory and Science

Applications International (SAI). Developed under the auspices of the Department of Energy's program in Advanced Simulation and Computing, it has been exposed throughout its development to very rigorous testing against problems with analytical solutions, for verification. See for example [2], which reports the results of a recent series of these tests and describes an automated scheme for continued testing of new versions of the code in the same manner. Validation, or testing against controlled laboratory-scale experiments is also done according to a timetable [3]. SAGE has additionally been applied to large-scale geophysical events including volcanic eruptions and tsunamis [4], where neither control nor precision testing is possible. In these cases we aim for consistency with the *a posteriori* geophysical data, and achieve this.

Because the equations of hydrodynamics are not in themselves closed, additional information regarding the response of materials to stress must be supplied. These are in the form of equations of state (for isotropic stresses) and constitutive relations, which relate the stress tensor and the internal energy to local densities and temperatures. In practice, these relations are known to be the weakest part of complex multi-fluid hydrocode simulations, because the codes often explore regimes in phase space that are not well covered by the laboratory experimentation that is used to derive these relations. SAGE includes a variety of analytical formulations of these equations of state and constitutive relations, but these are inadequate for complex geophysical use. Better are the equation of state and strength tables from the Los Alamos SESAME library, which unfortunately does not have good coverage of geological material. What exists in SESAME is mostly derived from light gas gun experiments carried out decades ago and extended to regions off the Hugoniot by theory. In the Chicxulub simulations we use SESAME tables for air, calcite, granite, and mantle material. We find, however, that we must modify the output from the SESAME tables to enforce thermodynamic consistency (including the latent heats of phase transitions, removing the van-der-Waals loops, etc). In addition, SAGE contains a special tabular equation for water designed by SAI to include nearly all known phase transitions.

It is important to realize that in a multimaterial Eulerian code like SAGE, some decision must be made as to how to treat cells that receive a mixture of materials.

There are interface treatments available within SAGE that allow one to keep track of the position of an interface on a sub-grid scale if desired. Such treatments allow one to inhibit or limit mixing, if so desired. We have not used any such interface treatment in these calculations. The default method, which we have used, is to assume that within each Eulerian cell local thermodynamic equilibrium obtains among the materials that occupy that cell. Because the adaptive grid mechanism ensures that adaption occurs to the maximum extent allowed by the user at a material interface, the equilibration that occurs within a single timestep occurs on the smallest cells in the problem. The equilibration is made thermodynamically consistent, ensuring conservation of total energy.

For materials in the problem that have strength, a simple elastic-perfectly plastic strength model is used, with pressure hardening, tensile failure, and melt energy. On impact, the transition from solid to liquid (indeed to vapor for much of the immediate target) is so rapid that the details scarcely matter, provided the latent heat of transition, the induced pressure, and the consequent volume change are properly accounted for. No specific fragmentation model was used in these calculations.

Because the material models are such an important part of the computational enterprise for a problem such as Chicxulub, it is important to have some validation, or at least benchmarking, experience with events at comparable scale that utilize the same material models. Realistically, the only geophysical events that even approach the scale of planetary impact craters while having known inputs of energy are underground nuclear explosions. We take in particular the Sedan nuclear test of July 1962, done for the Plowshare program, and intended to investigate possible peaceful uses of nuclear explosions. The Sedan device was buried 194 m below the surface of the Nevada test site desert and exploded with an energy of 104 kT. The emplacement depth was close to the optimum depth for cratering, and the resultant crater is a good test for cratering simulations. Fig. 1 shows the result of a comparison between a SAGE calculation (colors indicating material density) of the crater resulting from Sedan, still at an early stage, before fallback has completed, and measurements taken at the crater itself (the solid lines). The agreement is remarkably good. The crater diameter of 360 m, the maximum melt depth of 246 m, and the final crater depth of 97 m are well matched by the calculation (only the melt depth being somewhat overestimated). The maximum height of the dome before its breach, 90 m, and the time of the dome breach, 3 seconds after initiation, are also reasonably well matched by the calculation.

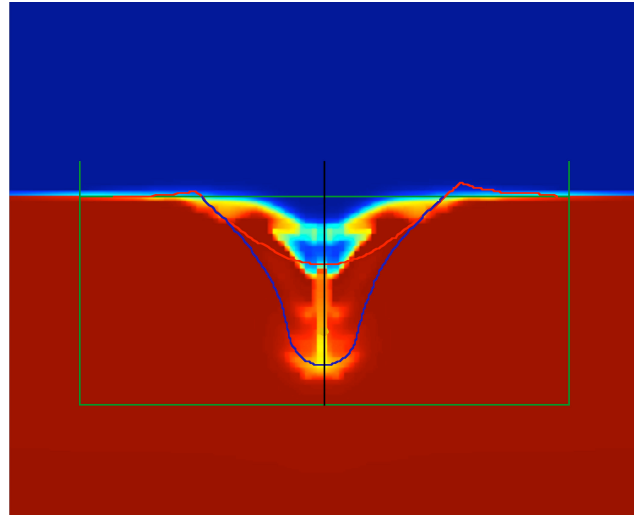


Fig. 1. Comparison between a SAGE calculation (colors representing density), and measurements taken on site of the Sedan underground nuclear explosion. The red solid line indicates the shape and size of the final crater, and the blue solid line indicates the extent of the below-ground melt.

3. SETUP FOR THE CHICXULUB SIMULATIONS

All simulations reported here were performed in a computational domain which is a box with horizontal dimension 256 km x 256 km and vertical dimension 128 km. The target consists of a US standard atmosphere of scale height 7 km, extending up to an altitude of 78 km, a water depth of 500 meters, a mixed water/solid calcite region 4.5 km thick, linearly stratified from pure water at the top to pure calcite at the bottom, a granite region 30 km thick, and a mantle region 15 km thick. This vertical stratification is illustrated schematically in Fig. 4 below. The target is homogeneous in the horizontal directions.

The projectile in the runs reported here is a sphere of 12 km diameter, with the density and equation of state of granite, but without strength, and having a velocity of 20 km/s. The total kinetic energy is therefore 113 Tt. An earlier series of runs performed with an earlier version of SAGE with a slower and lighter projectile is mentioned here only in passing. The 4 runs here reported have projectile trajectories of 15°, 30°, 45° and 60° with respect to the horizontal. All projectiles were started at an altitude of 40 km, except for the 15° run, in which a 20 km initial altitude was used. Outflow boundary conditions (freeze regions) are used.

We run these simulations until most of the ejected material has either achieved ballistic trajectories or been deposited locally. This generally requires two to three minutes of physical time, or several months of computational time on 512 processors. So far we have achieved this with all but the 60° simulation, which has only run out to 17 seconds past impact. These longer-time studies supplement earlier work by Pierazzo and

collaborators on effects of impact angle [5].

4. RESULTS

The only free energy at the start of the problem is the asteroid's kinetic energy. Upon impact, this energy is shared with the target, which responds both by being accelerated out of the way and by heating up. In Fig. 2 we plot the partition of kinetic and internal energies as a function of impact angle for the projectile and target at 5 seconds after the asteroid's kinetic energy is reduced to 75% of its initial value. The lines indicating internal energy represent the changes from initial values of internal energy, of course. As is expected, shallow impacts deliver much less energy to the target than deep impacts do. For very shallow impacts, much of the energy is retained in the form of the asteroid's kinetic energy, whose material propagates downrange on flattened "skipping" trajectories to impact again downrange.

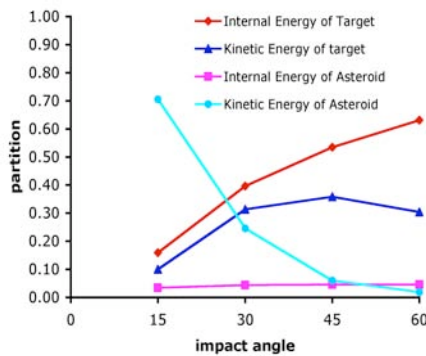


Fig. 2: Partition of energies (relative to the initial asteroid kinetic energy) at 5 seconds after the time at which the projectile's kinetic energy is 75% of its initial value for the 4 runs reported here. At shallow angles of impact, most of the initial kinetic energy is retained by the asteroid, whose material skips downrange in a relatively tightly focussed stream. At angles of impact greater than about 45°, more than 90% of the energy of impact is transmitted to relatively deeply excavated target material.

Because impacts at shallow angles deliver much less energy to the target, they also do not excavate very deeply. The worldwide distribution of ejected material suggests that significantly deep excavation has taken place in this event. In particular, shocked quartz, which is produced by the rapid application of high pressure to granite, is found in the K/T boundary layer at places very far distant from Chicxulub [6]. Since the granite of the continental crust at Chicxulub lies buried beneath several kilometers of carbonate platform, it is clear that deep excavation must be relatively efficient to account for the worldwide distribution of shocked quartz.

We diagnose excavation efficiencies by studying the trajectories and histories of Lagrangian tracer particles that are placed at particular positions at the beginning of the calculation. These tracers are massless points that move with the local flow and record as many local variables as desired. Typically we record pressure, temperature, density, and the three components of velocity. Unfortunately the treatment of tracers in SAGE has been rather clumsy and inefficient (the tracer data is written out in text format from a single processor, for example), so that it is deleterious to the parallel performance of the code to follow more than a few hundred such tracers in a given calculation.

In these calculations we have sprinkled a total of 213 tracers, 69 of them in the projectile and the remainder around the impact site down to mantle depths. Each target tracer originates within a given target layer, but it may later reflect the characteristics of a different material, or a mixture of materials. If a tracer that began in a one-material cell ever lands in an Eulerian cell that is a mixed cell, it will adopt the local variables of that cell, which is of course a mixture. Because of this change in the material that a tracer might represent, for more reliable statistics it would obviously be much more desirable to have hundreds of tracers for every one that we have used in these simulations, and improvements in SAGE will make it possible to do so in the future.

Nevertheless, with the limited tracer data that we have, we can make some generalizations about the relative excavation efficiencies of shallow versus steep impact angles. Shallow angle impacts simply do not excavate enough granite to account for the distribution of shocked quartz from the Chicxulub event. In fact, at an angle as low as 15°, most of the energy of impact is retained in the fragmented and vaporized asteroid material, which mainly propagates downrange at relatively low altitude (Fig. 3).

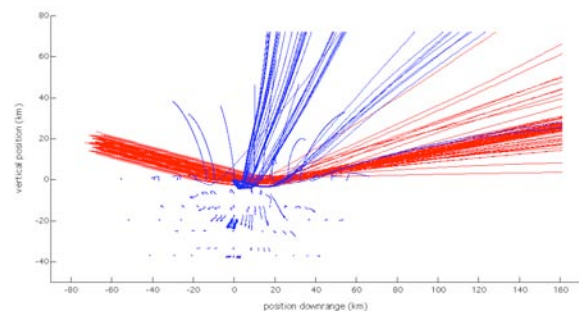


Fig. 3: X-Y projection of tracer particle trajectories out to 120 seconds for projectile (red) and target (blue) tracers for the 15° run. Excavation of target material is very shallow, very little projectile material is deposited in the crater, and the projectile remains are strongly focussed downrange.

At successively greater angles of impact (Figs. 4 and

5) more granite is excavated, and with more energy and greater isotropy. The dispersal of projectile material also becomes more uniform with steeper angles of impact. These results suggest that a relatively steep angle of impact (45° or greater) may be necessary to account for the worldwide distribution of platinum-group elements in the K/T boundary layer and also for the similarly broad distribution of shocked quartz [7]. We do not yet have similar results for our 60° run, as it is still in progress at this writing, but what we have seen so far is consistent with the arguments we make here.

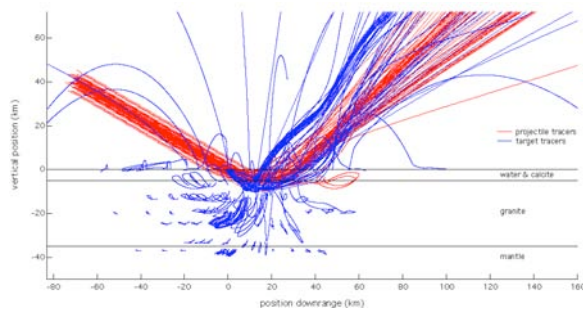


Fig. 4: X-Y projection of tracer particle trajectories out to 240 seconds for projectile (red) and target (blue) tracers for the 30° run. There is more spreading of both target and projectile material than in the 15° run, and some projectile tracers end up buried within the crater. The vertical stratification in the graph indicated here is the same in all model runs.

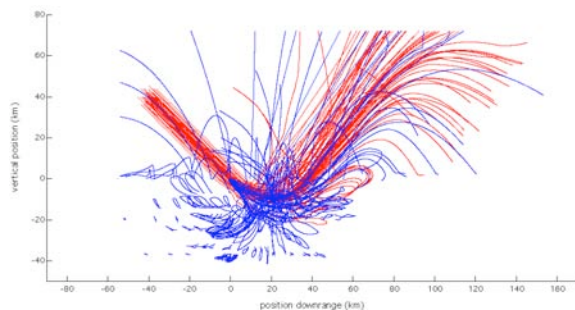


Fig. 5: X-Y projection of tracer particle trajectories out to 160 seconds for projectile (red) and target (blue) tracers for the 45° run. The ejection of target tracers is more symmetric than in the shallower runs, and a larger proportion of them achieve injection into the stratosphere or into suborbital ballistic trajectories. Still more projectile material is buried within the crater, and more rains back locally than in the shallower impact runs.

Similar conclusions can of course be derived from consideration of the peak pressures achieved in impacts at different angles. Of particular interest for excavation efficiency is the peak pressure at the calcite/granite interface which is shown as a function of angle in Fig. 6.

We see once again that the steeper impact angles are much more likely to result in greater distribution of shocked quartz than impacts at shallow angles.

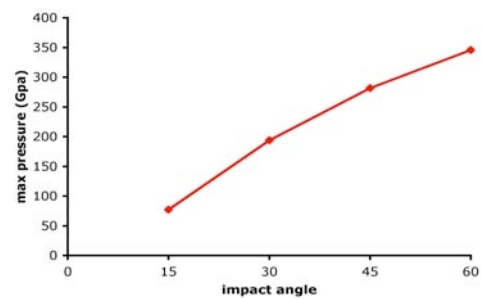


Fig. 6: Peak pressures seen at the calcite-granite interface for the 4 runs reported here, presented as a function of the impact angle.

An estimate of the actual amount of target material that is excavated and ejected into the stratosphere can be obtained by examining the trajectories of the tracers that originated within those materials of the target, and for those tracers that have achieved ballistic trajectories, extending them to their apogees. Each tracer is then taken as representing some volume of the material it originated within, and if this tracer has an apogee greater than stratospheric altitude the volume associated with it is regarded as deposited into the stratosphere. Fig. 7 illustrates the stratospheric input from the asteroid and three components of the target.

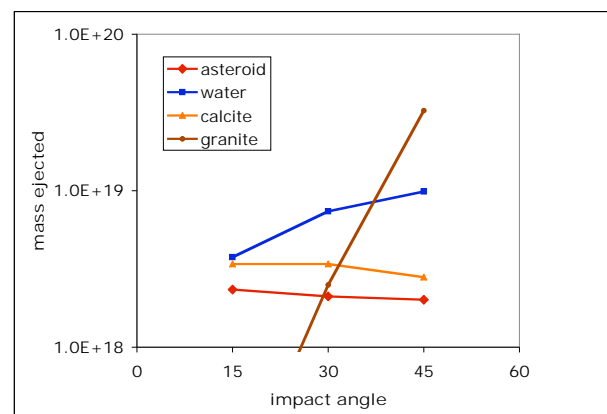


Fig. 7: Mass deposited into the stratosphere for four materials in the problem as functions of the impact angle.

While mass deposition into the stratosphere is perhaps the most significant influence of the Chicxulub impact event upon the environment in the late Cretaceous, another factor to be considered is the direct input of thermal energy into the troposphere via the atmospheric shocks that are produced during the course of the impact itself and the explosive vaporization of volatile materials that subsequently ensues. The atmospheric shocks are asymmetric. First there is the shock that is produced

surrounding the trajectory of the meteor in its passage through the atmosphere. Following passage of the shock, a hot and rarefied medium persists uprange of the asteroid for some minutes. If the trajectory is flat (shallow impact angle), this low-density channel is inaccessible to most of the heated material produced in the second shock, due to the excavation and explosive vaporization of the target. Instead, the horizontal component of the asteroid's momentum causes entrainment of the vaporized target material in the downrange direction. This effect may be seen in Figs. 3 and 4. Much of this very hot material is injected forcefully into the troposphere and could cause ignition of vegetation at considerable distance downrange, as well as effecting a serious and potentially devastating, but undoubtedly temporary, disruption to global atmospheric circulation patterns.

On the other hand, if the trajectory is steep, the rarefied channel produced by the incoming projectile is high in the atmosphere and therefore remains accessible to some of the rising material from the explosive vaporization of the target. The horizontal component of the asteroid's momentum is less, and there is consequently less entrainment of heated material in the downrange direction (see Fig. 5), and the entrainment that does occur is at higher altitude than in the flat case, providing less direct thermal input into the troposphere.

Thus more thermal energy is injected directly into the troposphere downrange of the impact point for shallow-angle impacts, while considerable thermal energy can escape through the top of the atmosphere when the impact angle is steep. In a shallow-angle impact, it would therefore be expected that fires would be immediately ignited on land downrange from the impact site, while for a steep-angle impact the first fires might well be set at points very distant from the impact site, even near the antipode, by the hot re-entry of ballistically ejected material. The lack of charcoal deposits in K/T boundary sediments in North American sites [8] might be seen as providing an additional argument that the impact angle must not have been shallow. On the other hand, the lack of charcoal could, and probably does, indicate much more complete combustion.

Summing up these considerations, we conclude that a shallow angle of impact might have resulted in an extinction mechanism involving the direct injection of thermal energy into the local troposphere, causing extensive local fires and strong hot winds. A steeper angle would be more likely to affect the global stratosphere within the first two hours, poisoning and darkening the atmosphere worldwide and heating via ballistic re-entry of asteroidal and target material. Signatures of these two distinct mechanisms would seem to be quite different, and the distribution of shocked quartz and tektites in very distant locations tends to support the steeper angle hypothesis.

Of course it is also the case that a shallower angle of impact will produce a smaller crater, so that a fair comparison of the amount of material ejected must be made with simulations that all produce a crater the size

of Chicxulub, which means that the simulations for shallower angles must be made with larger or faster projectiles, or both. We have not done this; we kept the same projectile diameter and speed for all four runs. We note, however, that the quantity of granite ejected into the stratosphere differs by *orders of magnitude* among the three runs plotted in Fig. 7, while the crater diameter (Fig. 8) differs by only ~30% among the same three runs.

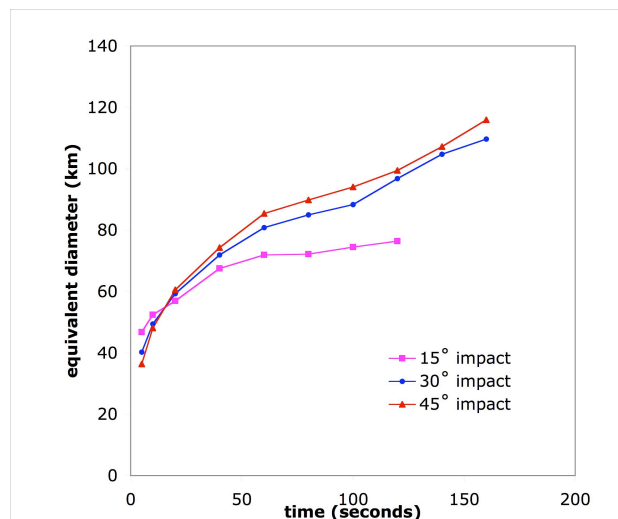


Fig. 8: Crater diameters as a function of time for the three runs that have gone out beyond 20 seconds. These diameters are defined by taking the position of the first zero-crossing of the density=1 isosurface averaged over all directions from the impact center, and may be taken as representing the early transient crater evolution. The transient crater diameter at Chicxulub is in dispute, but is at any rate not much greater than the numbers reported here.

We therefore consider our result on excavation efficiency robust, although our future simulations of this event will adjust the energies accordingly, and also make use of better tracer handling and other improvements to the SAGE code.

5. REFERENCES

1. Smits J. *Ann. Rev. Earth Planet. Sci.* 27:75-113, 1999.
2. Timmes F., Gisler G., Hrbek G., Los Alamos Unclassified Report LA-UR 05-6865, 2005.
3. Zoldi C., Los Alamos Unclassified Report LA-UR 02-6600, 2002.
4. Mader C. L. & Gittings M. L., "Modeling the 1958 Lituya Bay mega tsunami, II", *Science of Tsunami Hazards*, **20**, 241, 2002.
5. Pierazzo E. and Melosh H. J. *Ann. Rev. Earth Planet. Sci.* 28:141-67, 2000.
6. Claeys P., Kiessling W., Alvarez W., *Geological Society*

of America Special Paper 356, 55-68, 2002

7. Crookell M. et al. *Geophys. Res. Lett.*, 29, No. 20, 2002.

8. Belcher C. M. et al. *J. Geol. Soc. Lond.* 162, 591-602, 2005.

GLASS SPHERULES IN UPPER EOCENE FLYSCH OF CROATIAN ADRIATIC - EVIDENCE OF AN IMPACT INTO CARBONATE TARGET?

T. Marjanac⁽¹⁾, V. Bermanec⁽¹⁾, V. Premec-Fuček⁽²⁾, Lj. Marjanac⁽³⁾ & A. M Tomša⁽¹⁾

(1) Department of Geology, Faculty of Science, Horvatovac 102a, 10000 Zagreb, Croatia, Email: marjanac@geol.pmf.hr

(2) INA-Industrija nafte d.d., Research and Development Sector, 10000 Zagreb, Lovinčičeva bb, Croatia

(3) Institute of Paleontology and Geology of Quaternary, Croatian Academy of Sciences and Arts, A. Kovačića 5, 10000 Zagreb, Croatia

ABSTRACT

Glass spherules occur at 7 levels in Late Eocene flysch marls of Central Dalmatian Basin (Croatian Eastern Adriatic), which are exposed in hinterland of the city of Solin. The spherules occur at one level in *Globigerinatheka semiinvoluta* zone, and in six levels of *Globigerinatheka index* zone, and their stratigraphic spacing ranges from 1,5 m to 93,3 m. The best studied, and with most spherules recovered, is a composite turbidite 2-7, which is youngest in the sequence. It comprises impact-generated debris in its marl part, which is represented by perfectly clear (sometimes slightly dimmed) glass spherules 91 to 530 μ across; teardrop transparent microtektites 1225 μ long, and fragments of vesicular glass 450 to 1000 μ across. Some spherules and microtektites comprise small bubbles with diameter up to 41 μ . Chemical composition of the spherules, poor in SiO₂ and relatively rich in CaO and MgO indicates possible carbonate target.

1. INTRODUCTION

The hypothesis on multiple impacts around the Eocene / Oligocene boundary [1, 2, 3, 4, 5, 6, 7] triggered continuous lively discussions in impact community. The number of Eocene impacts is a very controversial issue [8, 9], and ranges from 2 [9, 10] to >6 [5]. The cited evidence of impacts were horizons with microtektites and spherules, the latter associated also with an Ir-anomaly. The microtektites horizon occurs in the upper part of the *Globigeraspis semiinvoluta* Zone (at 38,2 Ma), whereas other two closely spaced horizons occur in the lower part of the *Globorotalia cerroazulensis* Zone (at 37,3 and 37,2 Ma) [2, 3]. It was also noted that microtektites and spherule horizons are depleted in CaCO₃, possibly as a consequence of carbonate solution caused by corrosive bottom water during periods of global cooling [2, 4]. The age of the younger two microspherule horizons was subsequently revised, and was attributed to the latest *Porticulasphaera semiinvoluta* Zone [6]. Multiple Ir-anomalies, which suggest a sequence of closely spaced impacts during a period of 35,7-34,7 Ma (lower part of *G. cerroazulensis* Zone) were documented from deepmarine sediments in central Italy [7]. However, no spherules

were found in association with those Ir-anomalies. Ref. [8, 11] differentiated true microtektites from glass spherules containing clinopyroxene. Spheroids with Ni-rich spinel were found in sediments of the lower part of the P16 Zone (35,7 Ma in age) at the Massignano section in Italy, in the horizon with Ir-anomaly [12].

Not only the number of impacts differs among various researchers, but also zonal boundaries (P 15 / P 16, P16 / P17) are attributed different ages by different authors [3, 6, 7, 12]. Thus, we will relay herein on biostratigraphical zonation, but also because we lack isotopic control of our sediment ages.

Late Eocene was a period of several well documented bolide impacts [13] (Table 1).

Table 1: Impact structures of Late Eocene age [13]

Impact structure	Location	diam. (km)	age (Ma)
Chesapeake Bay	U.S.A.	90	35.5 \pm 0.3
Popigai	Russia	100	35.7 \pm 0.2
Crawford	Australia	85	> 35
Flaxman	Australia	10	> 35
Mistastin	Canada	28	37 \pm 1*
Wanapitei	Canada	75	37.2 \pm 1.2

* age revised in 2006 [14]

At present time, only two Eocene impact structures are recognized of sources of tektites/microtektites or spherule layers. The American tektite strewn field is associated with Chesapeake Bay impact crater [15, 16], and microkrystites of Indian and Pacific ocean are associated with Popigai impact crater of Northern Siberia [17].

2. THE STUDIED AREA AND DEPOSITS

The studied area is located in Central Dalmatia, Croatian Adriatic, near the Solin city (Fig. 1). Geologically, the studied area belongs to the "External Dinarides" unit [18,

19] and it is made of two stratigraphically and paleogeographically distinct units: a) carbonate platform succession of the late Mesozoic to early Tertiary age, and b) Tertiary flysch and molasse clastics [20].

The eastern Adriatic flysch stratigraphically spans from Middle Eocene [21], Bartonian [22] to the late Miocene [23, 24]. In the studied area, it is of carbonate composition and is overlain by, as well as locally interfingers with conglomeratic Promina Beds which are interpreted as molasse (Fig. 2). The Dalmatian flysch can be subdivided into three informal flysch “zones”; the lower-, middle- and upper flysch zone [24, 25, 26]. These zones correspond to the syn-rift (lower- and middle flysch zone) and post-rift (upper flysch zone) successions of the basin fill [25, 26]. The Lower Flysch Zone (LFZ) is ca. 750 m thick, but poorly exposed. Here predominate megabeds, whereas other lithofacies and their groups, such as turbidites, heterolithic sediments and conglomerates are subordinate. The Middle Flysch Zone (MFZ) is represented by ca. 180-190 m thick olistostrome [27] which is a single-event deposit, and represents a boundary between the ponded basin (LFZ) and a wider one (UFZ) without significant ponding of gravity flows [26]. The Upper Flysch Zone (UFZ) is ca. 860 m thick, and comprises various types of turbidites (which occur in the lower part of the Zone only), heterolithic sediments, sandy marls, sandy calcarenites, and conglomerates. Conglomerate wedges occur in the upper part of the LFZ

and throughout the UFZ. They are interpreted as alluvial fans and their distal wedges [25], and attributed to episodes of relative sea-level falls [28].

Detailed descriptions of all faces represented in the studied succession is beyond the scope of this paper, and we will focus only on spherule-bearing turbidites.

Turbidites encompass two types of beds: a) Bouma-type Ta-e and Tc-e turbidites, some of which attain up to 47 m in thickness, and b) megabeds which are defined by thickness > 10 m, and comprise two types of beds, based on the bed architecture: i) composite turbidites, and ii) complex beds [25, 26, 29, 30]. Megabeds are dominant bed-type in the LFZ, but in the UFZ occur restricted only to its lowermost part [26]. Composite turbidites are rare, only few being described in the literature. They are characterized by several lithologically uniform and normally graded thinning-upward units which are clearly erosive with contacts marked by slightly coarser debris, e.g. bed 2-7. In addition to current structures, the beds are also characterized by water-escape dish- and pillar structures, and convolutions of post-depositional origin. The 2-7 bed is made of 14 m thick calcarenite, and 24 m thick marls which comprise alternating massive and laminated units [29]. Complex beds are defined as bipartite beds composed of debrite in the lower part and turbidite above, with a clear transitional contact between the two [25, 26]. The thickest bed studied is 180-190 m

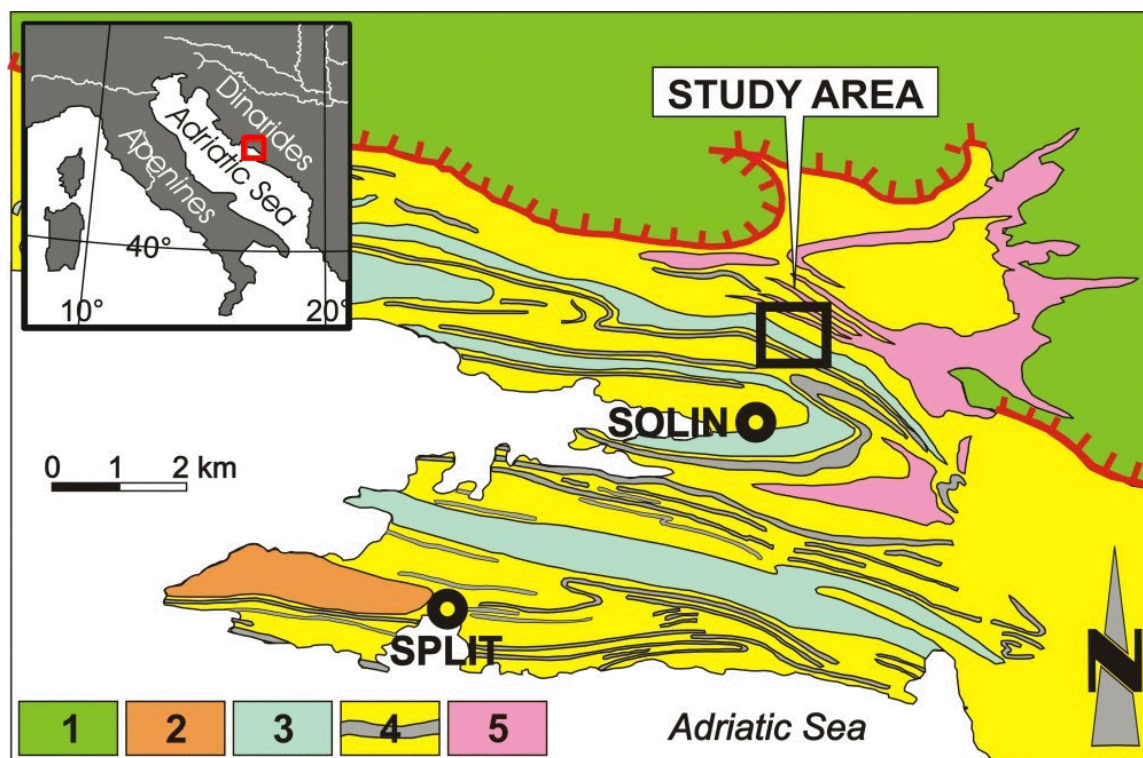


Fig 1: Simplified geological map of Central Dalmatia. Key: 1 = Mesozoic carbonates, 2 = Lower-Middle Eocene carbonates, 3 = K-S olistostrome, 4 = Middle-Upper Eocene flysch with megabeds, 5 = Eocene-Oligocene conglomerates. Map after [24], modified.

thick K-S olistostrome [25, 26, 27], which contains olistolites some of which reach up to 500.000 m³ in volume.

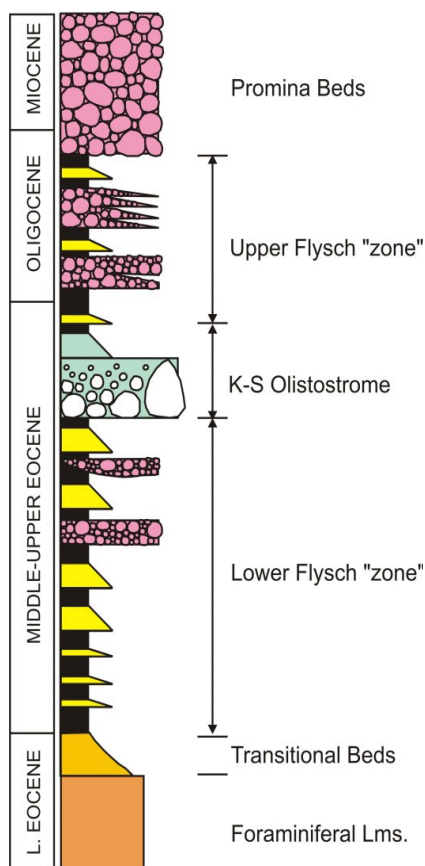


Fig.2. Depositional succession of Central Dalmatia.

Bouma-type turbidites were deposited from low-density turbidity currents [31]. The final stage in their deposition was from the ponded turbidity current tails to account for large thickness of turbidite marls.

Megabeds were deposited from turbidity currents with high initial volume, and lutites were deposited from ponded turbidity current tails. The composite turbidites were deposited from closely-spaced sequence of flows which could be treated as essentially a single depositional event. Sharp contacts of component units are probably a result of successive flow surges. Intervals of the massive marls were deposited from ponded turbidity current tail, but laminated intervals were probably deposited under influence of bottom waves, such as seiches, or bottom currents. The complex beds are also single-event deposits, deposited from large-volume gravity flows. Their lower part (debrite) was deposited by freezing of a debris flow, whereas their upper part was deposited from high-density turbidity current [31]. The initiation mechanism of such catastrophic events is commonly related to high-magnitude seismicity [32, 33, 34].

3. METHODS

The outcrop conditions allowed detailed sampling, and we attempted to avoid the weathering crust and altered sediments. Sampled were contacts of very finegrained arenite and marls in turbidites, turbidite marls at various levels above the bed base, and marl interbeds in heterolithic sediments. Typical sample was 100-200 grams, but the horizons with impactoclastic debris were successively re-sampled. To avoid contamination, samples were crushed in polyethylene bags, and disintegrated in 3 % solution of H₂O₂ and tap water, sieved through 65, 90, and 500 µ sieves and dried in microwave oven for 3-5 min. at 500 W. Mineral grains, spherules, microtektites and microfossils were hand-picked under stereomicroscope. Small magnetic spherules (ca. 60 µ across) were recovered by hand-magnet, although the procedure resulted in their magnetization. Chemical composition of spherules was made on JEOL JSM-6460LA electron microscope.

4. SPHERULE-BEARING BEDS

The studied turbidite succession comprises seven different stratigraphic horizons with glass spherules, metallic spherules, fragments of vesicular glass, and teardrop microtektites.

The spherules of *Globigerinatheka semiinvoluta* zone (former P 15, now E14 [35]) occur in the LFZ, ca. 20 m below the K-S olistostrome base. They occur in T_{ae} turbidite bed 315. Although the K-S olistostrome was a candidate for an syn-impact bed, only rare scattered metallic spherules are found at various levels of its marl part.

The spherules of *Globigerinatheka index* zone (former *cerroazulensis* zone, P16, now E15) occur at six levels in the UFZ, which are stratigraphically referred to prominent sequence boundary in base of coarsegrained fan delta III [25] (SB) (Fig. 3). The first spherule horizon of this zone occurs in the bed 3-45 which is 3.5 m thick T_{ce} turbidite 11,5 m below the SB. The second horizon is 5 cm thick marl layer of the 3-69 bed, located 50 cm below the SB. The third horizon is 2,5 m thick T_{be} turbidite 3-83 located 2,25 m above the SB. The fourth horizon is 1 m thick T_{ce} turbidite 3-88 located 4,75 m above the SB. The fifth horizon is marl layer associated with heterolithic interval 2-5, located 85 m above the SB. The sixth horizon is 38 m thick composite turbidite 2-7 located 93,3 m above the SB. It yielded largest number of glass spherules, vesicular glass fragments, metallic spherules, and microtektites, which occur in largest number at arenite-marl transition, and exclusively in units of the laminated marl.

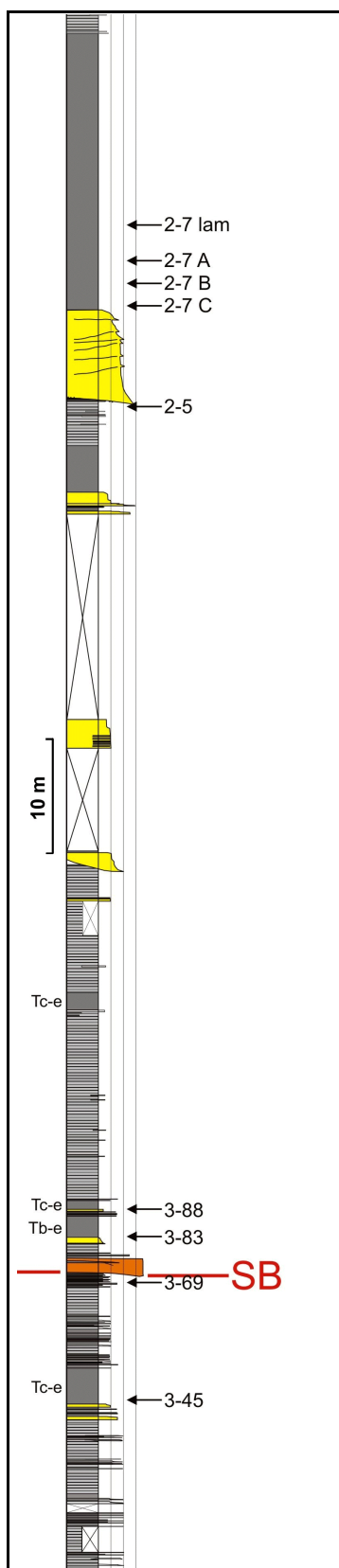


Fig. 4. Sedimentological log of studied sediments. *Globigerinatheka index* zone (E15).

5. IMPACT GRAINS

The spherules in *Globigerinatheka semiinvoluta* zone (E14) are up to 80 μ in diameter. The glass spherules are yellowish tinted and transparent, some are black opaque, whereas metallic ones are grey with metallic luster.

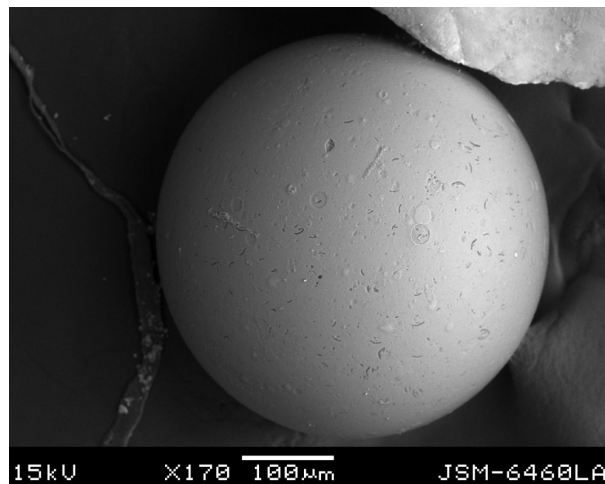


Fig. 4. Glass spherule 2-7C-6

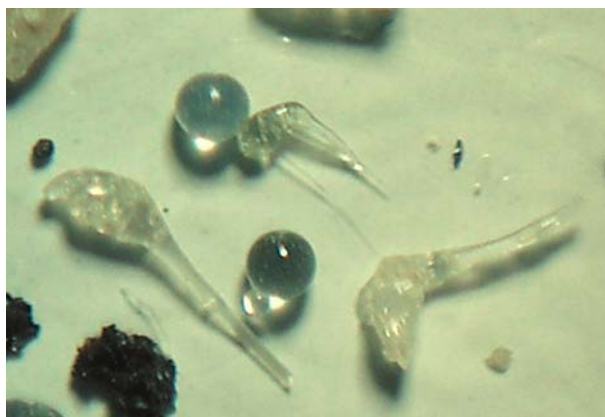


Fig. 5. Glass spherules and microtektites. Bed 2-7.

The glass spherules, vesicular glass, metallic spherules and microtektites in *Globigerinatheka index* zone (E15) are morphologically all very similar. The glass spherules are perfect spheres (Figs. 4, 5), 91 μ to 530 μ in diameter. Usually they are water-clear (Fig. 5), sometimes slightly dimmed, or with pearl luster. Sometimes small spherules are attached at the large ones, and close inspection (SEM) of their surface revealed small and shallow, flat-bottom, crater-like structures probably formed by escaping fluids. The metallic spherules are 80 μ to 180 μ in diameter. They are commonly highly magnetic, sometimes with metallic luster, sometimes dull. The fragments of vesicular glass measure 450 μ to 1000 μ across, and are made of whitish to yellowish, commonly untransparent glass. Teardrop microtektites are up to 1225 μ long, most commonly made of transparent milky glass. Sometimes they have one "tail", sometimes two (Fig. 5). The

microtektite glass commonly comprises small vesicles with diameter up to 41 μ , and their surface is pitted with small fluid-escape craters.

Table 2: composition of typical spherule from the bed 2-7:

SiO ₂	28.90
Al ₂ O	--
Al ₂ O ₃	--
Fe ₂ O ₃	--
CaO	17.22
MgO	7.84
FeO	0.80
ZnO	0.50
TiO ₂	0.42
MnO	0.36
CuO	0.19
Na ₂ O	0.28
K ₂ O	0.25
P ₂ O ₅	0.23
SO ₃	1.17
SO ₂	--
CO ₂	41.01
NiO ₂	--
NiO	--
Cr ₂ O ₃	--
L.O.I.	--
	99.17

6. DISCUSSION

Spherules of *G. semiinvoluta* and *G. index* zone differ in size and colour; the former are smaller, partly transparent, partly opaque, yellowish to brownish in colour, whereas the latter are larger and usually perfectly clear. The two very likely represent impactites of different impact events. We will try to address this hypothesis in continuation of our research.

Although spherules of the *G. index* occur at six (!) levels, they are all morphologically almost identical, they all have the same association of vesicular glass, metallic spherules, and mineral grains, so resedimentation can not be positively ruled-out as possible cause of stratigraphic repetition of one spherule horizon. However, many samples were analyzed from intermediate levels/beds, with no spherules or other impact grains found.

Composition of analyzed spherule from *G. index* zone (Table 2) shows significant difference from spherules of

North American strewn field [36, 37, 38], as well as spherules from Italian sections attributed to Popigai impact [12]. The major difference is in low SiO₂ content (28,9 %), and higher CaO and MgO content. The difference is also marked by ZnO, CuO, P₂O₅, SO₃, and particularly by high CO₃ content, which are unreported in published data on Upper Eocene spherule composition.

7. CONCLUSION

The Central Dalmatian Upper Eocene flysch succession comprises two horizons of impact-derived spherules, the older in *G. semiinvoluta* and younger in *G. index* zone.

The composition of spherules recovered from the 2-7 composite turbidite indicates possible sedimentary target of a large impact, very likely composed of limestones and dolomites. Since their composition greatly differs from other Upper Eocene spherules, particularly North American strewn field, as well as Popigai-derived microkrystites, we speculate that the source of analyzed spherules is yet undiscovered Late Eocene large impact structure.

8. REFERENCES

1. Keller G., Eocene-Oligocene boundary reference sections in the Pacific. In: *Terminal Eocene Events* (eds. Pomerol Ch. & Premoli Silva I.). Dev. in Paleont. and Strat. 9, Elsevier, 209-212, 1986
2. Keller G., Late Eocene impact events and stepwise mass extinctions. In: *Terminal Eocene Events* (eds. Pomerol Ch. & Premoli-Silva I.). Developments in Paleontology and Stratigraphy 9, 403-412, Elsevier, 1986.
3. Keller G., Stepwise mass extinctions and impact events: Late Eocene to Early Oligocene. *Marine Micropaleontology*, vol. 10, 267-293, 1986.
4. Keller G., D'Hondt S.L., Orth C.J., Gilmore J.S., Oliver P.Q., Shoemaker E.M. and Molina E., Late Eocene impact microspherules: stratigraphy, age and geochemistry. *Meteoritics*, vol. 22, 25-60, 1987.
5. Hazel J.E., Chronostratigraphy of Upper Eocene Microspherules. *Palaos*, vol. 4, 318-329, 1989.
6. Miller K.G., Berggren W.A., Zhang J. and Palmer-Julson A.A., Biostratigraphy and Isotope Stratigraphy of Upper Eocene Microtektites at Site 612: How Many Impacts? *Palaos*, vol. 6, 17-38, 1991.
7. Montanari A., Asaro F., Michel H.V. and Kennett J.P., Iridium Anomalies of Late Eocene Age at Massignano (Italy), and ODP Site 689B (Maud Rise, Antarctic). *Palaos*, vol. 8, 420-437, 1993.
8. Glass B. P. and Burns C. A., Late Eocene crystal-bearing spherules: two layers or one? *Meteoritics*, vol. 22, 265-279, 1987
9. Glass B.P., Tektites and microtektites: key facts and inferences. In: *Cryptoexplosions and Catastrophies in the Geological Record, with Special Focus on the Vredefort*

- Structure* (eds. Nicolaysen L. O. & Reimold W. U.) Tectonophysics, vol. 171, 393-404, 1990.
10. Poag W.C. and Aubry M-P., Upper Eocene Impactites of the U.S. East Coast: Depositional Origins, Biostratigraphic Framework, and Correlation. *Palaios*, vol. 10, 16-43, 1995.
 11. Glass B.P., Late Eocene Microtektites and Clinopiroxene-bearing spherules. In: *Terminal Eocene Events* (eds. Pomerol Ch. & Premoli-Silva I.). Developments in Paleontology and Stratigraphy, vol. 9, 395-401, Elsevier, 1986.
 12. Pierrard O., Robin E., Rocchia R. and Montanari A., Extraterrestrial Ni-rich spinel in upper Eocene sediments from Massignano, Italy. *Geology*, vol. 26, 307-310, 1998.
 13. Earth Impact Database, <<http://www.unb.ca/passc/ImpactDatabase/Age.html>> (Accessed: 26/6/2006)
 14. Kelley S., Testing for clustering in the terrestrial impact record: progress through dating ancient craters. <http://www.rssd.esa.int/SYS/docs/11_transfers/296311_kelley_pres.pdf> (Accessed: 28/6/2006)
 15. Poag W., Powars D.S., Poppe L.J. and Mixon R.B., Meteoroid mayhem in Ole Virginy: Source of the North American tektite strewn field. *Geology*, vol. 22, 691-694, 1994.
 16. Koeberl Ch., Poag W.C., Reimold U.W. and Brandt D., Impact Origin of the Chesapeake Bay Structure and the Source of the North American Tektites. *Science*, vol. 271, 1263-1266, 1996.
 17. Whitehead J., Papanastassiou D.A., Spray J.G., Grieve R.A.F. and Wasserburg G.J., Late Eocene impact ejecta: geochemical and isotopic connections with the Popigai impact structure. *Earth and Planetary Science Letters*, vol. 181, 473-487, 2000.
 18. Chorowicz J., Stratigraphie et tectonique d'un secteur de la Dalmatie moyenne, pres de Split (Yougoslavie). *Bull. Soc. géol. Fr. (7)*, vol. 11/6, 862-870, Paris, 1969.
 19. Aubouin J., Blanchet R., Cadet J-P., Celet P., Charvet J., Chorowicz J., Cousin M. and Rampnoux J-P., Essai sur la géologie des Dinarides. *Bull. Soc. géol. Fr. (7). ser.*, 12, 1060-1095, Paris, 1970.
 20. Marjanac T. and Čosović V., Tertiary Depositional History of Eastern Adriatic Realm. In: *Outline of the geology of the Dinarides and south Tisia with field guidebook* (eds. Pamić J. & Tomljenović B.), *Vijesti Hrvatskoga geol. društva* vol. 37, 93-103, 2000.
 21. Piccoli G. and Proto Decima F., Ricerche biostratigrafiche sui depositi flyschoidi della regione Adriatica settentrionale e orientale. *Mem. Ist. Geol. Miner. Univ. Padova*, vol. 27, 1-23, 1969.
 22. Benić J., Vapnenački nanoplankton i njegova primjena u biostratigrafiji krednih i paleogenskih naslaga Hrvatske. Doctoral Thesis. University of Zagreb. 1-159, 1983.
 23. de Capoa, P., Radoičić, R. and D'Argenio, B., Late Miocene deformation of the External Dinarides (Montenegro and Dalmatia). New biostratigraphic evidence. *Mem. Sci. Geol.*, vol. 47, 157-172. Padova, 1995.
 24. Kerner F., Gliederung der Spalatiner Flysch Formation. *Verhandl. Geol. Reichsanst.*, vol. 5, 87-102, Wien, 1903.
 25. Marjanac T., Evolution of Eocene-Miocene flysch basin of Central Dalmatia, Croatia. Doctoral Thesis, University of Zagreb, 1-348, 1993.
 26. Marjanac T., Importance of megabeds for reconstruction of Paleogene flysch basin in Split hinterland (Middle Dalmatia). *Geol. vjesnik*, vol. 44, 201-213, Zagreb, 1991.
 27. Marjanac T., Sedimentacija Kernerove "srednje fliške zone" (paleogen, okolica Splita). *Geol. vjesnik*, vol. 40, 177-194, Zagreb, 1987.
 28. Marjanac T., Deposition of megabeds (megaturbidites) and sea-level change in a proximal part of Eocene-Miocene flysch of central Dalmatia (Croatia). *Geology*, vol. 24, 543-546, 1996.
 29. Marjanac T., Anatomy of a composite turbidite in flysch of middle Dalmatia (Yugoslavia). Abstracts 8. I.A.S. Reg. Mtg., Tunis. 338-339, 1987.
 30. Marjanac T., Reflected sediment gravity flows and their deposits in flysch of Middle Dalmatia, Yugoslavia. *Sedimentology*, vol. 37, 921-929, Oxford, 1990.
 31. Lowe D.R., Sediment gravity flows: II depositional models with special reference to the deposits of high-density turbidity currents. *Jour. Sed. Petrol.*, vol. 52, 279-297, Tulsa, 1982.
 32. Johns D.R., Mutti E., Rosell J. and Séguret M., Origin of a thick, redeposited carbonate bed in Eocene turbidites of the Hecho Group, South-central Pyrenees, Spain. *Geology*, vol. 9, 161-164, 1981.
 33. Labaume P., Mutti E. and Séguret M., Megaturbidites: A Depositional Model From the Eocene of the SW-Pyrenean Foreland Basin, Spain. In: *Megaturbidites* (eds. Doyle L.J. & Bourrouilh R.). Geo-Marine Letters, vol- 7, 91-101, New York, 1987.
 34. Séguret M., Labaume P. and Madariaga R., Eocene seismicity in the Pyrenees from megaturbidites of the South Pyrenean Basin (Spain). *Marine Geology*, vol. 55, 117-131, Amsterdam, 1984.
 35. Berggren W.A. and Pearson P.N., A revised tropical to subtropical paleogene planktonic foraminifera zonation. *J. Foram. Research*, vol. 35, 279-298, 2005.
 36. D'Hondt S.L., Keller G. and Stallard R.F., Major element compositional variation within and between different Late Eocene microtektite strewnfields. *Meteoritics*, vol. 22, 61- 79, 1987.
 37. Glass B.P., North American tektite debris and impact ejecta from DSDP Site 612. *Meteoritics*, vol. 24, 209-218, 1989.
 38. Dressler B.O. and Reimold U., Terrestrial impact melt rocks and glasses. *Earth-Science Reviews*, vol. 56, 205-284, 2001.

THE CRATER “YAMA KORCHAZHIKHA” ON THE WEBSITE “CATALOGUE OF THE EARTH’S IMPACT STRUCTURES”

A.V. Mikheeva⁽¹⁾, P. G. Djadkov⁽²⁾, G.M.Ivanova⁽²⁾

⁽¹⁾*Institute of Computational Mathematics and Mathematical Geophysics, Siberian Branch of the Russian Academy of Sciences, pr. Lavrentieva, 6, Novosibirsk 630090, Russia, anna@omzg.sccc.ru*

⁽²⁾*Institute of Geophysics, Siberian Branch of the Russian Academy of Sciences, pr.Koptyuga, 3, Novosibirsk 630090, Russia djad@uiggm.nsc.ru*

INTRODUCTION

For solving problems of comprehensive understanding of the regularities of the internal properties of meteoritic craters, processes of impact crater formations, the composition of crater-forming meteorites, the information about impact structures is needed.

In 1990-1991, a researchers of ICM&MG [1], began to create the computer databank (DB) from a large volume of data, allowing one to carry out estimations of some relations of parameters and analysis of data on the Earth’s meteoritic craters, their plotting onto a geographical map.

As an extension of the previous studies, this paper presents the descriptions of the catalogue on the ICM&MG website:

<http://omzg.sccc.ru/impact/english.html>

(Fig.1); and a convenient control and visualization system for that DB, named “Impact Structures Catalogue” (ISC).

1. THE DESCRIPTION OF THE CATALOGUE

The original table of the catalogue includes 755 records, each being characterized by 41 attributes.

As compared to [1], in which there are 125 proven and 110 probable and doubtful structures, the given catalogue is supplemented with 520 new records (among them 72 are proven) [2]. The information sources are both the recent publications, and Internet sites.

The information on attributes is contained in appropriate DB fields, such as: the name of a structure, coordinates, age (relative and absolute), the size and the shape of a structure, a degree of erosion, the structure of rocks, the data on the presence of geophysical (gravitational and magnetic) anomalies, etc. All these features reflect morphological, geological, impact-metamorphic and some other attributes.

By the present time, on the website, there are only fifteen basic fields from the above-mentioned ones, however the descriptive part of each record will be added with a card of the detailed description (Fig.4) with decoding of the coded data (with a view of economy of the volume). The whole information of this card is divided into three basic groups of attributes: shape-structure, mineral-petrographic and geophysical. For anomalies, their values are specified, for the structure of rocks, which have undergone transformations when impacting, a meteoritic substance, diaplect mineral and glass, impactites, breccias are specified.


Catalogue of the Earth's Impact structures (755 records)														
<div> Probability 197-proven 0 210-probable 1 300-possible 2 48-discredited 3 </div>  <div> ABCDEFGHIJ KLMNOPQRS TUVWXYZ </div>														
Name of structure	C o n t	P r o b	LAT	LONG	Age (Ma)	Diam (km)	M o r p h	Anomaly		R o c k s	M e t a b.	D i a p l e c t	H i s t o r y	I m p a c t
								G r a v	M a g n					
Acraman (Ecremen), S.Aust	Au	0	-32,02	135,43	~590	80	d			CR	+			+
Aflou* (D'Afrou), Algeria	Af	1	38,07	2,05	< 100	5								+
Agheir, Mauritania	Af	1	20	-15			d							
Agnak (5 cr.), Canada	AN	1	67,5	-108		0,17								
Aimores, Brazil	AS	2				8,5								
Alchokoy, Kazakhstan	As	1	47,7	72,38		10								
Akonivesi, Finland	Eu	2	63,02	28,27		2,5								
Al Hashime, Saud Arab.	As	2	27,85	43,1		15								

Fig.1. A website view.

The coded data (in Fig.1, Fig.4) means:

For morphology: d – depression; b – bank; cr – center raising; rr – ring raising; rd – ring depression.

For mishen (target) rocks characters: CR – crystal; SE – sedimentary; VO – volcanic; MI – mixed.

A complex study of the geophysical data may be of interest for the search and diagnostics of the subsurface structures with the deprived morphological attributes and located under the thickness of deposits, and, also, morphologically inexpressive astroblems at the bottom of the ocean and in the coastal zones (in our DB, there are about 60), their names on the website list are marked with * (Fig.1). In the tsunami database [3,4], there are events of presumably a cosmogenic origin.

Among the recently added structures more widespread are such, which were detected by indirect attributes, on the basis of results of seismic investigations or other geophysical methods. One of the recently entered in the DB structures is the Korchazh crater in the Selenga river delta (Fig.2 a).



Fig.2a. The structure “Yama Korchazhikha” (near the village of Bykovo, Baikal lake)

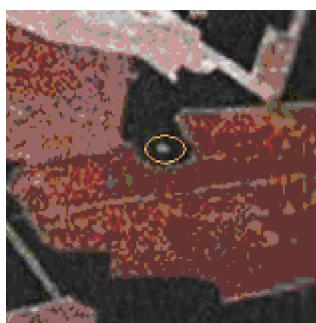


Fig.2b. View from space, the crater is marked with the yellow ellipse.

2. THE IMPACT STRUCTURE “YAMA KORCHAZHIKHA”

This paper presents one of new records of the “Catalogue of the Earth’s impact structures” that was discovered by scientists of Siberian Division.

This structure looks like a funnel with a small lake in the center (see the snapshot from space in Fig.2b) and is named by natives as “Yama Korchazhikha”, its diameter – ca 200-300 m, coordinates: 52,183°N, 106,767°E. The depth of structure about 20 m (see the topography map in

Fig.3). Not far from it (< 1 km), the second smaller funnel locates (d ~ 20m) that has more clear and expressive section profile. Its cosmic origin was confirmed by a special Moscow meteoritic commission headed by Dr. U. V. Kestlane of the Estonian Academy of Sciences in the 80-s years, but for a long time those materials were forgotten.

According to spoken message of U. V. Kestlane, the age of this structure can be supposed about 80-100 thousands years and its origin is purely of impact. His assumptions are based on the geomorphology of structure. The more exact age will be determined by the end of this spring with the radiocarbon method. By the present time, this record is marked in the catalogue as a possible structure (probability >50%).

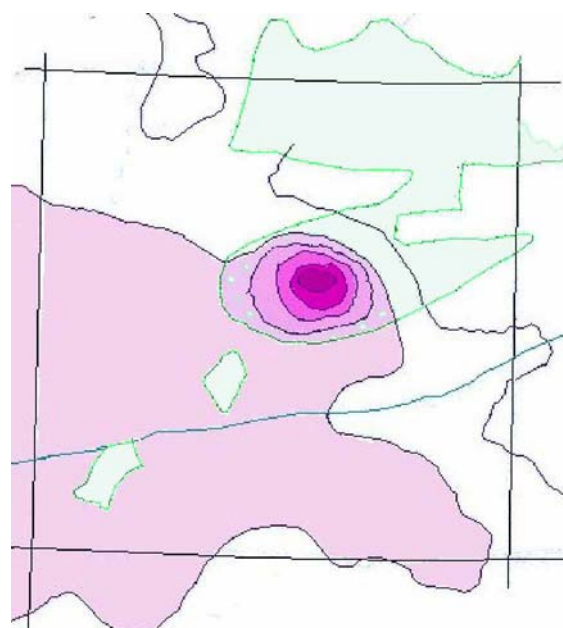


Fig.3. The crater’s topography map. M 1:25000, the isolines – in 5m.

3. THE DESCRIPTION OF THE DATA MANAGER SHELL.

Also, we present the data manager system ISC as supplement to the Impact Structures databank [2]. This software was created specially to collect all those materials and was written in C++ Builder 5. It can be used for the utilization in scientific research and for information purposes. The shell ISC is supported by the operational systems MS Windows beginning with version 98 and further. The data are kept in tables MS Access standard.

An example of this shell visual card is shown in Fig.4. The fotos, schemes, maps of gravity and magnetic anomalies are kept on page “fotos”. Bibliographic and http references are contained on

Event Card

General | Text | Photos | Reference

Name
 Name of structure:
 Russian name:

Age of event
 Age: ()
 Reduce age (Age/S):
 Period name:
 Periods of p-a:

Locate params
 Continent: Latitude:
 Land: Longitude:

Structure characters
 Number of objects: Structure depth in km:
 Diameter:
 Diameter of center rising:
 Type of formation: Type of structure:
 Morphology: Relief of true bottom:
 Erosion degree:
 Form: View from Earth orbit:
 Distruction cone:

Rocks characters
 Mishen rocks characters: -
 Meteorit substance: -
 Dialect material: -
 Highbar phase: -
 Impactits and brekchieis: -

Anomalies:
 Gravitation: -
 Magnit: -
 Basic reference:

Comments:

Next Previous OK Cancel

Fig.4. A record card window containing detailed parameters, textual descriptions and the photos of the allocated structure.

page 'Reference' (Fig.4) and, also, bibliographic records are kept in a separate table representing the common list of literature. This program shell can be installed on any personal computer and used for information collecting.

4. SUMMARY

The database consists of 197 proven, 210 probable, 300 possible (expected) and 48 discredited cosmogenic structures and is open for extension with new information

REFERENCES

- [1] Alekseev A. C., Petrenko V.E., Lyapidevskaya Z.A. An estimation of frequency of falling of celestial bodies onto the Earth, research into a possibility of their preliminary detection and change of trajectories // Report of SR, AS USSR, CC, Novosibirsk, 1991. 128p.
- Alekseev A.C., Mikheeva A.V., Lyskovskaya E.V., Lyapidevskaya Z.A., Petrenko V.E. Database "Catalog of impact structures on the Earth". All-Russian conference "Asteroid-Comet Hazard – 2005", 3-7 Oct.2005, St. Petersburg, p. 11-14.
- Gusakov V.K., Marchuk An.G., Osipova (Micheeva) A.V. From expert tsunami database (ETDB) toward expert system for tsunami risk assessment // IAMAS-IAPSO Joint Assemblies, Melbourne, Australia, 1997.
- Gusakov V.K., Lyskovskaya E.V. HTDB/PDM (Historical tsunami database /parametric data manager), Version 1.3, CD ROM // Tsunami Laboratory, ICMMG SD RAS, Novosibirsk, 2002.